GEOSTATIC STRESS STATE EVALUATION BY DIRECTIONAL SHEAR WAVE VELOCITIES, WITH APPLICATION TOWARDS GEOCHARACTERIZATION AT AIKEN, SC

A Dissertation
Presented to
The Academic Faculty

by

Taeseo Ku

In Partial Fulfillment
of the Requirements for the Degree
Doctor of Philosophy in the
School of Civil and Environmental Engineering

Georgia Institute of Technology
December 2012

GEOSTATIC STRESS STATE EVALUATION BY DIRECTIONAL SHEAR WAVE VELOCITIES, WITH APPLICATION TOWARDS GEOCHARACTERIZATION AT AIKEN, SC

Approved by:

Dr. Paul W. Mayne, Advisor
School of Civil & Environmental Engineering
Georgia Institute of Technology

Dr. Susan E. Burns
School of Civil & Environmental Engrg.
Georgia Institute of Technology

Dr. J. Carlos Santamarina
School of Civil & Environmental Engineering
Georgia Institute of Technology

Dr. Glenn J. Rix
School of Civil & Environmental Engrg.
Georgia Institute of Technology

Dr. Yuhang Wang
School of Earth & Atmospheric Science
Georgia Institute of Technology

Dr. Brent J. Gutierrez
US Department of Energy
Aiken, SC

Date Approved: October 24, 2012

To my dear parents and wife

ACKNOWLEDGMENTS

I would like to deeply thank to my advisor Dr. Paul W. Mayne for his patient guidance, mentorship, and encouragement during my Ph.D. study. His passion and dedication about research always inspired me. I wish to express my sincere gratitude to my defense committee: Dr. Susan E. Burns, Dr. Glenn J. Rix, Dr. J. Carlos Santamarina, Dr. Yuhang Wang, and Dr. Brent J. Gutierrez for their kind guidance, valuable suggestions, and insightful advice. Special thanks to my research project team members and US department of energy for financial and technical support.

I would like to thank the Georgia Tech in-situ testing group member Fawad Niazi for his friendship and support. We together conducted several geotechnical in-situ testing such as seismic dilatometer test and memocone penetration test. It was great field experiences and fun time for me. I am also grateful to former and current Geosystems group students: Sihyun Kim, Junbong Jang, Aditya Bhatt, Hyunwook Choo, Fengshou Zhang, Minsu Cha, Joan Larrahondo, Bate Bate, Seunghee Kim, Seokho Jeong, Aaron Geiger and other graduate student colleagues as well. They have been my supporters and friends through the years. I will always miss the Geo-party, weekly coffee breaks, and happy hour with you.

I would also like to express my deepest gratitude to my family. My wife, parents, sister, and brother have been the reason of who I am and what I am. Their limitless love, dedication, support and encouragements get me through all the difficulties and made me to become a person.

TABLE OF CONTENTS

LIST OF TABLES

Page

LIST OF FIGURES

Page

SUMMARY

Evaluations of stress history and the geostatic state of stress of soils are ascertained on the basis of field geophysical measurements that provide paired complementary types of shear waves. It is well-established that multiple types of shear waves occur in the ground due to their directional and polarization properties. The shear wave velocity (V_s) provides the magnitude of small strain stiffness (G_0) which depends on effective stress, void ratio, stress history, and other factors (cementation, age, saturation). Herein, this study examines a hierarchy of shear wave modes with different directions of propagation and particle motion from in-situ geophysical tests (HH, VH, and HV) and laboratory bender element data. A special compiled database from well-documented worldwide sites is assembled where full profiles of stress state, stress history, and several paired modes of V_s profiles have been obtained from crosshole tests (CHT), downhole tests (DHT), and rotary crosshole (RCHT). Reference profiles of the lateral stress coefficient (K_0) are available from direct in-situ measurements (self-boring pressuremeter, hydrofracture, and push-in spade cells). Stress history is documented in terms of yield stress ratio (YSR) from consolidation testing and careful engineering geology studies. A methodology is developed that relates both the YSR and K_0 to stiffness ratios obtained from directional shear wave velocities. In further efforts, means to extract reliable shear wave profiles from continuous downhole testing via a new GT autosource and seismic piezocone testing are outlined and applied to results from three test sites in Windsor/VA, Norfolk/VA, and Richmond/BC.

A driving impetus to this research involves the geologic conditions at the US Dept. of Energy's Savannah River Site (SRS) in South Carolina. Here, the overburden soils in the upper 60 m depths consist of very old Miocene and Eocene sediments, primarily layered deposits of sands, clayey sands, silty sands, and interbedded clays which exhibit an apparent and unusual stress history profile. Special geologic conditions include the dissolutioning of old calcareous sediments (Santee Formation) at depths of 40 to 50 m below grade, similar to karstic limestone deposits. As a consequence, caves, voids, and infilled soft soil zones occur within the soil matrix at these elevations, probably resulting in localized collapse of the overlying soil column. Based on conventional laboratory and in-situ test data conducted during geotechnical investigations at SRS, available interpretative relationships for assessing the soil stress history and geostatic stress states show scattered and inconsistent results. Complications abound in the systematic assessments of these geomaterials due to effects of very old ageing, cementation, desiccation, and diagenesis, as evidenced by unusual in-situ shear wave velocity profiles that decrease in magnitude with depth, as measured by CHT and DHT. Based on the findings of this study, it is recommended that a new set of shear wave velocity measurements be made at SRS to obtain HH waves (and complementary VH waves) needed for an independent assessment of YSR in the upper soil column

CHAPTER 1

INTRODUCTION

1.1 Geotechnical Site Characterization

Prior to each and every geotechnical project, site characterization is an initial important step in the procedures which must be conducted in order to establish the localized ground conditions. Site-specific investigations are necessary because every project site has a unique location with variable subsurface conditions consisting of one or more geomaterials, strata thicknesses, groundwater table(s), stress histories, and geologic background. Drilling, augering, and sampling are conventional methods used to procure specimens together with laboratory testing in order to develop the stratigraphic layout and evaluate the corresponding soil engineering parameters and properties. While important, however, laboratory testing through various sampling methods has inevitable disadvantages. Sample disturbance causes detrimental effects on the magnitude, uncertainty, and reliability of soil properties. Moreover, laboratory testing is limited to selected recovered samples at discrete points in subsurface space and is rather time-consuming and expensive, on a specimen by specimen basis.

As an alternate and/or complement to the traditional laboratory testing approach, multitudes of in-situ geotechnical tests and geophysical methods have been developed, with well over 200+ different probes, devices, penetrometers, and specialized techniques now available (Robertson 1986; Mayne 2007). Representative in-situ tests include the classical standard penetration test (SPT), cone penetration test (CPT), flat dilatometer test (DMT), pressuremeter test (PMT), and vane shear test (VST), while some newest to the family of field devices include the ball-penetrometer and T-bar (Randolph 2004).

Of more recent vintage, the utilization of field geophysical methods has shown considerable value and benefits to geotechnical site exploration. These include two broad categories of geophysics: mechanics waves and electromagnetic waves. The geophysical methods that obtain mechanical wave measurements focus on body waves (P- or compression waves and S- or shear waves) that include crosshole testing (CHT), downhole testing (DHT), seismic refraction, reflection, suspension logging, and surface wave techniques of both active and passive types. A summary depiction of the various geophysical test methods available for mechanical wave measurements is shown in Figure 1.1. Actually, for evaluating initial stiffness characteristics in soils, more various testing methods are available (here, small-strain shear modulus G_{max}). Figure 1.2 summarizes the current methods (McGillivray 2007). For completeness, both field and laboratory tests are included.

The shear wave velocity (V_s) obtained from mechanical wave measurements provides the small-strain shear modulus, $G_0 = G_{max} = \rho_t \cdot V_s^2$, and corresponding initial Young's modulus, $E_0 = E_{max} = 2 \cdot G_{max}(1+\nu)$, which are useful for both static and dynamic geotechnical problems; where ρ_t = total mass density and ν = Poisson's ratio of the ground. In fact, E_{max} is the beginning of all stress-strain-strength curves in soils and rocks (Tatsuoka and Shibuya 1992). The magnitudes of initial elastic moduli have a tremendous range that spans over 3+ orders of magnitude, from as low as 500 bars in soft clays to as high as $2 \cdot 10^6$ bars in rock materials as shown in Figure 1.3 (Tatsuoka and Shibuya 1992). Thus, the initial modulus (E_{max} and G_{max}) of geomaterials measured by the various geophysical techniques is a most useful parameter to represent intrinsic soil characteristics and fundamental stiffness. One aspect of this dissertation will be to present

a novel and advanced approach for geophysical shear wave profiling by continuous measurement in a downhole test manner.

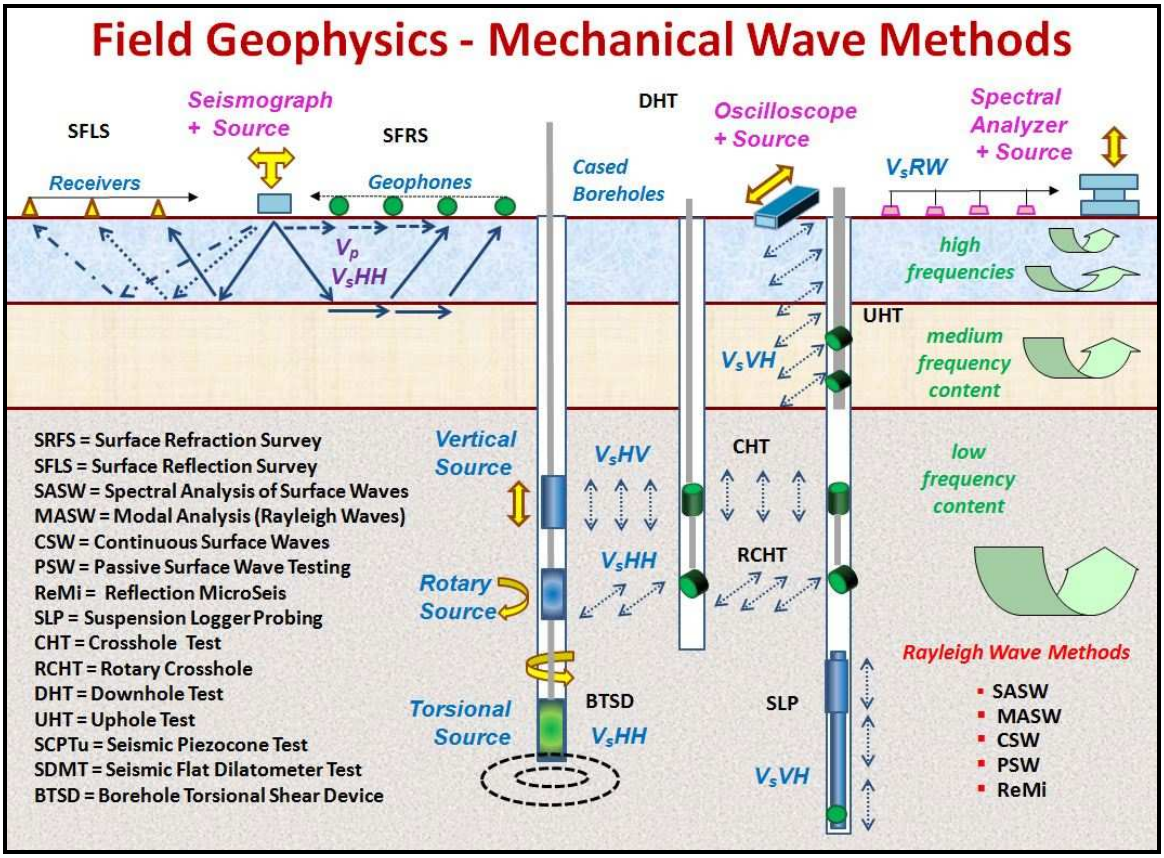

Figure 1.1. Schematic of various geophysical methods for in-situ mechanical shear wave velocity measurements in geomaterials.

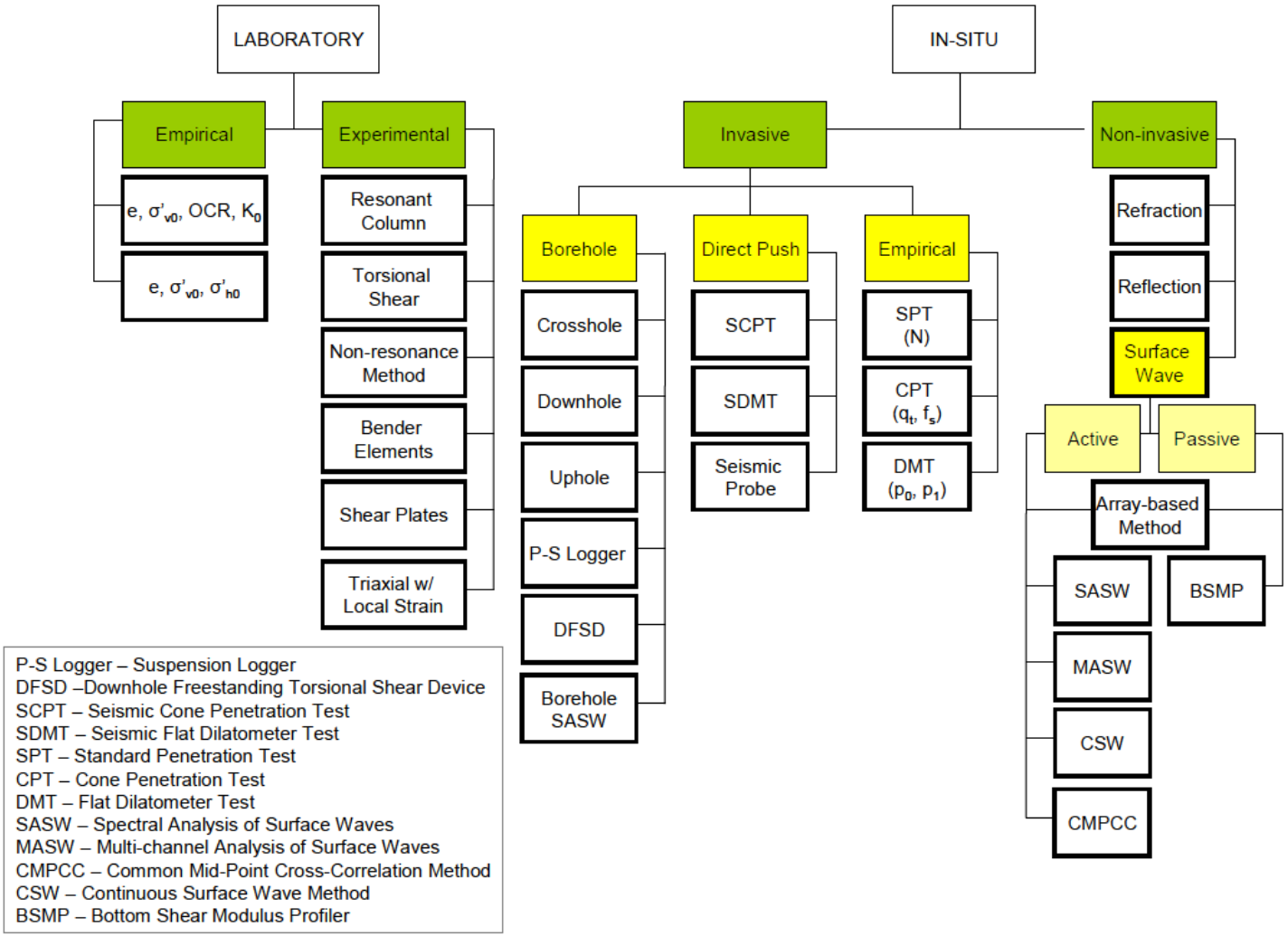

Figure 1.2. A variety of small-strain shear modulus (G_0 or G_{max}) evaluation methods from field and laboratory (Casey 2000; McGillivray 2007).

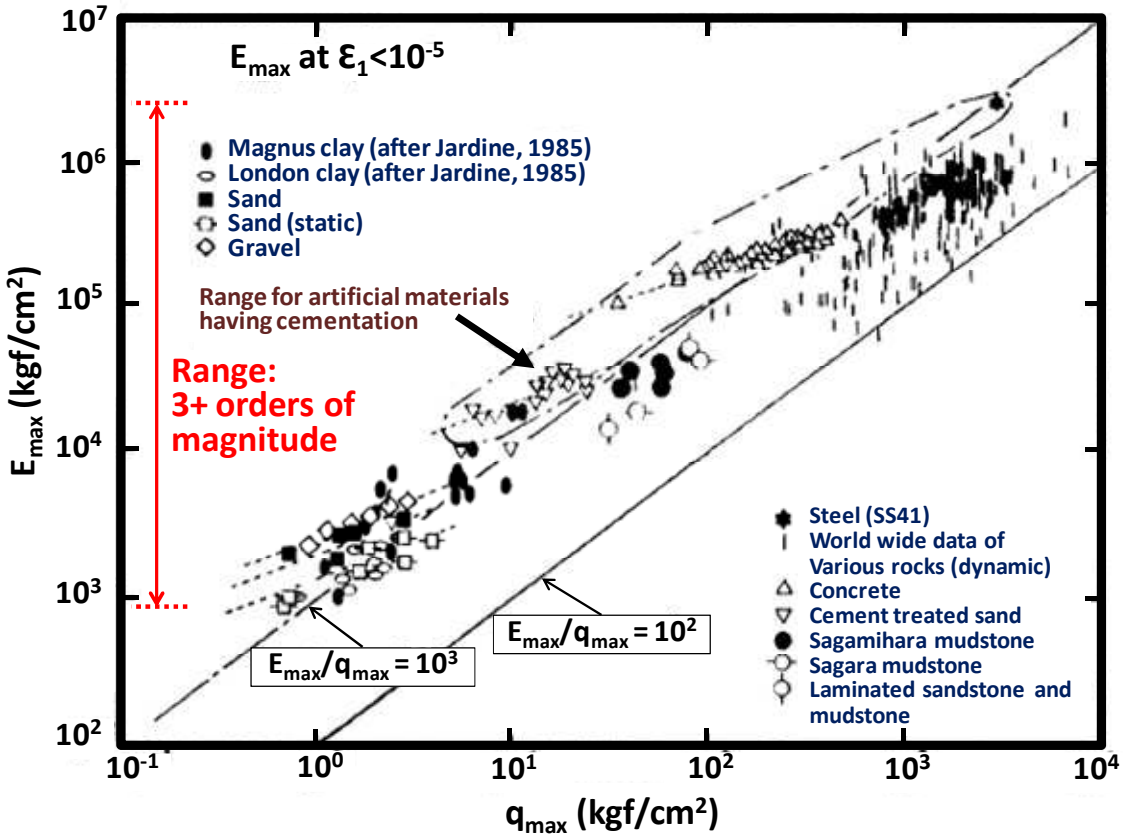

Figure 1.3. E_{max} versus q_{max} measured from laboratory shear test based on various geomaterials. Note: E_{max} = maximum Young's modulus, q_{max} = strength or maximum deviator stress (Kim et al. 1991; Tatsuoka and Shibuya 1992).

1.2 Field Testing Program: Traditional vs. Modern

Inherent complexities of natural soil behavior require a comprehensive set of complementary geotechnical site explorations based on laboratory testing and in-situ test measurements. In a traditional approach to soil site characterization, laboratory tests are performed on samples for obtaining reference values of engineering parameters. Yet, lab testing requires rotary drilling, special undisturbed sampling, sealing of tubes, transportation, and storage in moisture rooms, with corresponding times for specimen extrusion, cutting, trimming, mounting, saturation, testing, dismantling, just for each

sample. In comparison, in-situ field tests are relatively fast, economical, and efficient in terms of both time and cost. Figure 1.4 illustrates a "best practices" approach that involves the traditional drilling, sampling, and laboratory testing approach, as supplemented by individual tests to focus on select geotechnical parameters for identification and quantification. In this case, SPT, PMT, VST, field pumping tests, and CHT can help hone in on the evaluation of density, strength, sensitivity, geostatic stress state, small-strain stiffness, and permeability.

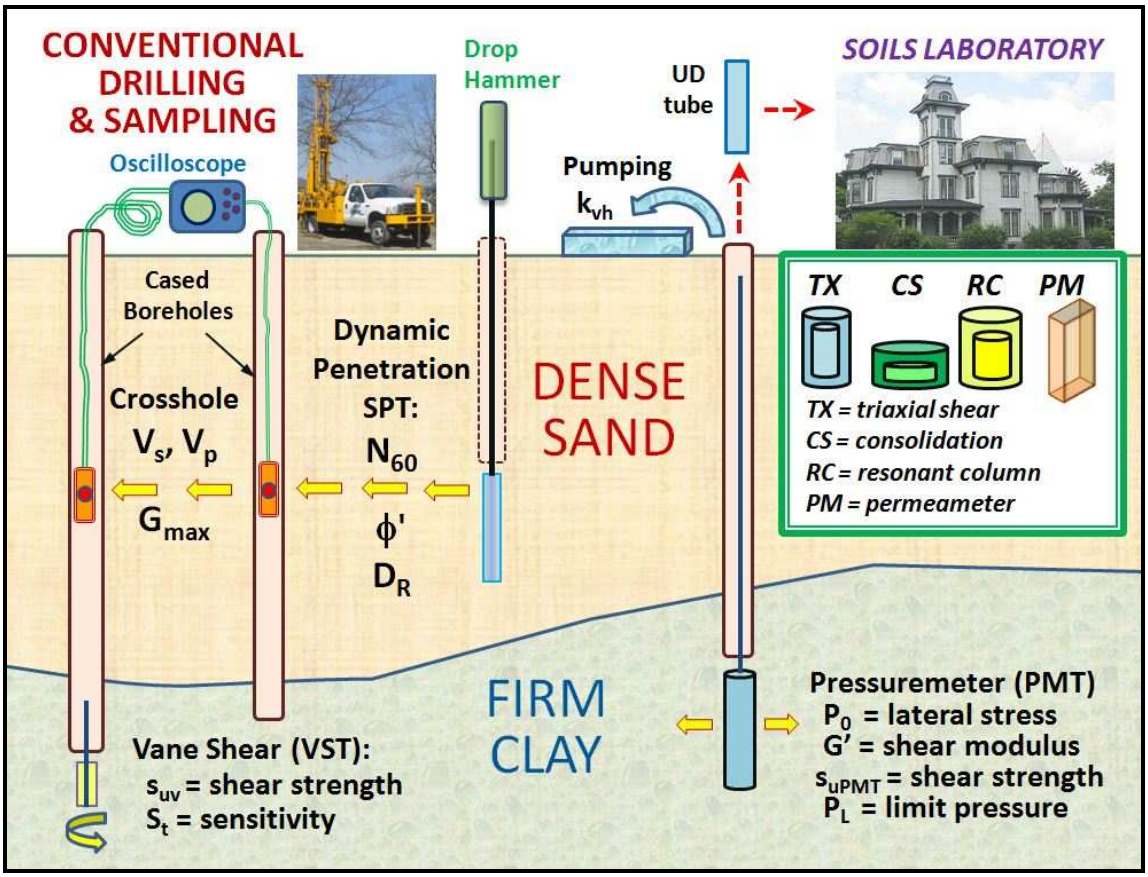

Figure 1.4. Schematic of conventional borehole drilling, sampling, and field tests with basic laboratory tests (Mayne 2012).

Of particular mention, hybrid geotechnical-geophysical in-situ tests make it possible to generate multiple types of readings and collect relatively continuous data, as well as investigate both vertical and lateral spatial variability. With the development of enhanced electronically-instrumented probes and digital data acquisition systems, direct-push technology is capable of merging cone penetration test (CPT) and flat dilatometer test (DMT) with the geophysical downhole test (DHT), so that one sounding can capture many readings in an efficient and economical manner. The seismic piezocone test with porewater dissipations (SCPTù) provides up to 5 independent readings with depth: cone resistance (q_t), sleeve friction (f_s), porewater pressure (u_2), time rate of dissipation (t_{50}), and shear wave velocity (V_{sVH}). Similarly the seismic flat dilatometer with A-dissipation readings (SDMTà) provides up to 5 separate records: blade resistance (q_D), contact pressure (p_0), expansion pressure (p_1), time for dissipation (t_{flex}), and downhole shear wave velocity (V_{sVH}). The relative homogeneity and/or heterogeneity of the project site can be first investigated using noninvasive electromagnetic geophysics (i.e., resistivity, ground penetrating radar, and/or electromagnetic conductivity) to decide where the hybrid SCPTu and SDMT soundings should be located. As such, Figure 1.5 shows the combinatory use of direct-push exploratory techniques and non-invasive geophysics for a routine yet modern means to exploration of the ground. More details concerning traditional and modern in-situ testing are provided in Appendix A.

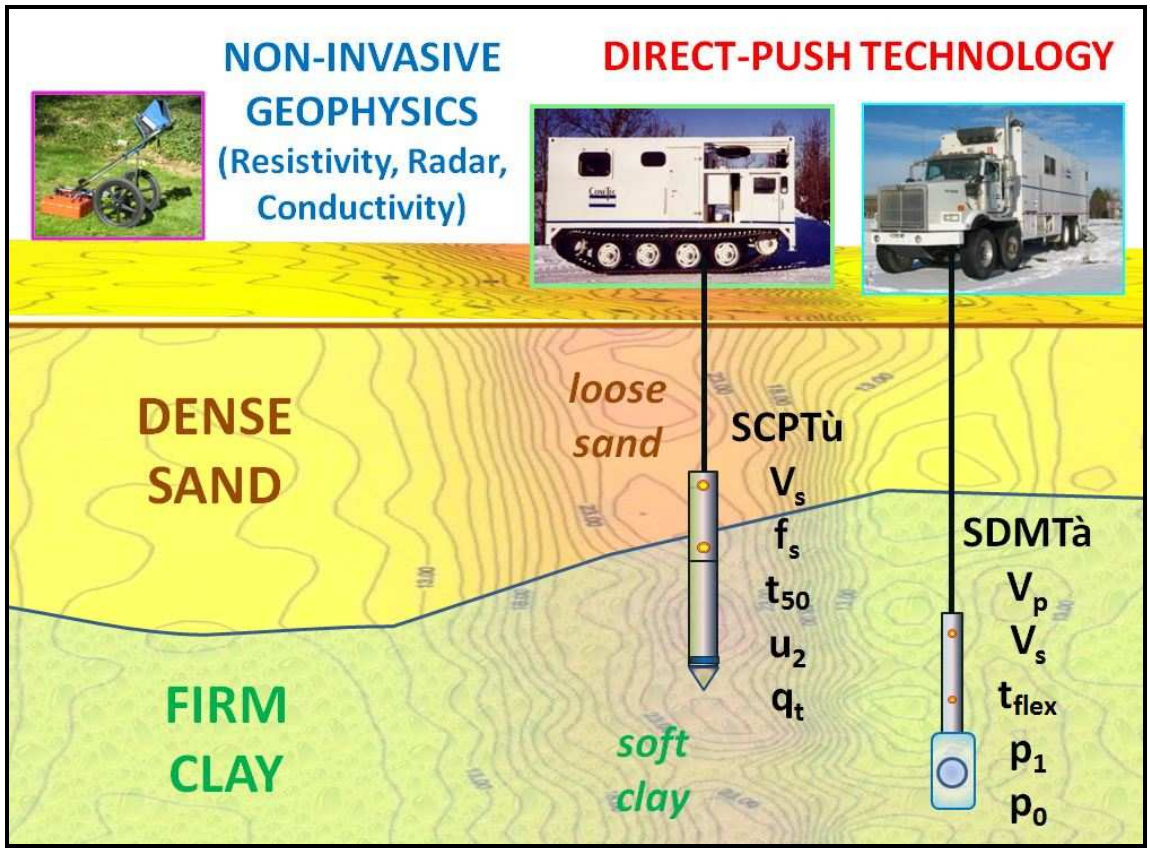

Figure 1.5. Modern exploration program involving both direct-push hybrid field testing and non-invasive geophysics (Mayne 2012).

1.3 Motivation and Objectives of Thesis: Better Utilizing Geophysical Methods

Doctoral research activities by the author were undertaken as part of a Georgia Tech team that focused on the geocharacterization of the Santee Formation in South Carolina for the US Department of Energy. Some anomalous geologic features and contradictory geotechnical information spurred a concerted effort on the part of DOE to undertake a more fundamental set of studies to unravel and elucidate the chemo-hydro-mechanical background and behavior of the old sedimentary deposits that underlie the

project site, specifically called the Savannah River Site (SRS). The author's tasks included a review and analysis of laboratory data, field testing, and geophysical measurements at the SRS. The information included data collection since as early as 1945 vintage, but primarily concentrated on more recent data obtained in the past 15 years at several SRS facilities, as detailed later. To understand and evaluate various soil parameters and the geostatic stress state at SRS, thousands of field tests have been accomplished (e.g. number of CPTu soundings = 3555+) with similar numbers of soil borings and laboratory tests completed todate. In particular, many prior independent investigations focused on the tasks of finding a rational evaluation of the stress history profile, yet it was difficult because the results were often contradictory and inconsistent due to various factors.

Considering the limitations of current in-situ methods of geocharacterizations, particularly using data from the SRS, the author decided to advance a new alternative and independent evaluation means for evaluating stress history and geostatic stress state, based on a shear wave velocity measurements. After reviewing prior efforts along these lines that were primarily based on formulated interrelationships for directional and polarized shear wave velocities in terms of effective principal stress, the approach reported herein took a more direct statistical approach by analysis of a carefully collected database derived from well-documented geotechnical test sites that contained paired sets of different shear waves (i.e., HH, VH, and HV) where reference profiles of OCR and K_0 were also fully detailed.

1.4 Thesis Outline

In this dissertation, novel approaches for geotechnical site exploration using geophysical measurements will be introduced. In particular, a review of existing methods to quantify certain soil parameters (e.g. small-strain shear modulus, stress history, and geostatic stress state) will be made and new developments made towards an independent means of quantification via shear wave velocity measurements. The contributions herein are three-fold: (1) evaluation of the unusual and apparent contradictory sets of laboratory, in-situ, and geophysical data at the Savannah River Site, SC; (2) development of a statistical algorithm for assessing the yield stress ratio (YSR) and lateral stress coefficient (K_0) from paired sets of directional shear wave velocities; and (3) methodology to evaluate continuous shear wave velocity data obtained during cone penetration testing.

The first task gives an overview on the unique geological and geotechnical conditions which underlie an important project site for the US Dept. of Energy (DOE) in western South Carolina in Chapter 2. In subsequent chapters, the document is composed of related yet independent technical papers from published proceedings and/or submitted/accepted to professional journals, thus each have a format that is self-contained within their limited page allocations (Chapter 3, 4, 5, 6, 7, and 8). As such, each of these chapters include separate introductions, data analyses, results, and conclusions, for completeness as an independent document. Therefore, background information is redundant in some cases, as each paper must provide information on a case-by-case basis. Chapter 9 provides additional specific analyses concerning data collected at the DOE site, as well as recommendations for future studies.

On a specific detailing for each chapter, the following content is addressed:

• Chapter 1 gives a brief review on geotechnical site characterization and sets the stage for the increased utilization of geophysical methods within our practice.

• Chapter 2 presents a brief overview on the unusual geological setting and related geotechnical site explorations conducted at the DOE Savannah River Site (SRS). Special geologic conditions include the dissolutioning of old calcareous sediments (Santee Formation) at depths of 40 to 50 m below grade, similar to karstic limestone deposits. As a consequence, caves, voids, and infilled soft soil zones (either with or without encapsulated carbonate shells) occur within the soil matrix at these elevations, probably resulting in localized to full collapse of the overlying soil column. Results from a considerable number of in-situ tests and laboratory test programs were analyzed based on standard evaluation methodologies through the soil column. Available interpretative relationships for assessing the soil stress history (i.e., preconsolidation stress or yield stress) from laboratory consolidation tests on recovered undisturbed samples show scattered results, ranging from underconsolidated to overconsolidated states. Analyses of in-situ test data from cone penetrometer testing (CPT) and flat dilatometer tests (DMT) suggest a normally-consolidated to lightly-overconsolidated state, in defiance of the very old age and history of these Eocene to Miocene sediments. Inferences can also be made from standard penetration tests (SPT) and geophysical data (CHT and DHT), further confounding the issue. As a consequence, the thrust of this research program was directed towards the development of an independent means to assess stress history and geostatic state of stress from field geophysical measurements using paired complementary types of shear waves having different directional and polarization characteristics.

• Chapter 3 presents a review of generalized relationships between shear wave velocity and effective confining stress level, void ratio, and other factors. Analytical formulations are examined within the context of compiled databases from both in-situ and laboratory V_s tests on a wide variety of geomaterials. A general V_s hierarchy in soils is observed from the database with consideration of stress history and directional-polarization type of test (Ku et al. 2011).

• Chapter 4 develops a set of expressions for small-strain shear modulus (G_0) using in-situ measurements collected from well-documented geotechnical test sites. In consideration of stiffness anisotropy which can be observed at many sites, separate global empirical G_0 relationships in different planes (VH, HV, HH) are examined in terms of confining stress, void ratio, and stress history.

• Chapter 5 suggests the utilization of shear wave velocities towards the evaluation of the in-situ geostatic horizontal stress state in soils, specifically the lateral stress coefficient K_0 (Ku and Mayne 2012a, Ku and Mayne 2012b). In these cases, reference benchmark values of K_0 were obtained from direct methods, including: self-boring pressuremeter tests (SBP), push-in total stress cells (TSC), and/or hydraulic fracturing (HF), as well as instrumented consolidometers, triaxial stress path testing, and laboratory suction measurements. The degree of inherent or fabric anisotropy appears to be approximately related to the ratio V_{sHV}/V_{sVH}. More significantly, the ratio V_{sHH}/V_{sVH} directly provides an assessment of K_0 in soils, especially if the age of the formation is also considered.

• Chapter 6 provides a means of evaluating stress history from the measured degree of G_0 anisotropy (i.e., small-strain stiffness ratio = G_{0HH}/G_{0VH}). Based on a special

compiled database, reference profiles of the yield stress ratio (YSR) for a variety of well-documented test sites were determined using series of laboratory consolidation tests on undisturbed samples at varied elevations, coupled with a good understanding on the engineering geology background of the formations. For stress history assessment in soils, expressions were derived from multiple regression analyses using the stiffness ratio and additional variables including depth and/or age.

• Chapter 7 includes an alternate stress history evaluation using the overconsolidation difference: OCD = (σ_p' - σ_{vo}') which has the benefits of a more reliable forecasting algorithm which is not reliant on point-to-point field measurement errors. Consistent and robust field OCR and preconsolidation stress profiles are derived using a formulation relating OCD to stiffness ratio (G_{0HH}/G_{0VH}), as evidenced in several case studies that are presented.

• Chapter 8 presents details concerning two new approaches to downhole testing (DHT) developed at Georgia Tech to obtain shear wave velocities (Ku and Mayne 2012c). This dissertation specifically addresses the post-processing issues related to handling of many wavelet data collected. The field procedures and equipment are documented in McGillivray (2007) and include: (a) frequent-interval method by seismic flat dilatometer (FiSDMT) and (b) continuous-interval method by seismic piezocone testing (CiSCPTu). A recently-awarded Georgia Tech patent for a roto-autoseis source assists in both methods by generation of consistent and repeatable wavelets that are recorded in the probes during advancement. In the case of frequent-interval SDMT, either pseudo-interval or true-interval V_s data are procured at the same depth intervals of 0.2-m as the normal lift-off pressure (p_0) and expansion pressure (p_1) and therefore is a

slowest version of downhole testing. This offers the advantage of accurate and detailed small-strain stiffness measurements (i.e., G_{max}) that can be useful in careful settlement calculations, pavement subgrade designs, and paleoliquefaction studies with shallow fine resolution requirements. In the continuous SCPTu, the autoseis generates wavelets as frequently as every 1 or 2 seconds, thus a fastest type of downhole testing. As there are considerable issues with signals that are complex because of extraneous noise, refracted waves, variable penetration rates, and vibration issues, special measures in post-processing raw wavelets are required in order to extract the V_s profile. The final result offers continuous profiles of q_t, f_s, u_2, and V_s with depth from a single CiSCPTu sounding.

• Chapter 9 provides a review of extensive V_s data obtained at the Savannah River Site (In-situ V_s trends were discussed in Ku et al. 2012). The V_s-stress relationships at SRS are investigated from both laboratory data and representative field V_s profiles. In particular, anomalous trends at the DOE site show V_s decreasing with depth in the upper 15 m and V_s nearly constant at 330 m/s in the profile over the next 30 m depths. As most "well-behaved" soil profiles show V_s increasing with depth, this chapter discusses and examines the expected reasons for this unusual behavior that can be attributed to capillarity, desiccation, overconsolidation, and/or cementation in the uppermost deposits, and/or collapse of the soil column due to dissolutioning of the underlying Santee formation at 45 m depth. This chapter also provides interrelationships between different types of in-situ tests performed at SRS. Due to the unusual geology, anomalous V_s trends, and the documented geomaterial conditions, a set of site-specific correlations for CPT-V_s at SRS is suggested.

• Chapter 10 provides final summary and conclusions based on all site investigation topics which are included in this thesis.

Appendices include followings:

• Appendix A – Field test review and current methodologies

• Appendix B – Void detection summary at SRS

• Appendix C – Evaluated geomaterial parameters at SRS

• Appendix D – Results of stress history evaluations using laboratory tests at SRS

• Appendix E – At rest lateral stress coefficient (K_0) versus shear wave velocity ratio (V_{sHH}/V_{sVH}) based on laboratory database.

• Appendix F – Case studies of stress history profiles based on shear stiffness ratios.

• Appendix G – Additional correlations between field tests (CPT-SPT, CPT-DMT) at SRS.

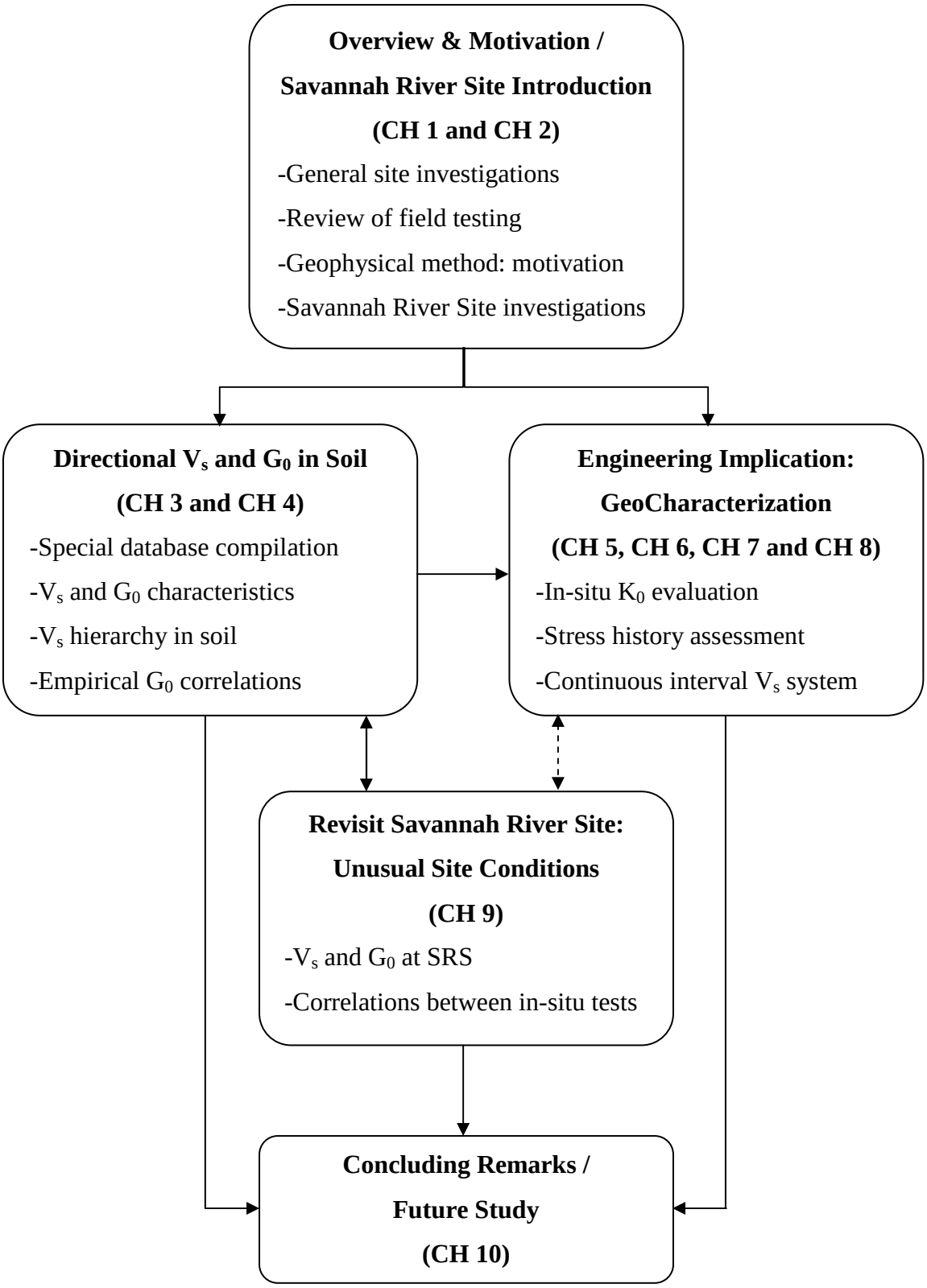

Figure 1.6. Brief explanation chart of thesis outline.

CHAPTER 2

GEOTECHNICAL SITE INVESTIGATIONS IN WEST CENTRAL SOUTH CAROLINA

2.1 Introduction of Savannah River Site

The Savannah River Site (SRS) is a large and important complex owned by the US Department of Energy which is located in west central South Carolina next to Georgia (Figure 2.1). The SRS is comprised of some various 30+ separate facilities on 803 square kilometers related to the development of nuclear materials processing and storage (Figure 2.1). Since the initial development of SRS after World War II, it has been discovered that the geologic soil column has unusual characteristics, particularly the presence of voids and caves at 45-m depths, causing concerns because of the critical utilization of the property. Moreover, SRS is located only 215 km from Charleston SC, where a M_w = 7.3 earthquake occurred in 1886.

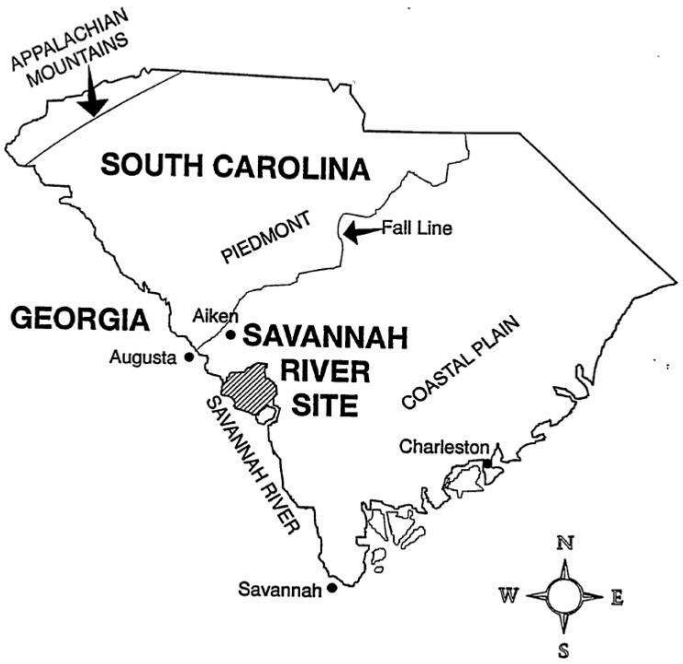

Figure 2.1. Location of Savannah River Site, USA (Cumbest et al. 1996).

2.1.1 Geologic Setting and Site Information of SRS

At SRS, the exposed overburden soils in the upper 60 m depths consist of very old Miocene and Eocene sediments, primarily layered deposits of sands, clayey sands, and silty sands, with interbedded clay strata which exhibit a variable and complicated constituency and stress history profile. The uppermost sandy soils appear to be primarily of quartz, silica, and/or glauconitic constituency while the lower sands below 25 m depth contain components with calcareous or carbonatic particles.

These old sediments appear to be either underconsolidated, normally-consolidated, and/or overconsolidated, depending upon location or test type (SPT, CPT, DMT, V_s, lab consolidation, lab triaxial), as well as the specific interpretative method employed to evaluate the magnitude of yield stress history and/or overconsolidation ratio. One lower unit (Santee formation) shows consistent but erratic soft zones and/or the presence of voids, due to dissolutioning and/or other complex geologic processes, resulting in caves, encapsulated karst-like features, and fluid-filled caverns at depths of between 40 to 50 m below grade.

A simplified geostratigraphic profile at the SRS APT (Accelerator Production of Tritium) site is shown in Figure 2.2 and includes the following strata from shallowest to deepest: (a) Upland Deposits/Altamaha Formation; (b) Tobacco Road; (c) Dry Branch; (d) Tan clay; (e) Dry Branch/Clinchfield sands; (f) Santee Formation. Another detailed stratigraphic cross-section for the overall SRS region is provided in Figure 2.3. As evident, heavily interbedded soil layers are observed and the overall thickness of the sedimentary deposits increases from northwest towards the southeast approaching the Atlantic Ocean.

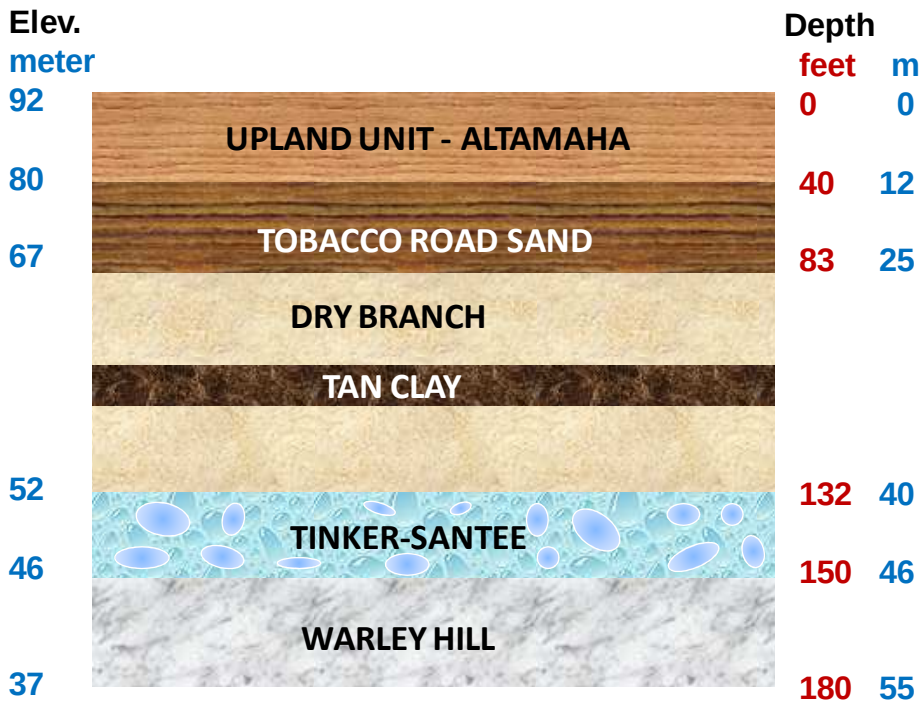

Figure 2.2. Simplified geostratigraphic soil profile at the SRS APT site (redrawn from Burns and Roe Enterprises Inc., 2001).

General geologic and age information at the SRS region are provided with approximate stratigraphic units in Figure 2.4. In the Santee formation, postulated void and cave features range from about 1 m to over 30+ m in length/width and 0.5 to 2 m in height that occur within a sedimentary soil matrix. These are anomalous compared with most other marine deposits along the Atlantic seaboard, yet have been confirmed in recent 30m deep excavations at the nearby nuclear Plant Vogtle in Augusta, Georgia located only 2 km west of SRS.

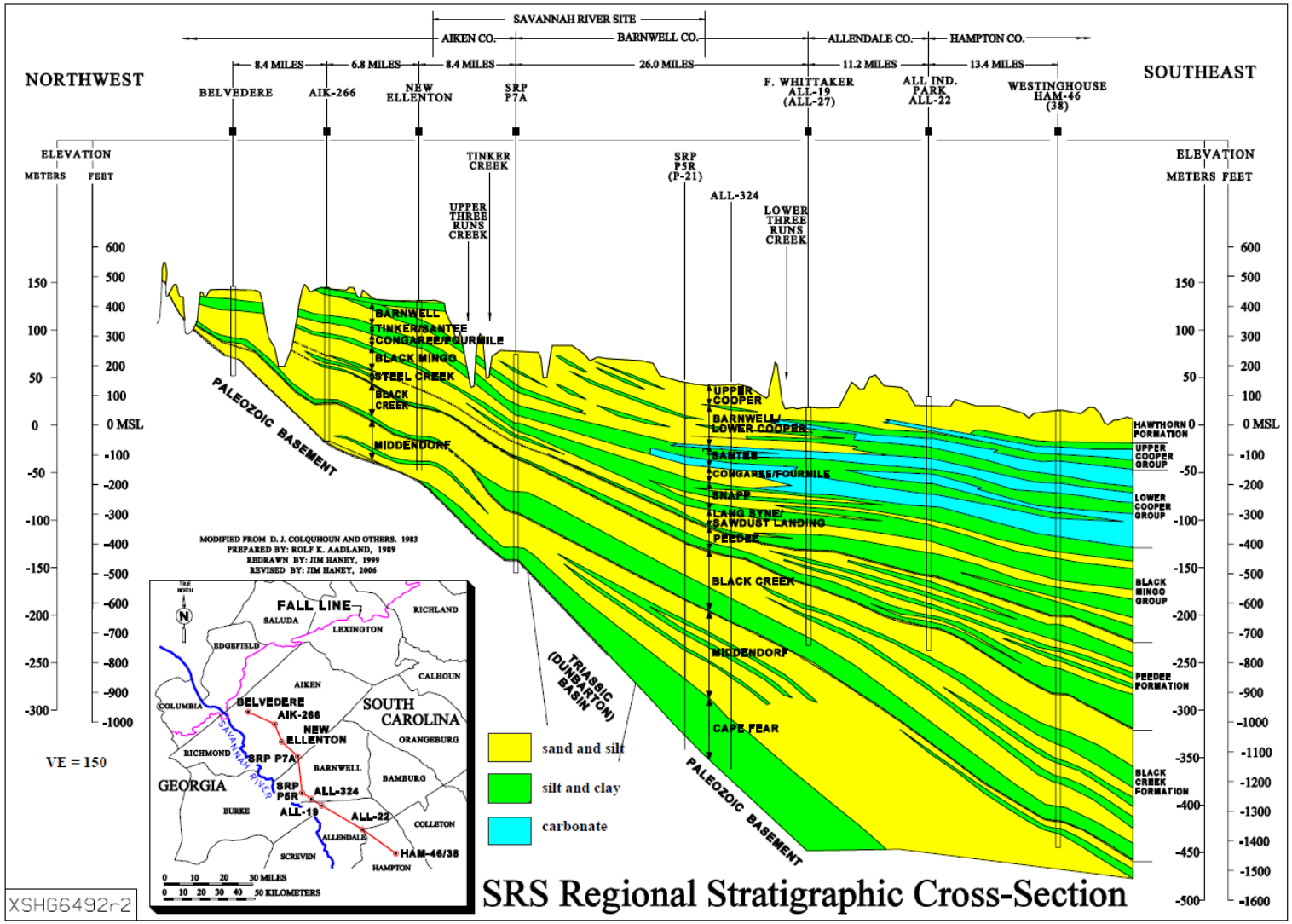

Figure 2.3. Detailed cross-section of SRS region (WSRC 2007).

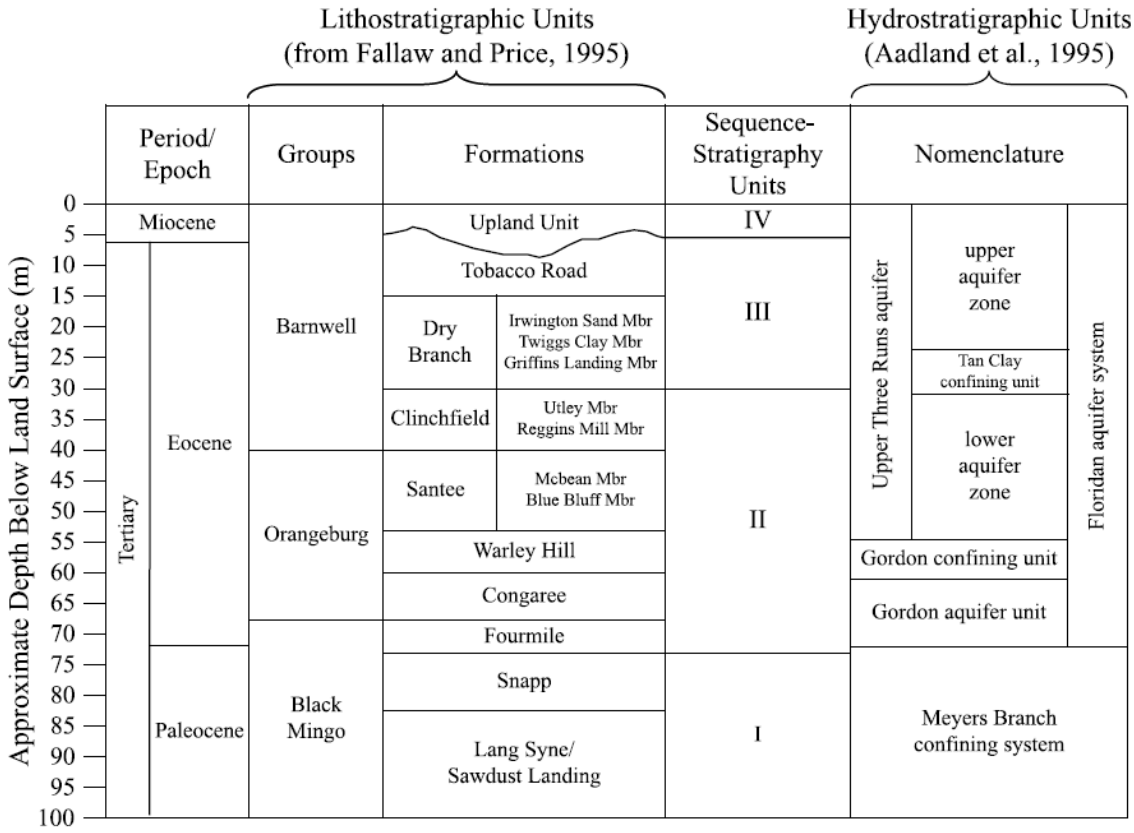

Figure 2.4. Stratigraphic units and geologic information at SRS (Cameron et al. 2010).

During the removal and replacement operations for 30-m deep excavations made for two new reactors at Plant Vogtle in 2009-2011, Figure 2.5 shows the uncovered caves observed at the Plant Vogtle site. The existence of dissolution features and soft zones/voids affects the construction of building and ancillary structures at the SRS because of concerns associated with possible collapse and/or settlements. These also include risks of settlements, subsidence, and/or ground deformations associated with soil liquefaction due to the proximity of the Charleston, SC seismic region. Therefore, a large number of site investigation programs have been conducted over the last half century towards a comprehensive geotechnical site characterization at SRS.

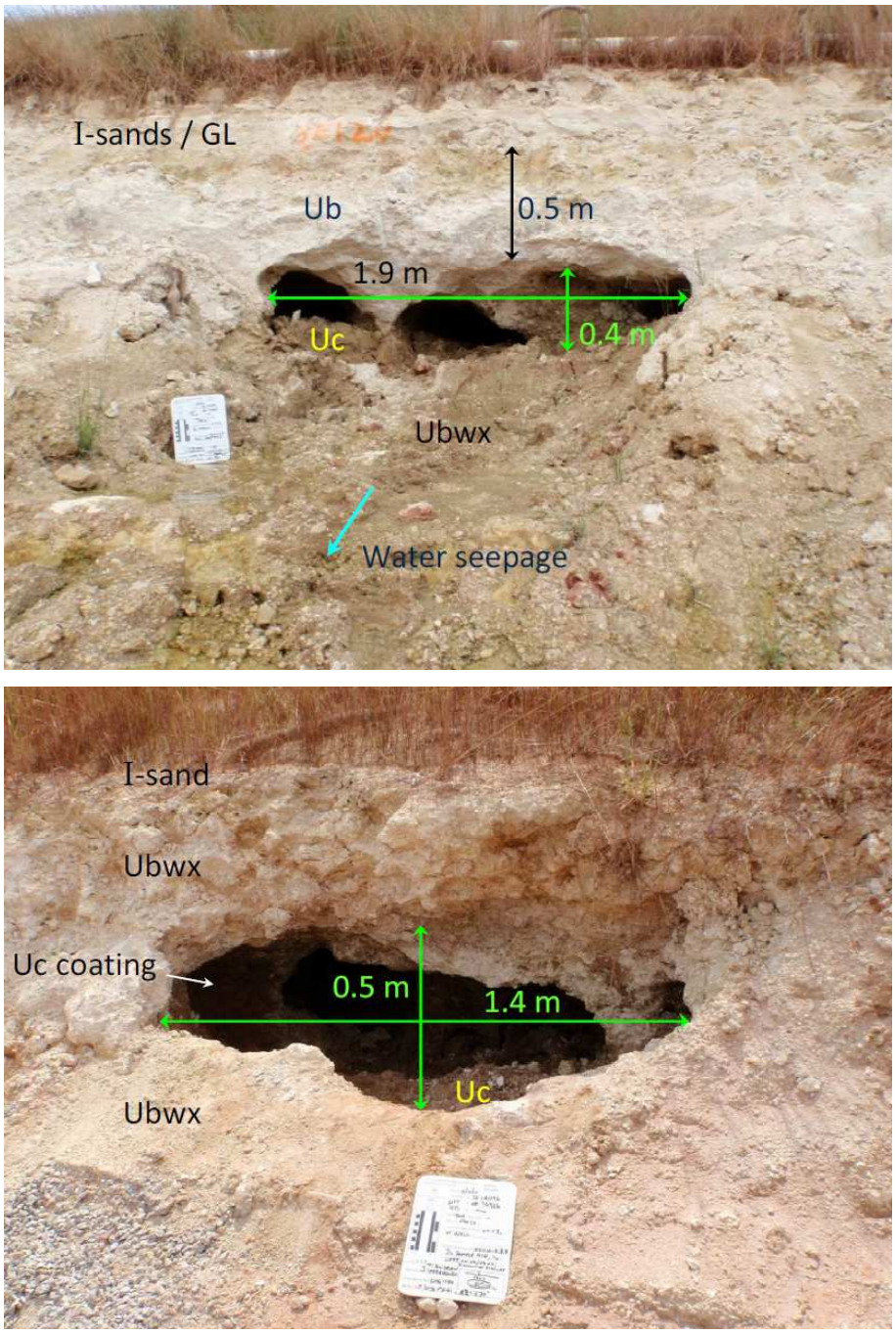

Figure 2.5. Examples of large void observed from deep excavations at Plant Vogtle, Augusta (Larrahondo-Cruz 2011).

Note: Ub – hard Utley limestone, Ubwx – brittle Utley limestone, Uc – Putley soil (clay deposits, bottom of observed caves)

2.1.2 Gap-Graded Soils at SRS

Much of the overburden soils at SRS classify as slightly to clayey sands (SP-SC to SC) based on mechanical analyses by sieves and the hydrometer analyses of geomaterials in the fines content portion. Surprisingly, the sand fraction is uniformly graded in the fine-medium sand size range, however, below the No. 200 sieve, very little silt sizes are found and a predominance of clay or colloidal particles occur. This results in gap-graded sands in the soil column. For instance, based on a sample boring (i.e., Boring B35 at the Salt Waste Processing Facility or SWPF site), grain size distribution curves are presented in Figure 2.6. The gap-graded soils are seen to have high clay fines contents, appreciable colloids, and plastic fines, as well as high specific surfaces. Other important special geologic conditions at SRS and their detection using in-situ tests are discussed in the next section.

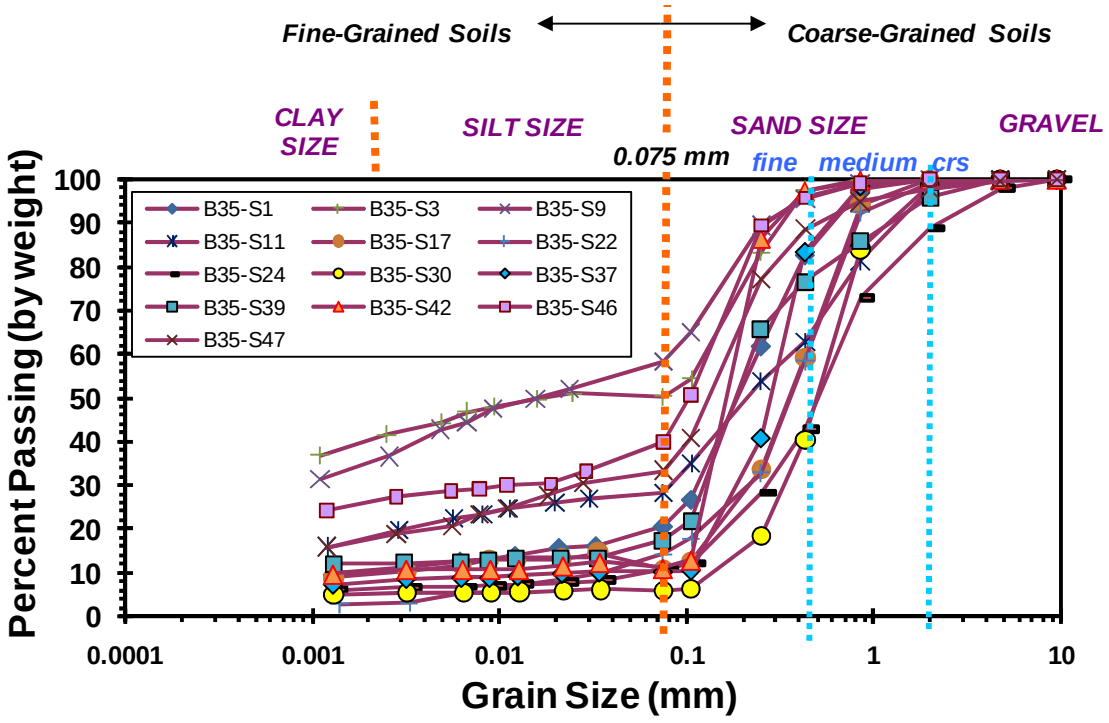

Figure 2.6. Grain size distribution curves at SRS (data from Shannon & Wilson, Inc. SWPF Report 2007).

2.2 Detection of Special Geologic Conditions through Field Testing

For the comprehensive site investigations at SRS, a large number of laboratory tests and field tests have been conducted from various plant locations and these are documented in many of the geotechnical reports. Figure 2.7 shows an overall map with the surface topography and the specific SRS site location information.

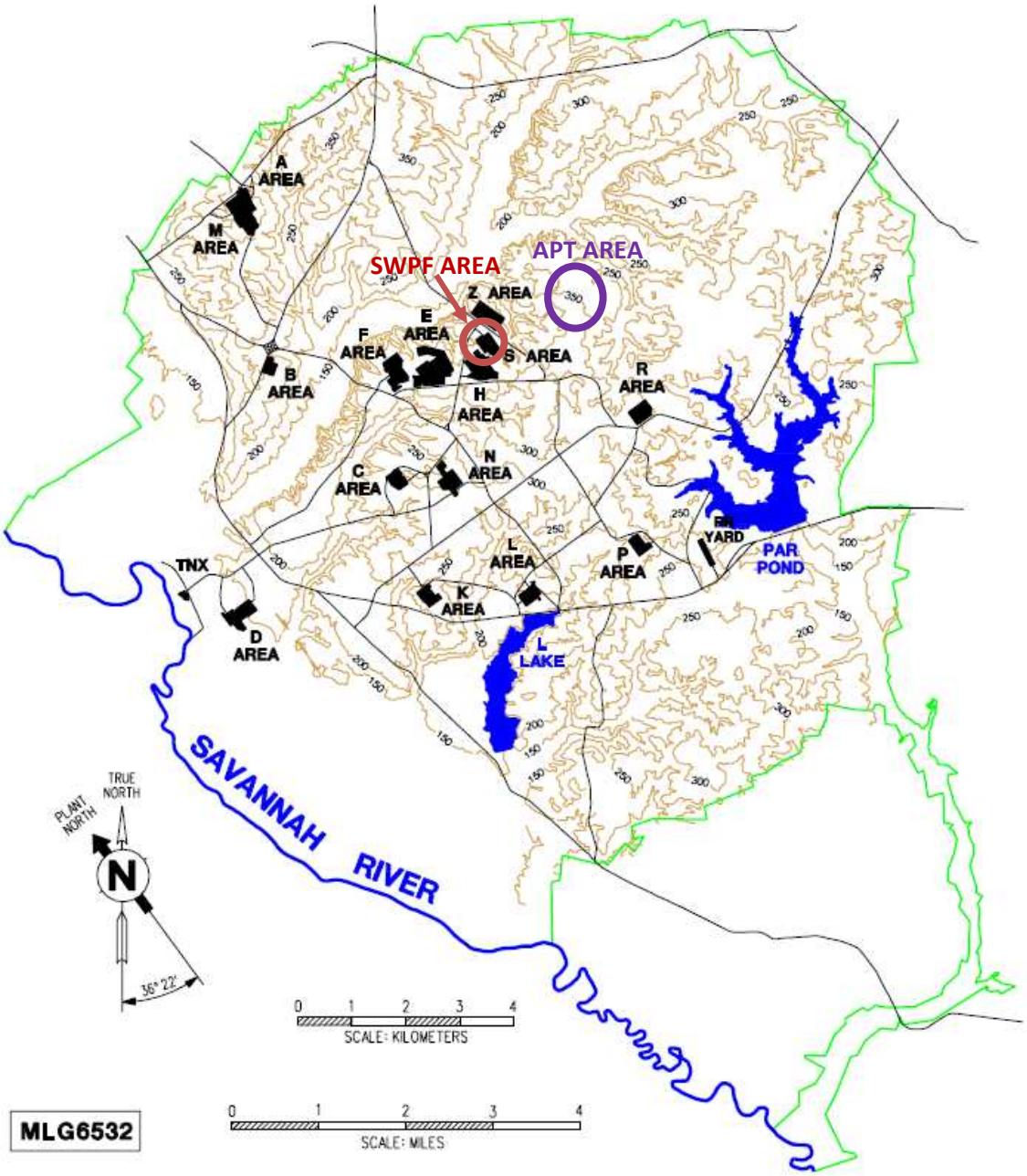

Figure 2.7. Surface topography and location names at SRS (WSRC 2007).

2.2.1 Compilation of In-Situ V_s Data at SRS: Unusual V_s Trend

The SRS consists of very complex geological conditions which play a significant influence on the geostatic stress state and stiffness anisotropy. For site characterization, numerous borings, samplings, and laboratory tests plus series of in-situ tests have been performed, including CPT, DMT, and SPT. Also, field geophysical measurements of P-wave and S-wave velocities were obtained at many locations within the SRS. Generally, field V_s provides information for site-specific dynamic shear modulus interpretations. In Figure 2.8, a total of 87 V_s profiles from downhole tests (DHT) have been compiled from the SRS APT site. Specifically, these DHT were obtained using SCPT. Surprisingly, it is noted that V_s measurements decrease with depth at this site, as the normal expected trend in soil deposits shows V_s increasing with depth (e.g. Lew and Campbell 1985; Brown et al. 2002). This unusual in-situ V_s trend is related to the geologic conditions at SRS and further details on these anomalous trends will be discussed in Chapter 9.

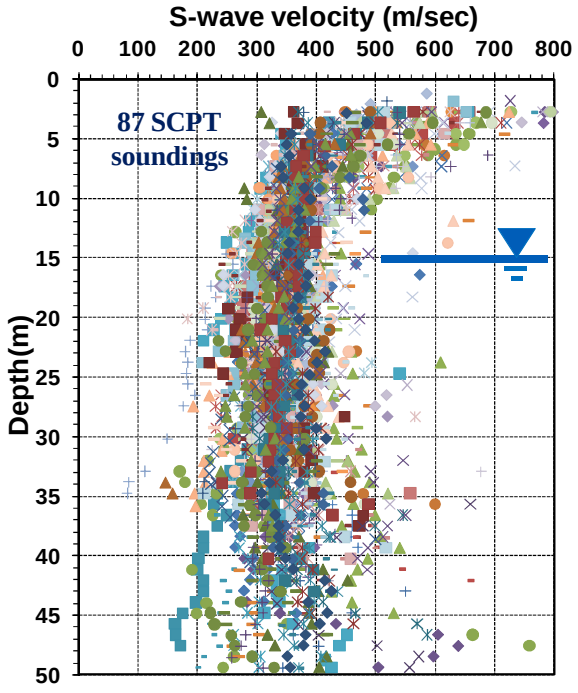

Figure 2.8. Compilation of downhole type V_s at SRS APT.

2.2.2 Cementious Bonding

The stiffness of cemented materials increases with bonding agent and/or cement content. Even a small amount of cementation can increase the dynamic shear moduli at small strain (e.g., Saxena et al. 1988; Fernandez and Santamarina 2001). As a result, an indirect assessment of cementation at SRS was made. The identification of cemented granular soils can be made using graphical relationships between normalized cone tip resistance (q_{t1}) and the ratio of G_{max} to q_t (Eslaamizaad and Robertson 1996; Schnaid et al. 2004).

Here, normalized cone resistance: $q_{t1} = (\frac{q_t}{P_a})\sqrt{\frac{P_a}{\sigma_v'}}$

With respect to empirical correlations linking estimate of G_{max} from cone tip resistance (q_t) in sands, Baldi et al. (1989) initially proposed the conceptual format using field SCPT data based on silica sands. Then, Rix and Stokoe (1991) compared the trends using chamber testing data on washed mortar sand and field testing data at Herber Road, California. It resulted in a wider banded trend of G_{max}/q_t versus q_{t1} for uncemented unaged sands. Later, Eslaamizaad and Robertson (1996) showed that the noted plot can provide the possibility of identifying cemented sands as the trend fell above the uncemented, unaged quartz to silica sands. It indicates that cementation effect tends to have more influences on the increase of G_{max} magnitude compared to q_t magnitude. The data have been expanded with in-situ data and suggested boundary expressions by Schnaid et al. (2004) and Schnaid (2005, 2009).

Hence, to quantify the degree of cementation, data from 143 CPT soundings were obtained with their associated V_s data at SRS APT. Values of cone tip resistance (q_t),

sleeve friction (f_s), and shoulder porewater pressure (u_2) are shown for mean plus and minus standard deviation in Figure 2.9.

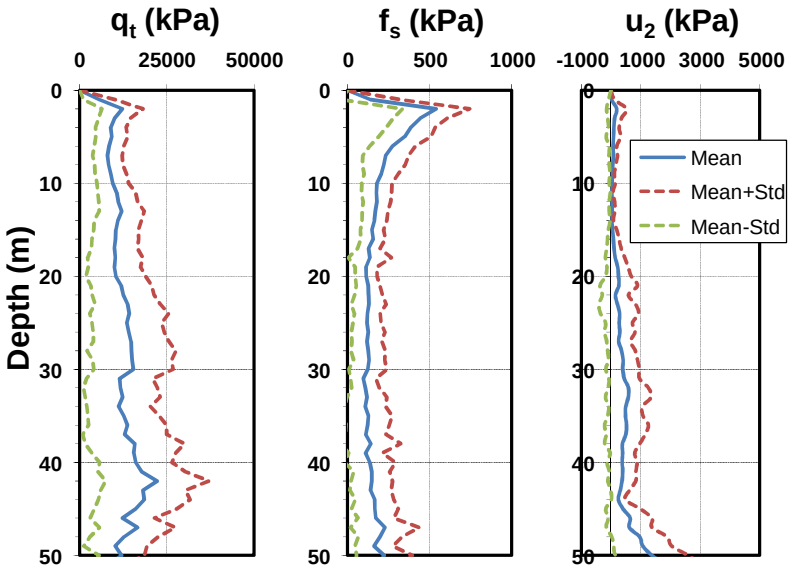

Figure 2.9. Mean values of (a) cone tip resistance; (b) sleeve friction; (c) shoulder porewater pressure from a total of 143 soundings at SRS APT.

Based on the CPT profiles and corresponding V_s data, the degree of cementation is quantified using the measured q_{t1} and G_{max}. Applied boundaries for an indirect identification of soil cementation evaluation are as follows (Schnaid et al. 2004):

Equation (2.1) $G_{max} = 800\sqrt[3]{q_t \cdot \sigma_v' \cdot P_a}$ for upper bound for cemented soil

Equation (2.2) $G_{max} = 280\sqrt[3]{q_t \cdot \sigma_v' \cdot P_a}$ for lower bound for cemented soil & upper bound for uncemented soil

Equation (2.3) $G_{max} = 110\sqrt[3]{q_t \cdot \sigma_v' \cdot P_a}$ for lower bound for uncemented soil

where $P_a = \sigma_{atm}$ = is a reference stress equal to atmospheric pressure. Figure 2.10 (a) shows the apparent degree of cementation at SRS APT. To consider the different soil layers, the G_{max}/q_t ratio is plotted per separation into each of the four distinct geologic

formations: Upland Unit (UU), Tobacco Road (TR), Dry Branch (DB), and Santee (S). In Figure 2.10, the Upland Unit (UU) clearly shows the highest G_o/q_t ratio, compared to the other geologic formations, thus inferring a highly cemented and/or structured geomaterial. However, this approach should be cautiously considered with limitations because the boundaries were established based on only for sands. In Figure 2.10 (b), CPT soil classification index profile shows the SRS mainly consists of sandy, but in the Santee formation it is identified as silty and clayey mixtures (More soil classification approaches will be provided based on CPT, DMT, and laboratory data in section 2.3.1). Thus, the assessment of cementation is not applicable for Santee formation.

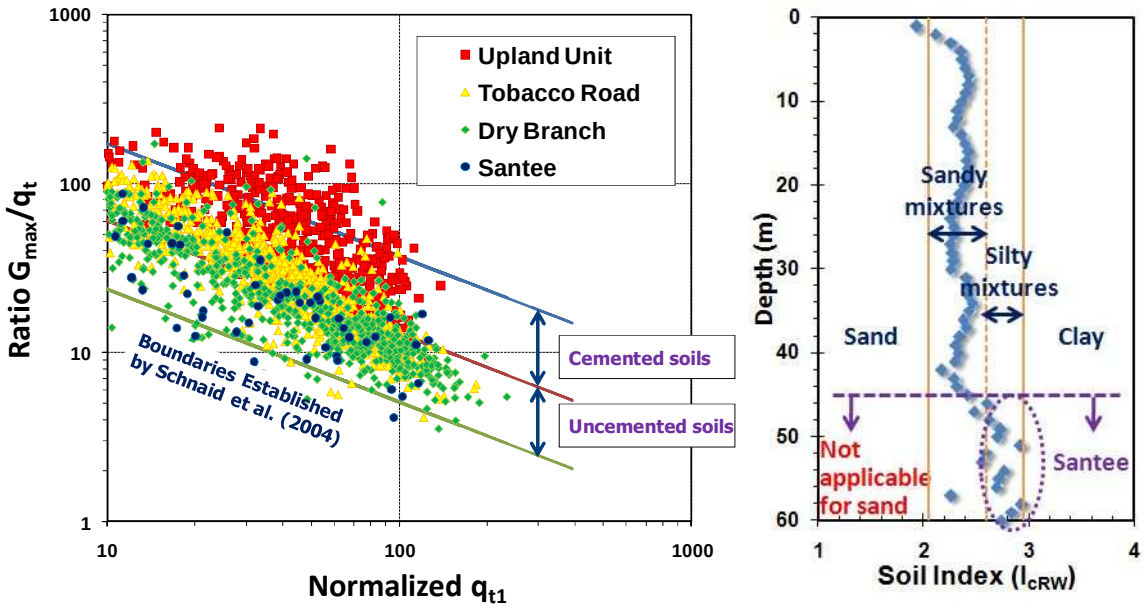

Figure 2.10. (a) Assessment of apparent cementation, (b) CPT soil classification index (I_{cRW}; Robertson and Wride 1998) profile at SRS APT site.

2.2.3 Calcareous Soils

According to downhole geophysical logging data from prior onsite studies (e.g., Laura Bagwell, SRNL 2008), certain soil layers show a calcareous and carbonate composition. Evidence of calcareous sediments at SRS was verified by x-ray diffraction testing (Larrahondo-Cruz 2011). With respect to testing of calcareous sands, it is known that grains are crushable and consist of angular particles, thus showing high void ratio and rather weak structure compared to silica soils (Semple 1988; Lunne et al. 1997). Variable cementation is often observed. Sample disturbance effects tend to be significant for calcareous soils.

The identification of carbonate sands can be indirectly detected by CPT measurements. For instance, it is observed that normalized cone resistance (i.e., q_{t1n}) magnitudes in calcareous sands can be about half the magnitudes of those in siliceous-quartz sands at the same relative density (D_R). Figure 2.11 shows a comparison of CPT data from chamber tests on 24 silica-quartz sands versus 6 series on calcareous-carbonate sands (data from Mayne 2007).

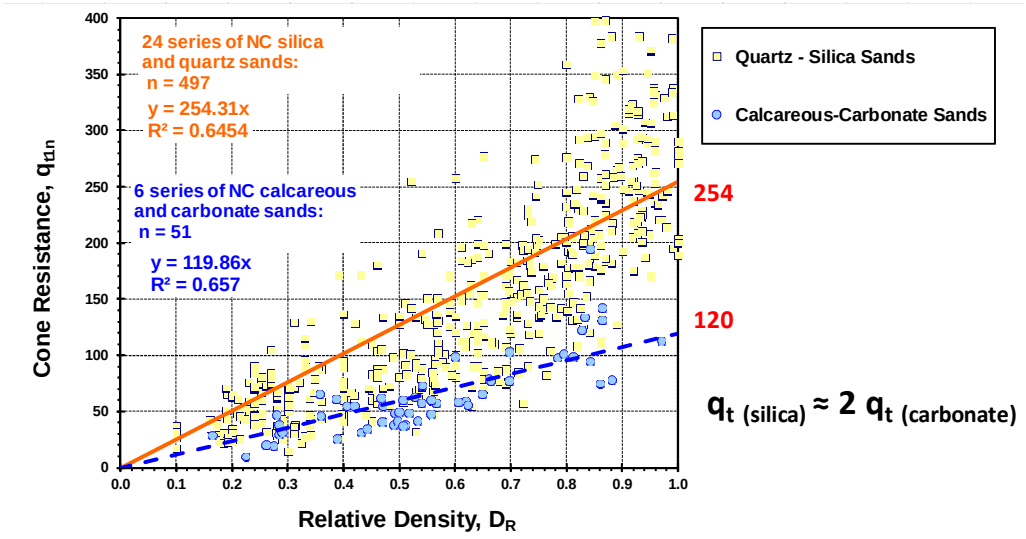

Figure 2.11. Cone resistance in different types of sands at same relative density from calibration chamber tests: siliceous versus calcareous.

The presence of calcareous soils can be identified using CPT soil classification charts. Ebelhar et al. (1988) applied data from CPT soundings in carbonate and calcareous soils to the simple q_t - FR chart. Figure 2.12 describes the identification of calcareous soils from SRS soil column based on a representative CPT sounding (#C21) recorded at the SRS K-site. The groupings show a reduced friction ratio for calcareous sands, compared with values in the upper sands that are siliceous type.

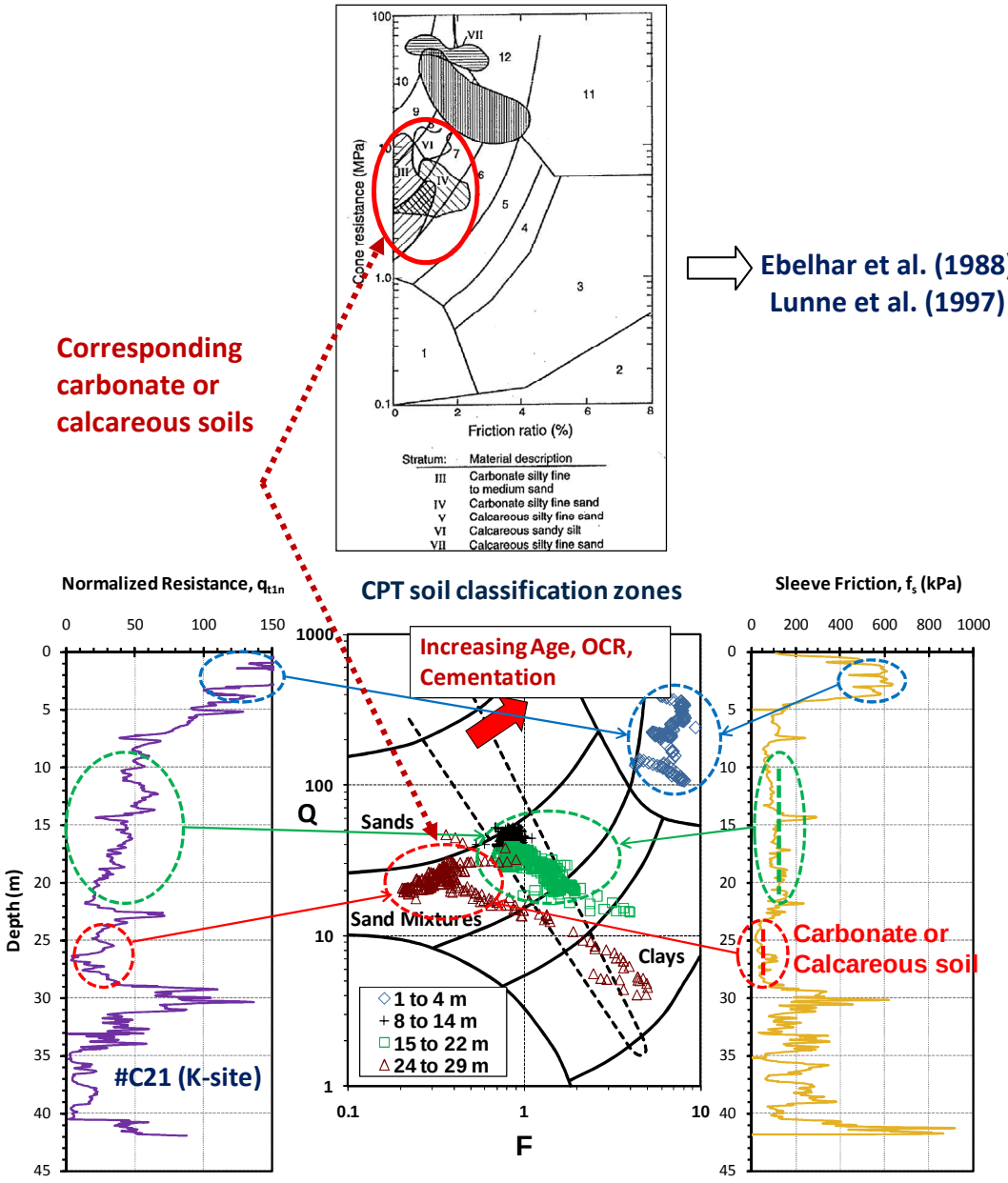

Figure 2.12. Example of identification of calcareous sands at SRS K-site.

2.2.4 Void Detection

As noted, the subsurface stratigraphy at SRS contains a special soft zone to karstic material named Santee formation which may include large voids or caves at about 45±5m depths. According to the summary report by the Washington Savannah River Company (WSRC 2007), the criteria for soft zone identification at SRS are defined as follows:

1) Criteria based on in-situ penetrometer testing:

    1.a. CPT : cone tip resistance (q_t) < 1.5 MPa (15 tsf)

    1.b. SPT : blow count (N) ≤ 5 blows/ft

2) Geologically located in Tinker/Santee formation or lower Dry Branch formation

3) Continuous vertical thickness ≥ 0.6 m (2 feet), or professional judgment

4) Consolidation test data : OCR < 1

5) Atterberg limit data indicating moisture content > liquid limit

Among the above multi-criteria, the possibility of soft zone and/or void detection is further investigated based on CPTu data. A total of 47 piezocone penetration tests (CPTu) were obtained at the SRS K-site by Lankelma Group under contract to DOE/SRS (2011). Mean values of cone tip resistance (q_t), sleeve friction (f_s), and excess porewater pressure (u_2) are provided in Figure 2.13 as a summary graph.

As noted, the magnitude of q_t is defined as less than 1.5 MPa in soft zone or void. Generally, for determining whether soil layers are either sand or clay, a rule of thumb is delineated by q_t = 5 MPa. Therefore, soil layers having q_t magnitudes less than 5 MPa are suggestive of clays, whereas sands exhibit values above 5 MPa. Additionally, the magnitude of porewater pressure (u_2) is approximately half of the q_t magnitude in clay. However, if there are partially large voids in Santee formation, the u_2 may be dissipated,

perhaps close to zero or hydrostatic (u_0). Hence, the magnitude of u_2 in soft zone including voids is expected to be much less than that in general clay layer. For instance, Figure 2.14 and Figure 2.15 show the detection of possible soft zone/or voids. In the soft zone material possibly including voids, the combination of u_2 and q_t behavior is definitely different from clay layers.

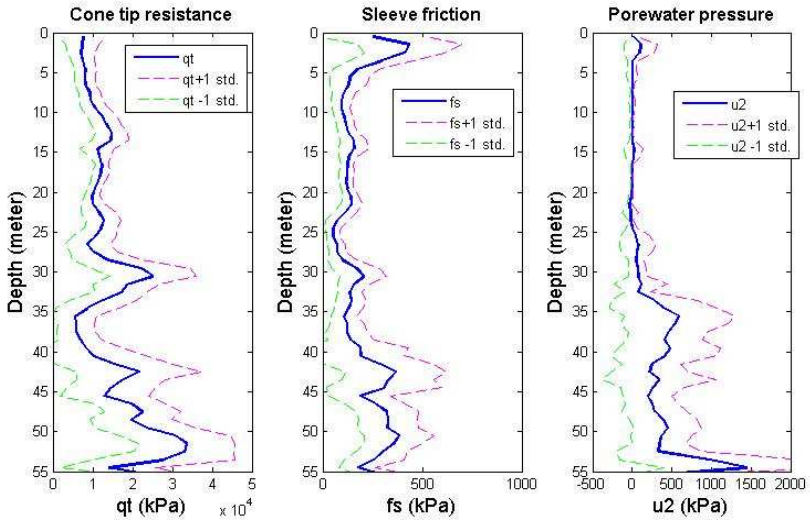

Figure 2.13. Mean profiles of a) CPT tip resistance, b) sleeve friction, and c) excess porewater pressure at SRS K-site.

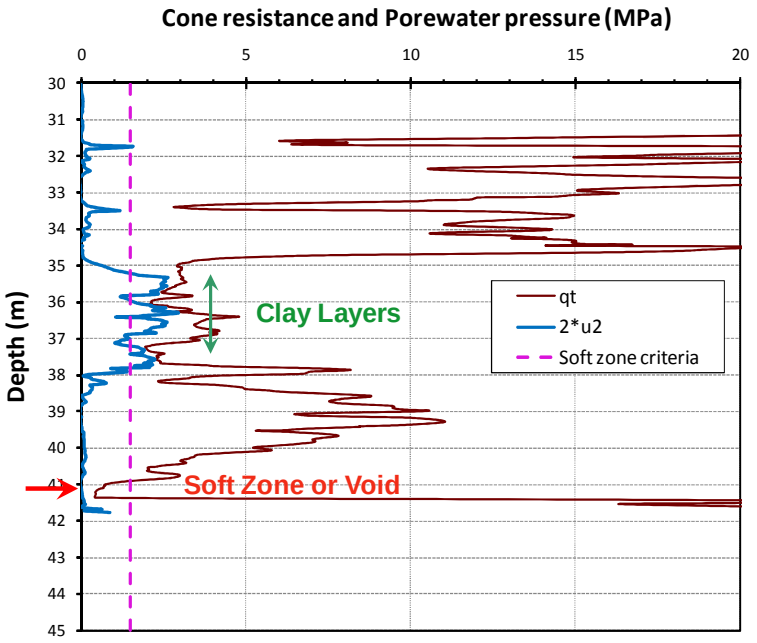

Figure 2.14. Identification of clay layers and detection of possible soft zone/or void using q_t and u_2 data (CPT ID:K-PDC-14) at SRS K-site.

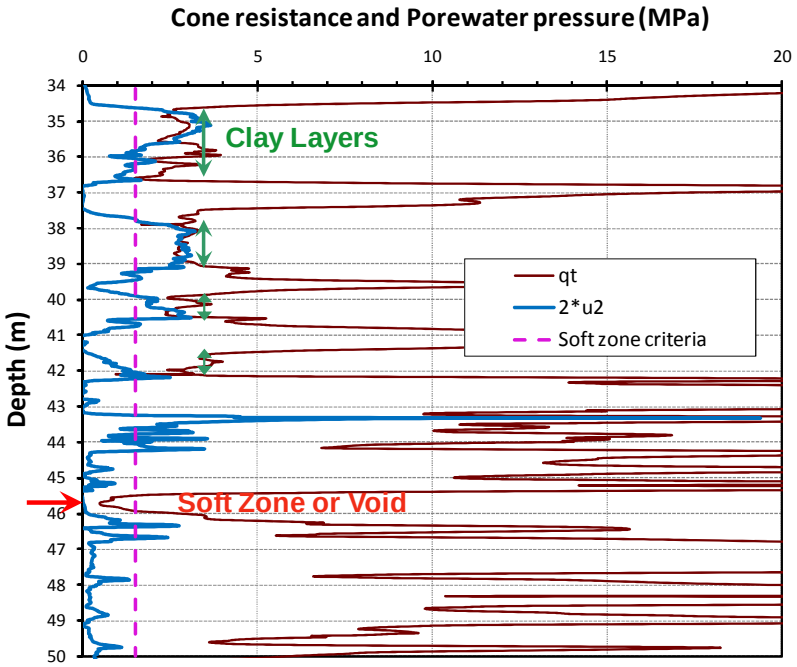

Figure 2.15. Identification of clay layers and detection of possible soft zone/or void using q_t and u_2 data (CPT ID:K-PDC-25) at SRS K-site.

In the same manner, all CPT data were reviewed with the aforementioned criteria to detect soft zones. Cone penetration profiles are shown in Figure 2.16 (East-West direction) and Figure 2.17 (North-South direction). The surface conditions here are nearly level. Most cone soundings were advanced more than 40 meters deep. Yellow zones indicate clays or organic clay soils which are evaluated based on CPT soil behavioral classification. Clay layers appear mainly located between the 30 and 40 meter depth interval. The soil identification is determined based on a CPT material index (I_{cRW}).

Possible soft zones/or voids are marked by red zones in Figure 2.16 and Figure 2.17. It is observed that the I_{cRW} value corresponding to the detected voids or soft zones is either a very large number or undefined, as due to a calculated negative Q value ($Q < 0$). Among a total of 47 CPT soundings, the detected voids or soft zones having q_t less than 1.5 MPa and relatively small u_2 have been found in 24 CPT data. Therefore, it seems that

about 50% CPT soundings detected the presence of voids or soft zones. Further details on this topic are provided in Appendix B

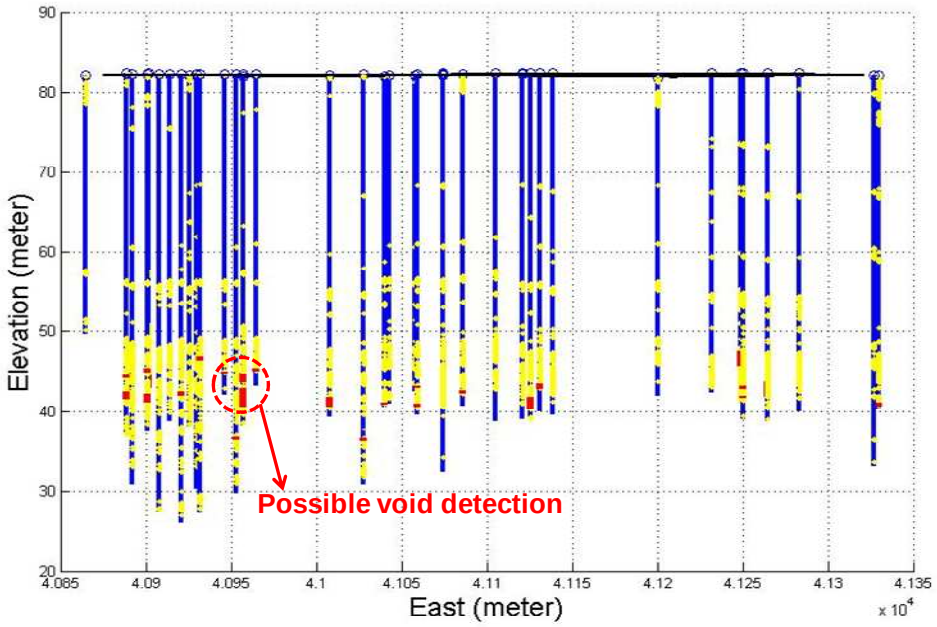

Figure 2.16. CPT profile (I – East-West direction) indicating estimated clay layers (yellow zone) and possible soft zone/or void (red zone).

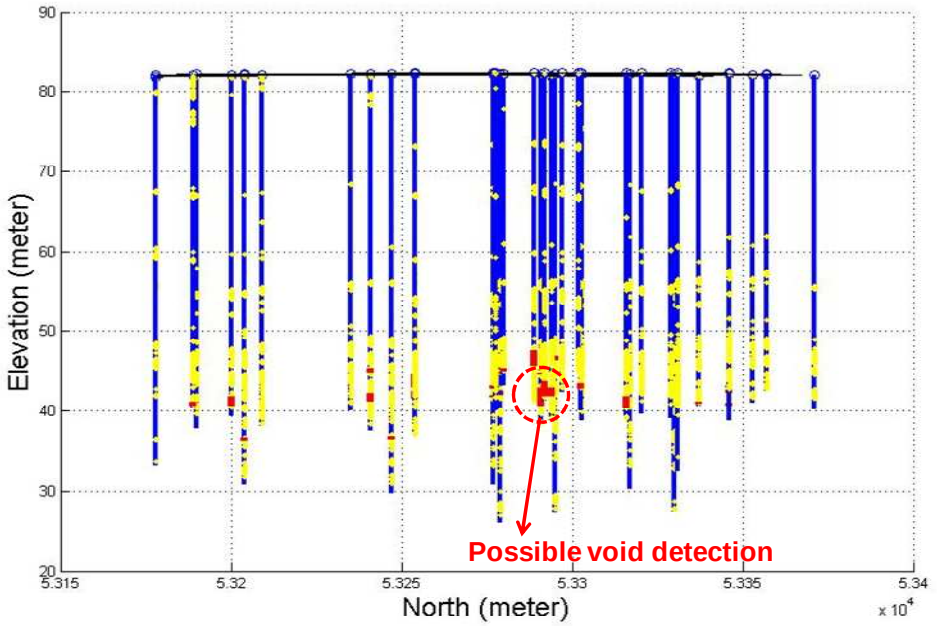

Figure 2.17. CPT profile (II – North-South direction) indicating estimated clay layers (yellow zone) and possible soft zone/or void (red zone).

In terms of vertical size magnitudes of the detected voids, additional detection frequency information is provided in Figure 2.18.

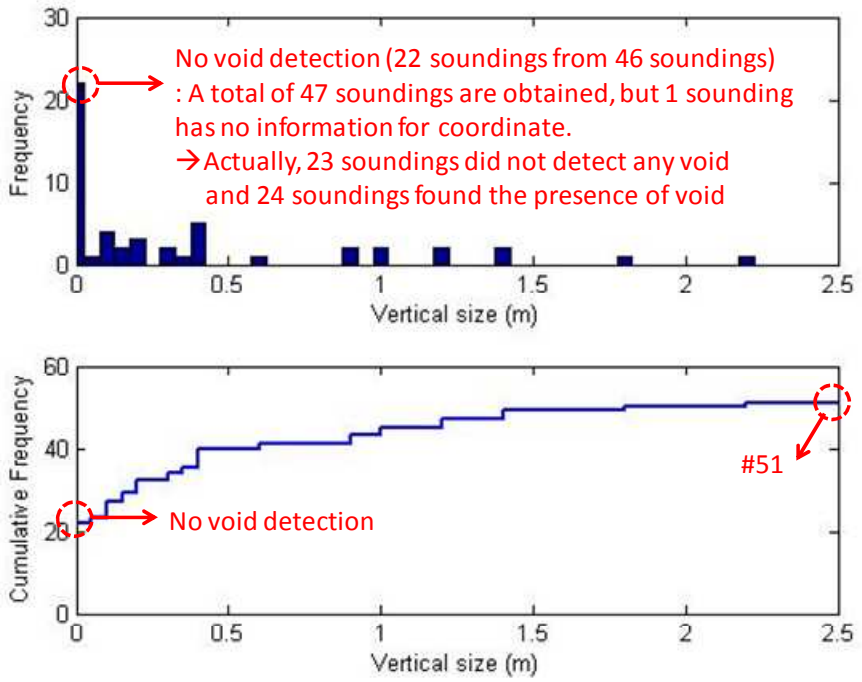

Figure. 2.18. Void detection frequency versus estimated vertical size of the detected voids at SRS K-site (CPT based).

2.3 Site Explorations at SRS

2.3.1 Soil Parameters and Classification from Field Tests

For geotechnical site characterization at SRS, extensive laboratory and field testing programs have been conducted over past several decades. For purposes related to geotechnical numerical simulations of computational stress and displacement predictions, it is necessary to assign parametric soil engineering values to the representative SRS geologic soil layers. Based on the current information, available data, and published reports, the recommend geomaterial parameters for different SRS geologic units are discussed in Appendix C. For details regarding the recommended values, evaluation

methods, and sources, refer to the Appendix C. Basically, field investigations using CPT and DMT apply empirical methodologies shown in Table A.1 (Appendix A).

Herein, in-situ soil classification approaches are provided based on traditional laboratory grain size distributions, CPT data, and DMT soundings. First, soil behavior profiles were obtained from two types of CPT soil classification indices (I_{cRW} and I_{cJB}; for Figures 2.19a and 2.19b, respectfully) using the CPT mean soundings (Figure 2.9) at SRS APT. As noted, it seems that the predominant soil types are sandy mixtures. This soil behavior type estimation can be reasonably compared with a gradation profile obtained from laboratory testing at the SRS (Figure 2.19c), with good agreement.

In addition, DMT data can provide an equivalent approach and indirect assessment of soil type (Marchetti, 1980). A total of 13 flat plate dilatometer test (DMT) soundings were obtained at the Salt Waste Processing Facility (SWPF) site at SRS. The mean values of contact pressure (P_0) and expansion pressure (P_1) profiles are shown in Figure 2.20a. Similar to the CPT analysis, a representative soil type profile on the basis of DMT material index (I_D) is provided in Figure 2.20b. Here the profile suggests mostly a sand profile having appreciable fines content, corresponding to either a silty sand to clayey sand over much of the sounding depths to 48 m. Again, the results are consistent with the lab mechanical analyses.

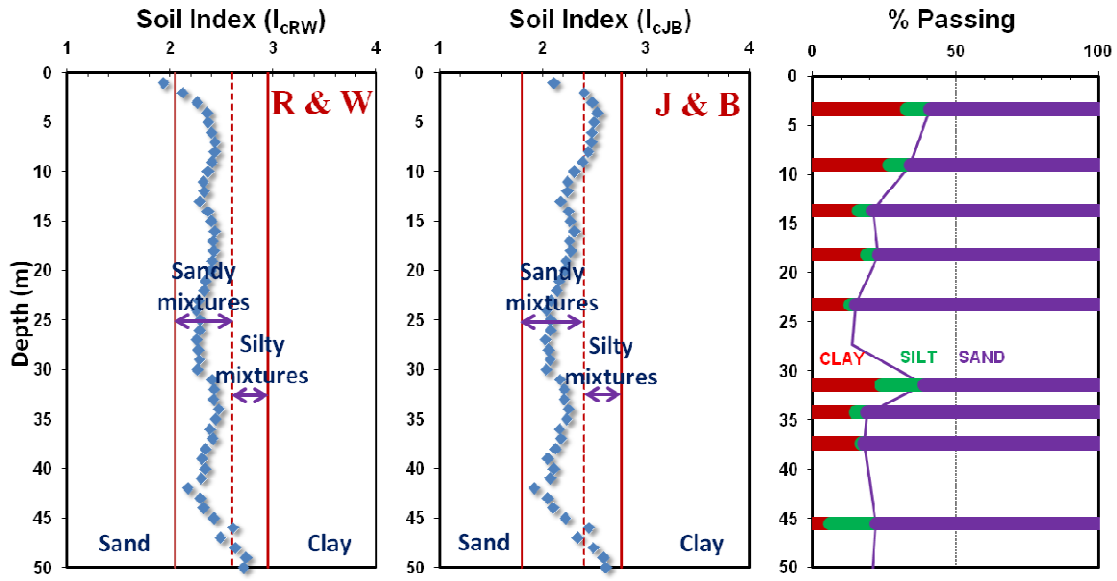

Figure 2.19. Soil behavior profiles based on CPT soil classification index (I_c) by (a) Robertson and Wride (1998); (b) Jefferies and Been (2006) at SRS; (c) Gradation profile from laboratory testing.

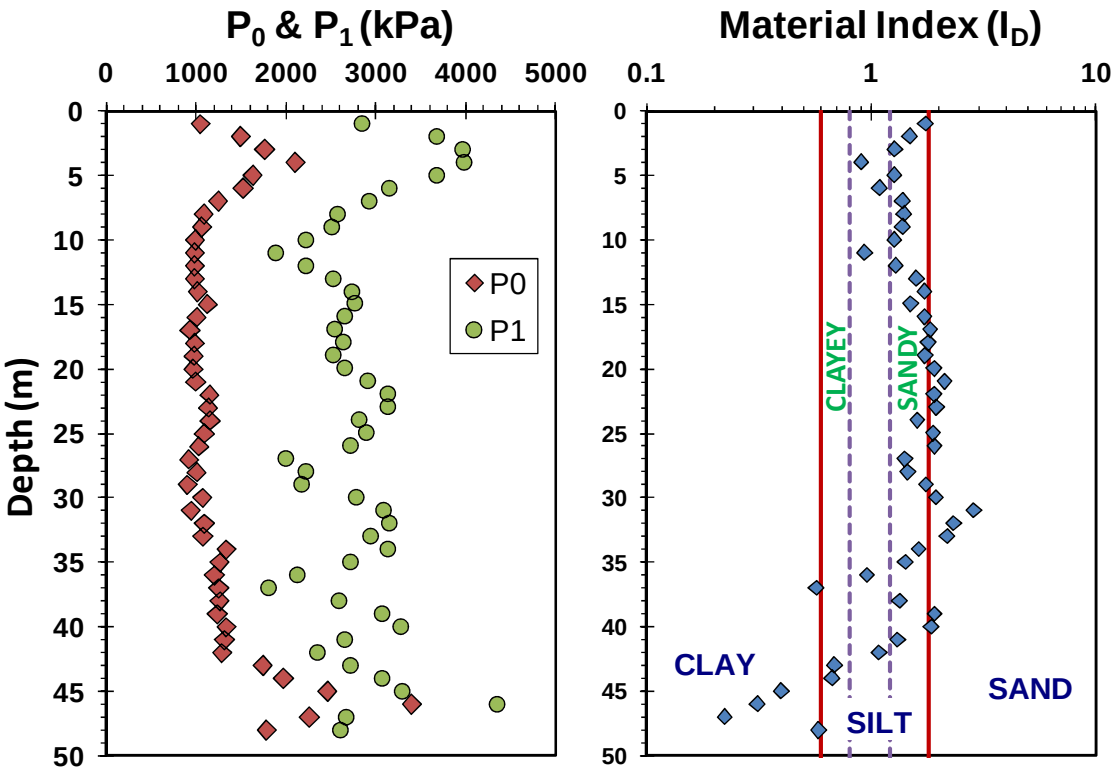

Figure 2.20. (a) Mean lift off pressure (P_0) and expansion pressure (P_1) with depth; and (b) representative soil profile based on DMT material index at SRS

2.3.2 Difficulties in Evaluating Stress History at SRS

The traditional means to evaluate stress history is via one-dimensional consolidation tests on undisturbed samples. In this regard, a review of the interpreted preconsolidation stress versus depth evaluated from the laboratory consolidation test data at the SRS SWPF was conducted (data from Shannon and Wilson Report 2007). A total of 41 incremental load (IL) tests and 58 constant rate of strain (CRS) tests were analyzed using interpretative schemes: (a) Casagrande (1936), (b) Becker et al. (1987), (c) Boone (2010), and other approaches. Additionally, to quantify the level of laboratory sample disturbance, a rating system developed by Terzaghi et al. (1996) is adopted. The ratings are categorized from 'A' (excellent) to 'E' (very poor quality), based on the volumetric strain [$\varepsilon_{vol} = \Delta e/(1+e_o)$] needed to reach the in-situ effective overburden stress level. The rating criteria are shown in Table 2.1.

Table 2.1. Ratings of sample disturbance for consolidation data
(after Terzaghi et al.,1996)

Volumetric strain (%)	< 1	1 - 2	2 - 4	4 - 8	> 8
Quality	A Excellent	B Good	C Fair	D Poor	E Very Poor

Note: where volumetric strain, $\varepsilon_{vol} = 100\cdot(\Delta e/(1+e_o)$ to return to σ_{vo}'

Herein, the preconsolidation stress (σ_p') evaluation results from the SRS consolidation test data are provided based on the common graphical Casagrande (1936) method (evaluated by Shannon and Wilson 2007). The profile of developed σ_p' from this method is shown in Figure 2.21. The profile is separated by approximate geologic formations at SRS SWPF. The evaluation results appear considerably scattered. In addition, sample disturbance seems significant. Alternative interpretations of σ_p' at SRS

have been made too as evaluated using the Becker et al. (1987) method (by Shannon and Wilson 2007) and Boone (2010) method (by author). Both results are provided in Appendix D. The σ_p' determination by more recent Boone (2010) method is also introduced. Later, details concerning the laboratory consolidation test data analyses will be provided with other attempted approaches for stress history evaluation at SRS (e.g., OCR estimation from CU triaxial tests).

Also, based on the noted profiles of CPT resistances (Figure 2.9) and DMT data (Figure 2.20) at the DOE site, the preconsolidation stress (σ_p') has been estimated for the geologic units (Figure 2.21). The magnitude of σ_p' is directly estimated using CPT data from Equation A.8 (Appendix A). In case of DMT data, σ_p' is calculated from the OCR value estimated by the Equation A.10 ($\sigma_p' = OCR \times \sigma_{vo}'$). In addition to the σ_p' estimations from CPT and DMT, in-situ V_s measurements from DHT(i.e., V_{sVH}) also make it possible to assess the σ_p' profile from the regression equation using small strain shear stiffness (Equation 2.4, Mayne 2003):

Equation (2.4) $$\sigma_p' = 0.101 \cdot (\sigma_{atm})^{0.102} (G_{max})^{0.478} \cdot (\sigma_{vo}')^{0.42}$$

All σ_p' profiles predicted from in-situ measurements are compared with the laboratory consolidation test results in Figure 2.21. The profile of yield stress (i.e. apparent preconsolidation) evaluated from various in-situ and laboratory tests show inconsistent and conflicting interpretations. The profiles indicate apparent normally consolidated or lightly overconsolidated characteristics, as well as moderately overconsolidated conditions, based on the particular test and/or method of interpretation.

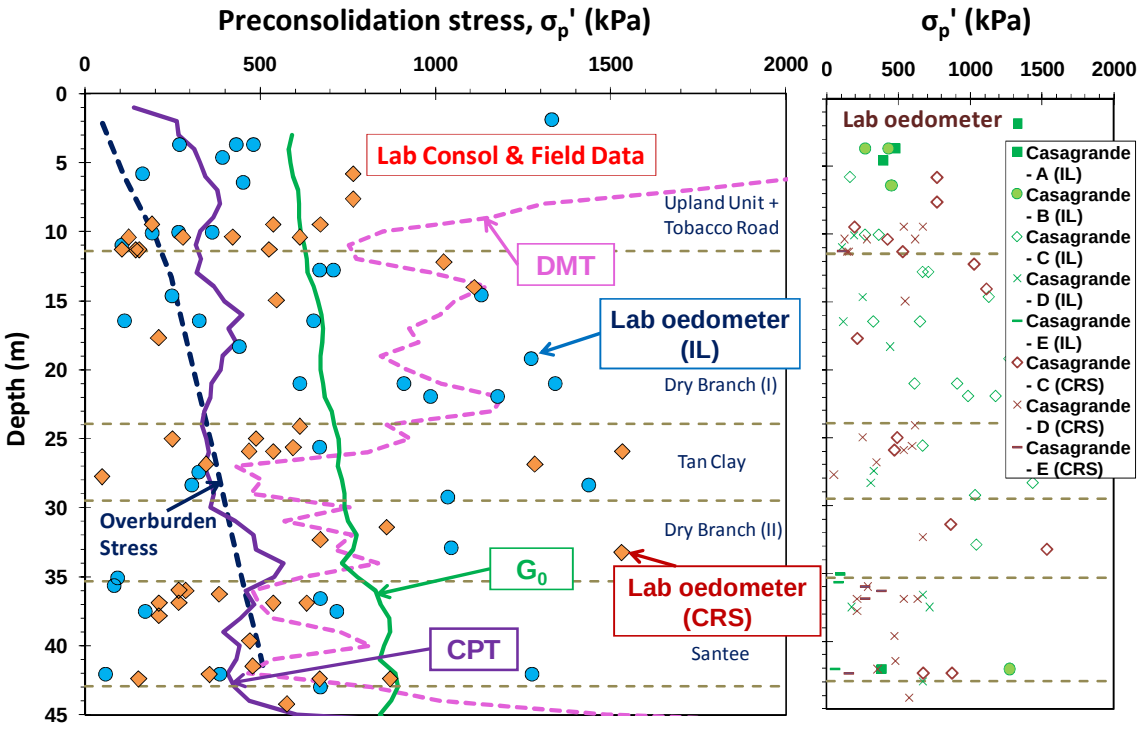

Figure 2.21. (a) Preconsolidation stress (σ_p') evaluations by various in-situ tests and laboratory consolidation data (Casagrande method) at SRS, (b) detailed laboratory oedometer test results with sample disturbance assessment.

Note: IL = incremental load, CRS = constant rate of strain, Sample quality: A = excellent, B = good, C = fair, D = poor, E = very poor.

Overall, considering the very old geologic age of the SRS deposits (Eocene and Miocene age), the stress history estimated from in-situ and laboratory tests appears unusual. It would be expected that such old deposits would have considerably higher OCRs. In fact, other Atlantic Coastal Plain deposits show higher OCR profiles than those at SRS including: (a) Calvert Formation, Richmond VA (Martin and Drahos 1986); (b) Yorktown Formation, Newport News VA (Mayne, 1989); (c) Calvert Cliffs, MD (UNS Report , 2010); and (d) Cooper Marl, Charleston SC (Camp 2004).

In addition to the sample disturbance effects, some low OCRs and scattered interpretations might have resulted from the noted complex geologic conditions at SRS. For instance, Santee alterations causing voids, soft zones, and cave formation by dissolution processes might have affected the overlying overburden soils, thus the geostatic stress state may have been altered. Collapsed soil columns coupled with arching and/or faulting and subsidence may have reduced the overburden stresses. For instance, if some localized portions of the upper soil column are assumed collapsed, some regions might be altered to active lateral earth pressure (K_A) state while other regions remain in relatively high at-rest lateral earth pressure (K_0) state, specifically in the case of highly overconsolidated intact soils. Figure 2.22 describes graphically the expected scenario.

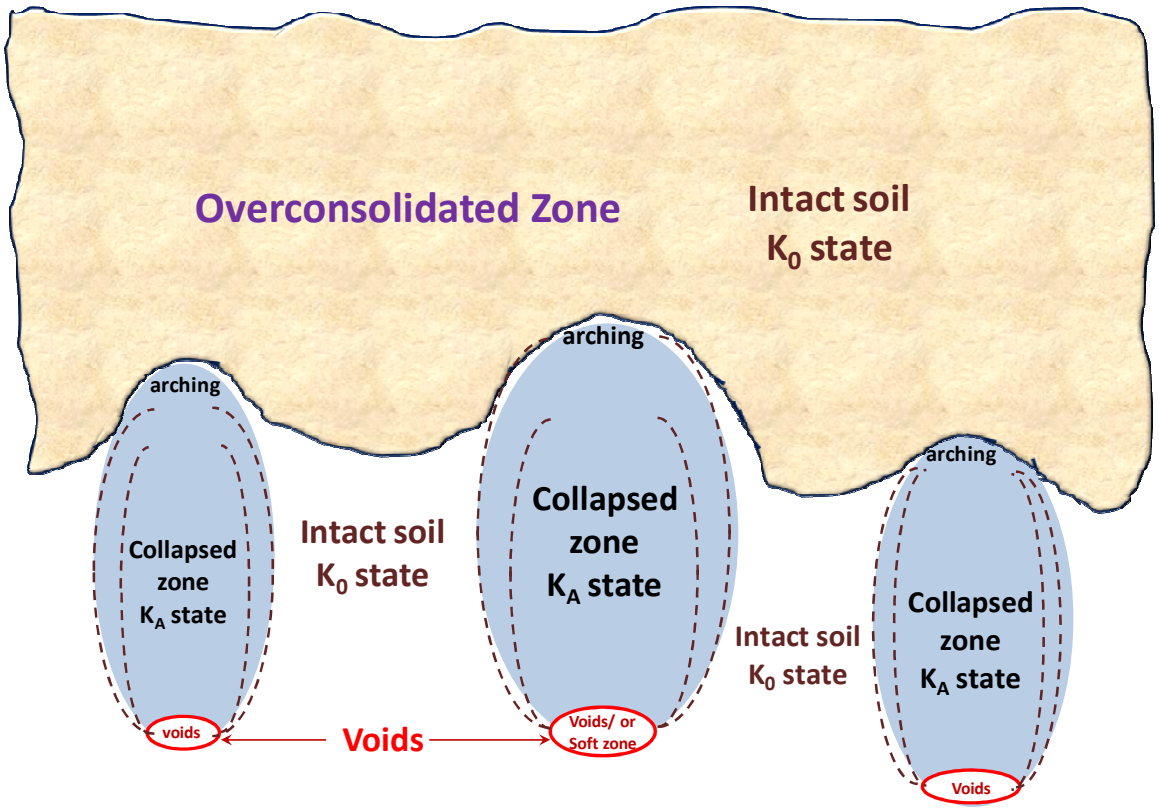

Figure 2.22. Hypothesis of collapsed soil column resulted from voids or soft zones.

This scenario might be demonstrated by the noted considerably scattered laboratory consolidation results from the Casagrande method (Figure 2.21). Also, it could be established by compilation of each stress history (σ_p') and K_0 evaluation result based on 13 DMT soundings as shown in Figure 2.23 and Figure 2.24. In some potential regions from limited DMT soundings, unusual evaluations are observed, including underconsolidated and/or significantly low earth pressure. Similarly, CPT soundings show highly variable results of overconsolidation ratio at SRS K-site in Figure 2.25. These inconsistent stress history and lateral earth pressure evaluation results might confirm that partial SRS soil layers are not horizontally homogeneous any more with respect to geostatic stress state.

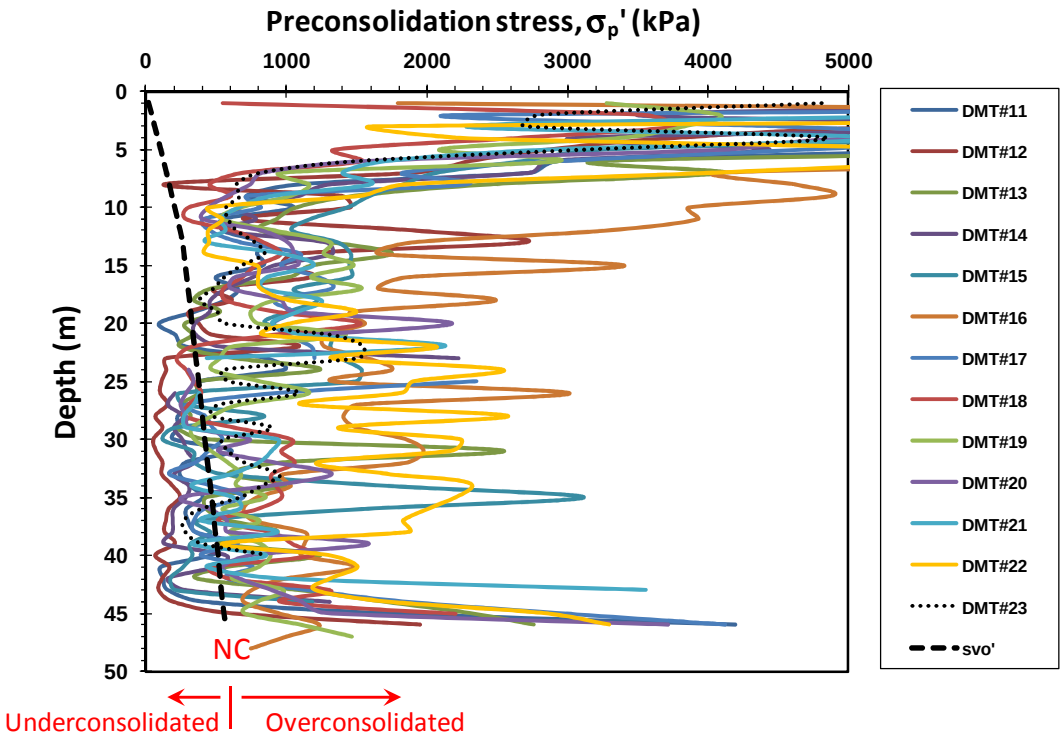

Figure 2.23. Compilation of preconsolidation stress assessments using DMT soundings at SRS SWPF (Equation A.10)

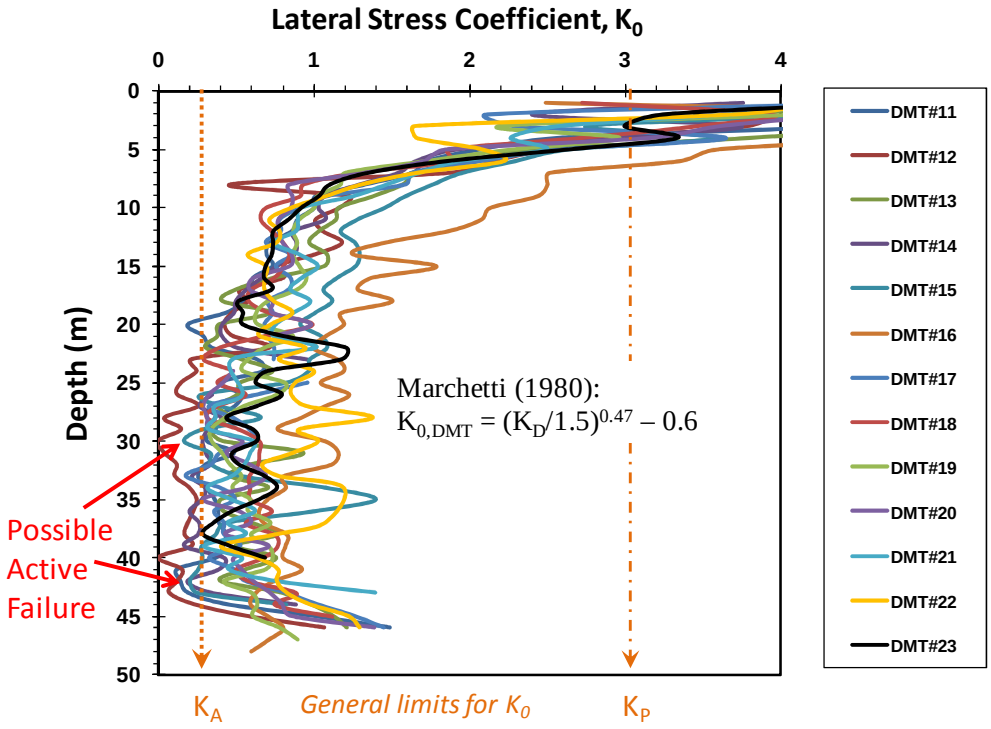

Figure 2.24. Compilation of K_0 assessments using DMT soundings at SRS SWPF.

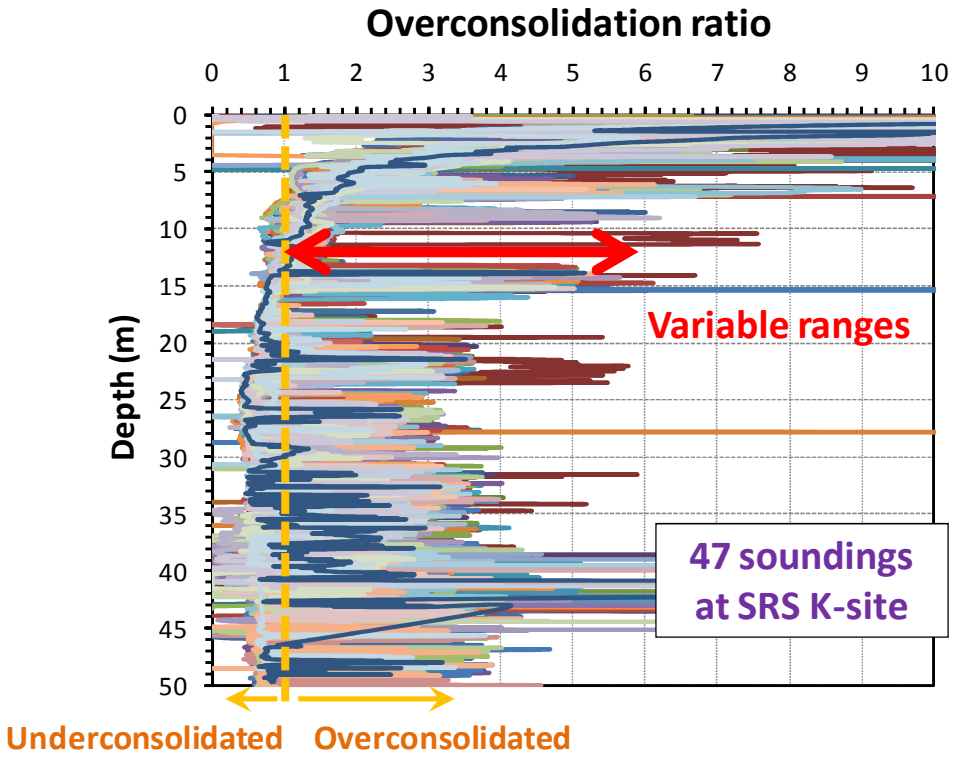

Figure 2.25. Compilation of overconsolidation ratio evaluations using CPT soundings at SRS K-site (Equation A.8).

Combined site-specific and complex geological conditions may have also affected typical estimations of soil behavior, properties, and stress history expected from conventional in-situ tests recordings (e.g., effects by gap-graded soils, calcareous soils, cementious bonding, desiccation, ageing, and Santee alteration). Therefore, it seems prudent to re-evaluate the stress history at SRS by a completely new approach such as use of geophysics, in order to provide a complementary and completely independent assessment.

CHAPTER 3

HIERARCHY OF V_S MODES AND STRESS-DEPENDENCY IN GEOMATERIALS

3.1 Introduction

Shear wave velocity (V_s) is widely used for geotechnical design problems, since it provides the small-strain shear modulus (G_0) which is a fundamental soil stiffness and the beginning of all stress-strain curves. The maximum shear modulus ($G_0 = G_{max}$) is obtained directly from: $G_0 = \rho \cdot V_s^2$, where ρ is the total mass density of the soil material and V_s is evaluated from one of several field and/or laboratory methods. The shear wave has directional and polarized characteristics, thus multiple types of V_s can be determined as follows: V_{sij} - where 'i' is the propagation direction and 'j' is the polarization direction (i.e. V_{sVH}, V_{sHV}, V_{sHH}) and the subscripts 'V' is for vertical and 'H' is for horizontal.

Different modes of V_s can be measured using bender element equipment on natural or reconstituted specimens in the laboratory. However, it may be preferable to use in-situ V_s measurements to preserve actual site-specific conditions and minimize sampling disturbance effects. Downhole tests (DHT) and crosshole tests (CHT) are representative field geophysical methods which can provide the specific V_s modes. With respect to the shear wave modes, this chapter examines the common hierarchy and general trend of shear wave velocity (V_s) with different directions of propagation and particle motion from mainly in-situ (i.e., crosshole, downhole) measurements and laboratory bender element data. The data sets are collected from worldwide sites where stress state, stress history, and several modes of V_s profiles have been obtained. The stress-dependency of V_s in geomaterials is also examined to observe site-specific trends and relationships for geostatic stress state.

3.2 Field Geophysics and Laboratory V_s Measurement Methods

In field testing, the most common shear wave mode is obtained by DHT (ASTM D 7400), which can be accomplished either in drilled-cased-grouted boreholes or by seismic CPT or seismic DMT (i.e. V_{sVH} mode). Standard CHT (ASTM D 4428) provides the V_{sHV} type using a downhole vertical hammer and geophones located in adjacent borehole(s) at the same elevation. The V_{sHH} type is produced by a special version of CHT using a horizontal triggering system like a rotary hammer (Butcher and Powell 1996), a special torsional vane (Sully and Campanella 1995), or an encased horizontal solenoid (Hiltunen et al. 2003). Herein, the nomenclature RCHT is used for rotary crosshole. If the depositional bedding plane is horizontal, it is noted that both propagation and polarization direction of V_{sHH} mode are parallel to the bedding plane.

In Figure 3.1, the schematics for these three geophysical methods are provided and the wave propagation and polarization directions corresponding to DHT, standard CHT, and rotary crosshole (RCHT) are depicted. There also exist V_s modes from suspension logger probing (SLP), surface refraction survey (SFRS), surface reflection survey (SFLS), and Rayleigh wave methods (SASW, MASW, CSW, PSW, ReMi), as discussed by Butcher and Powell (1995). For completeness, the various geophysical techniques for determining mechanical wave velocities can be shown in Figure 1.1 (Chapter 1), including non-invasive methods. A summary of all acronyms used for the field geophysical methods was provided in Figure 1.1 as well. Comprehensive application and details of geophysical methods were discussed by Wightman et al. (2003): Geophysics manual - Federal Highway Administration (FHWA).

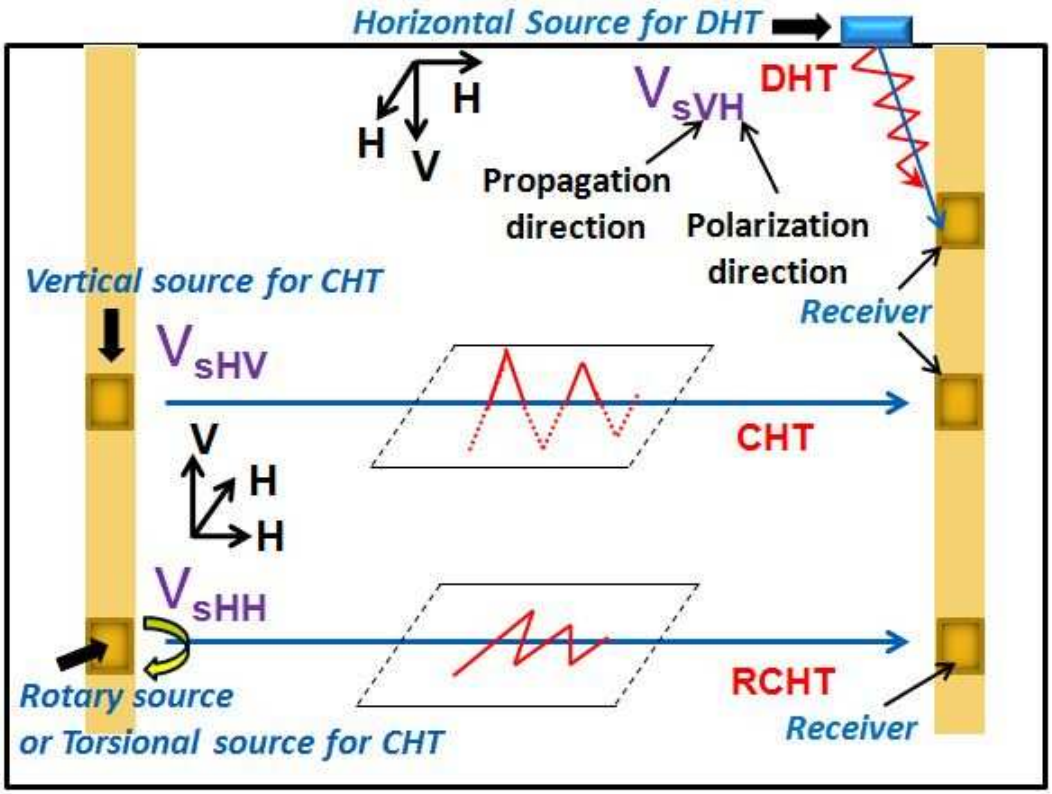

Figure 3.1. Types of in-situ V_s measurement methods in boreholes (DHT = downhole test, CHT = crosshole test, and RCHT = rotary crosshole).

On the other hand, as alternative approaches to measure V_s, laboratory testing methods can be applied. Recently, a widely adopted laboratory technique is bender element (BE) tests. The bender element consists of piezoceramic elements and can both generate and receive elastic waves. Particularly, it is relatively easy to generate different modes of V_s which depend on their propagation and polarization direction. The directional Vs modes (V_{sVH}, V_{sHV}, V_{sHH}) are described in Figure 3.2(a), (b), and (c). Also, Figure 3.2(d) describes approximate bender element testing system combined with an oedometer cell (Lee et al. 2006). Also, for reliable V_s measurements, Lee and Santamarina (2004) discussed many details regarding the bender element performance and generated shear wave interpretation.

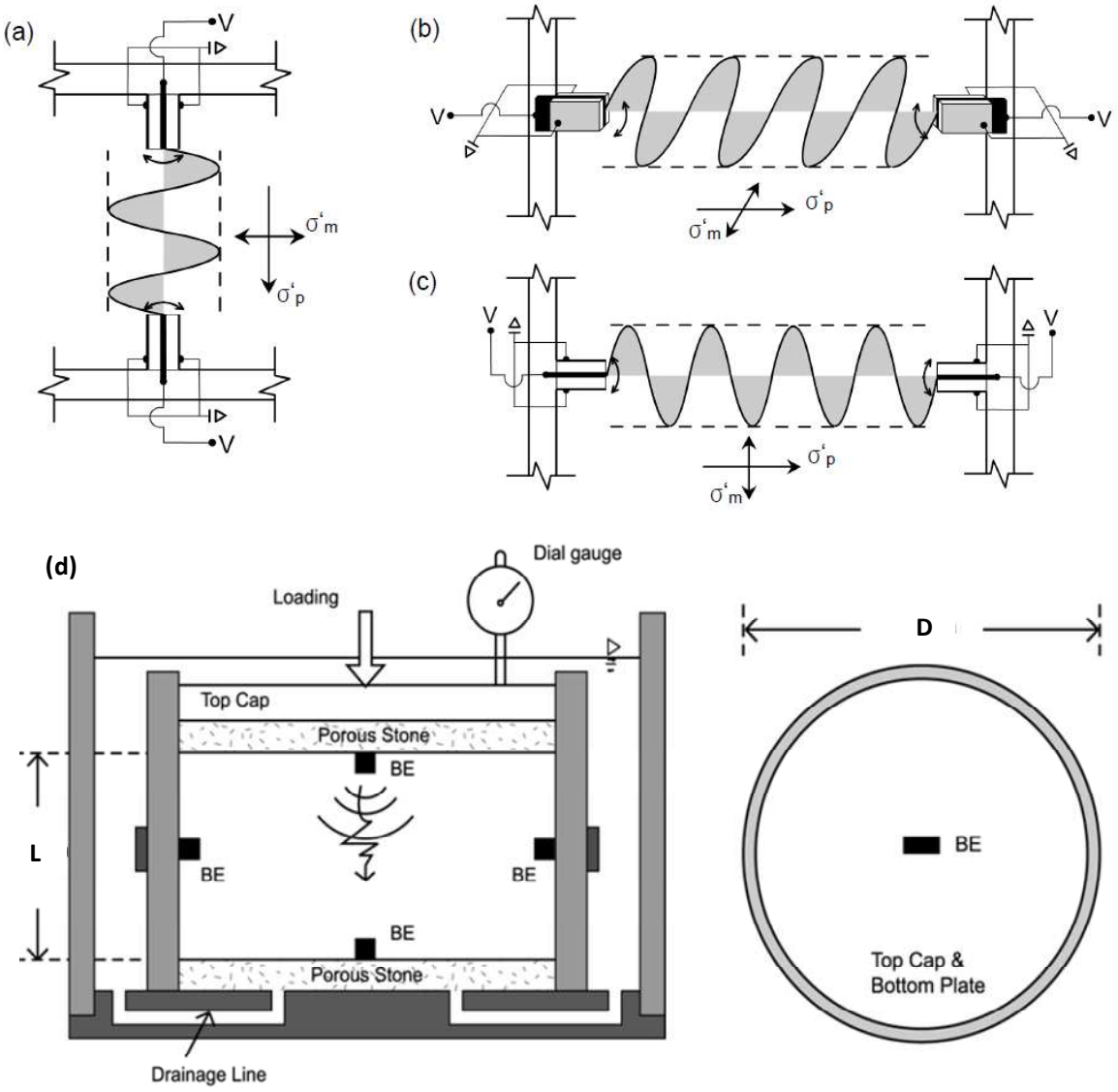

Figure 3.2. Three types of V_s modes depending on propagation and particle motion direction by bender setup: (a) V_{sVH}, (b) V_{sHV}, (c) V_{sHH} and (d) schematic of bender element testing system with oedometer (Lee et al. 2006).

Note: σ_p' = effective stress in propagation direction, σ_m' = effective stress in particle motion direction.

Resonant column (RC) test is also a representative laboratory G_0 and V_s measurement method. Basically, the RC test can measure shear modulus (G) and damping ratio (λ) from very small strain to medium strain levels. A cylindrical specimen

is placed with fixed bottom cap, then harmonic torsional shear is derived from top cap connected to accelerometer. The measured free vibration response is used to evaluate the dynamic soil properties. The test procedures and more details can be sought by ASTM D4015. A schematic of Stokoe-type RC device is shown in Figure 3.3. Other laboratory V_s or G_0 measurements may also be available from torsional shear (TS) test, non-resonance method, and triaxial test with local strain measurement system.

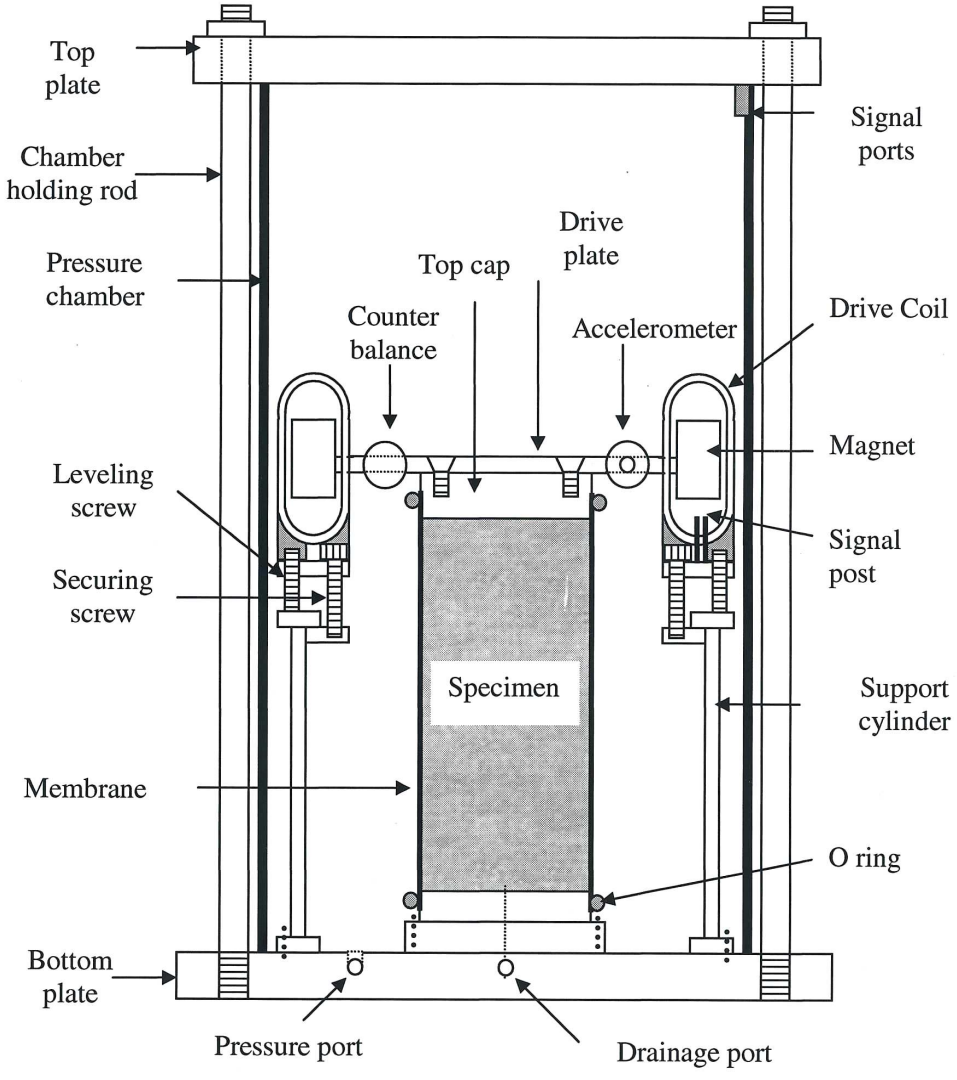

Figure 3.3. Schematic of Stokoe-type resonant column system (Meng 2003).

3.3 Factors Affecting Shear Wave Velocity

A number of factors influence the magnitude of shear wave velocity, as found from laboratory test programs on both undisturbed natural soils and reconstituted specimens and from field geophysical measurements.

3.3.1. Established V_s Relationships from Laboratory Testing

In order to quantify reliable G_0 and V_s, several empirical correlations have been suggested based on laboratory tests. Particularly, many early expressions were derived for G_0 based on mainly resonant column tests. Some notable early studies are introduced in chronological order. To begin with, Hardin and black (1968) suggested a specific equation for both clean sand and clay:

Equation (3.1) $$G_0 = 1230 \frac{(2.973 - e)^2}{1 + e} (OCR)^k (\sigma_o')^{0.5}$$

where $e < 2.97$, $0 < k < 0.5$, $\sigma_o' = (\sigma_1' + \sigma_2' + \sigma_3')/3$, G_0 and σ_o' have psi unit. It is noted that mean normal stress (σ_o'), void ration function and OCR are included in the equation. For sands, Seed and Idriss (1970) proposed the following expression:

Equation (3.2) $$G = 1000 K_2 (\sigma_o')^{0.5}$$

where G and σ_o' are in psf unit. K_2 represents void ratio effect and varies depending on shear strain levels. For K_2 determination, a graphical chart was provided in the study (e.g., $30 < K_{2,max} < 75$). As other empirical expression, Anderson and Stokoe (1978) suggested ageing or time-dependent effect for G_0:

Equation (3.3) $$G_{0,time-dependent} = G_0 (t = t_{ref}) \times \left(1 + N_G \log \frac{t}{t_{ref}} \right)$$

where t_{ref} = reference time (e.g., time at the end of primary consolidation), N_G = $\Delta G_0/G_0(t=t_{ref})$. This expression indicates that G_0 generally increases with time. Figure 3.4 shows the observed time effects on G_0 (Anderson and Stokoe 1978). Also, many other studies examined to derive the proper G_0 correlations. More general and comprehensive G_0 expressions (e.g., Hardin 1978, Hardin and Blandford 1989) will be discussed in Chapter 4. From these early studies for G_0, the expression can be replaced in terms of V_s (i.e, $G_0 = \rho \cdot V_s^2$).

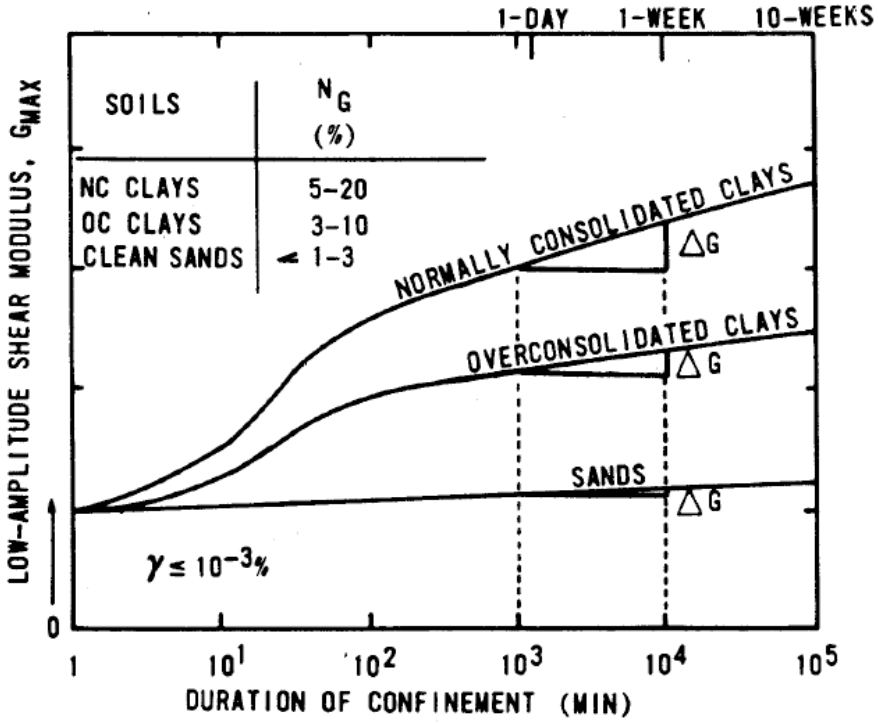

Figure 3.4. Observed time effects on G_0 for clays and sands (Anderson and Stokoe 1978).

Afterward, with respect to the confining stress states, an important observation was found. It was known that V_s depends on the effective stress in the direction of propagation and the stress in the plane of polarization, thereby leaving out one of the three principal stresses from a Cartesian coordinate system (Roesler 1979; Stokoe et al.

1991). The directional property and stress dependency of V_s can relate to stress-induced anisotropy in soils.

Based on these characteristics of shear wave velocity, various V_s – stress relationships have been suggested (Table 3.1). In terms of primarily the effective confining stress, the more widely acknowledged models are the mean normal stress method (Yan and Byrne 1990, Santamarina et al. 2001):

Equation (3.4) $$V_s = \alpha \cdot (\sigma_o')^{\beta}$$

where $\sigma_o' = (\sigma_1'+\sigma_2'+\sigma_3')/3$ and the individual stress method:

Equation (3.5) $$V_s = C \cdot (\sigma_x')^{n_x} (\sigma_y')^{n_y}$$

where σ_x' is the principal effective stress in the propagation direction, σ_y' is the principal effective stress in the polarization direction. The parameters α and C are stiffness values and exponents β and n indicate stress level dependency. Using a collected special database, the stress-dependency of V_s in soil geomaterials will be discussed later based on the representative V_s – stress relationships.

As indicated the early G_0 expressions (i.e., Equation 3.1, 3.2, 3.3), the V_s relationships might be reasonably extended to more general concepts using three primary factors: the stiffness/ageing coefficient (C_S; relating to soil structure, fabric, and other variables), void ratio, and stress state. The first two factors are related to inherent (structural) soil anisotropy. The inherent anisotropy at any site location may result from a variety of causes such as depositional processes, stratification, fabric, or cementation. The inherent soil anisotropy might have a critical influence on V_s measurements in different soil planes.

Table 3.1. Proposed V_s-σ' relationships for uncemented soils

V_s – Stress relationships	**References**
$V_s = (\sigma_x')^{nx} \cdot (\sigma_y')^{ny} \cdot (\sigma_z')^0$ σ_x : Wave propagation direction σ_y : Particle-motion direction σ_z : Orthogonal to σ_x and σ_y	Roesler (1979)
▪ *Inherent (structural) Anisotropy* $V_s = C \cdot (\sigma_o')^n$ where, $\sigma_o' = (\sigma_x' + \sigma_y' + \sigma_z')/3$ ▪ *Stress-Induced Anisotropy* $V_s = C \cdot (\sigma_x')^{nx} \cdot (\sigma_y')^{ny}$	Stokoe et al. (1991)
$V_s = C \cdot (\sigma_x')^{nx} \cdot (\sigma_y')^{ny}$ *For Rotary Crosshole* ; $\sigma_{ho}' = \sigma_x' = \sigma_y'$ $V_{sHH} = C \cdot (\sigma_{ho}')^{[nx+ny]}$	Butcher and Powell (1995, 1997)
▪ *Mean normal stress method* $V_{sVH} = C_{sVH} \cdot (\sigma_o')^n$ where $\sigma_o' = [(1+2K_0)/3] \cdot \sigma_{vo}'$ $V_{s\,HH} = C_{sHH} \cdot (\sigma_o')^n$ ▪ *Average stress method* $V_{sVH} = C_{sVH} \cdot [(\sigma_v' + \sigma_h')/2]^n = C_{sVH} \cdot (\sigma_{vo}')^n \cdot [(1+K_0)/2]^n$ $V_{sHH} = C_{sHH} \cdot [(\sigma_h' + \sigma_h')/2]^n = C_{sHH} \cdot (\sigma_{vo}')^n \cdot K_0^n$ ▪ *Individual stress method* $V_{sVH} = C_{sVH} \cdot (\sigma_v')^{n/2} \cdot (\sigma_h')^{n/2} = C_{sVH} \cdot (\sigma_{vo}')^n \cdot (K_0)^{n/2}$ $V_{sHH} = C_{sHH} \cdot (\sigma_h')^{n/2} \cdot (\sigma_h')^{n/2} = C_{sVH} \cdot (\sigma_{vo}')^n \cdot (K_0)^n$ K_0 : at-rest lateral stress coefficient	Yan and Byrne (1990) Sully and Campanella (1995)
▪ *Downhole* $V_{sVH} = C_{sVH} \cdot [F(e)]^{0.5} \cdot (\sigma_x')^{nx} \cdot (\sigma_y')^{ny}$ ▪ *Conventional Crosshole* $V_{sHV} = C_{sHV} \cdot [F(e)]^{0.5} \cdot (\sigma_x')^{nx} \cdot (\sigma_y')^{ny}$ ▪ *Special Rotary Crosshole* $V_{sHH} = C_{sHH} \cdot [F(e)]^{0.5} \cdot (\sigma_x')^{nx} \cdot (\sigma_y')^{ny}$ F(e) : the void ratio function	Fioravante et al. (1998)
▪ *Isotropic state of stress* $V_s = \alpha \cdot (\sigma_o'/1\ \text{kPa})^{\beta}$ where, $\beta \approx 0.36 - \alpha/700$ ▪ *Stress Anisotropy* $V_s = \Omega \cdot (\sigma_x'/1\ \text{kPa})^{\theta} \cdot (\sigma_y'/1\text{kPa})^{\delta}$ $V_s = \Theta \cdot [(\sigma_x' + \sigma_y')/2\ \text{kPa}]^{\varsigma} \cdot [(\sigma_x' - \sigma_y')/2\ \text{kPa}]^{\psi}$ Ω, Θ represent the stiffness of the particle and the void ratio	Santamarina, Klein, and Fam (2001)

Note : For all equations, coefficients (C, C_{sVH}, C_{sHV}, C_{sHH}, α, Ω, Θ) and exponents (n, n_x, n_y, β, θ, δ, ς, ψ) are material constants related to the soil properties

3.3.2. Established V_s Relationships from Field Testing

It is well-appreciated that the magnitude of in-situ V_s measurements generally increases with depth. For a variety of Quaternary age soils, Lew and Campbell (1985) suggested an empirical equation based on over 270 V_s surveys including data from refraction, DHT, and CHT measurements. The regression-based empirical expression for shear wave velocity (V_s in feet/second) includes the following:

Equation (3.6) $$V_s = K \cdot (d+c)^n$$

where d = depth (feet) and the parameters K, c and n are constants dependent on the specific soil type and geotechnical classification: (a) soft natural soils (K = 5.39, n = 0.385, c = 5.33); (b) intermediate soils (K = 5.57, n = 0.402, c = 5.24), and (c) firm natural soils (K = 6.26, n = 0.280, and c = 0.54). Also, Foti (2012) compared borehole seismic tests (DHT, CHT) and noninvasive SASW results at some Italian sites. The in-situ V_s profiles at the sites show the equivalent trends which generally increase with depth. Example sites are shown in Figure 3.5. Similarly, Brown et al. (2002) observed the same trends using downhole V_s and SASW at 10 strong-motion sites, CA.

More recently, Andrus et al. (2007) showed several empirical equations for V_s estimation of soils having various geologic ages. The depth factor is included with other variable factors such as cone tip resistance (q_t), soil type, and geologic age for the V_s prediction. One general format is as follow:

Equation (3.7) $$V_s = 2.27 \cdot q_t^{0.412} \cdot I_c^{0.989} \cdot D^{0.033} \cdot ASF$$

where V_s = shear wave velocity (m/s), q_t = cone tip resistance (kPa), I_c = CPT soil behavior type index (here, $I_c=[(3.47-\log Q)^2+(\log F+1.22)^2]^{0.5}$; Q and F are normalized cone tip resistance and friction ratio), D = depth (meter), and ASF = age scaling factor (1

for Holocene age, 1.22 for Pleistocene age, 2.29 for Tertiary age: Cooper Marl). In these V_s studies, it was found the V_s trend increases as a power law with depth.

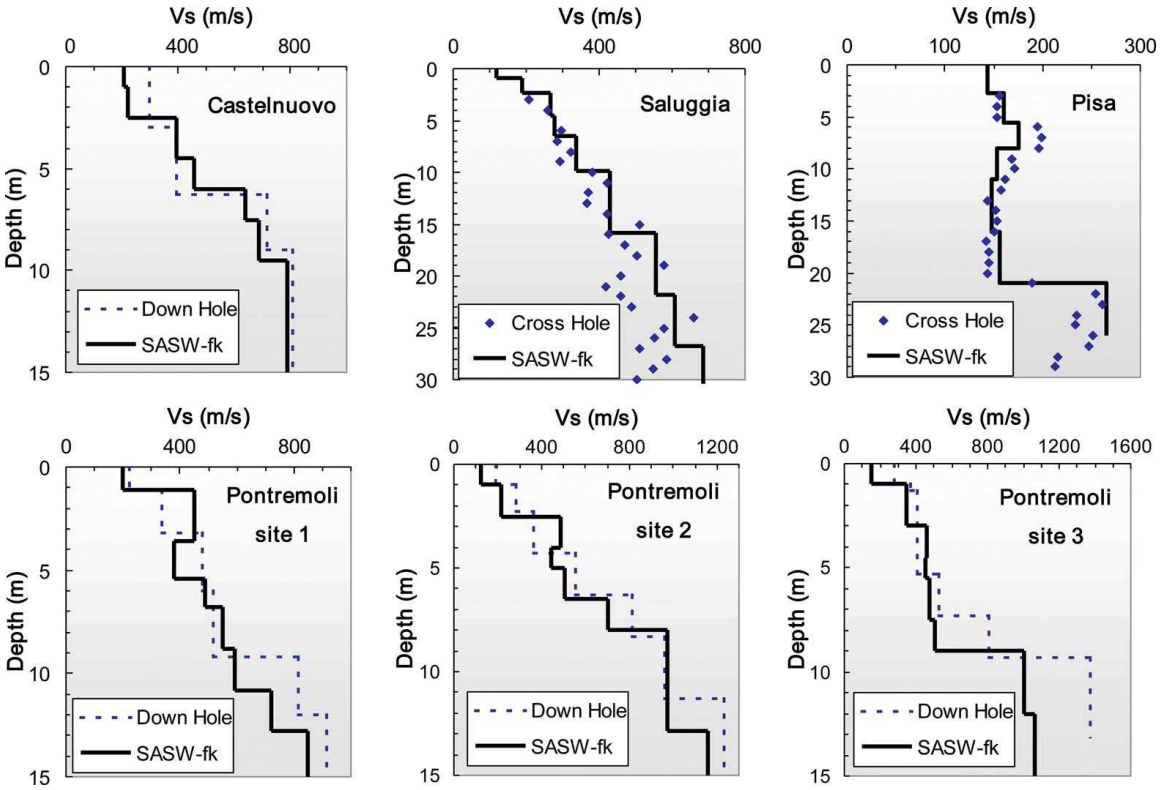

Figure 3.5. Examples of in-situ V_s profiles (downhole/crosshole and SASW) measured at some Italian sites (Foti 2012).

As shown in laboratory V_s measurements, the in-situ V_s can be also expressed using effective confining stress. For example, Butcher and Powell (1995) and Fioravante et al. (1998) applied the individual stress method based on field test results (Table 3.1). In fact, field V_s measurements are more preferable for geotechnical design practice because of two main reasons: 1) sample disturbance effects for laboratory tests, 2) ageing or time-dependent effect. With respect to the sample disturbance effect, Figure 3.6 shows considerable unwanted stress path changes which tend to occur during sampling process, transportation, and specimen preparation (Ladd and DeGroot 2003). The estimated reduction in true in-situ value will be discussed (i.e., based on G_0 values) in Chapter 4.

For the second issue, an example of time-dependent effect was already introduced in Figure 3.4 (Anderson and Stokoe 1978). Apparently the laboratory samples lose their age effects once extruded from tube to trim a specimen. In addition, they are exposed to zero isotropic state of stress in the process. Consequently, it is expected that in-situ V_s measurements can represent actual soil conditions in pristine status.

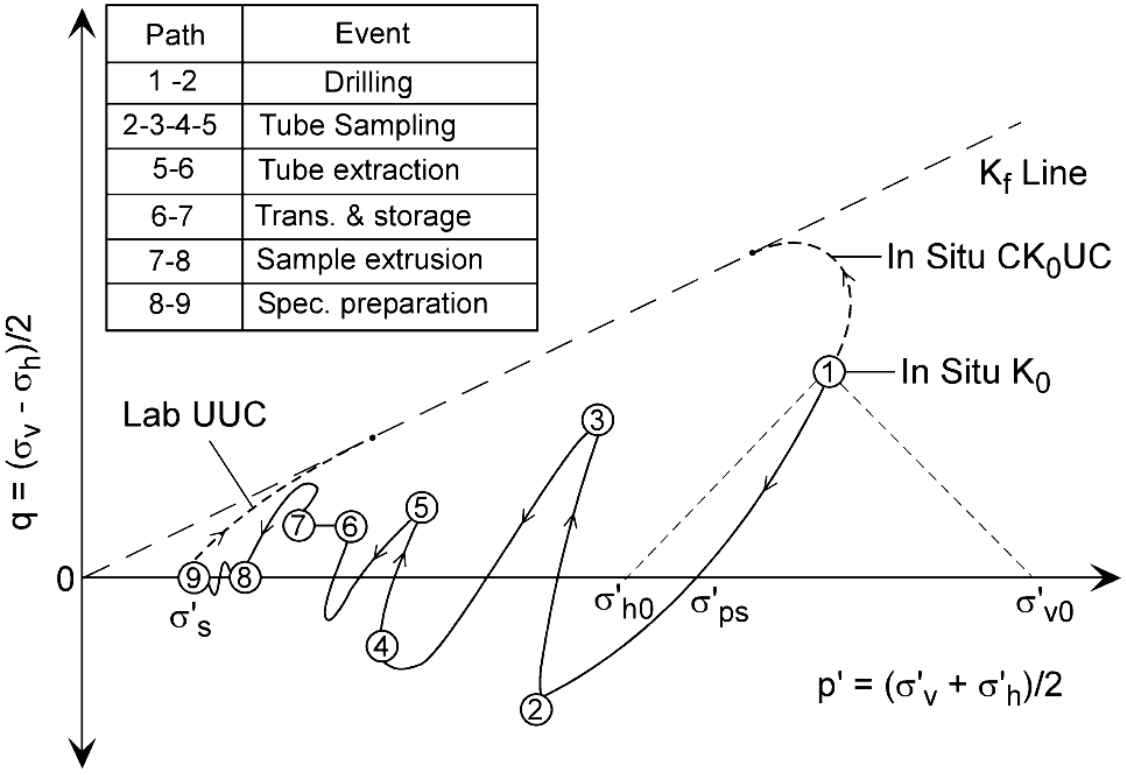

Figure 3.6. Possible stress path changes of lightly overconsolidated clay during sampling, transportation, and specimen preparation (adopted from Ladd and DeGroot 2003).

3.4 Shear Wave Velocity Database and Modal Hierarchy in Geomaterials

To investigate the "normal" trends of V_s with depth and the corresponding effects of geostatic stress state, shear wave anisotropy, direction, and mode, two database sets of shear wave velocity have been compiled: (a) field data and (b) laboratory data. Specifically, multiple types of shear wave velocity measurements on various geomaterials have been obtained (i.e., V_{sHH}, V_{sVH}, V_{sHV}), as available from either the open literature and/or unpublished reports and technical documents.

With respect to in-situ V_s measurements, data collected at 7 UK sites by Butcher and Powell (1995, 1997), Hight et al. (2003), and Bates and Phillips (2000) showed specific trends among different types of V_s magnitudes. Normally consolidated soils exhibiting low lateral stress K_0 values have similar V_s magnitudes for all modes. On the other hand, hard overconsolidated soils ($K_0 > 1$) show a hierarchy as follows: $V_{sHH} \geq V_{sHV} \geq V_{sVH}$. Interestingly, at the overconsolidated UK sites, the V_{sHV} data show rather higher magnitudes than V_{sVH} types. It might be due to the effects of inherent anisotropy, or possibly fissuring. Stress-induced anisotropy theoretically has to result in same magnitudes for V_{sVH} and V_{sHV} in terms of V_s-stress relationships. For further in-situ V_s data analysis, a large set of field data has been compiled. The specific site location, soil type, available V_s types, and reference source details are given in Table 3.2.

Table 3.2. Database listing of sites, soil types, V_s modes, and references for in-situ data

Field Site	Soil type	V_s modes	OCR	Void ratio	Reference Source
San Matteo, Italy	Po river sand	VH,HV,HH	1.3-1.9	0.77-1.19	Fioravante et al.(1998)
Texas A&M, TX	Deltaic Sand	VH,HV	1.8-4.5	0.75-0.78	Gibbens & Briaud (1994)
Holmen, Norway	Loose Sand	VH,HV	1	0.83-1.1	Butcher & Powell (1996)
Higashi-Ohgishima, Japan	Loose Sand fill	VH,HV,HH	1	1.0	Shibuya et al.(1995)
Treasure Island, CA	Loose Sand, Silty sand	VH, HV,HH	1	0.68	Henke and Henke (2002); Rollins et al. (1994)
Vincent Thomas Bridge, CA	Silty sand	HV,HH	1	N/A	Hiltunen et al.(2003)
Laing Bridge South, BC	Sand & clayey silt	VH,HV,HH	1	1.18	Sully (1991)
Opelika, AL	Residual silty sand and sandy silt	VH,HV,HH	2-6	0.76-0.83	Henke and Henke (2002), Mayne & Brown (2003)
Vagverket (Borlange), Sweden	Silt, clayey silt, silty clay	VH	1-5	0.8	Svensson & Moller (2001)
Vatthammar, Sweden	Silt, clayey silt, silty clay	VH	3	0.69	Svensson & Moller (2001)
Malamocco, Italy	Sandy silt, Clayey silt	VH,HV	2-7.6	0.7-0.8	Simonini (2004)
Lower 232 St., BC	Soft to firm NC & OC clayey silt	VH,HV,HH	1.2-10	1-1.9	Sully (1991)
200th St., BC	Soft to stiff NC & OC clayey silt	VH,HV,HH	1.2-12.9	1-2	Sully (1991)
University of Porto, Portugal	Residual sandy silts, silty sands	VH,HV	1-2	0.73	Viana da Fonseca et al.(2005)
Museumpark, Norway	Soft Drammen clay	VH,HV	1.2	0.8-1.8	Butcher & Powell (1995)
Bothkennar, UK	Soft silty clay	VH,HV,HH	1.3-2.2	1.3-1.9	Butcher & Powell (1997)
Lake Fill (Northwestern), IL	Soft to medium clay	VH, HV	1.4	0.5-0.53	Tumay (1997)
Norrkoping, Sweden	Clay, Varved clay	VH	1.2-1.6	1.2-3.2	Svensson & Moller (2001)
Lilla Mellosa, Sweden	Clay, organic clay	VH	1.1-1.5	2.7-3.5	Svensson & Moller (2001)
Montalto di Castro, Italy	Stiff Clay	HV,HH	2.3-3.3	0.7	Fioravante et al.(1998)
Fucino, Italy	Calcareous Clay	VH,HV	1.6-3	1.6-2.7	Foti et al.(2006)

Table 3.2. continued

Field Site	Soil type	V_s modes	OCR	Void ratio	Reference Source
Onsoy, Norway	Soft clay	VH	1.2-3.1	1.6-1.8	Long and Donohue (2007)
Eberg, Norway	Sensitive Clay	HV	1.5-3	0.7-0.75	Long and Donohue (2007)
Pisa tower, Italy	Soft to Firm Clay	VH,HV,HH	1.4-2	1.1-1.5	LoPresti et al.(2003)
Amherst, MA	Varved Clay	VH,HH	1.7-8.5	1.2-1.6	Henke and Henke (2002)
Cowden, UK	Clay till	VH,HV,HH	3.8-10.1	0.4-0.46	Butcher & Powell(1997); Powell & Butcher(2003)
Texas A&M, TX	Very stiff clay	VH	3.3-3.9	0.7	Tumay (1997)
Tornhill, Sweden	Stiff Clay till	VH	4-25	0.5	Svensson & Moller (2001)
U-Houston, TX	Fissured Beaumont clay	VH,HV	3.6-8.3	0.43-0.84	Tumay (1997) & O'Neill (2000)
Madingley, UK	Gault clay (Fissured)	VH,HV,HH	20+	0.78-0.84	Butcher & Powell (1995)
Chattenden, UK	London clay (Fissured)	VH,HV,HH	19+	0.77	Butcher & Powell (1995)
London clay site	London clay (Fissured)	VH,HV,HH	25+	N/A	Butcher & Powell (1997)
Heathrow, UK	London clay (Fissured)	VH,HV,HH	14+	0.68	Hight et al. (2003)
Southern England (Purton) UK	Very old Oxford clay	VH,HV,HH	14+	0.54	Bates and Phillips (2000)

Notes: V_{sVH} = Downhole shear wave; V_{sHV} = Standard crosshole shear wave using a conventional vertical downhole hammer; V_{sHH} = Special crosshole shear wave using a special rotary or vane hammer

Based on the above in-situ database, Figure 3.7 presents a comparison of DHT (V_{sVH}) and standard CHT (V_{sHV}) mode. The V_s values for DHT and standard CHT are comparable in magnitudes for normally consolidated (NC) to lightly overconsolidated (LOC) soils (low $K_0 < 1$). For overconsolidated (OC) to heavily overconsolidated (HOC) soils, the CHT V_s are rather larger than the DHT V_s. Considering the basic V_s-stress formats, the discrepancy of V_s magnitudes between VH and HV mode represent degree of inherent anisotropy in soils. In Figure 3.8, V_{sHH} values are similar to V_{sVH} as soils are

NC to LOC. However, V_{sHH} show considerably higher magnitudes than V_{sVH} in the case of OC and HOC stiff soils. Heavily overconsolidated soils usually have high lateral stress coefficient (K_0). Consequently, the large K_0 value mainly leads to high ratio of V_{sHH} and V_{sVH} (e.g., significant stress-induced anisotropy).

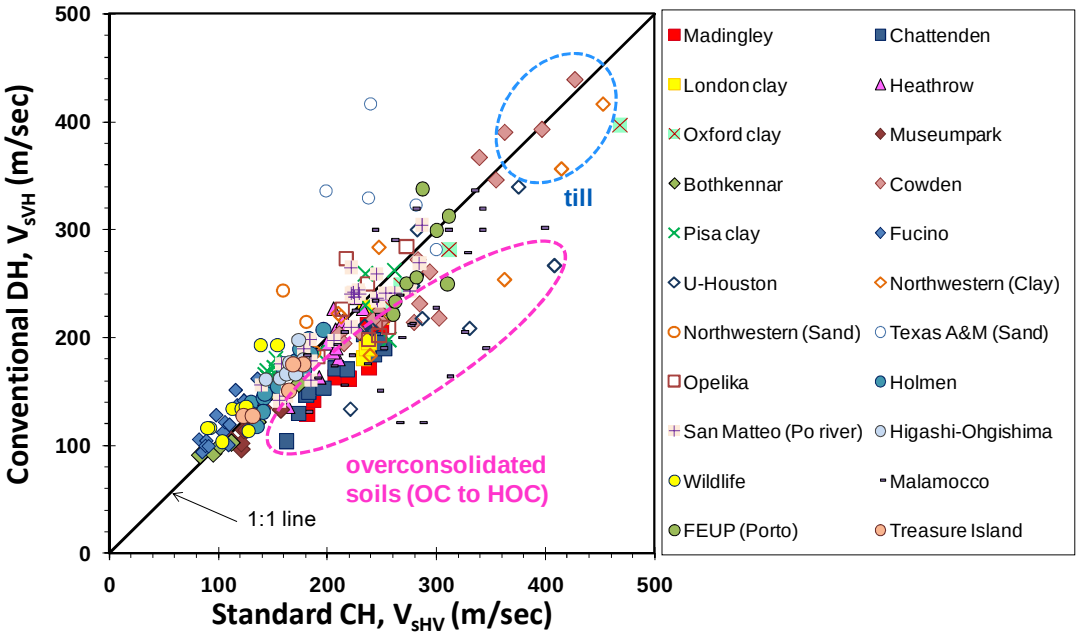

Figure 3.7. Downhole mode (V_{sVH}) versus standard crosshole mode (V_{sHV}) from in-situ database.

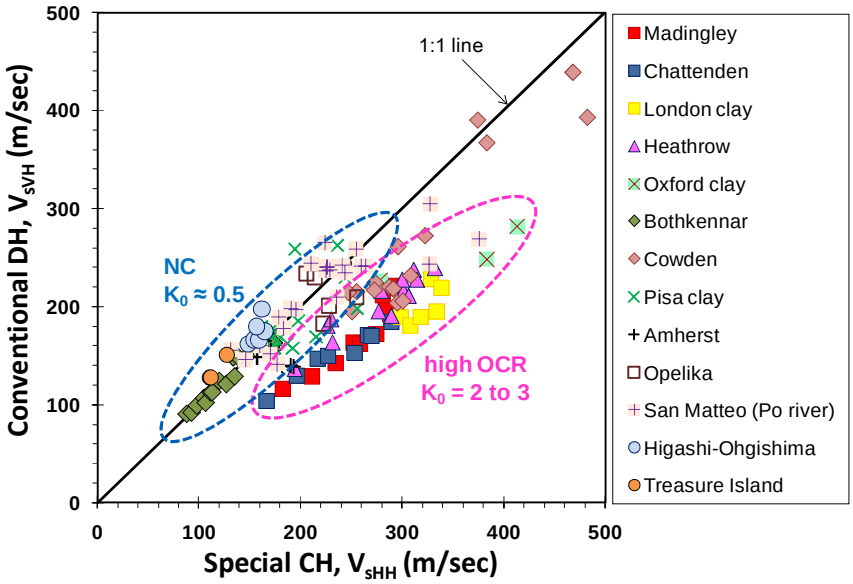

Figure 3.8. Downhole mode (V_{sVH}) versus special crosshole mode (V_{sHH}) from in-situ database.

A similar trend is confirmed by laboratory data in Figure 3.9. Table 3.3 provides details on soil type, test specimens, V_s modes, and sources for the collected laboratory data. Overall, the relative hierarchy for magnitude of different V_s modes trends as follows:

- Normally or lightly overconsolidated soil (NC or LOC)

  $V_{sHH} \leq V_{sHV} \approx V_{sVH}$

- Overconsolidated soil (OC to HOC)

  $V_{sHH} \geq V_{sHV} \geq V_{sVH}$

Table 3.3. Database listing of geomaterials, soil type, specimen details, shear wave modes, and laboratory data sources

Soil type	Specimen	Applied K_0	V_s modes	Test method	Reference
Medium dense sand	Reconstituted sand	0.5 - 2	$V_{s,VH}$,$V_{s,HV}$,$V_{s,HH}$	Bender test	Stokoe et al., 1991
Ticino sand	Reconstituted sand	0.5 - 2	$V_{s,VH}$,$V_{s,HH}$	Bender test	Belloti, 1996
Higashi-Ohgishima sand	Undisturbed sand (freezing)	0.5 - 1	$V_{s,VH}$,$V_{s,HV}$,$V_{s,HH}$	Bender test	Yamashita et al., 2003
Natori River sand	Undisturbed sand (freezing)	0.5 - 1	$V_{s,VH}$,$V_{s,HV}$,$V_{s,HH}$	Bender test	Yamashita et al., 2003
Yodo River sand	Undisturbed sand (freezing)	0.5 - 1	$V_{s,VH}$,$V_{s,HV}$,$V_{s,HH}$	Bender test	Yamashita et al., 2003
Edo River sand	Undisturbed sand (freezing)	0.5 - 1	$V_{s,HV}$,$V_{s,HH}$	Bender test	Yamashita et al., 2003
CDT (ML-Clayey silt)	Undisturbed silt (Mazier sample)	N.A.	$V_{s,VH}$,$V_{s,HV}$,$V_{s,HH}$	Bender test	Ng et al., 2004
CDT (ML-Clayey silt)	Undisturbed silt (Block sample)	N.A.	$V_{s,VH}$,$V_{s,HV}$,$V_{s,HH}$	Bender test	Ng et al., 2004
Pisa Clay	Undisturbed clay	0.5 - 2.5	$V_{s,VH}$,$V_{s,HH}$	Bender test	Jamiolkowski et al., 1995
Gault clay	Undisturbed clay	1.0 - 2.0	$V_{s,VH}$,$V_{s,HH}$	Bender test	Pennington et al., 1997
Boom clay	Undisturbed & reconstituted clay	0.5 - 2.0	$V_{s,VH}$,$V_{s,HV}$,$V_{s,HH}$	Bender test	Piriyakul, 2006
London clay	Undisturbed clay	1.0	$V_{s,VH}$,$V_{s,HV}$,$V_{s,HH}$	Bender test	Jovicic and Coop, 1998
Boston blue clay	Reconstituted clay	0.5	N.A.	TX local strains	Santagata et al., 2005

Notes: CDT = Completely decomposed tuff; TX = Triaxial

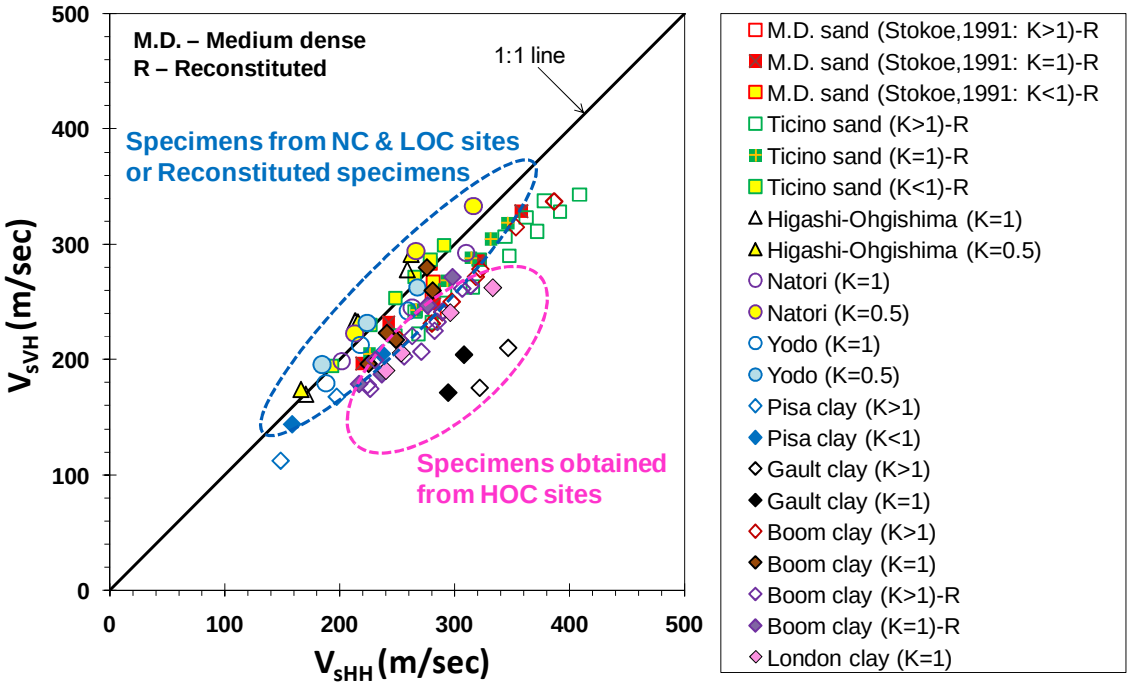

Figure 3.9. V_{sVH} versus V_{sHH} from collected laboratory data.

3.5 Examination on Stress-Dependency of V_s in Geomaterials

Various V_s-σ' relationships for geomaterials are summarized in Table 3.1. A fundamental concept is that V_s depends on effective confining stress state. For instance, Figure 3.10 shows an example for the well-known Boston blue clay (BBC) where the initial small-strain stiffness values come from triaxial data (Santagata et al. 2005) as follows:

Equation (3.8) $$E_{max} = 2G_0 \cdot (1+\nu)$$

Equation (3.9) $$V_s = (G_0 / \rho)^{0.5}$$

where E_{max} is Young's modulus and ν is Poisson's ratio. The initial stiffness values were obtained from K_0-NC re-sedimented BBC specimens (ν = 0.5 for undrained conditions). In Figure 3.10, V_s are plotted with effective mean normal stress. It is observed that V_s can be expressed as a specific power function of stress state: $V_s = \alpha \cdot (\sigma_o')^{\beta}$. The coefficient α is

determined as the constant value at a reference stress level (1 kPa) and the exponent β is the slope of the regression equation. More discussions for V_s – stress relationships are provided in the next paragraph.

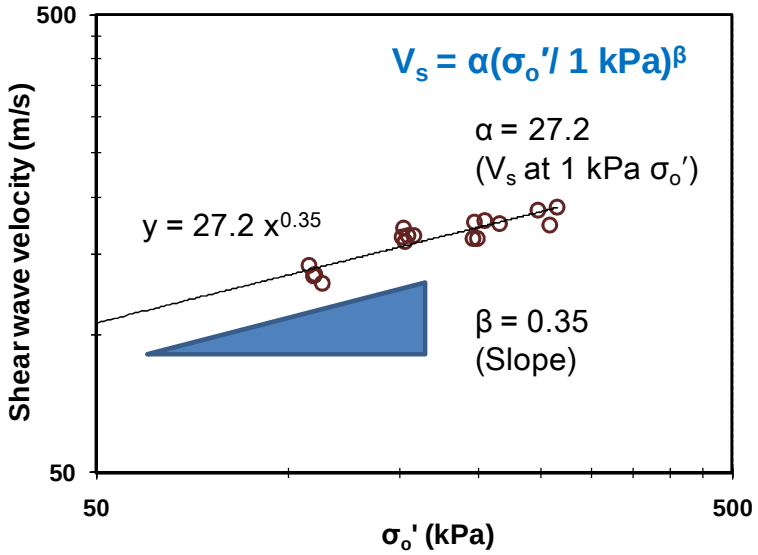

Figure 3.10. Relationship between V_s and σ' for reconstituted Boston blue clay (data from Santagata et al 2005).

Note: data obtained from triaxial local strain measurement system (0.0001% strain level)

Based on the collected V_s data sets, it is possible to investigate more extensive relationships between V_s and different stress states for a variety of geomaterials. Hence, as the widely accepted V_s-σ' models, the mean normal stress method and the individual stress method are mainly examined to discern trends and relationships. First, as briefly introduced before, the V_s can be expressed by mean normal stress. A representative expression under isotropic state of stress is shown below (Santamarina et al. 2001):

Equation (3.10) $$V_s = \alpha \cdot (\sigma_o'/1\ \text{kPa})^{\beta}$$

The constants α and β values are experimentally determined. The exponent β value represents the amount of stress-dependency effect. Theoretical β values have been proposed by contact effects [0 for cemented soil, 1/6 for Hertzian contacts (elastic

spherical particles), 1/4 for cone-to-plane contacts (rough or angular particles), 1/4 for spherical particles with contact yield]. The coefficient α is determined by packing type, material properties, contact behavior, and fabric changes. It is noted that the α is inversely proportional to the β term according to: $\beta \approx 0.36 - \alpha/700$ (Santamarina et al. 2001).

Laboratory test data are used to investigate the relationship between coefficient α and exponent β with the trend line in Figure 3.11. Employed data have K_0-consolidated conditions. Most data are located near the trend line and β values range approximately from 0.2 to 0.36. The mean β value is about 0.256. Compared with the theoretical β values from Santamarina et al. (2001), this range looks reasonable. Among the laboratory database, Patel et al. (2009) additionally examined the best-fit parameters for α and β and suggested empirical correlations using mean particle size (D_{50}), maximum and minimum void ratio (e_{max}, e_{min}), and regularity ($\xi = (R+S)/2$, here R = roundness, S = sphericity).

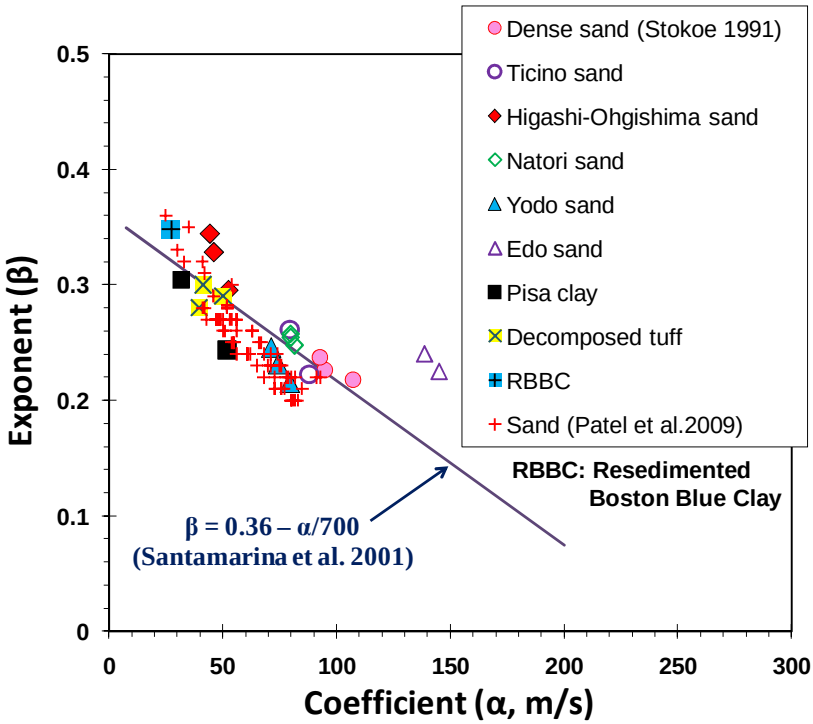

Figure 3.11. Relationship between coefficient (α) and exponent (β) using laboratory test data (V_s- stress model : mean normal stress method).

Similarly, previous studies have suggested that G_0 depends on $(\sigma_o')^{0.5}$ (Hardin and Black 1968; Schmertmann 1978; Tatsuoka et al. 1979; Yu and Richart 1984). Moreover, this specific β value (e.g., average β = 0.256) can be reasonably linked to the conventional approach for stress-normalized shear wave velocity:

Equation (3.11) $V_{s1}=V_s\cdot(\sigma_{atm}/\sigma_{vo}')^{0.25}$

where σ_{atm} = atmospheric pressure = 1 bar = 100 kPa. For liquefaction analysis (Youd et al. 2001), the empirical criterion has been developed based on relationships between cyclic resistance ratio (CRR) and V_{s1}. The equation uses an exponent of 0.25 in terms of stress as a traditional procedure. It is noted that the 0.25 value is very close to the mean β value from the above laboratory data.

In the same manner, the mean normal stress method is examined using in-situ data. An example study for V_s-σ_o' relationship is provided in Figure 3.12 (London clay at Chattenden, U.K.). With respect to the relationship between coefficient α and exponent β, Figure 3.13 shows in-situ data sorted by soil types. Laboratory data are plotted together as solid square symbols.

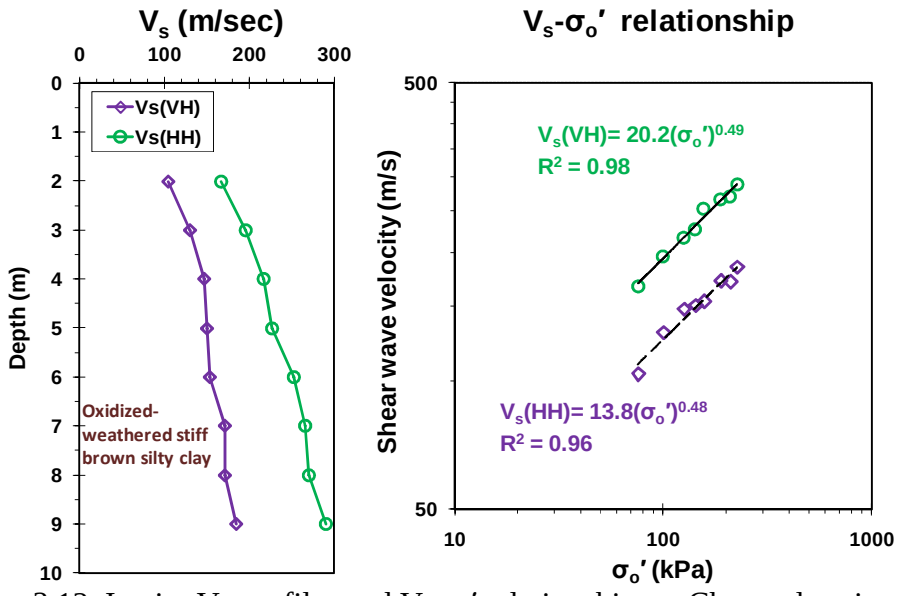

Figure 3.12. In-situ Vs profiles and V_s-σ_o' relationships at Chattenden site, U.K.

Whereas the laboratory data have narrow ranges of both α and β, the field data provide relatively wide ranges. The constant α remains inversely related to β. However, it seems that the stress-dependent β exponents at some specific field sites have remarkably high values which are almost approaching up to 0.8 - 0.85 with corresponding low α values (please refer to section 4.2.2 for high exponent examples, page 82). It appears more likely to happen particularly in clay sites. Some of significantly large exponent values might be influenced by undetected variations of soil layers which tend to have different void ratio, particle structure, and stress history condition. In summary, the constants α and β values from field data appear to be influenced by additional factors.

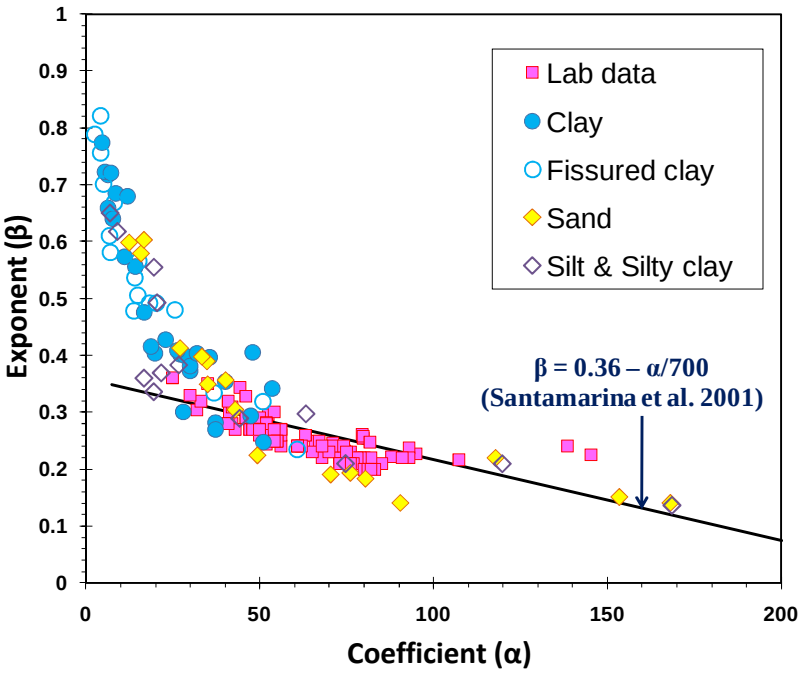

Figure 3.13. Relationship between coefficient (α) and exponent (β) using field test data (V_s- stress model : mean normal stress method).

In another approach, various field and laboratory test data are examined by application of the individual stress method: $V_s = C \cdot (\sigma_x')^{nx} \cdot (\sigma_y')^{ny}$. Figure 3.14 shows the

trend between the coefficient (C) and the exponent (assuming $n_x \approx n_y$) using field test data in terms of the individual stress method. It is observed that the general trend of Figure 3.14 looks similar to that of Figure 3.13, except that the exponents have almost half values ($n_x \approx n_y \approx \beta/2$). V_s modes and site information are provided in Figure 3.15.

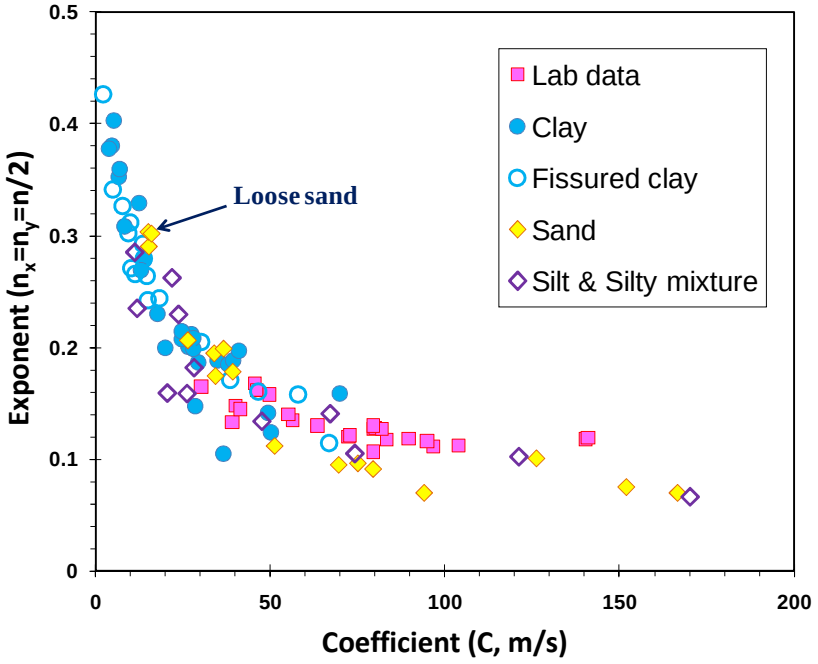

Figure 3.14. Relationship between coefficient (C) and exponent ($n_x \approx n_y$) using field test data (V_s- stress model : individual stress method).

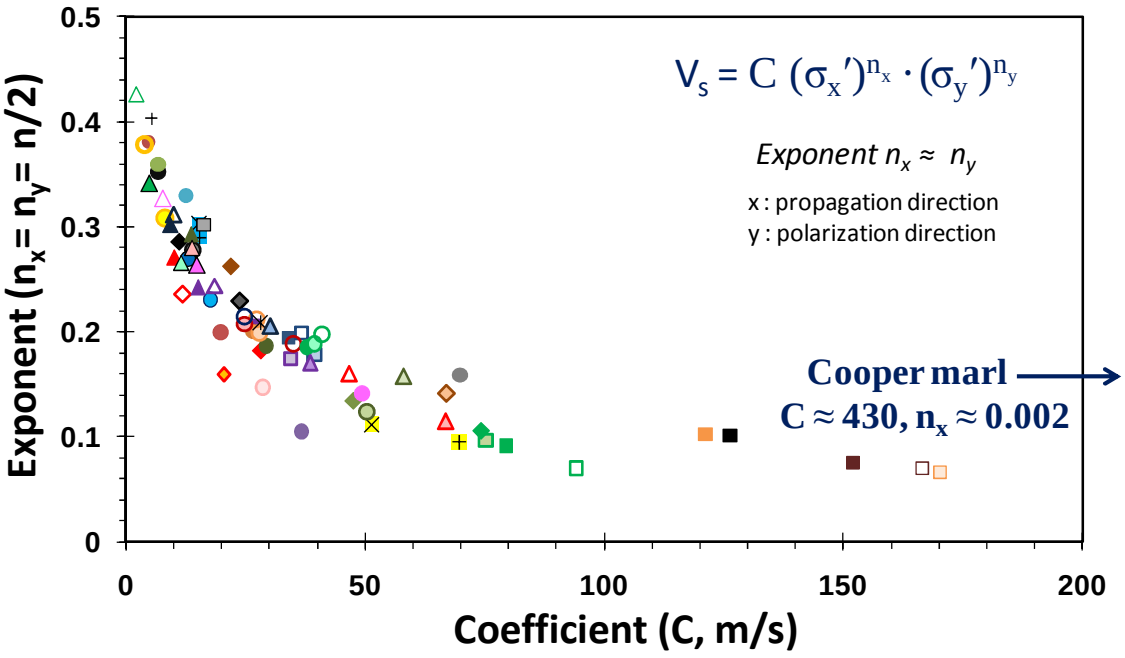

Po river (Vs,vh)	Po river (Vs,hv)	Po river (Vs,hh)	Texas A&M (Vs,vh)
Holmen (Vs,vh)	Holmen (Vs,hv)	Higashi-Ohgishima (Vs,vh)	Higashi-Ohgishima (Vs,hv)
Higashi-Ohgishima (Vs,hh)	Treasure Island (Vs,hv)	Treasure Island (Vs,hh)	V.T. Bridge (Vs,hv)
V.T. Bridge (Vs,hh)	Laing Bridge South (Vs,vh)	Laing Bridge South (Vs,hv)	Laing Bridge South (Vs,hh)
Opelika (Vs,vh)	Opelika (Vs,hv)	Vagverket (Vs,vh)	Vatthammar (Vs,vh)
Malamocco (Vs,vh)	Malamocco (Vs,hv)	Lower 232 St.(Vs,vh)	Lower 232 St.(Vs,hv)
Lower 232 St.(Vs,hh)	FEUP (Vs,vh)	FEUP (Vs,hv)	Museumpark (Vs,vh)
Museumpark (Vs,hv)	Bothkennar (Vs,vh)	Bothkennar (Vs,hv)	Bothkennar (Vs,hh)
Northwestern (Vs,vh)	Northwestern (Vs,hv)	Norrkoping (Vs,vh)	Lilla Mellosa (Vs,vh)
Montalto di Castro1 (Vs,hv)	Montalto di Castro1 (Vs,hh)	Montalto di Castro2 (Vs,hv)	Montalto di Castro2 (Vs,hh)
Fucino (Vs,vh)	Fucino (Vs,hv)	Onsoy (Vs,vh)	Eberg (Vs,hv)
Cowden (Vs,vh)	Cowden (Vs,hv)	Cowden (Vs,hh)	Texas A&M (Vs,vh)
Tomhill (Vs,vh)	Pisa clay (Vs,vh)	Pisa clay (Vs,hv)	Pisa clay (Vs,hh)
Amherst (Vs,vh)	Amherst (Vs,hh)	U-Houston (Vs,vh)	U-Houston (Vs,hv)
Madingley (Vs,vh)	Madingley (Vs,hv)	Madingley (Vs,hh)	Chattenden (Vs,vh)
Chattenden (Vs,hv)	Chattenden (Vs,hh)	London clay (Vs,vh)	London clay (Vs,hv)
London clay (Vs,hh)	Heathrow (Vs,vh)	Heathrow (Vs,hv)	Heathrow (Vs,hh)
Oxford clay (Vs,vh)	Oxford clay (Vs,hv)	Oxford clay (Vs,hh)	Cooper marl (Vs,vh)
USP,Brazil (Vs,vh)	USP,Brazil (Vs,hv)		

Figure 3.15. Site information for relationship between coefficient (C) and exponent ($n_x \approx n_y$) using field test data (V_s- stress model : individual stress method).

Note: additional data added (e.g., Cooper marl and residual soil [USP, Brazil]).

3.6 Summary and Conclusions

The multiple types of V_s modes (V_{sVH}, V_{sHV}, V_{sHH}) are affected by both inherent anisotropy and stress-induced anisotropy. In this chapter, the hierarchy of different in-situ V_s modes is examined from data obtained at worldwide sites (Ku et al. 2011). In general, field data show that the order has been identified:

- NC or LOC soil: $V_{sHH} \leq V_{sHV} \approx V_{sVH}$
- HOC soil: $V_{sHH} \geq V_{sHV} \geq V_{sVH}$

Laboratory test data from bender elements provide similar results. Considering the noted general V_s-stress relationships, in cases that V_{sVH} and V_{sHV} modes have different magnitudes (e.g., $V_{sHV} > V_{sVH}$ at HOC sites), inherent anisotropy seems to have a significant influence on V_s.

Empirical V_s relationships for determining V_s were examined with respect to stress states; that is, V_s is stress dependent. In the laboratory dataset, the mean value of stress-dependency β [mean normal stress method: $V_s = \alpha \cdot (\sigma_o')^{\beta}$] is approximately 0.256. It is noted that this specific value (0.256) can be related to the traditional exponent value (0.25) of the overburden-stress (σ_{vo}') corrected V_s : [$V_{s1} = V_s \cdot (P_a/\sigma_{vo}')^{0.25}$]. Whereas laboratory data provide rather limited ranges of β values, the degree of stress-dependency in field is significantly site-specific. As a result, the parameters α and β from in-situ data are still inversely proportional, but have relatively wider ranges. Individual stress model (i.e., $V_s = C \cdot (\sigma_x')^{nx} \cdot (\sigma_y')^{ny}$) also showed similar results.

In this chapter 3, relationships for V_s in terms of solely stress condition were reviewed, particularly their directional and polarization facets. For future studies, further investigations that consider important factors such as soil type, void ratio,

overconsolidation, age, desiccation, cementation, degree of fissuring and the presence of discontinuities, and strain rate, as well as the complex interrelationships of various different V_s modes, may be necessary for a complete analysis. In the following chapter 4, based on the collected in-situ V_s database, global empirical G_0 correlations in different soil planes (i.e., VH, HV, HH) will be sought in terms of stress states, void ratio, and overconsolidation ratio.

CHAPTER 4

SMALL STRAIN SHEAR STIFFNESS IN SOILS: DIRECTIONAL PROPERTIES

4.1 Introduction

The stiffness of soils is highly nonlinear, complex, and governed by strain magnitude, stress level, anisotropy, fabric, cementation, and stress history. True linear elastic stiffness response occurs only at small strain levels corresponding to nondestructive testing ($\gamma_s < 10^{-6}$ %), and for strains that extend beyond this threshold, the soil modulus decreases with increasing strains into the medium-range (i.e., working deformations) and high-range (i.e., strength). The small-strain shear modulus G_0 is a fundamental stiffness which relates to the undisturbed initial soil state and serves as the beginning of all stress-strain-strength curves for static/monotonic, cyclic, and dynamic loading, and for drained and undrained conditions (Burland 1989; Jardine et al. 1998). For the G_0, typical ranges of the linear threshold strain (γ^{ℓ}_t) for uncemented materials are shown in Figure 4.1a (Darendelli 1991; Jamiolkowski 2012). The ranges of volumetric threshold strain (γ^{V}_t) which represents the boundary between non-linear elastic and non-linear elasto-plastic area are compared. Figure 4.1b describes the equivalent threshold strains for a normalized stiffness degradation curve (Menq 2003; Jamiolkowski 2012). Monotonic and cyclic loadings show different behaviors after the volumetric threshold strain point in Figure 4.1b (i.e., number of cycles (N) = 1 for monotonic loading).

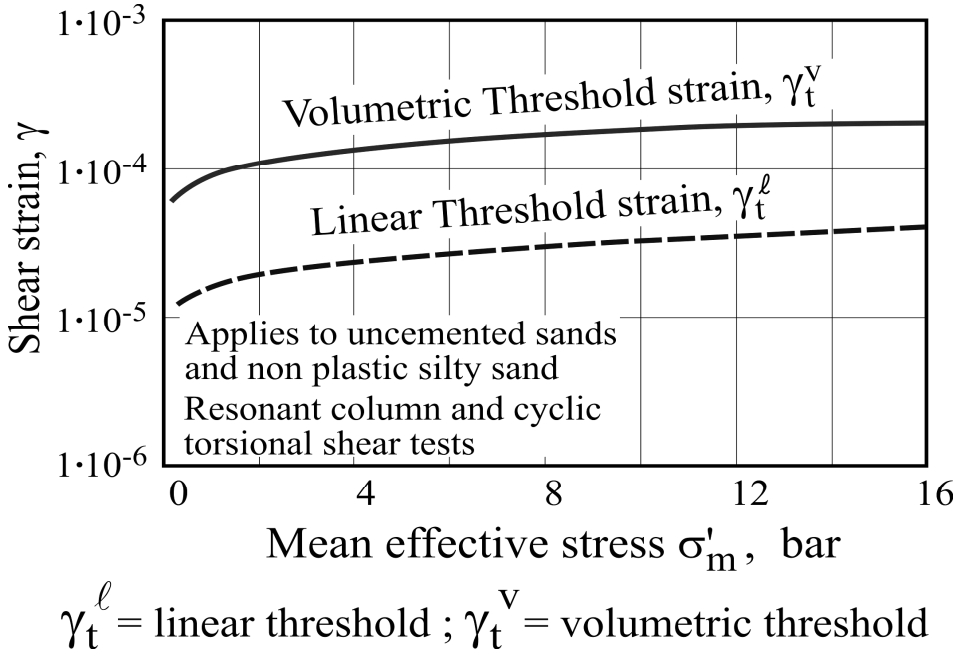

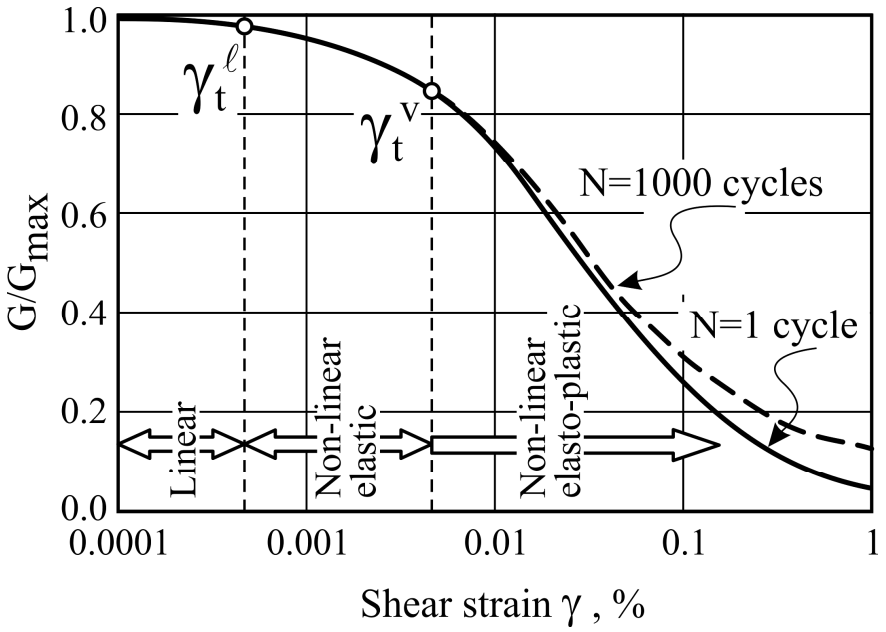

Figure 4.1. (a) Observed linear threshold strain and volumetric threshold strain from laboratory seismic tests (Darendelli 1991), (b) Normalized shear stiffness degradation curve with threshold strains (Menq 2003)

Note: figures from Jamiolkowski 2012

Understanding the soil stiffness behavior over a range of strains is critical for practical design purposes such as ground movements, seismic site amplification, and foundation settlement predictions. For instance, the idealized soil stiffness variation with level of strain and typical strain ranges applicable to various geotechnical situations have been well detailed already (e.g., Atkinson and Sallfors 1991; Shibuya et al. 1992; Benz 2007; Clayton 2011). Conceptual stiffness-logarithm of strain behavior is provided with the geotechnical applications in Figure 4.2. To obtain reliable stress-strain relationships in soils, it is important to evaluate both the initial shear stiffness (G_0 or G_{max}) at very small strains and the appropriate modulus reduction curves (G/G_0) which represent nonlinear stiffness changes due to loading conditions (Vucetic and Dobry 1991; Tatsuoka and Shibuya 1992; Fahey 1998; Mayne 2005).

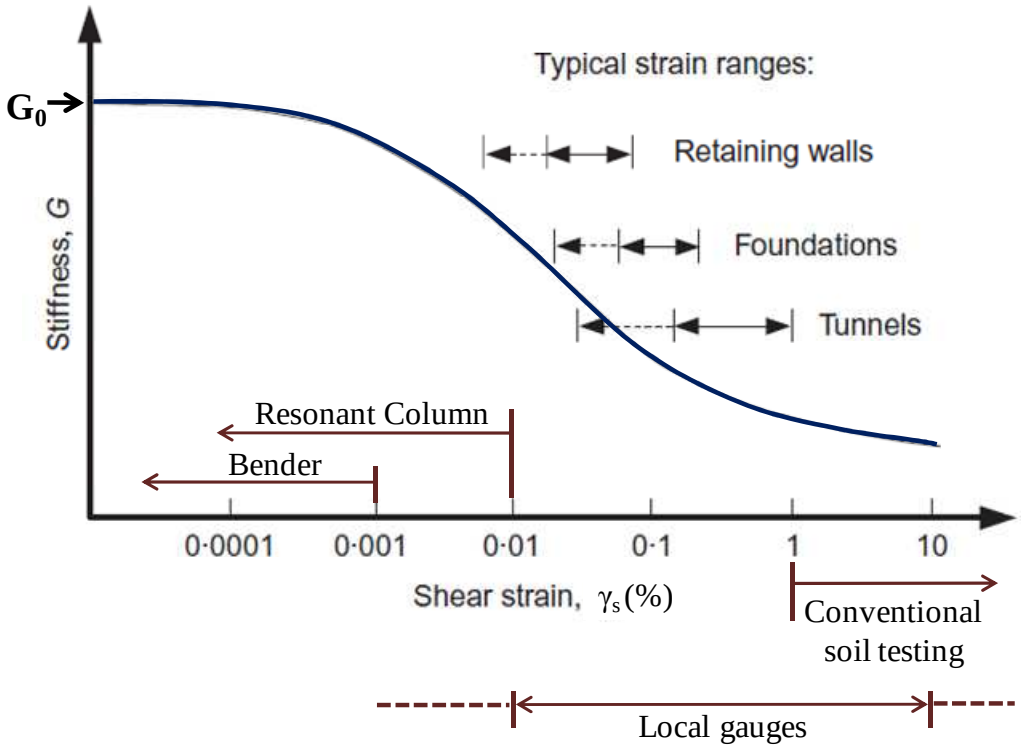

Figure 4.2. Conceptual stiffness-strain behavior in soils and typical strain levels of geotechnical design problems and testing (adapted from Atkinson and Sallfors 1991).

The linear elastic small strain stiffness of soils can be represented in terms of either the initial shear modulus G_0 or the related Young's modulus $E_0 = 2G_0(1+\nu)$, where ν = Poisson's ratio. The initial stiffness is assessed from the shear wave velocity (V_s) using field geophysics or laboratory tests on specimens cut from undisturbed samples (Woods 1978). At the laboratory scale, the magnitude of G_0 is usually obtained from resonant column tests (RCT), bender elements (BE), ultrasonics, torsional shear (TS), and/or triaxial tests with local strain measurements. Common field testing methods for V_s include crosshole, downhole, and noninvasive Rayleigh wave type measurements (Campanella 1994). Various field tests were discussed in Chapters 1 and 3. For the lab tests in particular, BE can provide directional G_0 measurements across different soil planes that are governed by both stress conditions and inherent soil fabric (refer to Figure 3.2). Based on shear wave velocity measurements which exhibit both polarization and propagation directional properties, the magnitude of G_0 is calculated as follows:

Equation (4.1) $$G_{0,ij} = \rho_t \cdot V_{s,ij}^2$$

where ρ_t is the total mass density of soil, V_s is shear wave velocity, 'i' is the propagation direction and 'j' is the polarization direction. Supposing that: (1) the propagation and particle motion direction of shear waves are parallel to the vertical and/or horizontal plane, and (2) the soil matrix has cross-anisotropic conditions, then three common types of V_s mode can be expressed: V_{sVH}, V_{sHV}, V_{sHH}, as shown in Chapter 3. In fact, the degree of stiffness anisotropy at small strains in soils and rocks can be measured by comparing the magnitudes of these three different V_s modes. From laboratory BE test data, it has been known that the shear stiffness anisotropy in soils has three main causes: (1) inherent (structural) anisotropy, (2) stress-induced anisotropy, and (3) strain-induced

anisotropy (Tatsuoka and Shibuya 1992; Jovicic and Coop 1998; Clayton 2011). Usually, strain-induced anisotropy is of concern only for laboratory measurements on reconstituted specimens. Considering stiffness anisotropy in natural soils, the directional G_0 should be carefully investigated with a corresponding plane direction.

A number of research studies have examined the various factors affecting the shear stiffness in soils and proposed G_0-stress relationships with potential parameters related to soil structure. Practically, most empirical equations for estimating G_0 have been derived from selective laboratory data (e.g., resonant column) or field measurements (e.g., downhole tests) at specific sites. Of recent, laboratory BE tests have been conducted because they are small and can be easily mounted in consolidometers, triaxial, and/or cubical apparatuses. In addition, sets of BE can be positioned to investigate directional stiffnesses, as well as other variables. Rate effects seem to have small influence on the magnitude of shear stiffness at very small strains for natural materials within the elastic range (Shibuya et al. 1992; Leroueil and Hight 2003; Mitchell and Soga 2005). However, the pronounced effects of sample disturbance and ageing can result in considerable discrepancies between laboratory-determined G_0 values and in-situ G_0 measurements conducted on the same geomaterial.

It has been observed that field G_0 values are most often greater than the G_0 obtained from laboratory tests (e.g., Ghionna and Jamiolkowski 1991; Tatsuoka and Shibuya 1992). As a result, laboratory G_0 measurements often may under represent the field value of G_0, leading Stokoe and Santamarina (2000) to recommend correcting lab G/G_{max} curves on the basis of field V_s measurements. Figure 4.3 provides the recommended ratios of laboratory-to-field G_0 from field V_s. As the magnitude of field V_s

increases, the observed V_s ratio generally decreases. Similarly, Figure 4.4 shows the modulus ratio ($G_{0,lab}/G_{0,field}$) which relates to soil type, sampling method, and age of soil sediments (Japanese case studies from Toki et al. 1995). In the case of loose sands, conventional thin-walled tube sampling might show lab G_0 greater than field G_0 because of inadvertent densification caused by the insertion process.

Basically, the field shear modulus (G) reduction curve (G−log γ curve) can be estimated from consideration of both the field V_s value to provide the reference anchor point (i.e., G_0) and lab measurements of G at higher strains: i.e., $G_{\gamma,field} = (G_{\gamma,lab}/G_{0,lab})\times G_{0,field}$. Figure 4.5 shows an example of the correction of laboratory G/G_{max} versus log γ curves to field equivalent values based on in-situ V_s measurements (Tatsuoka and Shibuya 1992; Stokoe and Santamarina 2000). Consequently, the field G_0 is critical for dynamic response analysis.

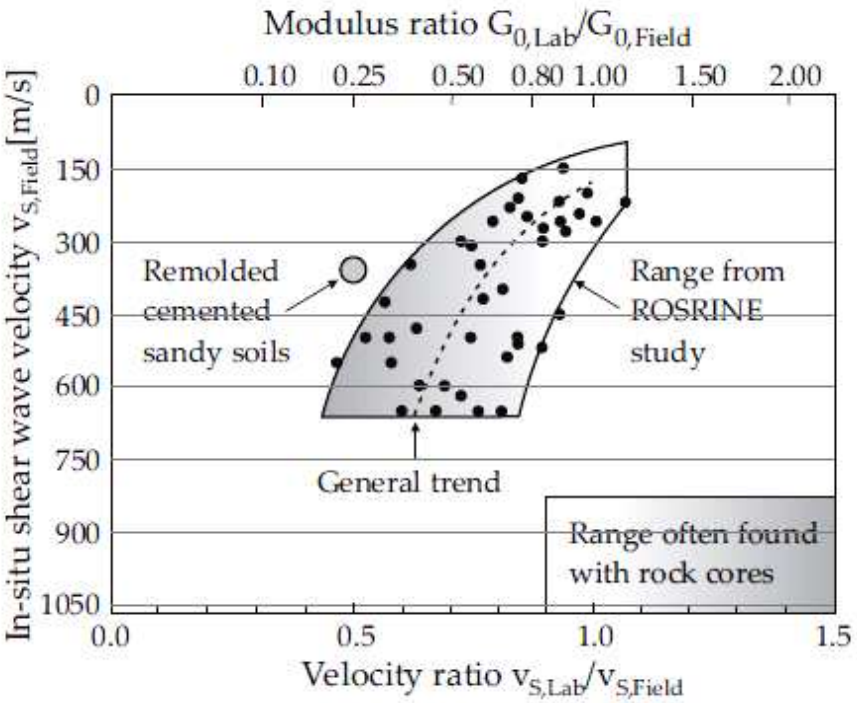

Figure 4.3. Variation of V_s ratio ($V_{s,lab}/V_{s,field}$) between laboratory and field measurements (Stokoe and Santamarina 2000; figure from Benz 2007).

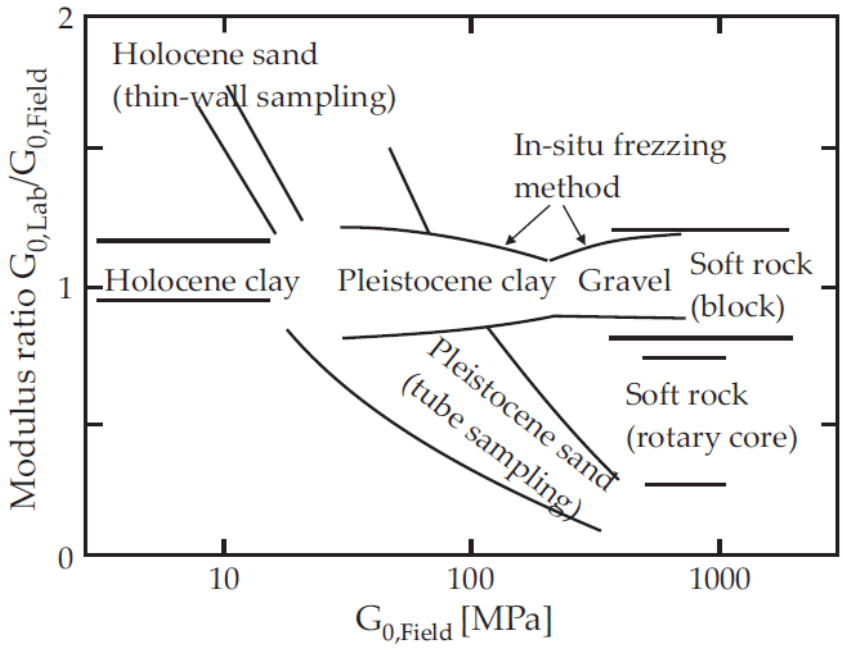

Figure 4.4. Observed ratio of laboratory-to-field G_0 (i.e., $G_{0,lab}/G_{0,field}$) versus $G_{0,field}$ (Toki et al. 1995, figure from Benz 2007).

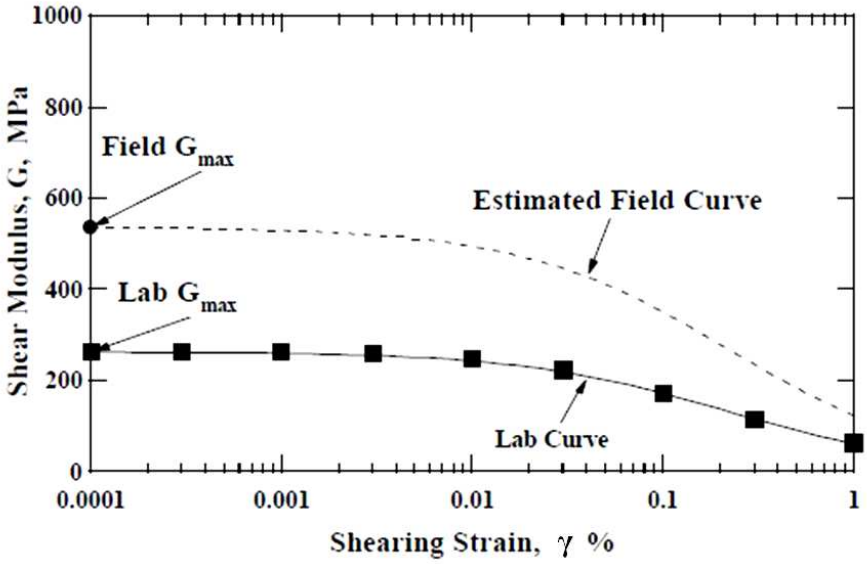

Figure 4.5. Field shear modulus curve with log strain based on correcting the laboratory measured results (Stokoe and Santamarina 2000).

Herein, using a special field G_0 database compiled from various sites that cover a variety of geomaterials, this study investigates global G_0 relationships in consideration of their different directional planes. The field data include in-situ V_s profiles (HH, VH, and

HV), effective stress conditions, and other relevant soil properties (i.e., void ratio) that were collected from published sources and reports. Directional G_0 values were evaluated from in-situ V_s data using sets of different geophysical methods. The various V_s modes were explained previously in Chapter 3 (Figure 3.1).

4.2 Background: Shear Modulus of Soils

4.2.1 Empirical G_0 Expressions

The shear stiffness of particulate materials is significantly affected by confinement, void ratio, particle properties (e.g., shape, size, stiffness), and contact behavior. In terms of micromechanics and particle contact behavior, analytical solutions for small-strain shear modulus have been discussed by Santamarina and Cascante (1996) and Santamarina et al. (2001). Basically, the magnitude of G_0 shows stress-dependent behavior in uncemented soils. As briefly noted, in order to identify additional factors that influence the shear modulus, numerous research studies have been based on results from laboratory resonant column testing (e.g., Hardin and Richart 1963, Hardin and Blandford 1989) and bender elements (e.g., Viggiani and Atkinson 1995, Jamiolkowski et al. 1995).

In an early study by Seed and Idriss (1970), the small strain shear modulus was associated with variations in effective friction angle (ϕ'), confining stress (σ_v'), void ratio (e), and at-rest lateral stress coefficient (K_0) from tests on sands. Figure 4.6 shows the relative effects of those parameters on the shear stiffness. Notably, G_0 is mainly influenced by void ratio and stress level according to the basic relationship provided in Equation 3.2 (i.e, $G = 1000 \cdot K_2 \cdot \sigma_o'^{0.5}$). Later, based on normally consolidated (NC) and moderately overconsolidated (OC) cohesive materials, Dobry and Vucetic (1987) summarized general effects of a variety of factors (e.g., confining pressure, void ratio,

geologic age, cementation, overconsolidation, plasticity index, strain rate, etc) on the magnitude of the initial $G_{0,}$ as well as modulus reduction curves (G/G_0) and damping ratio (D) that both vary with logarithm of strain. A rather comprehensive study by Tatsuoka and Shibuya (1992) on a large assessment of many soils and rocks confirmed and elaborated on these findings. More recently, Clayton (2011) remarked that the initial stiffness parameters (i.e., G_0, E_0) depend on void ratio, grain characteristics (particle size and shape), current effective stresses, structure, stress history, fabric and particle arrangement, discontinuities, and loading rate.

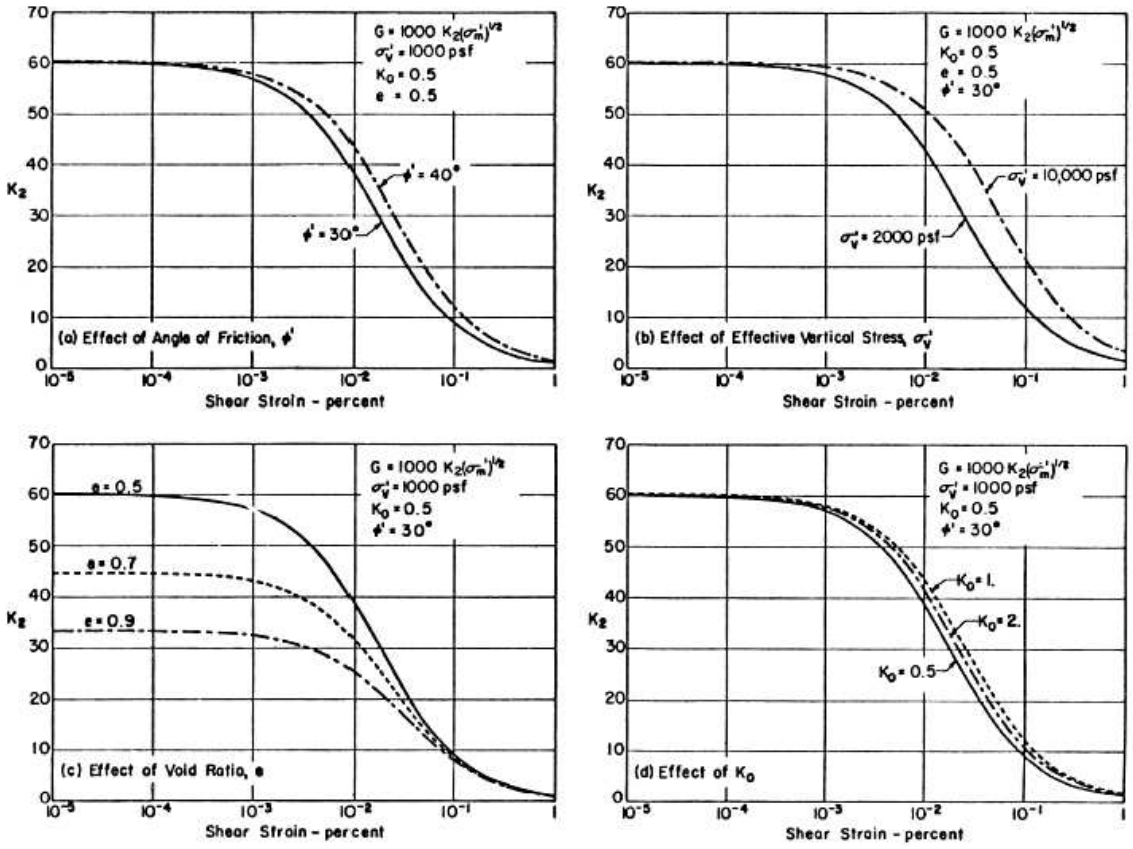

Figure 4.6. Shear stiffness variation influenced by a) effective friction angle, b) confining stress (σ_v'), c) void ratio, and d) at-rest lateral stress coefficient (K_0) (Seed and Idriss 1970).

One representative early empirical formula for G_0 can be written as follows (Hardin and Black 1968, Hardin 1978):

Equation (4.2) $$G_0 = S \cdot F(e) \cdot OCR^k \cdot (\sigma_o')^n$$

where F(e) is a void ratio function (see Table 4.1), OCR = overconsolidation ratio, σ_o' is mean effective stress, and S, k, and n are empirical material constants. Many early studies investigated the G_0 parameters via RC tests and proposed the above empirical format using a mean effective stress as confining pressure. Particularly, under isotropic stress conditions, the mean effective stress seems an appropriate useful term.

On the other hand, several later studies based on data from a special V_s exciter or torsional vibrator system (Roesler 1979) and directional BE tests (Stokoe et al. 1991, 1995), as well as RC tests (Ni 1987, Hardin and Blandford 1989), it was shown that the orthogonal stress which acts on out of plane has no influence on the G_0 or V_s. That is, only two (of the three principal) effective stresses control the magnitude of G_0; those in the directional planes of propagation and particle motion. Figure 4.7 indicates the noted observation (Stokoe et al. 1995). Consequently, the following formulation can be expressed based on the two individual stresses:

Equation (4.3) $$G_{0,ij} = S_{ij} \cdot F(e) \cdot OCR^k \cdot (\sigma_i')^{ni} \cdot (\sigma_j')^{nj}$$

where σ_i' is effective stress in the wave propagation direction (i), σ_j' is effective stress in the polarization direction (j), and S_{ij}, ni, nj are empirical material constants. It was observed that the stress exponent 'ni' and 'nj' have approximately same magnitudes (Yu and Richart 1984, Ni 1987, Pennington et al. 1997). The noted empirical expressions are not dimensionally matched when the stress exponent n (Equation 4.2) and the exponent

sum ni+nj (Equation 4.3) are not equal to one. In the case that dimensional consistency is required, additional reference pressure term should be included for stress normalization (e.g., P_a^{1-n} for Equation 4.2, $P_a^{1-ni-nj}$ for Equation 4.3, here P_a = atmosphere pressure). Actually, Equation 4.2 and Equation 4.3 can be related to the mean normal stress method, where $V_s = \alpha \cdot (\sigma_o')^{\beta}$ and individual stress method, where $V_s = C \cdot (\sigma_x')^{n_x} (\sigma_y')^{n_y}$, respectively, as mentioned in Chapter 3.

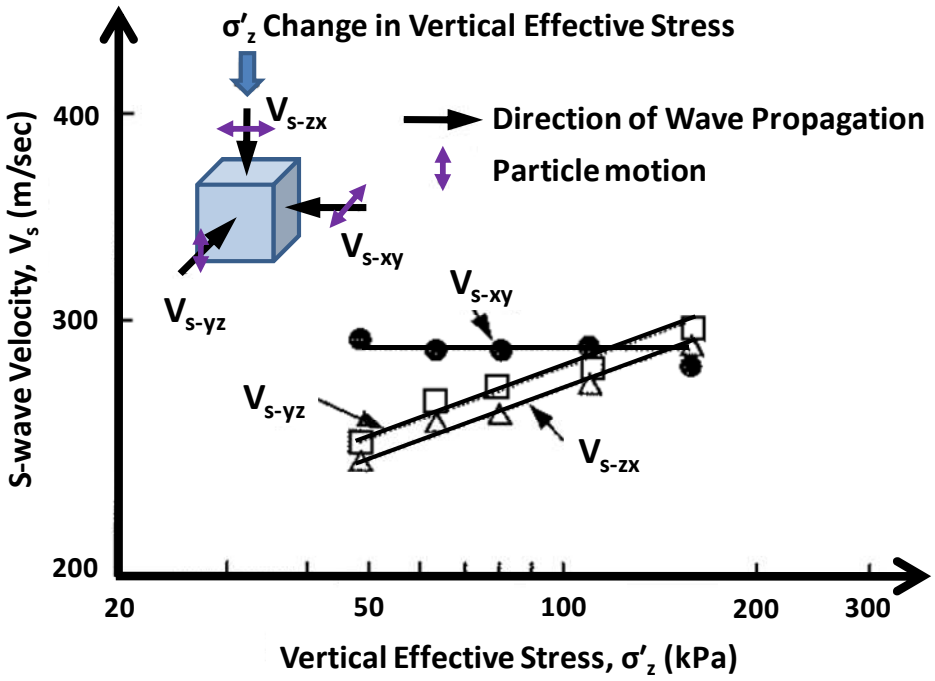

Figure 4.7. Directional V_s variations in different soil planes (Stokoe et al. 1995).

4.2.2 Effect of Confining Stress

In terms of the earlier Equation 4.2 form using a mean effective stress (here, k=0), Mitchell and Soga (2005) provided summary results which included soil type, void ratio functions, test methods, and observed material constant values on a number of prior empirical studies. Benz (2007) also provided summaries of a good number of prior G_0 expressions. Herein, some summary results are provided based on the aforementioned in

Table 4.1 for sands and Table 4.2 for clays. With respect to the stress-dependent behavior, the results show that the stress exponent n values are approximately 0.5 for these selected soil materials.

These observed experimental values are supported by analytical approaches at laboratory micromechanics scales. Within a classical contact theory such as Hertzian contacts, the exponent n is expected to be 1/3 for elastic spherical particles. Particles having angular shapes or rough surfaces result in cone-to-plane contacts, thus the higher $n \approx 0.5$ is observed. Contact yield can also produce the exponent $n \approx 0.5$ for spherical particles (Santamarina et al. 2001, Mitchell and Soga 2005). Evolution of contact forces and fabric alterations in soils might result in higher stress-dependent G_0. In simple G_0-stress relationships excluding void ratio functions, large n values were often observed in natural geomaterials. For instance, Weiler (1988) performed RC tests on undisturbed specimens of six naturally deposited clays and found larger n values (i.e., $0.84 \leq n \leq 1.18$) based on G_0-σ_o'-OCR expressions. Shibuya et al. (1997) showed significantly high n values and wider ranges for soft clays in terms of G_0-σ_v' relationships (here, σ_v' is effective vertical stress) as follows: (1) $0.75 \leq n \leq 1.27$ for seven in-situ seismic surveys [two clays among 9 total surveyed were excluded due to exceptionally high $n > 2$], (2) $0.64 \leq n \leq 0.94$ for eight series of BE tests on reconstituted clay specimens. Chang and Cho (2010) observed $n = 1.12$ from BE measurements with consolidation test on normally consolidated Kwang-Yang clay (estimated from V_s-σ_v' relationship). Also, based on Holocene clay deposits (i.e., BE test data using Bangkok clay, Ariake clay/Japan, and Louiseville clay/Canada), Lohani et al. (1999) found variable ranges of n values: $0.12 \leq n \leq 1.05$ in terms of G_0-σ_v' correlation. Lohani et al. (2008) showed $n = 1$ for both remolded and undisturbed sensitive Ariake clay.

Similarly, Ku et al. (2011) showed comparable results from various geomaterials based on compiled in-situ V_s data. In Equation 4.3, the sum of the stress exponent terms (i.e., ni + nj) is expected to be close to the exponent n of Equation 4.2, since two individual stress components are applied. Particularly, Equation 4.3 can consider directional G_0 values under anisotropic stress conditions. Assuming the two stress exponents are equivalent (ni ≈ nj) and the i-j plane is vertical or horizontal direction, the Equation 4.3 might be alternatively represented by adopting effective vertical stress (σ_v'). For example, $G_{0,VH}$ is expressed by:

Equation (4.4) $$G_{0,VH} = S_{VH}' \cdot F(e) \cdot OCR^k \cdot (\sigma_v')^{2nv}$$

where S_{VH}' is $S_{VH} \times (K_0)^{nv}$ (derived from Equation 4.3) and $K_0 = (\sigma_{ho}'/\sigma_{vo}')$ is the at-rest lateral stress coefficient. Similar expressions are possible in the HV and HH planes as well.

Table 4.1. Selected G_0 parameters for sands (from Mitchell and Soga 2005)

Soil type	S	F(e)	n	Void ratio	Test method	Reference
Round-grain Ottawa sand	6900	$\frac{(2.174-e)^2}{1+e}$	0.5	0.3-0.8	RC	Hardin and Richart (1963)
Angular-grain crushed quartz	3270	$\frac{(2.973-e)^2}{1+e}$	0.5	0.6-1.3	RC	Hardin and Richart (1963)
Several sands	9000	$\frac{(2.17-e)^2}{1+e}$	0.4	0.6-0.9	RC	Iwasaki et al. (1978)
Toyoura sand	8000	$\frac{(2.17-e)^2}{1+e}$	0.5	0.6-0.8	Cyclic TX	Kokusho (1980)
Several cohesionless and cohesive soils	4500-140000	$\frac{1}{0.3+0.7e^2}$	0.5	NA	RC	Hardin and Blandford (1989)
Ticino sand	7100	$\frac{(2.27-e)^2}{1+e}$	0.43	0.6-0.9	RC & TS	Lo Presti et al. (1993)

Note: RC – resonant column test, TX – triaxial test, TS – torsional shear test

Table 4.2. Selected G_0 parameters for clays (from Mitchell and Soga 2005)

Soil type	S	F(e)	n	Void ratio	Test method	Reference
Reconstituted NC kaolin	3270	$\frac{(2.973-e)^2}{1+e}$	0.5	0.5-1.5	RC	Hardin and Black (1968)
Several undisturbed NC clays	3270	$\frac{(2.973-e)^2}{1+e}$	0.5	0.5-1.7	RC	Hardin and Black (1968)
Reconstituted NC kaolin	4500	$\frac{(2.973-e)^2}{1+e}$	0.5	1.1-1.3	RC	Marcuson and Wahls (1972)
Reconstituted NC bentonite	450	$\frac{(4.4-e)^2}{1+e}$	0.5	1.6-2.5	RC	Marcuson and Wahls (1972)
Several undisturbed silts and clays	893-1726	$\frac{(2.973-e)^2}{1+e}$	0.46-0.61	0.4-1.1	RC	Kim and Novak (1981)
Undisturbed NC clay	90	$\frac{(7.32-e)^2}{1+e}$	0.6	1.7-3.8	Cyclic TX	Kokusho et al. (1982)
Undisturbed Italian clays	4400-8100	$e^{-1.3}$ ($e^{-1.1}$ to $e^{-1.43}$)	0.40-0.58	0.6-1.8	RC & BE	Jamiolkowski et al. (1995)
Several soft clays	5000	$e^{-1.5}$	0.5	1-5	SCPT	Shibuya and Tanaka (1996)
Several soft clays	18000-30000	$\frac{1}{(1+e)^{2.4}}$	0.5	1-6	SCPT	Shibuya et al. (1997)

Note: RC = resonant column; BE – bender element test, SCPT – seismic cone

4.2.3 Void Ratio and Stress History

Generally, the magnitude of G_0 decreases with increasing void ratio (e). In packing of soils, the void ratio is inversely related to coordination number (CN) which indicates the average number of contacts per particles. In granular materials, experimental relationships between the void ratio and coordination number were observed in prior studies (Oda 1977, Chang et al. 1991; Mitchell and Soga 2005). Dense packing results in small void ratios which represents a large coordination number, hence the magnitude of G_0 increases. In the G_0 expressions (i.e., Tables 4.1 and 4.2), various void ratio functions have been suggested for different types of soils. A comparison of

these void ratio functions are presented in Figure 4.8. As some natural soft clays exhibit quite large void ratios (e.g., Mexico City clay with $3 < e_0 < 10$), it would appear that the power law formats for the void ratio functions hold merit over the earlier expressions.

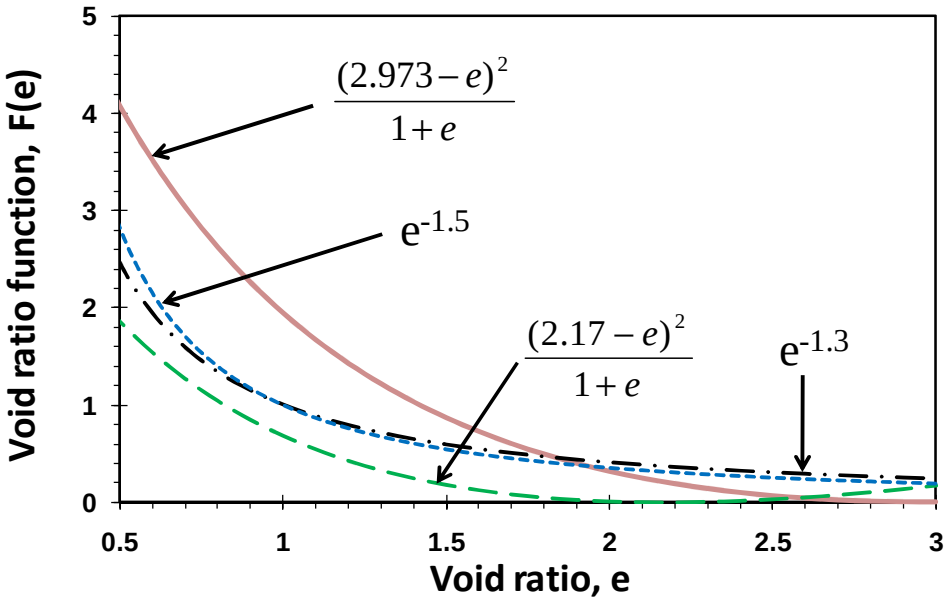

Figure 4.8. Comparison of observed trends of several void ratio functions.

With respect to the effects of stress history, it has been known that G_0 generally increases with OCR (i.e., $k > 0$ in Equation 4.2 and Equation 4.3). The OCR has more influence on G_0 when geomaterials have a higher plasticity index, as noted by Hardin and Black (1968), Dobry and Vucetic (1987), and Viggiani and Atkinson (1995). In normally consolidated soils (OCR = 1), the effective confining stress and void ratio mainly control the initial shear stiffness. However, there have been some conflicts regarding the specific influence of overconsolidation in soils, as separate from stress state. Based on laboratory tests, several studies have suggested that only two variables (i.e., confining stress and either void ratio or OCR) are among the three main factors necessary for G_0 assessment because the information is redundant (Viggiani and Atkinson 1995, Rampello et al. 1997,

Santagata et al. 2005). For instance, based on results from tests on Boston Blue clay (BBC), Santagata (2007) showed that two variables can sufficiently describe the stiffness ($E_{u,max}$), as shown in Figure 4.9.

In fact, current stress state and void ratio function have been usually adopted as controlling factors on G_0. For instance, some prior empirical studies suggested that OCR has a negligible effect on G_0 if it is appropriately normalized by the void ratio function (Tatsuoka and Shibuya 1992, Jamiolkowski et al. 1995, Santagata 2008). However, the OCR might be preferred in preconsolidated fine grained soils because void ratio changes in overconsolidated clays are much smaller than in normally consolidated clays (Viggiani and Atkinson 1995, Choo et al. 2011). In Figure 4.9 (Boston Blue clay), the OCR in fact provides a robust stiffness correlation. Conceptually, it can be illustrated in Figure 4.10 where an idealized void ratio versus logarithm of effective vertical stress plot is obtained from consolidation testing (here: initial void ratio e_o = 0.86 at 40 kPa, compression index C_c = 0.25, recompression index C_r = 0.03, preconsolidation stress σ_{p1}' = 100 kPa, stress at initial swelling point σ_{p2}' = 200 kPa). During loading and unloading steps, typical variations of void ratio and corresponding OCR are depicted. It is indicated that the variation of OCR seems significant with stress level change in overconsolidated areas.

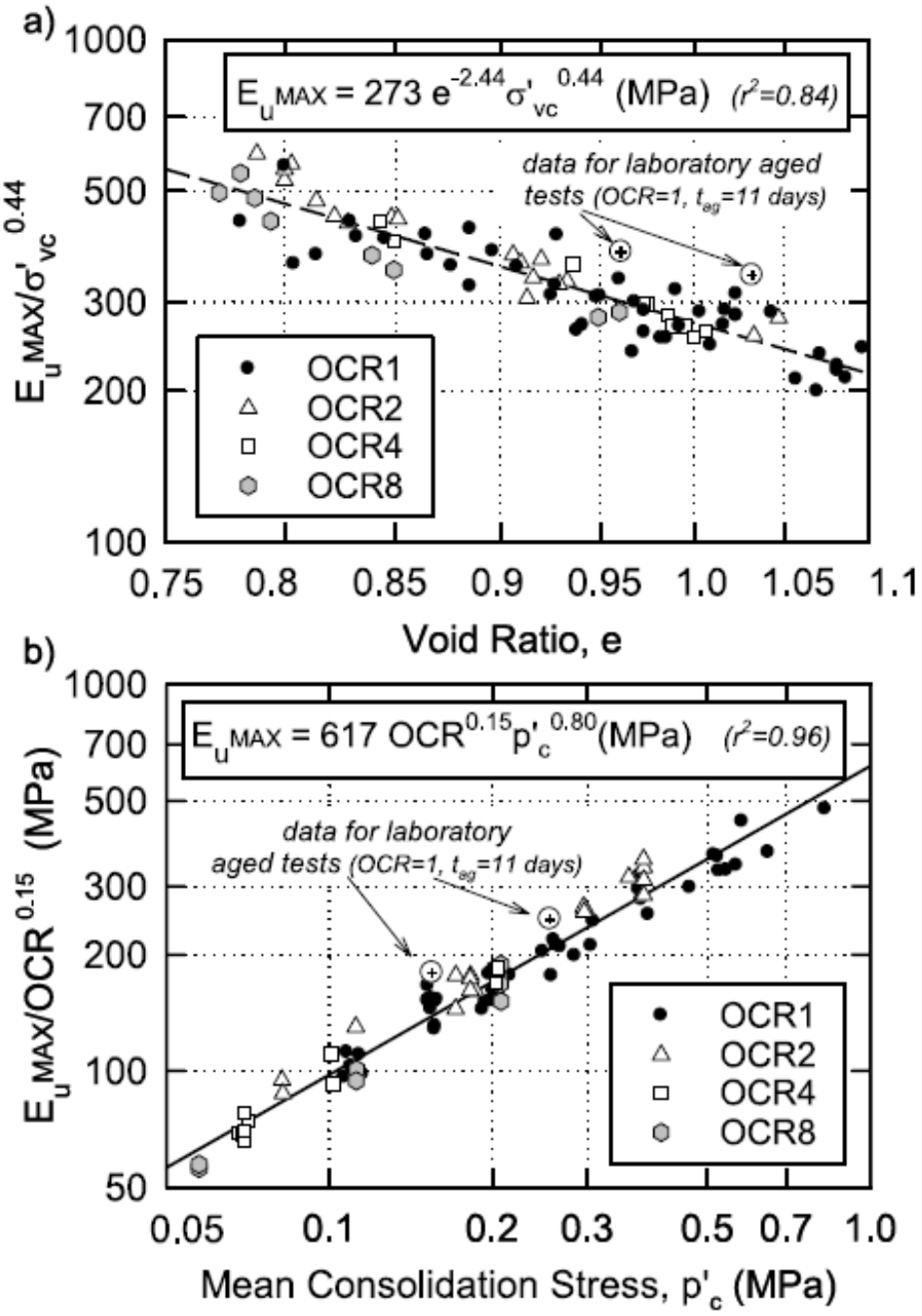

Figure 4.9. $E_{u,max}$ correlations using two variables: a) confining stress (σ_v') and void ratio, b) confining stress (σ_o', here expressed by p'_c) and OCR for Boston Blue clay (Santagata et al. 2005, Santagata and Kang 2007, Santagata 2008).

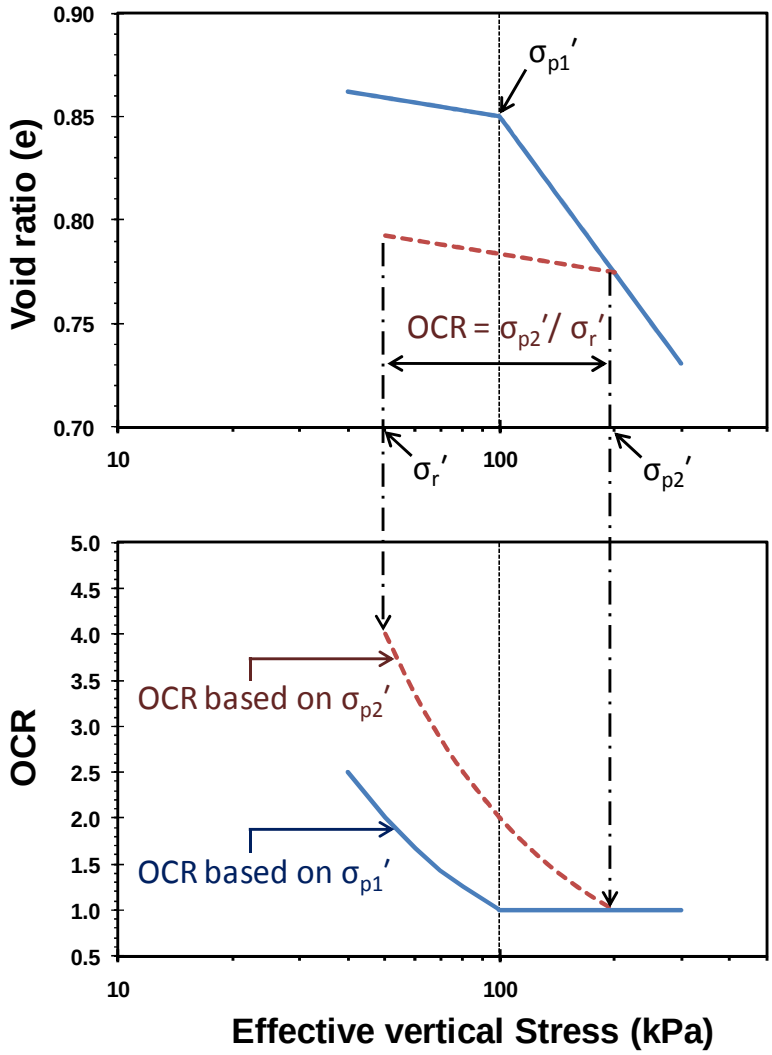

Figure 4.10. Typical relationship between void ratio and effective vertical stress from consolidation test and corresponding OCR variations (here, initial void ratio e_0 = 0.86 at 40 kPa, compression index C_c = 0.25, recompression index C_r = 0.03, preconsolidation stress σ_{p1}' = 100 kPa, stress at initial swelling point σ_{p2}' = 200 kPa).

4.2.4 Other Factors Influencing G_0

For the aforementioned G_0 relationships, the primary influence factors (i.e., effective confining stress, void ratio, and/or OCR) have been documented and verified. Several secondary level parameters of influence have also been identified in earlier

research efforts that are briefly summarized in Table 4.3 (Hardin and Drnevich 1972, Dobry and Vucetic 1987, Benz 2007).

Table 4.3. Additional factors affecting small strain shear modulus, G_0
(adapted from Dobry and Vucetic 1987; Benz 2007)

Parameters	**Small-strain shear stiffness, G_0**
Plasticity index, PI	1) Increases with PI (if OCR > 1) 2) Stays about constant (if OCR = 1)
Geologic age, t	Increases with time (specifically lab specimens)
Sample disturbance	Decreases with level of disturbance (lab specimens)
Cementation, c	Increases with amount of cement or bonding agent
Strain rate, $\partial\gamma/\partial t$ (and frequency of cyclic loading)	Slight increase with $\partial\gamma/\partial t$
Number of loading cycles, N	Decreases after N cycles of loading at large γ_c but recovers later with time
Effective material strength	Slightly influenced by ϕ' for granular soils
Grain characteristics	1) D_{50} and grain size distribution has more effects for poorly graded soils 2) G_0 (well graded sand) < G_0 (poorly graded sand) 3) Decreases with more fines contents
Degree of saturation, S	1) Relatively unimportant for clean sand 2) Important in cohesive soils (decreases with S) 3) Very important during desaturation and desiccation*

Notes: γ_c = cyclic strain, D_{50} = mean grain diameter; *Cho and Santamarina (2001)

The aforementioned developed relationships for G_0 were accomplished primarily via laboratory testing programs using data from RC and/or BE tests. Laboratory testing can control or adjust selected variables to specified soil conditions, hence investigate the

relative effects of each factor. However, it appears that several major deleterious changes occur when soil samples are removed from their natural environment: (1) sample disturbance that often is irrecoverable; (2) loss of natural time or ageing effects. When soil samples are removed from the ground, there are irrecoverable issues related to the loss of in-situ stresses, particularly when the specimen is cut from the sample before mounting in a resonant column device or triaxial or consolidation with bender elements (Tatsuoka and Shibuya 1992). Figure 4.11 verifies that the laboratory to field V_s ratio (or G_0 ratio) significantly relates to the sample quality (DeGroot el al. 2011; Jamiolkowski 2012). The data indicate even undisturbed samples tend to under estimate the field V_s value.

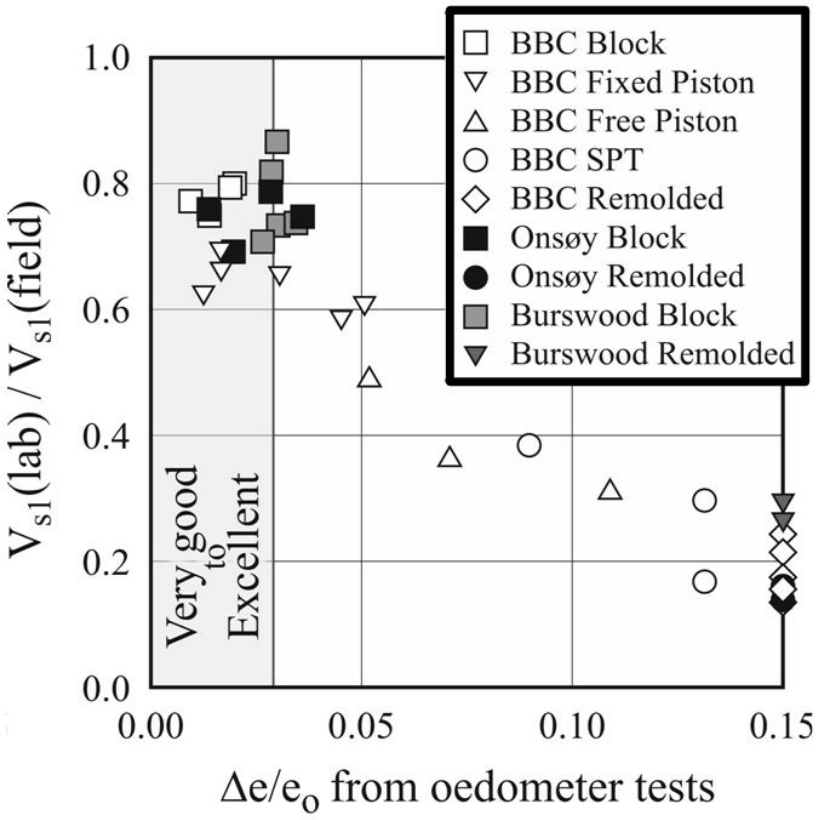

Figure 4.11. Example of sample quality evaluation using laboratory to filed V_s ratio (DeGroot el al. 2011; Jamiolkowski 2012)

Moreover, early studies by Anderson and Stokoe (1978) indicated a correction factor for time or age effects (N_G) was needed in order to relate lab testing G_0 values to field G_0 values (Equation 3.3, Figure 3.4; Chapter 3). Later, these time effects were confirmed and expanded upon by Mesri and Choi (1983), Leroueil and Hight (2003), Santagata and Kang (2007) and others. For instance, Santagata and Kang (2007) compared field and laboratory stiffness ($E_{u,max}$) data with consideration of ageing effect. Figure 4.12 shows the magnitudes of field stiffness are relatively larger than laboratory stiffness values based on Boston Blue Clay (BBC). Also, appropriate ageing correction factor (N_G) ranges were derived (Figure 4.12). Once the soil is removed from the ground, it would appear that the "clock is restarted", and therefore these unavoidable sampling issues add confusion and uncertainty into the overall assessment of G_0 facets in the laboratory. Field soil conditions tend to be more complex because various natural factors (e.g., ageing, diagenesis, depositional process, particle bonding, etc.) are involved and yet the soils remain under their natural anisotropic state without losses due to sample disturbance and/or age.

Herein, a developmental study of G_0 relationships acquired from different directional and polarized planes (VH, HV, HH) are examined using in-situ geophysical data collected from various field sites. The focus on field data is necessary in order to avoid the difficulties of sample disturbance and ageing/time effects. This study considers separate directional G_0 modes because significant stiffness anisotropy is observed under field conditions, particularly as the OCR increases (e.g., London clay, Gault clay) and the noted hierarchy of in-situ V_s modes in soils is further developed ($V_{sHH} \geq V_{sHV} \geq V_{sVH}$).

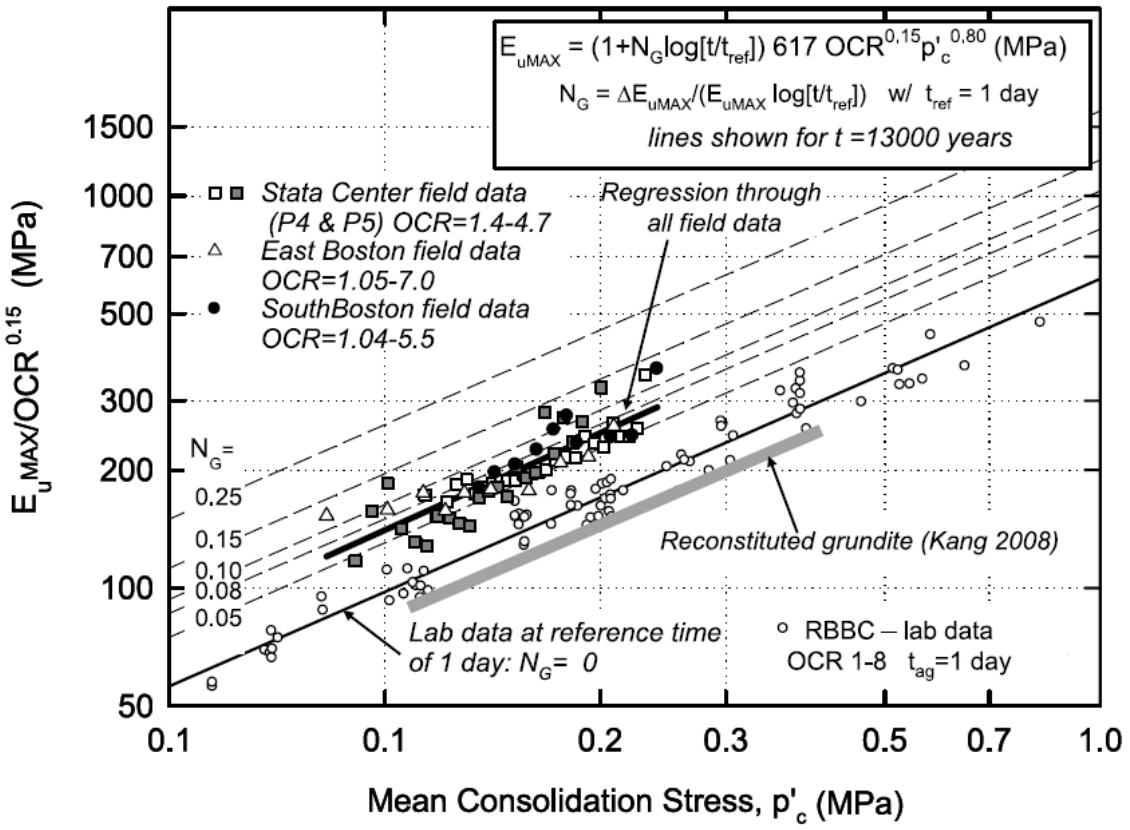

Figure 4.12. Stiffness comparison of unaged reconstituted Boston Blue Clay (RBBC) and natural field soil with application of ageing correction factor (Santagata 2008).

4.3 Field G_0 Database

For this study, a special field database has been collected from 33 well-documented geotechnical test sites, including: 14 sands and silt-sand mixtures and 19 clay sites. The database includes geophysical surveys from three different modes: 29 $G_{0,VH}$, 24 $G_{0,HV}$, and 17 $G_{0,HH}$ from in-situ shear wave velocity profiles. The $G_{0,HH}$ type has the smallest dataset because the corresponding V_{sHH} mode requires a special wave-generating system like a rotary hammer, horizontal sparker, or torsional source.

In field testing, it is not possible to control many of the testing variables and soil conditions. Thus, the current in-situ geostatic stress state and natural soil properties must

be assessed in order to relate to the measured G_0. Herein, the noted three main variables (i.e., confining stress, void ratio, and OCR) are considered in order to quantify the G_0 expressions. In fact, details of the applied database including G_0 planes (or V_s modes) have already been provided in Table 3.2. Most of reference G_0 data were derived from published sources, reports, and detailed studies conducted at the well-documented sites.

4.4 G_0 Relationships in Different Planes

4.4.1 G_0 Correlations in Clays

Based on the compiled field database, empirical G_0 correlations were examined from regression analyses. First, simple G_0-stress relationships in different planes were sought for cohesive soils. Table 4.4 summarizes the equations derived using three different types of confining stresses (i.e., σ_v'; σ_o'; $\sigma_v' \times \sigma_h'$ or $\sigma_h' \times \sigma_h'$) with additional statistical information. Figure 4.13 shows plots of G_0 versus adopted confining stresses and regression lines. Some notable observations are as follow:

▪ Empirical G_0 expressions using vertical stress (σ_v') seem less consistent in magnitudes of stress exponents and/or material constants. Also, compared to cases using mean normal stress (σ_o') and individual stress ($\sigma_v' \times \sigma_h'$ or $\sigma_h' \times \sigma_h'$), the G_0-σ_v' data are rather more scattered, thus relatively small determination of coefficient (R^2) values are observed. Consequently, it seems that mean normal stress and individual stress provide better correlations.

▪ Whereas stress exponent values in different planes are a little variable in limited ranges or equivalent, material constants have a general hierarchy in magnitude: HH > HV > VH (e.g., material constant values: 944 (Eq. 4.5.3b) > 686 (Eq. 4.5.2b) > 329 (Eq. 4.5.1b) and 1101 (Eq. 4.5.3c) > 647 (Eq. 4.5.2c) > 405 (Eq. 4.5.1c) for intact clays; 1012 (Eq.

4.6.3b) > 808 (Eq. 4.6.2b) > 645 (Eq. 4.6.1b) and 1037 (Eq. 4.6.3c) > 830 (Eq. 4.6.2c) > 520 (Eq. 4.6.1c) for both intact and fissured clays).

▪ Within the compiled dataset, the G_0 measurements in VH plane appear to have lower R^2 values maybe due to some sensitive errors and lack of data having very high stress levels.

▪ In Figure 4.13, discrepancies between regression lines from intact clays and from both intact and fissured clays are not significant mostly for correlations using mean normal stress and individual stress.

Table 4.4. Directional G_0-stress relationships from clays in database (source: Table 3.2)

Soil type	Plane	Empirical equation	R^2	S.E.	N	Eq.
Intact clay	VH	$G_{0,VH} = 954 \cdot (\sigma_v')^{0.811}$	0.263	0.344	146	4.5.1a
		$G_{0,VH} = 329 \cdot (\sigma_o')^{1.113}$	0.510	0.285	136	4.5.1b
		$G_{0,VH} = 405 \cdot (\sigma_v' \cdot \sigma_h')^{0.528}$	0.456	0.300	136	4.5.1c
	HV	$G_{0,HV} = 482 \cdot (\sigma_v')^{0.973}$	0.764	0.231	127	4.5.2a
		$G_{0,HV} = 686 \cdot (\sigma_o')^{0.928}$	0.789	0.219	127	4.5.2b
		$G_{0,HV} = 647 \cdot (\sigma_v' \cdot \sigma_h')^{0.467}$	0.784	0.221	127	4.5.2c
	HH	$G_{0,HH} = 1139 \cdot (\sigma_v')^{0.870}$	0.784	0.183	91	4.5.3a
		$G_{0,HH} = 944 \cdot (\sigma_o')^{0.915}$	0.882	0.135	91	4.5.3b
		$G_{0,HH} = 1101 \cdot (\sigma_h' \cdot \sigma_h')^{0.447}$	0.908	0.119	91	4.5.3c
Intact clay & fissured clay	VH	$G_{0,VH} = 574 \cdot (\sigma_v')^{0.961}$	0.373	0.324	200	4.6.1a
		$G_{0,VH} = 645 \cdot (\sigma_o')^{0.939}$	0.554	0.270	189	4.6.1b
		$G_{0,VH} = 520 \cdot (\sigma_v' \cdot \sigma_h')^{0.497}$	0.539	0.275	189	4.6.1c
	HV	$G_{0,HV} = 1089 \cdot (\sigma_v')^{0.854}$	0.613	0.265	175	4.6.2a
		$G_{0,HV} = 808 \cdot (\sigma_o')^{0.905}$	0.727	0.222	174	4.6.2b
		$G_{0,HV} = 830 \cdot (\sigma_v' \cdot \sigma_h')^{0.452}$	0.710	0.229	174	4.6.2c
	HH	$G_{0,HH} = 3236 \cdot (\sigma_v')^{0.713}$	0.625	0.218	127	4.6.3a
		$G_{0,HH} = 1012 \cdot (\sigma_o')^{0.911}$	0.862	0.130	126	4.6.3b
		$G_{0,HH} = 1037 \cdot (\sigma_h' \cdot \sigma_h')^{0.452}$	0.896	0.113	126	4.6.3c

Note: (1) G_0 and stress units in kPa. (2) If G_0 and confining stress are normalized by reference pressure (i.e., $\sigma_{atm}' = 100$kPa), dimensionless correlations are derived.

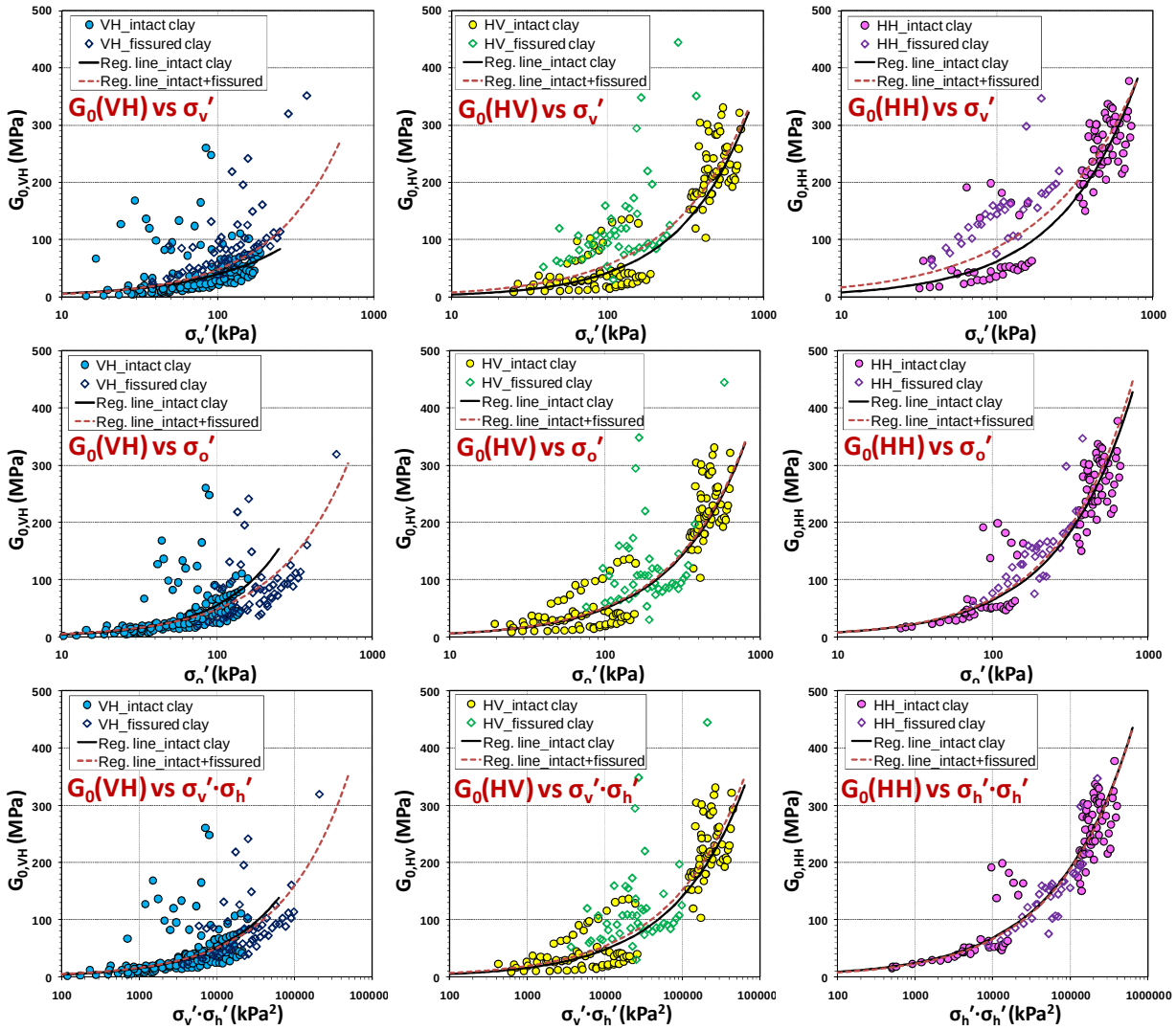

Figure 4.13. Apparent relationships between G_0 ($G_{0,VH}$; $G_{0,HV}$; $G_{0,HH}$) and confining stresses (σ_v'; σ_o'; $\sigma_v' \times \sigma_h'$ or $\sigma_h' \times \sigma_h'$) in clays. For equations and statistic information of regression lines, refer to Table 4.4.

For improved G_0 relationships, the in-situ void ratio (e_0) and OCR factors were considered along with effective confining stresses. For simplicity, the void ratio function is adopted as a power law function (i.e., e_0^{-x}) which was used by Jamiolkowski et al. (1995). As shown in Figure 4.8, the void ratio function (e_0^{-x}) is expected to have reasonable ranges. Table 4.5 summarizes G_0 correlations for different directional planes from multiple regression analyses conducted on data from intact clays. Table 4.6 shows results for both intact and fissured clays. Compared to the results in Table 4.4, two variables (confining stress, and either void ratio or OCR) generated apparent improved G_0 relationships. However, in most cases excepting $G_{0,VH}$ for intact clays, three variables (stress, e_0, OCR) did not provide good statistical results for correlations (e.g., low significance levels for variables or negligible effects of one variable), maybe because of redundant effects between void ratio and OCR.

It is observed that G_0 correlations using σ_v' have a relatively higher dependency (i.e., large exponents) on the basis of e_0 and/or OCR than other correlations with σ_o' or $\sigma_v' \times \sigma_h'$. The OCR seems to have more influence on G_0 correlations for intact clay than those for both intact and fissured clays. This seems to be resulting from significantly large OCR values in many fissured clays. Based on RC and BE tests on six undisturbed clays, Jamiolkowski et al. (1995) reported the range of the void ratio function: $e_0^{-1.11}$ to $e_0^{-1.52}$ derived from $G_{0,VH}$ correlations using confining stress and void ratio. In Table 4.5, the derived exponent values of void ratio function are close to the range or slightly lower (i.e., $e_0^{-1.206}$ in Eq. 4.7.1a; $e_0^{-1.030}$ in Eq. 4.7.1b; $e_0^{-1.070}$ in Eq. 4.7.1c). Figure 4.14 compares measured G_0 (y-axis) and predicted G_0 (x-axis) from regression analyses for intact clays. When two variables (stress and either e_0 or OCR) are involved in G_0

relationships, the overall correlations are quite improved albeit some discrepancies and uncertainties are still observed. Particularly, regressions including the void ratio provide almost the best predictions in all planes (VH, HV, HH).

Table 4.5. Directional G_0 correlations for intact clays (source: Table 3.2)

Plane	Empirical equation	R^2	S.E.	N	Eq.
VH	$G_{0,VH} = 5817 \cdot (\sigma_v')^{0.457} \cdot (e_0)^{-1.206}$	0.809	0.178	133	4.7.1a
	$G_{0,VH} = 3309 \cdot (\sigma_o')^{0.610} \cdot (e_0)^{-1.030}$	0.844	0.164	123	4.7.1b
	$G_{0,VH} = 3697 \cdot (\sigma_v' \cdot \sigma_h')^{0.291} \cdot (e_0)^{-1.070}$	0.838	0.168	123	4.7.1c
	$G_{0,VH} = 152 \cdot (\sigma_v')^{1.070} \cdot (OCR)^{1.053}$	0.780	0.189	140	4.7.1d
	$G_{0,VH} = 320 \cdot (\sigma_o')^{0.998} \cdot (OCR)^{0.699}$	0.746	0.207	130	4.7.1e
	$G_{0,VH} = 283 \cdot (\sigma_v' \cdot \sigma_h')^{0.504} \cdot (OCR)^{0.779}$	0.756	0.203	130	4.7.1f
	$G_{0,VH} = 1045 \cdot (\sigma_v')^{0.742} \cdot (e_0)^{-0.725} \cdot (OCR)^{0.571}$	0.866	0.150	133	4.7.1g
	$G_{0,VH} = 1945 \cdot (\sigma_o')^{0.681} \cdot (e_0)^{-0.806} \cdot (OCR)^{0.273}$	0.863	0.155	123	4.7.1h
	$G_{0,VH} = 1727 \cdot (\sigma_v' \cdot \sigma_h')^{0.347} \cdot (e_0)^{-0.785} \cdot (OCR)^{0.339}$	0.865	0.154	123	4.7.1i
HV	$G_{0,HV} = 2767 \cdot (\sigma_v')^{0.639} \cdot (e_0)^{-1.112}$	0.958	0.093	117	4.7.2a
	$G_{0,HV} = 3574 \cdot (\sigma_o')^{0.606} \cdot (e_0)^{-1.032}$	0.947	0.104	117	4.7.2b
	$G_{0,HV} = 3437 \cdot (\sigma_v' \cdot \sigma_h')^{0.305} \cdot (e_0)^{-1.049}$	0.949	0.102	117	4.7.2c
	$G_{0,HV} = 449 \cdot (\sigma_v')^{0.875} \cdot (OCR)^{0.761}$	0.824	0.201	127	4.7.2d
	$G_{0,HV} = 690 \cdot (\sigma_o')^{0.848} \cdot (OCR)^{0.521}$	0.815	0.206	127	4.7.2e
	$G_{0,HV} = 643 \cdot (\sigma_v' \cdot \sigma_h')^{0.425} \cdot (OCR)^{0.572}$	0.815	0.205	127	4.7.2f
HH	$G_{0,HH} = 5522 \cdot (\sigma_v')^{0.551} \cdot (e_0)^{-1.143}$	0.948	0.090	90	4.7.3a
	$G_{0,HH} = 3837 \cdot (\sigma_o')^{0.632} \cdot (e_0)^{-0.904}$	0.967	0.072	90	4.7.3b
	$G_{0,HH} = 3808 \cdot (\sigma_h' \cdot \sigma_h')^{0.321} \cdot (e_0)^{-0.800}$	0.968	0.071	90	4.7.3c
	$G_{0,HH} = 400 \cdot (\sigma_v')^{0.899} \cdot (OCR)^{0.975}$	0.967	0.072	91	4.7.3d
	$G_{0,HH} = 621 \cdot (\sigma_o')^{0.888} \cdot (OCR)^{0.622}$	0.957	0.082	91	4.7.3e
	$G_{0,HH} = 874 \cdot (\sigma_h' \cdot \sigma_h')^{0.430} \cdot (OCR)^{0.456}$	0.947	0.091	91	4.7.3f

Notes: (1) G_0 and stress units in kPa. (2) Except $G_{0,VH}$ in intact clays, correlations obtained from multiple regression using three variables (stress, e_0, OCR) are not provided because significance levels are not adoptable (less than 99% for variables) or OCR has limited effect. (3) If G_0 and

confining stress are normalized by reference pressure (i.e., σ_{atm}' = 100kPa), dimensionless correlations are derived. (4) Void ratio function (e_0^{-x}) format is adopted from Jamiolkowski et al. 1995.

Table 4.6. Directional G_0 correlations for both intact and fissured clays

(source: Table 3.2)

Plane	Empirical equation	R^2	S.E.	N	Eq.
VH	$G_{0,VH} = 4747 \cdot (\sigma_v')^{0.501} \cdot (e_0)^{-1.185}$	0.835	0.170	187	4.8.1a
	$G_{0,VH} = 6441 \cdot (\sigma_o')^{0.430} \cdot (e_0)^{-1.034}$	0.822	0.175	176	4.8.1b
	$G_{0,VH} = 5285 \cdot (\sigma_v' \cdot \sigma_h')^{0.239} \cdot (e_0)^{-1.040}$	0.831	0.170	176	4.8.1c
	$G_{0,VH} = 564 \cdot (\sigma_v')^{0.856} \cdot (OCR)^{0.377}$	0.580	0.268	194	4.8.1d
	$G_{0,VH} = 883 \cdot (\sigma_o')^{0.835} \cdot (OCR)^{0.104}$	0.562	0.271	183	4.8.1e
	$G_{0,VH} = 795 \cdot (\sigma_v' \cdot \sigma_h')^{0.422} \cdot (OCR)^{0.173}$	0.570	0.269	183	4.8.1f
HV	$G_{0,HV} = 4093 \cdot (\sigma_v')^{0.570} \cdot (e_0)^{-1.209}$	0.899	0.127	165	4.8.2a
	$G_{0,HV} = 3625 \cdot (\sigma_o')^{0.594} \cdot (e_0)^{-0.987}$	0.882	0.137	164	4.8.2b
	$G_{0,HV} = 3608 \cdot (\sigma_v' \cdot \sigma_h')^{0.298} \cdot (e_0)^{-1.033}$	0.893	0.130	164	4.8.2c
	$G_{0,HV} = 540 \cdot (\sigma_v')^{0.908} \cdot (OCR)^{0.322}$	0.732	0.222	175	4.8.2d
	$G_{0,HV} = 799 \cdot (\sigma_o')^{0.892} \cdot (OCR)^{0.057}$	0.731	0.221	174	4.8.2e
	$G_{0,HV} = 748 \cdot (\sigma_v' \cdot \sigma_h')^{0.445} \cdot (OCR)^{0.135}$	0.732	0.221	174	4.8.2f
HH	$G_{0,HH} = 9173 \cdot (\sigma_v')^{0.464} \cdot (e_0)^{-1.326}$	0.897	0.114	126	4.8.3a
	$G_{0,HH} = 3274 \cdot (\sigma_o')^{0.662} \cdot (e_0)^{-0.846}$	0.943	0.084	125	4.8.3b
	$G_{0,HH} = 2811 \cdot (\sigma_h' \cdot \sigma_h')^{0.347} \cdot (e_0)^{-0.666}$	0.938	0.088	125	4.8.3c
	$G_{0,HH} = 519 \cdot (\sigma_v')^{0.938} \cdot (OCR)^{0.408}$	0.879	0.124	127	4.8.3d
	$G_{0,HH} = 751 \cdot (\sigma_o')^{0.929} \cdot (OCR)^{0.130}$	0.895	0.114	126	4.8.3e
	$G_{0,HH} = 1004 \cdot (\sigma_h' \cdot \sigma_h')^{0.451} \cdot (OCR)^{0.027}$	0.898	0.113	126	4.8.3f

Note: (1) G_0 and stress units in kPa. (2) If G_0 and confining stress are normalized by reference pressure (i.e., σ_{atm}' = 100kPa), dimensionless correlations are derived. (3) Void ratio function (e_0^{-x}) format is adopted from Jamiolkowski et al. 1995.

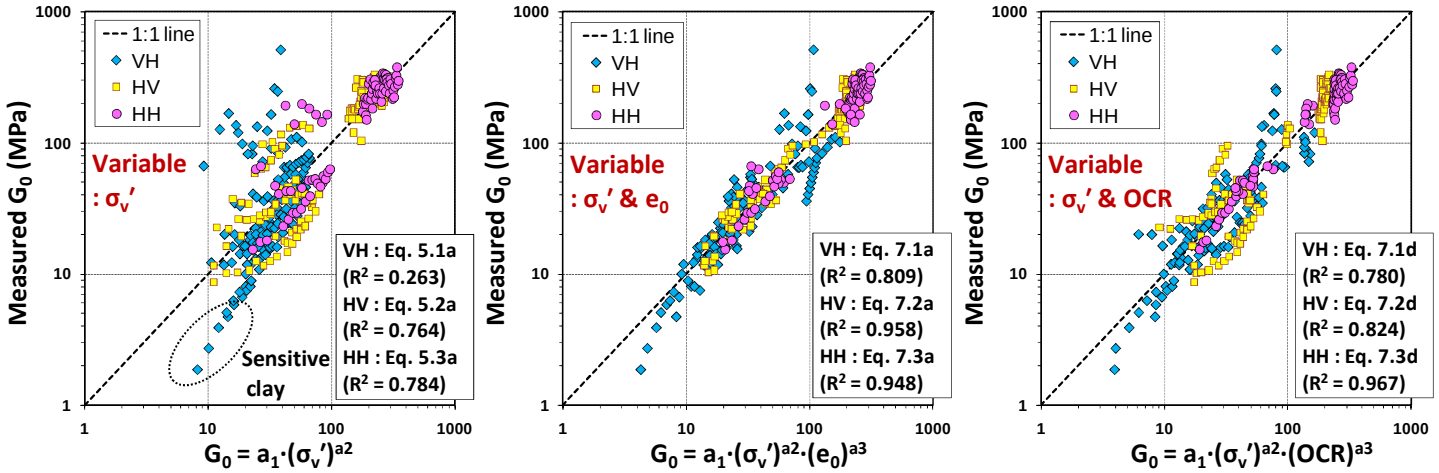

Figure 4.14 (a). Comparison of measured G_0 and predicted G_0 from regression analyses in intact clays (confining stress: vertical overburden stress = σ_v'). For equations and statistic information of regression lines, refer to Table 4.5.

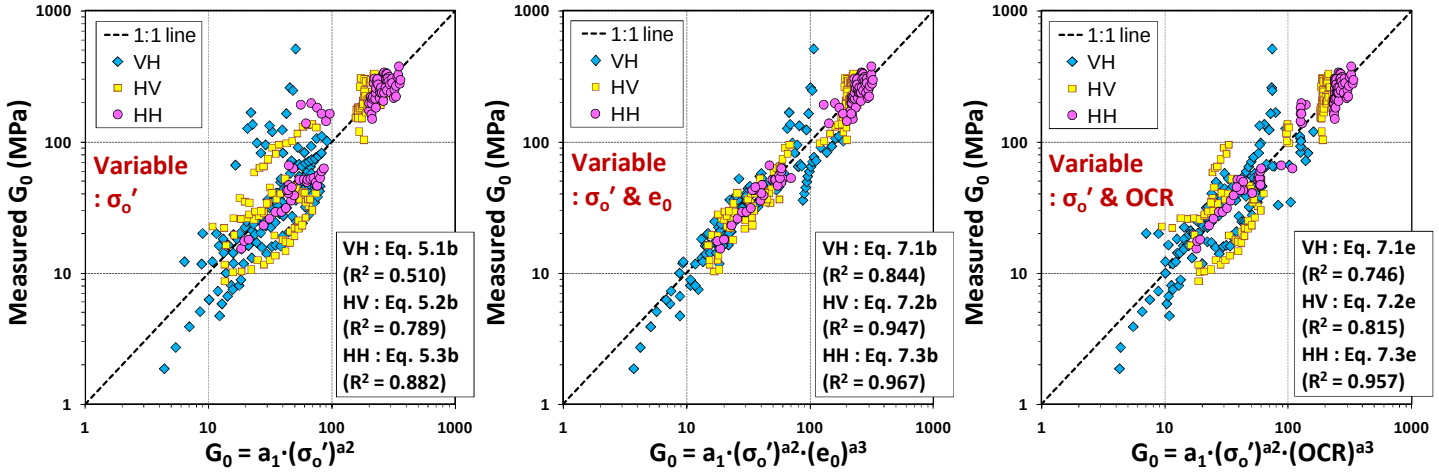

Figure 4.14 (b). Comparison of measured G_0 and predicted G_0 from regression analyses in intact clays (confining stress: mean normal stress = σ_o'). For equations and statistic information of regression lines, refer to Table 4.5.

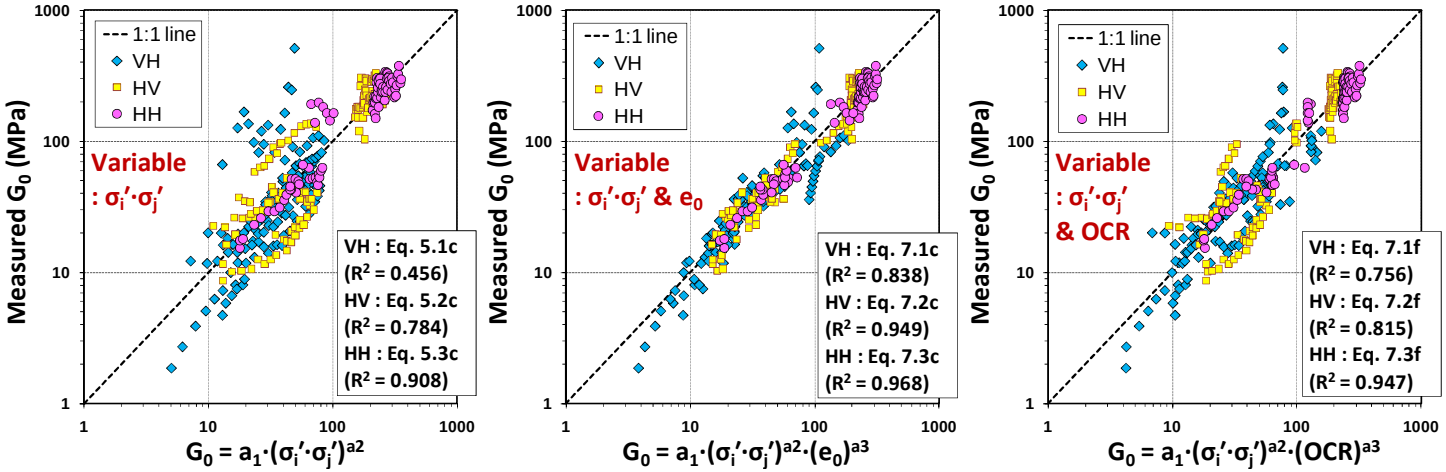

Figure 4.14 (c). Comparison of measured G_0 and predicted G_0 from regression analyses in intact clays (confining stress: individual stresses = $\sigma_i' \cdot \sigma_j'$). For equations and statistic information of regression lines, refer to Table 3.

Notes: $\sigma_i' \cdot \sigma_j' = \sigma_v' \cdot \sigma_h'$ in VH and HV plane; $\sigma_i' \cdot \sigma_j' = \sigma_h' \cdot \sigma_h'$ in HH plane.

In Figure 4.15, the value of G_0 is normalized by F(e) that is plotted with σ_o' for intact clays. The derived regression lines in different planes represent stiffness anisotropy in the compiled intact clays ($G_{0,HH} > G_{0,HV} > G_{0,VH}$). Figure 4.16 shows similar plots for both intact and fissured clays. The data seem rather scattered due to the group of data from fissured clays. In Figure 4.17, the stiffness anisotropy is still observed when the G_0 is normalized by stress function in multiple regression equations.

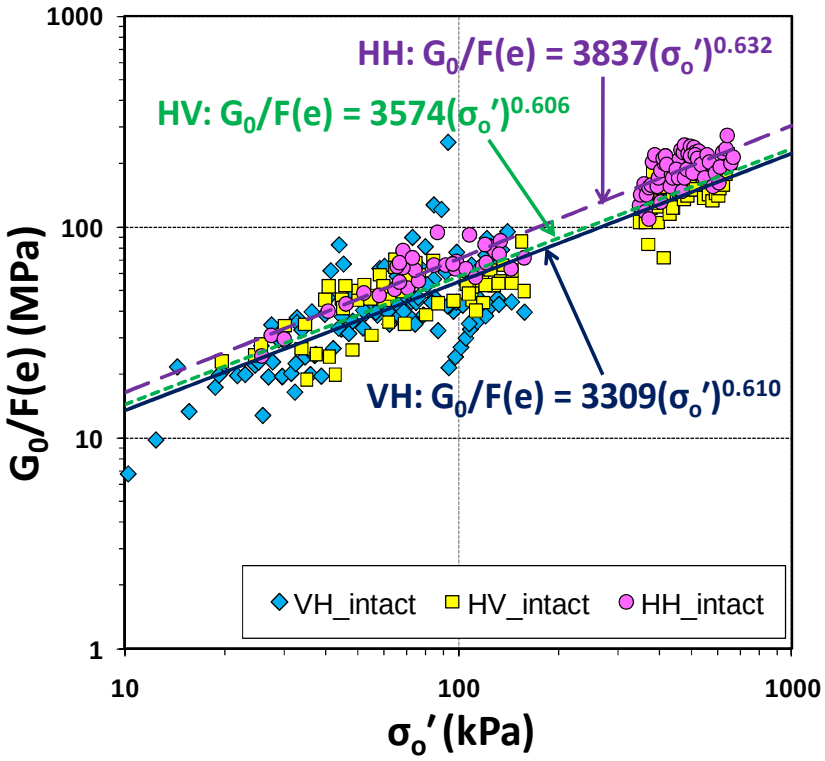

Figure 4.15. G_0 normalized by void ratio function (e_0^{-x}) in different planes (VH, HV, HH) versus mean normal stress (σ_o') in intact clays.

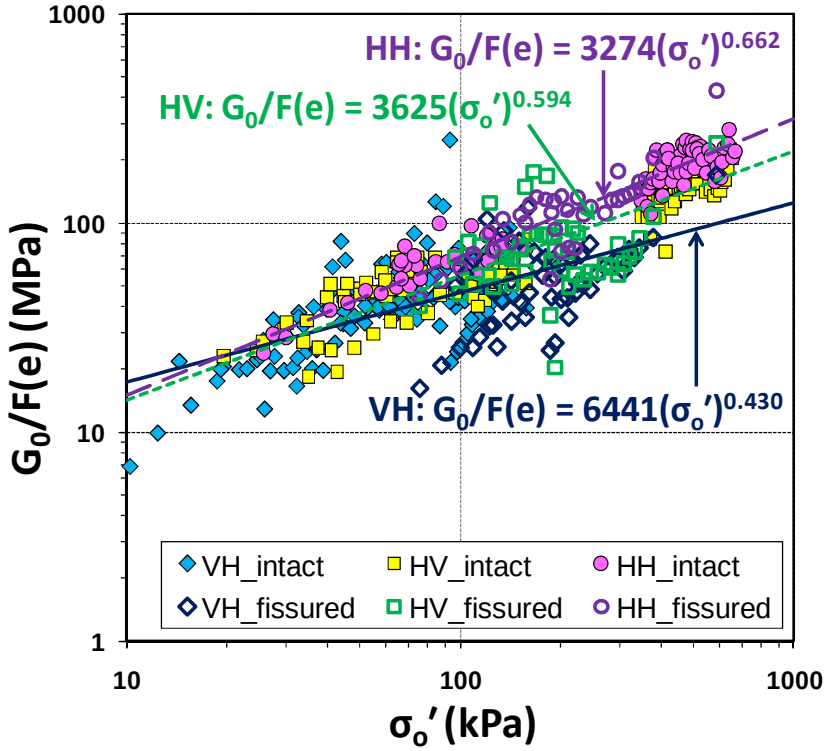

Figure 4.16. G_0 normalized by void ratio function (e_0^{-x}) in different planes (VH, HV, HH) versus mean normal stress (σ_o') in intact and fissured clays.

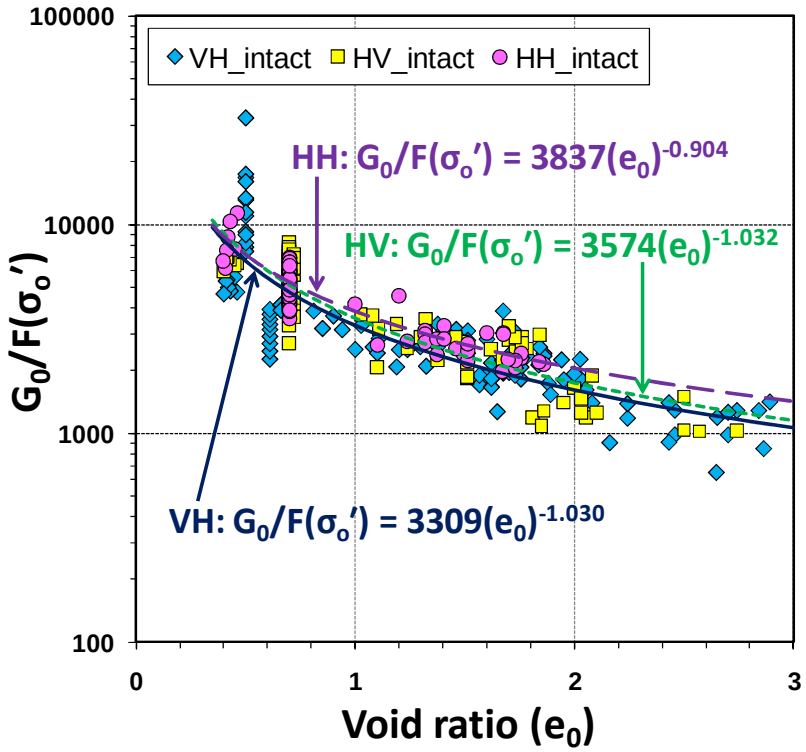

Figure 4.17. G_0 normalized by mean normal stress function ($\sigma_o'^n$) in different planes (VH, HV, HH) versus in-situ void ratio (e_0) in intact clays.

4.4.2 G_0 Correlations in Sands and Silt Mixtures

In the same manner, G_0 correlations were examined for sands and silt-sand mixtures. Table 4.7 summarizes the results from regression analyses. If the statistical results are compared with those in clays, the G_0 correlations in sands and silt mixtures seem less robust specifically when a single stress variable is only applied. For instance, Figure 4.18 shows rather scattered data from plots of G_0 versus σ_o' in different planes. In Figure 4.19, the magnitude of G_0 appears to be considerably related to void ratio (e.g., relatively high R^2). When G_0 is expressed in terms of both stress and void ratio variables, eventually improved correlation results are obtained as shown in Table 4.7. Compared to G_0 relationships in clays, the void ratio has a more pronounced influence on G_0 in sands and silt mixtures. In terms of e_0, higher exponent values are observed in the correlative expressions (Eq. 4.9) with a range between $e_0^{-1.364}$ to $e_0^{-2.550}$. In sands and silt mixtures, some additional hierarchies for regression equations are observed such as: HH > HV > VH for stress exponents; while VH > HV > HH for the material constants.

On the other hand, the OCR parameter does not really improve G_0 correlations in compiled sand and silt mixture dataset. Reliable G_0 correlations were not derived because most relationships have low significance levels and/or negligible exponent values for the OCR term. Measured G_0 and estimated G_0 from regression analyses using the two variables (σ_o' and e_0) are compared in Figure 4.20. Although the G_0 correlations are a bit more sensitive and scattered than those in clays, the predictions seem overall reasonable. In order to obtain improved G_0 relationships, it might be necessary to consider other variables such as grain characteristics (i.e., mineralogty, shape, and size), fabric, and soil

structure which were not examined in this study because of the incompleteness of information in the datasets.

Table 4.7. Directional G_0 correlations for sands and silt mixtures (source: Table 3.2)

Plane	Empirical equation	R^2	S.E.	N	Eq.
VH	$G_{0,VH} = 4594 \cdot (\sigma_v')^{0.571}$	0.365	0.244	192	4.9.1a
	$G_{0,VH} = 3878 \cdot (\sigma_o')^{0.642}$	0.348	0.247	179	4.9.1b
	$G_{0,VH} = 3924 \cdot (\sigma_v' \cdot \sigma_h')^{0.317}$	0.347	0.247	179	4.9.1c
	$G_{0,VH} = 14079 \cdot (\sigma_v')^{0.293} \cdot (e_0)^{-1.364}$	0.519	0.216	184	4.9.1d
	$G_{0,VH} = 13318 \cdot (\sigma_o')^{0.320} \cdot (e_0)^{-1.368}$	0.485	0.221	176	4.9.1e
	$G_{0,VH} = 13180 \cdot (\sigma_v' \cdot \sigma_h')^{0.160} \cdot (e_0)^{-1.370}$	0.487	0.220	176	4.9.1f
HV	$G_{0,HV} = 1076 \cdot (\sigma_v')^{0.871}$	0.506	0.281	177	4.9.2a
	$G_{0,HV} = 858 \cdot (\sigma_o')^{0.978}$	0.534	0.270	172	4.9.2b
	$G_{0,HV} = 877 \cdot (\sigma_v' \cdot \sigma_h')^{0.482}$	0.530	0.271	172	4.9.2c
	$G_{0,HV} = 10855 \cdot (\sigma_v')^{0.314} \cdot (e_0)^{-2.550}$	0.807	0.179	167	4.9.2d
	$G_{0,HV} = 8184 \cdot (\sigma_o')^{0.398} \cdot (e_0)^{-2.457}$	0.811	0.175	163	4.9.2e
	$G_{0,HV} = 8386 \cdot (\sigma_v' \cdot \sigma_h')^{0.194} \cdot (e_0)^{-2.468}$	0.810	0.176	163	4.9.2f
HH	$G_{0,HH} = 597 \cdot (\sigma_v')^{0.937}$	0.411	0.326	92	4.9.3a
	$G_{0,HH} = 467 \cdot (\sigma_o')^{1.063}$	0.400	0.330	89	4.9.3b
	$G_{0,HH} = 638 \cdot (\sigma_v' \cdot \sigma_h')^{0.518}$	0.359	0.341	89	4.9.3c
	$G_{0,HH} = 5584 \cdot (\sigma_v')^{0.445} \cdot (e_0)^{-2.141}$	0.648	0.263	84	4.9.3d
	$G_{0,HH} = 4091 \cdot (\sigma_o')^{0.541} \cdot (e_0)^{-2.155}$	0.647	0.263	82	4.9.3e
	$G_{0,HH} = 4681 \cdot (\sigma_v' \cdot \sigma_h')^{0.266} \cdot (e_0)^{-2.230}$	0.642	0.265	82	4.9.3f

Note: (1) G_0 and stress units in kPa. (2) If G_0 and confining stress are normalized by reference pressure (i.e., $\sigma_{atm}' = 100$kPa), dimensionless correlations are derived. (3) Void ratio function (e_0^{-x}) format is adopted from Jamiolkowski et al. 1995.

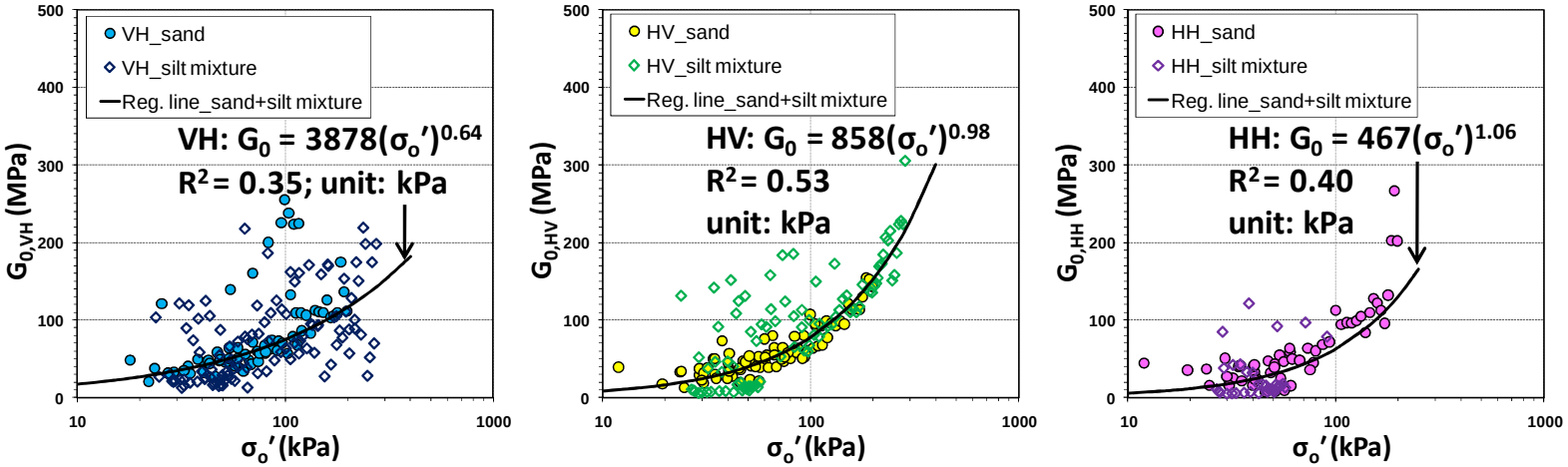

Figure 4.18. Observed trends between G_0 ($G_{0,VH}$; $G_{0,HV}$; $G_{0,HH}$) and mean normal stress (σ_o') in sands and silt mixtures.

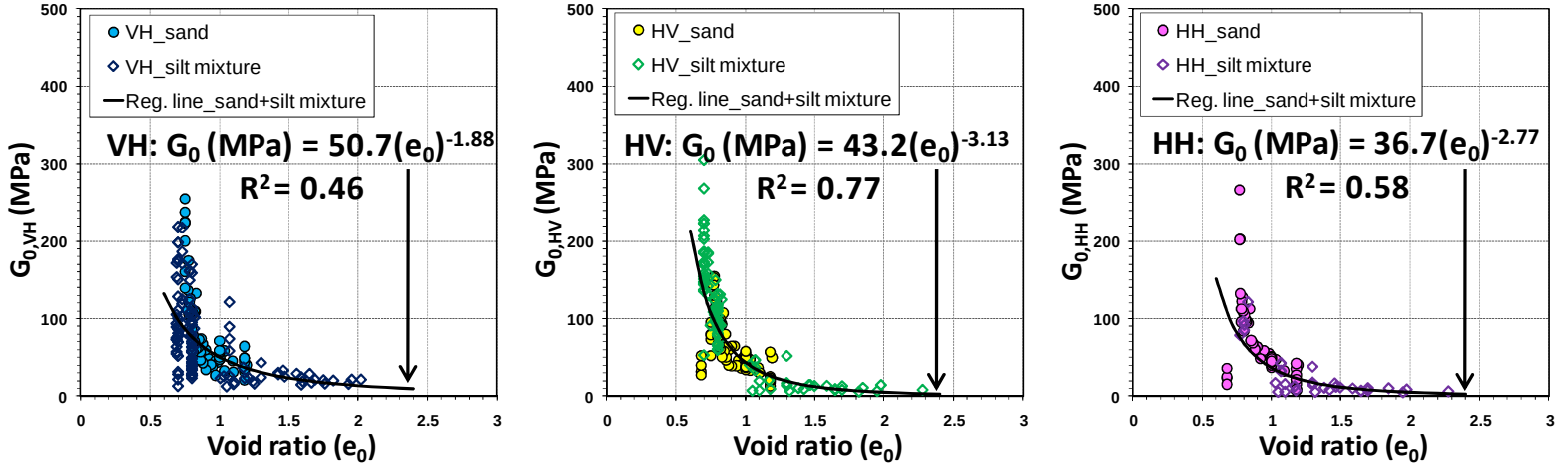

Figure 4.19. Observed trends between G_0 ($G_{0,VH}$; $G_{0,HV}$; $G_{0,HH}$) and in-situ void ratio (e_0) in sands and silt mixtures.

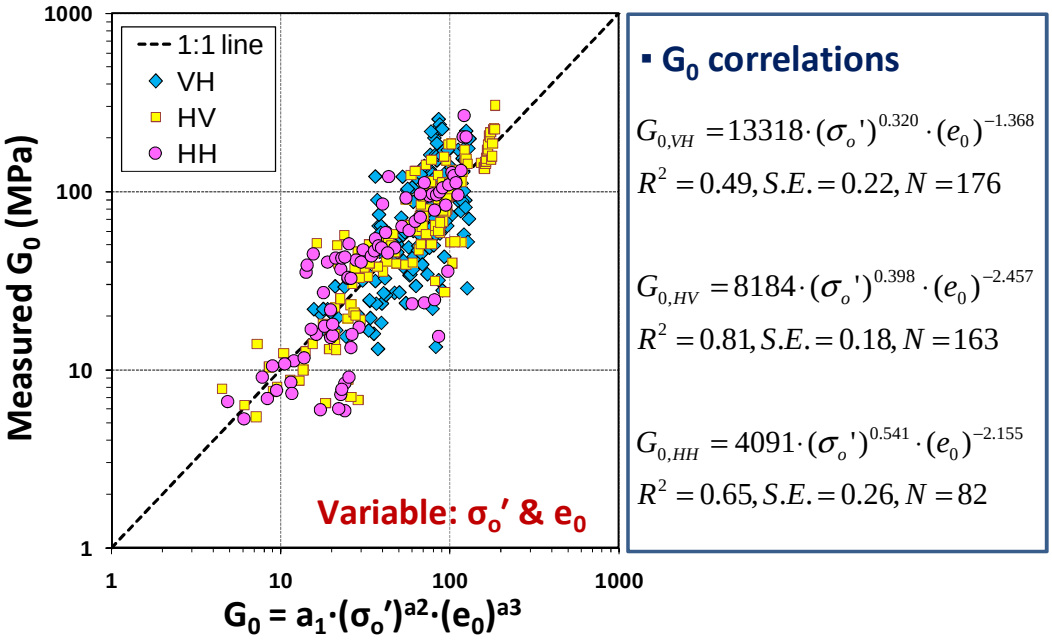

Figure 4.20. Example of measured G_0 versus predicted G_0 from regression analysis in sands and silt mixtures.

4.4.3 G_0 Correlations in All Soils

The multiple regression approaches for G_0 relationships were conducted for the entire database including all soil types: sands, silt mixtures, intact clays, and fissured clays. These results are summarized in Table 4.8. Here, results from the regressions are provided using confining stress (σ_v', σ_o', $\sigma_i' \cdot \sigma_j'$) and void ratio. The G_0 correlations were not notably influenced by OCR maybe due to the effect of sands and silt mixtures and associated uncertainty of the stress history of these geomaterials. Compared to the regression equations using a single variable (confining stress), the G_0 correlations are considerably improved by inclusion of both the confining stress and void ratio. It can be observed by comparison of Figure 4.21(a) and 4.21(b). Figure 4.21(a) shows the plot of measured G_0 versus predicted G_0 using the single variable (σ_o') regression. Figure 4.21(b) compares measured G_0 and estimated G_0 from the multiple regression (σ_o' and e_0).

Table 4.8. Directional G_0 correlations for all soil types (source: Table 3.2)

Plane	Empirical equation	R^2	S.E.	N	Eq.
VH	$G_{0,VH} = 1533 \cdot (\sigma_v')^{0.785}$	0.370	0.307	413	4.10.1a
	$G_{0,VH} = 1501 \cdot (\sigma_o')^{0.815}$	0.407	0.296	388	4.10.1b
	$G_{0,VH} = 1278 \cdot (\sigma_v' \cdot \sigma_h')^{0.425}$	0.415	0.294	388	4.10.1c
	$G_{0,VH} = 8429 \cdot (\sigma_v')^{0.390} \cdot (e_0)^{-1.265}$	0.730	0.198	371	4.10.1d
	$G_{0,VH} = 10286 \cdot (\sigma_o')^{0.355} \cdot (e_0)^{-1.182}$	0.696	0.208	352	4.10.1e
	$G_{0,VH} = 8613 \cdot (\sigma_v' \cdot \sigma_h')^{0.198} \cdot (e_0)^{-1.172}$	0.707	0.204	352	4.10.1f
HV	$G_{0,HV} = 1586 \cdot (\sigma_v')^{0.794}$	0.510	0.294	368	4.10.2a
	$G_{0,HV} = 1961 \cdot (\sigma_o')^{0.769}$	0.530	0.286	361	4.10.2b
	$G_{0,HV} = 1788 \cdot (\sigma_v' \cdot \sigma_h')^{0.393}$	0.533	0.285	361	4.10.2c
	$G_{0,HV} = 4327 \cdot (\sigma_v')^{0.544} \cdot (e_0)^{-1.475}$	0.826	0.173	332	4.10.2d
	$G_{0,HV} = 4919 \cdot (\sigma_o')^{0.532} \cdot (e_0)^{-1.347}$	0.811	0.178	327	4.10.2e
	$G_{0,HV} = 4531 \cdot (\sigma_v' \cdot \sigma_h')^{0.274} \cdot (e_0)^{-1.361}$	0.820	0.174	327	4.10.2f
HH	$G_{0,HH} = 661 \cdot (\sigma_v')^{0.976}$	0.662	0.292	219	4.10.3a
	$G_{0,HH} = 616 \cdot (\sigma_o')^{1.000}$	0.784	0.230	215	4.10.3b
	$G_{0,HH} = 952 \cdot (\sigma_v' \cdot \sigma_h')^{0.461}$	0.782	0.232	215	4.10.3c
	$G_{0,HH} = 3034 \cdot (\sigma_v')^{0.632} \cdot (e_0)^{-1.575}$	0.811	0.220	210	4.10.3d
	$G_{0,HH} = 1946 \cdot (\sigma_o')^{0.737} \cdot (e_0)^{-1.137}$	0.847	0.195	207	4.10.3e
	$G_{0,HH} = 2579 \cdot (\sigma_v' \cdot \sigma_h')^{0.344} \cdot (e_0)^{-1.102}$	0.840	0.200	207	4.10.3f

Note: (1) G_0 and stress units in kPa. (2) If G_0 and confining stress are normalized by reference pressure (i.e., $\sigma_{atm}' = 100$kPa), dimensionless correlations are derived. (3) Void ratio function (e_0^{-x}) format is adopted from Jamiolkowski et al. 1995.

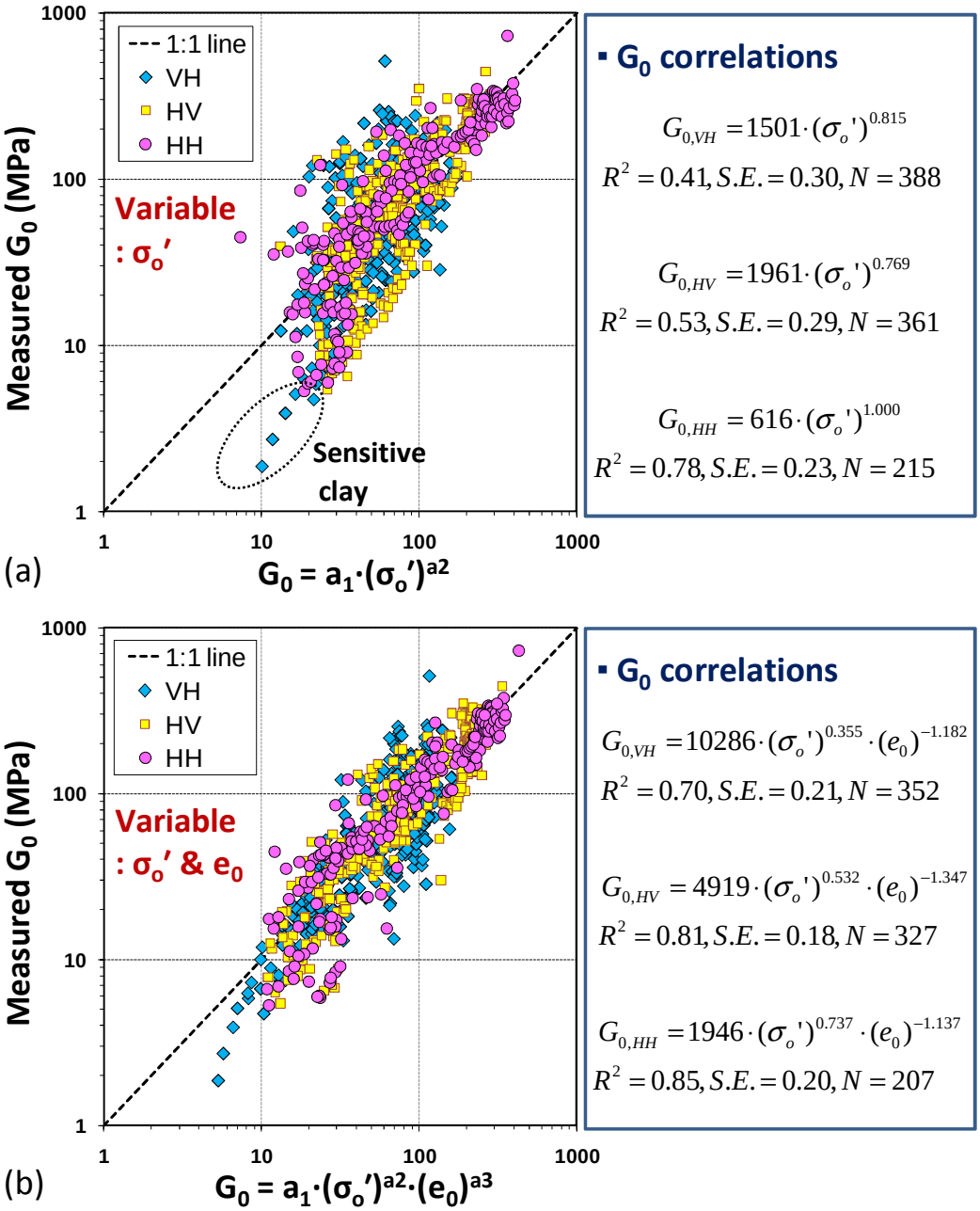

Figure 4.21 (a) Measured G_0 versus predicted G_0 using a single variable regression (variable: σ_o'), (b) measured G_0 versus predicted G_0 using multiple regression (variables: σ_o' and void ratio) for all soil types.

4.5 Summary on G_0 Relationships and Conclusions

This chapter examined a comprehensive set of G_0 correlations in terms of confining stresses (σ_v'; σ_o'; $\sigma_v' \times \sigma_h'$ or $\sigma_h' \times \sigma_h'$), void ratio ($e_0$), and OCR based on in-situ directional shear wave data obtained at various sites. Generally, natural sediments are expected to have a combination of both inherent and stress induced anisotropy, thus global G_0 relationships were derived for different soil types with consideration of different soil planes (VH, HV, HH). A special in-situ database in lieu of laboratory measurements has been collected from well-documented worldwide geotechnical test sites (19 clay sites and 14 sand to silt mixture sites). Most of the compiled field data included benchmark G_0 measurements, in-situ void ratio (e_0), and stress history that were obtained from published sources with detailed understanding on the site-specific geologic conditions. For clays, both e_0 and OCR parameters quite improved the G_0 correlations. The magnitudes of G_0 were reasonably expressed by two variables (i.e., effective confining stress and either e_0 or OCR), albeit some scattered data and outliers were observed. Yet, from multiple regression analyses, both e_0 and OCR showed redundant effects such that a single variable dominates. On the other hand, OCR does not seem to have as significant effects on G_0 in sands and silt mixtures but this may be due to the fact that OCRs are quite difficult to assess in such geomaterials. Still then, it was observed that e_0 rather significantly relates to G_0. Similar results were observed from G_0 regressions using all soil types (e.g., intact clays, fissured clays, sands, silt mixtures).

CHAPTER 5

EVALUATING IN-SITU LATERAL STRESS COEFFICIENT (K_0) VIA PAIRED SHEAR WAVE VELOCITY MODES

5.1 Current Practices on K_0 Evaluation

The at-rest lateral stress coefficient (K_0) is a fundamental geotechnical parameter which represents the anisotropic geostatic stress state relating the effective horizontal stress (σ_{ho}') to the effective vertical stress (σ_{vo}') such that: $\sigma_{ho}' = K_0 \cdot \sigma_{vo}'$. The magnitude of σ_{ho}' can be an important input parameter for geotechnical design problems, including: the initial laboratory consolidation setup of triaxial specimens, calculation of pile foundation side friction (i.e., beta method), numerical finite element simulations, and liquefaction studies. Even though the magnitude of K_0 may be needed for analyses, the direct evaluation requires specialized in-situ devices or laboratory testing equipment, therefore, an estimation of K_0 often serves purpose for many practical problems. As a consequence, a number of theoretical and empirical approaches have been developed for the assessment of K_0 in soils.

For soft clays and loose sands, it is commonly recognized that K_0 decreases with increasing effective friction angle (ϕ'). For normally consolidated (NC) soil, Jaky (1944) presented the following expression from limit plasticity considerations:

Equation (5.1) $$K_{0,NC} = 1 - \sin\phi'$$

Further studies using experimental laboratory testing and analytical developments found that K_0 relates to stress history, in particular the overconsolidation ratio (OCR), as documented elsewhere (Brooker and Ireland 1965, Pruska 1973, Mitachi and Kitago

1976). Based on data from 171 different soils tested under laboratory triaxial stress-path testing or instrumented oedometer setups, Mayne and Kulhawy (1982) linked K_0 during mechanical loading-unloading stages to both parameters via the following approximate expression:

Equation (5.2) $$K_{0,OC} = (1 - \sin\phi') \cdot OCR^{\sin\phi'}$$

While the above simple expression may provide a reasonable K_0 estimation, there may also exist additional important factors not considered, such as geologic origin, soil type, mineralogy, fabric, reloading, cementation, and ageing that can affect the magnitude of K_0. It might be difficult to comprehensively quantify all these effects on K_0 in natural soils based solely on laboratory testing. For instance, sample disturbance effects can mask or muddle the expected results from laboratory K_0 methods such as suction measurements, triaxial stress-path testing, and instrumented consolidometers that are available. Consequently, in-situ tests are likely necessary for a true K_0 state determination because the field data retain the ambient environment and intact status of the prevailing stress regime.

The K_0 stress state can be assessed directly or indirectly using in-situ tests (Lunne and Mayne 1998). Representative direct in-situ measurements include the self-boring pressuremeter test (SBPMT), total stress cell (TSC), and hydraulic fracture (HF), as well as the self-boring load cell (SBLC) and field suction probe (Ridley and Burland 1993). The SBPMT is a direct test approach which provides a lift-off pressure (P_o) during inflation that corresponds to the ambient total horizontal stress (σ_{ho}), as detailed by Powell (1990). Similarly, the TSC (also known as Glötzl cells or push-in spade cells)

provides a final equilibrium stress at σ_{ho} (Sully and Campanella, 1990). Finally, the HF test measures a closure pressure corresponding to σ_{ho} (Hamouche, et al. 1995).

The use of paired shear wave modes have also been purported to be viable in assessing K_0 stress states (e.g., Butcher and Powell, 1995; Sully and Campanella, 1995; Fioravante, et al.1998), which serves as the topic of this study. Figure 5.1(a) depicts the three main types of shear wave measurements (downhole, standard crosshole, and rotary crosshole) that serve as the basis for data in this study. For completeness, additional geophysical techniques for determining mechanical waves are also shown, including the non-invasive methods. Figure 5.1(b) shows a depiction of the benchmark in-situ methods which provide direct K_0 determinations in soils (SBP, HF, and TSC) along with special laboratory methods (suction measurements, instrumented consolidometer, triaxial stress path testing).

In routine site explorations, K_0 values are often estimated by indirect field methods such as the flat dilatometer test (DMT), cone penetration test (CPT), and/or Iowa stepped blade (ISB), or using expressions related to soil stress history (e.g., OCR). However, indirect empirical methods are primarily based on data from certain soil types, specific geologic units, and often from a few limited sites. Select examples of empirical K_0 assessment via some indirect in-situ methods are provided in Figure 5.2 where SBP, HF, and/or TSC were generally used for the reference benchmark K_0 values that were in turn correlated to more common tests, included CPT, DMT, and/or OCR from lab consolidation testing. These include trends relating the following: (2a) K_0 from SBP with DMT in clays (Cruz 2009), (2b) CPT results on sands in chamber tests (Cruz 2009); (2c) K_0 from SBP to CPT resistances in clays (Mayne and Kulhawy 1990), (2d) K_0 from HF

tests in clays (Hamouche, et al. 1995) and (2e) K_0 from TSC in clays related to OCR (Mayne 2005), and (2f) K_0 from SBP vs. OCR in clays (Mayne 2007). As evident in these trends, considerable scatter and uncertainty reside with all of these methods.

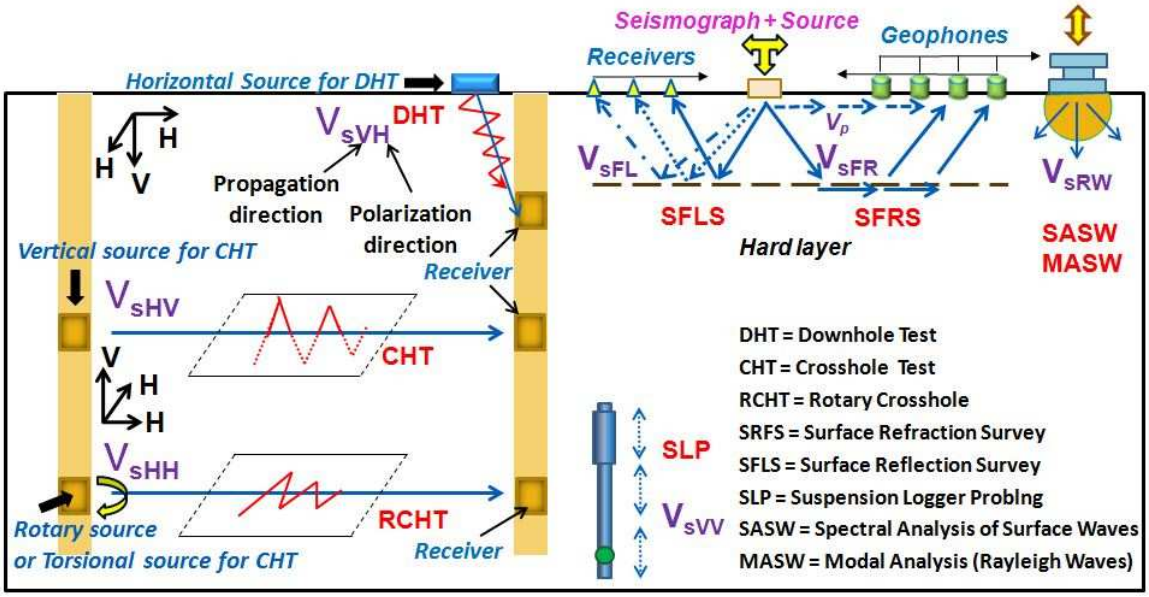

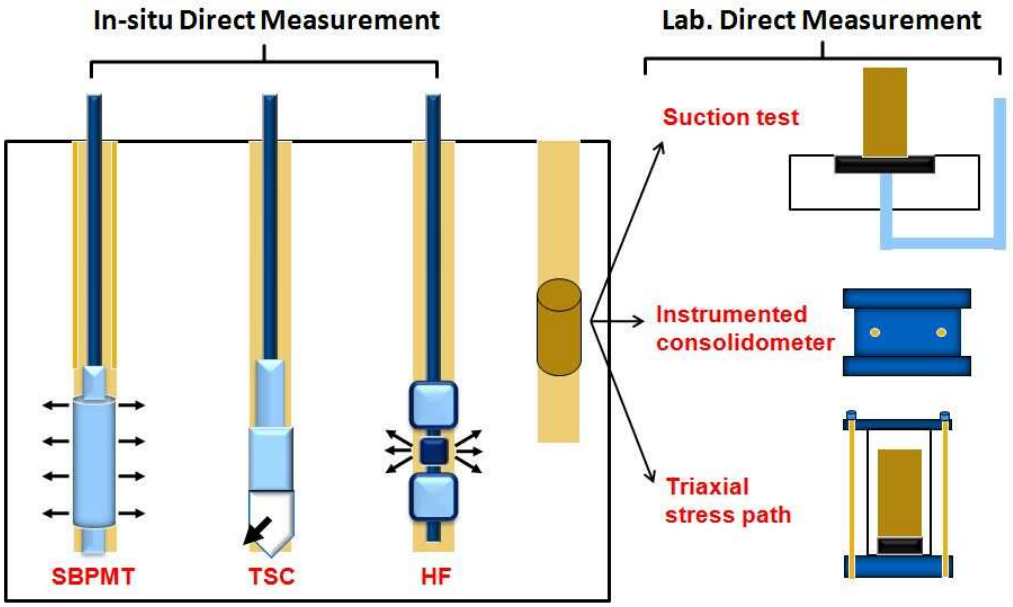

Figure 1(a). Types of in-situ V_s measurement methods in boreholes (DHT = downhole test, CHT = crosshole test, and RCHT = rotary crosshole) and various noninvasive geophysical methods.

Figure 1(b). Direct K_0 evaluation methods including in-situ tests (SBPMT = self-boring pressuremeter, TSC = total stress cells, HF = hydrofracture) and laboratory measurements on undisturbed samples.

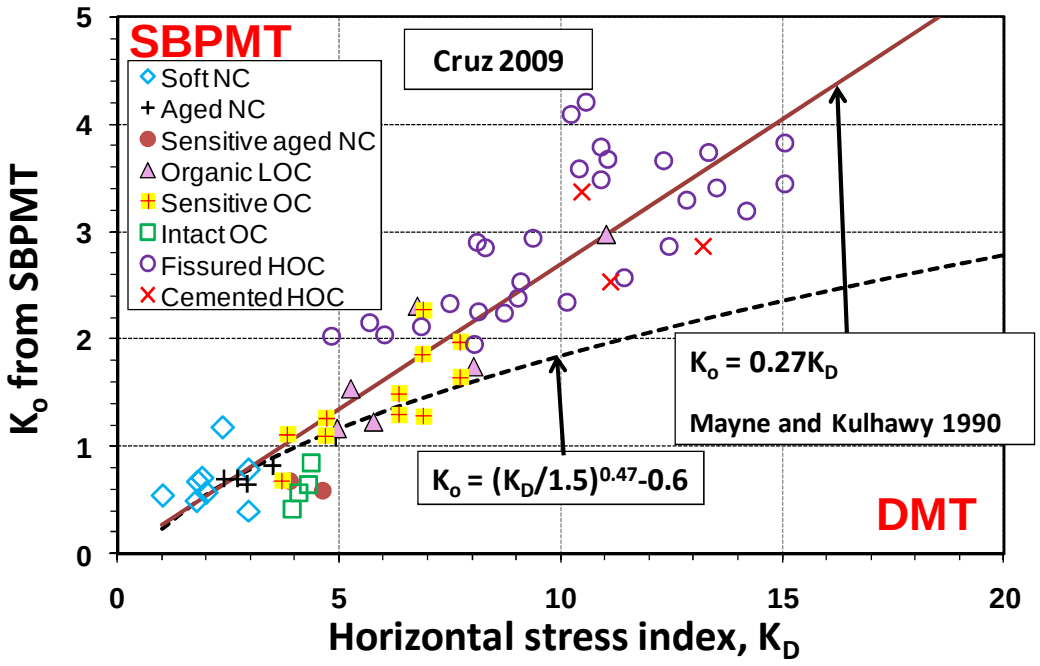

Figure 5.2(a) General indirect K_0 evaluation methods: DMT−SBPMT trends in clays.

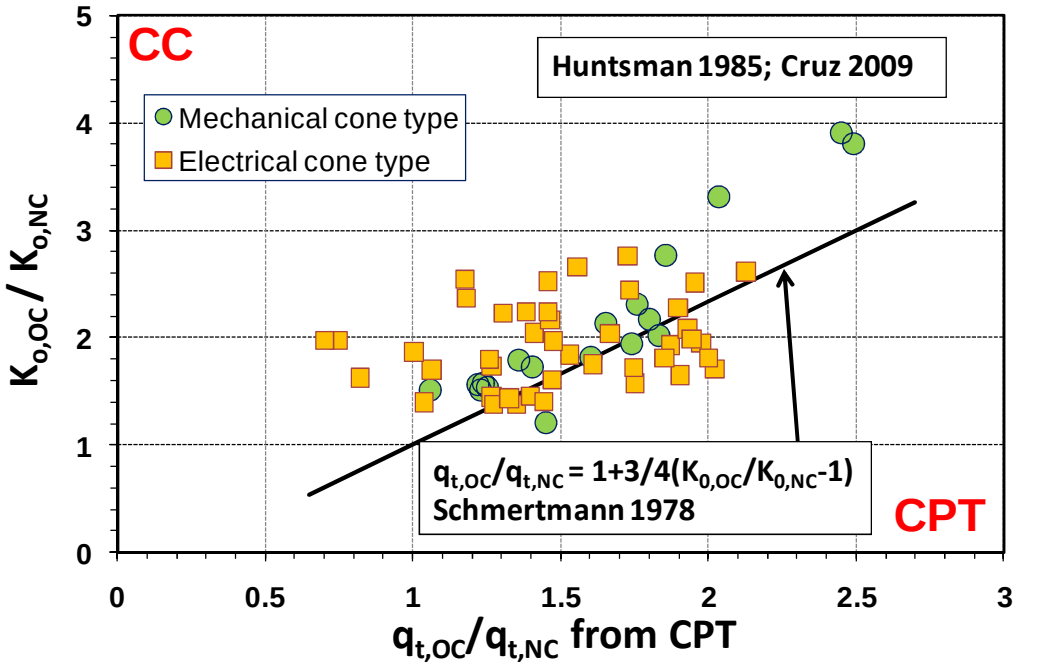

Figure 5.2(b) General indirect K_0 evaluation methods: CPT−Calibration chamber data in sands (CC).

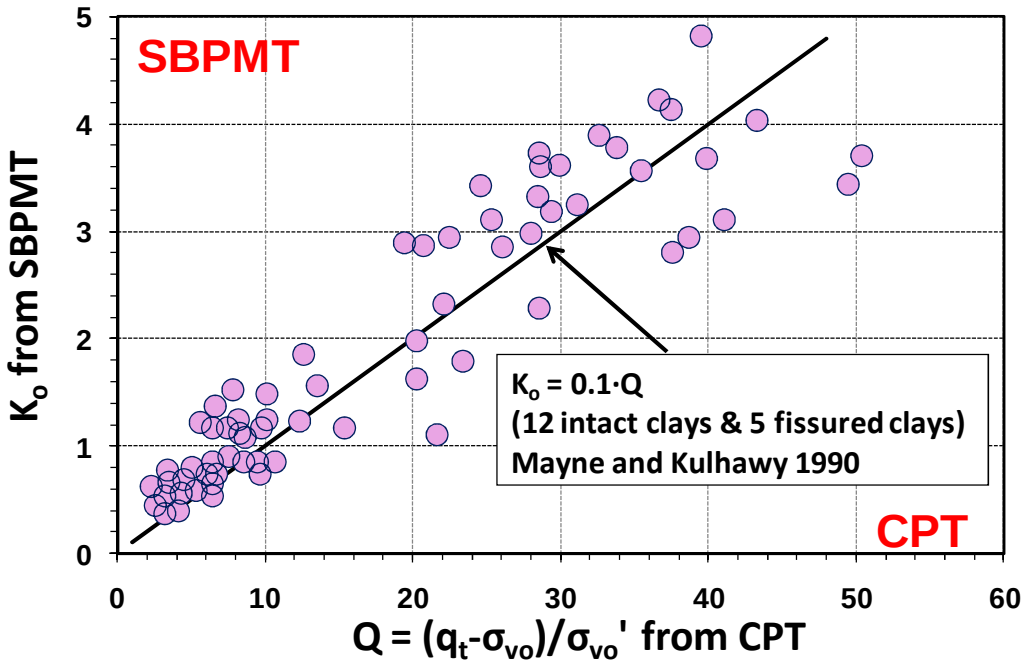

Figure 5.2(c) General indirect K_0 evaluation methods: CPT−SBPMT in clays.

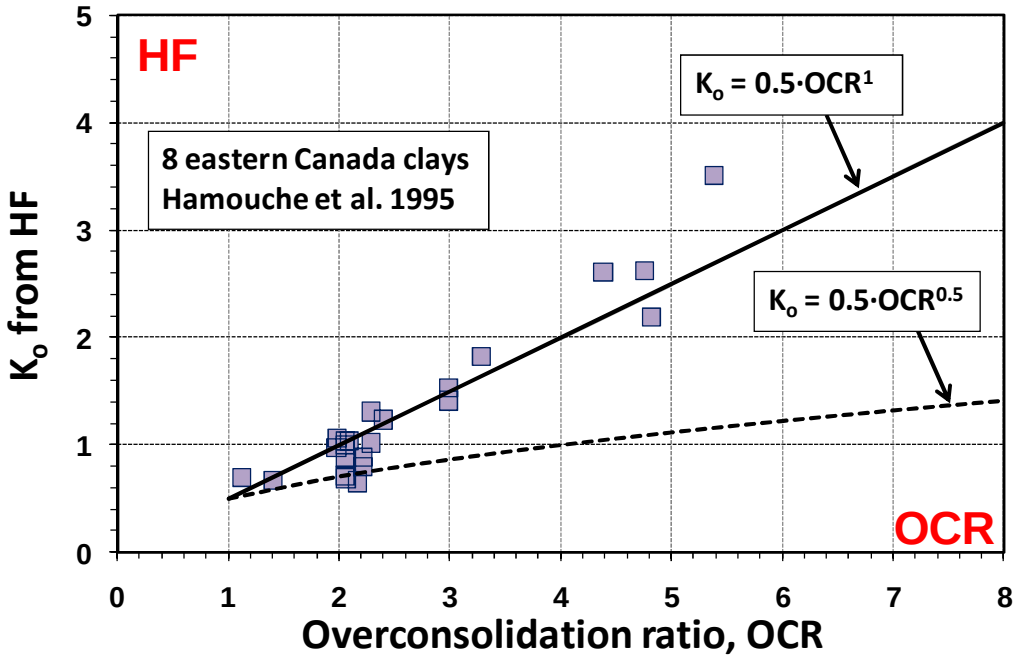

Figure 5.2(d) General indirect K_0 evaluation methods: OCR−HF in clays.

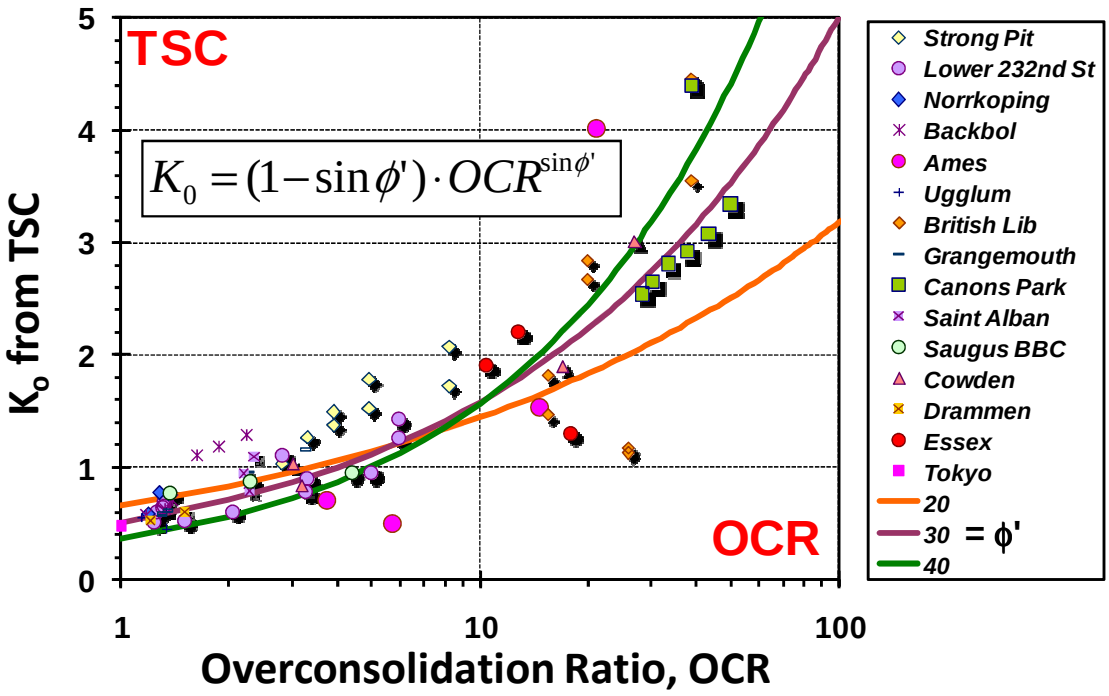

Figure 5.2(e) General indirect K_0 evaluation methods: OCR−TSC trends in clays.

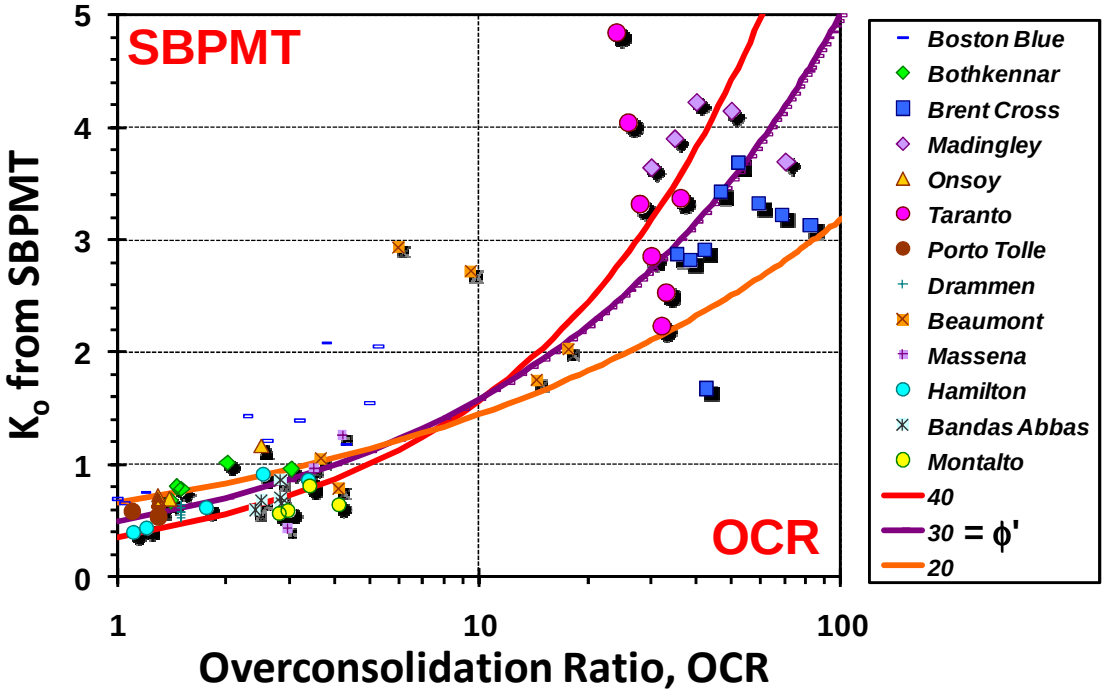

Figure 5.2(f) General indirect K_0 evaluation methods: OCR−SBPMT in clays.

Most in-situ tests are intrusive and therefore have inevitable soil displacement issues during penetration that might cause significant changes from the actual K_0 state of stress. Figure 5.3 shows the expected conceptual change of lateral stress coefficient (K) state as affected by a variety of in-situ test methods (Sully and Campanella 1990). The full range could extend as low as K_A, the active lateral stress coefficient, to as high as K_P, the passive lateral stress coefficient. The SBPMT test might be considered one of the most reliable or true field probing tests for K_0 evaluation, as it attempts to minimize soil displacements during installation. While the TSC is a direct K_0 approach, even a thin blade must impart some disturbance during insertion.

A truly non-intrusive approach using geophysical measurements of shear wave velocity (V_s) has been investigated herein. Sure, the soil just next to the borehole casing might be slightly disturbed (≈ 10 to 20mm), but this represents a very small mass of the total soil matrix involved in the testing with borehole-to-borehole spacings of 5 to 6 m. Thus, for geophysical tests, the soil matrix located between adjacent cased boreholes remains in a pristine and undisturbed state and the wave velocities represent readings on a large mass of natural soils. Paired sets of different types of shear wave velocities from standard downhole tests (DHT) and crosshole tests (CHT), and particularly special rotary-type crosshole (RCHT), are shown to provide a clear opportunity for K_0 determinations. Specific to this study, results from modal shear waves that have varied directional and polarization properties were reviewed, as obtained from a compiled dataset of well-documented test sites with known K_0 reference values for calibration.

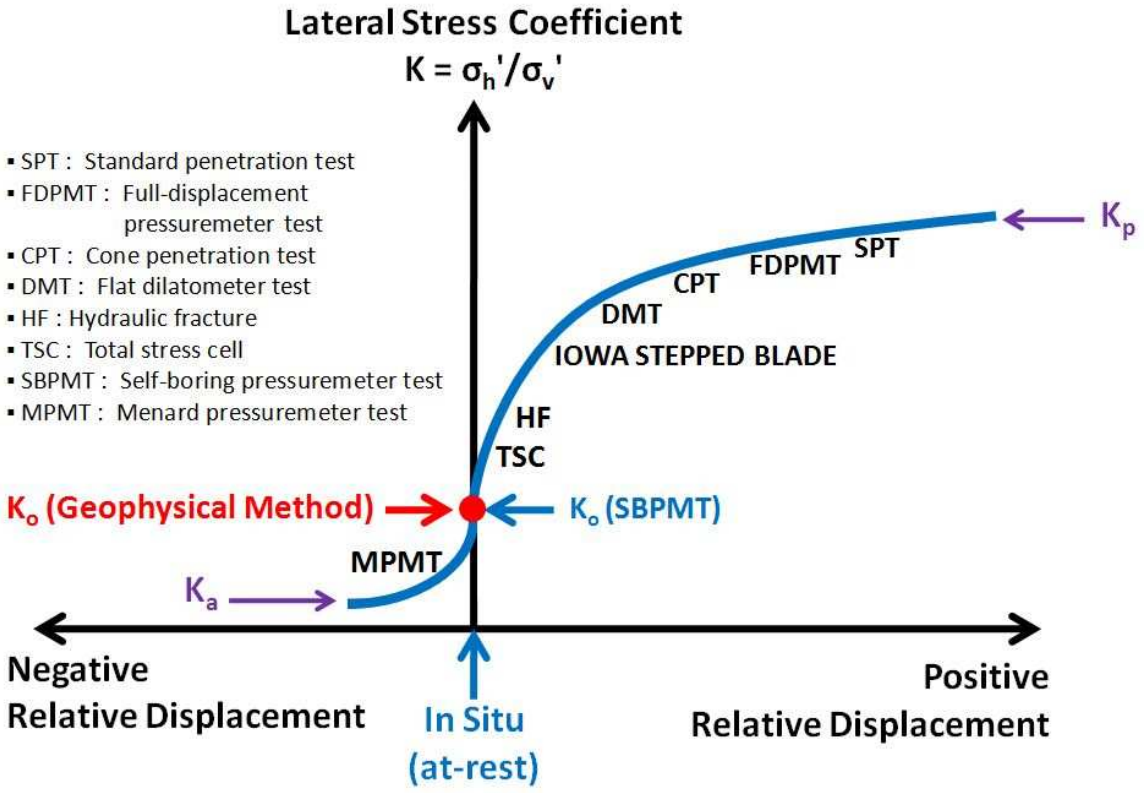

Figure 5.3. Conceptual change of lateral stress coefficient (K) state caused by insertion of various in-situ test devices (modified after Sully and Campanella 1990).

5.2 Background: Use of Shear Wave Dependency on Stress

Body waves comprise both compression and shear waves that can be formulated in terms of moduli from elastic continuum theory (Clayton 2011). The magnitude of the velocity of the shear waves relates to the effective stress conditions (Hryciw and Thomann 1993). Moreover, it is noted that shear waves have both directional and polarization characteristics. When the wave propagation direction is assumed parallel to vertical or horizontal major axis, mainly three different types of shear waves can be defined: V_{sVH} from DHT, V_{sHV} from CHT, and V_{sHH} from RCHT.

Various available formulations linking V_s with effective stress were provided earlier in Table 3.1. In this chapter, a selection of the important postulated V_s-stress relationships which are usually necessary for K_0 evaluation approach are briefly summarized with corresponding in-situ tests and extended expressions (Table 5.1). Based on the specific formulation between V_s and effective stress, the modal V_s ratio between paired shear waves can be obtained in terms of material constants (C_{VH}, C_{HV}, C_{HH}, n) and the in-situ lateral stress parameter K_0.

Table 5.1. Representative expressions for shear wave velocity-stress models

	Mean normal stress	Average stress	Individual stress	Propagation /polarization direction
General expression	$V_s = C\cdot(\sigma_o')^n$ *where* $\sigma_o' = (\sigma_x'+\sigma_y'+\sigma_z')/3$	$V_s = C\cdot(\sigma_{avg}')^n$ *where* $\sigma_{avg}' = (\sigma_x'+\sigma_y')/2$	$V_s = C\cdot(\sigma_x')^{nx}\cdot(\sigma_y')^{ny}$	X/Y
Downhole test (DHT)	$V_{sVH} = C_{VH}\cdot(\sigma_o')^n$ *where* $\sigma_o' = [(1+2K_0)/3]\cdot\sigma_{vo}'$	$V_{sVH} = C_{VH}\cdot[(\sigma_v' + \sigma_h')/2]^n = C_{VH}\cdot(\sigma_{vo}')^n\cdot[(1+ K_0)/2]^n$	$V_{sVH} = C_{VH}\cdot(\sigma_v')^{nx}\cdot(\sigma_h')^{ny}$ *if* $n_x=n_y=n/2$ $V_{sVH} = C_{VH}\cdot(\sigma_{vo}')^n\cdot(K_0)^{n/2}$	Vertical / Horizontal
Standard crosshole (CHT)	$V_{sHV} = C_{HV}\cdot(\sigma_o')^n$	$V_{sHV} = C_{HV}\cdot[(\sigma_v' + \sigma_h')/2]^n = C_{HV}\cdot(\sigma_{vo}')^n\cdot[(1+ K_0)/2]^n$	$V_{sHV} = C_{HV}\cdot(\sigma_v')^{nx}\cdot(\sigma_h')^{ny}$ *if* $n_x=n_y=n/2$ $V_{sHV} = C_{HV}\cdot(\sigma_{vo}')^n\cdot(K_0)^{n/2}$	Horizontal / Vertical
Rotary crosshole (RCHT)	$V_{sHH} = C_{HH}\cdot(\sigma_o')^n$	$V_{sHH} = C_{HH}\cdot[(\sigma_h' + \sigma_h')/2]^n = C_{HH}\cdot(\sigma_{vo}')^n\cdot K_0^n$	$V_{sHH} = C_{HH}\cdot(\sigma_h')^{ny}\cdot(\sigma_h')^{ny}$ *if* $n_y=n/2$ $V_{sHH} = C_{HH}\cdot(\sigma_{vo}')^n\cdot(K_0)^n$	Horizontal / Horizontal

Notes:

a. σ_x' = principal effective stress in wave propagation direction, σ_y' = principal effective stress in particle motion direction, σ_z' = principal effective stress in the direction perpendicular to σ_x' & σ_y'

b. Exponents n, nx, and ny are empirically-fitted parameters

c. Coefficients C, C_{HV}, C_{VH}, and C_{HH} are empirical stiffness parameters

As shown in Table 5.1, the most complex formulations consider different parametric values specifically determined for each geomaterial, including different exponent terms n for various stresses (e.g., σ_{vo}' and σ_{ho}'). If the simpler versions of the formulations are rearranged, a direct means to assess K_0 values can be obtained (Fioravante et al. 1998, Cai et al. 2011). Consequently, once a paired set of different modes of shear wave profiles (either V_{sHH} and V_{sHV}; or V_{sHH} and V_{sVH}) are measured, K_0 may be evaluated from either:

▪ Average stress method:

$$\text{Equation (5.3)} \quad K_o = \frac{1}{\left(\frac{V_{sVH} \cdot C_{HH}}{V_{sHH} \cdot C_{VH}}\right)^{(1/n)} - 1} \quad \text{or} \quad K_o = \frac{1}{\left(\frac{V_{sHV} \cdot C_{HH}}{V_{sHH} \cdot C_{HV}}\right)^{(1/n)} - 1}$$

▪ Individual stress method:

$$\text{Equation (5.4)} \quad K_0 = \left(\frac{V_{sHH} \cdot C_{VH}}{V_{sVH} \cdot C_{HH}}\right)^{(2/n)} \quad \text{or} \quad K_0 = \left(\frac{V_{sHH} \cdot C_{HV}}{V_{sHV} \cdot C_{HH}}\right)^{(2/n)}$$

In Equations 5.3 and 5.4, the V_{sHH} type is noted to play a critical role for K_0 assessment. For simplicity, assuming the soil is inherently isotropic in fabric (i.e., setting C_{VH}/C_{HH} or $C_{HV}/C_{HH} = 1$), Equation 5.4 can be expressed:

$$\text{Equation (5.5)} \quad K_0 = \left(\frac{V_{sHH}}{V_{sVH}}\right)^{(2/n)} \quad \text{or} \quad K_0 = \left(\frac{V_{sHH}}{V_{sHV}}\right)^{(2/n)}$$

Zeng and Ni (1999) showed an identical format with Equation 5.5 for reconstituted sand samples. Yet, in a separate approach, Hatanaka et al. (1999) found a relationship based on mean effective stress where $\sigma_o' = \{(1+2K_0)/3\} \cdot \sigma_v'$ given by:

$$\text{Equation (5.6)} \quad K_0 = [(3/\sigma_v') \cdot (V_s/C)^{1/n} - 1] / 2$$

so that a single mode of shear wave velocity might provide the desired results, at least in principle.

Using paired sets of shear waves per Equations 5.3 and/or 5.4, it is necessary to identify two unknown factors: the material constant ratios (either C_{VH}/C_{HH} or C_{HV}/C_{HH}) and the exponent n value that represents the degree of stress-dependency in geomaterials. Assuming the soil structure is isotropic, the ratio C_{VH}/C_{HH} or C_{HV}/C_{HH} can be initially assumed as unity. Deviations from the material constant ratio of unity indicate the degree of inherent anisotropy of soil fabric and structure. Different values for the C_{HV}/C_{HH} ratio have been reported in published studies: e.g., 1.0 - 1.2 for Ottawa sand (Yan and Byrne 1990); average of 0.93 for seven granular soils and a range of 0.9 - 1.0 for two Pleistocene marine clays (Fioravante et al. 1998). Concerning the stress-dependent behavior of soils, an exponent n = 0.25 has been commonly adopted (e.g., Yu and Richart 1984, Stokoe et al. 1985), however most results have been derived based on limited laboratory data on clean quartz and silica sands.

Recently, Cai et al. (2011) showed reasonable agreement in K_0 predictions assuming n= 0.25 and specific C_{HV}/C_{HH} = 0.93 for granular soils and C_{HV}/C_{HH} = 0.85 for clays with the average stress model based on V_{sHV} and V_{sHH} measurements obtained at two test sites in China. However, there remained some deviations for K_0 predictions in overconsolidated (OC) soils, thus empirical correction factors were applied. In Chapter 4, in terms of G_0-stress relationships, experimental data showing higher n exponent values > 0.25 were introduced (Weiler 1998, Shibuya et al. 1997). Moreover, as detailed in Chapter 3, data collected from a diverse grouping of geomaterials have shown relatively wider ranges in values for both the coefficient C and exponent n.

5.3 K_0 Database from Sites with Paired Shear Waves

Towards this intent of this study, a special database has been compiled from 16 well-documented test sites where K_0 profiles had been specially investigated and at least two types of shear wave profiles from different modes (SV and SH) were available. For these test sites, Table 5.2 summarizes details and information on each geomaterial including: site location, soil type, geologic age of soil, V_s modes, K_0 benchmark test, and reference sources. At these test sites, benchmark K_0 states have been directly evaluated in the field either by SPBMT, TSC, and/or HF methods, and/or using independent relationships between stress history (OCR), laboratory suction measurements, triaxial testing, and/or instrumented consolidometers on undisturbed samples. The database includes 4 sand sites, 3 silty mixtures, and 9 clay sites.

Each of the 16 sites has a profile of the V_{sHH} type from RCHT. In addition, the V_{sVH} mode from DHT was available from 12 sites and the V_{sHV} mode obtained by CHT at 15 of the sites. This permits pairing of the ratios V_{sHH}/V_{sVH} or V_{sHH}/V_{sHV}, or both. Based on the in-situ V_s database, the magnitudes of different V_s modes are compared with consideration of soil types in Figure 5.4. Whereas all V_s modes seem relatively comparable for normally consolidated soil sites, data from overconsolidated geomaterials show a general hierarchy for magnitudes of different V_s modes which is observed as follows: $V_{sHH} \geq V_{sHV} \geq V_{sVH}$. In terms of simple statistical means (± 1 standard deviation), the overall database indicates: V_{sHH} = 282.9 ± 63.1 m/sec (N = 57), V_{sHV} = 224.9 ± 42.4 m/sec (N = 65), V_{sVH} = 195.6 ± 42.8 m/sec (N = 61) for OC soils. These hierarchical trends were noted earlier in Chapter 3.

Table 5.2. Database listing of documented sites and reference sources for shear wave data

Site	Soil type	Mark	K_0	OCR	Years (10^3 yr)	Applied V_s modes	K_0 source	V_s reference
Treasure Island, CA	Sand to Silty sand	◇	0.5-0.6	1	0.075	HV, HH	SBPMT (Pass 1994)	Henke and Henke (2002)
Higashi-Ohgishima, Japan	NC sand fill	■	0.5	1	0.1	VH,HV,HH	K_0 profile recommended from V_s reference	Shibuya et al.(1995)
200th Street, BC	Soft to stiff NC & OC clayey silt	+	0.6-1.0	1.3-5.0	6	HV, HH	TSC & LS oedometer data	Sully (1991)
Lower 232 Street, BC	Soft to firm NC & OC clayey silt	✱	0.6-1.0	1.2-5.0	6	HV, HH	TSC	Sully (1991)
Bothkennar, Scotland	Soft silty clay	✚	0.5-0.9	1.3-2.2	7	VH,HV,HH	SBPMT (Nash et al. 1992)	Butcher & Powell (1997)
Pisa tower, Italy	Pisa clay	×	0.5-1	1.3-2	10	VH,HV,HH	K_0 profile from V_s reference (Oedometer, TX data)	LoPresti et al.(2003)
San Matteo (Po river), Italy	Po river sand	□	0.5-1.0	1-2	10	VH,HV,HH	SBPMT	Fioravante et al.(1998)
Amherst, MA	Clay	◇	0.7-1.8	1.5-7.5	15	VH, HH	SBPMT and TSC (Benoit and Lutenegger 1992, DeGroot and Lutenegger 2003)	Henke and Henke (2002)
Cowden, UK	Glacial till HOC to LOC	●	1-2	2-10	75	VH,HV,HH	SBPMT (Powell & Butcher 2003); TSC & suction tests reviewed	Butcher & Powell (1997); Powell & Butcher (2003)
Chattenden, UK	London clay (Fissured clay)	○	2-3	20+	30,000	VH,HV,HH	K_0 profile calculated from V_s reference	Butcher & Powell (1995)
London clay site, UK	London clay (HOC)	✕	2-3	25+	30,000	VH,HV,HH	K_0 profile calculated from V_s reference (SBPMT & suction test)	Butcher & Powell (1997)
Heathrow (T5), UK	London clay (HOC)	△	1.5-2.5	14+	30,000	VH,HV,HH	K_0 profile from suction measurements	Hight et al.2003
Madingley, Cambridge	Gault clay (Fissured clay)	◆	2-3.5	25+	100,000	VH,HV,HH	SBPMT (Coop and Wroth 1989, Powell 1990)	Butcher & Powell (1995)
Southern England: Purton, UK	Oxford clay	✱	2-3	20-45+	160,000	VH,HV,HH	K_0 profile from Hird and Pierpoint (1997)	Bates and Phillips (2000)
Vincent Thomas Bridge, CA	Silty sand	◇	0.4-0.5	N/A	N/A	HV, HH	K_0 profile from φ'	Hiltunen et al.(2003)
Opelika, AL	Silty sand, Sandy silt	+	0.7-1.1	2-5	N/A	VH,HV,HH	K_0 profile from equation using OCR and φ'	Henke and Henke (2002)

Notes: TX = triaxial, LS oedometer = instrumented lateral stress oedometer, TSC = total stress cell, SBPMT = self-boring pressuremeter test

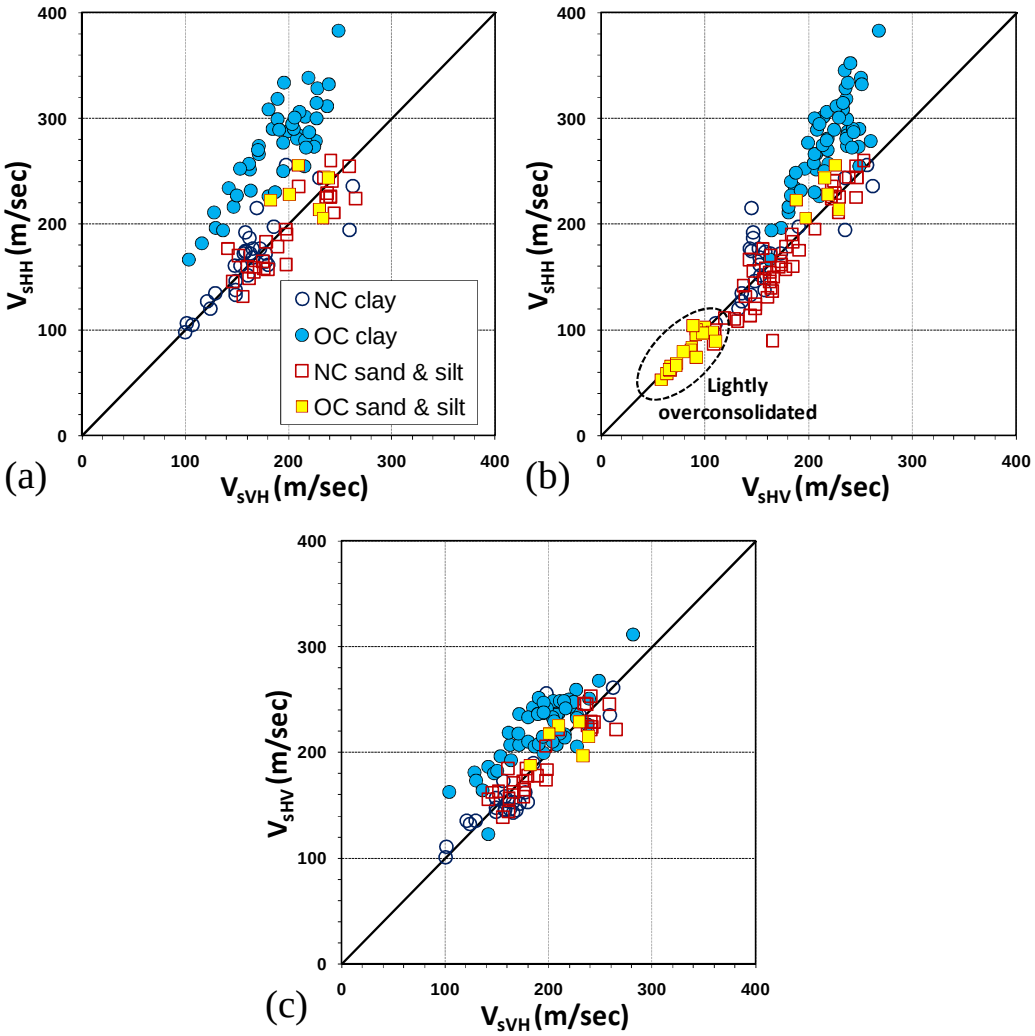

Figure 5.4. Shear wave data hierarchy: (a) Rotary crosshole mode (V_{sHH}) versus downhole mode (V_{sVH}), (b) rotary crosshole mode (V_{sHH}) versus standard crosshole mode (V_{sHV}), (c) standard crosshole mode (V_{sHV}) versus downhole mode (V_{sVH}) from in-situ database.

5.4 Feasibility and Sensitivity Analysis for K_0 Prediction

In order to develop a means for K_0 assessment using modal V_s ratios, the following simple semi-empirical equation was adopted as an initial approach:

Equation (5.7) $$K_0 = \alpha \cdot \left(\frac{V_{sHH}}{V_{sVH}} \right)^{\beta} \quad \text{or} \quad K_0 = \alpha \cdot \left(\frac{V_{sHH}}{V_{sHV}} \right)^{\beta}$$

Equation 5.7 has a similar format with Equation 5.4 derived from the individual stress method. The coefficient α is equivalent to $(C_{VH}/C_{HH})^{2/n}$ or $(C_{HV}/C_{HH})^{2/n}$ and the exponent term β corresponds to 2/n. Based on the aforementioned V_s database, a set of regression analyses were conducted. Figure 5.5 shows the plot of the reference K_0 as a function of the V_s ratios. Although the observed data are rather scattered, both modal V_s ratios appear to have strong relationships with K_0. The simple expression seems to produce moderately reasonable K_0 predictions. In particular, the ratio of V_{sHH}/V_{sVH} results in an overall better estimation for in-situ K_0 than the V_{sHH}/V_{sHV} ratio. The best fit lines using the regression analyses are as follows:

▪ HH-VH modes:

Equation (5.8a) $K_0 = 0.78 \cdot \left(\frac{V_{sHH}}{V_{sVH}} \right)^{2.55}$; $R^2 = 0.809$, N = 124, R.S.E = 0.112

▪ HH-HV modes:

Equation (5.8b) $K_0 = 0.85 \cdot \left(\frac{V_{sHH}}{V_{sHV}} \right)^{3.19}$; $R^2 = 0.593$, N = 150, R.S.E = 0.179

where R^2 = coefficient of determination, N = number of data points, and R.S.E = residual standard error from log regression. To examine propagation of uncertainties through calculations, error propagation analyses were conducted (here, $\varepsilon_{K0} = b\sqrt{\varepsilon_{VsHH}^2 + \varepsilon_{VsVH}^2}$ for $K_0 = a \cdot (V_{sHH}/V_{sVH})^b$):

▪ HH-VH modes:

Equation (5.8c) $\frac{u_{K0}}{K_0} = 2.55 \cdot \sqrt{\left(\frac{u_{VsHH}}{V_{sHH}} \right)^2 + \left(\frac{u_{VsVH}}{V_{sVH}} \right)^2} = 1.003$

▪ HH-HV modes:

Equation (5.8d) $$\frac{u_{K0}}{K_0} = 3.19 \cdot \sqrt{\left(\frac{u_{VsHH}}{V_{sHH}}\right)^2 + \left(\frac{u_{VsHV}}{V_{sHV}}\right)^2} = 1.407$$

where, u = uncertainty (here, 1 standard deviation), V_{sVH} =186.3 ± 44.3 m/sec, V_{sHV} =186.4 ± 57.9 m/sec, V_{sHH} =226.1 ± 70.8 m/sec. Error propagation will be decreased if the exponent values become lower (e.g., multiple regression equations in section 5.5). In fact, for the simplified Equation 5.5 assuming n = 8, the error propagation will be much more sensitive due to the high exponent value (i.e., HH-VH mode: u_{K0} / K_0 = 3.146, HH-HV mode: u_{K0} / K_0 = 3.529).

If Equation 5.8a and 5.8b links to Equation 5.4, then α values of 0.78 and 0.85 can be expressed by $0.91^{2.55}$ and $0.95^{3.19}$, respectively (i.e., C_{VH}/C_{HH} = 0.91, C_{HV}/C_{HH} = 0.95), indicating approximately the degree of fabric anisotropy. It is noted that the exponent β values of 2.55 and 3.19 are considerably different from the value which was suggested from the prior methodology using the individual stress expression in Equations 5.4 and 5.5, respectively (i.e., β = 2/n ≈ 2/0.25 ≈ 8). The results indicate it might be difficult to evaluate the specific in-situ K_0 conditions based solely on theoretical backgrounds. Consequently, it became necessary to further examine the parametric effects of both the coefficient α and the exponent β which in fact may very well be site-specific.

As noted, the best fit lines have very small β values (or equivalent large n values). Hence, in order to link the standard exponent n=0.25 (i.e., β = 2/n = 8 for equation 8) to the regression Equation 5.8a, an additional modification factor (MF_1) for the exponent term can be included as follows:

Equation (5.9) $$K_0 = \left(\frac{V_{sHH} \cdot C_{VH}}{V_{sVH} \cdot C_{HH}} \right)^{\frac{2}{n \cdot MF1}}$$

The above framework is applied to the case using HH and HV modes as well. In the regression Equations 5.8a and 5.8b derived from the V_s database, the values $\beta = 2.55$ and 3.19 correspond to the MF_1 values of 3.14 and 2.51, respectively. Once the material constant ratio is assumed as a fixed value (i.e. $C_{VH}/C_{HH} \approx 0.91$ or $C_{HV}/C_{HH} \approx 0.95$) which is obtained from the regression Equation 5.8a or 5.8b, it is possible to investigate the sensitivity of K_0 assessment using the modal V_s ratio. Figure 5.5(a) shows multiple sets of prediction lines having different MF_1 parametric values and the site-specific data for the K_0 versus the ratio V_{sHH}/V_{sVH}. When the V_s ratio is near unity, the various prediction lines show relatively narrow bands. However, the parameter MF_1 has significant effects on K_0 predictions in the high ratios of V_{sHH}/V_{sVH} around 1.5. In heavily overconsolidated (HOC) soils (i.e., where OCR > 10+) exhibiting large K_0 values, most data are located between the prediction line having $MF_1=2$ and the regression line ($MF_1 \approx 3.14$). Similarly, Figure 5.5(b) shows the K_0 values versus the ratio V_{sHH}/V_{sHV}. The general trend of prediction lines is similar to Figure 5.5(a), however the data appear more scattered. Sites having large K_0 values appear to deviate from the regression line ($MF_1 \approx 2.51$) toward the line corresponding to $MF_1 = 1$ or 2.

A second regression-based parametric study involved the sensitivity of K_0 evaluations considering the variations of the α parameter by fixing the exponent terms $\beta = 2.55$ and 3.19, corresponding to $\alpha = (C_{VH}/C_{HH})^{\beta}$ or $(C_{HV}/C_{HH})^{\beta}$. Here, the modification factor (MF_2) was applied for the sensitivity analysis as follows:

Equation (5.10) $$K_0 = \left(\frac{V_{sHH} \cdot C_{VH}}{V_{sVH} \cdot C_{HH}} \cdot MF_2 \right)^{\beta}$$

Figures 5.5(c) and 5.5(d) show the predicted K_0 lines as varied by the parameter MF_2. For HOC sites having very large K_0 values, the regression line seems to underestimate at the same V_s modal ratio. The higher MF_2 yields a larger K_0 value.

Consequently, based on the modal V_s ratios, it seems possible to roughly predict K_0 using the regression lines. In particular, the V_{sHH}/V_{sVH} ratio provides the best overall evaluations. To improve the K_0 assessment, it might be helpful to adopt site-specific MF values especially for HOC sites consisting of old soil deposits. However, the determination of the appropriate calibrated MF will pose other challenges because of reliance on additional variables such as fabric, age, fissuring, and cementation.

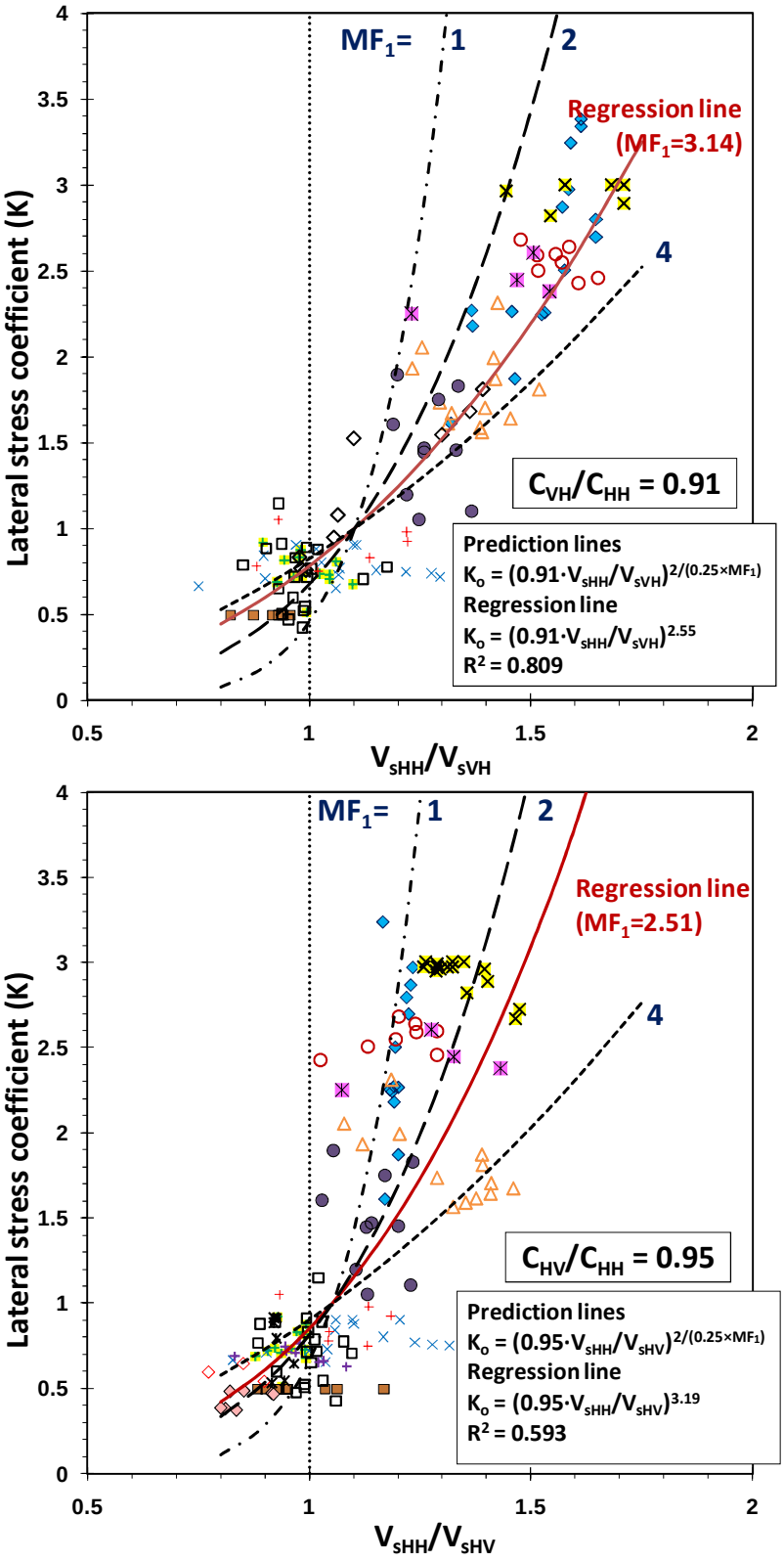

Figure 5.5. Regression analysis between in-situ K_0 and V_s ratio and corresponding sensitivity analysis on the exponent n including modification factor (MF_1): (a) K_0 versus V_{sHH}/V_{sVH}, (b) K_0 versus V_{sHH}/V_{sHV}

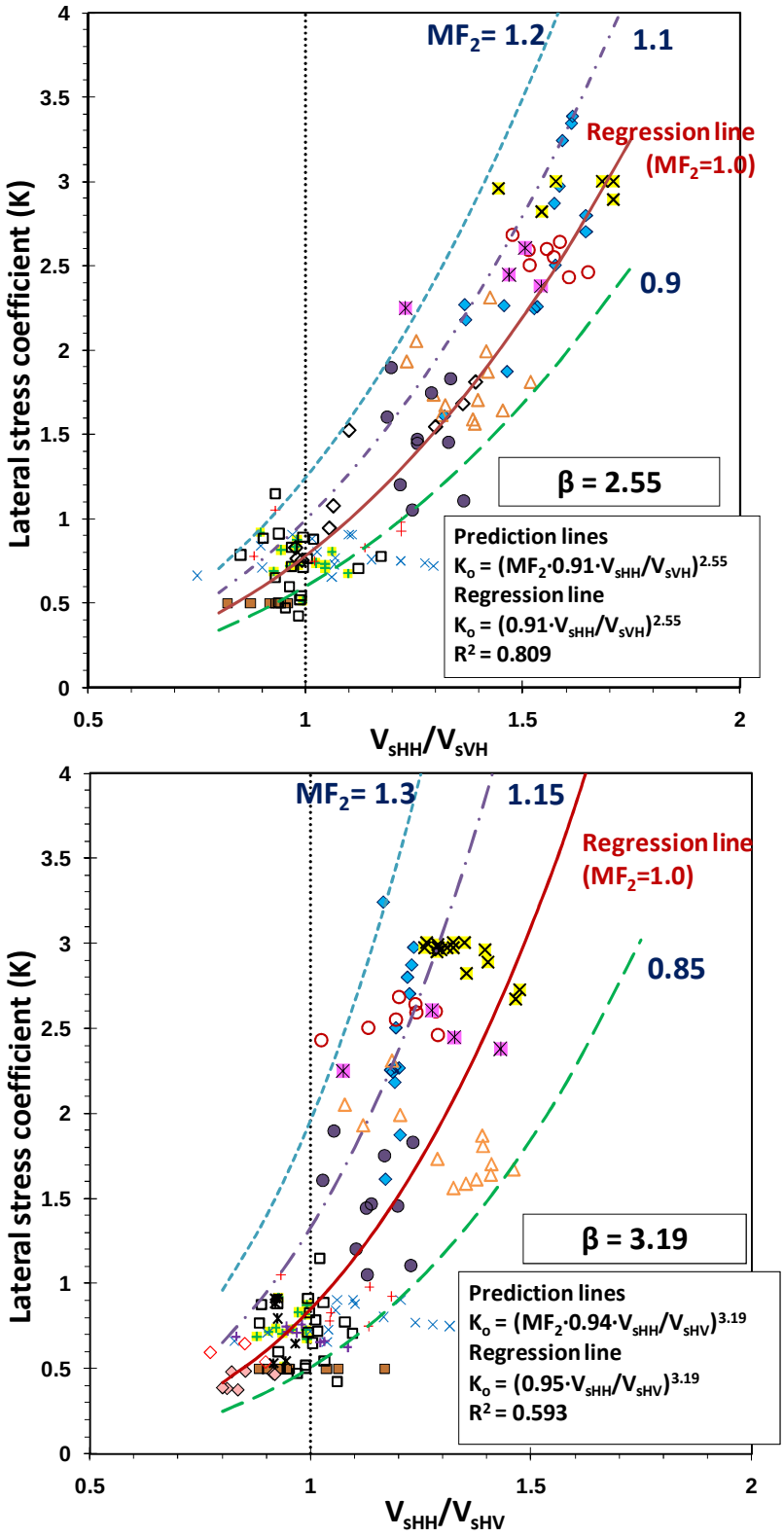

Figure 5.5. Regression analysis between in-situ K_0 and V_s ratio and corresponding sensitivity analysis on the C_{VH}/C_{HH} including modification factor (MF_2): (c) K_0 versus V_{sHH}/V_{sVH}, (d) K_0 versus V_{sHH}/V_{sHV}.

5.5 Age Effects on Shear Wave Ratio Expressions for K_0

In most cases, the age of the depositional formation of the various sites were known based on geological history, as reported in Table 5.2. Exceptions include the Opelika site and Vincent Thomas Bridge. Figure 5.6 shows that the V_{sHH}/V_{sVH} ratios appear to generally increase with the geologic age of the various deposits. Therefore, empirical relationships were sought from multiple regression analysis in consideration of shear wave ratios and age:

▪ HH-VH modes:

$$\text{Equation (5.11)} \quad K_0 = 0.428 \cdot \left(\frac{V_{sHH}}{V_{sVH}}\right)^{1.387} \cdot AGE^{0.0652}$$

with $R^2 = 0.877$, N = 118, R.S.E = 0.092 and AGE =geologic time of soil in years.

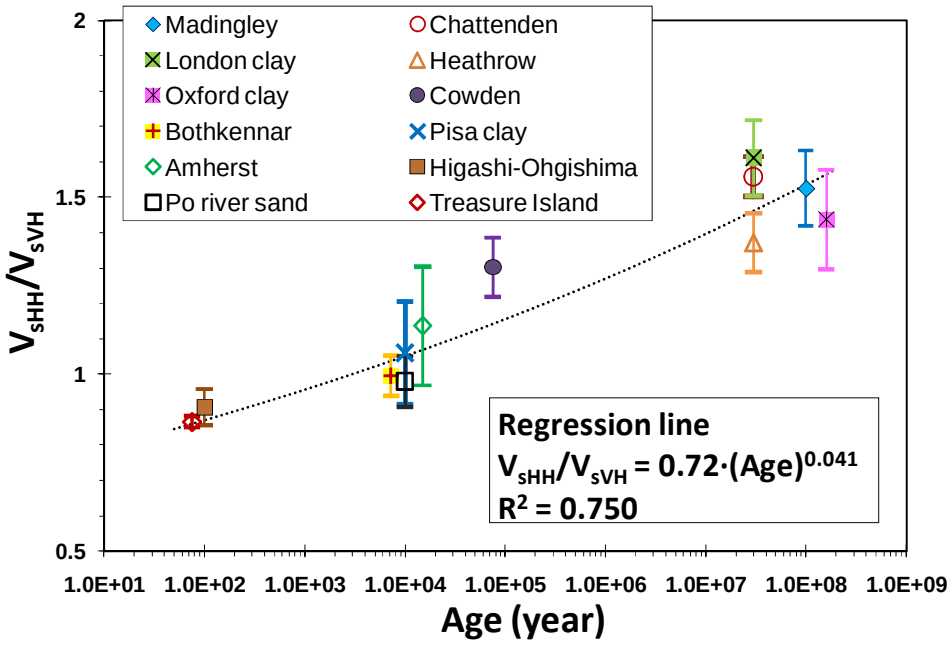

Figure 5.6. Trend between ratio V_{sHH}/V_{sVH} and geologic age of soil.
Note: range bars indicate mean ± 1 standard deviation

In Equation 5.11, the K_0 value is predicted using only the V_{sHH} and V_{sVH} mode. In another multiple regression including the V_{sHH}/V_{sHV}, it is observed that the modal

V_{sHH}/V_{sHV} ratio has very limited influences on K_0 prediction because of a small exponent value (β=0.326). The regression using the V_{sHH}/V_{sHV} provides a sound R^2 value as well, however it seems mainly affected by soil age. Furthermore, the t-statistic value for the V_{sHH}/V_{sHV} variable is not acceptable in 95% significance level: i.e., probability (>|t|) = 0.109 > 0.05. Relatively more scattered V_{sHH}/V_{sHV} data seems to hinder to obtain an accurate relationship. Thus, from Equation 5.11, this study suggests use of the K_0 prediction via the V_{sHH} and V_{sVH} modes. Compared to Equation 5.8a, Equation 5.11 provides higher R^2 value (i.e., R^2: 0.809 → 0.877). Whereas Figure 5.7 shows the plot of the measured K_0 versus the predicted K_0 based solely on the V_s ratio parameter, Figure 5.8(a) provides site-specific K_0 evaluation from the multiple regression analysis using two variables (i.e. V_s ratio and age of soil). Although some deviations are still observed, the predictions using the two variables seem generally improved over the K_0 evaluation using the single modal V_s ratio parameter. Yet, the K_0 prediction (Equation 5.11) might still require further improvement. In further consideration, the effect of depth (D) at which the V_s measurements were obtained was investigated, as shown influential by Andrus et al. (2007) in their correlative studies. A multiple regression for K_0 was conducted using three variable factors: (a) V_s ratio, (b) soil age, and (c) depth, which provided:

Equation (5.12) $$K_0 = 0.640 \cdot \left(\frac{V_{sHH}}{V_{sVH}} \right)^{0.797} \cdot AGE^{0.0802} \cdot D^{-0.220}$$

R^2 = 0.904, N = 112, R.S.E = 0.0788

where AGE =geologic time of soil in years ; D = depth in meter. Note that the (unidentified) London clay site (Butcher & Powell, 1997) was excluded here due to lack of information on the measured depths. In Figure 5.8(b), it is shown that Equation 5.12 provides a reasonable K_0 prediction for the results considered.

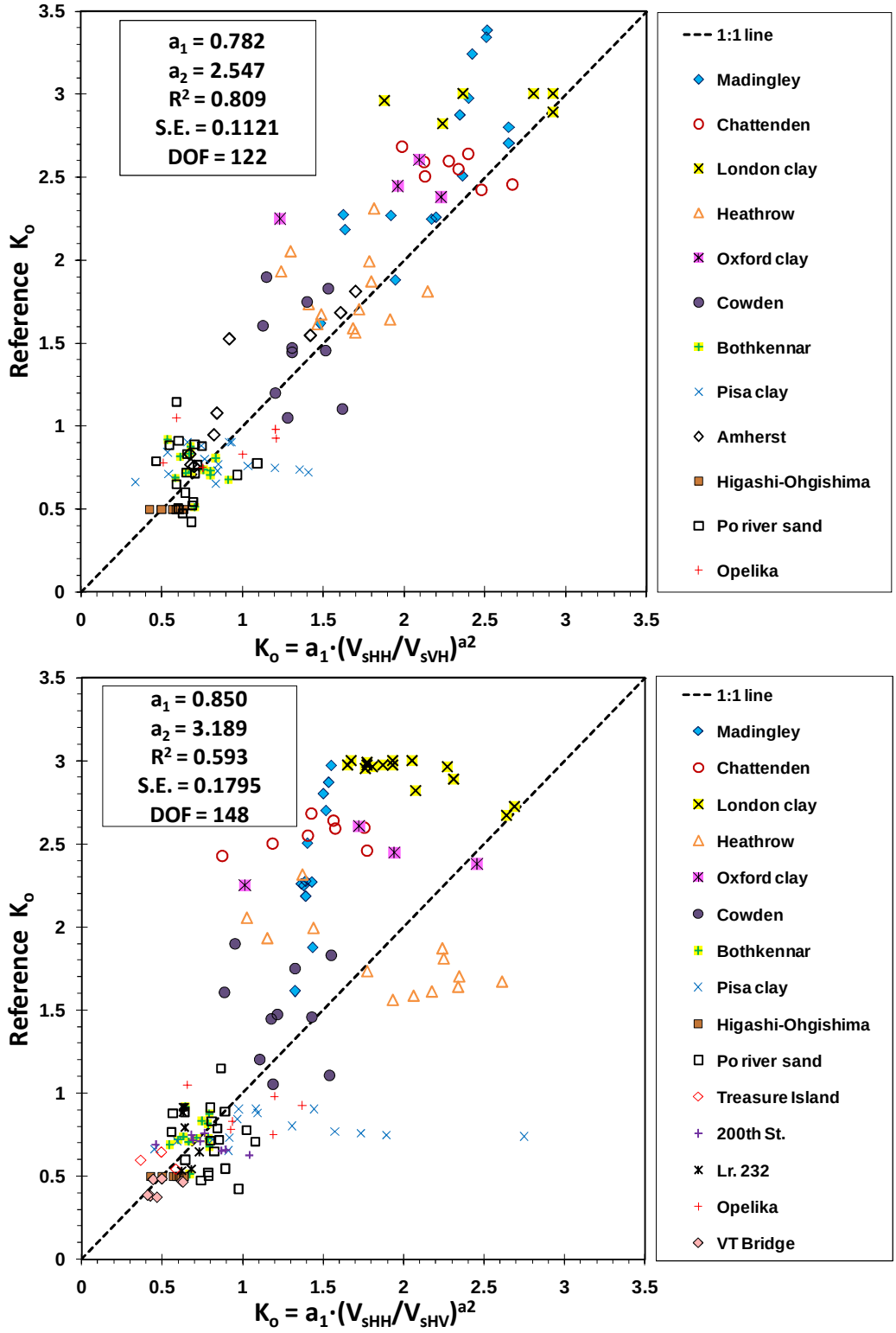

Figure 5.7. (a) Comparison of reference K_0 and predicted K_0 as a function of V_{sHH}/V_{sVH}; (b) comparison of reference K_0 and predicted K_0 as a function of V_{sHH}/V_{sHV}.
Note) S.E.: residual standard error, DOF: degree of freedom = number of independent observations

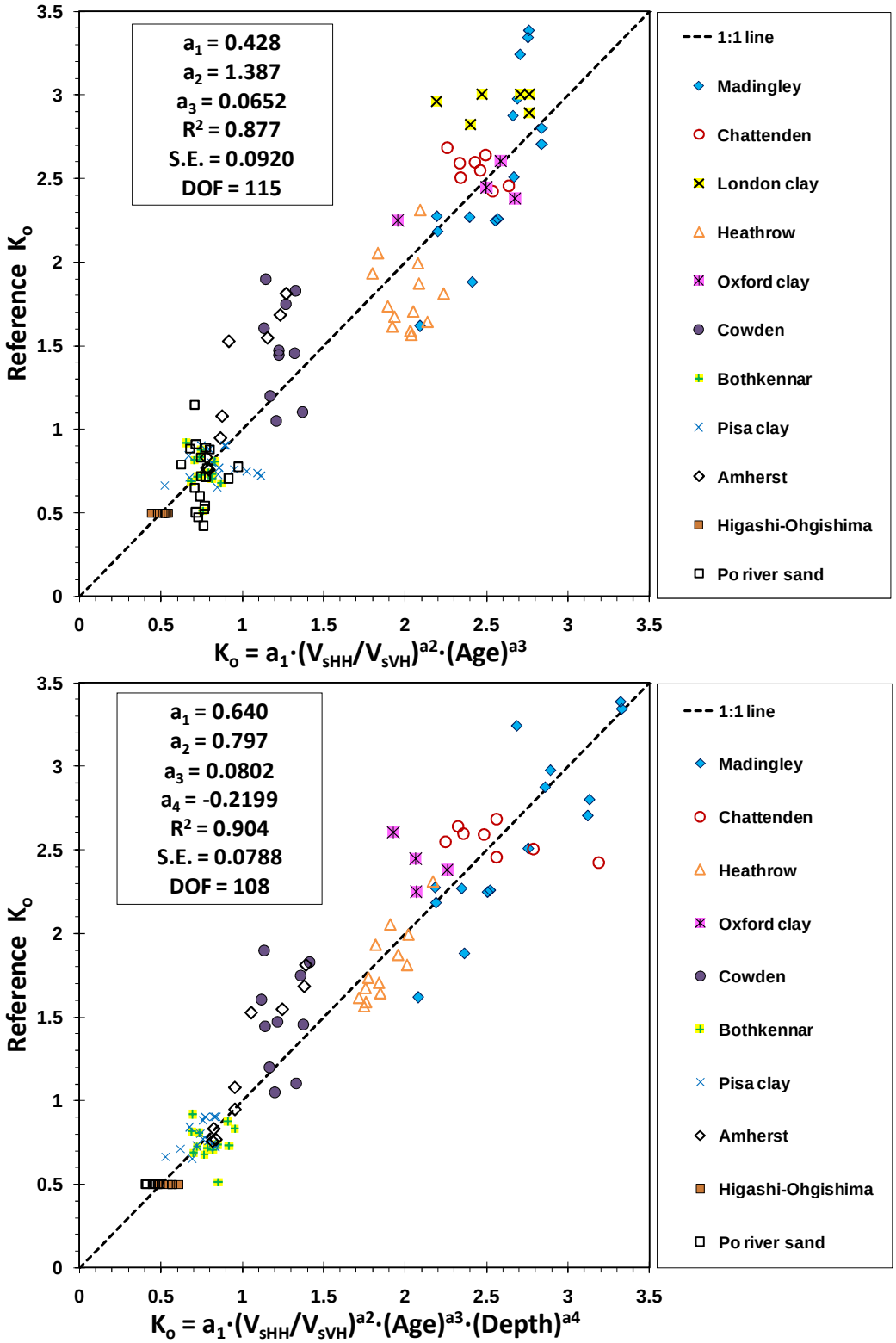

Figure 5.8. (a) Comparison of reference K_0 and predicted K_0 as a function of V_{sHH}/V_{sVH} and soil age, (b) reference K_0 and predicted K_0 based on multiple regression analysis (variable factors: V_{sHH}/V_{sVH}, soil age in years, and depth in meters).

Alternative to the regression-based K_0 predictions, a novel approach is made based on the simplified individual stress model for inherent isotropic soil (i.e., $K_0 = (V_{sHH}/V_{sVH})^8$ from Equation 5.5) and additional parameter as follow:

▪ HH-VH modes:

$$\text{Equation (5.13)} \quad K_0 = \left(\frac{V_{sHH}}{V_{sVH}}\right)^8 \cdot (1 - a_x{}^f) + b_x$$

where, a_x and b_x= modifier term (here, a_x = 0.6 and b_x = 0.4), exponent f = $(V_{sVH}/V_{sHH})^{[\log(t) - 3]}$, and t = geologic age of the soil formation in years.

The expression given by Equation 5.13 is an attempt to consider site-specific ageing effects especially for heavily overconsolidated sites. Figure 5.9 shows multiple sets of K_0 prediction lines adopting the term a_x=0.6 and b_x=0.4 with various age scaling. The prediction lines are not expected to be perfectly matched because the in-situ V_s and/or K_0 measurements often tend to be very sensitive and scattered relationships In addition, geomaterials are affected by other variables which are not easy to quantify. However, the general tendency of prediction lines is moderately acceptable with age scaling. A set of prediction lines can be shifted adjusting the magnitude of a_x = 0.6 and/or b_x = 0.4.

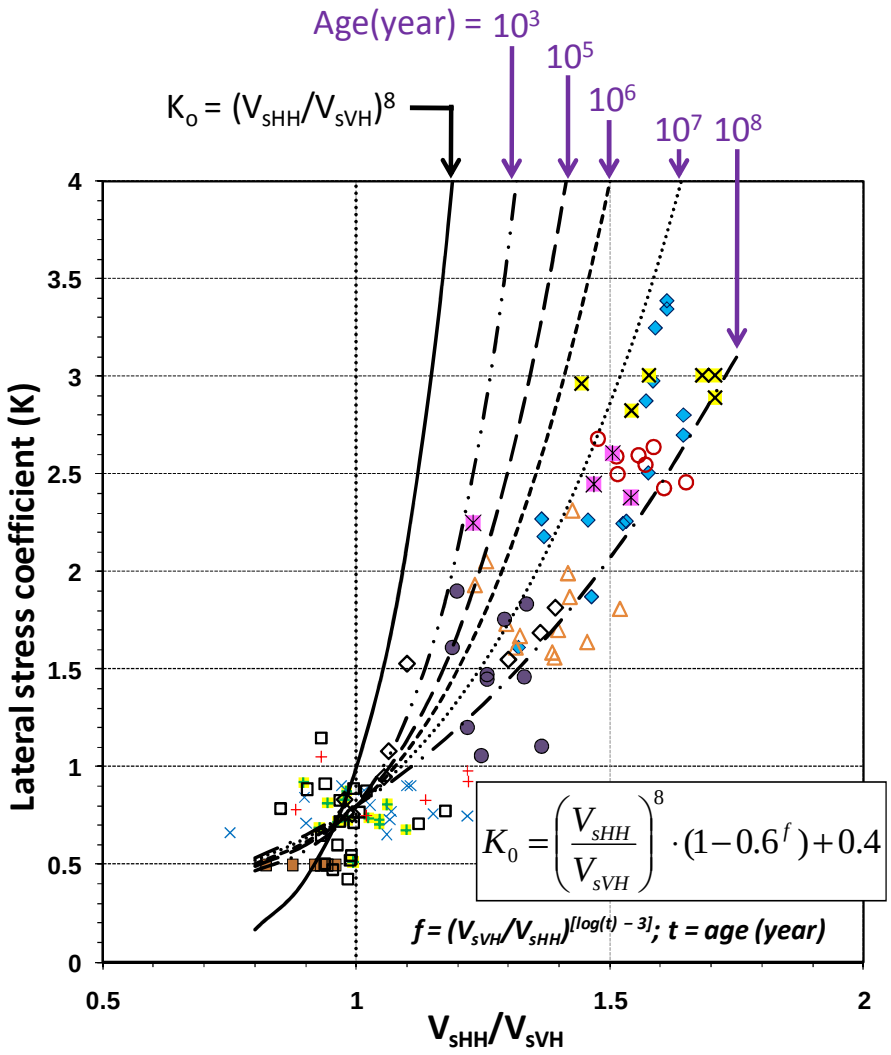

Figure 5.9. Lateral stress coefficient K_0 in terms of V_{sHH}/V_{sVH} ratio and age.

5.6 Case Studies

5.6.1 Po River Valley – NC Sand Site

To illustrate the applications of the derived K_0 expressions, results from the well-known Po River Valley site in Italy are reviewed. The Po River site consists of normally consolidated to lightly-overconsolidated alluvial sands of Holocene age. For the Po River site investigations, various in-situ tests have been conducted over several decades (e.g., Bruzzi et al 1985, Baldi et al 1988; Fioravante et al. 1998). The benchmark K_0

measurements with depth were obtained from self-boring pressuremeter tests (SBPMT). Figure 5.10a shows profiles of the measured shear wave velocity profiles from CHT (V_{sHV}), RCHT (V_{sHH}), and DHT (V_{sVH}) modes. As shown in Figure 5.10b, both of the proposed K_0 assessment methods provide reasonable agreements with the reference K_0 values.

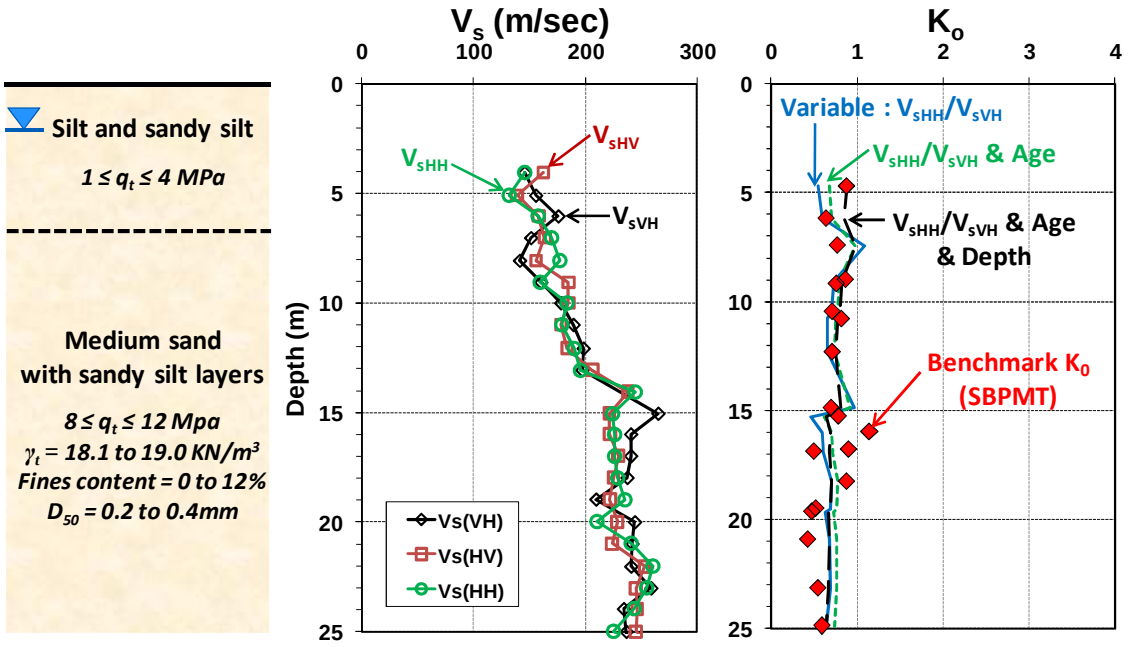

Figure 5.10. Case study for sands at Po River Valley, Italy (data from Fioravante et al. 1998): (a) modal shear wave profiles; (b) benchmark K_0 compared with wave velocity ratio evaluation.

5.6.2 Madingley – OC Clay Site

To illustrate the applications in overconsolidated soils, field data from the well-documented Madingley site in Cambridge, U.K. are reviewed (Coop and Wroth, 1989). Madingley consists of heavily overconsolidated fissured Gault clay and details on the benchmark K_0 measurements obtained from SBPMT are given by Powell (1990). The shear wave velocity profiles from DHT, CHT, and RCHT reported by Butcher and

Powell (1995) are presented in Figure 5.11a. Using these results, approximate K_0 evaluations are made using the aforementioned methods and these are presented in Figure 5.11b with good comparison shown against the pressuremeter values.

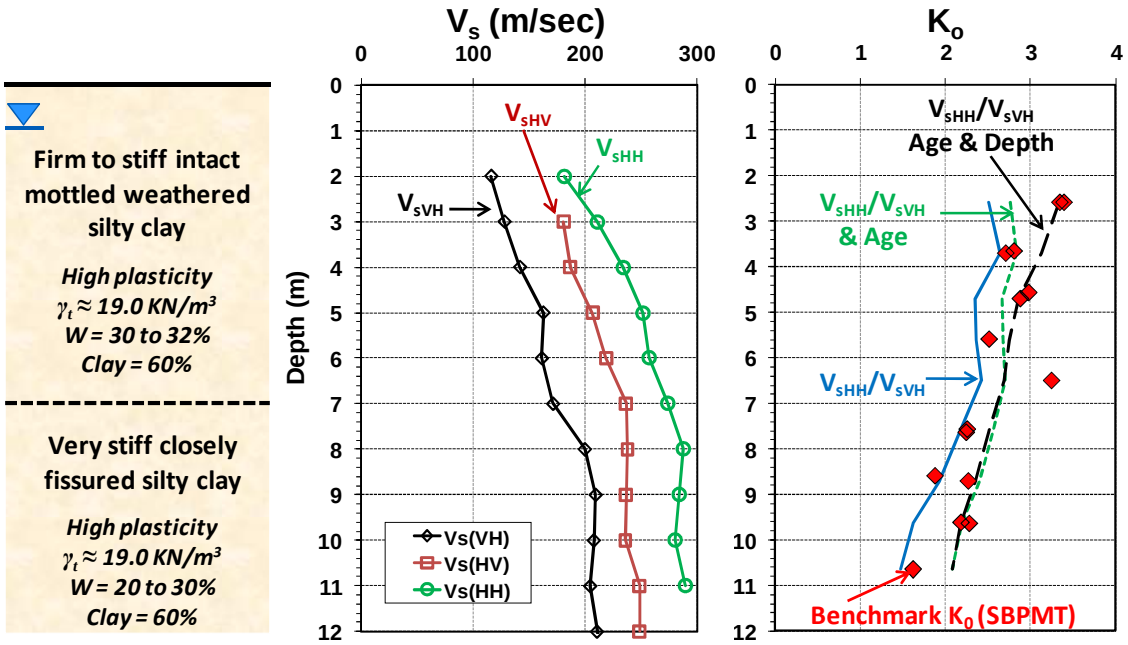

Figure 5.11. Case study for OC clay at Madingley, UK (data from Butcher & Powell, 1995): (a) modal shear wave profiles; (b) benchmark K_0 compared with wave velocity ratio evaluation.

5.7 Summary and Conclusions

In this study, in-situ K_0 evaluations using paired sets of shear wave velocity modes (SV and SH) were examined via a special database compiled from 16 well-documented geotechnical test sites that included 9 clay deposits, 3 silty mixed soils, and 4 sands (Ku and Mayne 2012a, 2012b). At these sites, profiles of two or three different shear wave modes (CHT, DHT, and RCHT) were available for paired matching. The reference K_0 values were obtained from direct methods including self-boring pressuremeter, hydrofracture, and/or push-in spade cells, and in some cases, from direct

laboratory measurements (sample suction, instrumented consolidometers, and/or triaxial stress path tests). Beyond the theoretical assessments, expressions for K_0 were derived using multiple regression studies that considered the ratio of HH/VH and/or HH/HV waves, as well as additional influences of depth and age. Based on overall observations on the suggested K_0 evaluation means, some recommendations for engineering applications within the collected dataset are as follows:

▪ The use of the ratio of HH/VH appears well suited to the evaluation of geostatic stress states in soils as it provides information on stress-induced anisotropy.

▪ The ratio HV/VH appears to indicate a degree of inherent or fabric anisotropy.

▪ A good first-order evaluation of K_0 is obtained simply from the ratio of shear wave velocities measured by rotary crosshole and downhole testing:

HH and VH modes: $$K_0 = 0.78 \cdot \left(\frac{V_{sHH}}{V_{sVH}} \right)^{2.55}$$

▪ If the age of the formation is known, a reasonable estimate of K_0 may be made from:

HH and VH modes: $$K_0 = \left(\frac{V_{sHH}}{V_{sVH}} \right)^{8} \cdot (1 - a_x{}^{f}) + b_x$$

where the modifier term $a_x = 0.6$, $b_x = 0.4$, exponent $f = (V_{sVH}/V_{sHH})^{[\log(t) - 3]}$, and t = geologic age of the soil formation in years

CHAPTER 6

YIELD STRESS RATIO EVALUATED FROM IN-SITU PAIRED DIRECTIONAL SHEAR MODULI

6.1 Introduction: Yield Stress

The stress history of soils is a primary characteristic that governs fundamental aspects of soil behavior and results from the complete geological evolution over time including various environmental factors. Considering the soil as an approximate elasto-plastic particulate media, the yield stress (σ_y') represents an important break point that separates elastic and plastic response regions. In conventional geotechnical terms, the preconsolidation stress (σ_p' or P_c') which indicates a past maximum vertical overburden stress, has been considered an equivalent parameter. However, the magnitude of σ_p' is commonly used to define the increased stress due to mechanical geologic experiences. For instance, Burland (1990) described the yield point at which a notable volumetric reduction occurs during ageing process of reconstituted samples as 'quasi-preconsolidation pressure'. It corresponds to the term σ_y' as distinguished from σ_p'. The yield stress σ_y' is a more accurate and comprehensive term which includes post-depositional processes such as ageing, weathering, cementation, and diagenesis of sediments (Gasparre, 2005; Boone, 2010). The overconsolidation ratio (OCR) is a well-known and classic normalized parameter which is the ratio of σ_p' to current effective vertical stress (σ_{vo}') such that: $OCR = \sigma_p'/ \sigma_{vo}'$. Similarly, yield stress ratio (YSR) can be defined as the magnitude of the σ_y' normalized by σ_{vo}'. In this study, the more complete terms yield stress (σ_y') and normalized YSR are both used to represent the stress history of natural soil deposits (Jardine et al., 2004).

After sedimentation, a natural normally-consolidated soil will become prestressed due to one or more overconsolidation mechanisms, as explained in prior studies (Skempton, 1961; Parry, 1970; Bjerrum, 1972; Mesri and Choi, 1979; Jamiolkowski et al., 1985; Chen and Mayne, 1994). The most common reason is mechanical loading-unloading that occurs from erosion, past glaciations, and excavation or removal of prior overburden. Another important cause of overconsolidation relates to changes in porewater pressures, including a rise in the groundwater table, artesian water, and/or desiccation by capillary effect. Additional mechanisms include the alteration of soil structure by ageing, weathering, cementation, wetting-drying cycles, and repetitive freeze-thaw processes, as well as a cementing or bonding caused by precipitation of calcium carbonates or other minerals from groundwater. In the field, the YSR profiles tend to be quite different for each mechanism. As a consequence, the genuine stress history might be rather complicated due to combined complex mechanisms (Chen and Mayne, 1994).

6.2 Background: Yield Stress Evaluation

A basic and conventional method to determine the yield stress is the laboratory one-dimensional consolidation test using an oedometer or consolidometer (e.g., ASTM D2435) or constant-rate-of-strain device (ASTM D4186). On the basis of this test, a number of interpretative approaches have been developed for delineation of the yield stress. Table 6.1 summarizes a number of various methodologies (modified after Arnal, 2009). While consolidation testing is expected to provide a reliable yield stress of the in-situ condition, there can be uncertainties and variances between the σ_y' evaluation methods because they are determined based on empirical procedures and graphical

observations (Boone, 2010). The original shape of the consolidation curve (e.g., e−logσ_v' plot) tends to be changed or shifted because of sample disturbance effects. The measured e-logσ_v' curve is also altered by test variables, including: the applied load incremental ratio (LIR=$\Delta\sigma/\sigma_{initial}$), strain rate of loading, porewater pressures, specimen diameter and thickness, swelling, side wall friction, and other variables (Van Zelst, 1948; Wahls, 1962; Ladd, 1991).

Table 6.1. Summary of σ_y' evaluation methods (modified after Arnal 2009)

Reference	Method type
Casagrande, 1936	e - logσ_v' plot, graphically constructed
Van Zelst, 1948	e - logσ_v' plot, rebound method
Burmister, 1951	e - logσ_v' plot
Schmertmann, 1955	e - logσ_v' plot, graphically constructed
Janbu, 1969	Stress-strain and modulus-strain
Jamiolkowski & Marchetti, 1969	$1/m_v$ - logσ_v' plot, graphically constructed
Pacheco Silva, 1970	e - logσ_v' plot, graphically constructed
Sällfors, 1975	e - logσ_v' plot, organic soils
Andersen et al., 1979	Backcalculated from s_u
Butterfield, 1979	ln(1+e) - logσ_v' plot
Graham et al., 1981*	Curve-fitting of experimental data
Oikawa, 1987	log(1+e) - logσ_v' plot
Becker et al., 1987	W - σ_v' Work-Energy method
Tavenas, 1987	e - logσ_v' plot
Jose et al., 1989	log(e) - logσ_v' plot
Hardin, 1989	$1/e - (\sigma_v'/\sigma_{atm})^p$ plot
Burland, 1990	I_{vo} - logσ_v' plot
Jacobsen, 1992	Empirical estimation or graphically constructed
Dias & Pierce, 1995	Spreadsheet procedure using a combination of methods
Onitsuka, 1995	ln(1+e) - logσ_v' plot
Chetia & Bora, 1998	Empirical expression based on OCR and e_L
DeGroot et al., 1999*	Relationship between σ_y', S_u, and index properties
Senol & Saglamer, 2002	Strain - stress plot
Wang & Frost, 2004	Energy - p space, Dissipated Strain Energy Method
Clementino, 2005*	e - logσ_v' plot, graphically constructed
Solanki & Desai, 2008	Empirical correlations (e/e_L)
Mesri & Vardhanabhuti, 2009	e - logσ_v' plot, granular soils
Boone, 2010*	e - logσ_v' plot, simple slope-intercept mathematics

Notes: References with * symbol are added after summary collection by Arnal (2009);

e = void ratio, $1/m_v$ = constrained modulus, W = work per unit volume, I_{vo} = void index, s_u = undrained shear strength, e_L = void ratio corresponding to liquid limit.

A most common reason for many uncertainties and discrepancies occurs due to sample disturbance (Ladd & DeGroot 2003). Samples are readily disturbed in the process of tube insertion, extraction, sample transportation, and specimen preparation (e.g., cutting, trimming, and mounting). Typical sample disturbance effects during the overall sampling process were shown previsously in Figure 3.6. Conceptually, the influences of sample disturbance and load increment ratio (LIR) on the resulting consolidation curve are depicted in Figure 6.1. In a standard moment-arm type oedometer test, a LIR = 1 is most common (i.e., load doubles with each successive load). However, in consolidation of simple shear specimens, direct shear box, and triaxial testing, a larger step is often applied, whereas in contrast, better definition of σ_y' results if a smaller LIR is used. Even 'undisturbed' specimens by professional research laboratories do not represent the actual conditions for the in-situ case because of inevitable stress release effects, exposure to zero isotropic total stress during trimming, temperature variations, material handling, and water content changes.

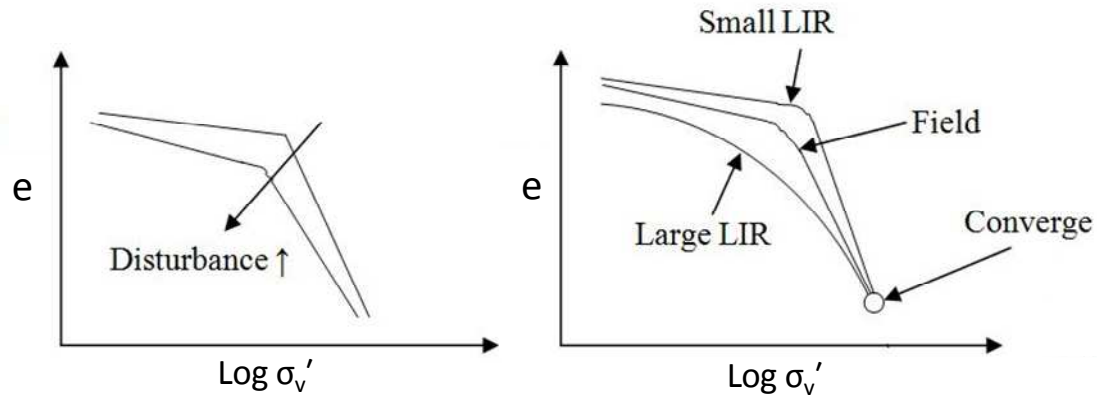

Figure 6.1. Conceptual changes on consolidation test results due to: (a) sample disturbance effects (Ladd 1991), (b) load incremental ratio effect (Wahls 1962).

Although the laboratory consolidation test is the primary method to define σ_y', it is relatively expensive (approximately US $500 to $700 per specimen), provides only a single value, and takes 2 to 3 days time (automated consolidometer) and up to 2 weeks for a manually-operated oedometer. Moreover, the consolidation test is rather problematic for silts and sands since undisturbed samples are very difficult and extremely expensive to procure. In addition, the resulting e-logσ_v' curves for sands are too flat to reasonably select a yield point. Therefore, alternative methods for evaluating stress history of soils have been proposed, specifically using in-situ tests. Methodologies have been developed to ascertain the stress history from cone penetration tests (CPT), flat dilatometer test (DMT), standard penetration test (SPT), and vane shear test (VST). Conceptually, it is possible to relate in-situ penetration data (e.g., q_t, p_0, N_{60}, s_{uv}) with the effective yield stress and yield surface (Mayne, 2007). In fact, each in-situ test has a unique stress path and reaches a different part of the yield surface (Mayne, 2005).

Two examples of the relationships for evaluating yield stress via field tests are provided in Figure 6.2: (a) σ_y' from CPT net cone resistance ($q_t - \sigma_{vo}$) in various soil types (Mayne et al., 2009), and (b) σ_y' from $s_{u,VST}$ and plasticity index (I_P) in clays (e.g., Leroueil & Jamiolkowski, 1991). In spite of the noted uncertainty and scatter in these data, the utilization of in-situ test data is an attractive and efficient means for profiling the yield stress because of multi-fold reasons: (1) results are available immediately, (b) continuous readings can be obtained with depth, and (c) data are collected quickly and economically. Furthermore, they can be used to corroborate the lab results as well as fill-in data between the discrete sampling elevations.

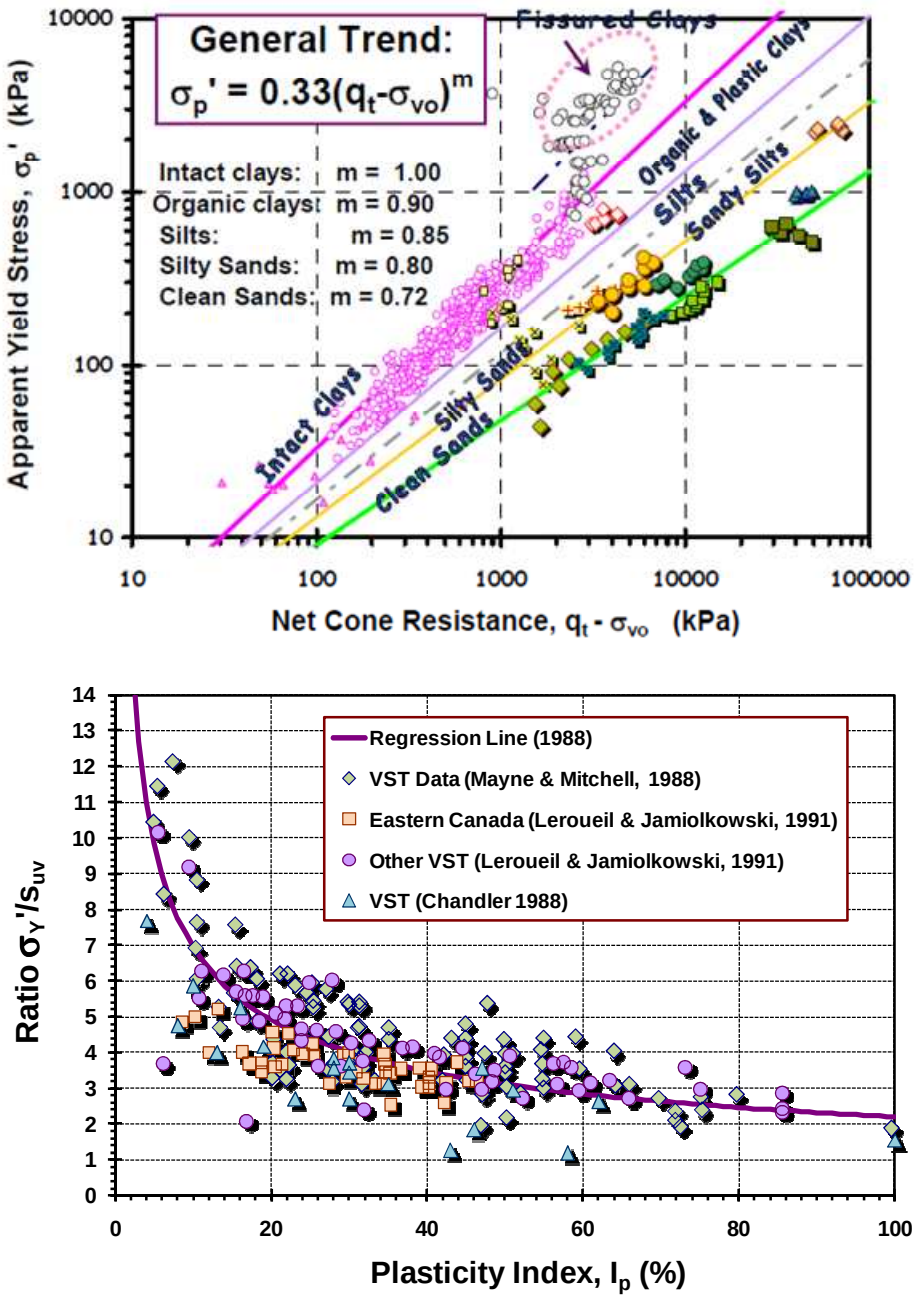

Figure 6.2. Experimental stress history evaluation methods via in-situ tests: (a) σ_y' via CPT readings in various soils, (b) σ_y' via VST in clays.

Other relationships for evaluation of the stress history from in-situ tests include the use of piezo-porewater pressures (Sully and Campanella 1990), pressuremeter (Kulhawy and Mayne 1990), flat plate dilatometer (Marchetti 1980), and standard penetration tests (Mayne 1992).

6.3 Shear Stiffness and Stress History Relationship

The shear modulus of soils at small strains (i.e., shear strain γ_s <10^{-4}) has been studied over the past half-century to understand the relative influences of various factors such as stress level, soil type, void ratio, strain rate, age, fabric, and other variables (Hardin and Richart, 1963; Hardin and Black, 1968; Hryciw and Thomann, 1993; Viggiani and Atkinson, 1995; Jamiolkowski et al., 1995; Pennington et al., 1997; Clayton, 2011). In consideration of dimensional consistency, the equations for the initial shear stiffness have led to a general expression based on three main variables (i.e., confining stress, void ratio, stress history) as follows (Hardin and Blandford, 1989):

Equation (6.1) $$G_{0,ij} = S_{ij} \cdot F(e) \cdot YSR^k \cdot P_a^{1-ni-nj} \cdot (\sigma_i')^{ni} \cdot (\sigma_j')^{nj}$$

where, $G_{0,ij}$ = elastic shear modulus in the i-j plane, F(e) = void ratio function, P_a = reference pressure (= 1 atm = 100 kPa), σ_i'= effective stress in the wave propagation direction, σ_j'= effective stress in the wave polarization direction, S_{ij}, k, ni, nj = empirical material constants. For fine-grained soils, it was noted that the initial stiffness is strongly related to two variables: (a) the effective confining stress state and (b) either void ratio or YSR (Viggiani and Atkinson, 1995; Rampello et al., 1997; Santagata et al., 2005), as detailed in Chapter 4. In consideration of G_0 magnitude, the void ratio is a dominating factor in normally consolidated (NC) soils whereas the YSR can appropriately explain the variations among overconsolidated (OC) soils. Particularly, Choo et al (2011) examined the effect of directional stress history on anisotropy of initial stiffness and suggested the YSR should be included in the empirical G_0 relationship to properly describe G_0 magnitudes in OC soils. By examining G_0 data ($G_{0,VH}$ and $G_{0,HH}$) obtained from different planes (e.g., VH-vertical plane, HH-horizontal plane), it was found that a directional YSR

seems more suitable for the relationship. Similarly, for cohesionless soils, Hryciw and Thomann (1993) developed a stress history-based model for G_0. The formulation was expressed based on directional stress history (i.e., YSR for vertical and horizontal directions). Consequently, the initial shear stiffness is strongly related to the soil stress history, albeit the parameter terms might depend on soil type and site-specific conditions.

The lateral stress coefficient (K_0) is related to stress history and frictional characteristics, as well as other variables. Mayne and Kulhawy (1982) proposed the following simple expression for one-dimensional mechanical loading-unloading of soils (equivalent to Equation 5.2):

Equation (6.2) $$K_{0,OC} = (1 - \sin\phi') \cdot YSR^{\sin\phi'}$$

where ϕ' is effective friction angle. Since this parameter relates the effective horizontal stress to effective vertical stress ($\sigma_{ho}' = K_0 \cdot \sigma_{vo}'$), it would be possible to include K_0 into a modified version of Equation 6.1 for G_0.

Several studies have indicated that K_0 can be evaluated using paired sets of shear wave modes; i.e., ratio of V_{sHH}/V_{sVH} or V_{sHH}/V_{sHV} (e.g., Sully and Campanella 1995; Fioravante et al. 1998; Griffin and Hiltunen 2001). For instance, in one formulation, the magnitude of K_0 might be evaluated using the following equation for inherent isotropic soils (Zeng and Ni, 1999; equivalent to Equation 5.5):

Equation (6.3) $$K_0 = \left(\frac{V_{sHH}}{V_{sVH}}\right)^{\zeta}$$

where ζ is material constant. The viability of utilizing in-situ V_s data has been discussed earlier in Chapter 5. If Equations 6.2 and 6.3 are combined, the YSR can be expressed in terms of V_s ratio and friction angle of geomaterials:

$$\text{Equation (6.4)} \quad YSR = (1-\sin\phi')^{-1/\sin\phi'} \cdot \left(\frac{V_{sHH}}{V_{sVH}}\right)^{\zeta/\sin\phi'}$$

Basically, Equation 6.4 is derived for inherently isotropic soils in fabric and structures. It might be much more complicated and difficult to quantify the stress history in actual in-situ sediments which have various depositional process and diagenesis. Nevertheless, considering the basic format of Equation 6.4, it is expected that the degree of V_s anisotropy or G_0 anisotropy (i.e., magnitude of V_s ratio or G_0 ratio) could be a critical parameter to assess the stress history in soils. In order to evaluate in-situ stress history condition, it seems more valid to use the in-situ anisotropy data because the in-situ shear stiffness tends to be quite different from that measured from laboratory (Chapter 4).

6.4 Yield Stress Ratio Relationship with Shear Wave Data

To investigate the feasibility of stress history evaluations using small-strain stiffness, a special in-situ V_s database has been compiled using results from 14 well-documented geotechnical test sites. Many site details were already provided in Table 5.2. The corresponding stress history profile (i.e., yield stress and YSR) were known from series of one-dimensional consolidation testing on undisturbed samples taken a different elevations in the formations, as well as well-documented engineering geologic studies at these sites. The YSR information, shear wave modes, and reference sources for each site are given in Table 6.2.

All sites have the V_{sHH} mode (rotary crosshole) and either downhole (V_{sVH}) and/or conventional crosshole (V_{sHV}), thus it is possible to pair the ratios of V_{sHH}/V_{sVH} and/or V_{sHH}/V_{sHV}. From the special database, the different V_s modes are plotted with the yield stress in Figure 6.3, with OC and NC soils approximately marked. Apparently, the V_s anisotropy is relatively significant in OC soils. Specifically, a hierarchy of V_s modes is observed in HOC soils (i.e., $V_{sHH} \geq V_{sHV} \geq V_{sVH}$). Hence, a larger yield stress seems to result in higher degrees of G_0 anisotropy because the G_0 ratio depends upon $(V_s \text{ ratio})^2$.

For instance, from the directional shear stiffness measured by seismic field testing, a considerable degree of stiffness anisotropy was observed in heavily overconsolidated soils (e.g., London clay). In the field, shear stiffness anisotropy in geomaterials is caused by a combination of stress-induced and inherent fabric anisotropy. Examples of significant stiffness anisotropy in overconsolidated soils are shown in Figure 6.4, including Gault clay and London clay (Butcher and Powell 1995). The directional field G_0 measurements were plotted with mean normal stress: $\sigma_o' = \frac{1}{3}\,\sigma_{vo}'\,(1 + 2 \cdot K_0)$. For both of these sites, a notable hierarchy of G_0 in different planes is observed, such that: $G_{0,HH} > G_{0,HV} > G_{0,VH}$. The $G_{0,HH}$ mode is the largest magnitude because of high K_0 stress states in both directional and polarization planes. In an ideal cross-anisotropic particulate medium, the $G_{0,VH}$ should be identical to $G_{0,HV}$, however, the observed difference may be due to the added effect of inherent anisotropy in soil fabric caused by deposition, strain history, and/or diagenesis, as well as the possibility of lateral directional differences (i.e., $G_x \neq G_y$).

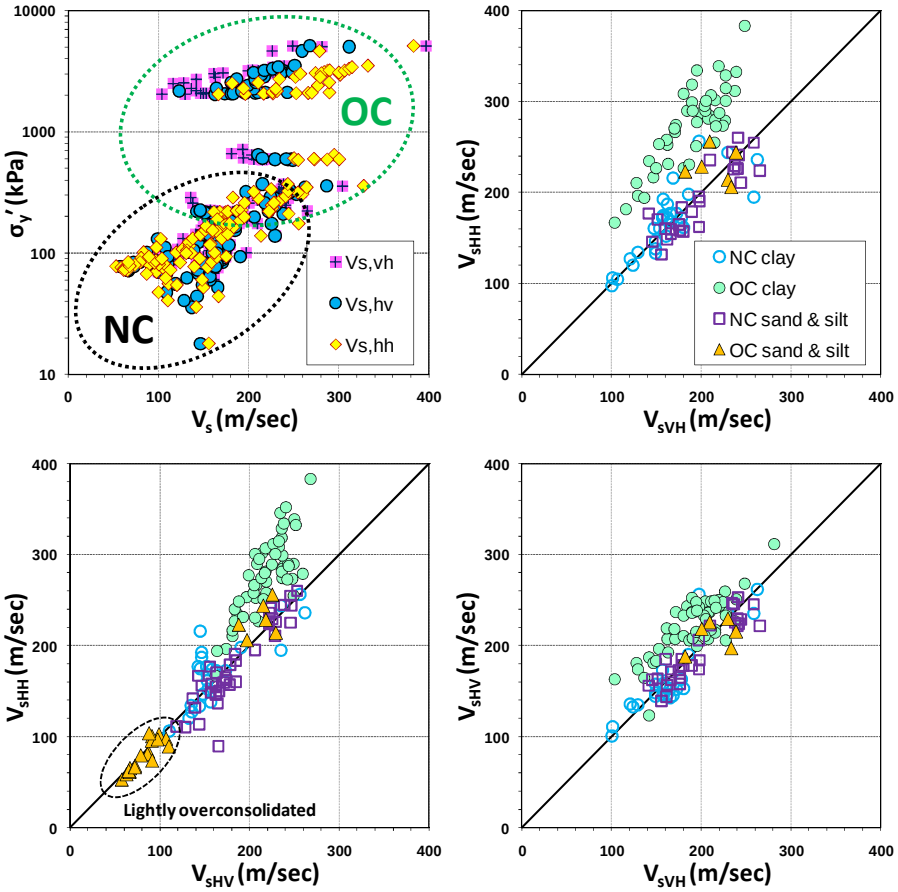

Figure 6.3. Hierarchy of shear wave data: (a) yield stress (σ_y') vs. shear wave velocity, (b) V_{sHH} (rotary crosshole type) versus V_{sVH} (downhole type), (c) V_{sHH} (rotary crosshole type) versus V_{sHV} (standard crosshole type), (d) V_{sHV} (standard crosshole type) versus V_{sVH} (downhole type).

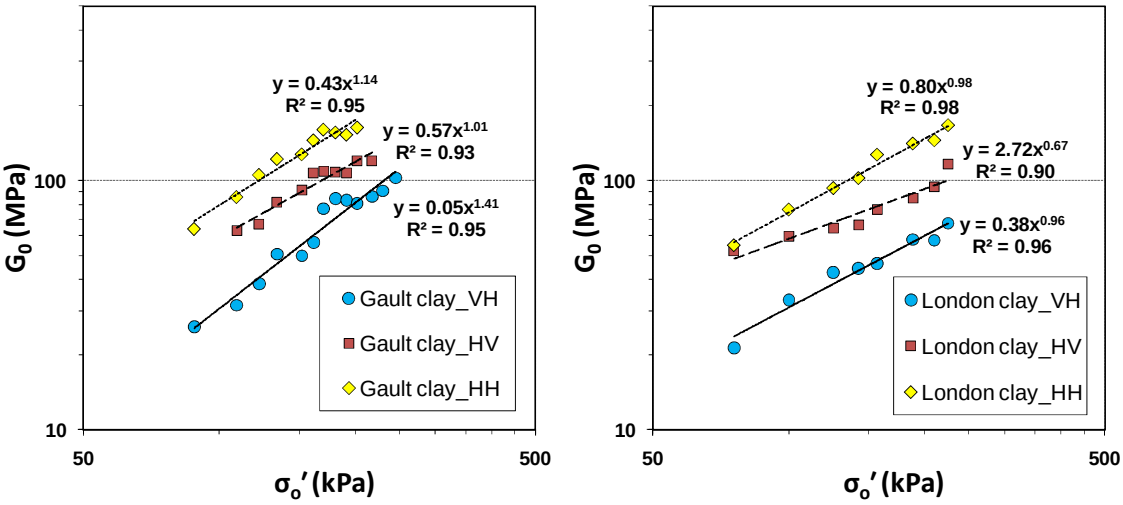

Figure 6.4. Small-strain shear modulus anisotropy with effective stress: (a) Gault clay at Madingley, UK (Butcher and Powell 1995), (b) London clay at Chattenden, UK (Butcher and Powell 1995).

Table 6.2. Summary of compiled database including YSR information

Site	Soil type	Applied V_s mode	YSR	YSR reference
Southern England (Purton)	Oxford clay	VH,HV,HH	14-44+	Hird and Pierpoint (1997)
Madingley, UK	Gault clay (Fissured clay)	VH,HV,HH	20+	Lunne et al. (1997)
Chattenden, UK	London clay (Fissured clay)	VH,HV,HH	20+	Powell and Butcher (1995) Apply OCD*=2000 kPa (Assumed based on geologic erosion information) YSR = $(OCD+\sigma_{vo}')/\sigma_{vo}'$
Heathrow T5, UK	London clay (HOC)	VH,HV,HH	14+	Gasparre (2005)
Cowden, UK	Glacial till; HOC to MOC	VH,HV,HH	3-10+	Powell & Butcher (2003)
Bothkennar, Scotland	Soft silty NC clay	VH,HV,HH	1.3-2.2	Nash et al. (1992); Hight (2003)
Pisa tower, Italy	Soft to firm Pancone clay	VH,HV,HH	1.3-2	LoPresti et al. (2003)
UMASS (Amherst)	Varved clay with shallow crust	VH, HH	1.6-8.5	DeGroot and Lutenegger (2003)
Higashi-Ohgishima, Japan	NC sand fill	VH,HV,HH	1	Shibuya et al. (1995)
San Matteo (Po river), Italy	Po river sand	VH,HV,HH	1.3-1.9	Bruzzi et al. (1985)
Treasure Island, California	Sand fill to silty sand	HV, HH	1	Henke and Henke (2002)
Opelika, Alabama	Residual fine sandy silt	VH,HV,HH	2.8-5	Hoyos & Macari, (1999)
200th St., British Columbia	Soft to stiff NC to LOC clayey silt	HV, HH	1.2-2.7	Sully (1991)
Lower 232 St., British Columbia	Soft to firm NC to LOC clayey silt	HV, HH	1.2-2.3	Sully (1991)

Notes: YSR = yield stress ratio = (σ_y'/σ_{vo}'); σ_y' = yield stress or preconsolidation; σ_{vo}' = current effective vertical overburden stress; OCD* = overconsolidation difference = $(\sigma_y' - \sigma_{vo}')$

6.5 Stress History Evaluated Directly from Stiffness Ratio

Considering the insights on the G_0 anisotropy-stress history relationships, regression analyses are investigated using the special database. Figure 6.5 shows plots of YSR versus the stiffness ratios of $G_{0,HH}/G_{0,VH,}$ $G_{0,HH}/G_{0,HV,}$ and $G_{0,HV}/G_{0,VH}$. For all cases, the YSR generally increases with the G_0 ratio albeit significant outliers and data discrepancies are evident. Best fit lines obtained from regression analyses employing a power function format and using an exponential function are provided with additional statistic information in Table 6.3 (HH-VH mode: Equation 6.5a and 6.5b, HH-HV mode: Equation 6.5c and 6.5d, HV-VH mode: Equation 6.5e and 6.5f). In the same manner, the yield stress is directly plotted with the G_0 ratios in Figure 6.6. It shows similar trends to the YSR-G_0 ratio relationship. Regression lines and statistic results for the yield stress are also summarized in Table 6.3 (HH-VH mode: Equation 6.6a and 6.6b, HH-HV mode: Equation 6.6c and 6.6d, HV-VH mode: Equation 6.6e and 6.6f).

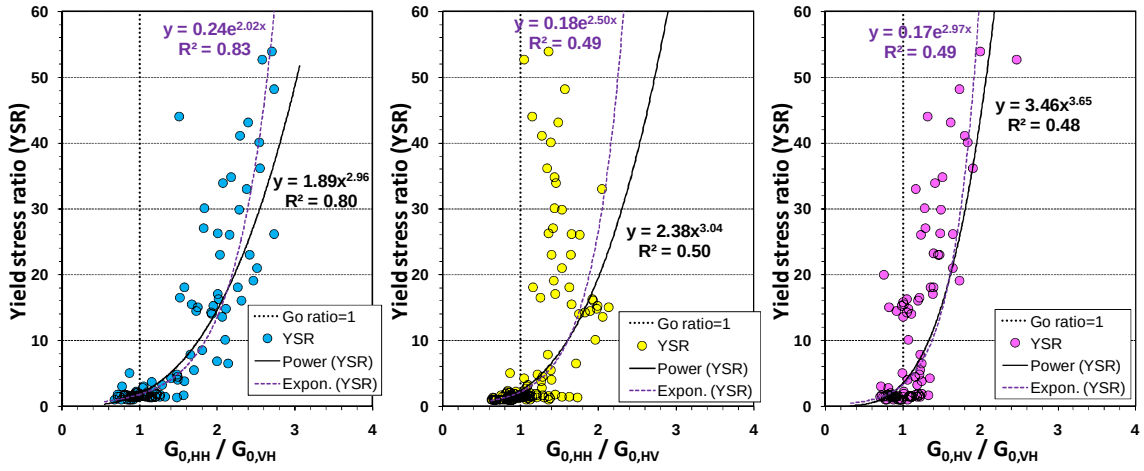

Figure 6.5. (a) Yield stress ratio versus $G_{0,HH}/G_{0,VH}$, (b) Yield stress ratio versus $G_{0,HH}/G_{0,HV}$, (c) Yield stress ratio versus $G_{0,HV}/G_{0,VH}$.

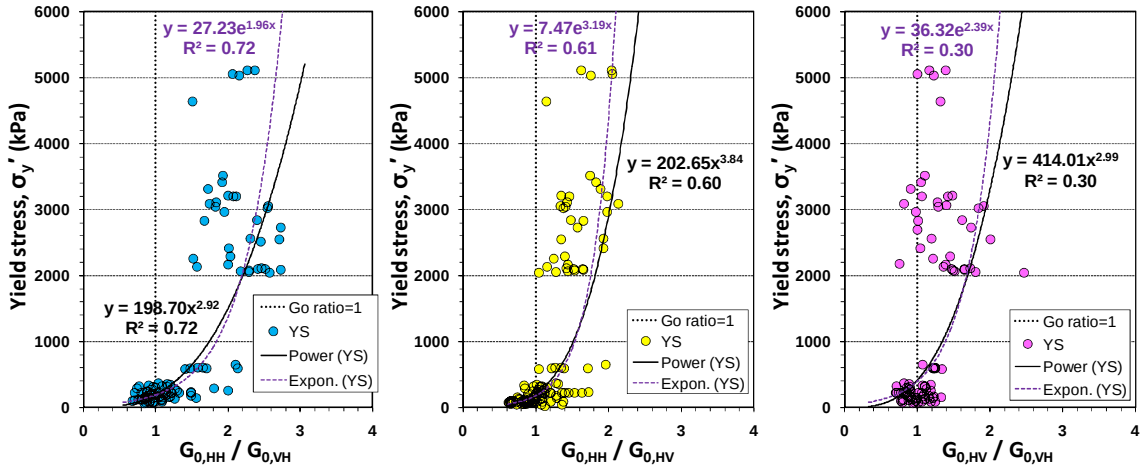

Figure 6.6. (a) Yield stress versus $G_{0,HH}/G_{0,VH}$, (b) Yield stress versus $G_{0,HH}/G_{0,HV}$, (c) Yield stress versus $G_{0,HV}/G_{0,VH}$.

Table. 6.3. Summary of regression analyses for stress history in terms of small-strain shear stiffness ratio (e.g., $G_{0,ij}/G_{0,ji}$)

	Paired mode	Regression equation	R^2	N	S.E.	Eq. no
YSR	HH-VH	$YSR = 1.89 \cdot \left(G_{0,HH}/G_{0,VH}\right)^{2.96}$	0.805	106	0.253	[6.5a]
	HH-VH	$YSR = 0.24 \cdot \exp\left(2.02 \cdot G_{0,HH}/G_{0,VH}\right)$	0.831	106	0.235	[6.5b]
	HH-HV	$YSR = 2.38 \cdot \left(G_{0,HH}/G_{0,HV}\right)^{3.04}$	0.499	130	0.400	[6.5c]
	HH-HV	$YSR = 0.18 \cdot \exp\left(2.50 \cdot G_{0,HH}/G_{0,HV}\right)$	0.495	130	0.401	[6.5d]
	HV-VH	$YSR = 3.46 \cdot \left(G_{0,HV}/G_{0,VH}\right)^{3.65}$	0.484	99	0.422	[6.5e]
	HV-VH	$YSR = 0.17 \cdot \exp\left(2.97 \cdot G_{0,HV}/G_{0,VH}\right)$	0.489	99	0.419	[6.5f]
σ_y' (kPa)	HH-VH	$\sigma_y'(kPa) = 198.7 \cdot \left(G_{0,HH}/G_{0,VH}\right)^{2.92}$	0.725	106	0.313	[6.6a]
	HH-VH	$\sigma_y'(kPa) = 27.2 \cdot \exp\left(1.96 \cdot G_{0,HH}/G_{0,VH}\right)$	0.725	106	0.312	[6.6b]
	HH-HV	$\sigma_y'(kPa) = 202.7 \cdot \left(G_{0,HH}/G_{0,HV}\right)^{3.84}$	0.602	130	0.410	[6.6c]
	HH-HV	$\sigma_y'(kPa) = 7.5 \cdot \exp\left(3.19 \cdot G_{0,HH}/G_{0,HV}\right)$	0.607	130	0.407	[6.6d]
	HV-VH	$\sigma_y'(kPa) = 414.0 \cdot \left(G_{0,HV}/G_{0,VH}\right)^{3.00}$	0.303	99	0.507	[6.6e]
	HV-VH	$\sigma_y'(kPa) = 36.3 \cdot \exp\left(2.39 \cdot G_{0,HV}/G_{0,VH}\right)$	0.295	99	0.510	[6.6f]

Notes: YSR = yield stress ratio; σ_y' = yield stress (preconsolidation); R^2 = coefficient of determination, N = number of applied data, S.E. = residual standard error from log regression.

Within the compiled database, in particular, the ratio $G_{0,HH}/G_{0,VH}$ seems significantly correlated with both YSR and σ_y', more so than the ratios $G_{0,HH}/G_{0,HV}$ or $G_{0,HV}/G_{0,VH}$. Therefore, further statistical-based analyses for the stress history evaluation are conducted using the ratio of $G_{0,HH}/G_{0,VH}$. Figure 6.7 shows site-specific data and best fit lines (i.e., 6.5(a) with a power function, 6.5(b) using an exponential function) with ±1 standard deviation for the YSR versus $G_{0,HH}/G_{0,VH}$ trends. Some outliers are observed, however most data are located within the ±1 standard deviation lines. Figure 6.8 provides comparable information for the yield stress. In the regression equations using the $G_{0,HH}/G_{0,VH}$, it is noted that the exponent values of both power function and exponential function for the yield stress are almost identical to the values for the YSR (i.e., power function: 2.96 [Eq.6.5a] ≈ 2.92 [Eq.6.6a], exponential function: 2.02 [Eq. 6.5b] ≈ 1.96 [Eq.6.6b]). It indicates that YSR regressions and σ_y' regressions (based on $G_{0,HH}/G_{0,VH}$) appear equivalent except different coefficient values. Hence, the stiffness ratio ($G_{0,HH}/G_{0,VH}$) dependencies on both YSR and σ_y' seem to have comparable sensitivity.

In an extended study from the available data, additional important variables relevant to G_0 anisotropy could be included to improve the stress history predictions. In this study, the geologic ages of the depositional sediments were documented. It has been indicated that ageing and time effects influence the magnitude of G_0 (e.g., Anderson and Stokoe, 1978). In Figure 5.6 (Chapter 5), it was observed that the V_s ratio ($V_{s,HH}/V_{s,VH}$) generally increases with the age (t) of soils. In consideration of this, multiple regression analyses for YSR are indicated in Table 6.4 (Equation 6.7a and 6.7b). Figure 6.9 shows plots of reference YSR versus predicted YSR based on the regression equations for YSR evaluation (Figure 6.9(a) − Eq.6.5a, Figure 6.9(b) − Eq.6.5b, Figure 6.9(c) − Eq.6.7a,

Figure 6.9(d) − Eq.6.7b). Although the data show variability, overall the equations provide reasonable estimations for YSR. Particularly, the predictions using both stiffness ratio and age seem to generate relatively better results (i.e., R^2 and S.E. improved).

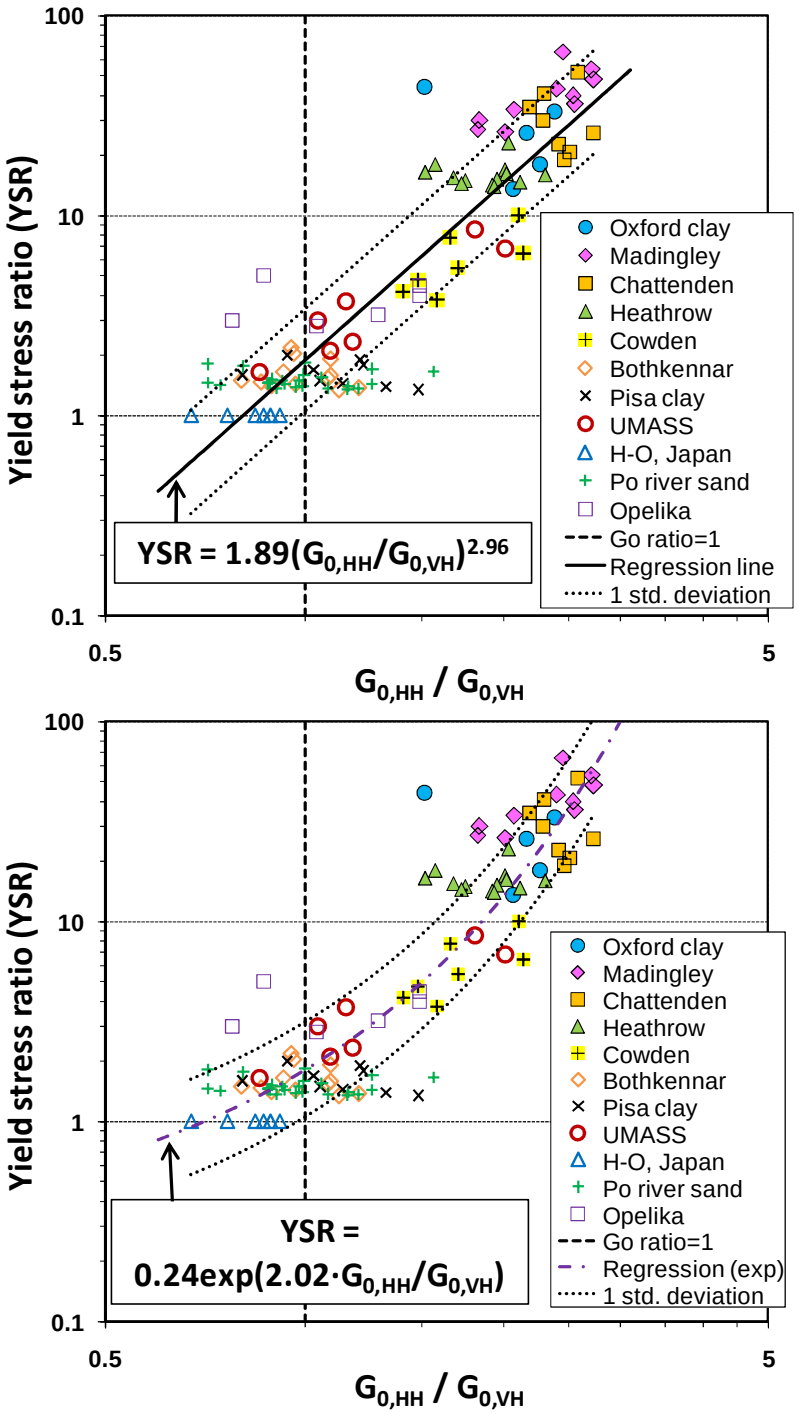

Figure 6.7. Observed trend by regression analysis between in-situ YSR and $G_{0,HH}/G_{0,VH}$: (a) Power law function using $G_{0,HH}/G_{0,VH}$, (b) Exponential function using $G_{0,HH}/G_{0,VH}$.

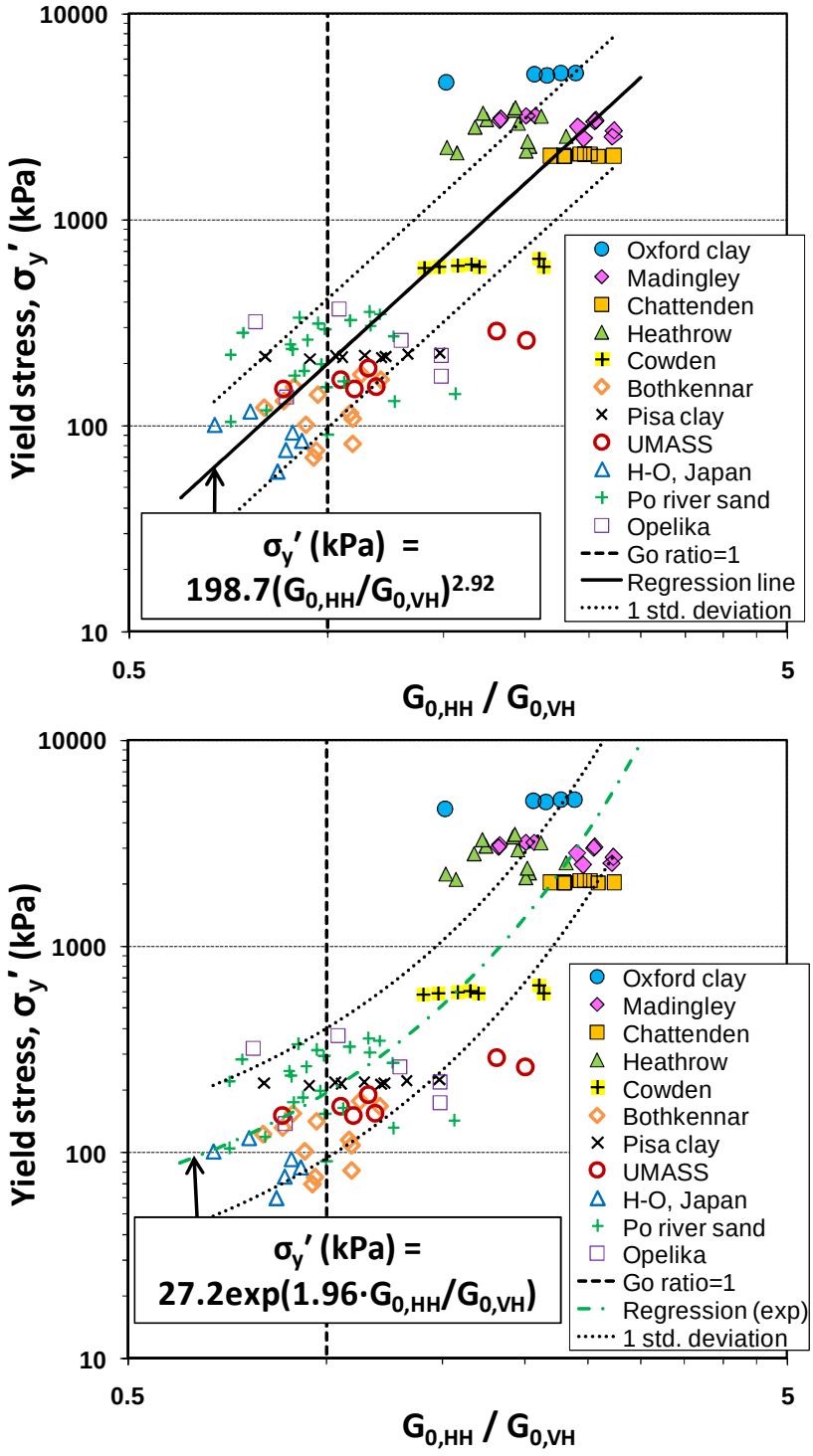

Figure 6.8. Observed trend by regression analysis between in-situ σ_y' and $G_{0,HH}/G_{0,VH}$: (a) Power law function using $G_{0,HH}/G_{0,VH}$, (b) Exponential function using $G_{0,HH}/G_{0,VH}$.

Table 6.4. Summary of multiple regression analyses for stress history (HH-VH mode)

	Regression equation (stress unit = kPa)	R^2	N	S.E.	Eq. no
YSR	$YSR = 0.29 \cdot \left(G_{0,HH}/G_{0,VH}\right)^{1.14} \cdot (t)^{0.199}$	0.934	100	0.152	[6.7a]
	$YSR = 0.13 \cdot \exp\left(0.86 \cdot G_{0,HH}/G_{0,VH}\right) \cdot (t)^{0.188}$	0.942	100	0.143	[6.7b]
σ_y' (kPa)	$\sigma_y'(kPa) = 5.11 \cdot \left(G_{0,HH}/G_{0,VH}\right)^{2.95} \cdot (\sigma_{vo}')^{0.79}$	0.827	106	0.250	[6.8a]
	$\sigma_y'(kPa) = 0.46 \cdot \exp\left(2.01 \cdot G_{0,HH}/G_{0,VH}\right) \cdot (\sigma_{vo}')^{0.86}$	0.847	106	0.234	[6.8b]
	$\sigma_y'(kPa) = 16.5 \cdot \left(G_{0,HH}/G_{0,VH}\right)^{0.38} \cdot (t)^{0.27}$	0.934	100	0.157	[6.9a]
	$\sigma_y'(kPa) = 12.8 \cdot \exp\left(0.20 \cdot G_{0,HH}/G_{0,VH}\right) \cdot (t)^{0.28}$	0.933	100	0.158	[6.9b]

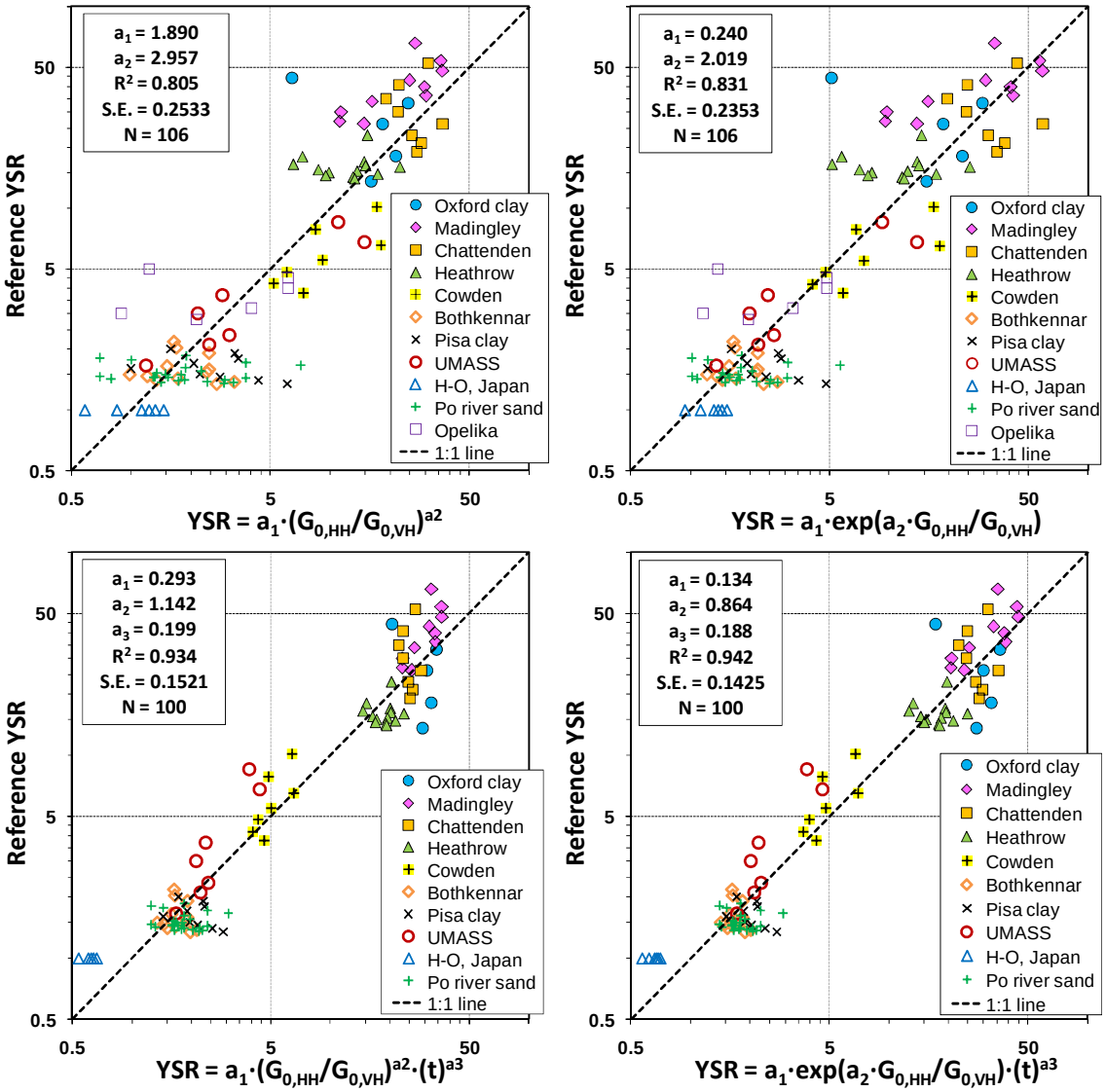

Figure 6.9. Comparison of reference YSR versus predicted value from regression analyses. Applied variables: (a) $G_{0,HH}/G_{0,VH}$, (b) $\exp(G_{0,HH}/G_{0,VH})$, (c) $G_{0,HH}/G_{0,VH}$ and geologic time, (d) $\exp(G_{0,HH}/G_{0,VH})$ and geologic time.

Separate multiple regression analyses have been conducted for the yield stress or preconsolidation stress, as well. As additional variables, the in-situ effective stress (σ_{vo}') and the age (t) of soil deposits are examined. Actually, the YSR is a normalized form of the yield stress divided by the σ_{vo}', thus multiple regressions adopting the σ_{vo}' for the yield stress evaluation might be more valid. Empirical yield stress correlations using the $G_{0,HH}/G_{0,VH}$ and σ_{vo}' are shown in Table 6.4 (Eq.6.8a and 6.8b). Equation 6.8 can be dimensionally equivalent when the stress terms (σ_y' and σ_{vo}') are normalized by a reference pressure. Compared to the regression equations (Eq.6.6a and Eq.6.6b) dependent upon a single variable (i.e., $G_{0,HH}/G_{0,VH}$), the predictions using Equation 6.8 generate improved statistic information (R^2: 0.725 [Eq.6.6a] → 0.827 [Eq.6.8a] ; 0.725 [Eq.6.6b] → 0.847 [Eq.6.8a]). Again, in case that the ratio $G_{0,HH}/G_{0,VH}$ and geologic age of soil deposits are employed as variables, similar empirical relationships for yield stress are derived (Equation 6.9a and 6.9b from Table 6.4). In Equation 6.9, it is indicated that the ratio $G_{0,HH}/G_{0,VH}$ has rather limited influence on the yield stress evaluation (i.e., small exponent or coefficient – 0.38 [Eq.6.9a] and 0.20 [Eq.6.9b]), albeit those provide high R^2 values. The statistic t-values for all variables from other regression equations (Eq.6.5 – Eq.6.8 in Table 6.3 and Table 6.4) were adopted at least in 99.9% significance level. However, the statistic t-value for the $G_{0,HH}/G_{0,VH}$ variable is acceptable within 95% significance level in Equation 6.9a (i.e., probability(>|t|) = 0.0397 < 0.05) and 90% significance level in Equation 6.9b (i.e., probability(>|t|) = 0.0974 < 0.10). In Figure 6.10, the reference σ_y' and predicted σ_y' values are compared based on the derived empirical correlations (Fig.6.10(a)–Eq.6.6a, Fig.6.10(b)–Eq.6.6b, Fig.6.10(c)–Eq.6.8a, Fig.6.10(d)–Eq.6.8b, Fig.6.10(e)–Eq.6.9a, Fig.6.10(f)–Eq.6.9b). Overall, reasonable stress history predictions using the ratio of $G_{0,HH}/G_{0,VH}$ appear viable.

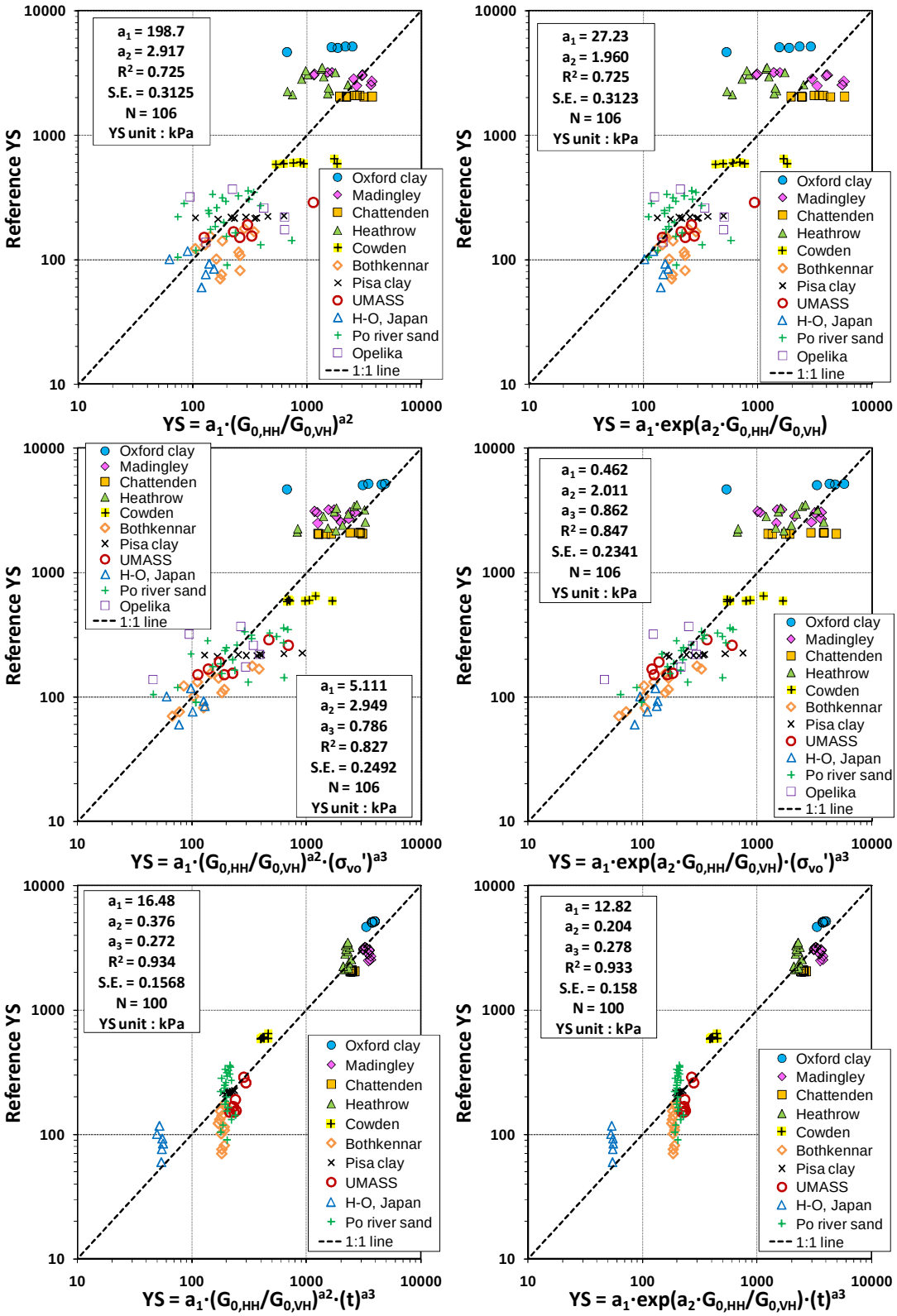

Figure 6.10. Comparison of reference σ_y' and predicted σ_y' by regression analyses. Applied variables: (a) $G_{0,HH}/G_{0,VH}$, (b) $\exp(G_{0,HH}/G_{0,VH})$, (c) $G_{0,HH}/G_{0,VH}$ and σ_{vo}', (d) $\exp(G_{0,HH}/G_{0,VH})$ and σ_{vo}', (e) $G_{0,HH}/G_{0,VH}$ and soil age, (f) $\exp(G_{0,HH}/G_{0,VH})$ and soil age.

6.6 K_0 Evaluation via OCR-Stiffness Ratio Correlation

Using statistical regression analyses on the database, several possible relationships between stress history and the field stiffness measurements were explored in prior sections. One promising trend between OCR (or YSR) and stiffness ratio ($G_{0,HH}/G_{0,VH}$) emerged in terms of a power law expression, as shown again in Figure 6.11 (semi-log plot):

Equation (6.10) $$OCR = \alpha_1 \cdot \left(\frac{G_{0,HH}}{G_{0,VH}} \right)^{\beta_1}$$

where α_1 = 1.89 and β_1 = 2.96 are fitting parameters, coefficient of determination (R^2) = 0.81, number of data points (N) = 106, and standard error (S.E) = 0.25 from log-log regression analysis (equivalent to Equation 6.5a).

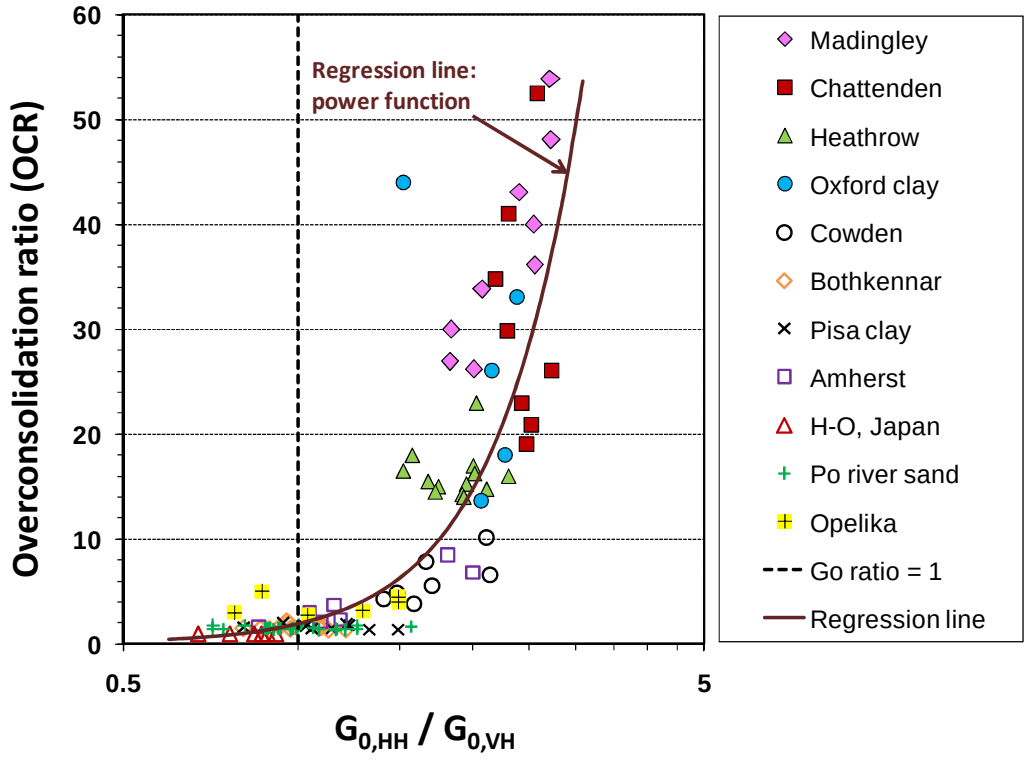

Figure 6.11. Correlation between OCR and shear modulus ratio ($G_{0,HH}/G_{0,VH}$) from database.

As is well-appreciated in Equation 6.2, the magnitude of K_0 depends strongly on stress history effects, particularly sediments which have undergone virgin loading followed by mechanical unloading, as well as other processes (ageing, desiccation, groundwater changes, etc.). The OCR (or YSR) expressions from Equation 6.10 can be subsituted into Equation 6.2 to provide the following equation relating K_0 to shear modulus ratio:

Equation (6.11) $$K_0 = (1-\sin\phi') \cdot \alpha_1^{\sin\phi'} \cdot \left(\frac{G_{0,HH}}{G_{0,VH}} \right)^{\beta_1 \sin\phi'}$$

Representative ranges of friction angle for clays are found in the range: $17^o \leq \phi' \leq 43^o$ (Diaz-Rodriguez et al. 1992) and for clean sands: $30^o \leq \phi' \leq 43^o$ (Mayne et al. 2009). The above expression is presented in Figure 6.12 showing K_0 variations with shear modulus ratio and probable friction angle values of 20º, 30º, and 40º. Data from the documented sites are superimposed on these graphs. Actually, in Chapter 5, a more simple power function was adopted for K_0 regression as follow:

Equation 6.12) $$K_0 = \alpha_2 \cdot \left(\frac{G_{0,HH}}{G_{0,VH}} \right)^{\beta_2}$$

where $\alpha_1 = 0.78$ and $\beta_1 = 2.55$, coefficient of determination (R^2) = 0.81 from a regression analysis (equivalent to Equation 5.8a in Chapter 5). Even though a few outliers are noted, overall reasonable K_0 evaluations are evident and within the typical expected ranges of variance for empirical geotechnical relationships and soil parameters.

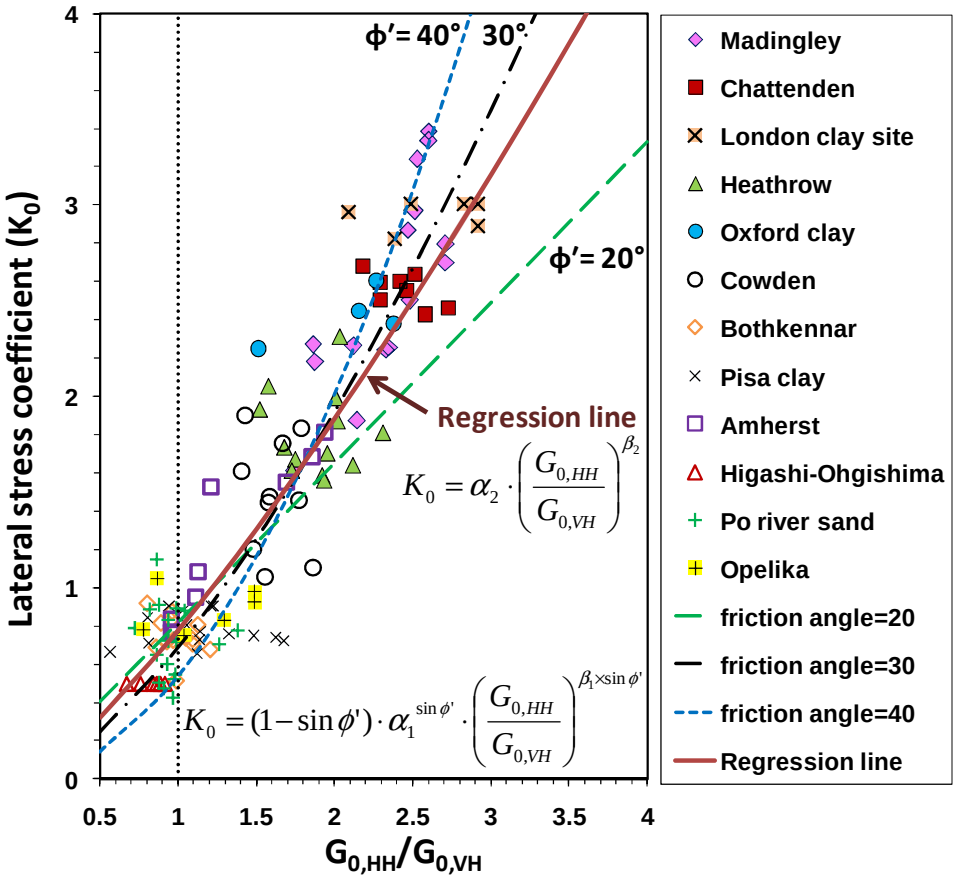

Figure 6.12. Lateral stress coefficient K_0 versus shear modulus ratio (prediction lines were derived using friction angle and G_0 ratio).

6.7 Case Studies: K_0 Evaluation from Small-Strain Shear Modulus Ratios

Two case studies are presented to illustrate use of the approach: (a) overconsolidated clay from London; (b) lightly-overconsolidated clay at Pisa.

6.7.1 Chattenden, UK – Heavily Overconsolidated Clay Site

The Chattenden site consists of a 40-m thick layer of heavily overconsolidated (HOC) and fissured London clay (Butcher and Powell 1995). The site is weathered stiff brown silty clay in the upper 11 meter depth and below this depth is grey and unweathered with increased spacing of fissures. This Eocene age deposit has been subjected to as much as 270 m of erosion, resulting is a hefty OCR profile with depth.

Figure 6.13a shows the measured geophysical results from two different V_s modes at the site (V_{sVH} and V_{sHH}) and the magnitude of V_{sHH} mode is much greater than the V_{sVH}. The corresponding K_0 evaluations resulting from Equations 6.11 and 6.12 are shown on Figure 6.13b. For comparison, benchmark K_0 values ranging from 2.0 to 3.0 obtained from suction measurements are also presented (Crilly et al. 1992). The K_0 prediction seems partially sensitive to friction angle, and in fact, London clay is associated with a characteristic value $\phi' = 22^o$ (Hight et al. 2003). With consideration of a reasonable ranges of K_0 lying between K_a (active coefficient) and K_p (passive coefficient), the predicted values should be cautiously adopted. Nevertheless, a good first order estimation is obtained with this novel approach.

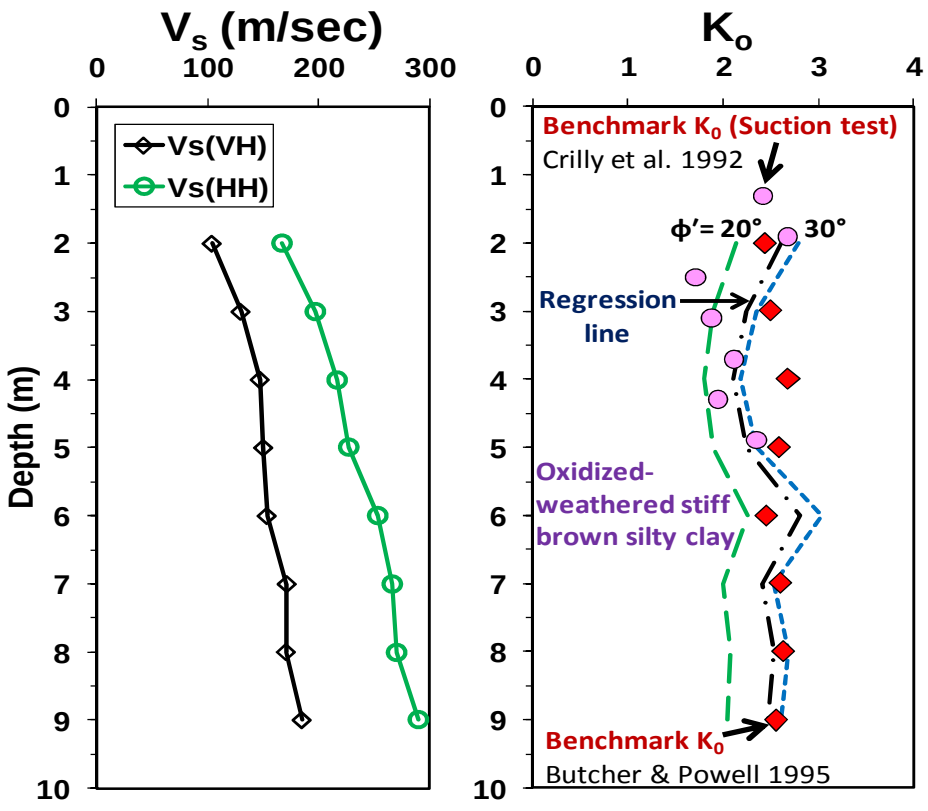

Figure 6.13. Data for London clay at Chattenden (Butcher and Powell 1995): (a) directional shear wave profiles, (b) benchmark K_0 profile and prediction using power function.

6.7.2 Pisa Tower, Italy – Lightly Overconsolidated Clay Site

The site of the famous Pisa tower is underlain by soft to firm alluvial deposits and interbedded clay and sand layers. Paired sets of V_{sVH} and V_{sHH} profiles were obtained in the upper marine clay zone between 10 and 20 meter depths (LoPresti et al. 2003), as presented in Figure 6.14a. The Pisa clay has a medium to high plasticity and low OCRs close to normally consolidated to lightly-overconsolidated conditions. Reference values of OCR and K_0 values were evaluated from oedometer and triaxial tests based on undisturbed specimens. This clay has relatively low K_0 values ranging between about 0.5 and 0.9. Figure 6.14b shows the K_0 assessment from the stiffness anisotropy ratio and 3 lines for adopted ϕ' = 20º, 30º, and a simple regression, noting that the characteristic ϕ' = 25º for Pisa clay.

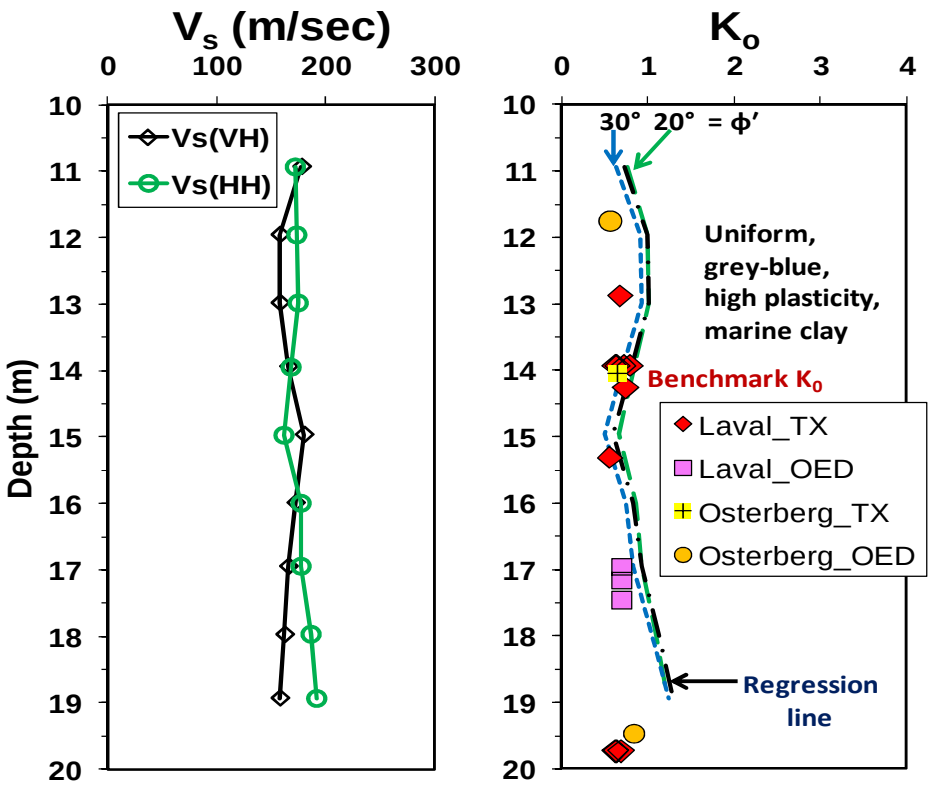

Figure 6.14. Data for Pisa clay, Italy (LoPresti et al. 2003): (a) directional shear wave profiles, (b) benchmark K_0 profile and prediction using power function.

(Notes: Laval = specimen retrieved from laval sampler, Osterberg = specimen retrieved from osterberg sampler, TX = triaxial test, OED = odeometer test)

The K_0 prediction appears reasonable at the Pisa site, with an overall low sensitivity to the friction angle value used.

6.8 Summary and Conclusions

This chapter addresses the evaluation of soil stress history from the degree of initial shear stiffness anisotropy, expressed in terms of a small-strain shear modulus ratio, specifically $G_{0,HH}/G_{0,VH}$. The G_0 values were obtained from different types of in-situ shear wave velocity modes including downhole (VH), crosshole (HV), and rotary crosshole (HH), with procedures for conduct of these tests as detailed by Hoar and Stokoe (1978). A special database was built based on well-documented geotechnical test sites (8 clay sites, 3 silt mixtures, and 3 sand sites) that included paired determinations of the stiffness ratios $G_{0,HH}/G_{0,VH}$ and $G_{0,HH}/G_{0,HV}$. The corresponding stress history profiles were determined by series of one-dimensional oedometer and/or consolidometer tests on recovered undisturbed samples, as well as engineering geology studies. Based on statistic-based regression analyses, various empirical correlations using the stiffness ratios were derived with additional considerations of geologic age of soils and in-situ stress condition. In engineering aspects, a sound first-order estimation of stress history can be obtained by adopting a ratio of initial soil stiffness in HH-VH plane. The simplest expressions are as follow:

$$OCR = 1.89 \cdot \left(\frac{G_{0,HH}}{G_{0,VH}} \right)^{2.96}$$

Also, this chapter revisited the K_0 evaluation based on combination of the K_0-OCR relationship (Mayne and Kulhawy 1982) and OCR-shear modulus ratio ($G_{0,HH}/G_{0,VH}$) correlation (Equation 6.10). In summary, some important highlights in Chapter 6 are as follow:

a) Small-strain shear modulus (G_0) in soils is related to stress history.
b) For stress history evaluation, a special in-situ shear wave database was compiled.
c) Basically, stress history can be assessed by degree of shear stiffness anisotropy (G_0 ratio).
d) Geologic time of depositional sediments seems related to G_0 ratio and stress history.
e) K_0 evaluation was viable through OCR-G_0 ratio correlation.

CHAPTER 7

STRESS HISTORY EVALUATED FROM RATIO OF DIRECTIONAL SHEAR MODULI IN SOILS

7.1 Introduction

In this chapter, an alternate approach for stress history evaluation is introduced based on a relationship between overconsolidation difference (OCD = σ_p' - σ_{vo}') and stiffness anisotropy ($G_{0,HH}/G_{0,VH}$). In Chapter 6, the importance of profiling the yield stress in soils was established, including its physical meaning in elasto-plastic particulate media, conceptual definitions, and causes due to various preconsolidation mechanisms. Then, based on empirical relationships between the shear stiffness ratio (e.g., $G_{0,HH}/G_{0,VH}$) and stress history, the YSR and yield stress were directly evaluated. Overall, the predictions provided reasonable trends. One issue that arose, however, is that small local V_s measurement errors could cause a high sensitivity in the results and thus reduce the reliability of the predictions.

7.2 Stress History Evaluation Using OCD - Stiffness Ratio Correlation

To alleviate the potential sensitivity of the aforementioned stress history evaluations, an alternative approach is suggested using the notion of overconsolidation difference (OCD; or prestress = $\Delta\sigma_p'$) which can represent the yield stress profile in soils. The OCD is defined simply as follow (Locat et al. 2003):

Equation (7.1a) $$OCD = \sigma_y' - \sigma_{vo}'$$

where σ_y' = effective yield stress (or more common preconsolidation stress, σ_p') and σ_{vo}' = effective vertical overburden stress. Details on OCD and associated profiles in soils are

explained by Locat et al. (2003) and Mayne (2007). Let's define a dimensionless OCD (OCD_1) normalized by a reference pressure (σ_{atm}' = atmospheric pressure) as follow:

Equation (7.1b) $$OCD_1 = (\sigma_y' - \sigma_{vo}') / \sigma_{atm}'$$

One clear advantage of OCD is that its general magnitude can be considered constant with depth, specifically for cases of preconsolidation resulting from common mechanical causes such as erosion, excavation, and glaciation. Therefore, evaluating an appropriate constant OCD magnitude (or mean OCD value) can provide a simple means to represent OCR values that most often decrease with depth, as well as corresponding σ_p' profiles which increase with depth.

Based on the compiled database which was developed in Chapter 6, a relationship between OCD and shear stiffness ratio (i.e., $G_{0,HH}/G_{0,VH}$) was examined. In the given depth ranges, mean G_0 and OCD values were applied for regression analysis. In Figure 7.1, an apparent strong correlation between the OCD and G_0 ratio was observed:

Equation (7.2a) $$OCD = 0.466 \cdot (\sigma_{atm}) \cdot (G_{0,HH}/G_{0,VH})^{5.57}$$

Equation (7.2b) $$OCD_1 = 0.466 \cdot (G_{0,HH}/G_{0,VH})^{5.57}$$

where σ_{atm} = reference atmospheric pressure, $R^2 = 0.968$, n =13 (each datum has a mean value), S.E. = 0.174 from log-log regression (Equation 7.2a). Equation 7.2 was derived based on pure empirical regression analyses considering insights that G_0 ratio relates to stress history. For uncemented geomaterials, Equation 7.2 should be applied within limited ranges of G_0 ratio: $0.5 \leq G_{0,HH}/G_{0,VH} \leq 2.5$ and 1 kPa $\leq$ OCD $\leq$ 5000 kPa. Roughly, the lower boundary 1 kPa OCD magnitude represents that soils are normally consolidated (OCR≈1).

As noted in earlier chapters, the shear moduli (G_0) are obtained from field shear wave velocity measurements taken with different directions and polarization. Thus the $G_{0,HH}$ is from a rotary crosshole test (RCHT) that uses either a horizontal sparker, rotary vane device, or torqued hammer and the $G_{0,VH}$ obtained from a standard downhole test (DHT, SCPT, SDMT) and horizontal source positioned at the surface. Once the OCD values are evaluated from the correlation (e.g., Equation 7.2), the effective vertical overburden stress, preconsolidation stress, and corresponding OCR profiles can be calculated from the following:

Equation (7.3) $\sigma_p' = \sigma_{vo}' + OCD$

Equation (7.4) $OCR = \sigma_p'/\sigma_{vo}' = (\sigma_{vo}' + OCD)/\sigma_{vo}'$

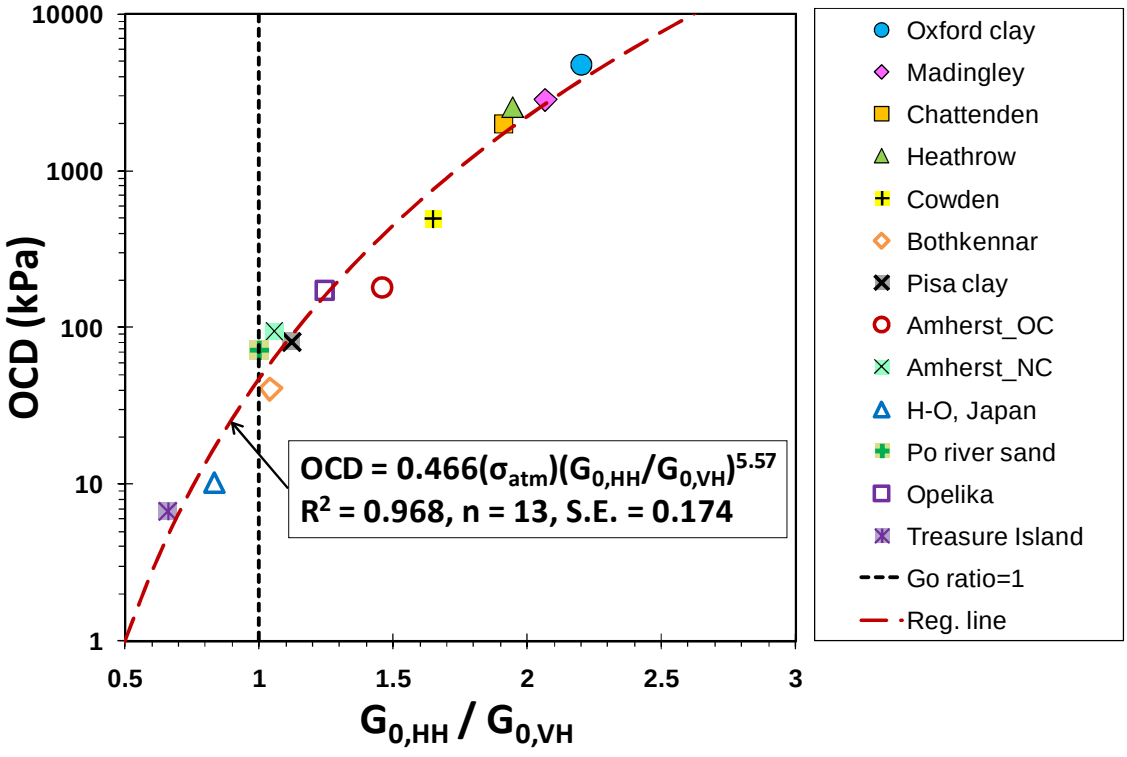

Figure 7.1. Relationship between OCD = (σ_p' - σ_{vo}') and stiffness ratio $G_{0,HH}/G_{0,VH}$.

To set-up reasonable aged values for OCDs for two sites which are normally consolidated (NC) in the database, specifically: Higashi-Ohgishima sand site, Japan and Treasure Island site, California, aged OCR values were approximately quantified considering quasi-preconsolidation effects caused by long-term creep effects over time as follows (Mesri and Choi 1979):

Equation (7.5) $$OCR_{quasi-age} = \left(t / t_p \right)^{\frac{C_{\alpha e}}{C_c - C_r}}$$

where t = age of soil, t_p = end of primary consolidation, $C_{\alpha e}$ = coefficient of secondary compression, C_c = compression index, C_r = recompression index (assumed $C_{\alpha e}/C_c \approx 0.015$ for limited creep effect, generally $0.015 \leq C_{\alpha e}/C_c \leq 0.03$ for sands, Mesri et al. 1990).

The advantage of using this approach based on the OCD-G_0 ratio relationship is that a single variable (i.e., G_0 ratio) can provide reasonable and reliable stress history evaluations. Some case studies are presented in the following sections, including a new site with documented stress history profile and shear wave data that became available to the author following the OCD derivation. This offered an excellent opportunity to check the reasonableness and robustness of the novel approach.

7.3 Case Study Applications Using OCD Method

7.3.1 Bothkennar – NC Clay Site

At the famous Bothkennar test bed site in Scotland, the OCR and preconsolidation stress profiles were predicted based on the derived OCD - $G_{0,HH}/G_{0,VH}$ relationship (Equation 7.2a). The Bothkennar site is underlain by (aged) normally consolidated soft silty clay that is a result of post-glacial deposition (Nash et al. 1992). An approximate stratigraphy at Bothkennar site is summarized in Table 7.1 (Hight et al. 1992).

Table 7.1. Stratigraphic layers at Bothkennar (Hight et al. 1992)

Unit	Thickness (meter)	Deposits
Grangemouth Beds	≈ 1.5	Modern tidal flat deposits
Claret Beds Letham Beds	13 - 21	Soft post-glacial organic clays and silty clays (primary focus material of the national geotechnical test site)
Bothkennar gravel Loanhead Beds	Not documented	Late glacial deposits
Till		Glacial deposits
Carboniferous coal measures		Bed rock

For the soft clay layer, the general site specifications are provided in Table 7.2. More detailed soil property profiles showing the characteristics of clay at Bothkennar are also given in Figure 7.2.

Table 7.2. Geotechnical site specifications for Bothkennar clay, Scotland (Nash, Powell, and Lloyd 1992)

	Geotechnical specification
Material	Homogeneous clay (without peat), with firm crust
Clay fabric	Not markedly laminated
OCR	Normally/lightly overconsolidated
Thickness	> 10 m
Shear strength	Usually s_u < 40 kPa, sensitivity not specified
Plasticity index	> 20%
Flooding	Does not flood regularly

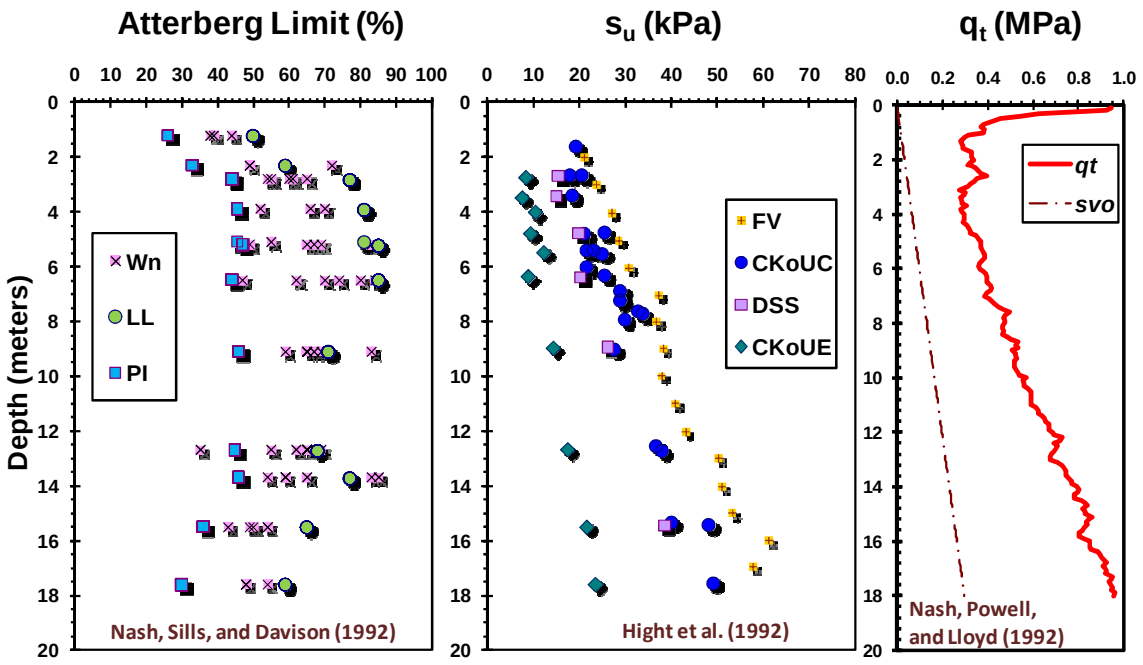

Figure 7.2. Soil property profiles at Bothkennar test site: (a) Atterberg limits (Nash, Sills, and Davison 1992), (b) undrained shear strength (Hight et al. 1992), (c) cone tip resistance profiles (Nash, Powell, and Lloyd 1992).

Notes: w_n = water content, LL = liquid limit, PI = plasticity index, FV = field vane, CK_0UC = undrained triaxial compression, CK_0UE = undrained triaxial extension, DSS = direct simple shear test.

Three different modal sets of V_s were obtained at the site from RCHT, CHT, and DHT, including HH, HV, and VH shear waves, respectively (Butcher and Powell, 1996, 1997). These are shown in Figure 7.3a. A number of laboratory oedometer and consolidation test data (Nash, Sills, Davison 1992) are available to confirm the stress history profiles at the site. In addition, results from CPTu and DMT are also available. Using Equation 7.2, the predicted OCD value from the HH/VH ratio is about 59 kPa. The corresponding derived profiles of preconsolidation stress and OCR from the interpreted OCD are shown together in Figure 7.3 with evidently very good agreement seen when compared with standard lab tests.

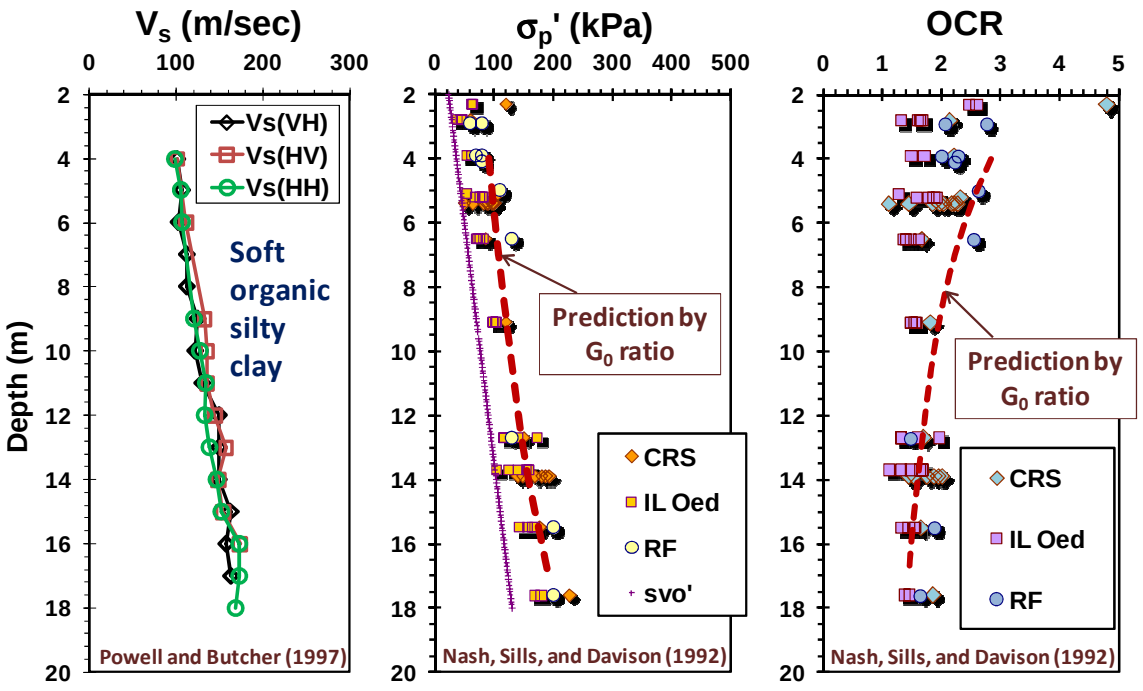

Figure 7.3. Profiles at Bothkennar soft clay: (a) directional V_s modes; (b) yield stress profile; and (c) OCR profile from consolidation tests and OCD-G_0 ratio trend.

Notes: CRS = constant rate of strain consolidation test (Bristol Polytechnic), IL = incremental load type (Bristol University), RF = restricted flow consolidation test (Oxford University).

7.3.2 Port of Anchorage, Alaska – Moderately Overconsolidated Clay Site

After the OCD-G_0 ratio relationship was developed, a new case study from Anchorage, Alaska became available for study following field and lab testing that were summarized in a recently completed dissertation at Northwestern University (Zapata-Medina 2012). The Port of Anchorage (POA) site is a near shore location with a mean water depth of 12 meter. The site has geologic conditions that include a thin soft estuarine silt (mud layer), glacio-estuarine clay deposit (Bootlegger Cove Formation = BCF), and underlying glacio-fluvial deposits. A general soil profile is given in Figure 7.4 (Zapata-Medina 2012). The focal study involves the BCF clays which average about 36 m thick.

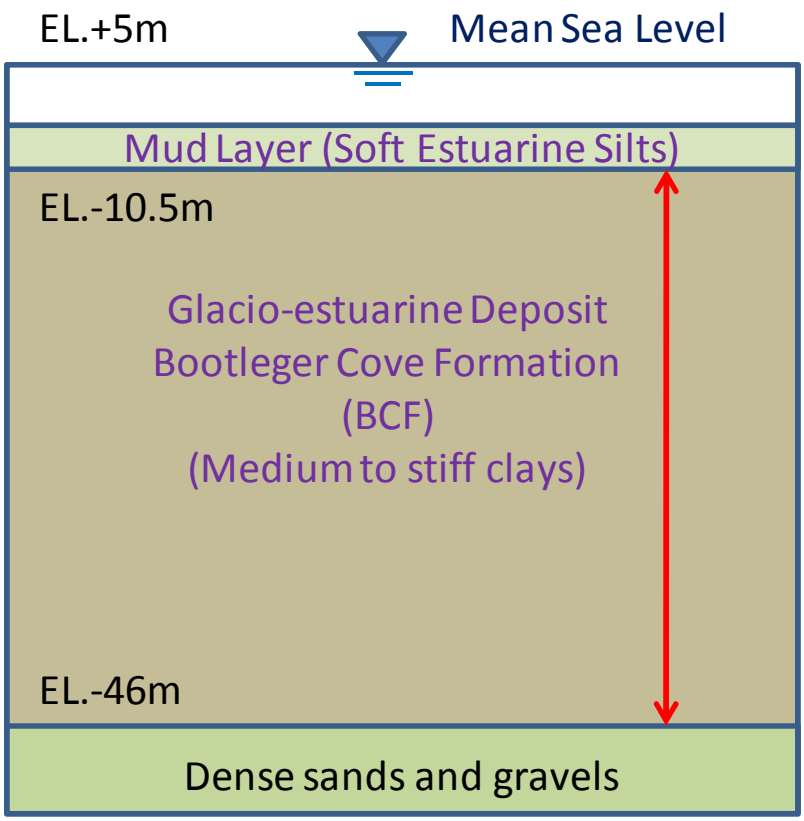

Figure 7.4. Generalized soil profile at Port of Anchorage (Zapata-Medina 2012).

Many laboratory and in-situ tests have been conducted for the POA expansion, particularly regarding the Bootlegger Cove Formation. The Bootlegger Cove Formation (BCF) consists of mainly stiff silty clay with occasional bedded sands with gravels. The clay has the following mean index characteristics: w_n = 20 to 31%; LL = 45%, PL = 21%, and PI = 24%). The BCF is moderately overconsolidated with an OCD = 450 kPa (Mayne and Pearce 2005). A summary of laboratory Atterberg limit and undrained strength data (triaxial testing and direct simple shear testing) is provided in Figure 7.5. Additional information is given in Figure 7.6 that shows undrained shear strength profiles and CPT soundings. Further details are given in Mayne and Pearce (2005) and Zapata-Medina (2012).

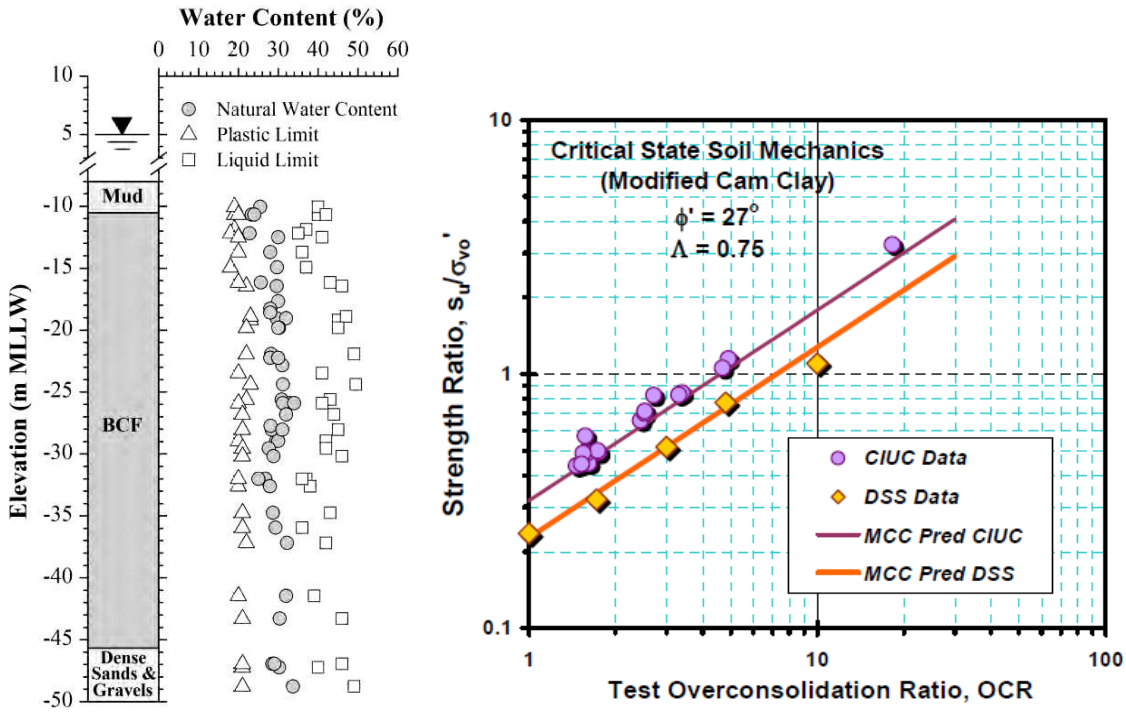

Figure 7.5. (a) Profile of Atterberg limit (Zapata-Medina 2012), (b) Laboratory undrained strength data (Mayne and Pearce 2005) for clays at BCF.

Notes: CIUC = Isotropically-consolidated undrained triaxial compression; DSS = direct simple shear

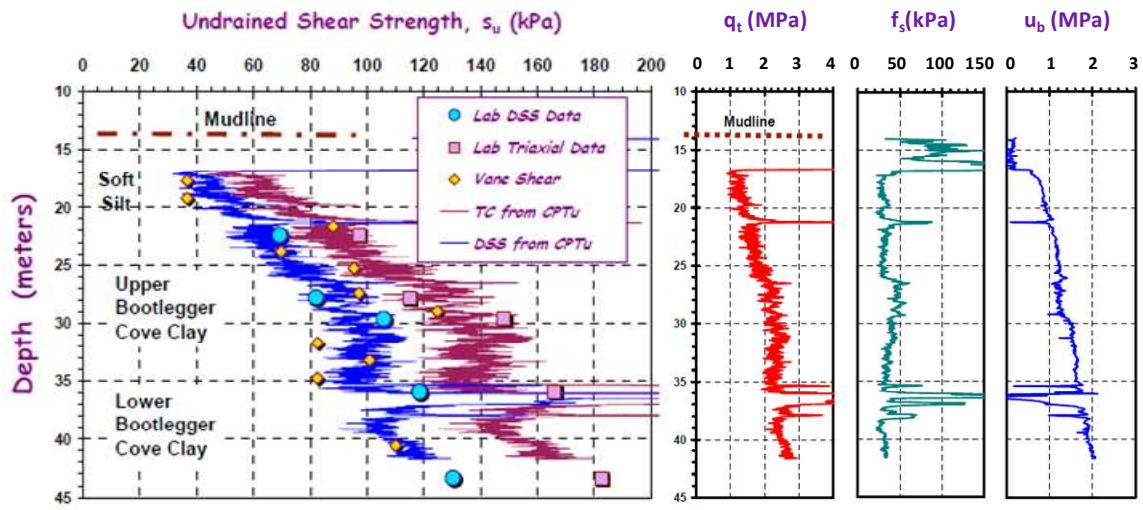

Figure 7.6. Undrained shear strength profiles and piezocone test soundings in Bootlegger Cove clay at Port of Anchorage (Mayne and Pearce 2005).

Different field V_s modes were obtained during recent geophysical explorations at the site including crosshole testing using both a vertical hammer (HV) and rotary hammer (HH) in onshore borings, as well as suspension logging geophysics with a reported VH profile in an offshore boring, as detailed in Zapata-Medina (2012). The study by NWU also involved CRS consolidation tests on newly-acquired samples that pretty much confirmed the earlier findings. Using the OCD-G_0 stiffness trend, the stress history profiles were evaluated at the POA site. As noted, this assessment at POA site was a kind of blind test study for the stress history prediction applying the OCD-G_0 ratio correlation because the site shear wave data were made available after deriving the relationship and the estimated OCD value was about 452 kPa. Figure 7.7 shows very solid predictions for the in-situ σ_p' and OCR profiles, both in excellent agreement with the consolidation results. Other case studies are also provided in Appendix F.

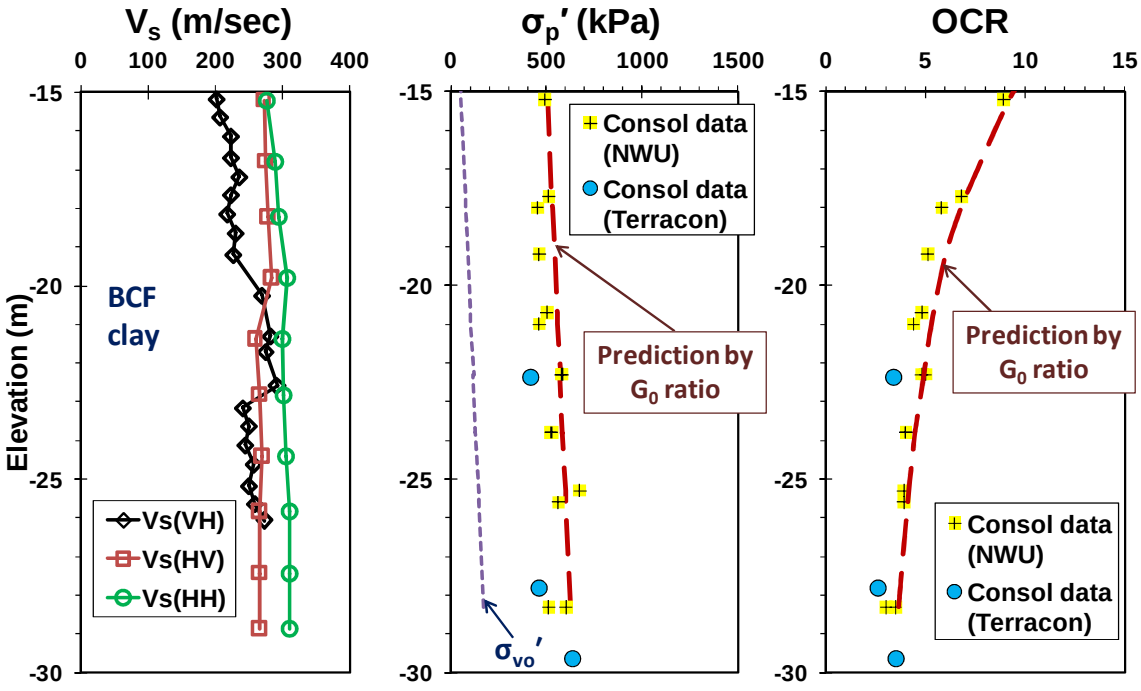

Figure 7.7. Profiles at Port of Anchorage BCF clay: (a) directional V_s modes; (b) yield stress profile; and (c) OCR profile from consolidation tests and OCD-G_0 ratio trend.

7.4 Summary and Conclusions

Herein, stress history of soils was represented in terms of the overconsolidation difference: OCD = $\sigma_y' - \sigma_{vo}'$ that was related directly to shear stiffness ratio ($G_{0,HH}/G_{0,VH}$). Quite consistent stress history evaluations are available using the OCD-stiffness ratio trend as follows:

$$OCD = 0.466 \cdot (\sigma_{atm}) \cdot (G_{0,HH}/G_{0,VH})^{5.57}$$

$$OCD_1 = 0.466 \cdot (G_{0,HH}/G_{0,VH})^{5.57}$$

$$OCR = \sigma_p'/ \sigma_{vo}' = (\sigma_{vo}' + OCD) / \sigma_{vo}'$$

The noted regression equations are derived based on uncemented geomaterials. To avoid physical contradiction with respect to geomaterial behavior, the equations are only applicable within limited ranges: $0.5 \leq G_{0,HH}/G_{0,VH} \leq 2.5$ and 1 kPa $\leq$ OCD $\leq$ 5000 kPa. The lowest 1 kPa OCD magnitude can approximately indicate that the soils are normally consolidated (i.e., OCR $\approx$ 1). Overall, this approach provided reliable results for in-situ stress history assessment based on a single variable (i.e., $G_{0,HH}/G_{0,VH}$). The approach was substantiated by data from a newly-acquired case study involving moderately OC clay at the Port of Anchorage that became available to the author to independently cross-validate the methodology.

CHAPTER 8

CONTINUOUS-INTERVAL SHEAR WAVE VELOCITY PROFILES BY AUTO-SOURCE AND SEISMIC CONE TESTS

8.1 Introduction

The in-situ measurement of shear wave velocity (V_s) is important as a basic mechanical property for geotechnical design problems as it relates directly to the initial tangent shear modulus (G_0) at very small strains corresponding to nondestructive testing ($\gamma_s < 10^{-6}$ %). The value of G_0 is a fundamental stiffness for evaluating dynamic ground response, vibration problems, and seismic site amplification from earthquake motions, as well as static deformation problems involving shallow and deep foundations. As discussed in Chapter 4, in-situ V_s measurements are critical because laboratory G_0 values tend to be reduced because of sample disturbance effects and stress relief (Ghionna and Jamiolkowski 1991; Tatsuoka and Shibuya 1992), as well as restarting the time clock due to loss of ageing effects (Anderson and Stokoe, 1978; Howie et al. 2002). In the area of seismic ground hazards, the profile of V_s plays a dual role: (a) providing site-specific information on the level of ground amplification caused by earthquake motions (Schneider et al. 2001), and (b) evaluation on soil liquefaction resistance (Youd et al. 2001). In-situ V_s profiling can provide a means to evaluate soil properties such as unit weight (Mayne 2001), stress history (Mayne 2005) and shear strength (Levesque et al. 2007). For instance, the trend for total unit weight in terms of V_s and depth is presented in Figure 8.1 for a wide range of particulate geomaterials, including clays, silts, sands, gravels, and mixed soils (Mayne et al. 2009). Consequently, reliable and detailed in-situ V_s measurements are essential for the fields of geotechnics and geophysics.

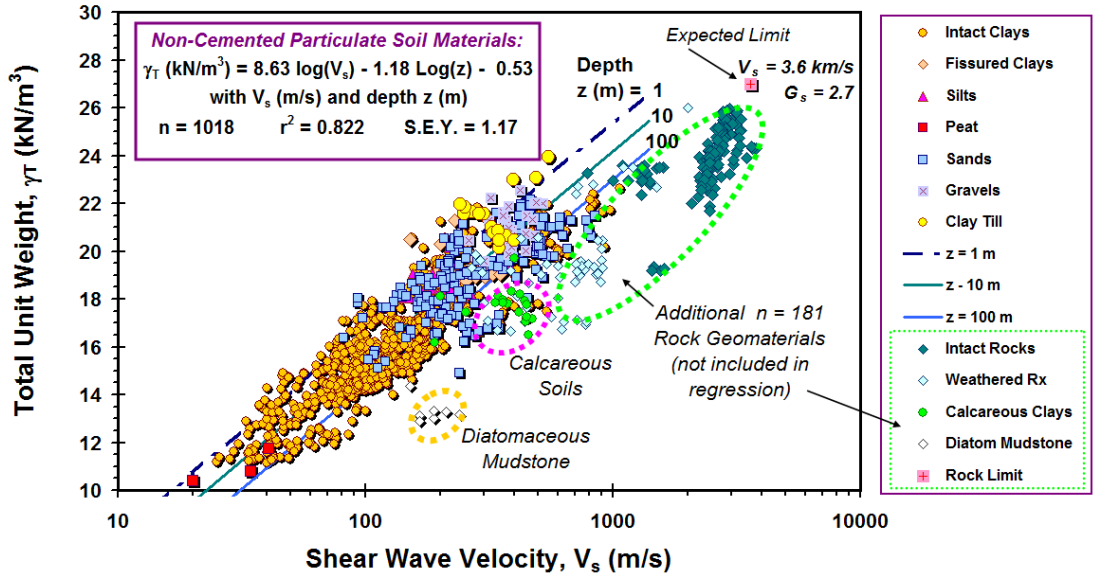

Figure 8.1. Trend between soil unit weight (γ_t), shear wave velocity (V_s), and depth (z) for a wide variety of soils (modified from Mayne et al. 2009). Also shown for reference (but not included in the regressions) are data for rocks and non-compliant geomaterials (calcareous sands, carbonate clays, and diatomaceous mudstone).

As summarized earlier in Figure 1.1, a variety of invasive and noninvasive field geophysics methods have been developed to measure mechanical body waves, particularly shear wave velocities, including: crosshole testing (CHT), downhole testing (DHT), suspension logger probing (SLP), surface refraction survey (SFRS), surface reflection survey (SFLS), and Rayleigh wave methods (SASW, MASW, CSW, PSW, ReMi), as detailed by Woods (1978) and Campanella (1994). Whereas the CHT and DHT are invasive tests which require cased boreholes, SLP uses a fluid filled drilled hole, and the SFRS, SFLS, and Rayleigh wave methods are non-invasive tests that are conducted entirely at the surface. These conventional V_s measurement techniques have their own advantages and increased use relying on geophysics or geotechnical project conditions. However, many of the common tests are rather time-consuming and expensive, thus not

utilized much in routine site investigations. In soils that are favorable for direct-push technology, seismic piezocone penetration testing (SCPTu) and seismic dilatometer testing (SDMT) are efficient means for V_s profiling in a DHT approach because the probings do not require any of the following: rotary drilling, casing, grouting, inclinometer readings, inflating of packers, or separate deployment of borehole-type geophones (e.g., Robertson et al., 1986, Martin and Mayne 1998). Thus, SCPT and SDMT are easier, more economical, and faster than borehole-type CHT and DHT.

For several representative geophysical tests, typical costs to profile V_s are compared in Table 8.1 for a 30-m depth investigation, corresponding to the necessary depth for an IBC seismic evaluation (Note: IBC = international building code). Although suspension logging is useful in geological explorations for the petroleum industry, the probe itself is 6 m long and thus only economical for cases where V_s profiling extends greater than 60 m deep. Cost wise, the SCPT is clearly the choice for budgetary reasons, when push penetration is possible. Furthermore, the SCPTu provides additional readings including: tip resistance (q_t), sleeve friction (f_s), and porewater pressure (u_2) with depth.

The collection of multiple measurements is beneficial towards a comprehensive site characterization program at any given site. Figure 8.2 shows a schematic of the pseudo-interval V_s measurement system often deployed using SCPTu soundings. The general setup and detailed procedures of the SCPTu are discussed in ASTM D 5778 and D 7400 guidelines. As shown, the most common approach to measure V_s uses a single geophone that has its axis parallel with the horizontal surface source (i.e., pseudo-interval method) and this is sufficient in accuracy for most projects (Campanella et al. 1986, Robertson et al. 1986). Yet, more robust V_s measurements can be accomplished by true-

interval evaluations via biaxial geophone receivers positioned at two elevations simultaneously (Burghignoli et al. 1991; Butcher & Powell, 1996).

The standard SCPTu produces V_s data at one-meter depth intervals after stopping penetration at rod breaks. The recent development of an automatic seismic source (McGillivray and Mayne 2008) combined with an enhanced data acquisition system allows for a much faster field production time because minimal stopping is required at the rod breaks. Since so many more wavelets are generated, elaborate V_s evaluation tools are required to handle large numbers of signals, very short distance intervals, overlapping wavelet response, and filtering of extraneous noise. This section shows the evaluation techniques for extracting reliable continuous-interval V_s profiles from the data.

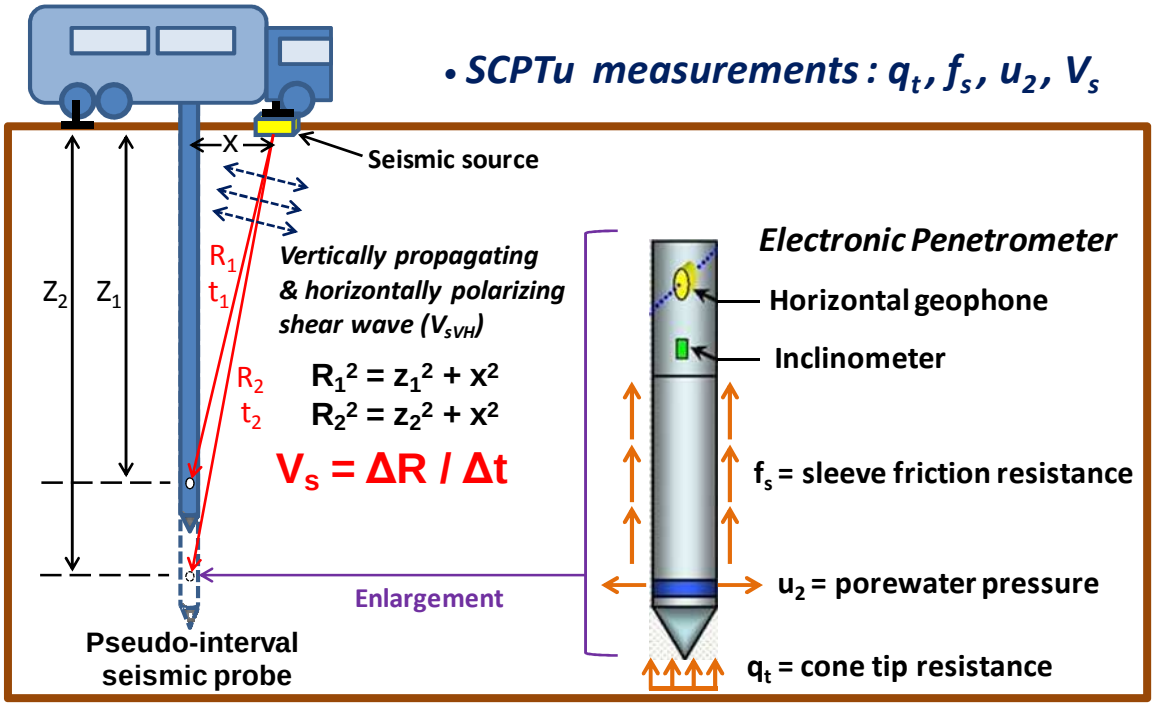

Figure 8.2. In-situ V_s measurement system using downhole-type direct-push technology.

Table 8.1. Estimated cost comparison for V_s profiling of 30 meter depth

Geophysical method	General Cost*	
	US $	Euro €
Suspension Logging (SL)	$25,000	€19,231
Crosshole Testing (CHT)	$15,000	€11,538
Downhole Testing (DHT)	$8,000	€6,154
Surface Waves (SASW, MASW)	$4,500	€3,462
ReMi Passive Surface Waves	$2,500	€1,923
Seismic Piezocone**	$2,000	€1,538

NOTES:

* Cost in US dollars converted to Euro taken at: 1.00 € = 1.30 $ US (Oct. 2012).

**In addition to shear wave velocity, price also includes measurements of cone tip resistance, sleeve friction, and penetration porewater pressure readings with depth.

8.2 Background of Experiments

For reliable field V_s measurements, an important issue is generating clear and repeatable shear wavelets with the appropriate setup of geophones. Several series of horizontal seismic sources and advanced data acquisition systems have been developed by the Georgia Tech In-Situ Research Group, resulting in a portable automated triggering system (McGillivray 2007). The new seismic source named 'RotoAutoSeis' can deliver vertically- propagated and horizontally-polarized shear wave signals at controlled speeds of between 1 to 10 seconds. The auto-source system is capable of producing continuous shear waves during cone penetration advances at 20 mm/sec, thus significantly reducing the field testing time for V_s profiling. Two versions of the latest series of RotoAutoSeis units are shown in Figure 8.3.

To produce consistent shear wave signals, an AC or DC powered electric motor connected to mechanical gears is used to deliver seismic strikes by a rotating mass hammer. In the field, electrical power of the portable seismic source is available from a vehicle battery, generator, or power supply of the cone truck. The rate of hammer strikes can be adjusted by changing the motor speed. Figure 8.4 illustrates the mechanical gear operation system. The hammer is attached to a large diameter gear and operated by a small diameter gear connected to the electric motor. Further details regarding this automated source are discussed in McGillivray and Mayne (2008). Repeatable shear wavelets generated by the RotoAutoSeis assist in field performance and operations during SDMT and SCPT. A conventional SCPTu often employs paired sets of reverse polarized left- and right- shear waves for a cross-over analysis (Campanella et al. 1986). While the RotoAutoSeis operates in only one direction, more reliable data are obtained by implementation of more robust processing techniques, including cross-correlation, frequency-domain analytics, and/or other enhanced data processing methods.

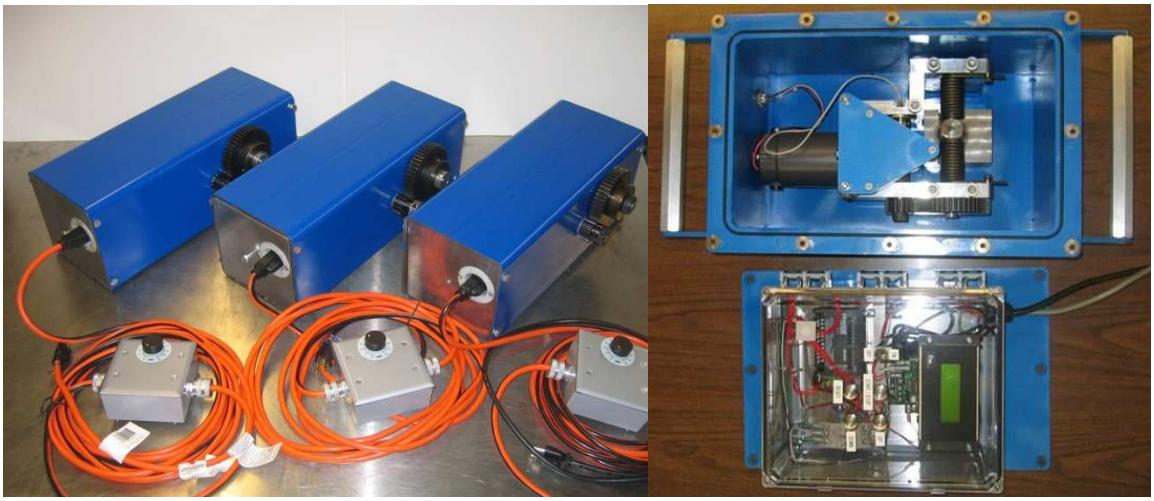

Figure 8.3. Two recent versions of GT RotoAutoSeis device including (a) design prototypes, and (b) commercial unit: top view of mechanical gear system.

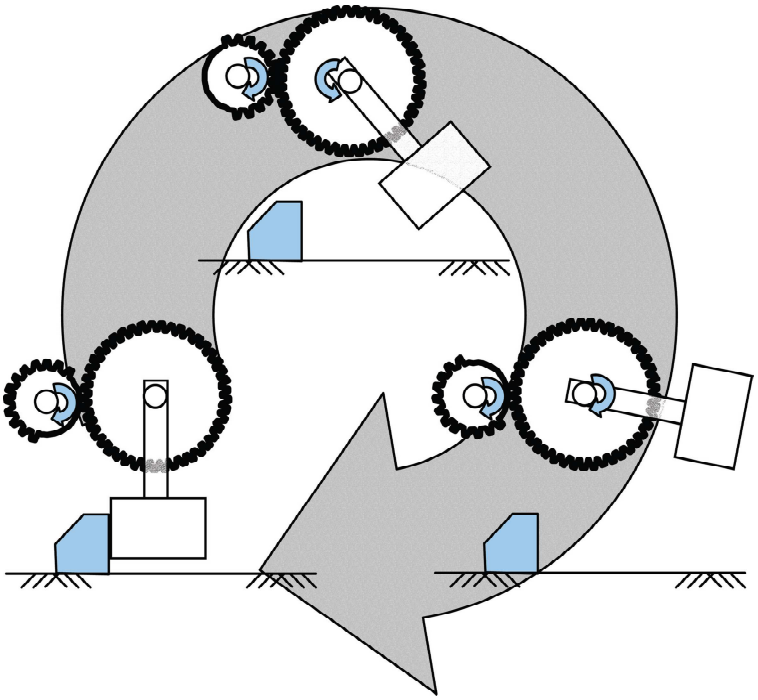

Figure 8.4. Schematic of mechanical gear system of the Georgia Tech patented RotoAutoSeis (McGillivray and Mayne 2008).

8.3 Direct-Push Downhole at 1-meter Interval and Frequent Interval V_s Testing

Downhole testing (DHT) and crosshole testing (CHT) have been the most commonly adopted geophysical methods for shear wave determinations in geotechnical applications (Woods 1978). Conventional DHT and CHT require rotary drilling and casing of boreholes, grouting, inclinometer measurements, and repetitious repositioning of downhole geophones and/or hammers at 1.5-m depth intervals for testing. These standard tests are quite expensive and time-consuming. In practice, the alternative seismic cone penetration test (SCPT) and seismic flat dilatometer test (SDMT) using direct-push technology are more efficient means for in-situ V_s profiling by DHT, thus provide a comprehensive site investigation approach. In terms of V_s profiling intervals, the 1.5-m interval by conventional DHT and CHT is replaced by a 1-m depth interval in

the normal SDMT and SCPTu. Yet, it is also plausible that V_s measurements can be procured more frequently by stopping these probes at smaller intervals.

In the case of SDMT, frequent-interval V_s data can be collected along with the basic pressure readings (i.e., p_0, p_1) from standard dilatometer testing. The frequent-interval seismic flat dilatometer (FiSDMT) provides V_s measurements every 0.2-meter depth intervals, thus a much finer detailed V_s profile is obtained. The enhanced resolution of the field V_s profile has more opportunity to delineate the geostratigraphy and detect the existence of possible thin soft layers. Moreover, the detailed V_s measurements are more conducive for accurate predictions of foundation movements, subgrade response, soil liquefaction potential, and other sensitive geotechnical concerns.

An example FiSDMT sounding is shown in Figure 8.5. The SDMT measurements were taken at the test site of the Treporti circular embankment northeast of Venice, Italy (McGillivray and Mayne 2008). For the V_s measurements, a true-interval seismic dilatometer system was used. The test site has complex interbedded alluvial-marine layers which consist of medium to fine sand (SP-SM), silt (ML), and silty clay (CL). The descriptions and properties of the soil layers have been detailed elsewhere (Simonini 2004, Simonini et al. 2007). Results from a standard downhole shear wave velocity profile produced by an adjacent SCPT sounding are also presented for reference and benchmarking purposes. Compared to the conventional coarse one-meter interval V_s data from the SCPT, it is evident that the FiSDMT provides much finer detailing in the V_s profile at 200 mm intervals. Both methods successfully detect the stiffer-harder layers at the 3 m and 7 m depth marks, yet the frequent-interval V_s does a better job in tracking the actual variations and subtle changes. Both V_s profiles were developed using cross-

correlation of raw wavelet data. In terms of V_s evaluation techniques, additional details on the processing will be discussed in the upcoming section.

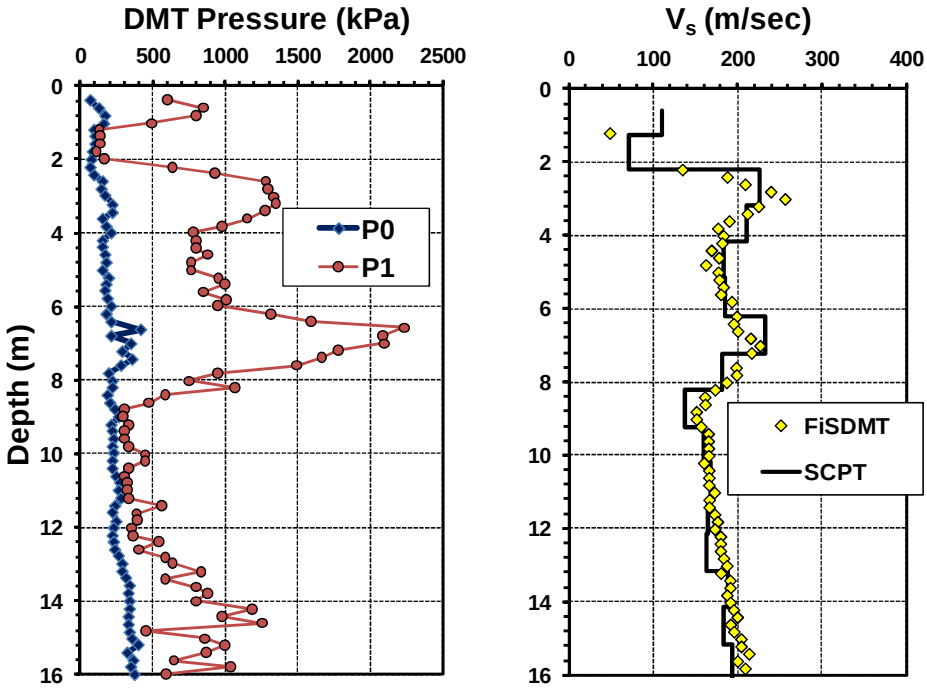

Figure 8.5. Frequent-interval SDMT soundings (p_0, p_1, 0.2-m interval V_s) and SCPT soundings (1-interval V_s) at Treporti site, Italy (McGillivray and Mayne 2008).

This frequent-interval method is not restricted to implementation with the seismic flat dilatometer, but can also be applied to conventional borehole type downhole tests (DHT), as well as seismic cone (SCPT) and/or use of special geophysics probes. In Figure 8.6, the results of special recent tests conducted at the Department of Energy site near Aiken, South Carolina are shown for a representative FiSCPTu in old Eocene deposits of the Atlantic Coastal Plain geology (i.e., SRS site at Chapter 2). These measurements were obtained by conducting two separate probings at the same location: (a) initially, a CPTu sounding was advanced using a 10-cm^2 penetrometer to collect cone tip resistance (q_t), sleeve friction (f_s), and porewater pressure (u_2) readings at 0.02-m intervals with depth, followed by: (b) a sounding at the same position using a special 15-

cm^2 geophysical true-interval probe that contained 6 geophones, specifically 3 sets of horizontal biaxial geophones at different elevations. The vertical offset distance between each set of geophones was approximately 0.5 m. The geophysics probe was incrementally advanced at 0.2-m intervals to collect the V_s data.

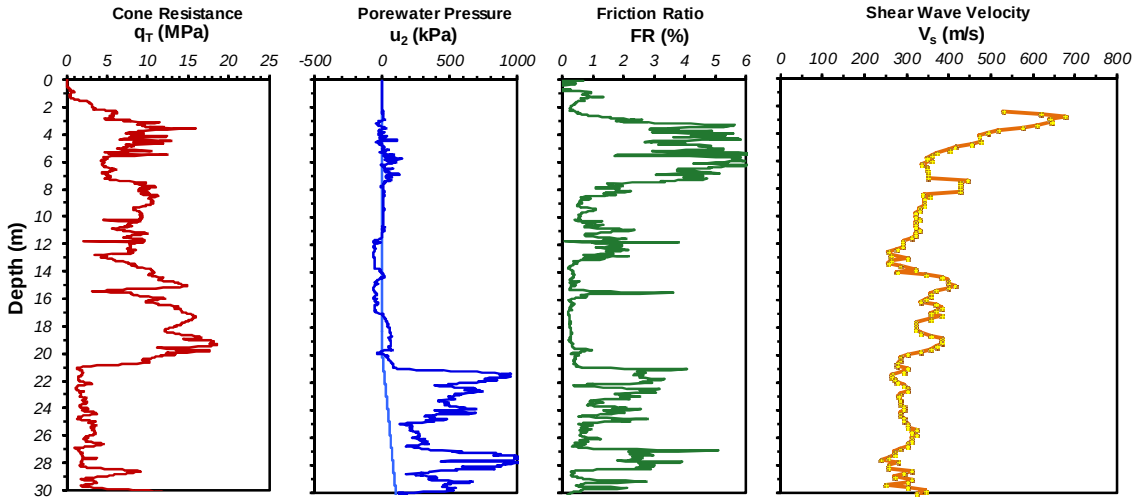

Figure 8.6. Results of frequent-interval seismic piezocone (FiSCPTu) obtained using a cone penetrometer and geophysics probe in Aiken, SC (data courtesy of McGillivray).

8.4 Methodology: Shear Wave Evaluation

Due to advancements in automated seismic sources and data acquisition systems, both frequent-interval and continuous-interval shear wave data can now be appreciated, resulting in higher resolution V_s profiling than before. On the other hand, the large overflow of numbers from incoming wavelets with increased noise and overlapping signals requires a more robust means to handle these data. This section explains how to handle and evaluate general in-situ shear wave data using selected signal post-processing methods. Downhole geophysical data from a SCPTu sounding performed in Norfolk, Virginia are used to illustrate the methodology and success of the approach. All soundings were generated by ConeTec Investigations, Inc.

8.4.1 Reference Standard SCPTu Sounding and Site Conditions at Norfolk, Virginia

Several sets of downhole V_s data were obtained from a site in Norfolk, Virginia and these are used to detail and compare several different methods of data reduction, including: first arrival, first crossover, peak, cross-correlation, and both time domain and frequency domain evaluations. All post-processing and evaluations of shear waves were conducted within the 'MATLAB' software program. The reference DHT-type shear wave velocity profile was obtained via a standard SCPT procedure, details of which are given by Campanella (1994) and Butcher et al. (2005). A continuous-interval sounding (CiSCPTu) was also performed at the site, as will be discussed later.

The soil conditions at the Norfolk site consist of upper 9 meters of Holocene sandy and clayey sediments (Norfolk formation) that are underlain by calcareous Miocene age marine deposits (Yorktown formation) that extend beyond the exploration depths of 20 m. The upper Norfolk sediments are variable across the region and often encountered in loose to soft to firm conditions, perhaps with a shallow crust. The deeper Yorktown formation is an older and more uniform deposit that serves as a strong foundation support medium for many large bridges, buildings, and port facilities in the Norfolk-Portsmouth-Newport News area of southeast Virginia (Mayne 1989). The groundwater table lies 2 m deep at this site. For more site information, Figure 8.7 shows the standard SCPTu soundings and corresponding soil behavioral type (SBT) profile at this site provided by ConeTec Investigations.

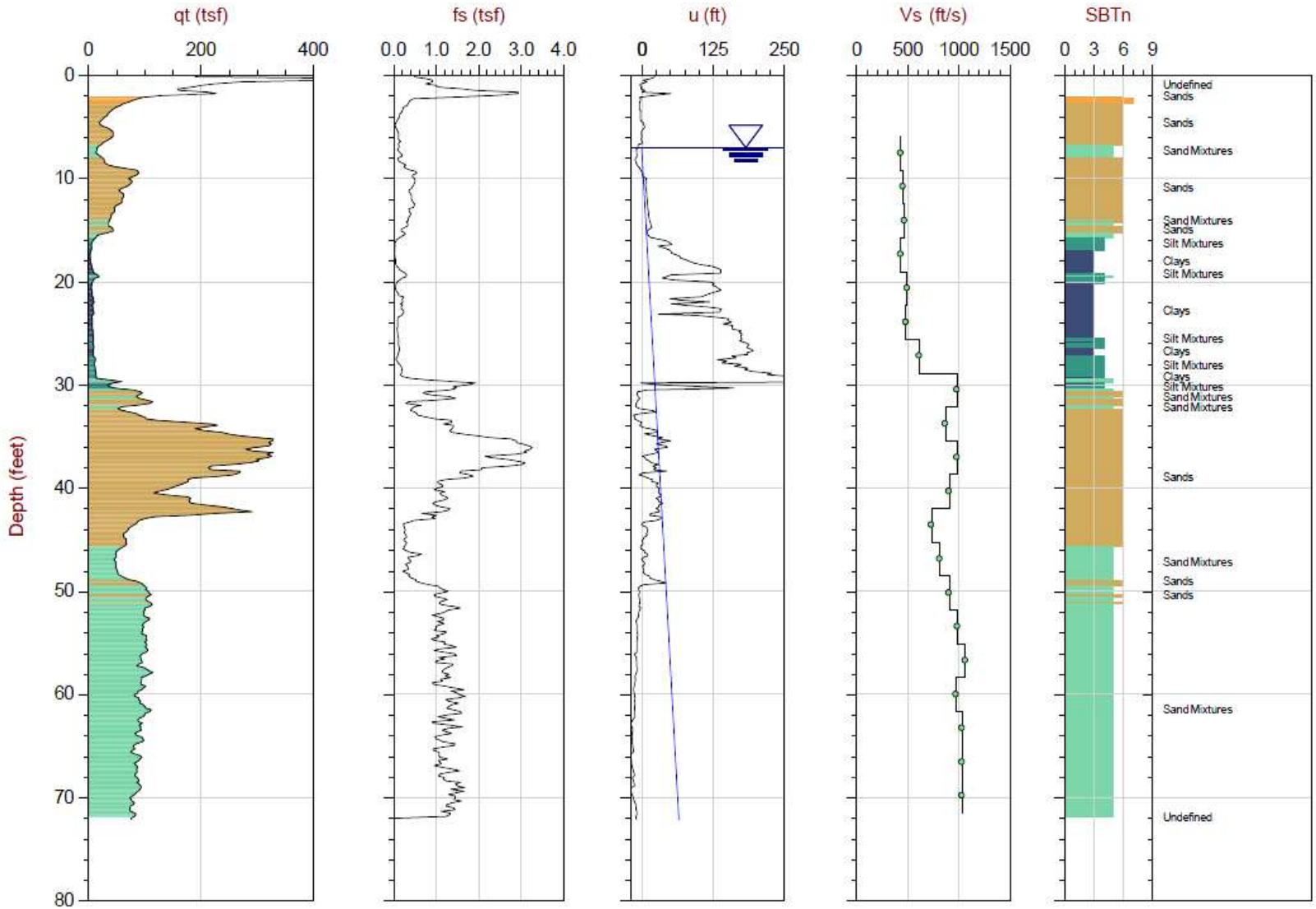

Figure 8.7. Standard SCPTu soundings and corresponding soil behavioral type (SBP) profile at Norfolk, VA (figure source: ConeTec).

8.4.2 Signal Processing

The successive 1-meter interval shear wave signals for the benchmark V_s profile were generated using a downhole procedure and surface seismic source. The summary of raw V_s wavelets from both left-sided and right-sided strikes (i.e., opposite directional strikes using a sledge hammer) is shown in Figure 8.8. The signal sampling rate was 20 kHz with a record length of 250ms for each event. The signal amplitude was normalized to the maximum value for each event for display. Before evaluating the V_s values between each successive set of wavelets, an appropriate processing methodology of shear wave signals is required.

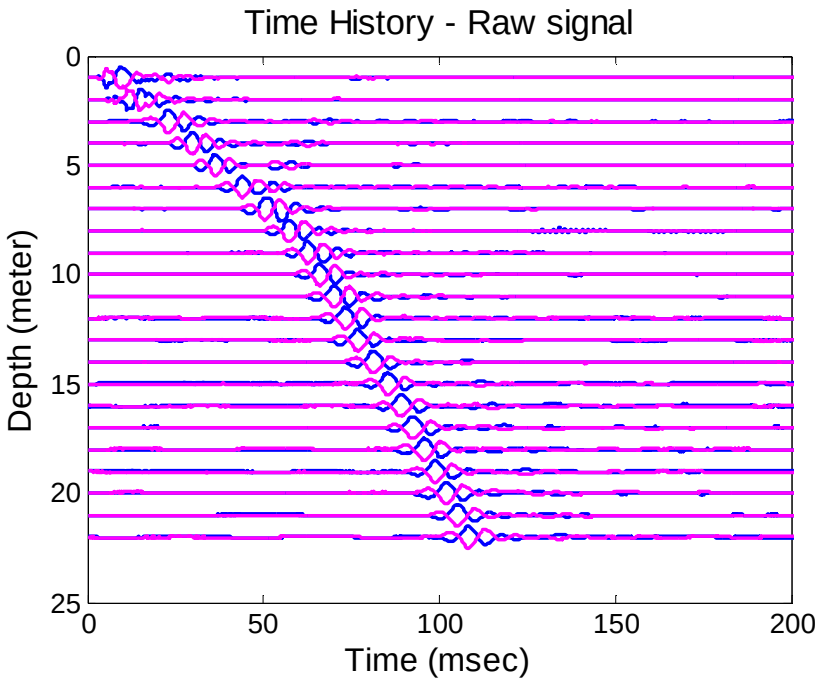

Figure 8.8. Summary of 1-meter interval raw shear wave signals recorded from a representative SCPTu at Norfolk, Virginia.

First, the time series signals might need to be detrended. The detrending is a statistical operation to remove unwanted trends or distortioning of data signals in time series. For instance, a slight linear trend tendency can be removed by subtracting the

least-squares fit of a straight line from the data. Subsequently, the detrending can make sure that overall raw data signals approach a baseline value. In some cases, simple zero-offset might be better. After detrending, it is necessary to control background noises superimposed on the signals at the lowest possible level. There are several noise control strategies that can be employed in both time and frequency domains. In time domain, signal stacking can improve effectively the signal-to-noise ratio for raw signals which have random noises (i.e., noise mean equal to zero). However a large number of signals might be required to gather clear signals, thus adding to field time for data collection. Also, this is not viable for continuous shear wave signals using the automatic triggering system because only a single strike is recorded at every depth. Signals can be smoothed by applying a moving average as well in time domain. A smoothing kernel (κ) operator is useful particularly for high frequency noises.

Equation (8.1a) $$y_i = \sum_{l=-(n-1)/2}^{(n-1)/2} \kappa_l \cdot x_{i+l}$$

where i = discrete element of signal, n= number of discrete elements of kernel, y = smoothed output signal, x = input signal. Mathematically, it can also be expressed by a convolution sum as follows (Santamarina and Fratta 1998):

Equation (8.1b) $$\underline{y} = \underline{x} * \underline{\kappa}$$

where $\underline{y}$ = smoothed signal, $\underline{x}$ = noisy signal, $\underline{\kappa}$ = smoothing kernel ($\sum\kappa = 1$). The kernel should be selected cautiously because too short of a chosen kernel only removes high frequencies and a long kernel may delete critical frequency components of the input wave (Santamarina and Fratta, 1998).

On the other hand, it is possible to reduce noise levels in the frequency domain. Based on estimated spectral densities of signals, different types of filters such as low-pass, high-pass, and band-pass filter can be adopted. In this study, undesired noise was efficiently controlled in the frequency domain using a band-pass filter to capture the frequency range of interest. This is a low and high cutoff frequency filter, and consequently, an appropriate frequency range to reduce noise level and preserve critical shear wave components must be determined. For this purpose, a coherence function can be a useful tool for judgment (Campanella and Stewart 1992). The coherence function or squared coherence can be defined in terms of Fast Fourier Transform (FFT) coefficients:

$$\text{Equation (8.2)} \quad C_{xy} = coh^2(k) = \frac{\left|\Phi_{xy}(k)\right|^2}{\Phi_{xx}(k) \cdot \Phi_{yy}(k)}$$

where, Φ_{xy} = cross-spectrum between two time series (x and y), Φ_{xx} = auto-spectrum of time series x, Φ_{yy} = auto-spectrum of time series y. It is noted that the coherence is equivalent to the correlation coefficient (r) at a particular frequency (k). The magnitude of coherence varies between zero and one (i.e., 0 indicates no correlation) and represents the degree of coupling between two consecutive signals at the given frequency, thus the frequency range of interest can be determined. Assuming the consecutive signals have similar shapes, relatively small coherence values may represent unwanted noise in signals. Also, frequency domain magnitudes and waveforms of each raw signal should be investigated to identify the validity of the determined band-pass filtering frequency range.

From the raw signals obtained at the Norfolk site, Figure 8.9 shows the coherence values between two successive signals which were recorded at 20.3 and 21.3 meter depths. A maximum magnitude is observed around 100 Hz. Eventually, based on visual

examinations and engineering judgment from the coherence values and additional power spectral density estimates of raw signals, a widely-used Butterworth filter was employed as a band-pass filter with a frequency range of 25 and 500 Hz which is a reasonable wide band width. An equation for the transfer function (H) using the n^{th} order Butterworth low pass filtering is as follow:

Equation 8.3) $$G^2(w) = |H(jw)|^2 = \frac{G_0^2}{1+\left(\frac{\omega}{\omega_c}\right)^{2n}}$$

where, n = order of filter (n=4 in this study), ω = angular frequency, ω_c = cutoff frequency, G_0 = gain at zero frequency. For the Butterworth filter, a Nyquist frequency (i.e., $f_N = 0.5 * f_s$ = 10 kHZ) was used to normalize the input parameters for the cut-off frequency in MATLAB (i.e., normalized cutoff frequency $\omega_n = [\omega_1, \omega_2]/f_N$).

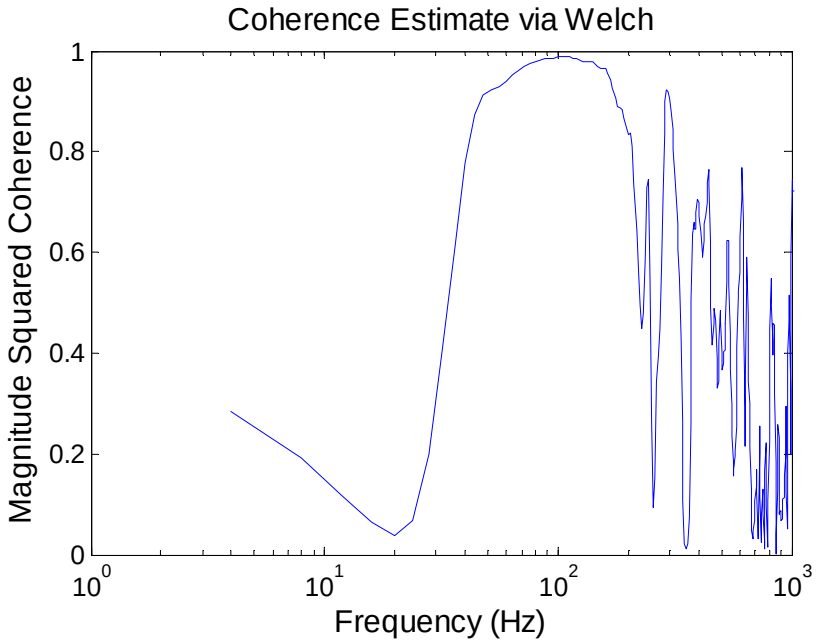

Figure 8.9. Coherence values between raw shear wave signals recorded from 20.3 and 21.3 meter depths at Norfolk, Virginia.

A windowed signal can help provide better results for V_s evaluations, especially for the cross-correlation method (Stewart 1992; Campanella and Stewart 1992; Liao and Mayne 2006). Furthermore, windowing can minimize the effect of spectral leakage of the data (Santamarina and Fratta 1998). Hence, in each signal, the zone of expected main shear wave of interest only remains for the V_s evaluation. Stewart (1992) studied various window types and recommended a simple rectangular window for a frequency range less than 200 Hz. Figure 8.10 shows the filtered signals (i.e, band frequency [25, 500 Hz]) with a rather wide window. A combined window using the rectangular window and a hamming window was applied. A rectangular window was used in the middle of the main waveform. At the borders between windowed and non-windowed zones, a hamming window which is one of the most common windowing functions was combined with the rectangular window.

8.4.3 Methods for Shear Wave Velocity Evaluation

For downhole-type shear wave data, the velocities can be calculated by different evaluation methods. A fundamental concept is to use path length difference over a known time interval, as shown in the aforementioned Figure 8.2. The V_s is calculated as follows:

Equation (8.4) $$V_s = \Delta R / \Delta t$$

where ΔR = difference in the lengths of the ray paths between the source and two continuous receivers, Δt = the travel time calculated directly from the observations at two receivers for true-interval. In the case that only one receiver is used, a pseudo-time interval is used at two different depths ($\Delta t = \Delta t_2 - \Delta t_1$: pseudo-time intervals). The obtained V_s value is plotted at the mid-point of the geophone depth locations. Regardless

of true-interval and/or pseudo-interval methods, for a reliable continuous V_s evaluation, it is crucial to find the accurate time lag between two consecutive shear wavelets. Therefore, several determination methods for finding the time difference (Δt) are discussed in the next section.

8.4.3.1 Manual picking methods – first arrival, first peak, and first cross-over

The simplest methods involve manually choosing the first arrival, first peak, and/or first crossover point. In the well-known crossover methods, paired sets of left and right strikes are needed, thus adding field time for data collection. In those cases where the shear wave is clearly observed, manual picking methods can be suitable yet do require judgment and experience by the user. However, if numerous datasets must be analyzed, it is quite time-consuming. In addition, it is sometimes difficult to accurately pick points due to uncertainty, baseline shifts of one or more wavelets, and excessive noise in the signals. A magnified plot in Figure 8.10 shows how to find the time difference (Δt) between two consecutive signals using the first arrival and first peak. The first arrival method has been widely used for V_s determinations, particularly from old analog signals (Stokoe and Woods 1972, Gillespie 1990; Sully and Campanella 1995), however the determination of the exact arrival point is contentious because the arrival time is likely to be masked by disturbances such as wave reflections and near field effects (Lee and Santamarina 2005, Liao and Mayne 2006). The "first peak" can be considered as an extended means for determining the first arrival time.

The "first cross-over" method utilizes the shear wave characteristic of polarization and thus requires data from two opposing wavelets for velocity determination (Robertson

et al 1986, Campanella and Stewart 1992, Sully and Campanella 1995). An example of the selected cross-over time is shown in the right side insert of Figure 8.10. Although the detection of the cross-over point seems simple, it can incur errors due to signal disturbance, electromagnetic interference, and/or baseline offsets. The method requires at least two repeatable and paired strike events having opposite directions (e.g., left- and right-strike for downhole tests; or paired up- and down-strikes for standard crosshole). Basically, it is noted that these manual picking methods provide only a single reference point of information for Δt out of the entire 20,000 digital data points which are available from two paired wavelets. Note that the crossover method was necessary back 3 decades ago when signals were recorded analog, but readings today are produced digitally.

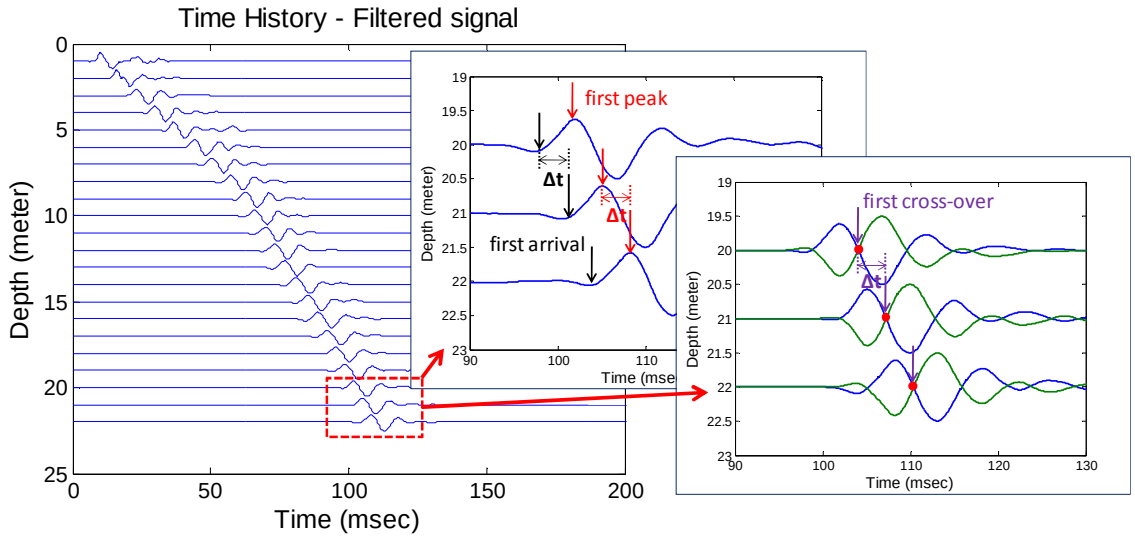

Figure 8.10. 1-meter interval filtered shear wave signals recorded from SCPTu at Norfolk, VA. Magnified figures show determining time shifts (Δt) via first arrival, first peak, and first cross-over methods with paired wavelet signals of opposite polarity.

8.4.3.2 Cross-correlation in time domain

The cross-correlation method has become more popular with the availability of faster computers, greater data storage, and user software packages. Time domain analysis is simpler than frequency domain and avoids the assumption of circularity occurring in the transformation process (Santamarina and Fratta 1998). The time shift between two independent shear wave series can be determined by cross-correlation functions in time domain as follows:

Equation (8.5a) $$R(m) = \int_{-\infty}^{\infty} x(t) \cdot y(t+m)dt$$

where x(t) and y(t) are two independent signals, and "m" is a time shift. Similarly, a basic operation form of the cross-correlation (or cross-covariance) for evenly spaced discrete time series can be expressed as follow:

Equation (8.5b) $$R(k) = \sum_{i} (x_i) \cdot (y_{i+k})$$

where, x and y = two independent time series signals, k = time shift. The cross-correlation is used to represent similarity between two signals. A normalized cross-correlation coefficient (r) between two signals can be defined (Lyon 2010):

Equation (8.6) $$r = \frac{\sum[(x_i - \bar{x}) \cdot (y_{i+k} - \bar{y})]}{\sqrt{\sum (x_i - \bar{x})^2} \cdot \sqrt{\sum (y_{i+k} - \bar{y})^2}}$$

The squared correlation coefficient value (r^2) is mathematically equivalent to the coefficient of determination (R^2). Therefore, additional statistical information between two time series is provided such that the degree of fitting ranges from no correlation (R^2=0) to perfect agreement (R^2=1).

Theoretically, the cross-correlation approach to find Δt requires some assumptions such as no signal distortion and minimal attenuation. Attenuation levels of shear waves vary depending on frequency component. For instance, more attenuation tends to occur for high frequency levels. Therefore, it is critical to use a consistent and repeatable seismic source like the RotoAutoSeis to maintain identically similar signal shapes. In reality, the assumption is maybe sufficient enough to accept specifically for two consecutive signals having a very short interval in soil media (e.g., CiSCPTu system). When the two consecutive signals are overlapped, the coefficient value (r) should be maximized. Time shift at the moment corresponds to the difference in shear wave arrival time (Δt). Figure 8.11(a) shows the maximum time lag between two signals recorded at 20.3 and 21.3 meter depths at the Norfolk site. The maximum correlation coefficient (r) value of 0.993 is observed at the equivalent time lag in Figure 8.11(b).

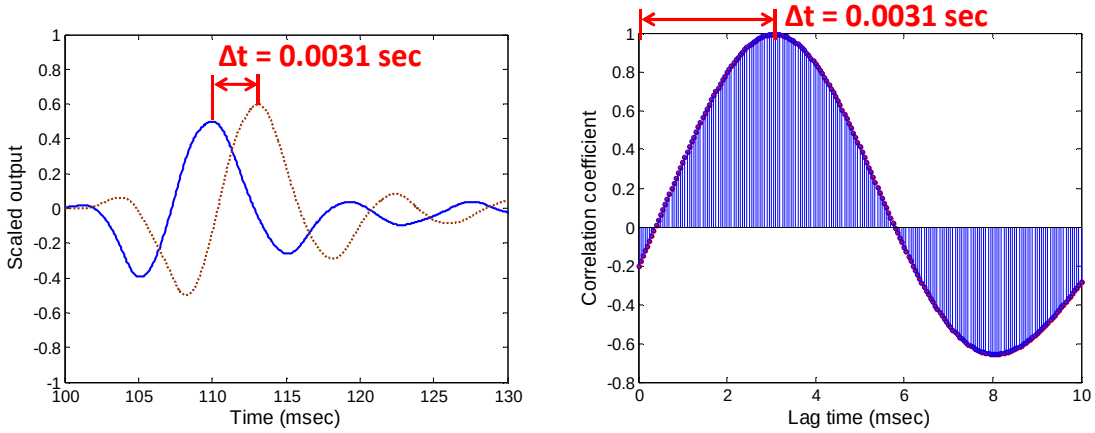

Figure 8.11. (a) Maximum time lag between two consecutive signals recorded at 20.3 and 21.3 meter depths at Norfolk, VA: (b) correlation coefficient (r) values varied with time shift for equivalent signals.

8.4.3.3 Cross-spectral analysis in frequency domain

The time shift (Δt) between shear wave arrivals can be alternatively determined from a frequency domain analysis. Herein, a phase lag at the estimated main peak frequency of shear waves is calculated to find the Δt. To estimate the predominant frequency of the shear wave signals, a power spectral density (PSD) should be obtained. The PSD represents physically how the power of time series signals is distributed with frequency range. Several techniques are available to assess the PSD of measured waves. For instance, auto-spectral density is evaluated by several means such as Fast Fourier Transform (FFT), Welch's method (Periodogram), and least-squares spectral analysis (LSSA; e.g., Lomb method or Lomb-Scargle method). Many prior studies have discussed the details of PSD evaluation methods (Welch 1967, Lomb 1976, Press et al. 1992, Bloomfield 2000, Trauth 2010). Figure 8.12 shows the PSD for the shear wave signal measured at 21.3 meter depth based on the several methods. It is noted that all of the applied techniques show an identical predominant frequency or response of approximate 100 Hz.

The single spectral (auto-spectral) analysis can be extended to cross-spectral analysis based on two time series. Cross-spectrum of two time series x and y are expressed as the sum of real and imaginary parts (Figure 8.13):

Equation (8.7) $$\Phi_{xy} = Co(k) + iQ(k)$$

where, Φ_{xy} = cross-spectrum between two time series (x and y), Co(k) = cospectrum at frequency k (real part), Q(k) = quadrature spectrum at frequency k (imaginary part). The cross-spectral analysis is used to find the correlation between two time series at given frequencies. Likewise, the normalized auto PSD in Figure 8.12, a cross PSD between two

signals (i.e., signals at 20.3 and 21.3 meter depth) is shown in Figure 8.14. For the cross-spectral FFT analysis, the periodogram which decomposes two time series into harmonic sinusoidal components was computed via Welch's method (i.e., 'cpsd' function in MATLAB). The periodogram is a representative and effective statistical tool for investigating periodic tendency of time series.

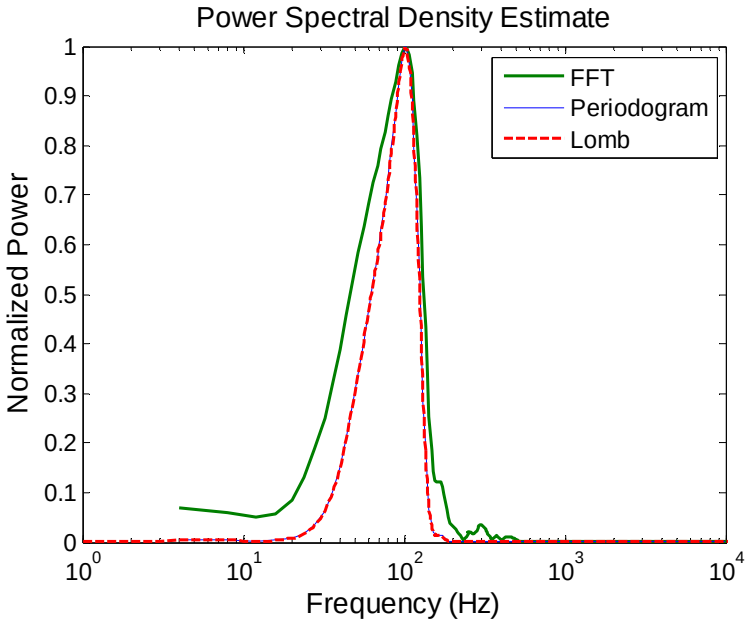

Figure 8.12. Normalized power spectral density (PSD) estimated from FFT, Welch spectral analysis (periodogram), and least-squares spectral analysis (Lomb method) for the signal recorded at 21.3 meter depth.

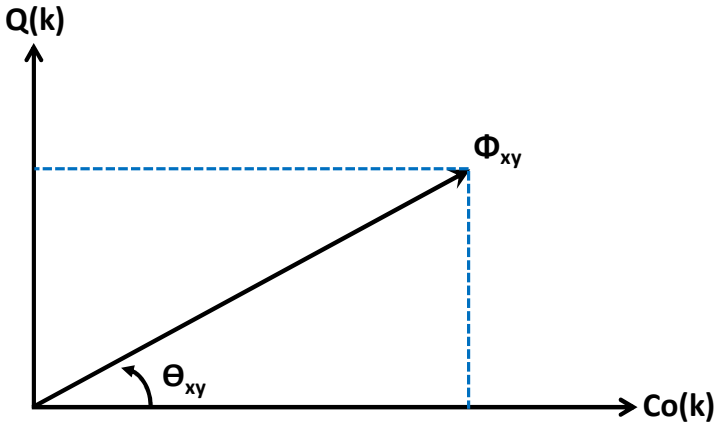

Figure 8.13. A conceptual phase diagram for cross-spectrum between two time series.

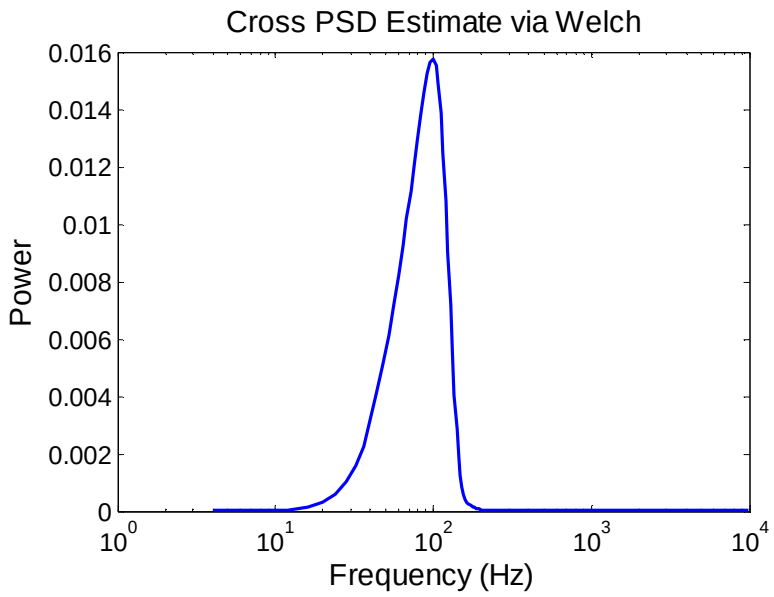

Figure 8.14. Cross PSD estimated using Welch's method for two signals recorded at 20.3 and 21.3 meter depths at Norfolk, VA.

An observed peak frequency is identical to that of auto PSD (i.e., 100 Hz). The analysis provides a phase spectrum in frequency domain, thus time shifts and phase velocities between two signals can be calculated for specific frequencies of interest:

Equation (8.8a) *Phase shift (angle) at frequency k*: θ (degree) = $\tan^{-1}(Q(k)/Co(k))$

Equation (8.8b) *Phase delay time*: $\Delta t_f = \theta / (360 \times f)$

Equation (8.8c) V*elocity*: $V_f = \Delta R / \Delta t_f$

The calculated velocities vary depending on frequencies. Using the noted spectrum in Figure 8.14, the phase angle and velocity for each frequency component are shown in Figure 8.15. Particularly, the phase velocity at the dominant frequency (i.e., 100 Hz) can be considered a reasonable value. Theoretically, Discrete Fourier Transform (DFT) of cross-correlation is equivalent to the cross-spectral density. In its strictest sense, if clear signals are analyzed perfectly, the velocity estimated from the peak frequency shifting may be identical to the results from the cross-correlation method in time domain.

However, discrepancies can occur due to a variety of reasons such as spectral leakage, resolution problems, and periodicity assumption, as well as the spectral density estimates which have bias and variance, as well as effects of stochastic decomposition processes.

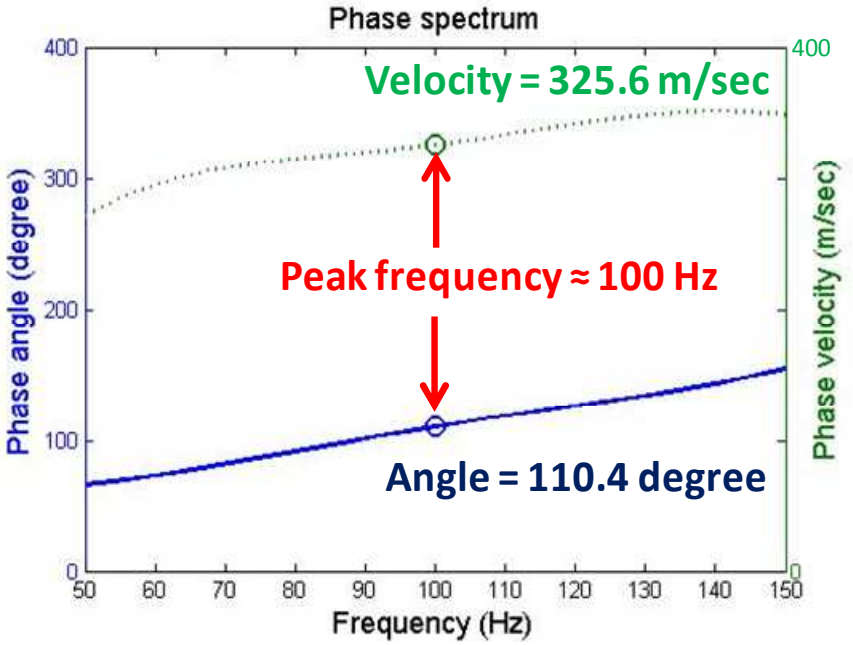

Figure 8.15. Phase spectrum (phase angle and velocity) between two signals recorded at 20.3 and 21.3 meter depths at Norfolk, VA.

8.4.3.4 Comparison of V_S evaluation methods from reference sounding

Based on the one-meter interval downhole shear wave signals recorded at the Norfolk site, the aforementioned V_s assessment results are compared in Figure 8.16. Holocene sediments are characterized by a representative $V_s \approx 140$ m/s while the lower older marine deposits of the Yorktown exhibit $V_s \approx 300$ m/s. The V_s evaluations using the cross-correlation and the cross-spectral analysis are derived via MATLAB program. Coefficient of determination (R^2) values between two consecutive signals are also provided. It is observed the evaluations are considerably well matched with the manual picking methods (i.e., cross-over, first peak). The results show that the applied post-

processing methods and V_s evaluation tools made via the MATLAB program are robust and adoptable. Both the time domain and frequency domain methods are valuable means to explain periodic patterns. Whereas the manual picking methods generate only an evaluation of time shift (Δt), cross-correlation in time domain and cross-spectral analysis in frequency domain provide additional information (e.g., coefficient of determination obtained from cross-correlation; phase spectrum from cross-spectral analysis). Moreover, traditional manual methods are time-consuming for both fieldwork (e.g., paired opposing strikes) and evaluation process (e.g., visually picking points). Consequently, coded software programs (e.g., MATLAB) using cross-correlation and/or cross-spectral analysis are advantageous for improved interpretations and handling of large datasets.

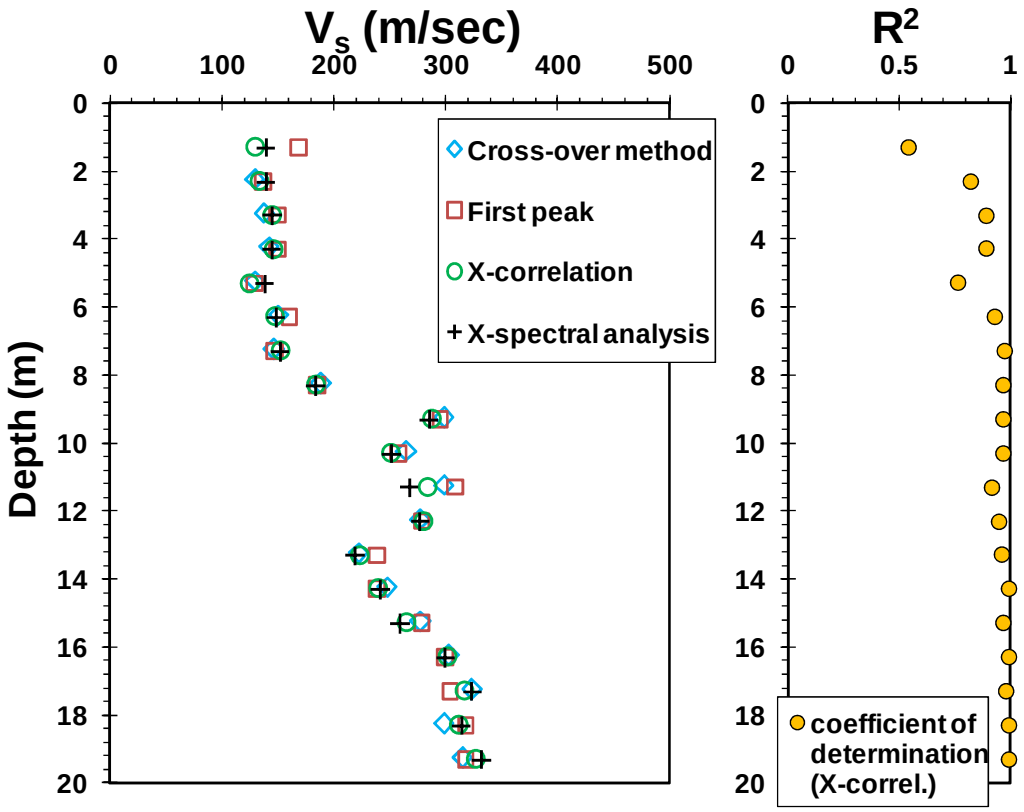

Figure 8.16. Downhole results showing comparison of various V_s evaluation methods and coefficient of determination (R^2) values between consecutive shear wave signals at Norfolk, VA.

8.5 Continuous-Interval V_s Profiling

Using the aforementioned data processing techniques, the feasibility of continuous-interval V_s profiling will be examined based on three test sites (Norfolk, VA; Windsor, VA; Richmond, BC).

8.5.1 Continuous-Interval V_s Profiling at Norfolk, VA

8.5.1.1 Continuous shear waves at Norfolk, VA

A special series of continuous shear wave measurements were taken at the Norfolk site. The site description was already provided for the reference SCPTu sounding in section 8.4.1. Here, the RotoAutoSeis unit was utilized to generate frequent wavelets approximately every 5 seconds. The signals were recorded by an advancing seismic cone penetrometer at the standard rate of 20 mm/s. A total of 220 successive shear wave signals were generated over the 20-m depth of the sounding. The distance from the center of the autoseis to the axis of the SCPTu push rods was 1.25 meters. Shear waves were regularly collected at 10 cm vertical intervals without stopping (except to re-grip the rods by the hydraulic actuator system). Compared to conventional 1.5-m V_s profiles collected by DHT or 1-m V_s data provided by SCPT and SDMT, the 0.1-m signals generated by the continuous-push seismic system are considerably closer together and larger in number, thus able to provide higher resolutions for geologic profiling.

8.5.1.2 Continuous V_S evaluation at Norfolk, VA

For continuous shear wave testing, the signal sampling rate was 50 kHz with a record length of 200 ms. Raw shear wavelets at Norfolk site exhibit significantly noisy signals as shown in Figure 8.17(a). To reduce the noise level, a band-pass filtering range [100Hz, 350Hz] was adopted on the basis of visual examinations on fluctuations of

signals and engineering judgment from observed coherence values and spectrum. Eventually, the filtered shear wavelets are shown with a windowed zone in Figure 8.17(b). After filtering, the full set of cascaded continuous shear waves are evident. For determining the appropriate filtering range, it was important to examine noise characteristics and the selection process is discussed for the recorded continuous signals.

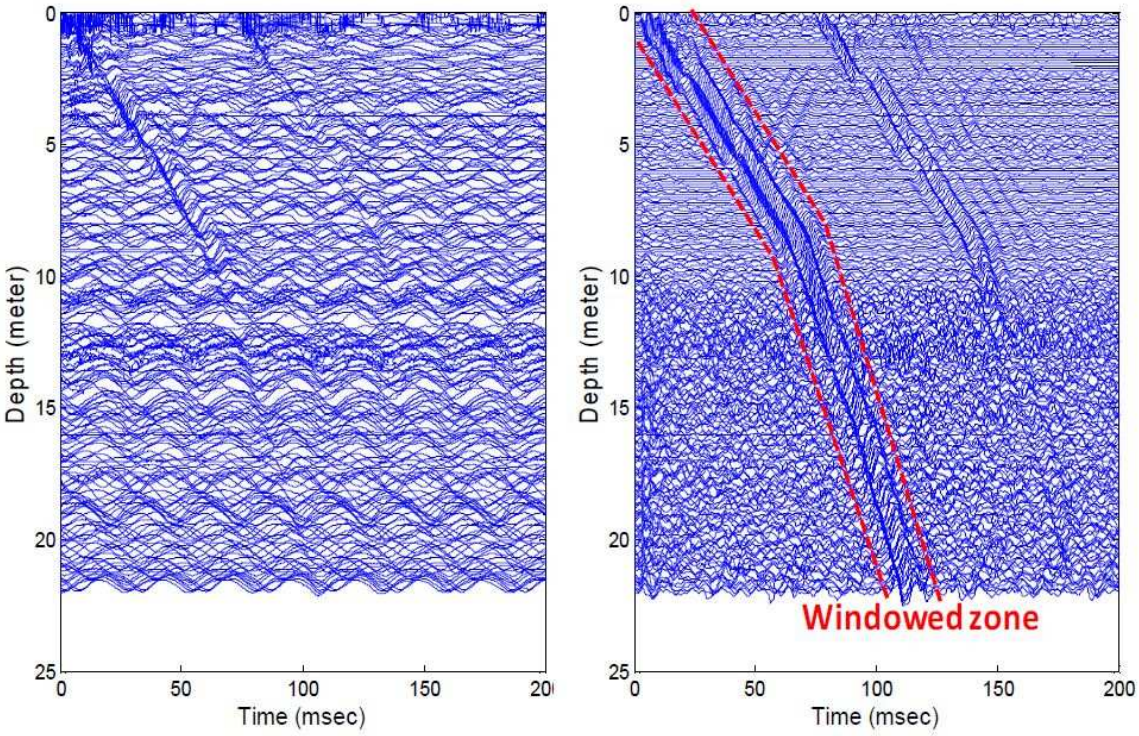

Figure 8.17. (a) Successive raw shear wave signals, (b) Successive filtered shear wave signals recorded from special continuous SCPTu conducted at Norfolk, VA.

In conventional SCPTu tests, it is usually not too difficult to obtain sound signals as shown in Figure 8.8. In most cases, slight random white noise (e.g., the noises are time invariant and mainly high frequency components) tend to be observed. The white noise can be identified from various mathematical approaches (i.e., mean, standard deviation, probability distribution function, zero auto-correlation, constant flat power spectral density). Generally, these slight random noises may be readily mitigated by the noted

appropriate filtering techniques. However, in the raw continuous V_s signals (Figure 8.17a), the main background noises seem to have different characteristics. It is not easy to identify shear waves from raw signals because the data include random noises that have visible long-term fluctuations, particularly below 10 meter depths. Definitely, those are not part of the main shear waves but appear to be a similar type to Flicker noise (fluctuation noise) which is caused primarily by vibration and source instability. It was known that the Flicker noise is close to pink noise (or 1/f noise) which is usually weighted to low frequency and inversely proportional to frequency rather than white noise.

To characterize and verify the background noises, further examinations are provided based on the raw signals recorded at 22 meter depth (the deepest depth). The data between 0 and 80 ms were applied to avoid the effect of main shear wave signal (i.e., total 4000 data points are applied until 80 ms). Basically, the zone should have a baseline value (i.e., zero) because the main shear wave is expected not to arrive within the zone. However, the actual signals are not constant, but considerably fluctuated. The unwanted background noises are not white random noises as demonstrated by auto-correlation function (i.e., auto-correlation coefficient or auto-covariance is not zero) in Figure 8.18. Based on the same dataset, auto power spectral density (raw signal at 22 meter depth) and cross spectral density (raw signals at 21.9 and 22 meter depth) are provided via Welch's method in Figure 8.19. Considering the observed power spectral densities, the main background noise seems to have similar characteristics with the aforementioned pink noise (i.e., low frequency weighted or inversely proportional to frequency). Hence, it seems reasonable that the background noises primarily consist of Flicker noise type due

to vibrations. Probably, cone truck vibrations (engine: 1100 RPM ≈ 18.4 Hz) generated the main noises when CSWV signals were recorded at non-stationary condition. Consequently, based on these spectral density examinations on raw signals, reasonable band-pass frequency filtering range was adopted (e.g., low cut-off frequency is 100 Hz).

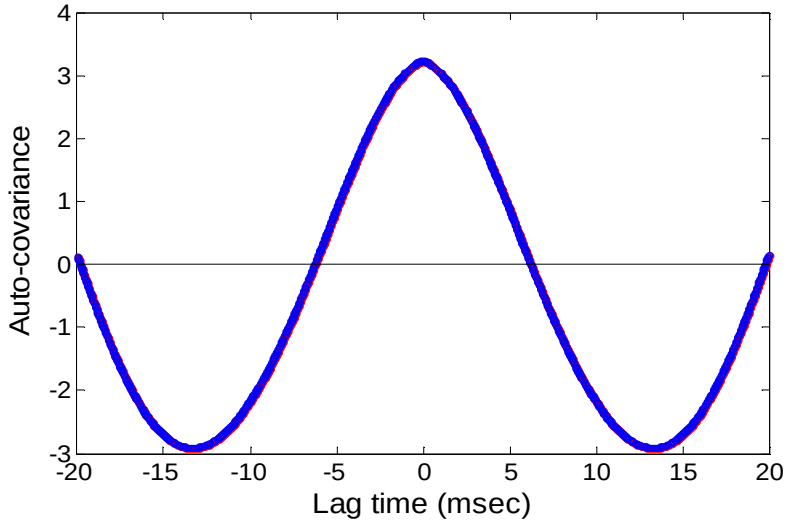

Figure 8.18. Auto-covariance values for raw signal recorded at 22 meter depth (applied data range is between 0 and 80 msec).

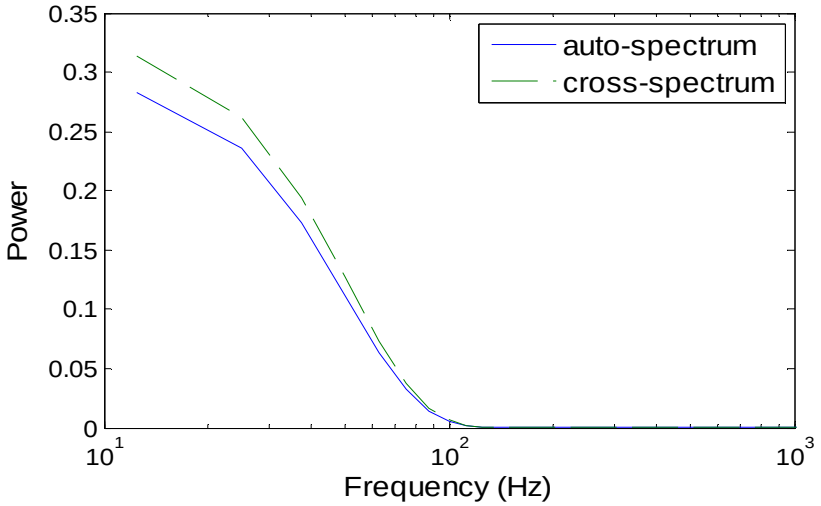

Figure 8.19. Auto spectral density for raw signal at 22 meter depth and cross spectral density for raw signals at 21.9 and 22 meter depth based on Welch's method (applied data range is between 0 and 80 msec).

Using the filtered signals, continuous V_s measurements were evaluated by both the cross-correlation and cross-spectral analyses, however the results were sensitive and scattered. The variable results were caused by various factors, including: extremely short times, rod vibrations caused by the cone penetration process, slight CPT rate variants, unfiltered noise, refracted and reflected signals, and unexpected random errors from the source. In order to obtain a reliable in-situ V_s profile, an additional zero-phase filtering technique was examined for the time intervals (Δt) where the algorithm of the filter function is discussed in Oppenheim and Schafer (1989). A conventional algorithm of $(n-1)^{th}$ order running-mean filter is as follow:

Equation (8.9) $$y_n = b_1 \cdot x_n + b_2 \cdot x_{n-1} + ... + b_{nb+1} \cdot x_{n-nb} - a_2 \cdot y_{n-1} - ... - a_{na+1} \cdot y_{n-na}$$

where, x = input data, y = filter data, b = filter coefficient vector (numerator coefficient), a = denominator coefficient vector, na = feedback filter order, nb = feedforward filter order. In this study, the author applied b = 1/n ×[1,1,…,1] and a = 1 ×[1,0,…,0] for simple application (default use in MATLAB). In fact, a zero-phase distortion filtering was accomplished using 'filtfilt' function in MATLAB. It reduces the filter initial transients and transforms phase delay into appropriate position. Eventually, it is expected that the zero-phase filtering provides equivalent results to the following simple expression (n^{th} order):

Equation (8.10) $$y_i = \frac{1}{n+1} \sum_{j=1}^{n+1} x_{i+(j-n/2-1)}$$

where, i and j = discrete element, n = even number. The evolution of V_s profiles using the n^{th} order running-mean filter are presented in Figure 8.20 (i.e., 2^{nd}, 6^{th}, 10^{th} order). The continuous V_s profile having a high order running-mean filter (e.g., 10^{th}) is relatively well

matched in comparison with the reference 1-meter interval V_s from DHT. The most appropriate n^{th} order might be determined with consideration of varying trends of other CPT soundings.

The final complete CiSCPTu is summarized in Figure 8.21 with profiles of 4 continuous readings with depth: cone tip resistance (q_t), sleeve friction (f_s), porewater pressure (u_2), and shear wave velocity (V_s). This combination offers an economic, expedient, and efficient means to procure information on the geostratigraphy, soil engineering parameters, and geophysical data in a single sounding. It is noteworthy that both the continuous V_s and conventional DHT results capture the significant step up in velocity at the Holocene-Yorktown interface at 9 m depth.

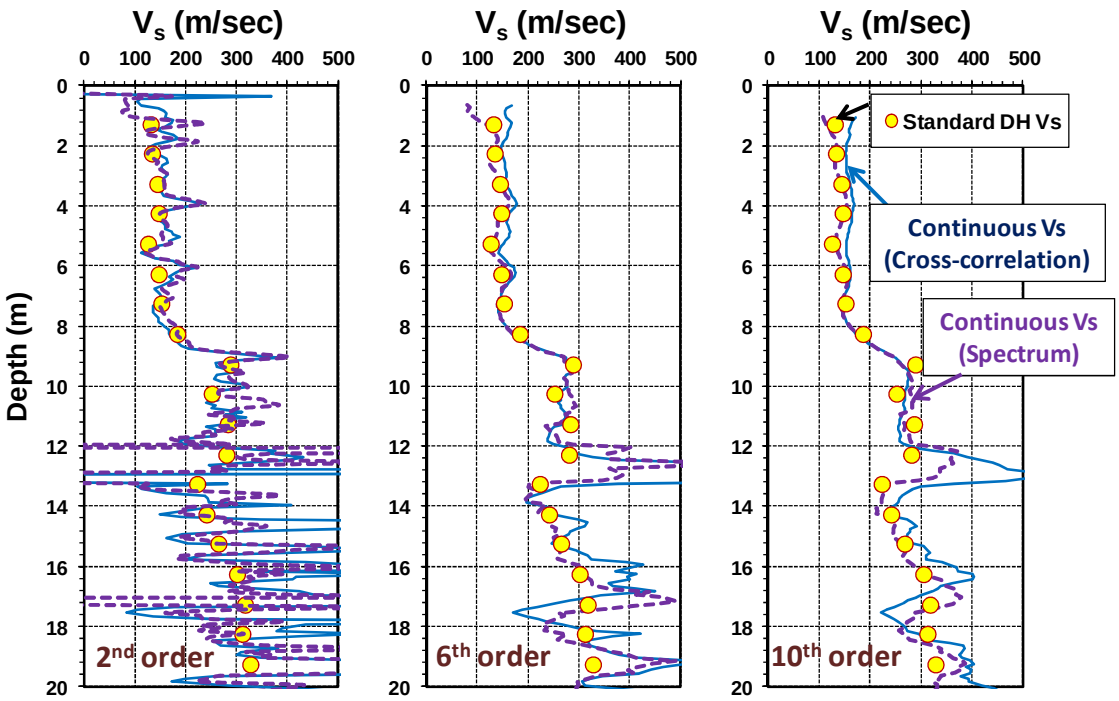

Figure 8.20. Evolution of continuous V_s profiles applying running-mean filter technique: (a) 2^{nd}, (b) 6^{th}, (c) 10^{th} order at Norfolk, VA.

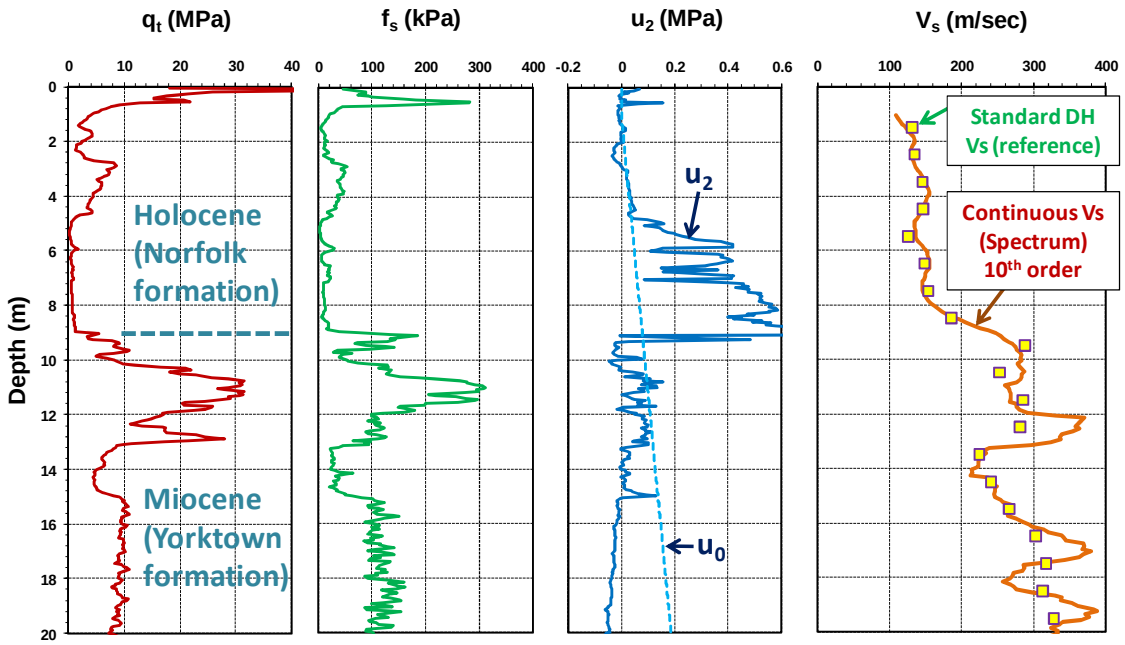

Figure 8.21. Results of continuous readings from CiSCPTu sounding at Norfolk site, Virginia: (a) cone tip resistance, (b) sleeve friction, (c) porewater pressure, and (d) shear wave velocity.

8.5.2 Continuous-Interval V_s Profiling at Windsor, VA

8.5.2.1 Continuous shear waves generation and site descriptions at Windsor, VA

Another series of standard and continuous-interval SCPT results were obtained using the automated seismic source and penetrometer system at a site in Windsor, Virginia. The ground conditions at the Windsor site consist of about 1 m gravelly sand fill overlying natural alluvial and deltaic sediments of the Windsor Formation to 8 m depths that are underlain by marine deposits of the Yorktown Formation which extends beyond the termination depths of exploration at 30 m. The Windsor Formation is comprised of Holocene sediments: silty clays, sands, and clayey sands. The Yorktown consists of stiff calcareous sandy clay of Miocene age and groundwater lies about 1 m

deep at this location. As already noted from Norfolk site, the Yorktown is well-known throughout southeast coastal Virginia as a rather strong foundation bearing stratum for structures.

Field testing for the CiSCPTu was performed using a 15 cm^2 cone with a single geophone positioned 0.2 m above the cone tip. The autoseis source was situated at ground level and offset 1.45 meters horizontally from the CPT rod string axis. In the same manner, as the cone was pushed into the ground, shear waves were generated at the ground surface every 5 seconds. Eventually, a total of 295 continuous shear wave signals were generated per every 10-cm interval throughout the 30 meter depth. For comparison and reference, a standard SCPTu sounding using pseudo-interval arrays at 1-meter stops was also performed to provide a benchmark profile of downhole-type shear wave velocity at the site. Whereas the automated triggering system provided only uni-directional strikes for the series of continuous shear waves, paired sets of left- and right- strikes were accomplished for the standard 1-meter interval SCPTu using the old "classic" sledge hammer and beam arrangement. Figure 8.22 shows the SCPTu measurements and evaluated soil behavioral type profile at Windsor (ConeTec).

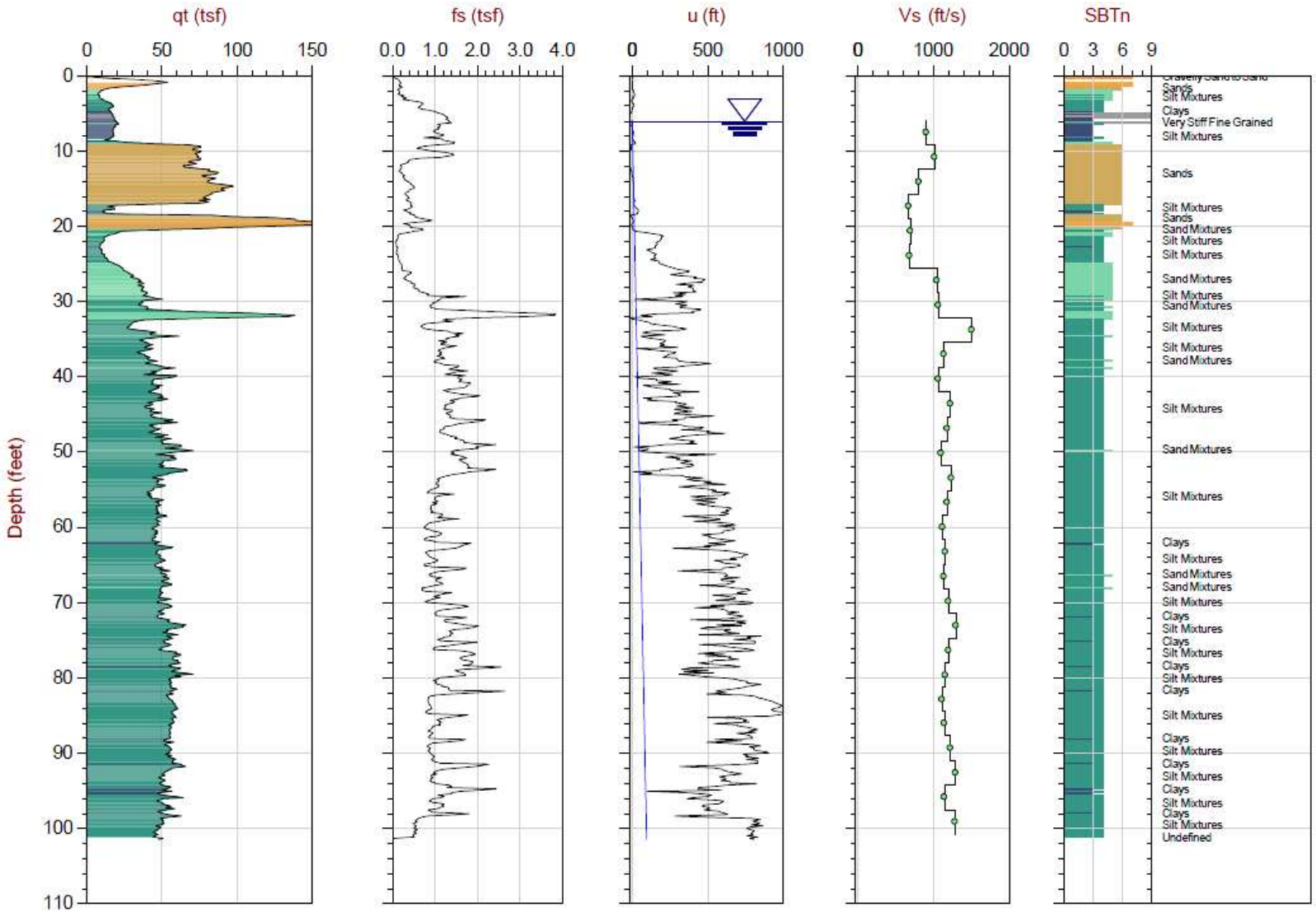

Figure 8.22. Standard SCPTu soundings and corresponding soil behavioral type (SBP) profile at Windsor (figure source: ConeTec).

8.5.2.2 Continuous V_s evaluation at Windsor, VA

In the field, each continuous shear wave signal was recorded per every 0.02 msec (i.e., sampling rate = 50 kHz) up to 200 msec length. An evenly-spaced sampling time is useful for automation of V_s calculations. After detrending the raw signals, the coherence values and cross-spectral densities between continuous signals were investigated. For instance, Figure 8.23 shows the coherence magnitudes between two consecutive signals measured at 30.8 and 30.9 meter depth (i.e., wave measurements at the deepest depths). It is noted that high coherence values are observed at a frequency range of about 50 and 100 Hz. Based on further examination on the coherence values, spectral densities, and engineering judgment, a band-pass range of 40Hz and 400Hz was applied for noise filtering. Significantly poor raw signals which were difficult to match were deleted.

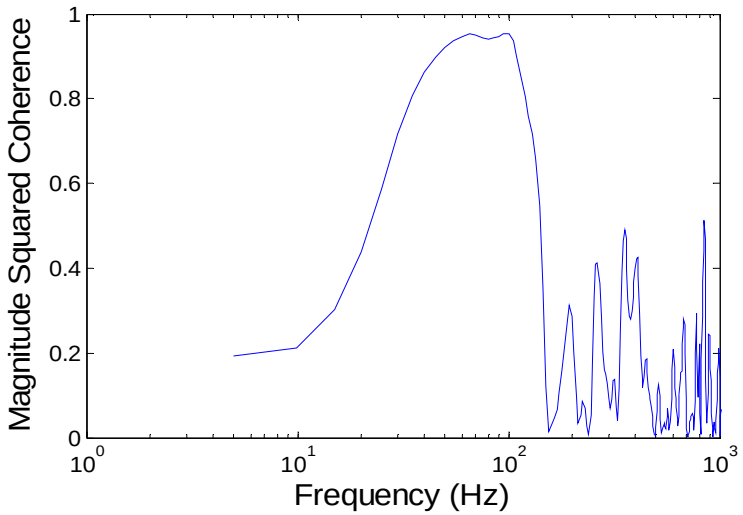

Figure 8.23. Magnitude of coherence function between two consecutive shear wave signals recorded at 30.8 and 30.9 meter depth at Windsor site, VA.

The benchmark DHT profile was provided in terms of one-meter depth intervals that was obtained from a standard SCPTu. The raw signals were recorded with 20 kHz sampling rate up to 250 msec length. An adopted cut-off band frequency range was [25,

300] Hz. Eventually, two sets of shear wave data were procured and analyzed for developing the in-situ V_s profiles at the Windsor site; (a) a total set of 285 continuous uni-directional wavelets; and (b) 31 paired sets of standard left-right strikes for standard downhole series. Figure 8.24 shows the entire family of raw continuous shear wave signals which are normalized by maximum magnitudes for display. As expected, the falling cascade of the initial arrival of the shear waves is quite apparent in this graph. In contrast, the conventional set of paired wavelets from left-right strikes every one meter depth intervals are provided in Figure 8.25.

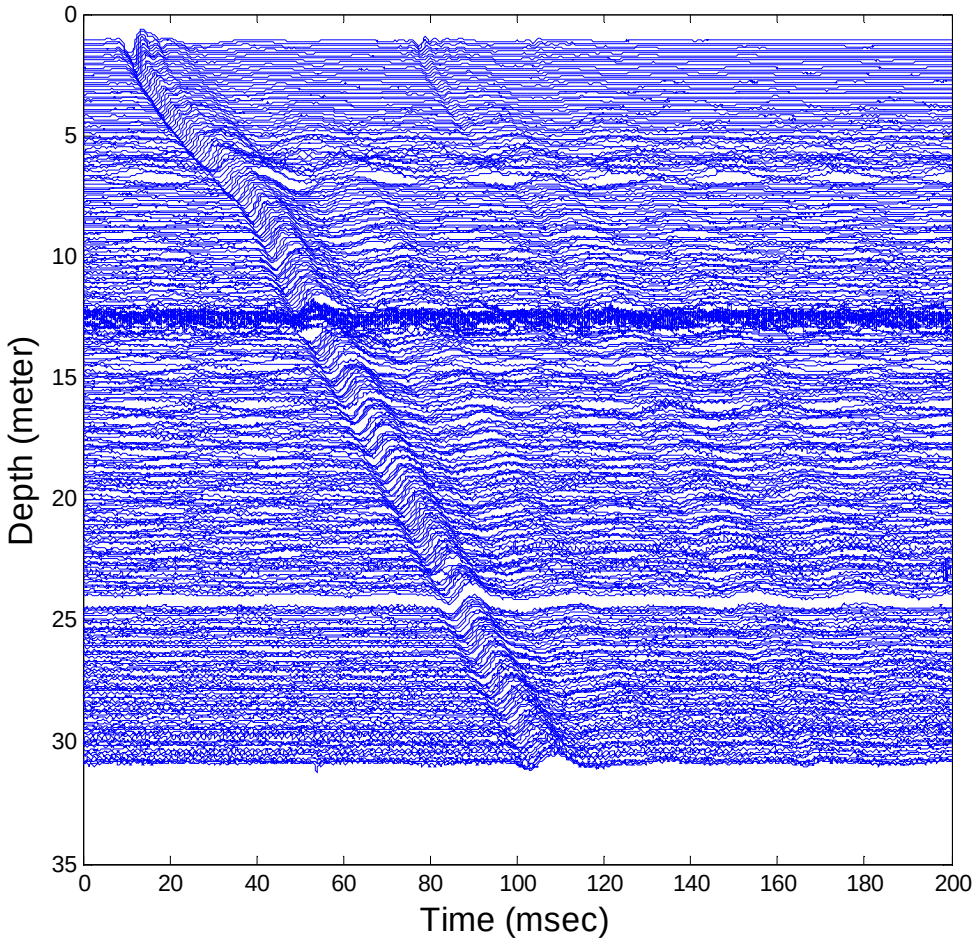

Figure 8.24. Successive raw shear wave signals recorded from special continuous-interval testing (CiSCPTu) at Windsor, VA.

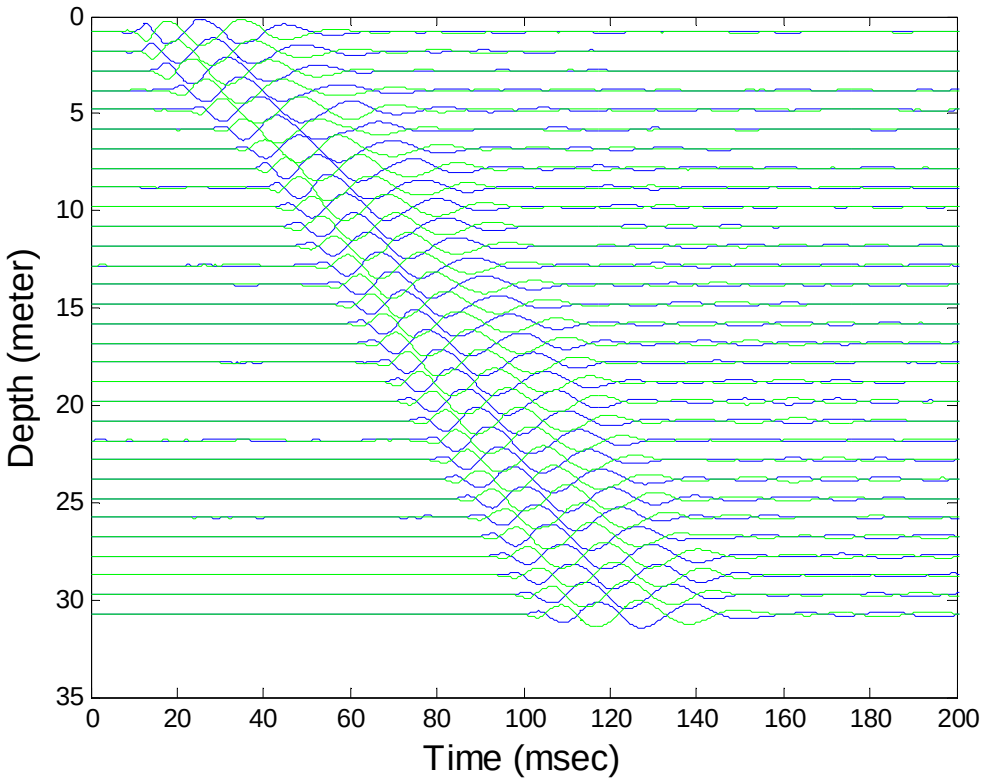

Figure 8.25. Filtered 1-meter interval paired (left and right strike) shear wave signals from downhole test arrangement using SCPT at Windsor, VA.

For the continuous V_s calculation at Windsor site, cross-correlation in time domain and spectral analysis in frequency domain were performed. For example, Figure 8.26 shows a time shift which provides the maximum correlation coefficient (r) obtained from two consecutive signals measured at 30.8 and 30.9 meter depth (i.e., maximum r = 0.9726 at Δt = 0.360 msec). Due to the short distance (i.e., 100 mm), a very small lag time was calculated. Automated Δt determinations are available as well with frequency-based analysis.

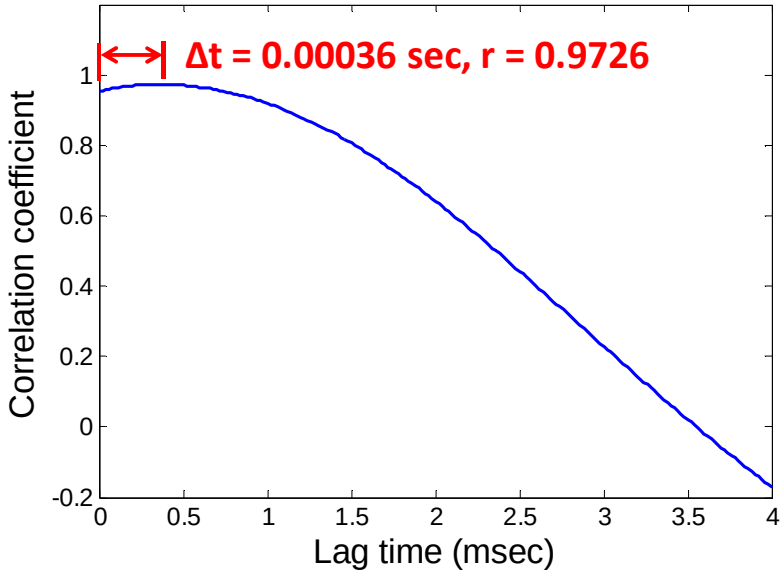

Figure 8.26. Correlation coefficient (r) values versus time shift (Δt) evaluated from normalized cross-correlation function for two consecutive signals recorded at 30.8 and 30.9 meter depth at Windsor, VA.

Using the continuous shear wave data, the PSD was obtained to examine the predominant frequency. Figure 8.27 shows normalized auto-spectral density values using FFT, Welch method, and LSSA for the signals measured at 30.9 meter depth. All PSD estimation techniques result in a same peak frequency of 80 Hz. Cross-spectral density (via periodogram) evaluated from two consecutive signals recorded at 30.8 and 30.9 meter depth is provided in Figure 8.28. It is observed that the predominant frequency of the cross-spectrum is identical to that of auto-spectral density (i.e., f_{peak} = 80 Hz). Consequently, the phase delay time (Δt) can be calculated using Equation 8.8b (i.e., $\Delta t = \theta_p/(360\times f_p) = 11.215/(360\times 80) = 0.389$ msec, where f_p = predominant frequency observed from cross-spectral density, $\theta_p = \tan^{-1}(Q(f_p)/Co(f_p))$ = phase shift (angle) at peak frequency).

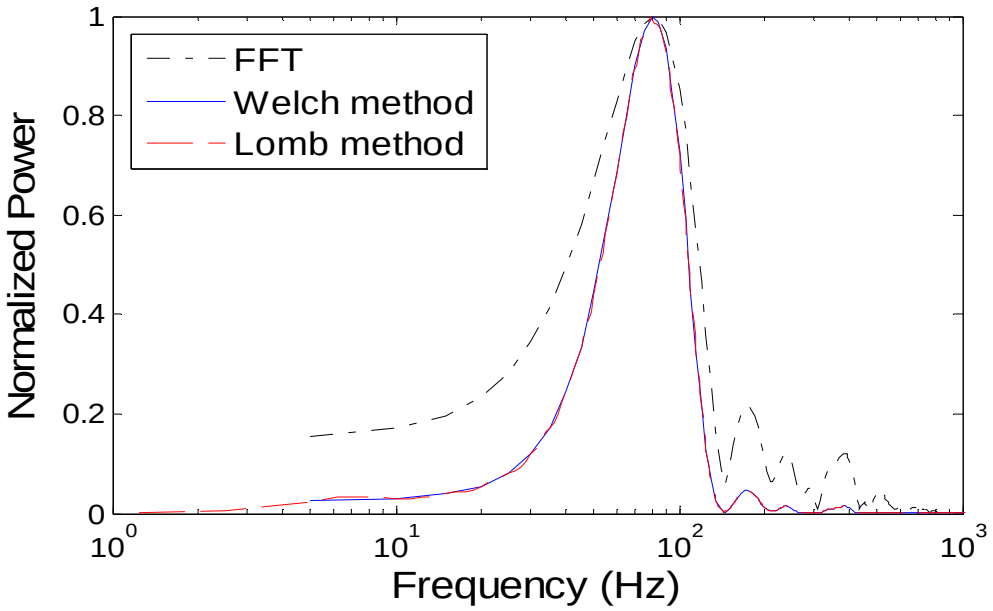

Figure 8.27. Normalized auto-spectral density estimated using FFT, Welch's method (periodogram), and least squares spectral analysis (Lomb method) for the signal recorded at 30.9 meter depth.

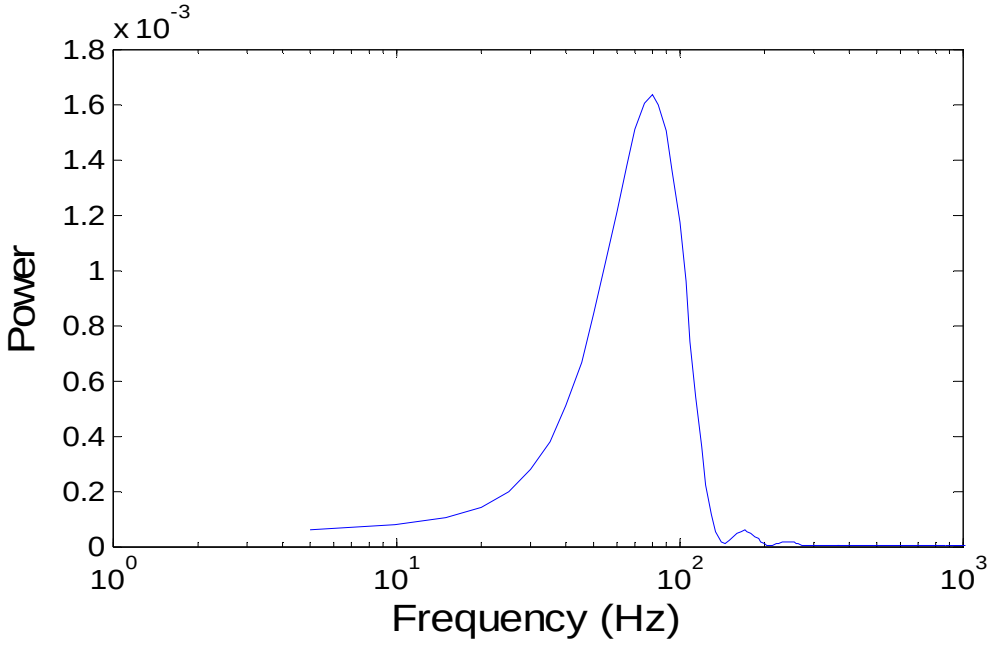

Figure 8.28. Estimated cross-spectral density (periodogram) for the two consecutive signals recorded at 30.8 and 30.9 meter depth at Windsor, VA.

In the same manner (i.e., automated cross-correlation and spectral analysis method), the reference 1-meter interval V_s from SCPTu (Figure 8.25) was evaluated as well. For the limited wavelet dataset, the manual picking methods (i.e., cross-over point, peak point) were also available. Figure 8.29 shows the evaluated 1-meter interval V_s results and corresponding R^2 values between two successive signals. Although some minor deviations are observed, all four evaluation methods show overall quite good agreement in their V_s profiles. Clearly there is a step in the profile at the interface where the lower-velocity Holocene soils meet with the deeper higher-velocity Yorktown Formation.

With this reference benchmark, the continuous-interval V_s profiles derived from both the automated cross-correlation and spectral density methods were compared at this Windsor. However, similar to Norfolk site, considerably sensitive V_s predictions were observed for both evaluation methods. Hence, the zero-phase running mean filtering technique (Equation 8.9) was applied again. Eventually, Figure 8.30(a), (b), and (c) show evolutions of the in-situ V_s profiles applying the running-mean filter technique (a-2^{nd}, b-6^{th}, c-10^{th} order). For both of the derived continuous V_s profiles (i.e., cross-correlation and spectral analysis), adopting the 10^{th} order filter seems to match well with the reference downhole test data. The final continuous seismic piezocone sounding (CiSCPTu) with four independent channels of collected information (q_t, f_s, u_2, V_s) is provided in Figure 8.31. All readings are seen to be good indicators identifying the different geologic units, stratigraphic conditions, and soil behavioral types. At this site, the upper Windsor group is characterized by shear wave velocities of 250 decreasing to 200 m/s. For the Yorktown Formation that is encountered at depths below 8 m, the shear

waves are consistently around 350 m/s. Thus, the contrast between the upper Holocene soils and underlying Miocene age marine deposits is quite evident.

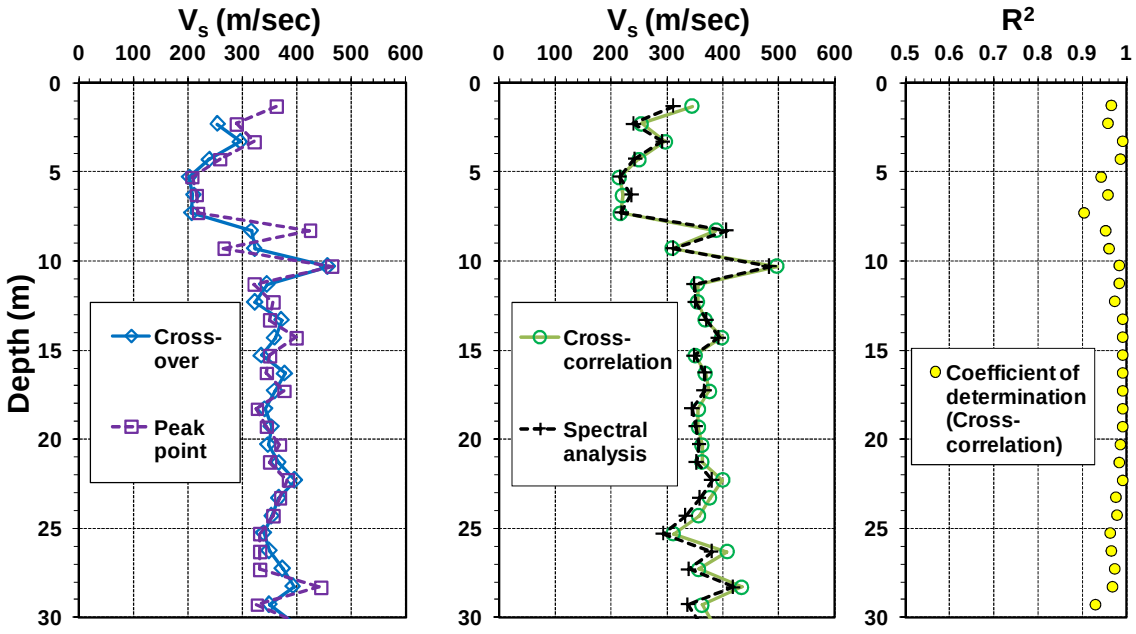

Figure 8.29. Comparison of 1-meter interval V_s profiles evaluated from various techniques (i.e., cross-over, peak, cross-correlation, spectral analysis) and corresponding R^2 values for two successive signals at Windsor, VA.

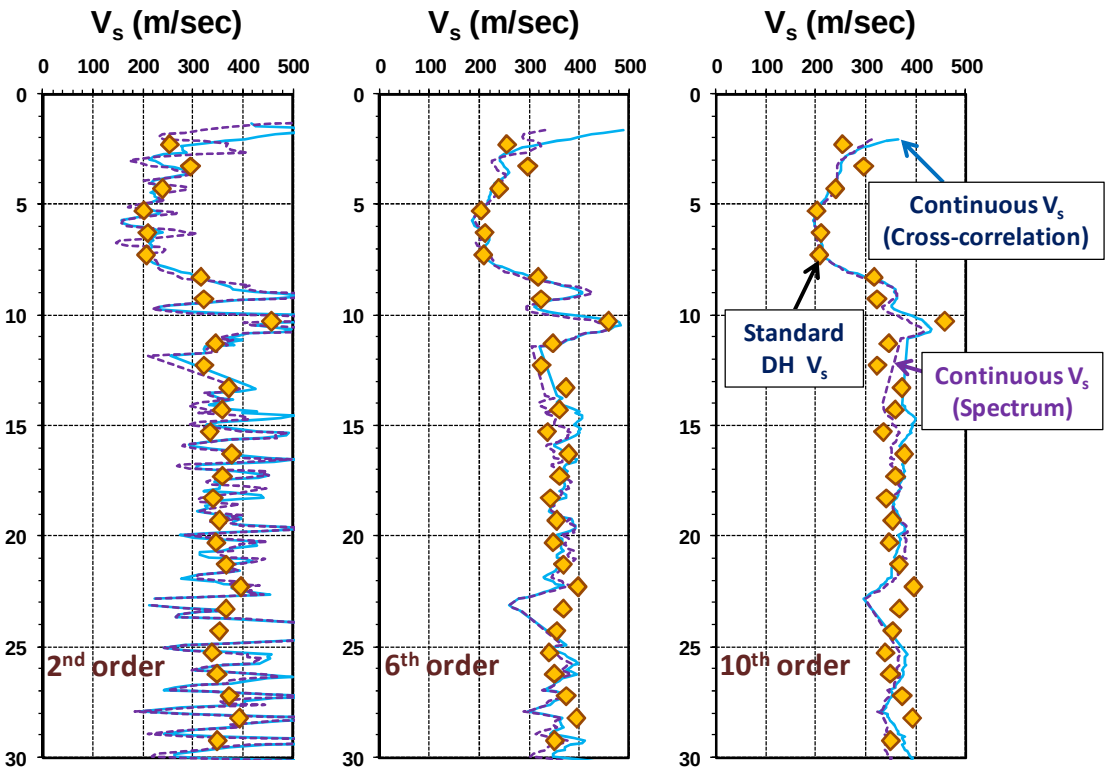

Figure 8.30. Evolution of continuous V_s profiles evaluated from cross-correlation and cross-spectral analysis adopting zero-phase running-mean filter technique: (a) 2nd, (b) 6th, (c) 10th order at Windsor, VA.

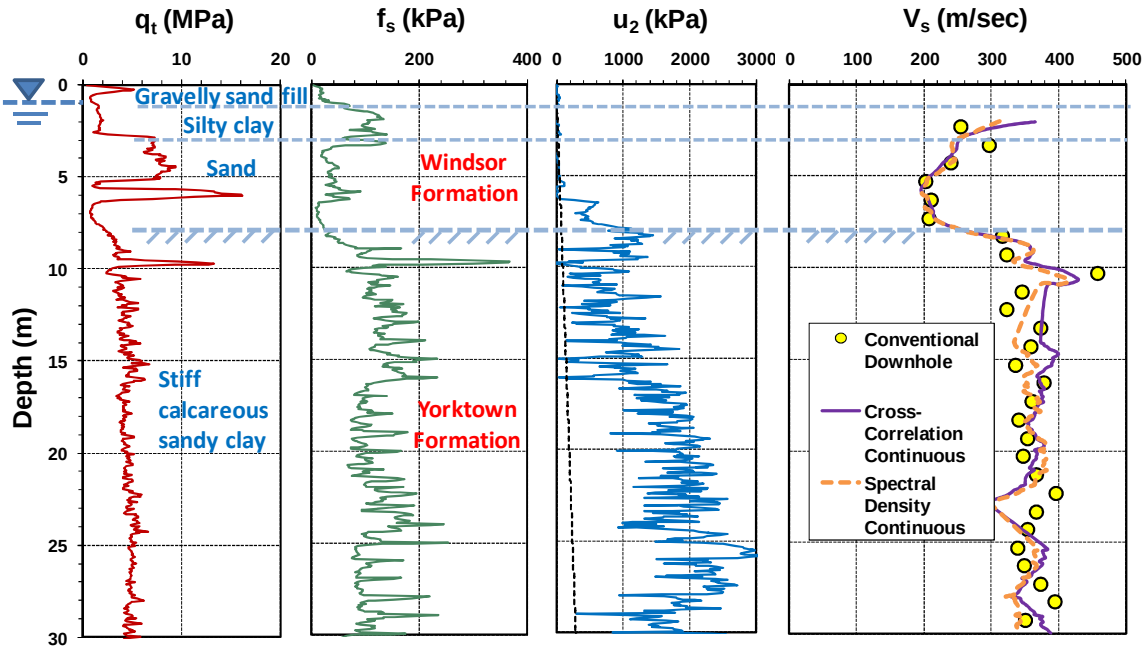

Figure 8.31. Results of continuous seismic piezocone tests (CiSCPTu) at Windsor, VA.

8.5.3 Continuous-Interval V_s Profiling at Richmond, BC

8.5.3.1 Continuous shear waves generation and site descriptions at Richmond, BC

Shear wave data taken at an industrial site in Richmond, British Columbia are presented here as a third example on the capabilities regarding continuous V_s profiling by CiSCPTu and related technical issues on post-processing of the wavelet data. For the information of the soil conditions and layers at the site, Figure 8.32 provides deep 45 meter depth CPT soundings and associated soil behavioral type (SPT) profile. The ground conditions at the Richmond project site consist of about 1 m of gravelly sand fill overlying natural alluvial and deltaic deposits of silty clay to 7 meters, a thick sand stratum which extends to 30 m, underlain by a thick layer of soft to firm clayey silt which resides beyond the termination depths of exploration at 45 m. Groundwater lies about 3.5 m deep at this location. A total of 445 successive shear wave signals were generated for the special continuous shear wave measurements at the Richmond site. As such, shear waves were collected at 100-mm vertical intervals using an autoseis source, pseudo-interval testing procedure, and bi-axial geophone arrangement in the penetrometer. The sampling rate of signals was 20 kHz with a record length of 400 ms. The distance from the center of the autoseis unit to the axis of the SCPTu push rods was 1.25 meters.

A summary of the continuous record of raw wavelets is shown in Figure 8.33. The primary shear wave is seen clearly as a falling cascade. For illustration purposes, the selected waveforms and frequency components of two consecutive raw signals recorded at 45.0 and 45.1 meter depths are provided in the subfigures. Due to the short distance interval of 100 mm, the identification of the time delay is not clearly evident. For the selected two raw signals, slightly different peak frequencies were observed at approximately 35 Hz in addition to some issues with noise and vibration.

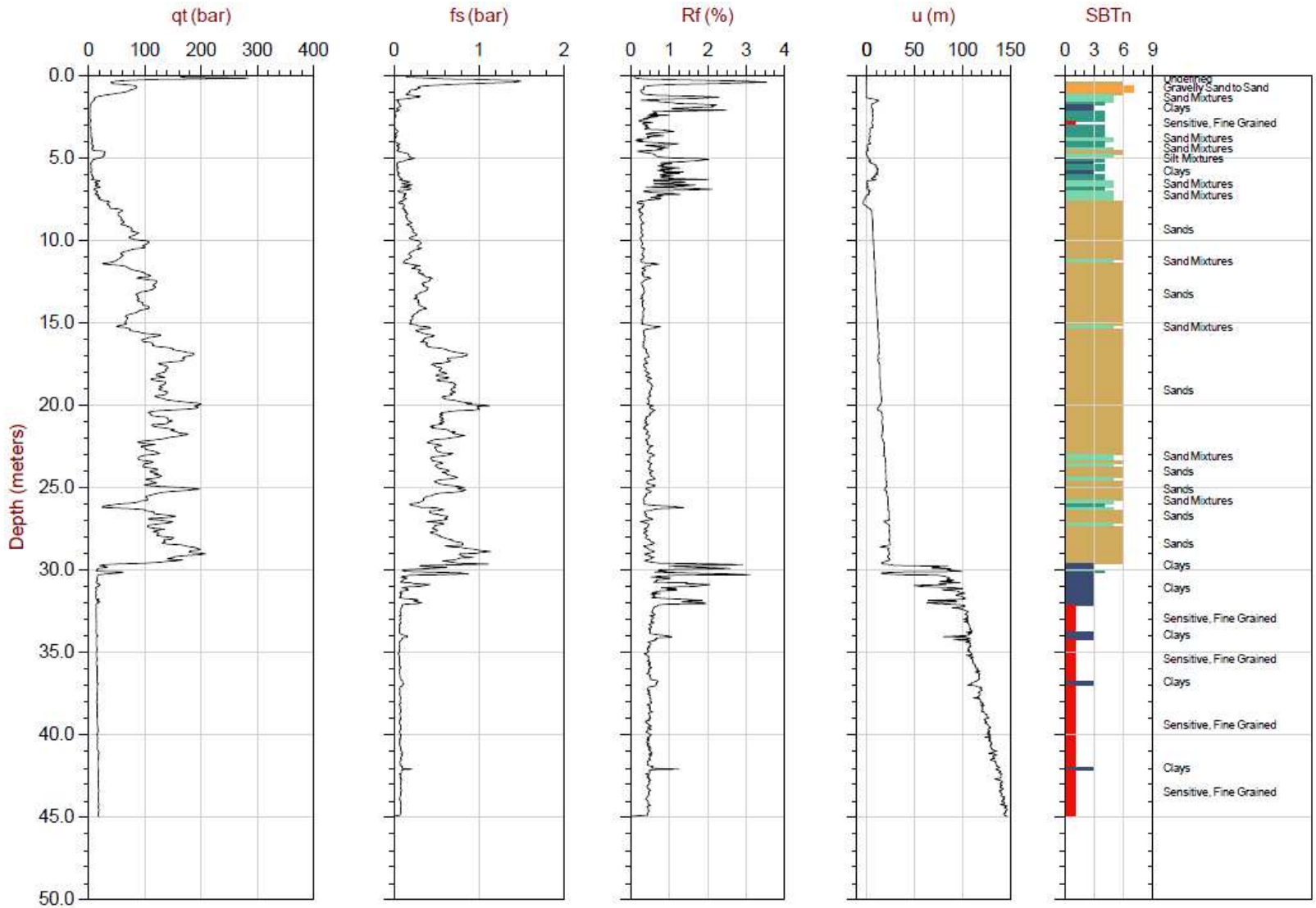

Figure 8.32. CPTu soundings and corresponding soil behavioral type (SBP) profile at Richmond, BC (figure source: ConeTec)

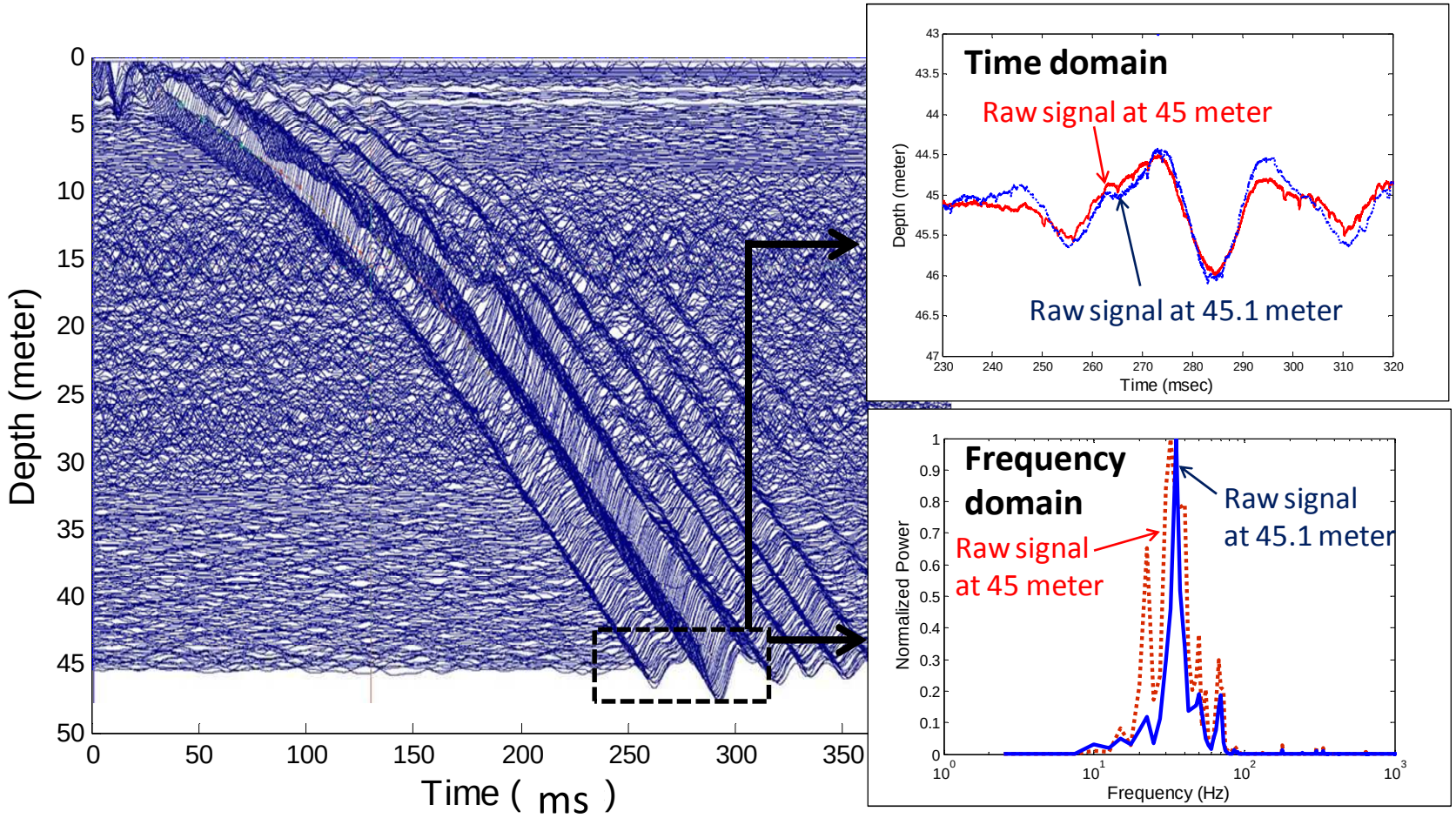

Figure 8.33. Continuous raw shear waves recorded every 0.1-m from CiSCPTu performed at Richmond, BC. In subfigures, two consecutive raw signals recorded at 45.0 and 45.1 meter depth are magnified in time domain and frequency domain.

8.5.3.2 Continuous V_s evaluation at Richmond, BC

To mitigate noise levels, the continuous raw shear wave signals were filtered (i.e., band-pass filtering in frequency domain) and windowed before V_s calculations. Figure 8.34 shows the magnitudes of the squared coherence evaluated from two consecutive raw signals recorded at 45.0 and 45.1 meter depths. It is observed that the coherence function has relatively high magnitudes for the frequency range between 30 Hz and 100 Hz. Eventually, based on further examination of coherence measurements and frequency components for all successive raw signals, the frequency range of [10 Hz, 300 Hz] was applied for band-pass noise filtering. Significantly poor raw signals that were difficult to identify clearly were deleted (e.g., signals recorded near 15 m and 26.5 m depths). Consequently, a total 418 shear wavelets met the quality requirements and were used for the V_s calculations.

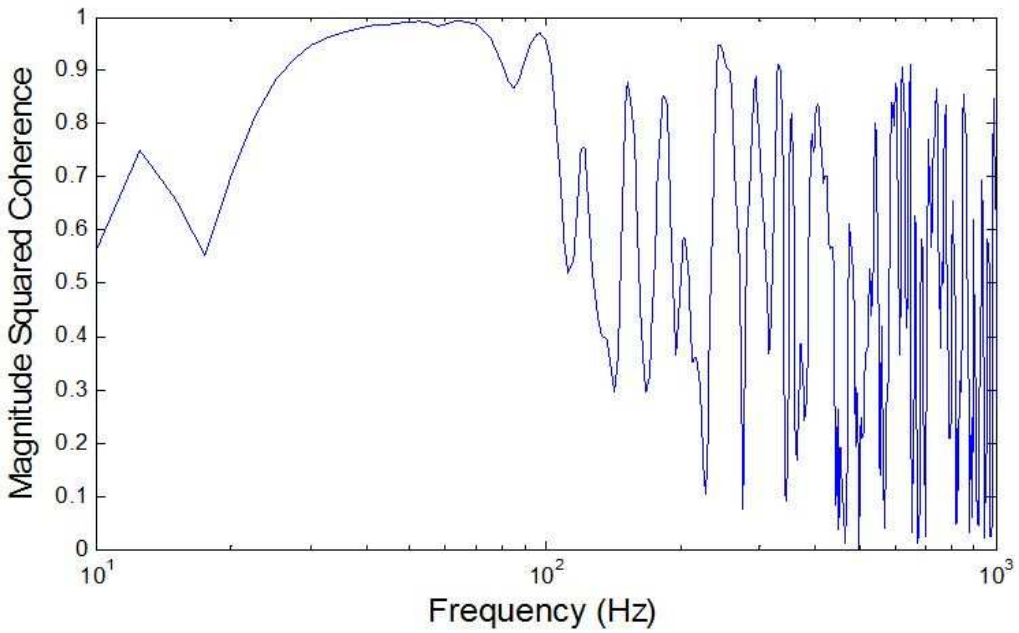

Figure 8.34. Coherence values evaluated from two consecutive raw signals recorded at 45.0 and 45.1 meter depth at Richmond, BC.

After signal processing of the continuous raw shear wave data at the Richmond site, the cross-correlation analysis was conducted in time domain. Figure 8.35 shows correlation coefficient values obtained from two consecutive filtered and windowed signals at 45.0 and 45.1 meter depth. A maximum *r value* of about 0.93 was observed at a Δt of 0.40 ms. In turn, the best value of Δt was also determined using power spectral density (PSD) in the frequency domain. Figure 8.36 compares auto-spectral densities evaluated from the noted PSD evaluation techniques based on the filtered signal recorded at 45.1 meter depth. Apparently, all techniques provide an identical peak frequency of about 35 Hz. Similarly, cross-spectral densities were examined from the periodogram (Welch method) which shows periodic tendency of signals. Figure 8.37 shows the cross-spectral density evaluated from two consecutive filtered signals recorded at 45.0 and 45.1 meter depth. The observed peak frequencies of both auto PSD (Figure 8.36) and cross PSD (Figure 8.37) are identical (i.e., 35 Hz).

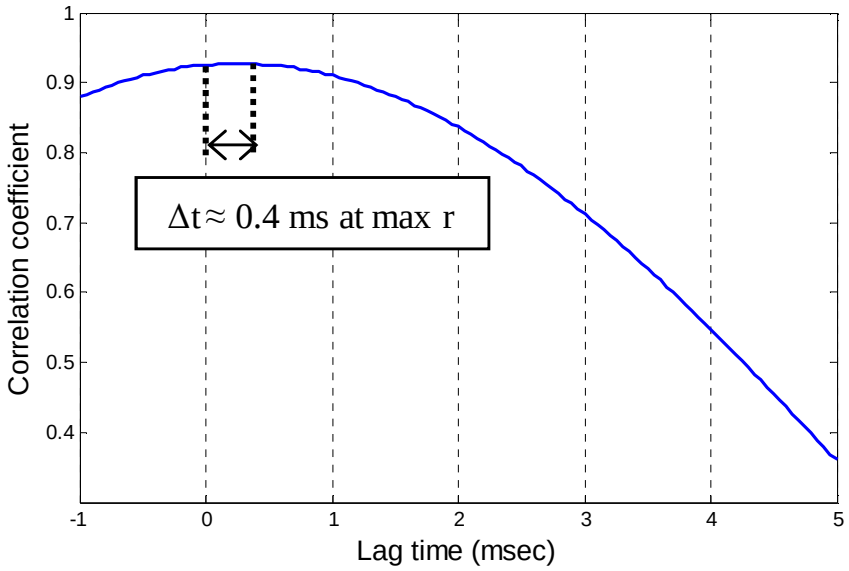

Figure 8.35. Magnitude of correlation coefficient (r) from two consecutive filtered signals at 45.0 and 45.1 meter depths at Richmond, BC.

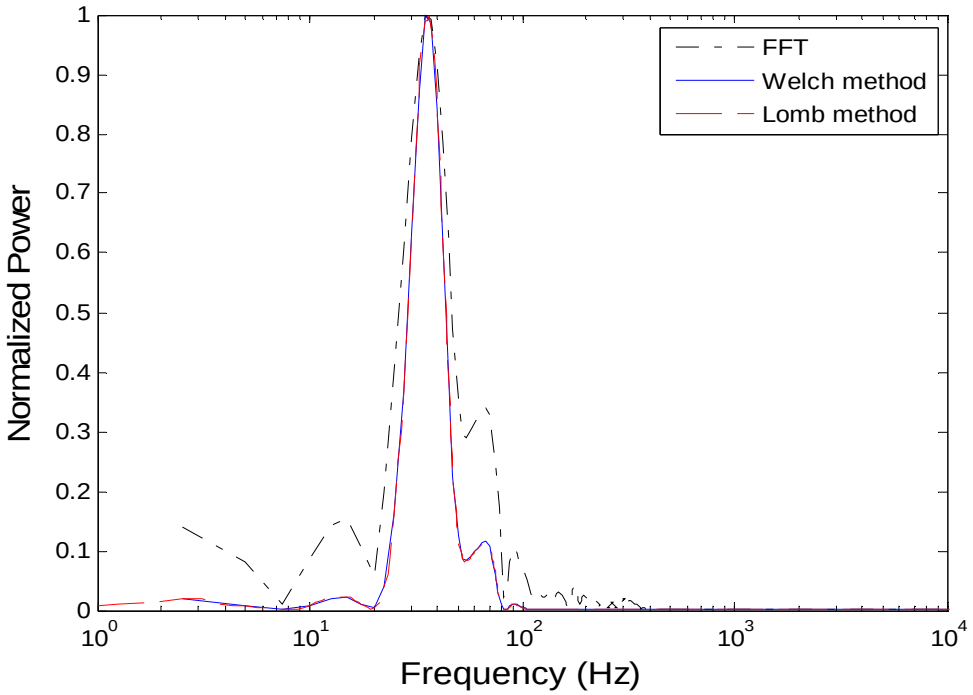

Figure 8.36. Normalized auto-spectral density estimated using various techniques (FFT, Welch method, Lomb method) for the filtered signal recorded at 45.1 meter depth at Richmond, BC (Note: Lomb method corresponds to LSSA technique).

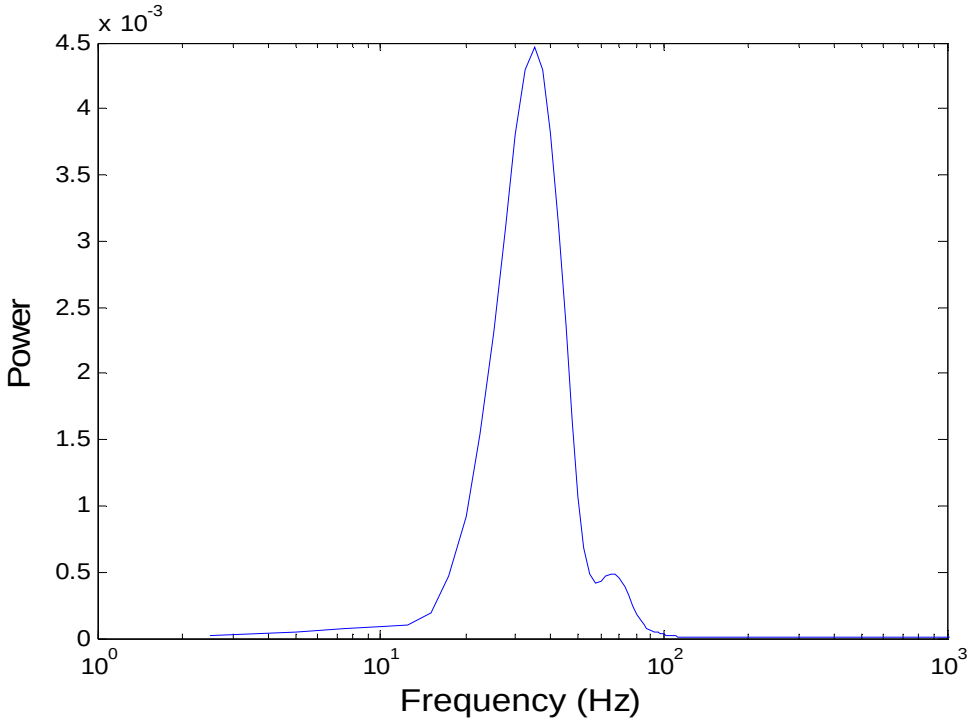

Figure 8.37. Cross-spectral density (periodogram) estimated from two consecutive filtered signals recorded at 45.0 and 45.1 meter depths at Richmond, BC.

For reference comparison and benchmarking purposes, conventional field V_s data were also obtained at the Richmond BC site including; 1-meter DHT interval V_s from SCPTu, 0.5-meter DHT interval V_s from SDMT, and coarser interval V_s from MASW surveys. As before, the continuous-interval V_s results were scattered and variable when the V_s profile was developed on the basis of matching each successive wavelet. In order to extract a reliable V_s profile, the noted zero-phase digital filtering technique was adopted and examined on its applicability again. Figure 8.38 shows the continuous V_s profiles evaluated from cross-correlation analysis in time domain and cross-spectral analysis in frequency domain with the special filtering technique; i.e., (a): 2^{nd} order, (b): 6^{th} order, (c): 10^{th} order. As the continuous V_s data adopt higher order running-mean filter, it is observed that the sensitive V_s profiles (i.e., cross-correlation and cross-spectral analysis) become well matched with the downhole reference V_s. The cross-correlation method shows rather large CiV_s values at very shallow depth. This may be due to boundary effects (e.g., near-field effect, reflection) that have influence on the shear wavelets recorded near the surface.

All available V_s results (i.e., CiV_s, 1-meter interval DHT, 0.5-meter interval SDMT, and MASW) at the Richmond site are compared in Figure 8.39. Although slight variants are observed due to lateral hetereogeneity and spatial variability between test locations, the V_s evaluations match very reasonably with overall comparable agreement. Values of the coefficient of determination (R^2) obtained from cross-correlation analyses (i.e., $r^2=R^2$) from continuous signal matchings are provided in Figure 8.39c. For a finale plot, the complete CiSCPTu sounding is given in Figure 8.40 showing the full continuous plots of q_t, f_s, u_2 and V_s readings throughout the 45 m depth.

Of special mention, it is also noteworthy to explain the sequential order and timing of the various tests made at the Richmond BC site, all performed by field crew and engineering staff of ConeTec at their office and yard facility. The SDMT and MASW data were acquired first to depths of 10 and 15 m, respectively. Later, the CiSCPTu was performed to 45 m. The data were conveyed to GT personnel, and initially, the shear wave wavelet data could not be interpreted with reasonable results, at least using traditional cross-correlation procedures. Later, after the raw data were carefully scrutinized, synthesized, and interpreted by the author, the resulting profile of Figure 8.40 was developed. Then, a request was made to David Woeller, president of ConeTec, to produce additional reference benchmark results on the shear wave velocity profile to 45 m using conventional geophysical methods. These data were obtained several months later by Ilmar Weemees of CT using a true-interval DHT system. The V_s interpretations from CiSCPTu are therefore a type of "class A" advance prediction, thus confirming the reliability of this approach.

On the other hand, an interesting observation was found by matching the raw continuous shear wave signals (Figure 8.33) and the final CPT plots (Figure 8.40). In the estimated sand layer between 10 and 30 meter depths, the raw continuous signals seem to have relatively significant noises due to cone vibration effects during advancement of the cone. Hence, the amount of noises captured on raw signals (e.g., signal-to-noise ratio) might be another means to distinguish sand and clay layers.

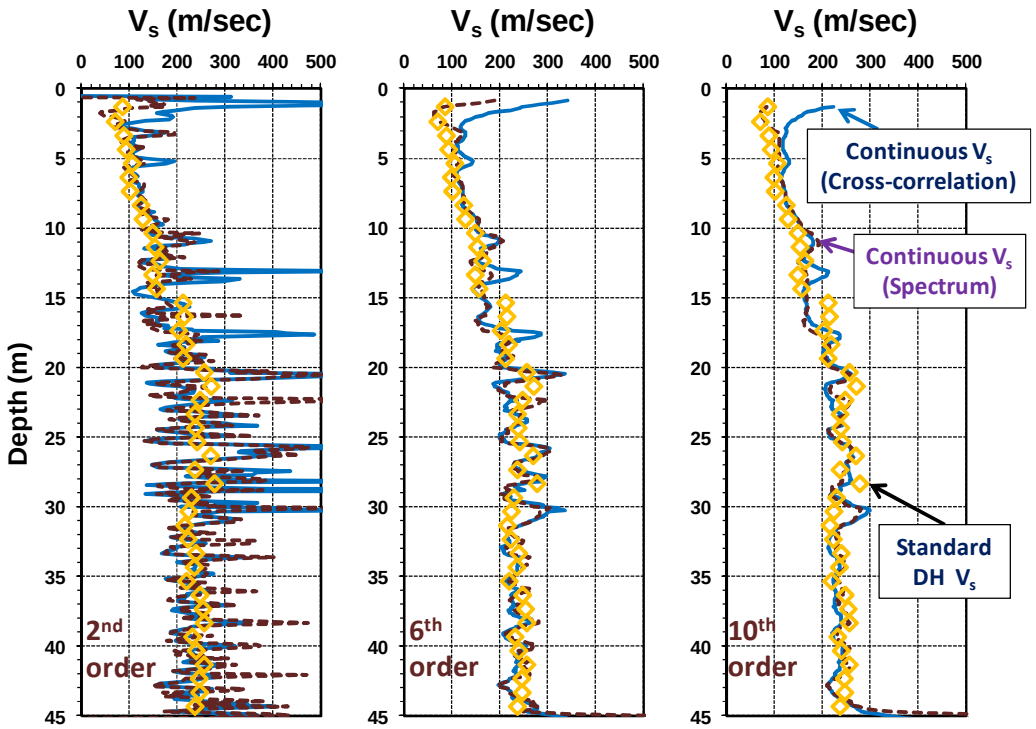

Figure 8.38. Continuous V_s evaluated from cross-correlation and cross-spectral analysis adopting different running-mean filters at Richmond, BC: (a) 2nd order, (b) 6th order, (c) 10th order.

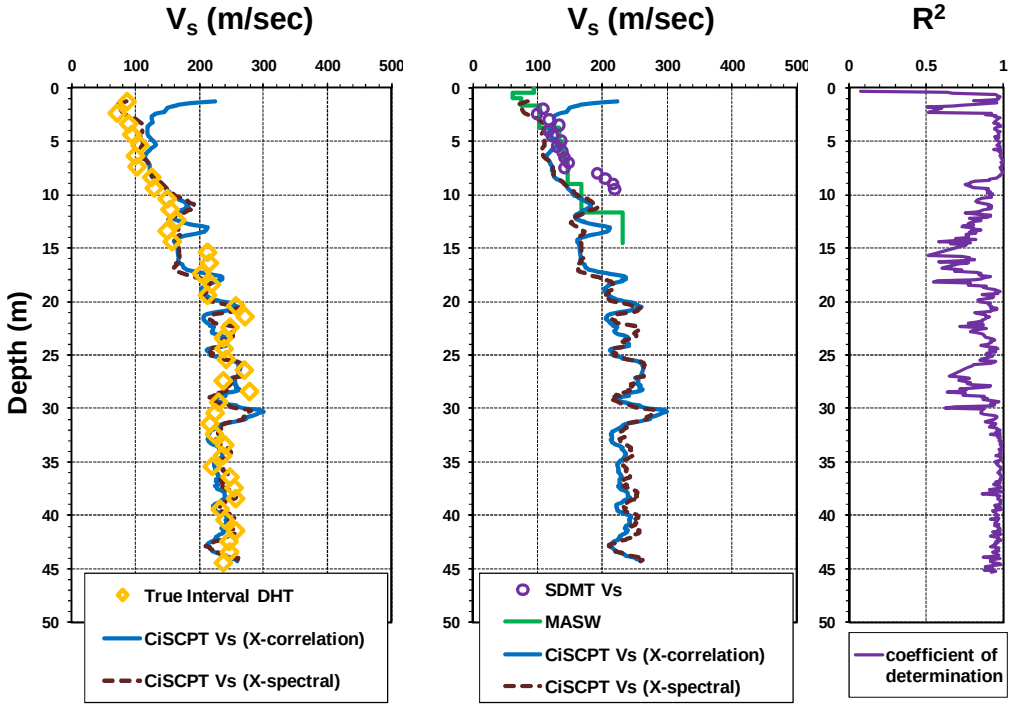

Figure 8.39. Comparison of various V_s data at Richmond BC site, including: downhole (DHT), seismic dilatometer (SDMT), Rayleigh waves (MASW), and continuous (CiSCPTu). The coefficient of determination (R^2) for continuous shear wave signals are shown in rightmost column.

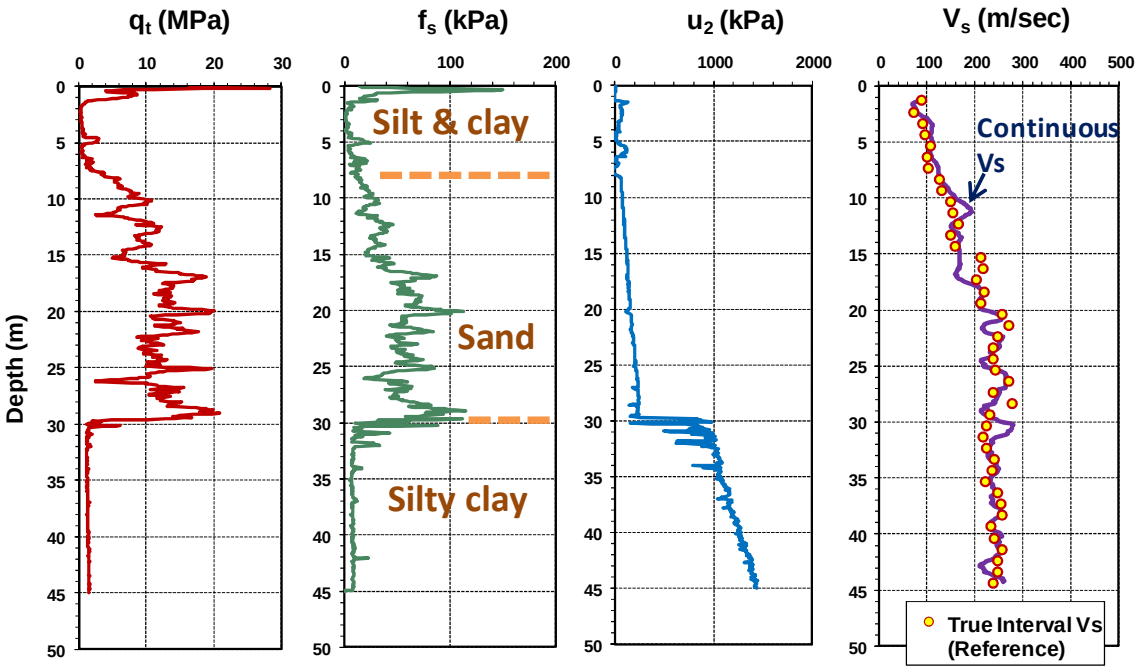

Figure 8.40. Summary results of continuous-interval seismic piezocone tests (CiSCPTu) in comparison with true-interval DHT shear wave velocity profile at Richmond, BC site.

8.6 Summary, Conclusions and Recommendation for Future Study

A new continuous V_s profiling technique using an automated surface seismic source coupled with cone penetration testing has been studied (Ku and Mayne 2012c). Compared to conventional downhole and crosshole geophysical methods, the continuous-interval seismic piezocone test (CiSCPTu) is considerably more efficient in field production time and a detailed V_s profile with depth can be obtained. In the test development, there were two important issues requiring special considerations: (1) use of a repeatable and consistent shear wave generating system, and (2) availability of a reliable means to interpret continuous wavelet data. With respect to the first issue, the recent development of an automatic seismic source named *RotoAutoSeis* makes it possible to deliver consistent and repeatable strikes at 1- to 10- second intervals during a constant rate of cone advancement at 20 mm/s.

In terms of the second issue, select signal post-processing techniques and different means of V_s interpretation were discussed. Due to the large numbers of wavelet data, automated V_s evaluation methods using cross-correlation in time domain and spectral density analysis in frequency domain were necessary. A zero-phase distortion filtering technique via a running-mean filter seems to mitigate the sensitivity of V_s evaluations. Field data from sites in Norfolk and Windsor, Virginia with contrasting shear waves in the upper and lower geologic formations were presented to illustrate the success of the approach in layered soil profiles. A third case study involving 45-m deep sediments in Richmond, British Columbia was presented where the CiSCPTu evaluations were made in advance of the reference benchmark DHT via true-interval procedure. In all 3 cases, the continuous shear wave profiles gave reasonable agreement with the benchmark values by conventional testing. An appropriate running-mean filter order can be determined by examining variations of other continuous CPT soundings.

Basically, this study presented a first look at continuous shear wave velocity measurements using seismic cone testing. The potential for finer and more detailed resolutions of V_s profiles and faster testing times in the field are partially offset by the need for more rigorous filtering and post-processing of wavelet signals and complexities in calculations. The V_s evaluation methods and data-processing techniques in this chapter should be verified by application to more sites. In future studies, use of true-interval geophone modules with this approach may help alleviate some of the aforementioned difficulties and improve the test procedures. Nevertheless, the potential and practical aspects of continuous shear wave velocity data should be further explored.

CHAPTER 9

SHEAR WAVE VELOCITY CHARACTERISTICS AT THE SAVANNAH RIVER SITE

9.1 Introduction

This section examines the V_s characteristics at the Savannah River Site, as introduced earlier in Chapter 2. Unusual in-situ V_s trends at the SRS APT site were discussed, specifically a trend showing V_s decreasing with depth in the upper 15 m followed by a constant V_s profile from 15 to 45 m. More details on site-specific investigations from field and laboratory dynamic measurements at SRS will be provided with final recommendations for further studies. Prior chapters have discussed the feasibility of advanced site investigations based on geophysical measurements that acquire directional and polarized V_s ratios (e.g., V_{sHH}/V_{sVH}), or anisotropic stiffness ratios, for assessing the geostatic K_0 stress state and/or stress history (i.e., OCD and/or YSR) at SRS. Therefore, it is prudent to evaluate existing V_s data and examine the shear wave characteristics at the DOE site in consideration of future studies.

9.2 In-Situ Geophysical Measurements at SRS

9.2.1 Comparison of Various In-Situ V_s Results at SRS

The stress-dependent behavior of shear waves in soil influences the trend of the measured in-situ V_s profile. Usually, the magnitude of field V_s generally increases with depth because they track with increasing effective overburden stress. The magnitude of V_s also increases with decreasing void ratio in soils. In contradiction, the shear wave profiles at SRS show distinctly contrasting trends. From a total of 87 downhole-type V_s

profiles (Figure 2.8) at the SRS APT, the corresponding mean V_s profile is shown in comparison with general V_s trends suggested by Lew and Campbell (1985) in Figure 9.1. A similar comparison is made with trends given by Andrus et al. (2007) in Figure 9.2.

Whereas many sites worldwide show a general increase of V_s with depth (e.g. Brown et al. 2002; Foti 2012), the representative profile at the SRS APT, in fact, it shows an opposite trend. The observed SRS data shows V_s decreasing with depth in the upper 15 m of overburden soils. After 15 m depth, V_s becomes almost constant with depth throughout the DHT depth investigations of 50 m.

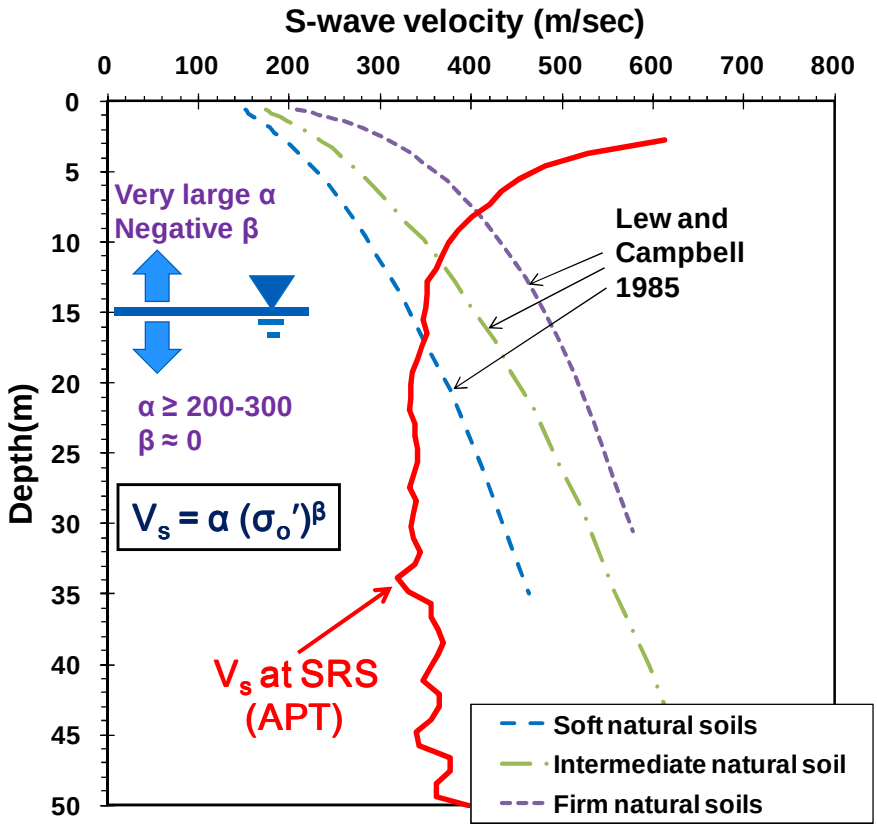

Figure 9.1. Comparison of anticipated V_s profiles from empirical trends noted by Lew & Campbell study (1985) with mean DHT V_s profile at SRS APT.

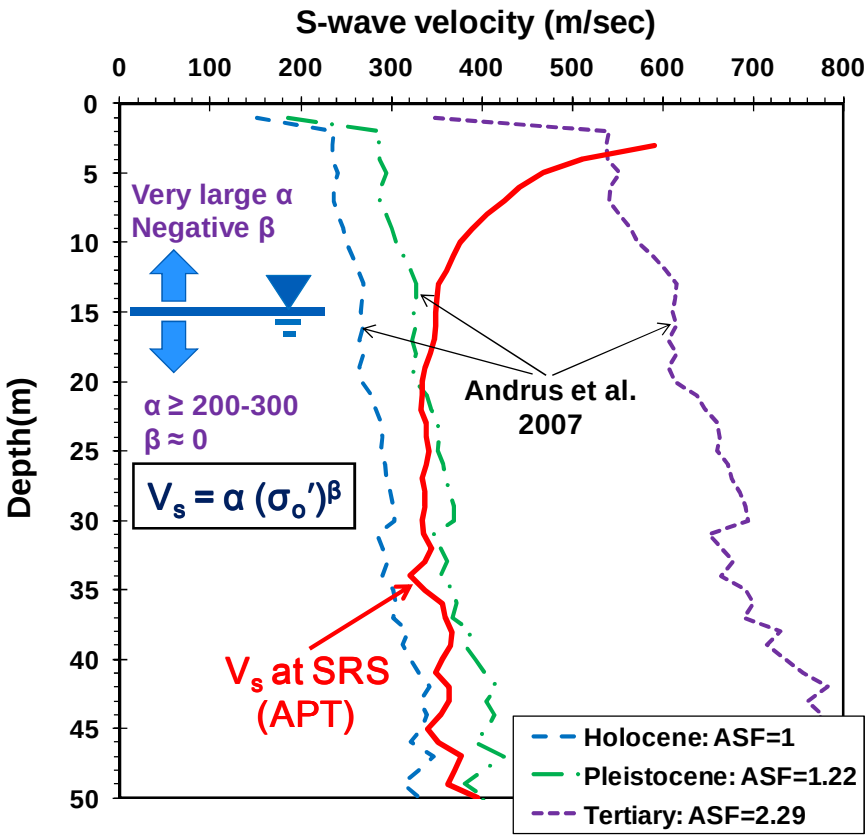

Figure 9.2. Comparison of expected V_s profiles from empirical equations noted by Andrus et al. (2007) with mean DHT V_s profile at SRS.

Towards a comprehensive study on in-situ shear wave velocity (V_s) profiles at SRS, recent series of Rayleigh wave measurements (SASW) were conducted (by Dr. Rix and GT graduate students) and these are compared with the downhole type mean V_s profile in Figure 9.3a for the upper 70 m. Overall, the V_s magnitudes seem comparable for both methods, excepting the uppermost 10 to 15 m. This upper zone consists of unsaturated sediments of the Altamaha formation and Upland Terrace Deposits. Here, the seasonal variations of capillarity, desiccation, infiltration, and degree of saturation could easily have affected the results depending upon the actual conditions during the specific days of the tests. At the Sand Borrow Pit, the V_s magnitudes from SASW are more

difficult to compare directly because the surface elevations are different because of 15 m of excavation. Nevertheless, the results appear comparable. Figure 9.3b provides averaged shear wave profiles at other SRS area locations (data summarized by Li et al. 2010). Most V_s data were downhole type (i.e., 579 SCPTu, 4 SDMT, 2 borehole-type DHT), although some are also derived from other techniques (32 crosshole and 11 suspension logger). It is observed that the in-situ V_s profiles show considerably similar trends across the region.

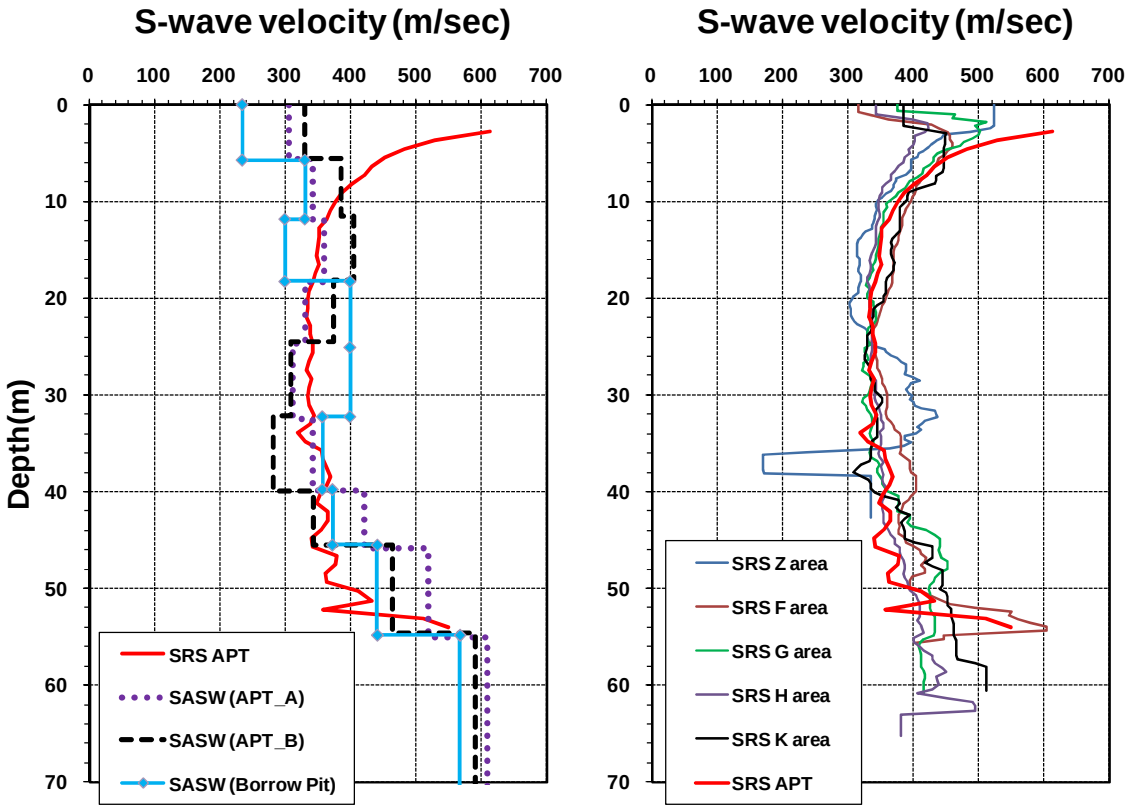

Figure 9.3. (a) Comparison of SASW and downhole type V_s profiles at SRS APT site, (b) comparison of averaged V_s profiles (mainly SCPTu data) at various SRS locations.

For the comprehensive investigations at SRS, crosshole V_s and suspension logging V_s measurements were also obtained beyond 90 meter to the deeper depths of 150 meter

(SRS report 2005). Figure 9.4 compares those V_s data with the downhole-type V_s and SASW measurements. In the upper 50 meter depth, the crosshole V_s are rather similar to the downhole-type V_s. However, the interpreted suspension logging data have coarser resolutions and rather lower values. In the much deeper and older sediments such as Blue Bluff Marl and/or Warley Hill beyond 50 meter depths, the Rayleigh wave measurements show the largest magnitudes of V_s in the profile.

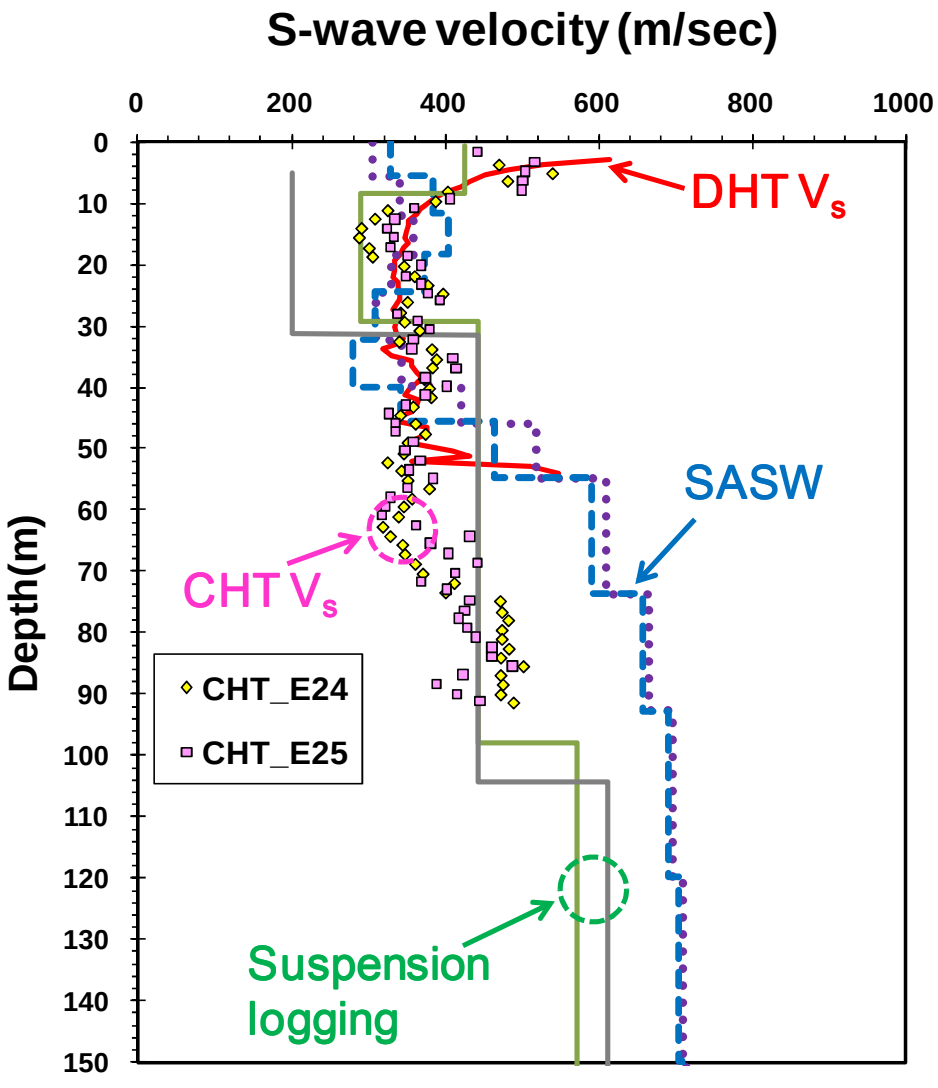

Figure 9.4. Comparison of various types of V_s measurements to 150 meter depths at SRS.

9.2.2 Stress-Dependent Behavior of In-Situ V_s at SRS

For uncemented geomaterials, a general V_s-stress relationship was given in power law form: $V_s = \alpha \cdot (\sigma_c')^{\beta}$ where the coefficient α and exponent β are material constants and σ_c' is the effective confining stress level (units-dependent). Assuming the confining stress (σ_c') as mean normal stress (σ_o') under isotropic stress state conditions, it was shown that the coefficient term α (m/s) is inversely proportional to the exponent β term according to relationship: $\beta \approx 0.36 - \alpha/700$ (Santamarina et al. 2001). Actually, the exponent β term represents the stress-dependent behavior of V_s in soils. Whereas the exponent $\beta = 0.25$ has been generally adopted as an empirical constant value based on laboratory testing of clean quartz-silica sands, it was noted that both field and laboratory data (e.g., Weiler 1988) have relatively wider ranges for both α and β, as detailed in Chapter 3.

In terms of V_s-σ_o' relationships, two constants α and β values are investigated using the mean V_s profiles at SRS. The groundwater table is located at approximate 15 m depth. Figure 9.5 shows the plot of field mean V_s versus σ_o' obtained from 15 to 45 meter depths at SRS APT (Note: assumed $K_0 = 0.5$ for σ_o'). The mean V_s profile below 15 meters is nearly constant with depth (Figure 9.1), thus result in a considerably high coefficient α value and low exponent β value which is close to 0. In the same manner, other SRS sites were also assessed based on their field V_s profiles (equivalent depth range from 15 meters to 45 meters) shown in Figure 9.3b. Then, the site-specific relationships between α and β values at SRS sites are compared with other data (Figure 3.13) in Figure 9.6. Even though the in-situ data appear to have relatively wide ranges for both constants α and β, some SRS data are notably deviated from other data. The observed trends seem definitely different from normal stress-dependent behavior of geomaterials. Surprisingly,

the V_s profiles decrease with depth within the shallow upper 15 m. These trends provide a significantly larger α coefficient and corresponding negative β exponent which are not commonly observed at many "well-behaved" sites.

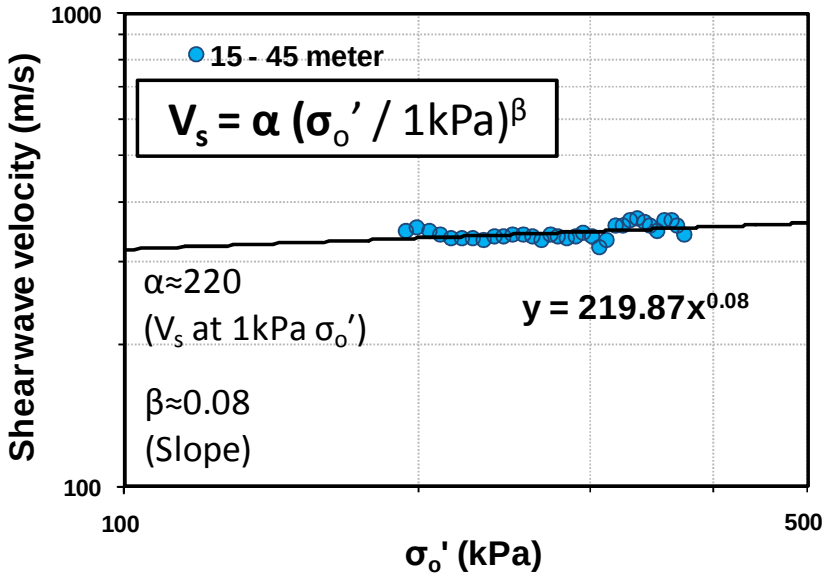

Figure 9.5. Relationship between in-situ V_s and σ_o' at SRS ATP site (data source: 1-meter interval V_s data between 15 and 45 meter depth in Figure 9.1).
Note: assumed $K_0 = 0.5$ for σ_o' (Burns and Roe Enterprises Inc. 2001)

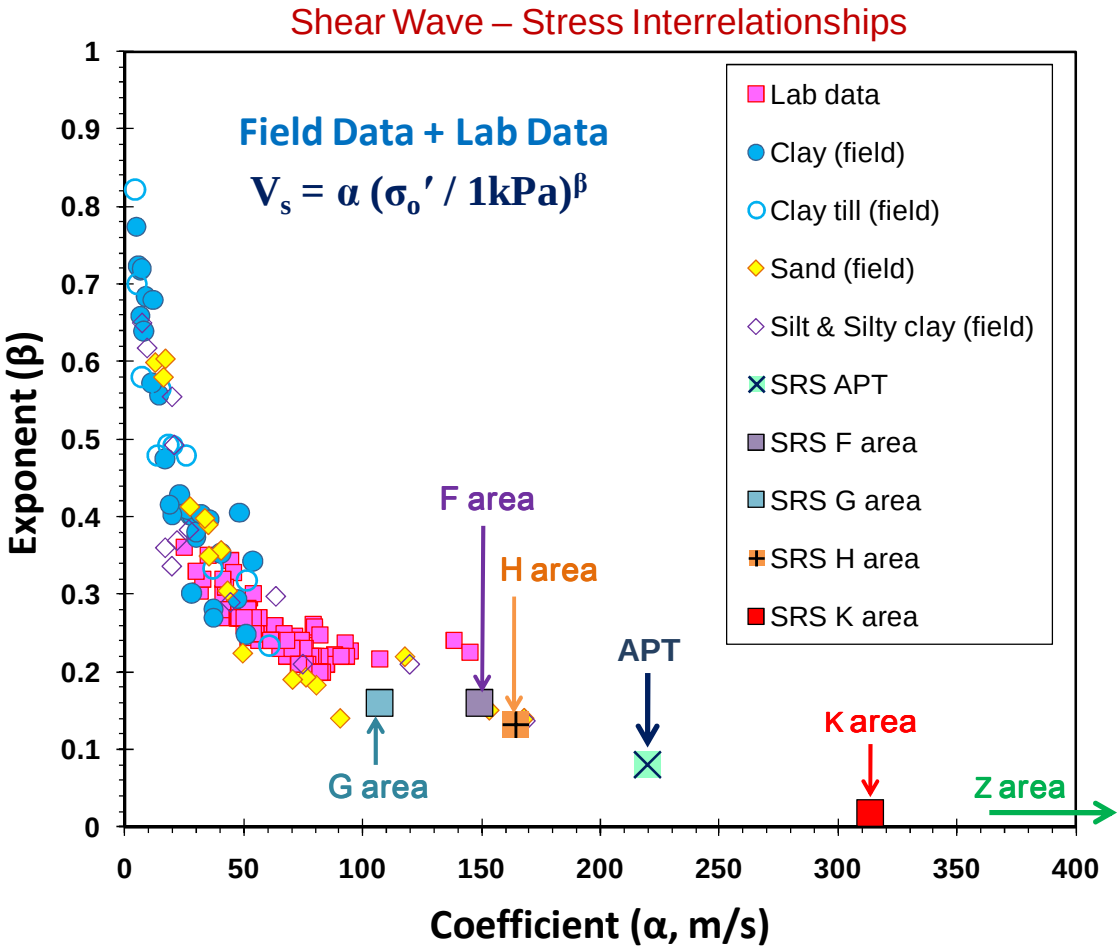

Figure 9.6. Relationship between shear wave coefficient (α) and exponent (β) in soils including data from several SRS sites.

9.2.3 Expected Causes for Unusual In-Situ V_s at SRS

The field V_s trends at SRS are different from many sites, perhaps due to one of more effects: cementation, desiccation, age, diagenesis, and/or dissolutioning followed by collapse of the upper soil column. No clear single explanation is cited because of the complex geologic conditions that prevail. Some possible scenarios are discussed subsequently.

First, the cementation effect can increase the magnitude of V_s and its corresponding G_0 (Saxena et al. 1988, Fernandez and Santamarina 2001). The apparent degree of cementation at SRS was quantified using the ratios of G_0 to q_t measurements and suggested boundaries for uncemented and cemented soils per Schnaid et al. (2004), as discussed in Chapter 2 (Figure 2.10). The uppermost soils of the Upland Terraces and Altamaha Formation fit within and even above the "cementation" threshold. Thus, cementation may have resulted in at least a partial role in the higher V_s measurements at uppermost depths.

A desiccated vadose zone due to capillarity and restricted groundwater flow may have also influenced the V_s trends. At SRS, the vadose zone extends from the ground surface down to approximately 15 meter depth at which elevation the groundwater table lies. In fine grained soils, the vadose zone might be fully saturated by large capillary forces. Much of the overburden soils at SRS classify as a clayey fine-medium sand based on the hydrometer analyses of materials in the fines content portion. Surprisingly, the sand fraction is uniformly graded in the fine-medium sand size range, however, below the No. 200 sieve, very little silt sizes are found and a predominance of clay or colloidal particles occur (e.g., grain size distribution curves in Figure 2.6). This results in gap-graded sands in the soil column. Therefore, high capillary forces are plausible in the SRS sandy soils due to the considerable plastic clay fines content. In fact, the specific surface of these soils is very high considering they are sands (Cha and Santamarina 2012). Consequently, the process of desaturation can have significant changes on the V_s measurement. For instance, Figure 9.7 shows V_s is highly variable depending on the degree of desaturation (Cho and Santamarina 2001). A low degree of saturation can result

in considerably high magnitude V_s that is anywhere from about 1.5 to as much as 20 times than for a fully-saturated state Hence, the decreasing V_s trends in the upper 15 meters might be explained in part by de-saturation effects on V_s.

Another possible scenario for the unusual V_s profile at SRS includes the following geologic tale: an initial highly overconsolidated soil profile with high V_s magnitudes followed by dissolutioning of the Santee at 45 m and subsequent collapse of the overlying soil column. Arching effects may play an additional or secondary role. As noted earlier, SRS contains interbedded layers including a special geological formation named Santee. The Santee alterations and voids/cavern formation by dissolutioning of calcium carbonates may have undermined the overlying overburden soils, thus altering the geostatic stress state. This scenario can be extended to collapse of soil column as well as stress alteration and/or reduction that might have affected the current V_s profile. The scenario would be expected to gradually decrease the V_s magnitudes with depth if the stress reduction is more significant near the deep Santee formation including soft zone. In terms of high yield stress ratio (YSR) or overconsolidation ratio (OCR), it has been recognized that G_0 increase with degree of overconsolidation (Chapter 4). The uppermost soil formations at SRS show relatively high YSR/or OCR values due to combinatorial effects of erosion, desiccation, wetting and drying cycles, and groundwater fluctuations. An apparent increase in YSR might also be attributed to ageing. High YSR would be expected to increase the V_s magnitudes particularly at shallow depth. Correspondingly, the K_0 stress state may have reduced to the active failure state (K_A) in collapsed locations, while in other locations the area may remain intact due to arching. Such a scenario may

explain the wide variability of σ_p' values and other geotechnical parameters across the SRS area at same elevations.

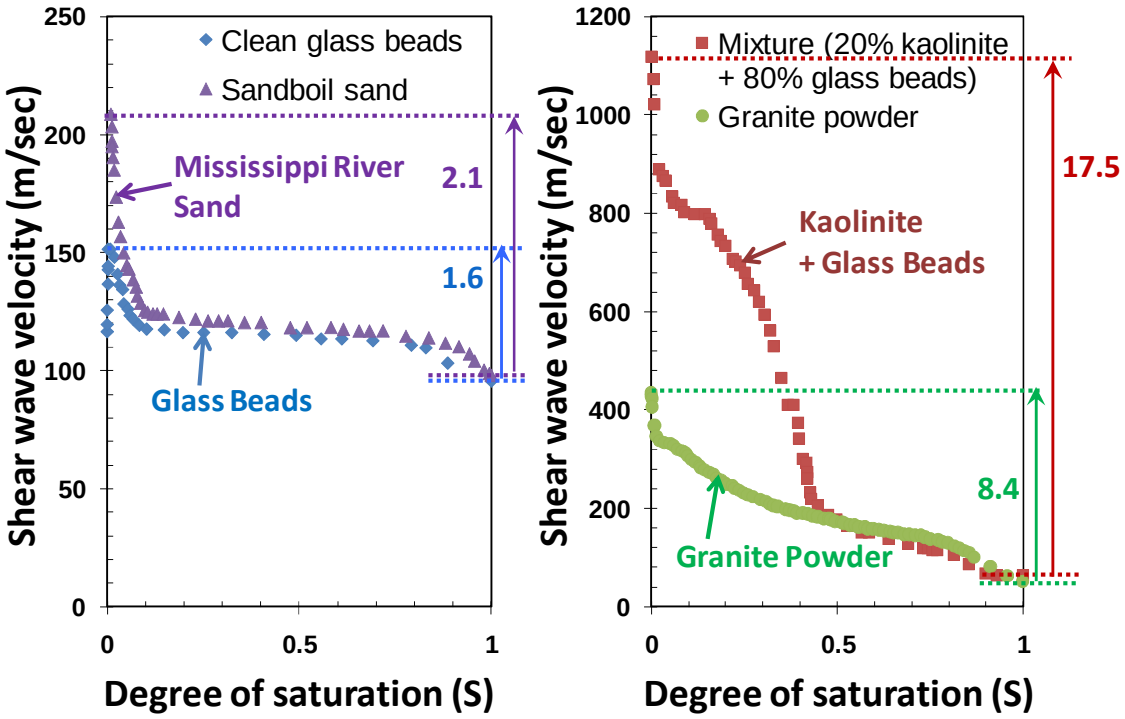

Figure 9.7. Effects of degree of saturation on shear wave velocity (redrawn from Cho and Santamarina, 2001).

9.3 V_s-Stress Relationships from Laboratory Data at SRS

In this section, the relationships between shear wave velocity (V_s) and stress state at SRS are investigated based on laboratory resonant column (RC) and bender element (BE) test data. The RC data were obtained by Stokoe et al. (1995). Specimens from the RC lab series were isotropically consolidated to an initial effective stress, σ_o'. Figure 9.8 shows the V_s-σ_o' relationships and specimen information such as soil types, sample depth, and each geologic unit (Upland, Tobacco Road, Dry Branch, and Warley Hill). At this time, data from the Santee formation are not included for the analysis. Most samples

consist of sands and sand mixtures, except one clay specimen which was obtained from within the Dry Branch formation.

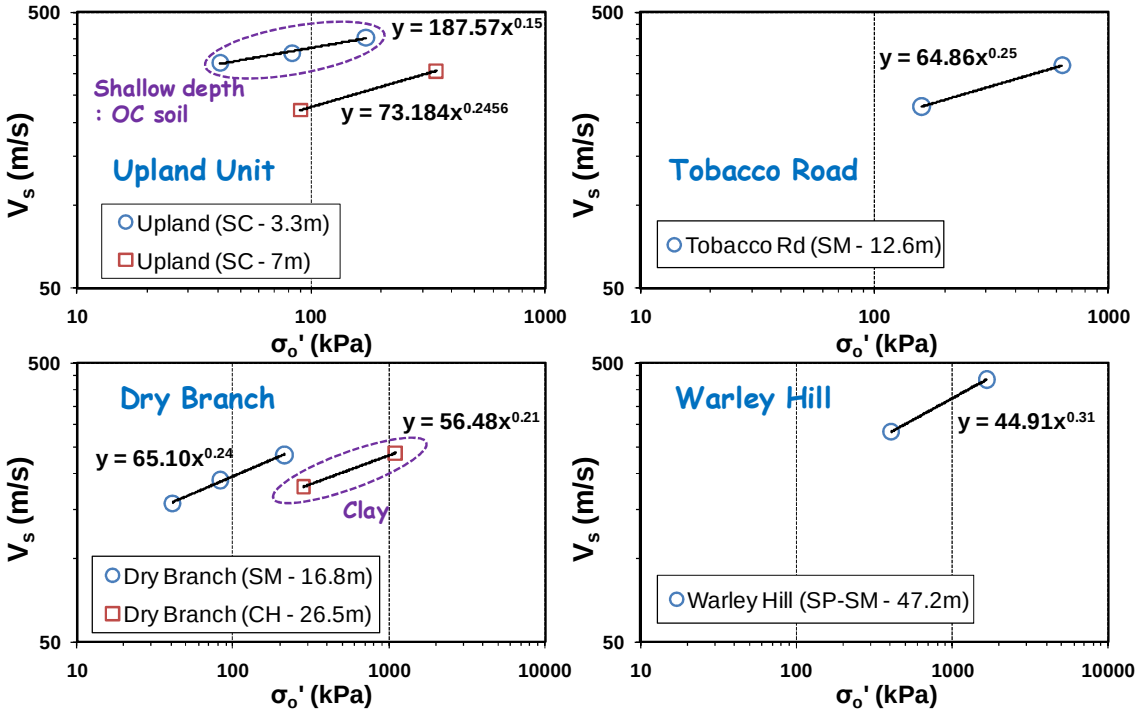

Figure 9.8. V_s-σ_o' relationships based on RC test data for various SRS geologic formations (data from Stokoe et al. 1995).

In Figure 9.9, sand mixtures from all of the SRS soil column units are examined together. In terms of the V_s-σ_o' relationships, the sand mixtures show similar behavior. The sand specimen obtained from the very shallow depth of Upland Unit is excluded, because it deviates from the general trend line most likely due to high overconsolidation, desiccation, and/or cementation. The general relationship based on RC data obtained from the selected upper 40-m SRS soil column is as follows:

Equation (9.1) $V_s = 61.12 \cdot \sigma_o'^{0.262}$

where V_s = shear wave velocity (m/s) and σ_o' = mean effective stress (kPa).

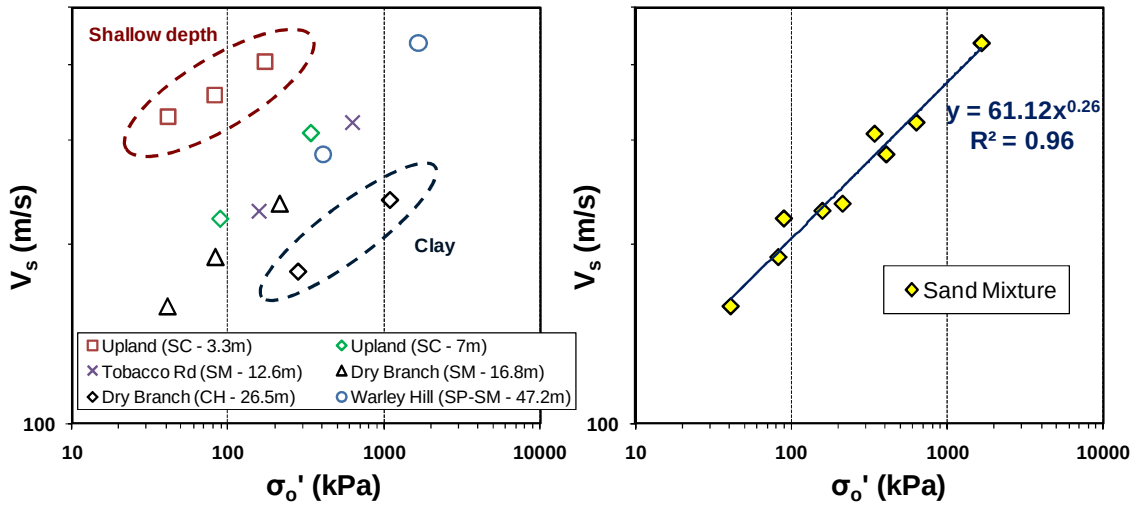

Figure 9.9. V_s-σ_o' relationships based on all sand mixture samples except one specimen obtained at shallow depth (data from Stokoe et al. 1995).

The RC data are compared with recent BE test data in Figure 9.10. The BE data were obtained from consolidation tests with special instrumentation at GT reported by Cha (2012). These samples consist of calcareous soils (calcite + quartz) and crushed to pass sieve #10 and retained on sieve #100. It is necessary to cautiously examine the dissolution process (Calcite content is dissolved by acetic acid), and loading-unloading steps for the BE test series. The V_s-stress relationships for the BE data are as follows:

Before dissolution

Equation (9.2) $V_s = 45.45 \cdot \sigma_v'^{0.327}$ for initial loading step (BE data)

Equation (9.3) $V_s = 115.78 \cdot \sigma_v'^{0.158}$ for unloading step (BE data)

After dissolution

Equation (9.4) $V_s = 28.18 \cdot \sigma_v'^{0.377}$ for loading step (BE data)

Equation (9.5) $V_s = 212.88 \cdot \sigma_v'^{0.076}$ for unloading step (BE data)

where V_s (m/s) and σ_o' (kPa).

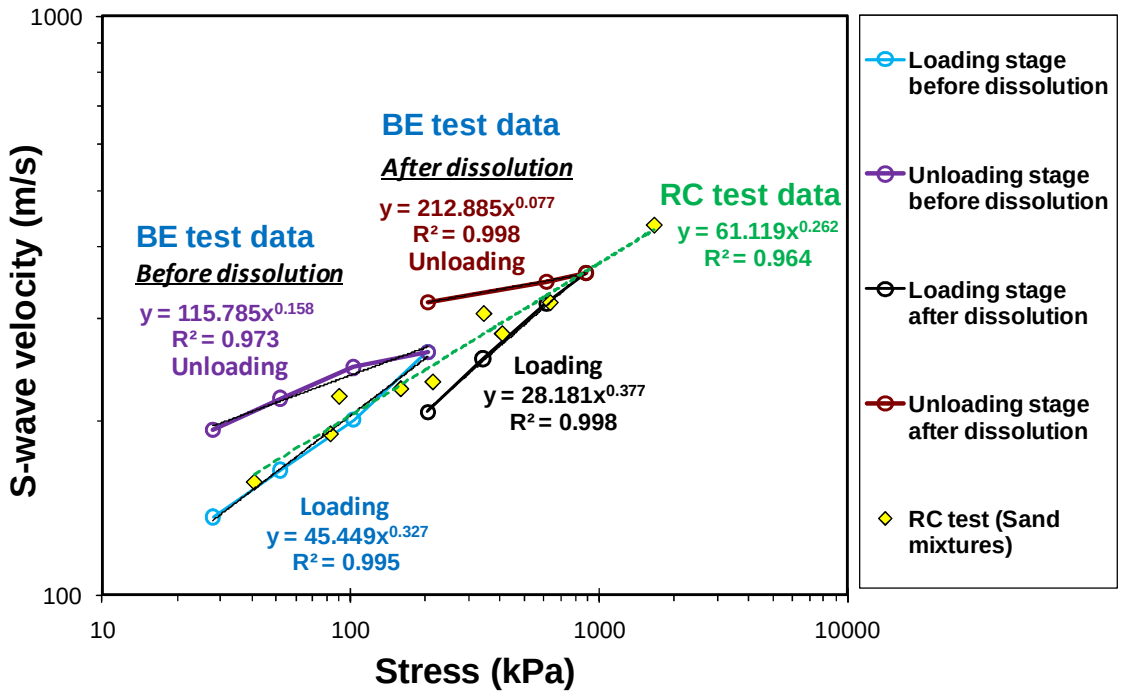

Figure 9.10. Comparison of V_s-stress relationships derived from RC data and BE data including dissolution process. Note: BE data obtained by Cha and Santamarina (2012) at Georgia Tech.

In the log V_s versus log stress plots, it is noted that the slope (i.e. stress exponent term) of RC data is between the loading steps and the unloading steps regardless of dissolution process. Using the form proposed by Santamarina et al. (2001), Figure 9.11 shows the coefficient (α) and exponent (β) values obtained from SRS RC and BE data with other laboratory test data given in Figure 3.11. Whereas the BE data under loading steps have small α and large β values, conversely the BE data under unloading stage seem to have relatively large α and small β. Contrary to some in-situ data which deviate from apparent general trends of geomaterials, the laboratory data seem to provide relatively reasonable results in terms of stress-dependent behavior. For further investigations on the V_s-stress relationships, the effects of void ratio (e_0) and yield stress ratio (YSR= σ_y'/σ_{vo}')

are considered together based on the BE data (Figure 9.12). The following equations are derived from multiple regression analysis:

Equation (9.6) $V_s = 46.64 \cdot \sigma_v'^{0.207} \cdot e_0^{-1.3}$ for all loading steps (BE data)

Equation (9.7) $V_s = 60.90 \cdot \sigma_v'^{0.123} \cdot e_0^{-1.87}$ for all unloading steps (BE data)

Equation (9.8) $V_s = 48.53 \cdot \sigma_v'^{0.197} \cdot e_0^{-1.35} \cdot YSR^{0.099}$ for all steps (BE data)

where V_s (m/s) and σ_o' (kPa).

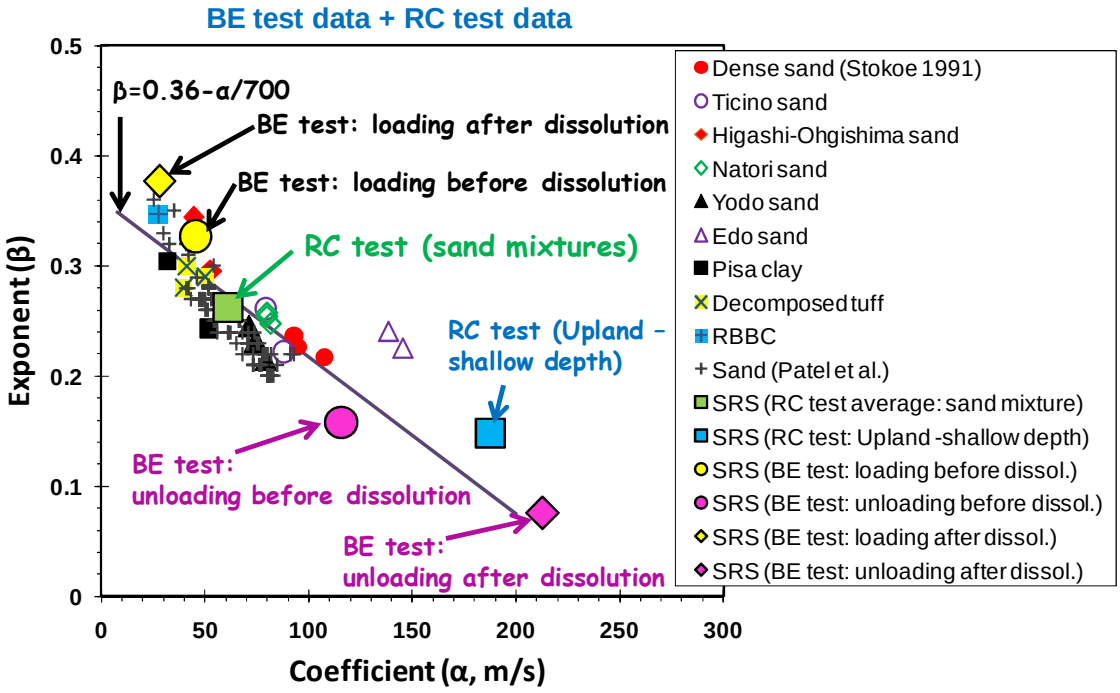

Figure 9.11. Shear wave velocity terms: coefficient (α) and exponent (β) plots for SRS RC and BE data compared with various reported soil samples (RC data from Stokoe et al. 1995; BE data from Cha and Santamarina 2012). Note: relationship: $V_s = \alpha \cdot (\sigma')^{\beta}$.

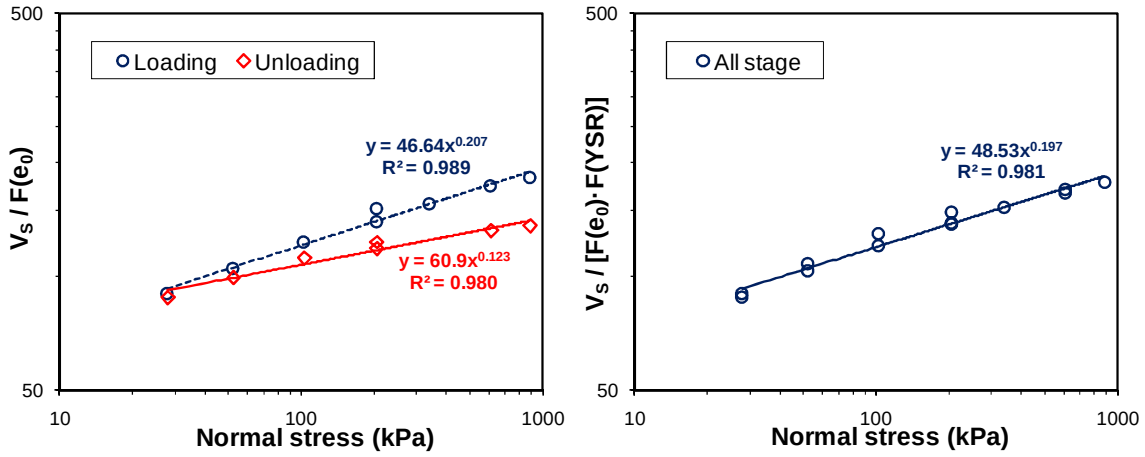

Figure 9.12. (a) V_s-stress relationships considering the effect of void ratio; (b) V_s-stress relationship including the effects of void ratio and yield stress ratio based on bender element data (BE data from Cha and Santamarina 2012).

Note: $F(e_0) = e_0^{-x}$, $F(YSR) = YSR^{0.099}$

9.4 Laboratory G_0 versus In-Situ G_0 Measurements at SRS

With consideration of the potential discrepancy between field and laboratory G_0 measurements, the G_0-stress relationships at SRS were examined based on the downhole-type in-situ V_s profile from the SRS APT site, laboratory RC, and lab BE test data. In Figure 9.13, the field G_0 is compared with laboratory RC data using undisturbed samples. It is observed that G_0-σ_o' regression line from RC sand mixture data is located below the field G_0 measurements. The regression line is expressed by:

Equation (9.9) $\quad G_0 = 7.62 \cdot (\sigma_o')^{0.52}$; $R^2 = 0.96$, $n=9$

where σ_o' is effective mean stress in kPa and G_0 is in MPa. The discrepancy seems significant at low stress conditions possibly due to cementation, desiccation, and/or high degree of overconsolidation. The magnitudes of G_0 are relatively close at lower Tobacco Road, Dry Branch, and Santee Formation, yet the field G_0 values are overall larger than the laboratory G_0 by more than about 25%. Interestingly, the laboratory G_0 measurements

of a sand specimen sampled at shallow depth (3.3 meter) have large magnitudes which are close to the field G_0 under low stress level.

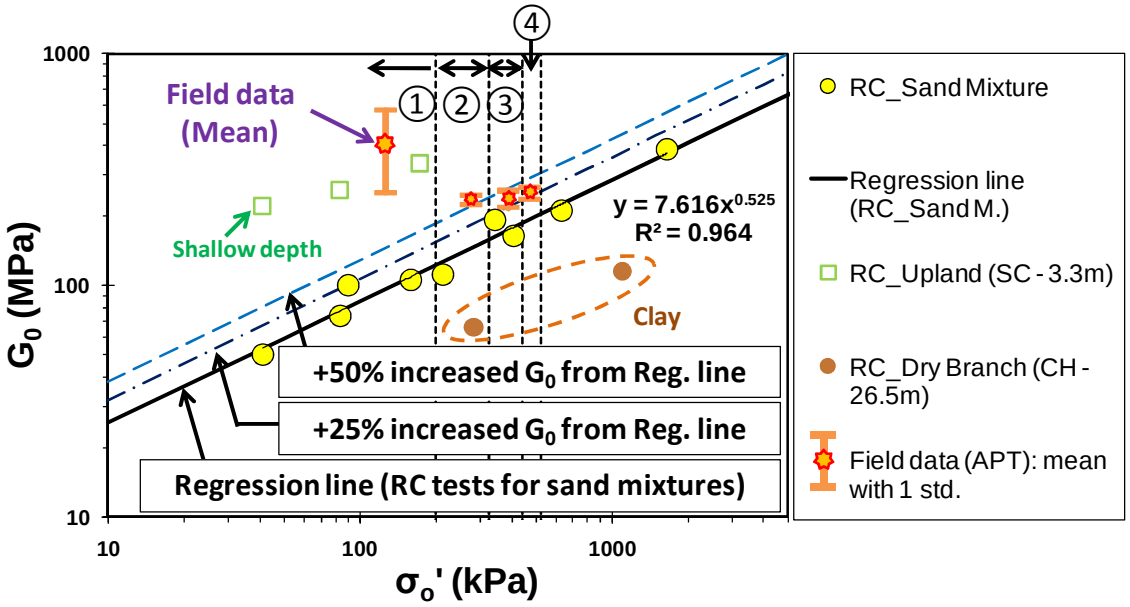

Figure 9.13. Comparison of laboratory G_0 (RC data) and field G_0 evaluated from V_s profile at SRS APT site. *Note: approximate geologic units for field G_0 −① Upland Unit, ② Tobacco Road, ③ Dry Branch, ④ Santee formation; 1 std. = 1 standard deviation.

From the laboratory BE data, Figure 9.14 shows the value of G_0 normalized by void ratio function, specifically: $F(e) = e_0^{-2.8}$, for the reconstituted calcareous specimen obtained at SRS under loading steps. Multiple regression analysis was conducted to determine the most appropriate expression in terms of the void ratio and stress. The derived regression equation is as follow:

Equation (9.10) $$[G_0/\ e_0^{-2.8}]_{lab} = 6.04\cdot(\sigma_v')^{0.49};\ R^2 = 0.98,\quad n = 8$$

where σ_v' = effective vertical stress in kPa and G_0 is in MPa unit. For comparison, the field G_0 value was normalized by the same void ratio function for a representative field

void ratio $e_0 \approx 0.75$. In Figure 9.14, it is not necessary to concern sampling effect issues because the laboratory G_0 were measured based on unaged reconstituted specimens. However, it will be reasonable to consider aging effects on the soil stiffness. The increase in G_0 with time is quantified by the following parameter (Anderson and Stokoe 1978):

Equation (9.11) $$N_G = \frac{\Delta G_0}{G_0(t = t_{ref}) \times \log(t_g / t_{ref})}$$

where, t_g = geologic time, t_{ref} = reference time, ΔG_0 = change of shear stiffness between t_g and t_{ref}, $G_0(t=t_{ref})$ = small-strain shear stiffness at a reference time. Based on the aforementioned normalized G_0 expression on the SRS reconstituted specimen, the aged natural SRS calcareous soil could be expressed as follow:

Equation (9.12a) $$[G_0/ e_0^{-2.8}]_{aged\ soil} = [1 + N_G \cdot \log(t_g/t_{ref})] \cdot 6.04 \cdot (\sigma_v')^{0.49}$$

where, σ_v' is effective vertical stress in kPa and G_0 is in MPa, t_g = 40 million years for SRS soils and t_{ref} = 1 day. For dimensional consistency, Equation 9.12a can be expressed:

Equation (9.12b) $$[G_0/ e_0^{-2.8}]_{aged\ soil} = [1 + N_G \cdot \log(t_g/t_{ref})] \cdot 577 \cdot (\sigma_v')^{0.49} \cdot (\sigma_{atm})^{0.51}$$

where σ_{atm} = atmospheric pressure (100 kPa), G_0, σ_v', and σ_{atm} are in same stress units. Aging effects in soils have been examined in prior studies (e.g., Schmertmann 1991, LoPresti et al. 1996). Values of aging coefficient N_G from various published sources have been summarized by Santagata and Kang (2007). In Figure 9.14, prediction lines adopting N_G = 0.05 and 0.10 are provided. It is observed that the field data in Tobacco Road, Dry Branch, and Santee formation are located near the two prediction lines (N_G = 0.05, 0.10).

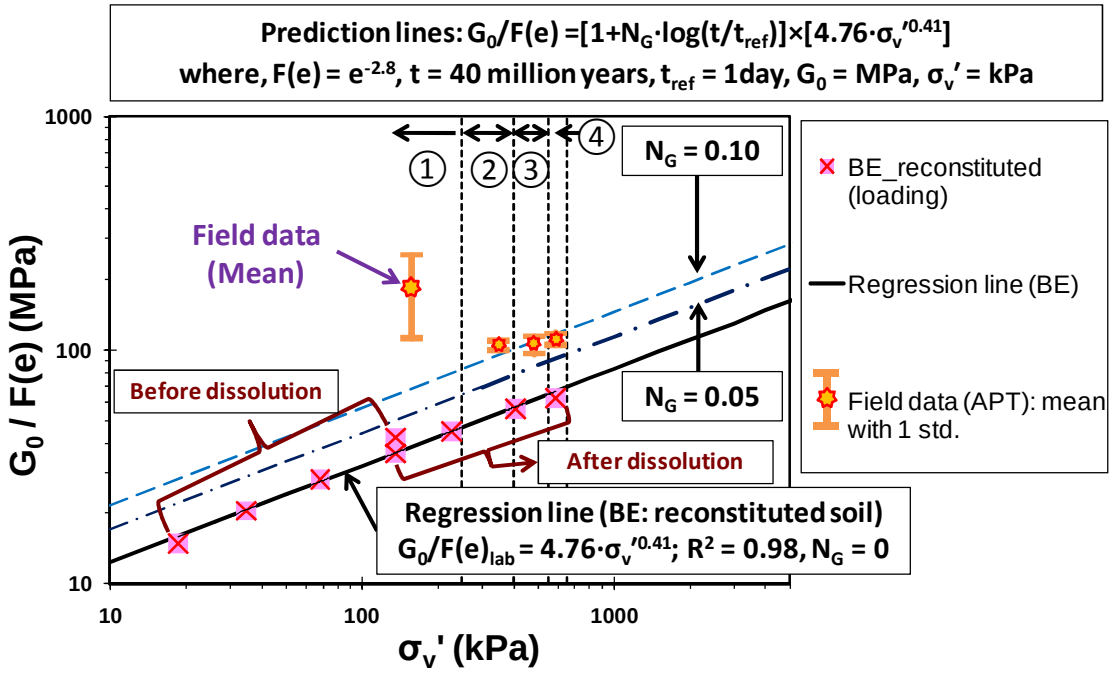

Figure 9.14. Comparison of laboratory G_0 (BE data) of reconstituted calcareous soils and field G_0 evaluated from V_s profile at SRS APT. For unaged reconstituted specimens, additional prediction lines considering aging effect are provided (N_G = 0.05, 0.10). *Notes: approximate geologic units for field G_0 −① Upland Unit, ② Tobacco Road, ③ Dry Branch, ④ Santee formation; 1 std. = 1 standard deviation.

9.5 Empirical V_s-CPT Relationships at SRS

Considering the special complex geologic conditions (e.g., very old soil deposits, cementation, calcareous soils, desaturation, possible stress alteration in upper soil column due to dissolutioning) and their influences on field test measurements at the SRS site, it is necessary to examine site-specific correlations between V_s and CPT resistances.

9.5.1 V_s Prediction Using Available Soil Correlations

In 2011, a series of SCPTu soundings were conducted at the SRS K-site by Lankelma Group. To investigate empirical relationships between V_s and CPT, raw shear wavelets sets of downhole data were evaluated and correlated with CPT readings. Based on those data, various prior V_s−CPT correlations were examined for their validity in the upper 40 meter depth range. The selected equations are shown in Table 9.1. Except for the newest trends given by Andrus et al. 2007, the selected empirical equations were primarily established from data on Holocene soils. In these relationships, the V_s (VH) mode applies as the data were obtained from downhole testing via SCPT.

Table 9.1. Selected published V_{sVH} − CPT relationships in soils

Reference	Empirical equation	Soil types
Baldi et al. 1989	$V_s = 277 \cdot (q_t/1000)^{0.13} \cdot (\sigma_{vo}'/1000)^{0.27}$	Clean sands
Hegazy and Mayne 1995	$V_s = (10.1 \cdot \log(q_t) - 11.4)^{1.67} \cdot (f_s/q_t \times 100)^{0.3}$	All soils
Mayne and Rix 1995	$V_s = 41.16 \cdot (q_t - \sigma_{vo})^{0.212} \cdot (e_0)^{-0.49}$	Intact and fissured clays
Mayne 2007	$V_s = 51.6 \cdot \ln(f_s) + 18.5$	All soils
Andrus et al. 2007	$V_s = 13 \cdot (q_t)^{0.382} \cdot D^{0.099}$	Tertiary-Age Cooper Marl
Andrus et al. 2007	$V_s = 2.27 \cdot (q_t)^{0.412} \cdot I_c^{0.989} \cdot D^{0.033} \cdot ASF$	Age scaling factor (ASF) ASF = 1 for Holocene ASF = 1.22 for Pleistocene ASF = 2.29 for Tertiary

Notes: V_s is VH mode in units of m/s; CPT readings q_t and f_s are in kPa. D = depth (m), e_0 = in-situ void ratio, I_c = CPT material index = $\sqrt{\{3.47 - \log(Q)\}^2 + \{1.22 + \log(F)\}^2}$, where $Q = (q_t - \sigma_{vo})/\sigma_{vo}'$, $F\ (\%) = 100 \cdot f_s/(q_t - \sigma_{vo})$, σ_{vo} = total vertical stress (kPa), and σ_{vo}' = effective vertical stress (kPa).

Figure 9.15 shows plots of measured V_s versus predicted V_s from the selected correlations: Figure 9.15(a) Baldi et al. 1989, (b) Hegazy and Mayne 1995, (c) Mayne and Rix 1995, (d) Mayne 2007, (e) Andrus et al. 2007, (f) Andrus et al. 2007 (adopting ASF=1.5). All predictions appear rather deviated and/or scattered. Interestingly, the empirical correlation for clays suggested by Mayne and Rix (1995) seems to provide the relatively better estimations for SRS soils which ironically mainly consist of sands and sand mixtures (albeit with clay fines contents). Yet, notable discrepancies are observed for all relationships when applied to SRS soils. Consequently, new site-specific empirical correlations are developed for the SRS geomaterials to accommodate the unusual V_s profiles and soil conditions which include very old Miocene and Eocene deposits and gap-graded sands with clay fines (yet little silt fractions).

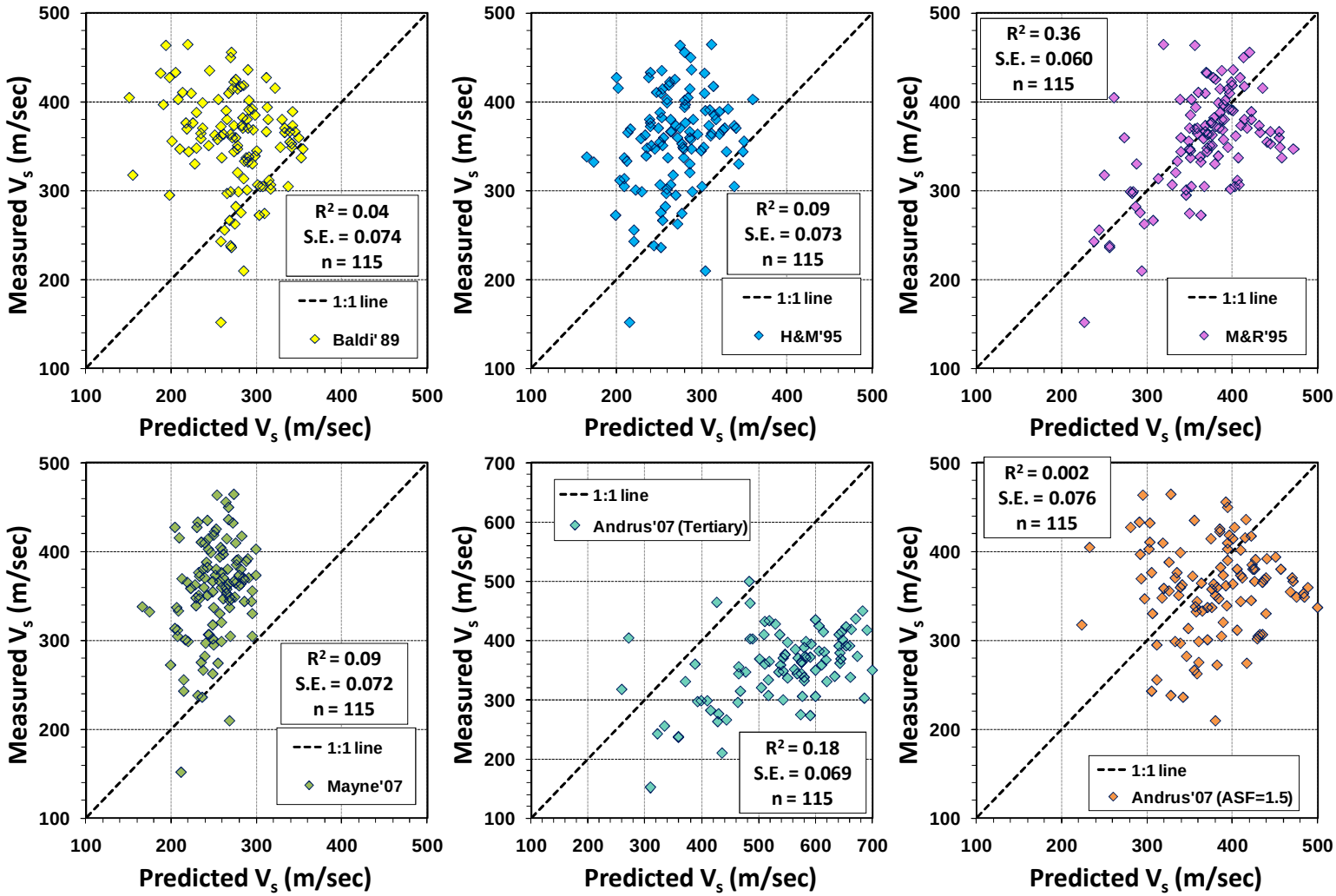

Figure 9.15. Application of selected V_s-CPT correlations to data from SRS; (a) Baldi et al. 1989, (b) Hegazy and Mayne 1995, (c) Mayne and Rix 1995, (d) Mayne 2007, (e) Andrus et al. 2007, (f) Andrus et al. 2007 (adopting ASF=1.5).

9.5.2 Regression Models at SRS

Due to the rather poor agreement achieved using prior correlative relationships, various potential V_s−CPT regression models for SRS were investigated. Eventually, the derived equations applicable to the upper 40 meter overburden depths are as follows:

▪Basic format: $V_s = a_1 \cdot (A)^{a2} \cdot (B)^{a3} \cdot (C)^{a4}$

▪Model 1: *variable A= Log(q_t)−α, B = σ_{vo}' where α = 3.19 ≈ log($q_{t,min}$)*

Equation (9.13) $V_s = 880 \cdot (\mathrm{Log}(q_t) - \alpha)^{0.121} \cdot \sigma_{vo}'^{-0.151}$

(R^2 = 0.629, S.E. = 0.0464, N = 114)

▪Model 2: *variable A= Log(q_t)−α, B = σ_{vo}', C = $10^{exp(Ic)}$ where α = 3.19 ≈ log($q_{t,min}$)*

Equation (9.14) $V_s = 720.8 \cdot (\mathrm{Log}(q_t) - \alpha)^{0.048} \cdot \sigma_{vo}'^{-0.104} \cdot 10^{-0.0034 \times \exp(Ic)}$

(R^2 = 0.651, S.E. = 0.0452, N = 114)

▪Model 3: *variable A= f_s, B = $10^{exp(Ic)}$*

Equation (9.15) $V_s = 315.2 \cdot f_s^{0.066} \cdot 10^{-0.0061 \times \exp(Ic)}$

(R^2 = 0.627, S.E. = 0.0465, N = 114)

▪Model 4: *variable A= f_s, B = σ_{vo}', C = $10^{exp(Ic)}$*

Equation (9.16) $V_s = 473.7 \cdot f_s^{0.062} \cdot \sigma_{vo}'^{-0.073} \cdot 10^{-0.0053 \times \exp(Ic)}$

(R^2 = 0.673, S.E. = 0.0437, N = 114)

▪Model 5: *variable A= Log(q_t)−α, B = f_s, C = σ_{vo}' where α = 3.19 ≈ log($q_{t,min}$)*

Equation (9.17) $V_s = 718.5 \cdot (\mathrm{Log}(q_t) - \alpha)^{0.115} \cdot f_s^{0.040} \cdot \sigma_{vo}'^{-0.147}$

(R^2 = 0.643, S.E. = 0.0457, N = 114)

Note that:

1) $q_{t,min}$ = minimum magnitude of cone tip resistance q_t,
2) $I_c = I_{c,RW}$ = CPT material index = $\sqrt{\{3.47-\log(Q_{tn})\}^2+\{1.22+\log(F)\}^2}$, where $Q_{tn}=\frac{(q_t-\sigma_{vo})}{\sigma_{atm}}\cdot\left(\frac{\sigma_{atm}}{\sigma_{vo}'}\right)^n$, $F = 100\cdot f_s/(q_t-\sigma_{vo})$, $n = 0.381(I_c)+0.05(\sigma_{vo}'/\sigma_{atm})-0.15$
3) R^2 = coefficient of determination, S.E. = residual standard error from log linear regression, and N = number of data.

Based on the above regression models, measured V_s and predicted V_s values are compared in Figure 9.16. It is noted that the predicted V_s is slightly inversely proportional to the σ_{vo}' in the models. The regression model 3 does not include the σ_{vo}' term as one of the variables, therefore the predicted V_s at uppermost depths might be rather underestimated compared to the other models. On the other hand, the calculation of σ_{vo}' in the upper 15 m is rather uncertain because of capillarity, degree of saturation, and possible negative hydrostatic porewater pressures. Apparently, the V_s predictions via the derived site-specific regression models provide improved results. However, coefficients of determination (R^2) values are not significantly high, albeit considerable scattering and outliers are not observed. This might be because the in-situ V_s measurements at SRS are less variable with depth and/or location, thus rather clustered and having comparable magnitudes.

Two representative SCPTu soundings are provided in Figure 9.17 and Figure 9.18 (Borings #18 and #58). The applied q_t and f_s are mean values obtained at the depth ranges corresponding to each V_s measurement. As per the aforementioned, regression model 3 seems to result in relatively small V_s estimation at shallow depths compared to other correlative expressions for both soundings. However, it seems that the new site-specific expressions produce overall reasonable V_s predictions. For completeness, additional correlations between field tests (i.e., CPT-SPT, CPT-DMT) are provided in Appendix G.

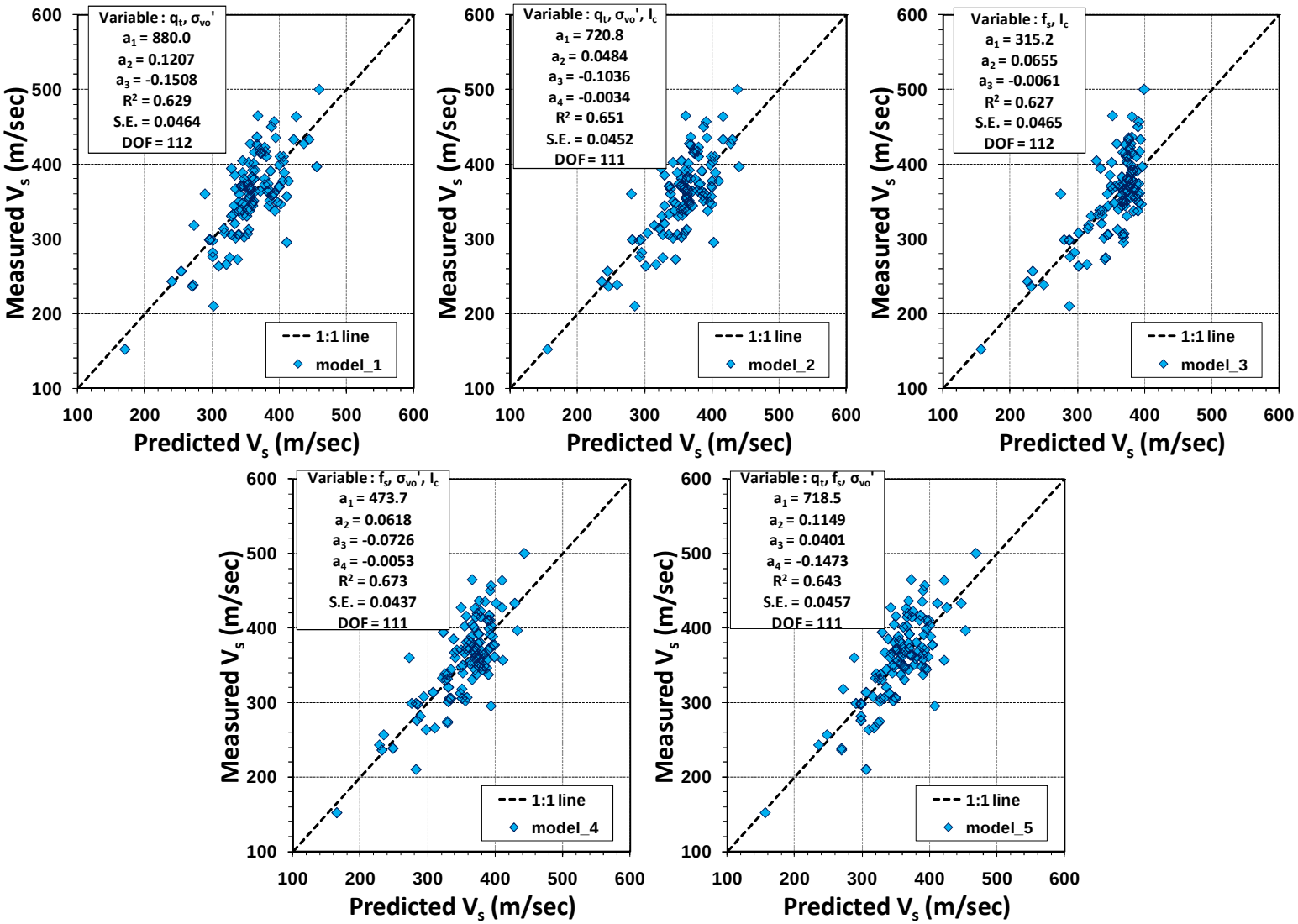

Figure 9.16. Comparison of measured V_s versus predicted V_s using regression models at SRS.

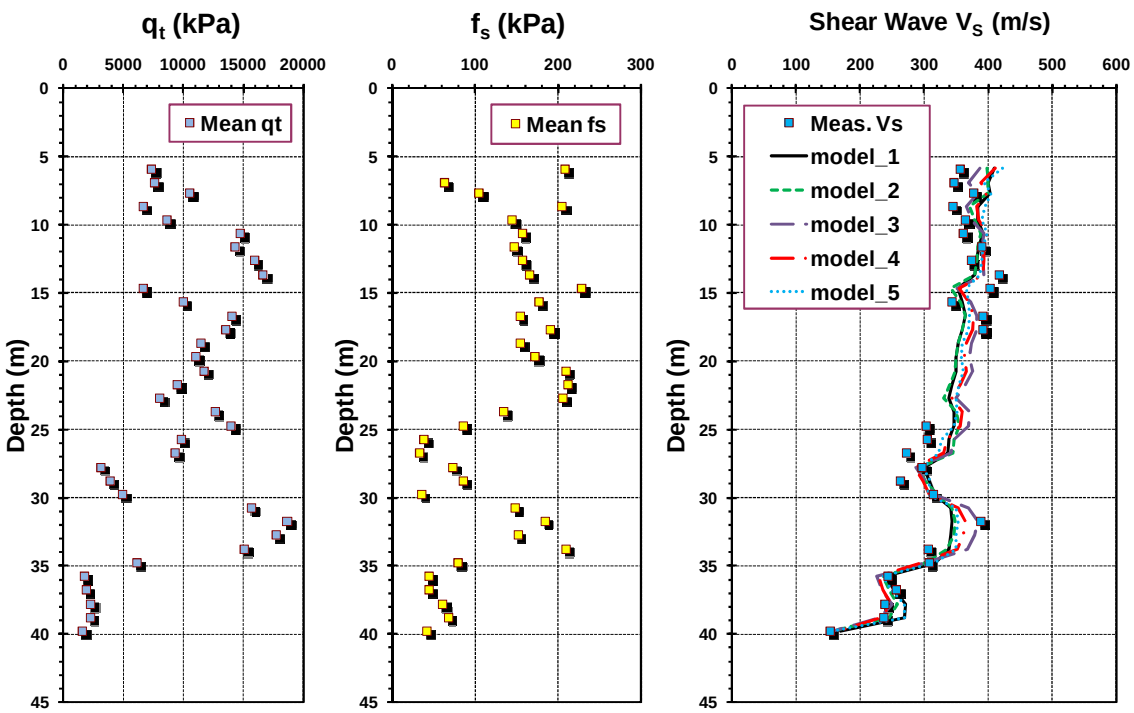

Figure 9.17. Result of standard SCPT and V_s prediction using regression models at SRS K-site (Boring #18).

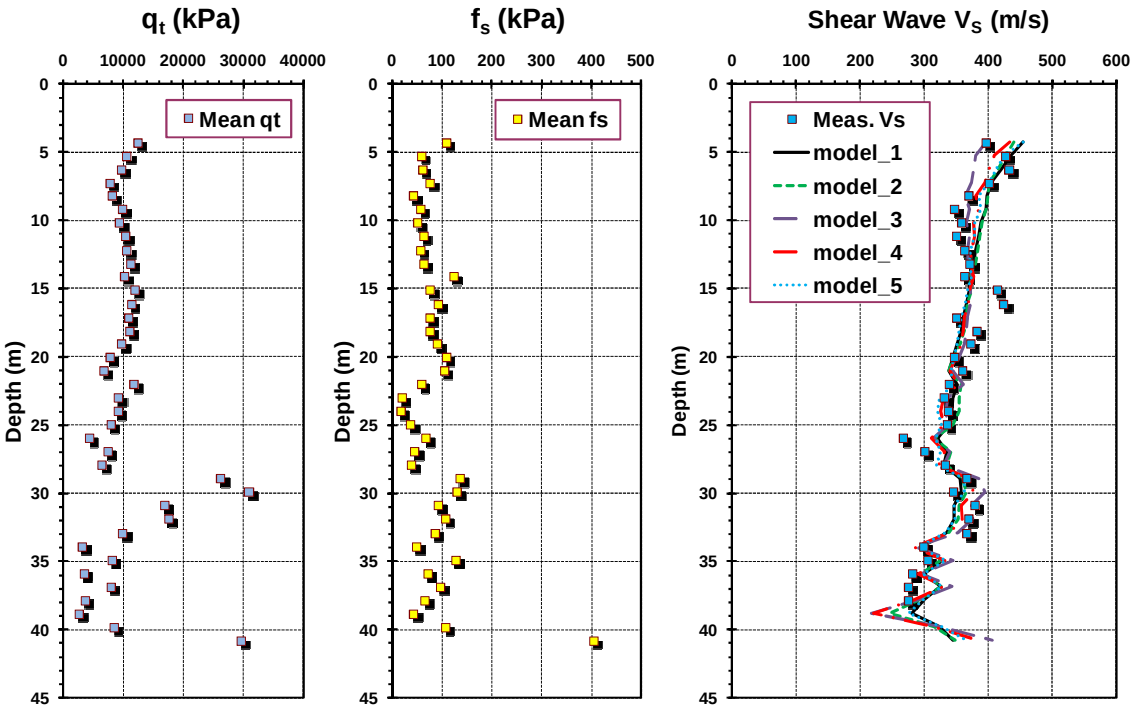

Figure 9.18. Result of standard SCPT and V_s prediction using regression models at SRS K-site (Boring #58).

Additionally, for the proposed regression models, error propagation analyses were conducted as follow:

▪ Basic regression format: $V_s = a_1 \cdot (A)^{a2} \cdot (B)^{a3} \cdot (C)^{a4}$

▪ Error propagation for the basic format: $\frac{u_{Vs}}{V_S} = \sqrt{\left(a_2 \frac{u_A}{A}\right)^2 + \left(a_3 \frac{u_B}{B}\right)^2 + \left(a_4 \frac{u_C}{C}\right)^2}$

where, u = uncertainty (here, 1 standard deviation), A, B, and C are assumed as independent variables for analysis.

▪ Error propagation for models: $\frac{u_{Vs}}{V_S} = 0.076$ (model 1), 0.061 (model 2), 0.076 (model 3), 0.074 (model 4), 0.076 (model 5)

9.6 Summary

This chapter discussed site-specific characteristics of shear waves measured at the Savannah River Site (refer to Ku et al. 2012 for in-situ V_s characteristics). Normally, shear wave velocity increases with depth in most soils. In contrast, in-situ V_s profiles at SRS showed unusual trends, specifically: (a) V_s decreases from the ground surface down to 15 meter depth, and (b) V_s magnitude is nearly constant from 15 m to 50 m depths. Several possible scenarios to explain such behavior include: cementation, desaturation, diagenesis, and/or stress alteration due to void formation and dissolutioning, coupled with high yield stresses at shallow depth. On the other hand, laboratory RC and BE test data showed realistic stress-dependent behavior of SRS soils similar to well-behaved uncemented geomaterials. In the case of similar samples retrieved from the same location, reasonable V_s-stress relations were derived. In the final section, considering the special complex geologic conditions at SRS, site-specific V_s-CPT correlations were sought for practical engineering purposes.

CHAPTER 10

CONCLUDING REMARKS AND RECOMENDATIONS

10.1 Summary and Conclusions

The research efforts for this dissertation have focused primarily on shear wave velocity (V_s) and the related small-strain stiffness (G_0) in soils, with particular interests related to geotechnical site characterization. As such, the dissertation offers three notable areas for contribution, as follows: (1) evaluation of stress history and geostatic stress state from paired sets of directional and polarized shear waves; (2) identification of shear wave velocity profiles from continuous wavelet data taken during cone penetrometer testing; and (3) assessment of unique and unusual karstic geologic conditions and related geotechnical properties at a major DOE facility in South Carolina.

In terms of the first topic, evaluations of stress history (e.g., yield stress ratio, overconsolidation) and the geostatic state of stress of soils (i.e., K_0 profiles) are ascertained on the basis of field geophysical measurements that provide paired complementary types of shear waves. It is well-established that multiple types of shear waves occur in the ground due to their directional and polarization properties. The shear wave velocity (V_s) provides the magnitude of small strain stiffness (G_0) which depends on effective stress, void ratio, stress history, and other factors (cementation, age, saturation). Herein, this study examines a hierarchy of shear wave modes with different directions of propagation and particle motion from in-situ geophysical tests (HH, VH, and HV), as well as laboratory bender element data. After a review of available analytical relationships, a special compiled database from well-documented worldwide sites is assembled where full profiles of stress state, stress history, and several paired modes of

V_s profiles have been obtained from crosshole tests (CHT), downhole tests (DHT), and rotary crosshole (RCHT). Reference profiles of the lateral stress coefficient (K_0) are available from direct in-situ measurements (self-boring pressuremeter, hydrofracture, and spade cells). Stress history is documented in terms of yield stress ratio (YSR), or more common term overconsolidation ratio (OCR), from consolidation testing and careful engineering geologic studies. A methodology was developed that relates both the YSR and K_0 to shear wave stiffnesses (HH/VH) obtained from directional shear wave velocities. It appears the ratio of standard crosshole to downhole shear waves (HH/VH) is a measure of fabric or inherent anisotropy.

With respect to the second contribution, a new exploratory procedure for collecting continuous shear wave velocity measurements via cone penetration testing using a special autoseis source was presented whereby wavelets can be generated and recorded every 1 to 10 seconds. The rotoautoseis was developed by Georgia Tech and received a US patent in February 2010. The continuous-interval seismic piezocone test (CiSCPTu) offers a fast, productive, and reliable means to expedite the collection of downhole shear wave velocity profiles, as well as additional readings on cone tip resistance, sleeve friction, and penetration porewater pressures with depth. Three test sites in Windsor/VA, Norfolk/VA, and Richmond/BC were utilized for illustrating the collection of data, calibration, and post-processing issues arising from large numbers of wavelets that contained noisy signals from truck vibrations, slight variances in penetrometer rates, random sources, refracted and reflected waves, and other factors. This necessitated thorough analyses that required filtering, windowing, smoothing of data, and selection of the final shear wave profile in terms of both time and frequency domain

analyses. The developed methodology was verified by a "class A" prediction using a 45-m deep CiSCPTu that was confirmed by standard DHT results obtained after the fact.

Contributions regarding the noted last topic resulted from the special geologic conditions at the US Dept. of Energy's Savannah River Site (SRS) in South Carolina. The SRS consists of layered marine deposits of quite old surficially-exposed Miocene age and rather shallow Eocene age soils, primarily sands to clayey sands with interbedded clays with varied quartzitic, silicaceous, to calcareous constituents. At depths of 40 to 50 m below grade is found the well-documented Santee formation, known for its soft-filled cavities and/or voids of low resistance and unusual "karstic" tendencies to form dissolutioned "caves" within an unconsolidated limestone matrix. Consequently, the overlying SRS soil columns are expected to experience considerable alterations of geostatic stress state and/or localized collapse.

Based on conventional laboratory and in-situ test data conducted during geotechnical investigations at SRS, available interpretative relationships for evaluating the geostatic stress states and stress history provided scattered and inconsistent results. In a number of cases, the geomaterials appear to be highly overconsolidated (HOC) at shallow depths, while deeper deposits ($z > 30$ m), the soils appear either lightly-overconsolidated (LOC), normally-consolidated (NC), and/or underconsolidated (UC). Extensive analyses were made in ascertaining the stress history at SRS on the basis of reviewing many dozens of consolidation tests (oedometer and CRS type), as well as lab triaxial tests. Moreover, the analyses included the assessments of stress history (YSR and/or OCR) on the basis of in-situ test data, including standard penetration tests (SPT), cone penetration tests (CPT), flat plate dilatometer (DMT), and other approaches.

Complications abound in the systematic assessments of these geomaterials due to combined effects of very old age, cementation, desiccation, and diagenesis, as evidenced by unusual in-situ shear wave velocity profiles that decrease in magnitude with depth, as measured by CHT and DHT. On the basis of the current findings at SRS, future studies are recommended, as detailed in the following section.

10.2 Recommendations for Future Study

• The relationships for geostatic stress state and stress history evaluation approaches can be upgraded and improved by including new field and laboratory data from additional well-documented test sites.

• The techniques to extract reliable continuous-interval shear wave velocity (CiV_s) profiles should be further verified based on new site studies. The issue of sensitive V_s results may be partially resolved and improved when a true-interval type CiV_s system is developed in the future. It will be also interest to examine frequency variations how to affect the continuous V_s results in cross-spectral analysis.

• Considering the complex geologic conditions at SRS, frequent-interval and/or continuous-interval V_s measurement system may be beneficial for better identifying details in soil layers, interfaces, and stratigraphic conditions. Currently, the SRS site has many numbers of DHT V_s measurements (V_{sVH}), a fewer number (e.g. dozen) of conventional CHT (V_{sHV}) profiles, several shear wave profiles from Rayleigh waves (SASW), and one deep suspension logger sounding. To data, however, the author is unaware that HH-wave measurements have been obtained at SRS. The pairing of HH waves from rotary crosshole tests (RCHT) with downhole type tests (DHT) that provide

VH waves would offer an unique assessment of the geostatic stress state (i.e., K_0 profile) as well as an independent evaluation of the stress history (i.e., OCR, OCD, and/or YSR) at SRS to help uncover the complex and elusive nature of these old aged and important geologic materials at SRS. These HH waves are needed at SRS to complete the picture towards understanding the ambient stress state of the soil column. Additional independent support in the K_0 assessment at SRS might be provided by use of direct in-situ test devices such as hydrofracture (HF) and self-boring pressuremeter (SBP). Together, these tests can assist in the validation and/or confirmation of geocharacterization of the subsurface soils conditions, future construction activities, and expected behavior of existing structures at the SRS facilities that are critical to DOE operations.

• This study mainly focused on the utilization of VH, HV, and HH shear wave modes from downhole, regular crosshole, and rotary crosshole tests, respectively. It was noted that the hierarchy of shear wave modes relates to geostatic stress states and stress history, as well as inherent or fabric-induced anisotropy. For future research studies, Rayleigh wave methods (e.g., SASW, MASW, CSW, ReMi, and PSW) might also play a role in evaluating the stress conditions. For instance, SASW data showed relatively high V_s magnitudes compared to other downhole and crosshole tests below 55 meter depth in Figure 9.1. Also, Rayleigh wave measurements currently focus only on the vertical wave component whereas useful information might be gathered by collection and analysis of the horizontal component. How the SASW and MASW type measurements fit within the hierarchy family of shear waves will also be of interest.

APPENDIX A

FIELD TEST METHODS FOR GEOTECHNICAL EXPLORATION

A.1 Traditional Methods of Field Testing

For many decades, in-situ field tests for site characterization have been conducted in concert with rotary soil borings with sampling and laboratory testing. As such, some of the more conventional field tests are reviewed here for completeness in the dissertation, including: standard penetration test (SPT), vane shear test (VST), pressuremeter (PMT), flat dilatometer (DMT), and cone penetration test (CPT), as well as several geophysical methods such as crosshole (CHT), downhole (DHT), and surface wave methods (SWM). Figure A.1 describes a variety of in-situ test methods (Mayne 2006).

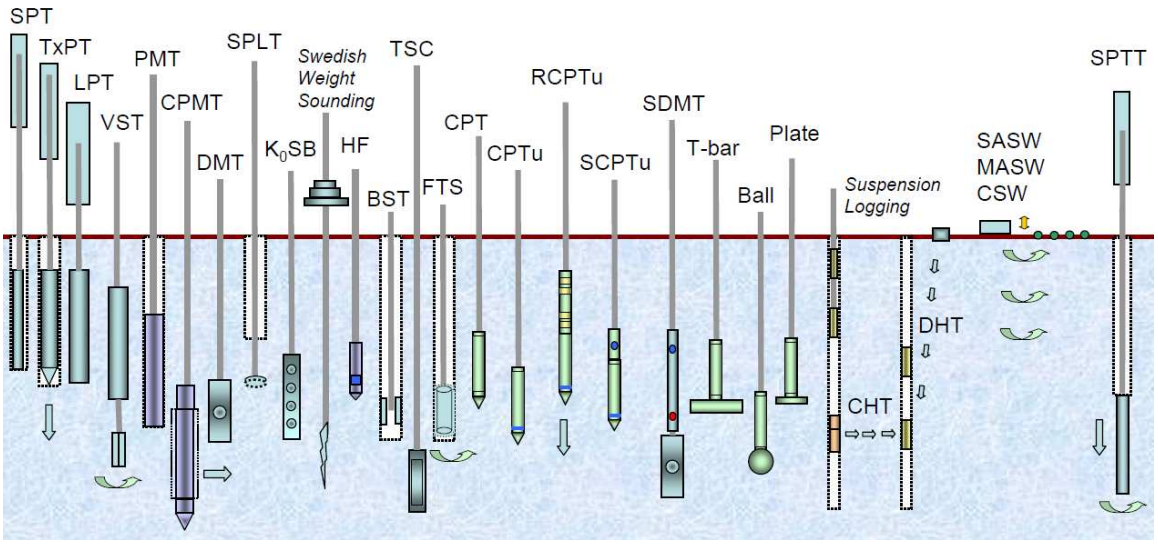

Figure A.1. Overview illustration of available in-situ field tests (Mayne 2006).

Since 1902, the standard penetration test (SPT) has been widely adopted over the past century due to its cost-effectiveness and operational simplicity. The SPT provides both a drive sample and dynamic resistance in the soil, specifically the “blow count” or N-value (reported in blows/foot or blows/0.3 m). The procedural details for SPT can be

found in ASTM D1586. The SPT is most adoptable in sand layers and can be also performed in firm to stiff clays, silts and weak rocks. However, the test acquires a disturbed sample and is not applicable in soft clays.

Currently, the energy-corrected N_{60} value corresponding to 60% energy efficiency ratio (ER) is desired because of the need to standardize results over the 110 year history of the test (ASTM D 4633). While the drop hammer system (140-lb hammer falling 30 inches) has theoretically been kept the same, the actual applied ER has increased over the years as the equipment upgraded from the original pin-weight hammer (ER ≈ 35%) to donut hammer (ER ≈ 45%) to safety hammer (ER ≈ 65%) to fully automatic systems (60% < ER < 100%). Details on the energy corrections are given in Kulhawy and Mayne (1990). Figure A.2 shows the various hammer types of SPT.

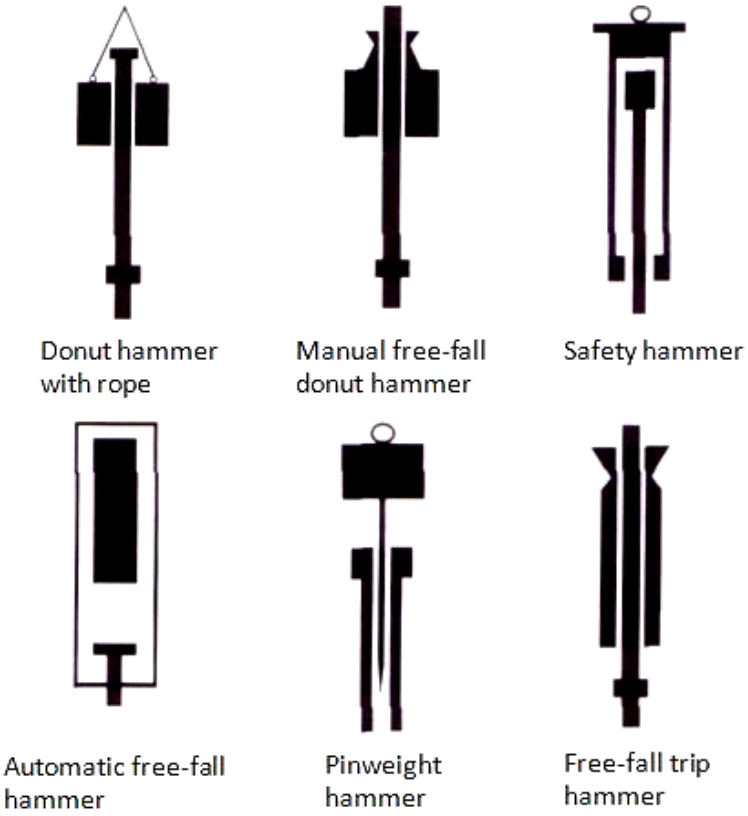

Figure A.2. Various hammer types of SPT.

The vane shear test (VST) is long-standing field test since 1940's which is performed in soft to stiff clays and silts to measure undrained strength and sensitivity. A four-bladed vane is inserted into the soil layer and rotated to measure a peak torque. The general guidelines are provided in ASTM D2573. To evaluate the undrained shear strength (s_{uv}) of clay, limit equilibrium analysis is applied. The VST also provides the sensitivity ratio (S_t) by dividing the measured peak strength by the remolded strength. Moreover, the measured vane strength should be corrected by an empirical reduction factor before application to field stability problems ($\tau_{mobililzed} = \mu \cdot s_{uv}$). Applied during borehole advancement, the test is a bit slow at 1-m test intervals and not applicable to sand layers nor to cohesionless silts. Improvements in recent years include the advent of the electromechanical vanes to facilitate field VST and recording of data. Figure A.3 shows components of electric vane system.

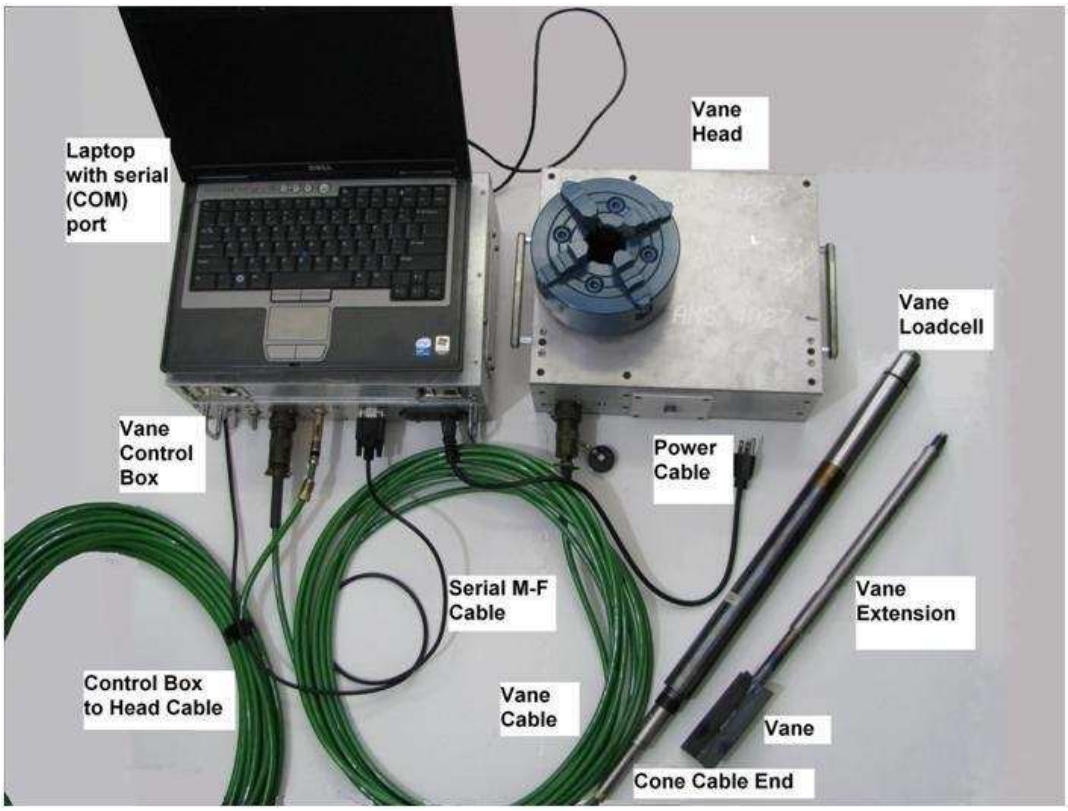

Figure A.3. A set of electric vane components (Courtesy ConeTec Investigations).

In the early Menard version of the device introduced in 1955, the pressuremeter test (PMT) inserts a longitudinal cylindrical probe into a cased borehole. To generate internal pressures and inflate the probe, it is connected to screw pump at the ground by tubing and tracks the volumetric changes as water is injected into the probe. The test procedure is given by ASTM D4719. The PMT can eventually provide a complete stress-strain-strength curve in soil at each test depth. Based on cylindrical cavity expansion (CCE) theory, it defines several readings and properties such as lift-off pressure ($P_0 = \sigma_{ho}$), shear strength (s_{uPMT}), stiffness modulus (G or E), rigidity index ($I_R = G/s_u$), and limit pressure (P_L). There are several types of PMT devices: (1) Pre-bored (Menard) type pressuremeter (MPMT), (2) Self-boring pressuremeter (SBP), (3) Push-in pressuremeter (PIP), (4) Full-displacement type (FDP). Particularly, it is acknowledged that the SBP can provide the most reliable value of at-rest lateral stress coefficient (K_0) since it attempts to become inserted with minimal disturbance to the ground and the interpretation relies solely on the measured volume change-pressure readings. Overall, the PMT has robust interpretation backgrounds of soil parameters. However, the test is rather time consuming and expensive, particularly when the Menard version is employed. Figure A.4 shows the pressuremeter probes and gages.

Figure A.4. Various pressuremeter probes and gage system.

Total Stress Cells (TSC) is usually conducted to measure the in-situ at-rest lateral stress coefficient (K_0) in cohesive soils (sometimes named Puch-In Spade Cells). A thin steel blade is inserted into the ground and measure a total horizontal stress by inflating membrane. It is assumed the test minimizes soil disturbance, thus reliable K_0 is obtained. However, it takes long time for dissipation and requires additional correction for stiff clays. More details regarding TSC test were introduced by Tavenas et al. (1975), Massarsch et al. (1975), Rankka (1990), and Sully (1991). Figure A.5 shows components of the TSC (Sully 1991).

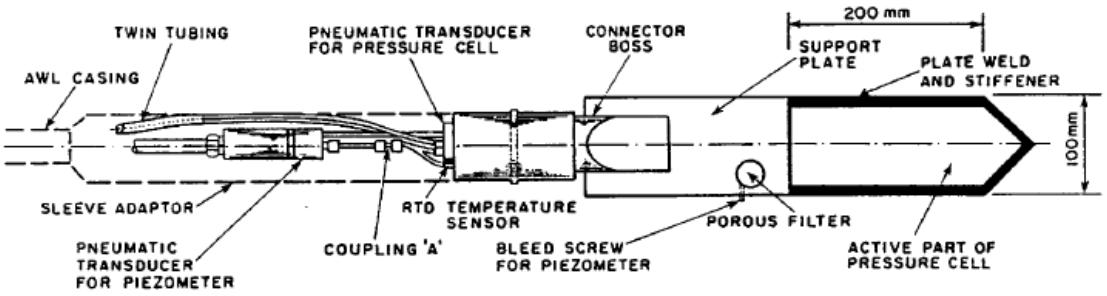

Figure A.5. Total Stress Cells components (Sully 1991).

Hydraulilc fracture (HF) test also provides direct measurements on K_0 stress state. The HF typically measures the in-situ K_0 in clays. Also, the HF test has been commonly adopted by rock mechanics and offshore engineering. High water pressure can occur hydraulic fracturing of soil medium. After fracturing, the water pressure decreases with time. An example (plot of pressure versus time) of HF test data is shown in Figure A.6 (Murdoch et al. 2006). The interpreted closing pressure is assessed as the in-situ horizontal stress. However, the assessment of the closure pressure measurement might not be straightforward. Further details for HT test were given by Bjerrum and Andersen (1972), Tavenas et al. (1975), Hamouche et al. (1995), Lunne and Mayne (1998).

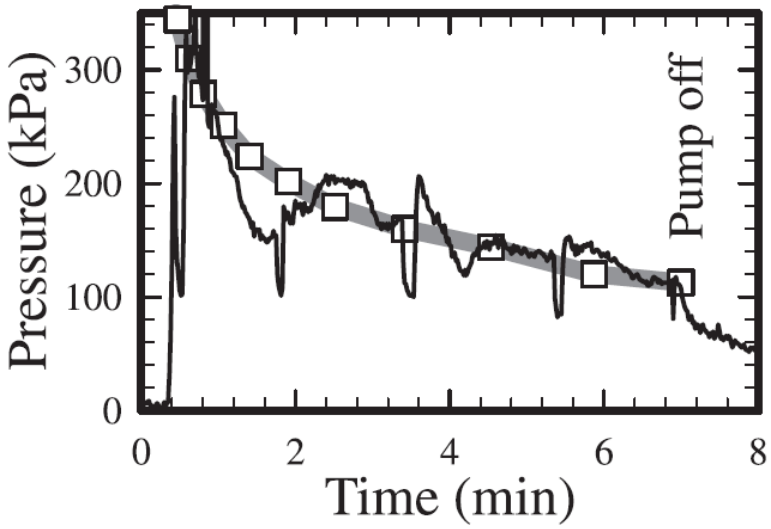

Figure A.6. An example of HF test data (Murdoch et al. 2006).

Since its beginnings in 1932 in Holland, cone penetrometer testing (CPT) has become an efficient, expedient, and economical means for site exploration that utilizes the direct-push technology. The cone penetrometer is hydraulically pushed at a constant rate of 20 mm/s with measurements of cone tip resistance (q_t), sleeve friction (f_s), and penetration porewater pressure (u_2) recorded at depth intervals of 10mm to 50mm. No borings or samples or spoils are generated during the CPT. Thus, it is possible to provide continuous soil layer profiling and evaluate geomaterial properties with fast field production time. Test procedures are provided by ASTM D3441 (mechanical system) and ASTM D5778 (electric and electronic system). Figure A.7 describes a general setup, approximate procedures, and available readings from the electronic CPT system. Compared with traditional rotary drilling and sampling from boreholes, the significant advantages of cone penetration testing are that it provides multiple independent readings on soil behavior during advancement and the results are logged directly to a field computer for immediate access and analysis.

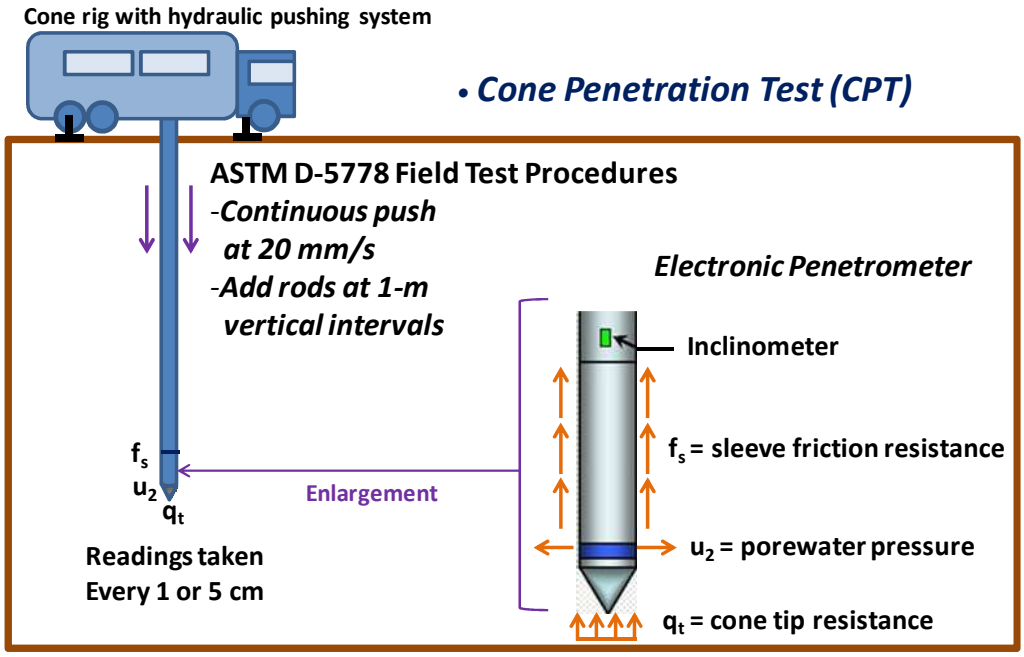

Figure A.7. General setup of CPT and multiple readings.

To identify soil types, empirical soil behavior type (SBT) charts have been suggested based on the basic CPT readings (e.g. Robertson 1990; Lunne et al.1997), as shown in Figure A.8. Soil behavior type is estimated using a soil classification index (I_c) which is derived from normalized piezocone parameters. Two types of material indices are applied for soil classification (Robertson and Wride, 1998; Jefferies and Been, 2006). Stress-normalized parameters (Lunne et al. 1997) and soil classification indices are defined as follows:

- Normalized tip resistance : $Q = (q_t-\sigma_{vo}) / \sigma_{vo}'$
- Normalized sleeve friction : $F = 100 \cdot f_s / (q_t-\sigma_{vo})$
- Normalized excess porewater pressure : $B_q = (u_2-u_o) / (q_t-\sigma_{vo})$
- Soil classification index:

$$I_{cRW} = \sqrt{\{3.47 - \log(Q)\}^2 + \{1.22 + \log(F)\}^2}$$ (Robertson & Wride, 1998)

$$I_{cJB} = \sqrt{\{3 - \log(Q \cdot (1 - B_q) + 1)\}^2 + \{1.5 + 1.3 \cdot \log(F)\}^2}$$ (Jefferies & Been, 2006)

In order to represent the stress normalization working for various soil types, the aforementioned normalized cone tip resistance (Q) has been modified (Robertson 2009):

- $Q_{tn} = [(q_t-\sigma_{vo}) / P_a] \cdot (P_a / \sigma_{vo}')^n$

where, P_a = 1 atmosphere, $n = 0.381(I_c) + 0.05(\sigma_{vo}'/P_a) - 0.15$.

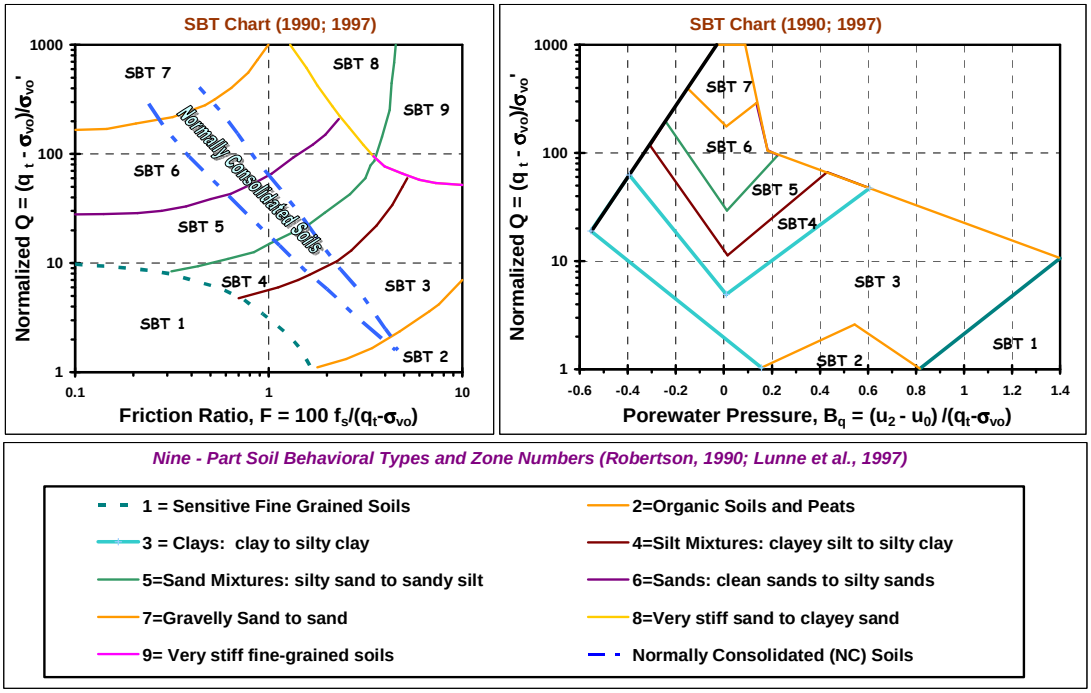

Figure A.8. CPT soil behavior type chart (Robertson 1990; Lunne, Robertson, & Powell 1997).

The flat plate dilatometer test (DMT) is also a reliable in-situ means for obtaining relatively quick profiling of the geostratigraphy and evaluation of soil engineering parameters. The DMT consists of a special taper-shaped blade which is connected to a pressure gauge. The blade has a 60 mm diameter flexible steel membrane in one side. Basically, two readings are taken: 1) A-reading: lift-off or contact pressure by membrane flush (no membrane deflection), 2) B-reading: expansion pressure where the membrane deflection is 1.1 mm outward. The DMT blade is shown with a new dilatometer seimic system in Figure A.9. Detailed test procedures are given by ASTM D6635. With consideration of proposed corrections for membrane stiffness and soft soil types (Schmertmann 1986), DMT readings (P_0, P_1) and indices are defined as follows:

- Contact pressure : $P_0 = 1.05(A+\Delta A) - 0.05(B- \Delta B)$

  where ΔA and ΔB = calibration factor for membrane stiffness in air

- Expansion pressure : $P_1 = B - \Delta B$
- I_D = material index = $(p_1-p_o)/(p_o-u_o)$ → clay when $I_D < 0.6$; Sand: $I_D > 1.8$
- E_D = dilatometer modulus = $34.7 \cdot (p_1-p_o)$
- K_D = horizontal stress index = $(p_o-u_o)/\sigma_{vo}'$

Figure A.9. DMT blade with a new seismic dilatometer system.

Geophysical seismic wave measurements are now a staple and important means of site investigation in geotechnical studies (Campanella 1994). As a traditional geophysical method, conventional crosshole tests (CHT) can produce field shear wave velocity (V_s) profiles which are important for geotechnical engineering problems, usually performed at 1.5 m depth intervals in the USA. The CHT requires at least two or three cased boreholes, therefore are relatively expensive because of the need for rotary drilling, casing and grouting operations, inclinometer measurements for verticality, and deployment of geophones for the time arrivals of V_s waves, each step requiring allocated

field times and performance. Test setup and procedures are described by Hoar and Stokoe (1978) and standardized guidelines given by ASTM D4428. In the USA, the standard CHT utilizes a downhole hammer with up- and down-movement to generate shear waves propagating in a horizontal direction and polarized in the vertical direction (HV waves). It is also possible to use a special rotary hammer, horizontal sparker, or torsional source that generates a shear wave propagating in a horizontal direction and polarized in the horizontal direction (HH waves).

A less expensive alternate geophysical method is the downhole test (DHT), detailed in ASTM D7400. The DHT uses only a single rotary-drilled and cased borehole to record shear wave time arrivals with depth. A horizontal source at the surface oriented perpendicular to the borehole axis is employed to generate shear wave propagating in a vertical downward direction and polarized in the horizontal direction (VH waves). Approximate configurations for both CHT and DHT are described in Figure A.10a (Wightman et al. 2003) and A.10b (ASTM D7400-08).

Noninvasive surface wave testing is also commonly conducted. A vibrating source on the surface generates Rayleigh waves which consist of a broad range of frequencies. From the propagating and dispersive characteristics of Rayleigh waves, shear wave velocity profiles are evaluated by complex inversion processes based on the measured dispersion curve. Several types of surface wave measurements are available depending on vibration types: Spectral Analysis of Surface Waves (SASW; Nazarian and Stokoe 1984), Continuous Surface Waves (CSW, Tokimatsu et al. 1992), Multi-channel Analysis of Surface Waves (MASW, Park et al. 1999), etc (reference information from McGillivray 2007). A configuration of MASW is shown in Figure A.11.

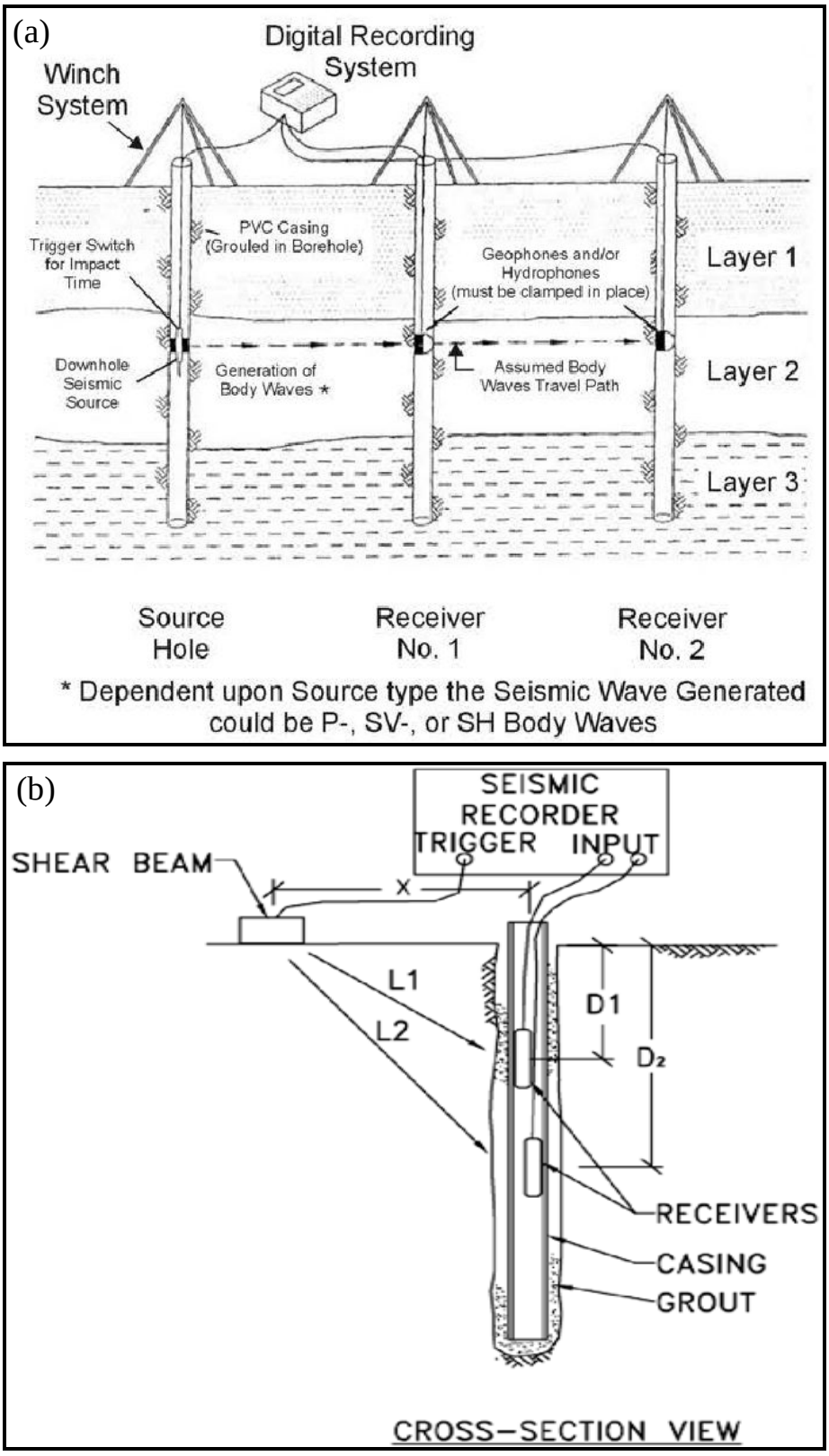

Figure A.10. Approximate configurations of (a) crosshole test (Wightman et al. 2003); (b) downhole test (ASTM D 7400 - 08).

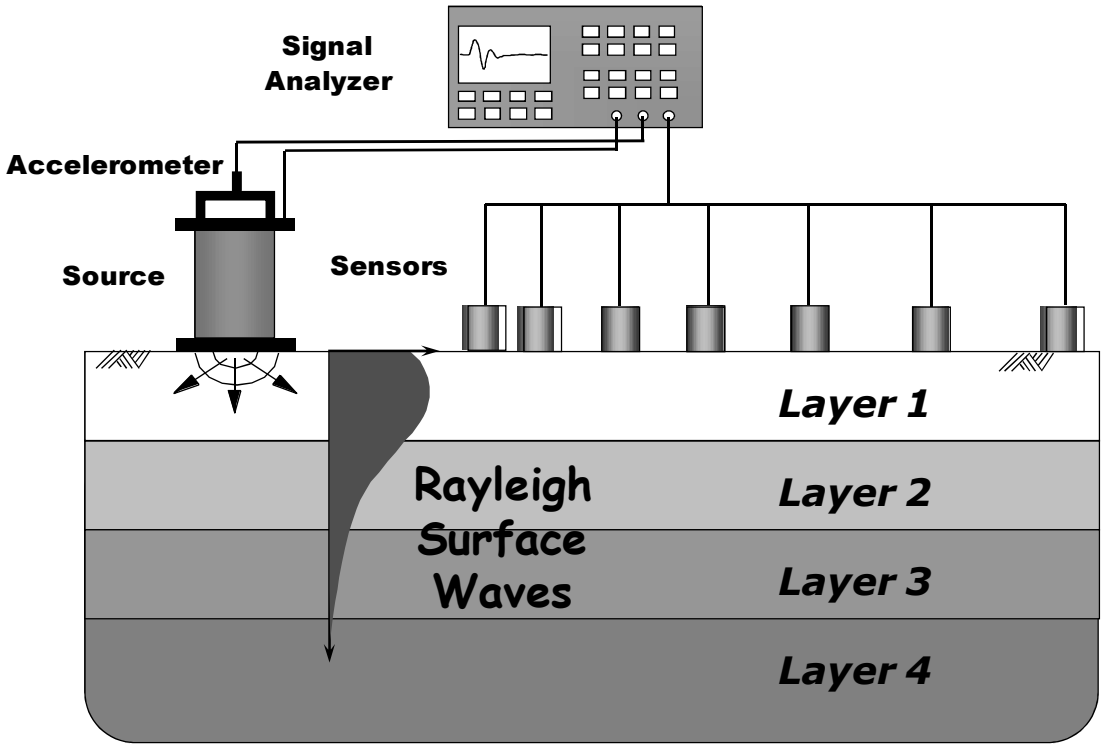

Figure A.11. Schematic of in-situ surface wave measurements (MASW; courtesy by Prof. Mayne).

On the other hand, suspension logging system can provide both P- and S-wave based on a single borehole. It is possible for the suspension logger to measure both waves at depths greater than 60 meter, thus widely adopted in explorations for the petroleum engineering and geophysics. A general set-up of the suspension logging is shown in Figure A.12. Figure A.13 shows P- and S-wave measurements using the suspension logger until deep 900 meter depths at Keiser, Arkansas. Although the wave magnitudes seem rather sensitive, it is possible to explore wave profiles up to considerably deep depths.

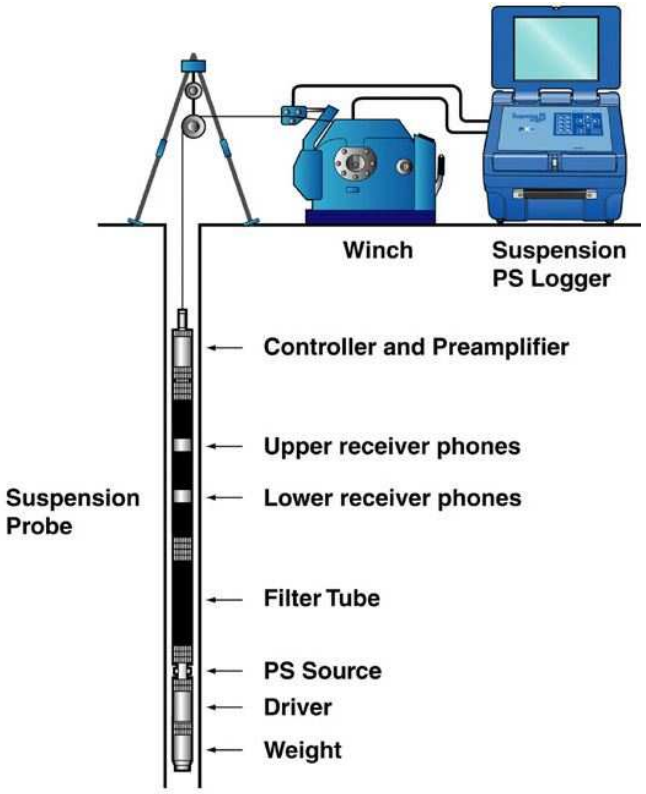

Figure A.12. A general set-up of suspension logging system (figure from OYO corporation).

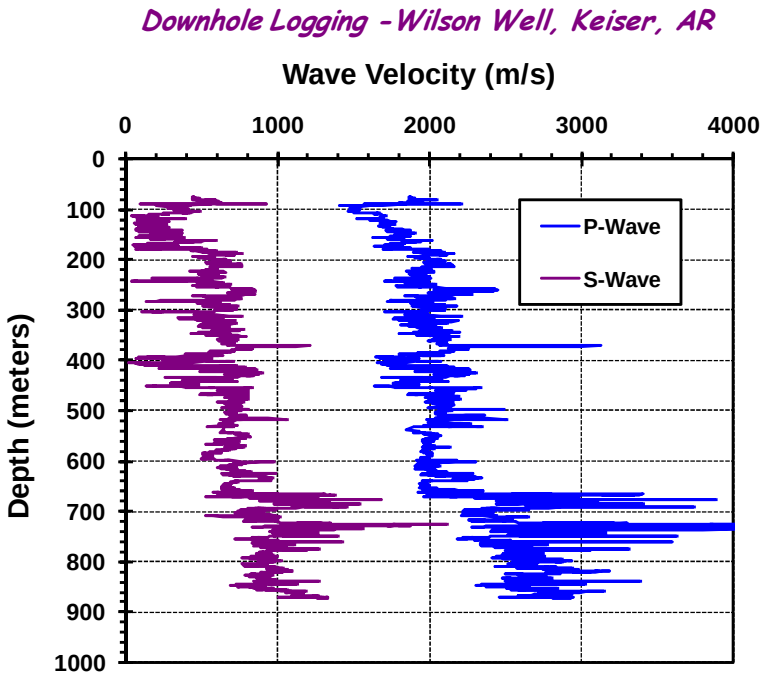

Figure A.13. P- and S- wave data using suspension logging system at Keiser, Arkansas (data courtesy of Dr. Mayne).

A.2 Hybrid Geotechnical-Geophysical Tests with Direct-Push Technology

The seismic piezocone test (SCPTu) is an enhanced version of CPT that obtains downhole shear wave velocity (V_s) measurements (usually at 1m rod breaks), thus collecting four separate sets of readings on soil behavior in a single sounding. Similarly, the seismic flat dilatometer test (SDMT) is available by adopting a single or double set of biaxial geophone receivers. Both SCPTu and SDMT are hybrid geotechnical-geophysical methods that use direct-push technology to obtain stress/pressure readings and provide downhole-type shear wave velocity (V_s). Compared to the conventional CHT and DHT in that obtain seismic velocities at 1.5 meter depth intervals, more frequent interval V_s profiling can be readily obtained from SCPTu and SDMT. In recent site investigation practices, these hybrid SCPTu and SDMT seem to provide sufficient data and robust analyses for routine engineering design purposes, including multiple readings from a single sounding for geostratigraphy, evaluation of soil properties, parameters, and small-strain stiffness.

A.3 Soil Parameters and Stress History Evaluated from SCPTu and SDMT

In addition to detailing the soil strata and layering, geotechnical parameters and properties can be estimated from various relationships, as listed in Table A.1, for the hybrid methods of seismic piezocone and seismic flat dilatometer testing.

Table A.1 Relationships for estimation of soil parameters from SCPTu and SDMT

Soil Parameter	**CPT Expressions**	**DMT Relationships**
Unit weight (γ_t)	γ_t (kN/m^3) = $1.95\gamma_w \cdot (\sigma_{vo}'/\sigma_{atm})^{0.06} \cdot (f_s/\sigma_{atm})^{0.06}$ (Mayne et al. 2010)	γ_t (kN/m^3) = $1.12 \cdot \gamma_w \cdot (E_D/\sigma_{atm})^{0.1} \cdot (I_D)^{-0.05}$ (Schmertmann 1986)
Relative density of sands (D_R)	D_R (%) = $100 \cdot [0.268 \cdot \ln(q_{t1}) - b_x]$ where b_x=0.525, 0.675, 0.825 for high, medium, and low compressibility, respectively (Jamilokowski et al.2001; Mayne 2006)	D_R (%) = $100 \cdot [\frac{K_D - 1}{7}]^{0.5}$ (Reyna & Chameau,1991)
Effective friction angle (φ')	SANDS: $\varphi'(°) = 17.6° + 11 \cdot \log[q_{t1}]$ (Kulhawy and Mayne,1990) CLAYS and SILTS: $\varphi'(°) = 29.5 \cdot B_q^{0.121} \cdot [0.256 + 0.336 B_q + \log(N_m)]$ where, $0.1 < B_q < 1$, $B_q = (u_2 - u_o)/(q_t - \sigma_{vo})$, $N_m = Q = \Delta(q_t - \sigma_{vo})/\sigma_{vo}'$ (Senneset, Sandven, & Janbu,1989)	SANDS: $\varphi'_{DMT}(°) = 28° + 14.6 \cdot \log(K_D) - 2.1 \cdot \log(K_D)^2$ (Marchetti,1997) CLAYS - no information
Lateral stress coefficient (K_0)	NC soil : $K_0 = 1 - \sin\varphi'$ (Jaky 1944) OC soil : $K_0 = (1 - \sin\varphi') \cdot OCR^{\sin\varphi'}$ (Mayne and Kulhawy 1982)	1. $K_{0,DMT} = (K_D/1.5)^{0.47} - 0.6$ (Marchetti,1980) 2. NC: $K_0 = 1 - \sin\varphi'$ OC: $K_0 = (1 - \sin\varphi') \cdot OCR^{\sin\varphi'}$
Small-strain shear modulus, G_0	$G_0 = 50 \cdot \sigma_{atm} \cdot \left[\frac{(q_t - \sigma_{vo})}{\sigma_{atm}}\right]^{m^*}$ where m*=0.6 for sands, 0.8 for silts, 1.0 for clays (Mayne 2007)	SANDS to CLAYS $G_0/E_D = f(K_0)$ (Hryciw and Woods 1988)

Notes: normalized cone resistance for clean sands: $q_{t1} = \frac{q_t/\sigma_{atm}}{\sqrt{\sigma_{vo}'/\sigma_{atm}}}$

Analytical CPTu relationships for penetration into soils have been derived using a variety of approaches such as cavity expansion theory (Vesic, 1977; Keaveny & Mitchell 1986), limit plasticity theory (Senneset et al. 1989; Sandven 1990), effective stress path methods (Konrad & Law 1987), state parameter (Jefferies & Been 2006), strain path method (Whittle & Aubeny 1993), and dislocation theory (Elsworth, 1993). In particular, a hybrid incorporation of spherical cavity expansion and critical state soil mechanics (SCE-CSSM) makes it possible to represent the cone tip resistance (q_t) and penetration pore water pressure (u_2) in closed-form (Mayne 1991; Chen & Mayne 1994; Mayne 2007). Sleeve friction (f_s) can be expressed by considering the shear-induced pore water pressure and the "beta" method for calculating side friction of pile. For undrained penetration, the resulting q_t, u_2, f_s expressions are as follows:

Equation A.1) $q_t = \sigma_{vo} + [(4/3)(\ln I_R + 1) + \pi/2 + 1]\cdot(M/2)(OCR/2)^{\Lambda}\cdot\sigma_{vo}'$

Equation A.2) $u_2 = u_0 + (4/3)(\ln I_R)\cdot(M/2)(OCR/2)^{\Lambda}\cdot\sigma_{vo}' + [(1 - (OCR/2)^{\Lambda})]\cdot\sigma_{vo}'$

Equation A.3) $f_s = [K_0\cdot\sigma_{vo}' - (1 - (OCR/2))^{\Lambda}] \cdot \sigma_{vo}']\cdot\tan\delta$

where $M = 6\sin\varphi'/(3-\sin\varphi')$, $\Lambda = (1 - C_s/C_c) \approx 0.8$ to 0.9, C_s = swelling index, C_c = virgin compression index, and $OCR = \sigma_p'/\sigma_{vo}'$.

The overconsolidation ratio (OCR), and its corresponding preconsolidation stress or yield stress (σ_p'), can be obtained from the hybrid cavity expansion-critical state model. For the purpose of engineering design, some specific parameters are assumed to obtain simplified equations ($\Lambda = 1$, $\varphi' = 30°$, $I_R = 100$). Consequently, first-order approximations in terms of preconsolidation stress are expressed using q_t, u_2, and σ_{vo}' (Mayne 2001, 2005, 2007).

Equation A.4) $\sigma_p' = \frac{(q_t - \sigma_{vo})}{M \cdot [1 + 1/3 \cdot \ln(I_R)]}$ → $\sigma_p' = 0.33 \cdot (q_t - \sigma_{vo})$

Equation A.5) $\sigma_p' = \frac{(u_2 - u_o)}{M / 3 \cdot \ln(I_R)}$ → $\sigma_p' = 0.54 \cdot (u_2 - u_o)$

Equation A.6) $\sigma_p' = \frac{(q_t - \sigma_{vo})}{0.975 M + 1/2}$ → $\sigma_p' = 0.60 \cdot (q_t - u_2)$

The hybrid SCE-CSSM framework might have a chance to be extended or generalized to explain more variety of geo-materials including even drained and partially drained cases. In particular, the applicability of cavity expansion theory for drained penetration has been reviewed (Mayne, 2006).

For stress history evaluation in clean sands, an empirical equation relating OCR to net cone resistance is derived from regression analyses from CPT calibration chamber data (Mayne, 2001). Again, if the equation is reduced to an approximate form, the formulation becomes similar to the simplified Equation A.4 for clay ($q_t \approx q_t - \sigma_{vo}$, $\varphi' = 35°$).

Equation A.7)

$$OCR = \left[\frac{0.192 (q_t / \sigma_{atm})^{0.22}}{(1 - \sin\phi')(\sigma_{vo}' / \sigma_{atm})^{0.31}} \right]^{\frac{1}{\sin\phi' - 0.27}} \Longrightarrow OCR \approx \frac{(q_{tnet} / \sigma_{atm})^{0.72}}{13.8 \cdot (\sigma_{vo}' / \sigma_{atm})^{1.02}} = \frac{\sigma_p'}{\sigma_{vo}'}$$

$$\Longrightarrow \sigma_p'(kPa) \approx 0.33 \cdot (q_t - \sigma_{vo})^{0.7}$$

Therefore, this similarity between the hybrid cavity expansion-critical state framework (Eq.A.4) for clay and the regression model (Eq.A.7) for sand offers an extended format (Eq. A.8, Mayne, et al. 2009). The applicability of the generalized equation for a variety of soil types is shown in Figure A.14.

Equation A.8) $\sigma_p' = 0.33 \cdot (q_t - \sigma_{vo})^{m'} (\sigma_{atm}/100)^{1-m'}$

where m' is a function of material index (I_c).

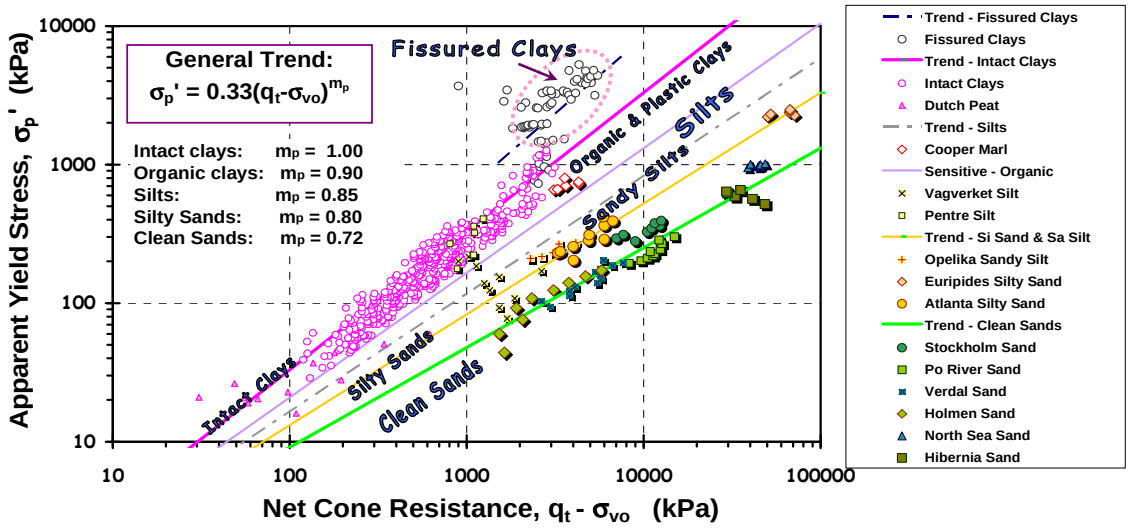

Figure A.14. General approach to preconsolidation stress interpretation by net cone resistance (Mayne, et al. 2009).

The hybrid SCE-CSSM model is also applied for dilatometer test. It assumes that lift-off pressure (p_o) and porewater pressures during cone penetration have similarities (Mayne & Bachus, 1989; Mayne 2006). For stress history evaluation using DMT, Kulhawy and Mayne (1990) proposed a first order estimation for σ_p'. Equation A.9 was derived from an average statistical trend based on 24 intact clays.

Equation A.9) $\sigma_p' = 0.509 \cdot (p_o - u_o)$

On the other hand, OCR equations (Eq.A.10) estimated from the horizontal stress index (K_D) were suggested based on the criteria of material index (I_D).

Equation A.10) $OCR_{DMT} = (0.5 \cdot K_D)^{1.56}$ if $I_D \leq 1.2$

$(0.67 \cdot K_D)^{1.91}$ if $I_D \geq 2$

$(m \cdot K_D)^n$ if $1.2 \leq I_D \leq 2$

where $m = 0.5+0.17 \cdot (I_D-1.2)/0.8$, $n = 1.56+0.35 \cdot (I_D-1.2)/0.8$ (Marchetti,1980; Viana da Fonseca, 2010)

APPENDIX B: DETECTION OF VOIDS AND SOFT ZONES BY CPT AT DOE SITE SOUTH CAROLINA

Possible void/soft zones were detected using piezocone tests at SRS K-site. Table B.1 provides the CPTu information including the detected void locations (refer to Chapter 2).

Table B.1. Void/Soft zone detection using CPT data at SRS K-site

ID	North	East	El. (m)	Void detection (depth, m)	I_{cRW}
C14	53189	41330	82.1	41-41.35	Q < 0
C15	53346	41059	82.2	39-39.2, 41.2-41.5	Q < 0
C16	53357	41074	82.2		
C17	53331	41074	82.3		
C18	53277	41250	82.4	39.25-39.4, 40.4-40.5	Q < 0
C19	53292	41265	82.3	38.6-40.4	Q < 0
C20	53279	40946	82.2	37.25-37.4	Q < 0
C21	53371	41074	82.1		
C22	53254	41265	82.4		
C23	53254	40957	82.2	37.6-38.5	Q < 0
C24	53291	40957	82.2	37.3-37.5, 39.3-41.5	Q < 0
C25	53204	41028	82.2	45.5-45.8	Q < 0
C26	53209	40926	82.1		
C27	53178	41200	81.9		
C28	53330	40908	82.2		
C29	53235	41121	82.3		
C30	53254	40902	82.3	35.9-36, 37.8-39.2	Q < 0
C31	53279	40921	82.2	39.7-40.1	>4
C32	53346	41105	82.3		
C33	53316	41126	82.4	40.5-41.9	>4
C34	53277	41283	82.4		
C35	53320	41139	82.4		
C36	53329	41121	82.4		
C37	53311	4114	82.4		
C38	53302	41131	82.4	38.9-39.5	>4
C39	53295	40932	82.2	35.3-35.7	>4
C40	53294	40957	82.0	39-40	Q < 0
C41	53302	41265	82.3		
C42	53204	40865	82.1		
C43	53280	40965	82.2	36.8-37.2	>4
C44	53247	40953	82.2	45.3-45.7	Q < 0
C45	53277	40892	82.2	45.2-45.3	Q < 0
C46	53254	40889	82.3	37.8-38, 39.8-40.7	Q < 0

Table B.1. continued

ID	North	East	El. (m)	Void detection (depth, m)	I_{cRW}
C47	53303	40914	82.2		
C48	53317	40930	82.3	44.95-45	Q < 0
C49	53297	41249	82.3		
C50	53277	41232	82.4		
C51	53241	40901	82.2	36.9-37.3, 40-42	Q < 0
C52	53289	41249	82.3	34.8-36.5	>4
C53	53357	41058	82.1		
C54	53353	41043	82.1		
C55	53337	41040	82.0	40.9-41	Q < 0
C56	53190	41028	82.2		
C57	53200	41008	82.1	40.3-41.5	Q < 0
C58	53346	41086	82.2	39.65-39.85	Q < 0
C59	53178	41327	82.1		
C60	53331	41074	82.3		

$$I_{cRW} = \sqrt{\{3.47 - \log(Q)\}^2 + \{1.22 + \log(F)\}^2}$$

APPENDIX C: GEOMATERIAL PARAMETERS AT DOE SITE, SC

Overview

For purposes related to geotechnical numerical simulations of computational stress and displacement predictions at the Savannah River Site (SRS), it was necessary to assign parametric soil engineering values to the representative geologic soil layers. The heavily interbedded complex geologic formations can be divided into the following units, beginning at the ground surface as follows: (1) Upland Unit, (2) Tobacco Road, (3) Dry Branch, (4) Santee, and (5) Warley Hill. Based on available published reports and technical documents, the various laboratory results, geophysical records, and in-situ test data obtained at the APT, SWPF and K-sites were reviewed by the author. The recommended geotechnical engineering parameters are discussed in subsequent sections.

Elasto-Plastic Material

1) Unit weight (γ_t)

Unit weight values are obtained from average values of measured tube samples taken at the APT, SWPF and K-sites. These values were also cross-checked using empirical correlations with available in-situ and geophysical data. Please refer to Figure C.1. Applied sources are as follows:

- APT site – cone penetration test (CPT), shear wave (V_s), B & P report
- SWPF and K-sites – cone penetration test (CPT), dilatometer (DMT), shear wave (V_s), S & W report
- The empirical equations consist of the following:

(a) CPT: $\gamma_t(kN/m^3) = 1.95 \cdot \gamma_w(\sigma_{vo}'/\sigma_{atm}')^{0.06} \cdot (f_s/\sigma_{atm})^{0.06}$ (ISFOG-II, 2010)

(b) DMT: $\gamma_t(kN/m^3) = 1.12 \cdot \gamma_w (E_D/\sigma_{atm}')^{0.1} \cdot (I_D)^{-0.05}$ (SOA-1, ICSMGE, 2009)

where, $E_D = 34.7 \cdot (p_1 - p_o)$ = dilatometer modulus; $I_D = (p_1 - p_o)/(p_o - u_o)$ = material index

(c) V_s : $\gamma_t(kN/m^3) = 8.64\log(V_s) - 0.74\log(\sigma_{vo}') - 0.40$ (SOA-1, ICSMGE, 2009)

Note: B & P report = Burns and Roe, Inc. 2001; S & W report = Shannon and Wilson, Inc. 2007

2) Shear wave velocity (V_s)

The shear wave velocity for each layer was evaluated from a review and averaging from a total of 87 SCPT downhole shear wave profiles obtained from the APT site. In addition, data summarized by Li et al. (2008) were averaged at other locations across the SRS areas, as documented in Chapter 9.

3) Small-strain shear modulus (G_{max})

The initial tangent shear modulus ($G_0 = G_{max}$) is directly calculated using γ_t and V_s.

- $G_{max} = (\gamma_t / g_a) \cdot V_s^2$

where $g_a = 9.8$ m/s^2 = gravitational constant

4) Young's modulus (E)

The stiffness of soils changes dramatically with level of strain, or alternatively with stress level. The initial stiffness (E_{max}) begins within the small-strain nondestructive region. Herein, the operational value of stiffness was expressed in terms of an equivalent (secant) value of Young's modulus (E), taken as 20 % of E_{max} which approximately corresponds to a factor of safety (FS) = 2.

- $E = 0.2 \times E_{max} = 2 \cdot G_{max} \cdot (1 + \upsilon')$, where the value of Poisson's ratio in working load region: $\upsilon' = 0.2$

5) Yield stress ratio (YSR)

Consolidation data obtained from SWPF site were averaged per each geologic formation. The yield stress (similar to preconsolidation stress) was evaluated for each consolidation test via a number of different graphical methods (e.g., Casagrande 1936, Becker et al. 1987, Boone 2010, etc). Please refer to Figure C.2(a). The normalized form is given as:

▪ YSR = yield stress (σ_y') / overburden stress (σ_{vo}')

which is similar to the more common term, overconsolidation ratio (OCR). The yield stress is important as an anchor point for the yield surface in constitutive modeling.

6) Yield stress

After YSR values are obtained from geologic formations, estimated effective overburden stress at mid-depth of each layer is multiplied. It is assumed ground water is located at about 15 meter depth. Original yield stress values are shown in Figure C.2(b).

▪ Yield stress = YSR × σ_{vo}'

7) Mohr-Coulomb friction angle (φ')

The effective friction angle φ' is determined from average values taken from evaluations of data from APT, SWPF and K-sites. Please refer to Figure C.3. Employed sources are as follows:

▪ APT – cone penetration test (CPT), B & P report

▪ SWPF and K-site – cone penetration test (CPT), dilatometer (DMT), S & W report

▪ Empirical equations

(a) CPT: $\phi'_{CPT}\,(\text{deg}) = 17.6^\circ + 11 \cdot \log(Q_{tn})$ where, $Q_{tn} = \dfrac{(q_t - \sigma_{vo})}{\sigma_{atm}} \cdot \left(\dfrac{\sigma_{atm}}{\sigma_{vo}'} \right)^n$

(b) DMT: ϕ'_{DMT} (deg) = $20° + 1/(0.04 + 0.06 / K_D)$

where, $K_D = (p_o - u_o)/ \sigma_{vo}'$ = lateral stress index

8) Mohr-Coulomb cohesion intercept (c')

The magnitude of effective cohesion intercept (c') is assumed as 2% of the magnitude of yield stress (σ_y').

- c' (kPa) = $0.02 \cdot \sigma_y'$

as detailed by Mayne and Stewart (JGE 1988) and Mesri and Abdel-Ghaffar (JGE 1993)

9) Drucker-Prager parameters (β and d)

The equivalent set of Drucker-Prager strength parameters (β and d) are determined as follows:

- $\tan\beta(\text{deg}) = \frac{6 \cdot \sin\phi'}{3 - \sin\phi'}$
- $d(kPa) = \frac{18 \cdot c' \cdot \cos\phi'}{3 - \sin\phi'}$

10) Dilation angle (ψ)

Dilation angle is obtained from numerical model input parameter shown in Li et al (2008).

11) Poisson's ratio (υ')

Poisson's ratio is taken equal to 0.2 for drained case for strains < 0.1%.

12) Lateral stress coefficient (K_o)

The coefficient of lateral stress (K_o) is calculated using the effective stress friction angle (φ') and yield stress ratio (YSR):

- $K_o = (1-\sin\varphi') \cdot OCR^{\sin\varphi'}$

where YSR is used in lieu of OCR. (Mayne and Kulhawy 1982)

Modified Cam Clay Material

1) Compression index (C_c)

The virgin compression index (C_c) is determined as a mean value derived from relatively undisturbed consolidation data at SWPF. To quantify the laboratory sample disturbance effect, a rating system developed by Terzaghi et al. (1996) is adopted. The ratings are determined from 'A' (excellent) to 'E'(very poor quality), based on the magnitude of volumetric strain [$(\Delta e/(1+e_o)$] measured to reach the in-situ effective overburden stress level. The rating criteria are shown in Table C.1. The specimens which have only rating A,B, and C are applied for recommended C_c value. Please refer to Figure C.4(a).

Table C.1. Ratings of sample disturbance effect for consolidation data (Terzaghi et al.,1996)

Volumetric strain (%)	<1	1-2	2-4	4-8	>8
Quality	A	B	C	D	E

2) Recompression index (C_r)

Values of the recompression index (C_r) from consolidation test data are obtained in the same manner as the virgin compression indices. Please refer to Figure C.4(b).

3) Isotropic compression index (λ) and isotropic recompression index (κ)

The CSSM parameter for compression and swelling are denoted by λ and κ, respectively, and are evaluated using following equations:

- $\lambda = C_c / \ln(10) = C_c / 2.3$
- $\kappa = C_r / \ln(10) = C_r / 2.3$

4) Critical state friction angle (φ'_{cs})

Critical state friction angle (φ'_{cs}) is taken equal to the Mohr-Coulomb friction angle (φ').

5) Friction parameter (M_{TXC})

The CSSM frictional parameter M_{TXC} is defined as follow:

- $M_{TXC} = \frac{6 \cdot \sin \phi_{cs}'}{3 - \sin \phi_{cs}'}$

Note : TXC – Triaxial Compression

6) Void ratio at 1kPa (e_{1kPa})

Based on consolidation data at SWPF, void ratio (e_0) under 1kPa is approximately calculated using C_r slope per each specimen. Mean values are adopted for recommended e_{1kPa}.

7) Specific volume at 1kPa (N) and specific volume on CSL at 1kPa (Γ)

Specific volume is defined as v = 1+e. Thus, the parameter N can be calculated using e_{1kPa}.

- $N = 1 + e_{1kPa}$

The parameter Γ on the critical state line (CSL) is related to N as follow:

- $\Gamma = N - (\lambda - \kappa) \cdot \ln(2)$

8) Void ratio (e_o)

The initial void ratio (e_o) is determined as the void ratio under the normal stress corresponding to the estimated geostatic stress state.

A complete summary listing of all interpreted geotechnical parameters is given in Table C.2 for the Elasto-Plastic Model and in Table C.3 for the Modified Cam Clay constitutive model.

Table C.2. Recommended parameters for elastic and elasto-plastic material

Parameter	Source	Upland Unit	Tobacco Road	Dry Branch	Santee	Warley Hill
Unit weight [γ_t, kN/m^3]	*Average (APT, SWPF)*	20.2	19.9	19.9	20.0	21.0
Shear velocity [V_s, m/s]	*87 Vs data*	433.9	342.1	344.2	353.9	375.9
G_{max} [MPa]	*Calculated*	388	237	240	255	302
Young's modulus [E, MPa]	*Calculated*	186	114	115	123	145
Yield stress ratio [YSR]	*Consol. Data (SWPF)*	5.98	2.59	2.53	1.08	1.97
Yield stress [σ_y', kPa]	*Consol. Data (SWPF)*	736	870	1205	631	1396
M-C Friction angle [ϕ', ^{o}]	*Average (APT, SWPF)*	35.1	34.9	33.7	31.6	33.8
M-C Cohesion intercept [c', kPa]	*Calculated*	14.7	17.4	24.1	12.6	27.9
D-P parameter [β, ^{o}]	*Calculated*	1.42	1.41	1.36	1.27	1.37
D-P parameter [d, kPa]	*Calculated*	89	106	148	78	171
Dilation [ψ, ^{o}]	*Li 2008*	14	13	13	0	13.3
Poisson's ratio [u]	*Assumed*	0.2	0.2	0.2	0.2	0.2
Earth pressure [K_0]	*Calculated*	1.19	0.74	0.75	0.49	0.65

Table C.3. Recommended parameters for Modified Cam Clay material

Parameter	Source	Upland Unit	Tobacco Road	Dry Branch	Santee	Warley Hill
Unit weight [γ_t, kN/m^3]	*Average (APT, SWPF)*	20.2	19.9	19.9	20.0	21.0
Compression index [C_c]	*Consol. Data (SWPF)*	0.22	0.24	0.08	0.13	0.37
Isotropic compression index [λ]	Calculated	0.096	0.103	0.035	0.059	0.160
Recompression index [C_r]	*Consol. Data (SWPF)*	0.013	0.013	0.006	0.007	0.002
Isotropic recompression index [κ]	Calculated	0.006	0.006	0.003	0.003	0.001
Yield stress [σ_y', kPa]	*Consol. Data (SWPF)*	736	870	1205	631	1396
Critical state friction angle [φ_{cs}']		35.0	34.8	33.2	31.1	33.3
Friction parameter, M_{TXC}	*Calculated*	1.42	1.41	1.36	1.27	1.37
Void ratio at 1kPa [e_{1kPa}]	*Consol. Data (SWPF)*	0.83	0.74	0.89	0.98	1.04
N (specific volume at 1kPa)	*Calculated*	1.83	1.74	1.89	1.98	2.04
Γ (specific volume on CSL at 1kPa)	Calculated	1.77	1.68	1.87	1.94	1.93
Void ratio [e_o]	*Consol. Data (SWPF)*	0.76	0.67	0.76	0.83	0.85

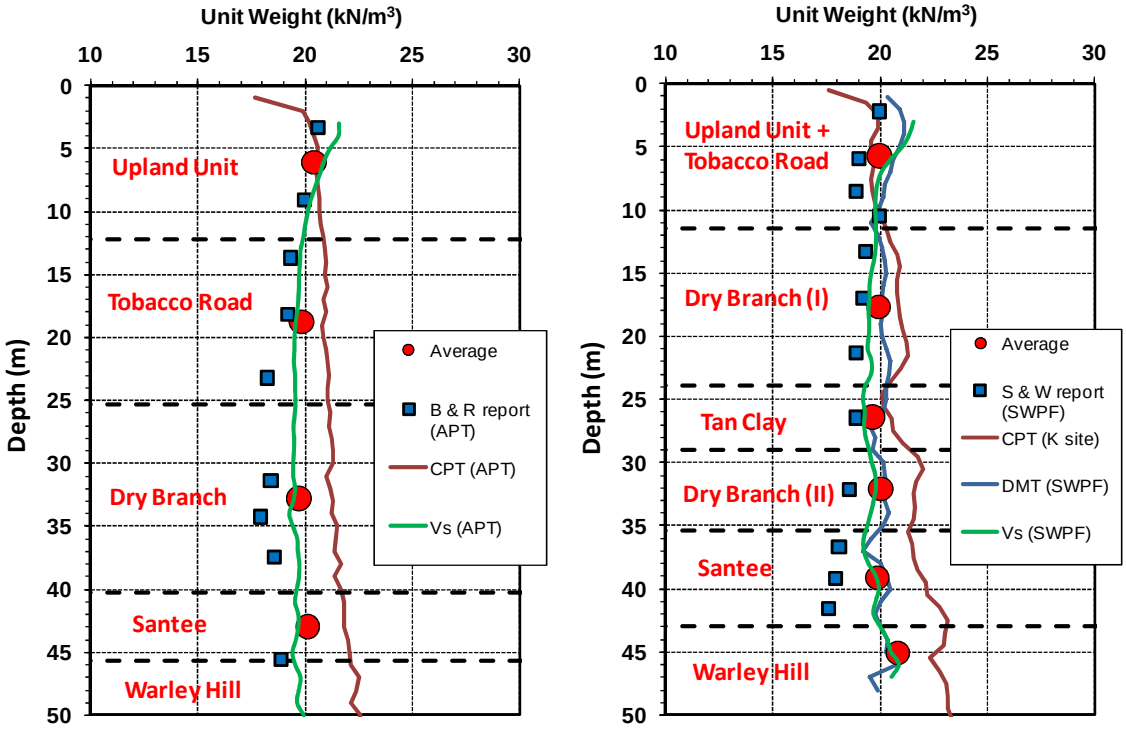

Figure C.1. Unit weight profile with approximate geologic formation: a) APT, b) SWPF and K-site.

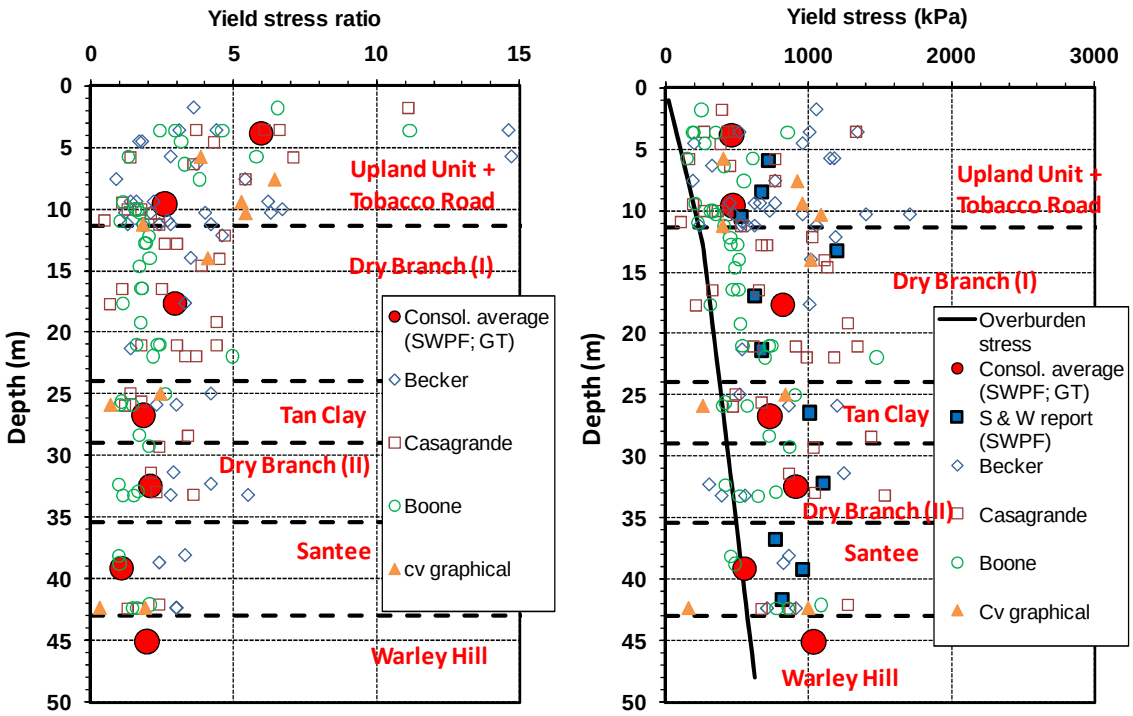

Figure C.2. Stress history profile with approximate geologic formation at SWPF: a) YSR, b) yield stress.

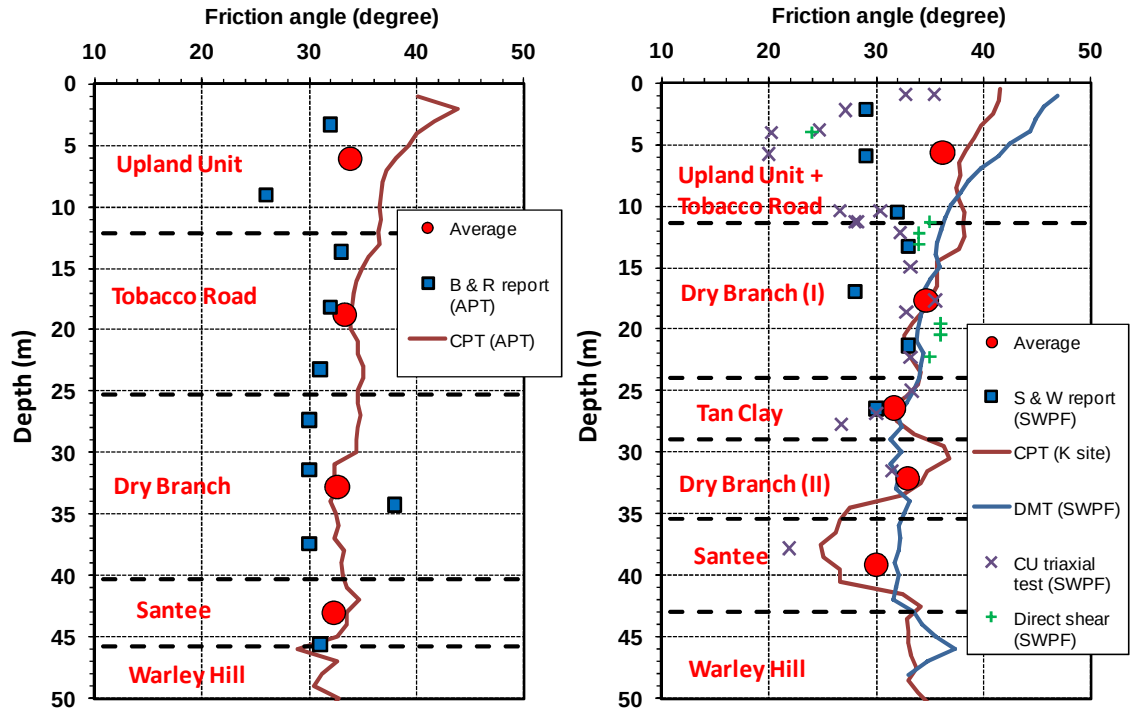

Figure C.3. Effective friction angle profile with approximate geologic formation: a) APT, b) SWPF and K-site.

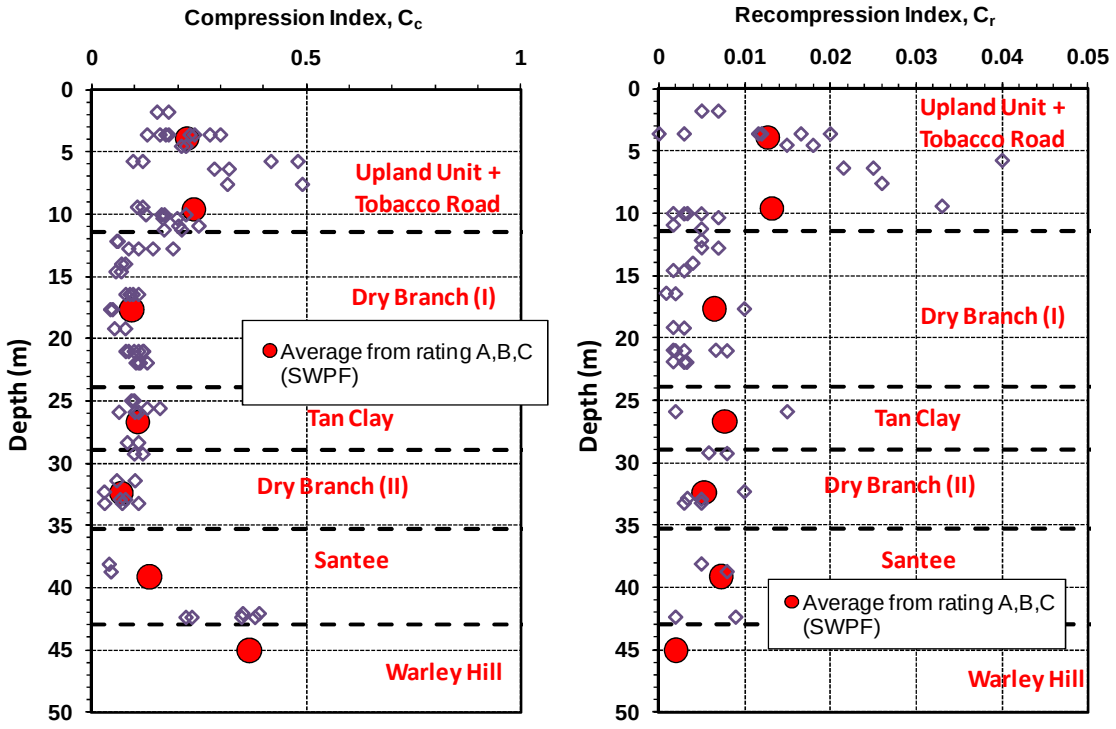

Figure C.4. a) Compression index (C_c) profile; b) Recompression index (C_r) profile with approximate geologic formation at SWPF.

APPENDIX D: STRESS HISTORY EVALUATION FROM LAB CONSOLIDATION TEST DATA AT DOE SITE, SC

D.1 Stress History Evaluation by Laboratory Consolidation Data

Results from a large number of laboratory consolidation tests were reviewed for interpretation of the preconsolidation stress (σ_p') values (or yield stress, σ_y'). Values obtained using the Casagrande (1936) method for σ_p' were shown in Figure 2.21. Herein, the σ_p' results (Shannon & Wilson 2007) analyzed using the Becker et al. (1987) method (Shannon & Wilson 2007) and Boone (2010) method (by author) are shown with interpretations from in-situ tests in Figure D.1 and D.2, respectively.

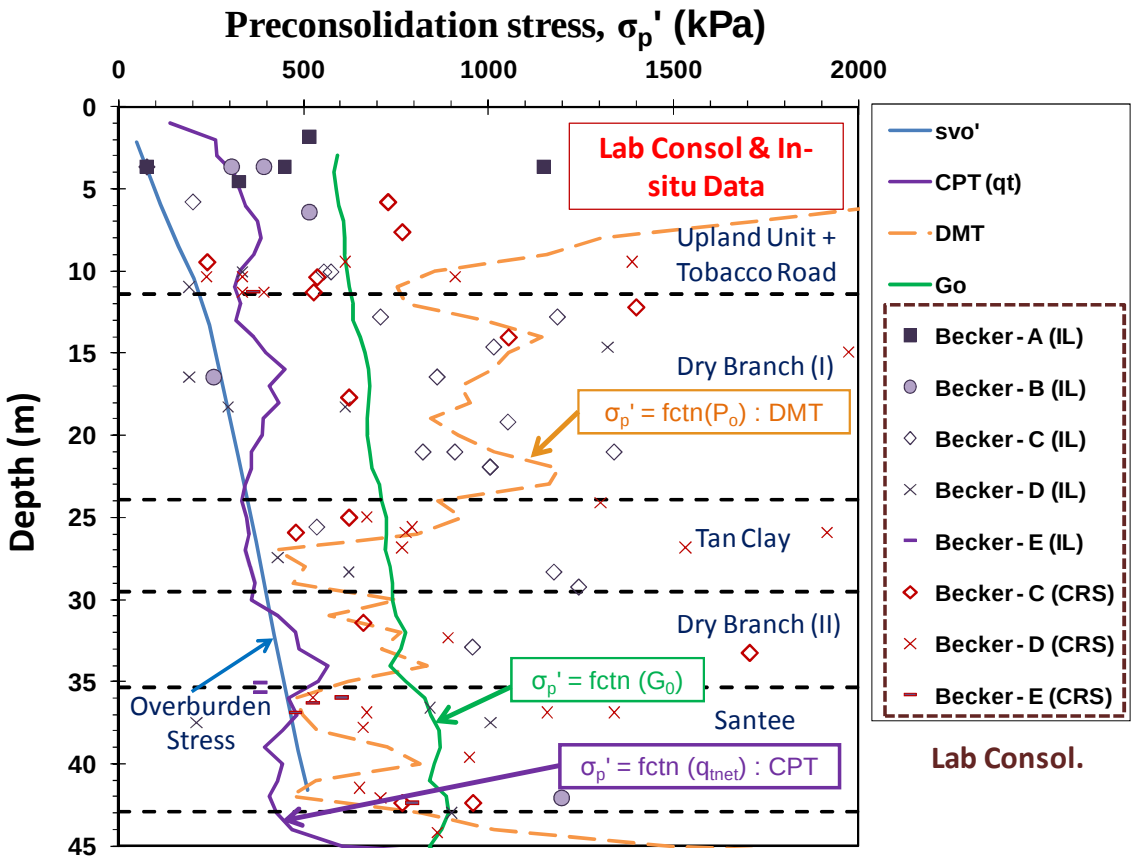

Figure D.1. Preconsolidation stress (σ_p') evaluations by various in-situ tests and laboratory consolidation data (Becker et al. method) at SRS SWPF.

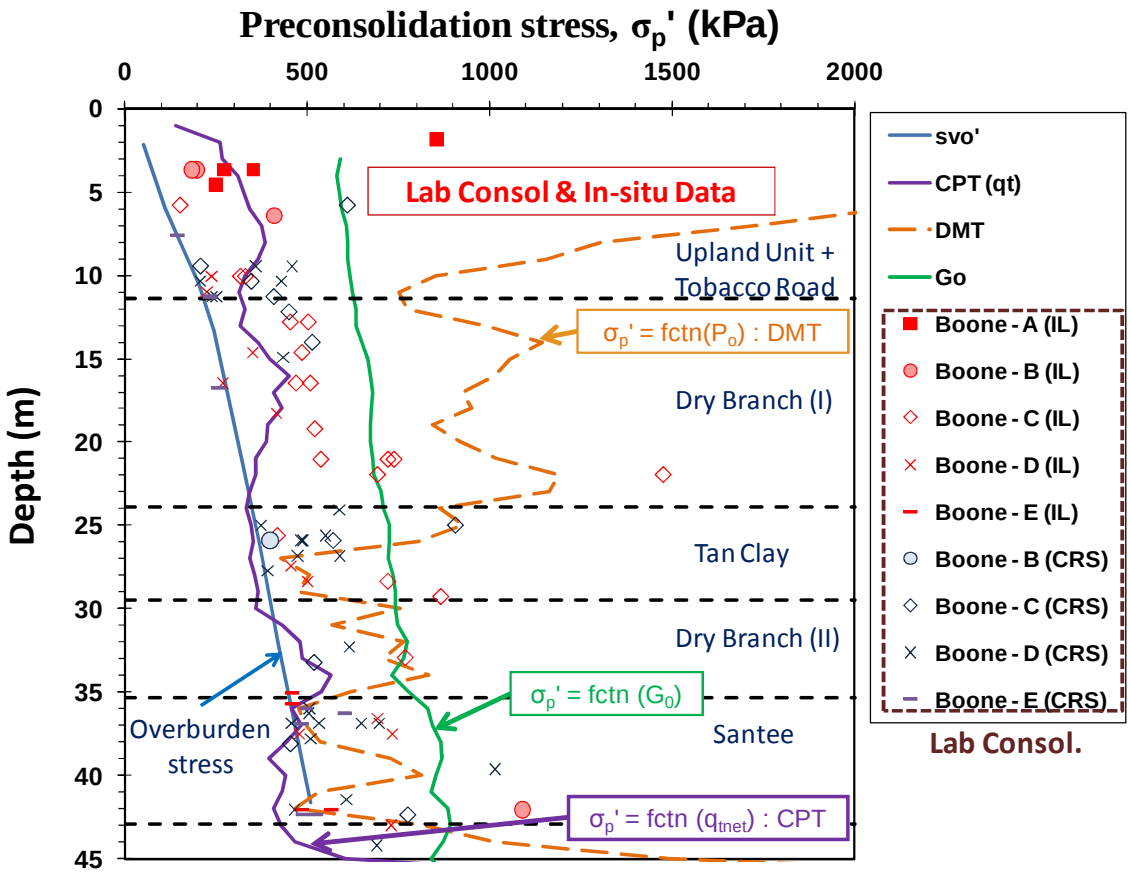

Figure D.2. Preconsolidation stress (σ_p') evaluations by various in-situ tests and laboratory consolidation data (Boone method) at SRS SWPF.

Figure D.3 depicts the determination of σ_p' using the recent Boone method. The σ_p' is determined as follow: $\sigma_p' = 10^{[(e_c-e_p)/C_{c,max}]}$; where $e_p = (e_c/C_{c,max} - e_r/C_r)/(1/C_{c,max} - 1/C_r)$; $e_c = C_{c,max}\cdot\log(\sigma_{v,max}') + e_{min}$; $e_r = C_r\cdot\log(\sigma_{vo}') + e_{vo}$). Both the strain-energy method by Becker et al. (1987) and the recent Boone (2010) method still show rather scattered results in comparison with other field test results. However, it seems the evaluation sensitivity decreases somewhat in Boone method. The profile is separated by approximate geologic formations. Table D.1 summarizes all consolidation results along for profile for the individual geologic formations.

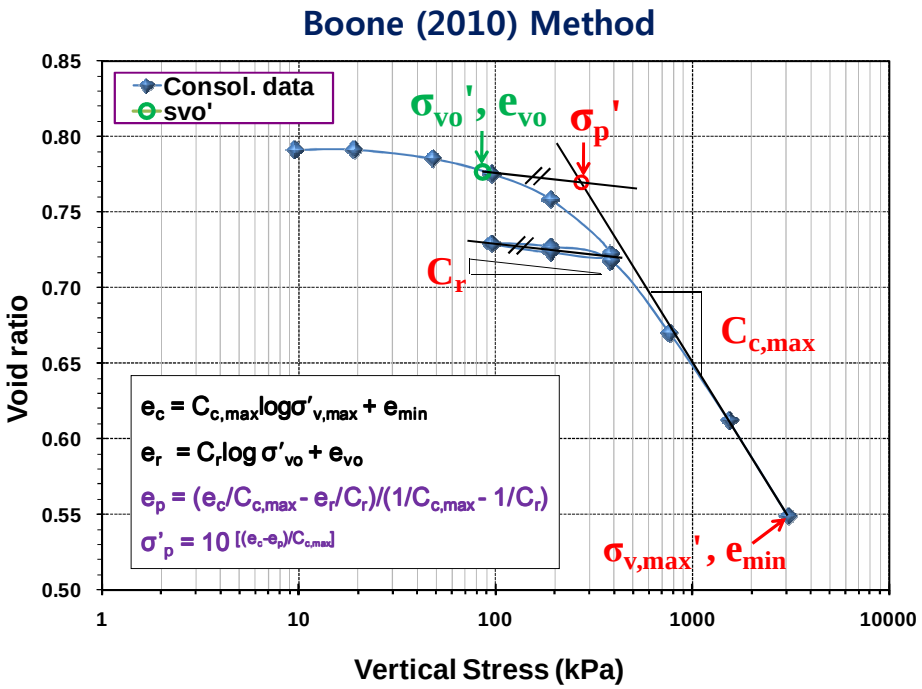

Figure D.3. Representative example of σ_p' determination using Boone (2010) method using consolidation data from SWPF.

Table D.1. Summary for preconsolidation stresses evaluated from consolidation data using three interpretative approaches at SRS SASW.

Unit	Depth (m)	USCS	Data no.	Preconsolidation stress (kPa)							
				Becker		Casagrande		Boone		All	
				Average	1 std.	Average	1 std.	Average	1 std.	Average	1 std.
UU, TR	11.4	SC, CH	26	515.6	291.1	404.9	279.0	329.4	162.0	416.6	259.1
Dry Branch (I)	23.9	SC, SP-SC, SP-SM	23	986.3	368.2	711.4	374.2	528.5	248.3	738.7	379.7
Tan Clay	29.5	SC, SP-SC	11	967.2	480.6	810.1	468.1	583.7	173.9	780.4	413.8
Dry Branch (II)	35.3	SC, SP-SC	13	726.7	421.2	530.8	489.2	531.1	114.7	589.7	368.9
Santee	42.9	SC,SM, SP-SM	21	777.6	278.1	410.0	221.5	588.7	142.7	588.2	253.3
Warley Hill	45.4+	SC, ML	5	1005.5	172.6	906.5	350.8	782.3	255.1	886.5	255.6

Note: std = standard deviation

D.2 Stress History Evaluation Using CU Triaxial Test Data

Laboratory strength data from isotropically-consolidated undrained triaxial compression tests (CIUC) at the SRS SWPF site have been reviewed and re-evaluated by author. The data were submitted by Shannon and Wilson, Inc. (2007) for the 'Geotechnical Investigation Phase II Project for the Salt Waste Processing Facility (SWPF)'. To determine the effective friction angle (φ') and effective cohesion intercept (c'), graphs of the effective stress [$p'=(\sigma_1'+\sigma_3')/2$] and shear stress [$q=(\sigma_1'-\sigma_3')/2$] at failure are plotted, then the slope ($m = \sin\varphi'$) and intercept ($a'=c'\cdot\cos\varphi'$) are determined from a trend line. Table D.2 shows CIUC triaxial test results in detail. Based on CIUC triaxial tests, the value of Skempton's parameter A_f [$(\Delta u-\Delta\sigma_3)/(\Delta\sigma_1-\Delta\sigma_3)$] is shown in Figure D.4. In clay soils, the parameter A_f values are related to OCR. For instance, A_f approaches zero or slightly negative values at high OCRs for clays (Mayne and Stewart, 1988). Thus, it might provide an insight for stress history evaluation at the SRS.

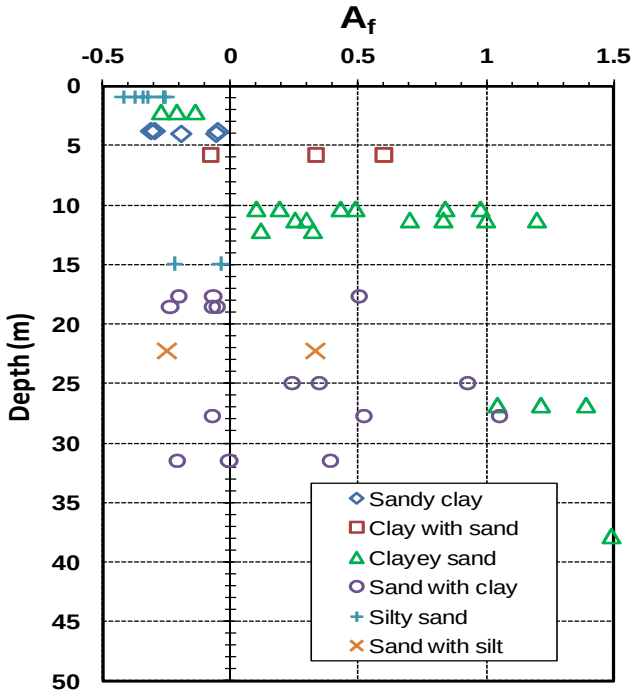

Figure D.4. Skempton's parameter A_f observed from CIUC triaxial tests at SRS SWPF.

Table D.2. Summary of CIUC triaxial test results at SRS SWPF site

ID	#	Depth	strain	A_f	p'	q	a'	m (slope)	c'	ϕ'	Soil type
		m	%		kPa	kPa	kPa		kPa	degree	
A-14 S-1	Test 1	0.91	20	-0.26	177.1	100.5	4.61	0.5409	5.48	32.7	Silty sand
	Test 2	0.91	20	-0.37	964.9	525.7					
	Test 3	0.91	20	-0.34	1134.1	618.7					
A-14 S-3	Test 1	3.81	18.07	-0.31	254.2	112.7	7.28	0.418	8.01	24.7	Sandy clay
	Test 2	3.81	20	-0.29	479.1	211.3					
	Test 3	3.81	16.47	-0.05	539.7	229.9					
A-16 S-1	Test 1	0.91	19.65	-0.42	880.8	466.1	0.07	0.5795	0.08	35.4	Silty sand
	Test 2	0.91	8.39	-0.25	894.8	563.5					
	Test 3	0.91	9.98	-0.32	1963.8	1137.5					
B-32 S-41	Test 1	37.8	0.36	3.59	179.9	45.3	8.36	0.3733	9.01	21.9	Clayey sand
	Test 2	37.8	4.03	1.53	448.1	228.2					
	Test 3	37.8	1.31	1.49	809.7	288.2					
B-33 S-11	Test 1	10.36	17.45	0.19	282.4	155.2	12.11	0.5067	14.04	30.4	Clayey sand
	Test 2	10.36	14.67	0.43	421.0	218.8					
	Test 3	10.36	16.15	0.84	420.2	231.6					
B-34 S-2	Test 1	2.21	10.76	-0.21	204.5	116.0	21.36	0.455	23.99	27.1	Clayey sand
	Test 2	2.21	16.56	-0.14	249.9	133.2					
	Test 3	2.21	19.34	-0.27	513.8	255.4					
B-34 S-12	Test 1	11.28	14.03	0.25	283.3	143.4	10.27	0.4702	11.63	28.0	Clayey sand
	Test 2	11.28	11.01	0.70	360.5	179.9					
	Test 3	11.28	14.01	1.00	427.1	211.1					
B-36 S-16	Test 1	14.94	19.82	-0.04	624.2	344.1	2.24	0.5476	2.68	33.2	Silty sand
	Test 2	14.94	14.87	-0.22	2391.9	1312.1					
	Test 3	14.94									
B-36 S-20	Test 1	18.59	18.42	-0.24	1535.8	845.4	24.65	0.5422	29.34	32.8	Sand with clay
	Test 2	18.59	20.01	-0.05	1568.6	887.7					
	Test 3	18.59	17.03	-0.07	2360.3	1304.0					
B-36 S-27	Test 1	24.99	20	0.24	496.6	283.0	10.28	0.5493	12.30	33.3	Sand with clay
	Test 2	24.99	0.78	0.93							
	Test 3	24.99	20	0.35	1268.8	707.2					
B-36 S-29	Test 1	26.82	19.92	1.04	230.1	125.6	10.64	0.4998	12.28	30.0	Clayey sand
	Test 2	26.82	0.77	1.21							
	Test 3	26.82	11.86	1.39	575.0	298.0					
B-38 S-11	Test 1	10.36	18.75	0.10	334.5	174.7	25.9	0.4477	28.96	26.6	Clayey sand
	Test 2	10.36	13.34	0.49	397.0	195.2					
	Test 3	10.36	7.93	0.98	390.7	210.2					

Table D.2. continued

ID	#	Depth	strain	A_f	p'	q	a'	m (slope)	c'	ϕ'	Soil type
		m	%		kPa	kPa	kPa		kPa	degree	
B-38 S-30	Test 1	27.74	20	-0.07	875.7	441.9	45.77	0.45	51.25	26.7	Sand with clay
	Test 2	27.74	20	0.52	725.6	358.8					
	Test 3	27.74	20	1.05	699.8	372.3					
B-39 S-6	Test 1	5.79	12.4	0.60	98.8	62.4	31.00	0.3419	32.99	20.0	Clay with sand
	Test 2	5.79	5.7	-0.08	437.7	167.2					
	Test 3	5.79	5.42	0.34	386.9	179.2					
B-39 S-12	Test 1	11.28	11.13	0.30	267.3	135.0	20.65	0.4738	23.45	28.3	Clayey sand
	Test 2	11.28	19.75	1.20	229.9	140.0					
	Test 3	11.28	11.84	0.83	473.7	247.0					
B-39 S-24	Test 1	22.25	15.31	-0.25	1737.6	950.5	N/A	N/A	N/A	N/A	Sand with silt
	Test 2	22.25	0.6	0.33	680.5	115.2					
	Test 3	22.25									
B-41 S-4	Test 1	4.04	20	-0.19	318.7	176.5	66.58	0.3448	70.93	20.2	Sandy clay
	Test 2	4.04	20	-0.06	483.2	233.2					
	Test 3	4.04									
B-41 S-34	Test 1	31.47	13.57	-0.21	1765.1	944.5	13	0.5231	15.25	31.5	Sand with clay
	Test 2	31.47	14.86	-0.01	1826.2	961.6					
	Test 3	31.47	16.64	0.39	1451.3	770.9					
B-42 S-13	Test 1	12.19	20	0.12	408.5	235.1	8.56	0.5326	10.12	32.2	Clayey sand
	Test 2	12.19	20	0.32	566.4	304.2					
	Test 3	12.19	1.6	6.17	88.9	52.9					
B-43 S-19	Test 1	17.68	20	-0.20	1856.7	1119.6	13.65	0.5813	16.77	35.5	Sand with clay
	Test 2	17.68	20	0.50	561.9	331.6					
	Test 3	17.68	10.46	-0.07	2480.2	1437.3					

The different OCR estimation methods based on strength data are examined in Table D.3. The OCR profile evaluated from a total of 20 CIUC test data is shown in Figure D.5. Table D.4 summarizes the selected strength data (σ_{vo}' condition) and OCR evaluation results.

Table D.3. OCR evaluation methods using strength data for clay soil

▪ SHANSEP or CSSM for OC clay soil	Eq. (D.1) $S_u/\sigma_{vo}' = S_u/\sigma_{vnc}' \cdot OCR^{\Lambda}$ where, $\Lambda = 1 - C_s/C_c$; strength rebound parameter
▪ In-situ OCR estimation for Modified Cam clay (Mayne, 1980)	Eq. (D.2) $S_u/\sigma_{vo}' = (M/2)\cdot(OCR/2)^{\Lambda}$ Original model: $OCR = \left[\left(\frac{2}{M}\right)\frac{s_u}{\sigma_{vo}'}(o.c.)\cdot\exp(\Lambda_0)\right]^{1/\Lambda_0}$ where, $M = 6\sin\varphi'/(3-\sin\varphi')$ is the ratio of Cambridge (q/p') at failure
▪ General limits based on observed relationships (Mayne, 1988)	Eq. (D.3) $(1.82\cdot S_u/\sigma_{vo}')^{1.43} \le OCR \le (4\cdot S_u/\sigma_{vo}')^{1.43}$ Eq. (D.4) $OCR_{CIUC} = \left[\frac{(s_u/\sigma_{vo}')}{0.75\sin\phi'}\right]^{1.43}$

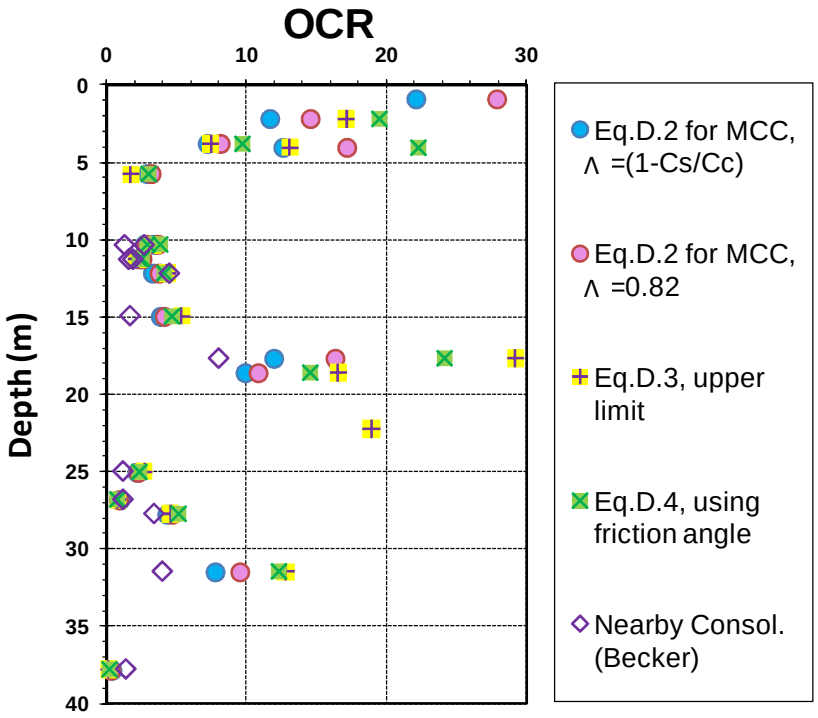

Figure D.5. Interpreted OCR profile evaluated by laboratory strength data.

Table D.4. Summary of CIUC triaxial tests for stress history evaluation

Boring ID	Depth m	σ_{vo}' kPa	σ_{vc}' kPa	A_f	p' kPa	q kPa	M	S_u/σ_{vc}'	Estimated test OCR	Estimated σ_p' kPa	Estimated In-situ OCR Eq.(D.3)	Estimated In-situ OCR Eq.(D.4)	Estimated In-situ OCR Eq.(D.2)	Soil type
A-14 S-1	0.91	17.5	23.7	-0.262	177.1	100.5	1.3	4.247	31.6	748.9	42.7	44.2	22.1	Silty sand
A-14 S-3	3.81	73.3	72.2	-0.309	254.2	112.7	1.0	1.561	7.6	546.2	7.4	9.7	7.2	Sandy clay
A-16 S-1	0.91	17.5	24.1	-0.419	880.8	466.1	1.4	19.367	277.1	6668.1	380.7	359.2	110.7	Silty sand
B-32 S-41	37.8	460.0	459.5	3.586	179.9	45.3	0.9	0.099	0.1	67.0	0.1	0.2	0.5	Clayey sand
B-33 S-11	10.36	191.5	187.0	0.193	282.4	155.2	1.2	0.830	3.1	572.7	3.0	3.0	2.7	Clayey sand
B-34 S-2	2.21	42.5	40.6	-0.208	204.5	116.0	1.1	2.859	18.0	729.0	17.1	19.5	11.7	Clayey sand
B-34 S-12	11.28	210.7	212.6	0.254	283.3	143.4	1.1	0.675	2.3	484.4	2.3	2.6	2.5	Clayey sand
B-36 S-16	14.94	285.0	268.8	-0.037	624.2	344.1	1.3	1.280	5.7	1530.3	5.4	4.7	3.9	Silty sand
B-36 S-20	18.59	320.0	297.5	-0.236	1535.8	845.4	1.3	2.841	17.8	5298.0	16.6	14.5	9.9	sand with clay
B-36 S-27	24.99	382.0	349.8	0.241	496.6	283.0	1.3	0.809	3.0	1033.6	2.7	2.3	2.2	sand with clay
B-36 S-29	26.82	402.0	366.3	1.043	230.1	125.6	1.2	0.343	0.9	317.2	0.8	0.8	0.9	Clayey sand
B-38 S-11	10.36	201.1	195.4	0.102	334.5	174.7	1.1	0.894	3.4	665.9	3.3	3.9	3.4	Clayey sand
B-38 S-30	27.74	418.0	370.3	-0.072	875.7	441.9	1.1	1.193	5.1	1907.0	4.6	5.1	4.3	sand with clay
B-39 S-6	5.79	111.5	111.6	0.601	98.8	62.4	0.8	0.559	1.7	194.4	1.7	3.1	2.9	clay with sand
B-39 S-12	11.28	210.7	212.9	0.298	267.3	135.0	1.1	0.634	2.1	443.9	2.1	2.3	2.3	Clayey sand
B-39 S-24	22.25	320.0	320.8	-0.245	1737.6	950.5	0.0	2.962	18.9	6064.6	19.0	N/A	N/A	sand with silt
B-41 S-4	4.04	77.8	75.2	-0.192	318.7	176.5	0.8	2.348	13.6	1018.9	13.1	22.3	12.7	Sandy clay
B-41 S-34	31.47	415.0	427.9	-0.208	1765.1	944.5	1.3	2.207	12.4	5310.3	12.8	12.4	7.8	sand with clay
B-42 S-13	12.19	218.0	229.8	0.120	408.5	235.1	1.3	1.023	4.1	949.7	4.4	4.1	3.4	Clayey sand
B-43 S-19	17.68	277.0	282.5	-0.203	1856.7	1119.6	1.4	3.962	28.7	8095.3	29.2	24.2	12.0	sand with clay

Notes *: Estimated test OCR = $4\cdot(S_u/\sigma_{vc}')^{1.43}$; Estimated in situ $\sigma_p' = OCR\cdot(\sigma_{vc}')$; In situ OCR (1) = $(\sigma_p' / \sigma_{vo}')$*

It was known Skempton's parameter A_f values are related to OCR in clay soil. OCR values interpreted from strength data are plotted with A_f values in Figure D.6. The observed trend at SWPF site is similar to other clays presented in Mayne and Stewart (1988). For further investigation, theoretical relationships (Equation D.5 and D.6) between the pore pressure parameter at failure (A_f) and OCR are provided together. It is noted that the theoretical lines using effective friction angle of 35 degree agree better with the observed data than the cases where effective friction angle of 30 degree is applied.

Eq. (D.5) Theoretical relationship for original Cam clay: $$A_f = \left[\left(\frac{e}{OCR}\right)^{\Lambda} - 1\right] \cdot M^{-1} + \frac{1}{3}$$

Eq. (D.6) Theoretical relationship for modified Cam clay: $$A_f = \left[\left(\frac{2}{OCR}\right)^{\Lambda} - 1\right] \cdot M^{-1} + \frac{1}{3}$$

(Mayne, 1980)

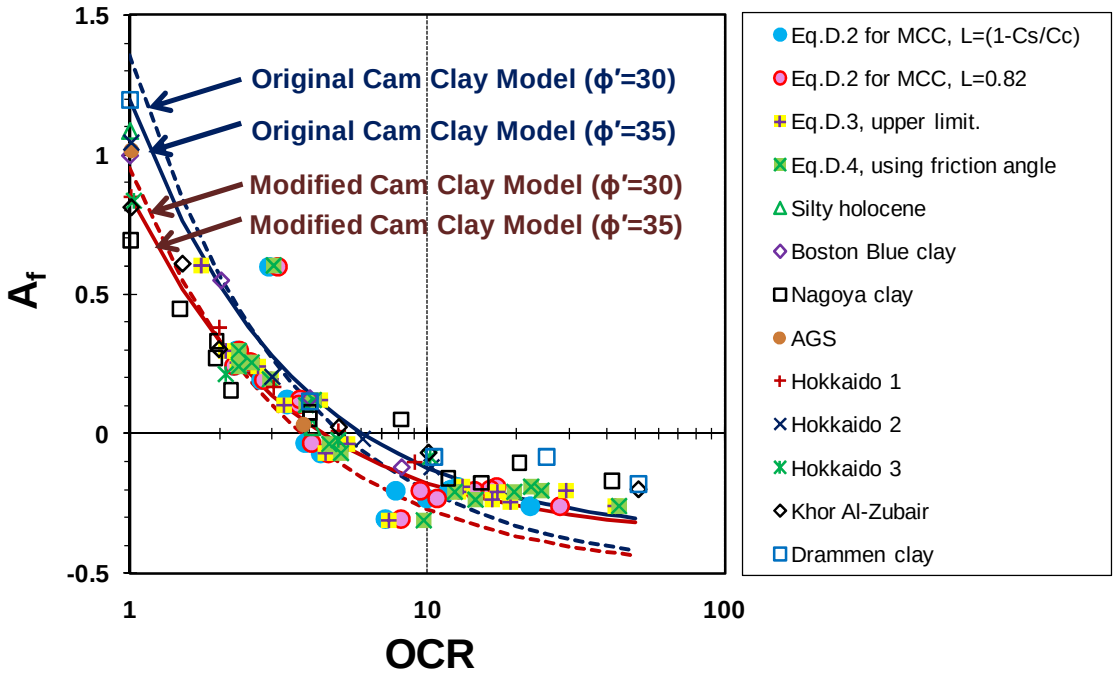

Figure. D.6. Observed trend between A_f and OCR for CIUC tests (Mayne and Stewart, 1988) with SRS data.

APPENDIX E: OBSERVED TREND BETWEEN K_0 AND PAIRED V_S RATIO FROM LABORATORY TESTING DATA

K_0 versus paired V_s ratio from laboratory testing data

As the relationship between in-situ K_o and V_s ratio is investigated, the similar approach is conducted using laboratory data. Bender element tests allow to generate multiple types of V_s. Details of employed laboratory testing data were provided in Table 3.3. Observed trends are shown in Figure E.1 (K_0 versus V_{sHH}/V_{sVH}) and Figure E.2 (K_0 versus V_{sHH}/V_{sHV}). K_0 prediction line which was suggested by Zeng and Ni (1999) and in-situ regression K_0 line are compared together.

• K_0 prediction for inherent isotropic soil (Zeng and Ni 1999):

$$K_0 = \left(\frac{V_{sHH}}{V_{sVH}}\right)^{(2/n)} \quad \text{or} \quad K_0 = \left(\frac{V_{sHH}}{V_{sHV}}\right)^{(2/n)}$$

where n is assumed as an empirical value of 0.25.

• K_0 regression line using in-situ data (Chapter 4)

(a) HH and VH mode: $K_0 = 0.78 \cdot \left(\frac{V_{sHH}}{V_{sVH}}\right)^{2.55}$; $R^2 = 0.809$, N = 124, R.S.E = 0.112

(b) HH and HV mode: $K_0 = 0.85 \cdot \left(\frac{V_{sHH}}{V_{sHV}}\right)^{3.19}$; $R^2 = 0.593$, N = 150, R.S.E = 0.179

where R^2 = coefficient of determination, N = number of data points, and R.S.E = residual standard error from log regression. Both lines do not seem really well matched for laboratory data which show rather scattered measurements. Further analyses are conducted based on HH and VH modes which have more dataset.

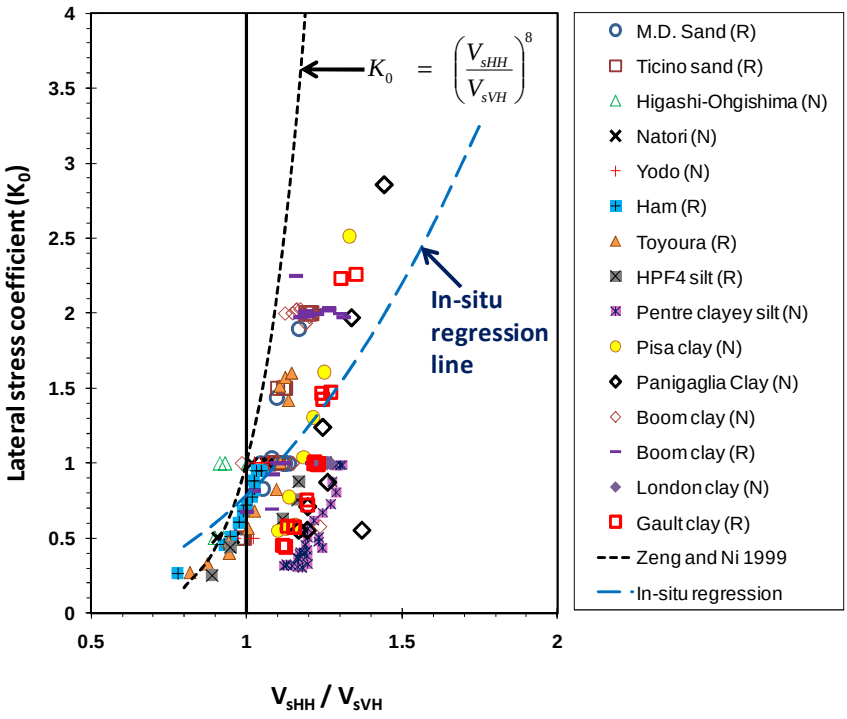

Figure E.1. K_0 versus V_{sHH}/V_{sVH} from various laboratory data.

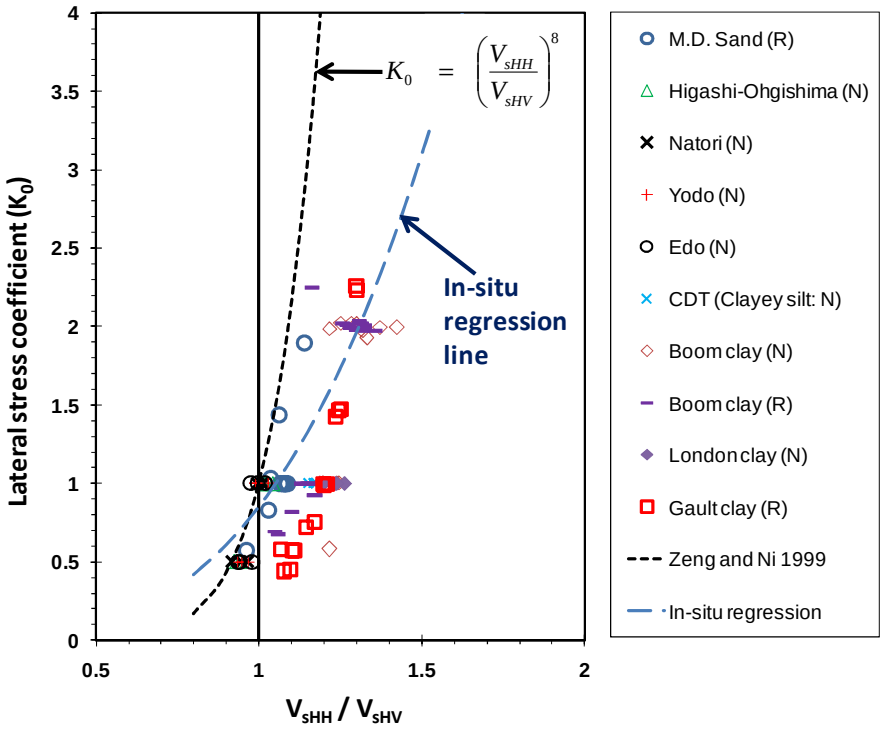

Figure E.2. K_0 versus V_{sHH}/V_{sHV} from various laboratory data.

Unlike in-situ data, the laboratory data can be separated into two groups: 1) reconstituted sample, 2) natural sample. First, the V_{sHH}/V_{sVH} data obtained from various reconstituted specimens are plotted with K_0 in Figure E.3. The data seem deviated from the K_0 estimation line for inherent isotropic soil (Zeng and Ni 1999), however look apparently parallel to the line. It might indicate the magnitude of exponent term n is close to 0.25. Therefore, fixing the n=0.25, additional prediction lines using different modification factor (MF) are shown together in Figure E.3:

• Parametric study format using MF

$$K_0 = \left(MF \times \frac{V_{sHH}}{V_{sVH}} \right)^8$$

Figure E.3 shows even reconstituted specimens can have considerable fabric anisotropy. In Figure E.4, the K_0 versus V_{sHH}/V_{sVH} data for natural specimens are plotted. The degree of anisotropy looks a little higher than the reconstituted specimens, however the general trend seems comparable. It appears that reconstituted specimens are also likely to have considerable V_s anisotropy particularly in silt and clay.

For further examination, the laboratory data are again separated into other two groups based on soil types as follows: 1) sand, 2) clay and silt. Figure E.5 shows the observed K_0 versus V_{sHH}/V_{sVH} data only for sand. Similarly, the clay data are plotted in Figure E.6. In sand, it is observed the trend between K_0 and V_{sHH}/V_{sVH} ratio is close to the K_o prediction suggested by Zeng and Ni (1999) regardless of reconstituted or natural specimens. In contrast, V_s anisotropy is relatively significant in clay at same K_0 value. Generally, the degree of inherent anisotropy in silt and clay seems higher than that in sand.

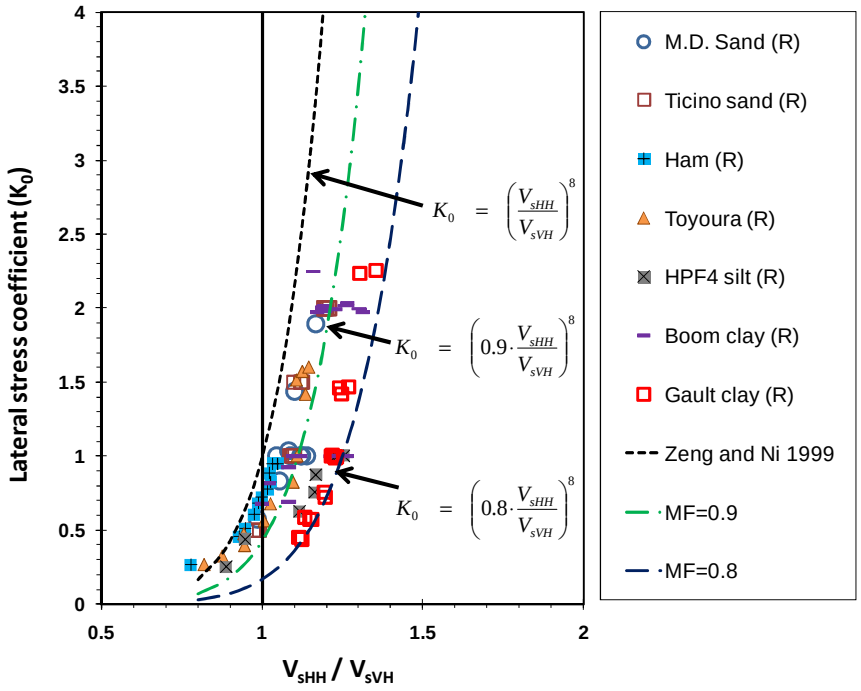

Figure E.3. K_0 versus V_{sHH}/V_{sVH} from various reconstituted specimens.

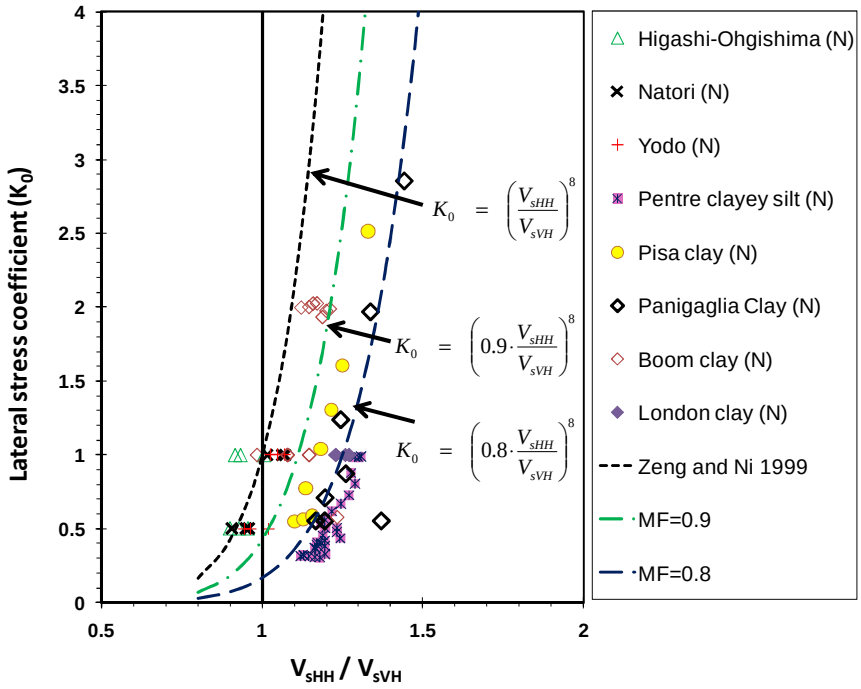

Figure E.4. K_0 versus V_{sHH}/V_{sVH} from various natural specimens.

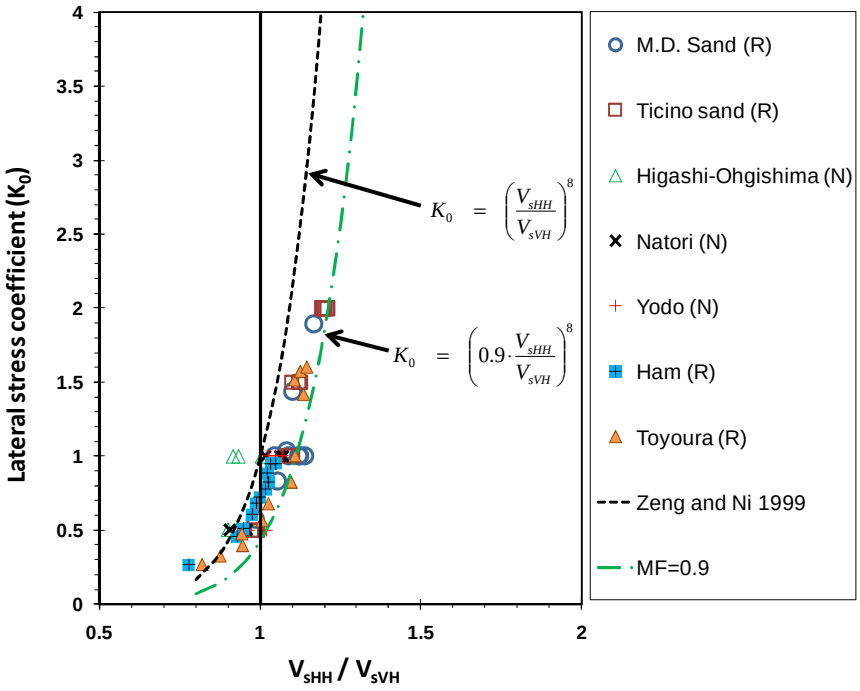

Figure E.5. K_0 versus V_{sHH}/V_{sHV} in sand.

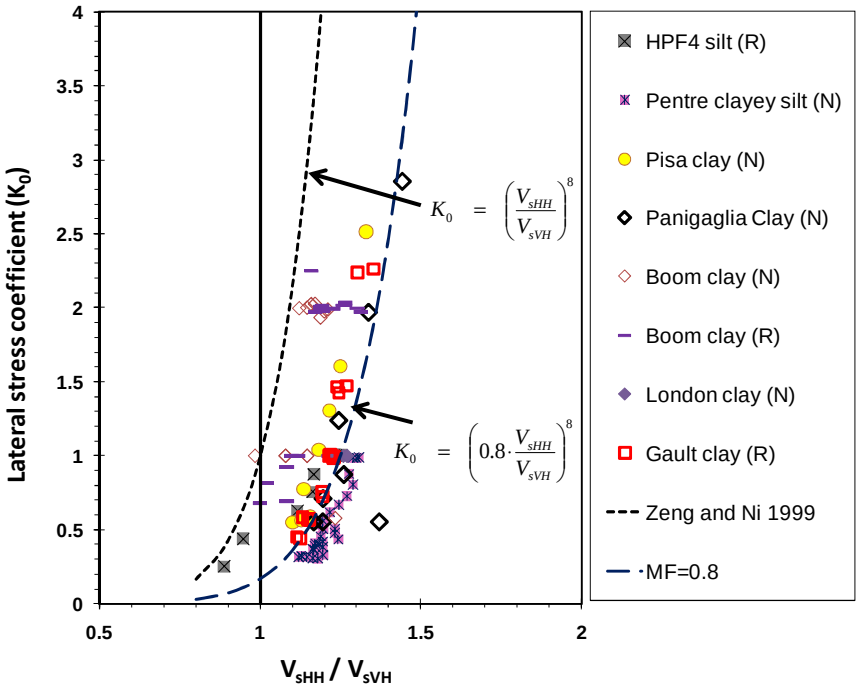

Figure E.6. K_0 versus V_{sHH}/V_{sHV} in silt and clay.

APPENDIX F

SHEAR WAVE VELOCITY PROFILES AND STRESS HISTORY EVALUATIONS FROM COMPILED TEST SITES

Overview: Information and data from a total of 12 well-documented test sites were collected and summarized for the study of paired directional shear wave velocities in evaluating stress history. These sites were explored using a variety of methods, lab and field tests, geophysics, and backgrounds. Details on each site are summarized in Chapters 6 and 7 of this dissertation.

The findings of parametric studies and multiple regression analyses showed the value of the stiffness ratio ($G_{0,HH}/G_{0,VH}$) in providing an assessment of the stress history in terms of overconsolidation difference: OCD = ($\sigma_p' - \sigma_{vo}'$), which is often constant with depth in a soil deposit. The OCD can be utilized to provide the profile of preconsolidation stress (σ_p') that often increases with depth, as well as the normalized form, YSR $\approx$ OCR = σ_p'/σ_{vo}', which usually decreases with depth.

The level of the groundwater table provides the hydrostatic porewater pressure (u_0) and the unit weight of the soil layers can be obtained from the V_{sVH} velocity via the relationship given in Appendix A. The difference in total overburden stress σ_{vo} and hydrostatic u_0 gives the effective vertical overburden stress and the OCD can be used accordingly to profile the yield stress and YSR.

In the following figures, shear wave data from each of the 12 documented sites are presented. The paired shear wave information is used in corresponding assessments of σ_p' and YSR that are in turn compared with available consolidation test results. Table F.1 summarizes the special database again for site information.

Table F.1. Listing of compiled database (equivalent to Table 6.2).

Site	Soil type	OCR	G_0 reference	OCR reference
Bothkennar, Scotland	Soft silty clay	1.3-2.2	Butcher & Powell 1997	Nash et al. 1992, Hight et al. 1992
Chattenden, UK	London clay	20+	Butcher & Powell 1995	Apply OCD=2000 kPa; OCR = (OCD+σ_{vo}')/σ_{vo}'
Cowden, UK	Glacial clay till	3-10+	Butcher & Powell 1997, Powell & Butcher 2003	OCR profile from Powell & Butcher 2003 (Oedometer, CPT)
Heathrow T5, UK	London clay	14+	Hight et al.2003	OCR profile estimated from Gasparre 2005
Higashi-Ohgishima, Japan	NC sand fill	1+	Shibuya et al. 1995	NC fill: OCR=1+ Qusi -ageing effect
Madingley, UK	Gault clay	20+	Butcher & Powell 1995	OCR profile from Lunne et al. 1997 (CPT)
Opelika, Alabama	Silty sand, Sandy silt	2.8-5	Henke & Henke 2002	OCR profile from Hoyos & Macari, 1999 (lab data)
Pisa tower, Italy	Pisa clay	1.3-2	LoPresti et al. 2003	OCR profile estimated from Laval sampler, LoPresti et al. 2003
San Matteo (Po river), Italy	Po river sand	1.3-1.9	Fioravante et al. 1998	OCR profile from Bruzzi et al. 1985 (lab data)
Southern England (Purton)	Oxford clay	14-44+	Bates & Phillips 2000	OCR profile from Hird & Pierpoint 1997
Treasure Island, CA	Sand fill	1+	Henke & Henke 2002; Rollins et al. 1994	NC fill: OCR=1+ Qusi -ageing effect
UMASS (Amherst)	Clay	1.6-8.5	Henke & Henke 2002	OCR profile from DeGroot & Lutenegger 2003 (lab data)

A) Madingley

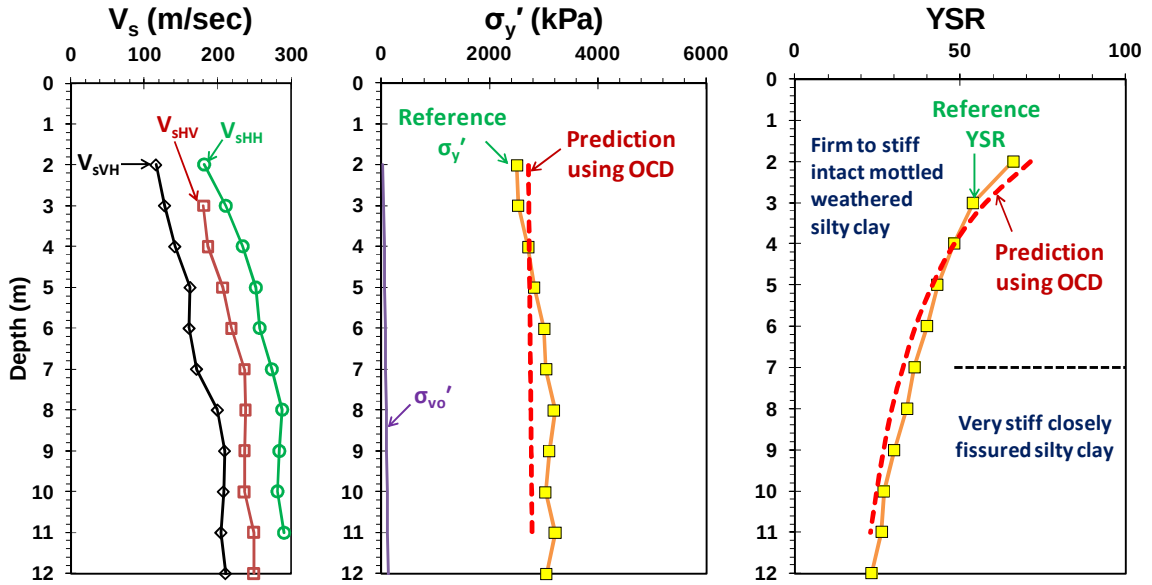

Figure F.1. Paired sets of V_s modes and stress history evaluation using OCD- $G_{0,HH}/G_{0,VH}$ relationship at Madingley, UK (Stress history reference profile: Lunne et al. 1997).

B) Chattenden

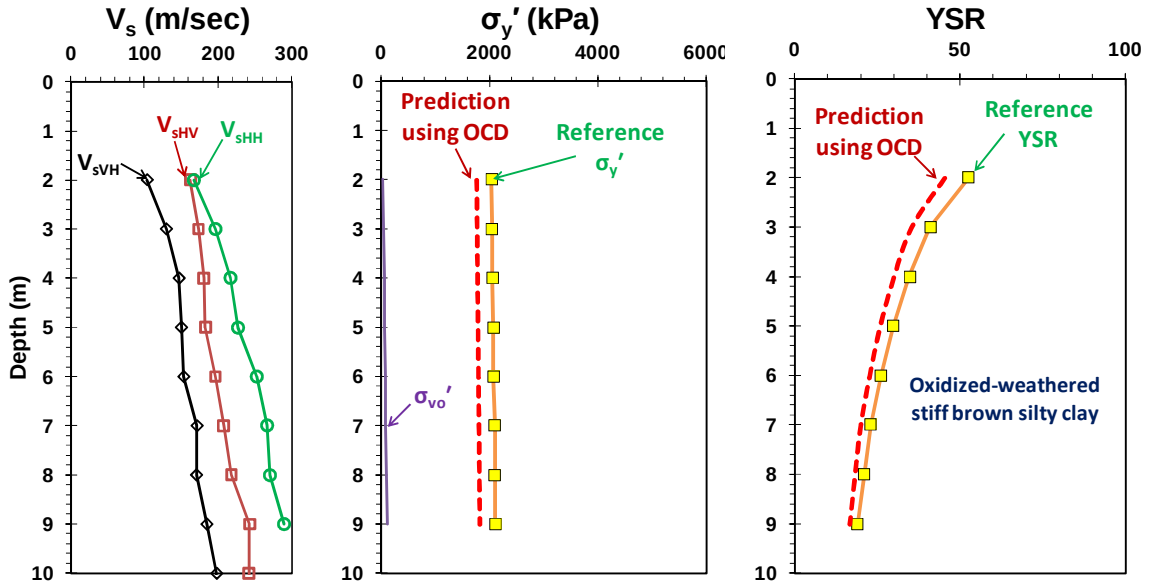

Figure F.2. Paired sets of V_s modes and stress history evaluation using OCD- $G_{0,HH}/G_{0,VH}$ relationship at Chattenden, UK (Stress history reference profile: apply OCD=2000 kPa; Butcher and Powell 1995).

C) Heathrow (T5)

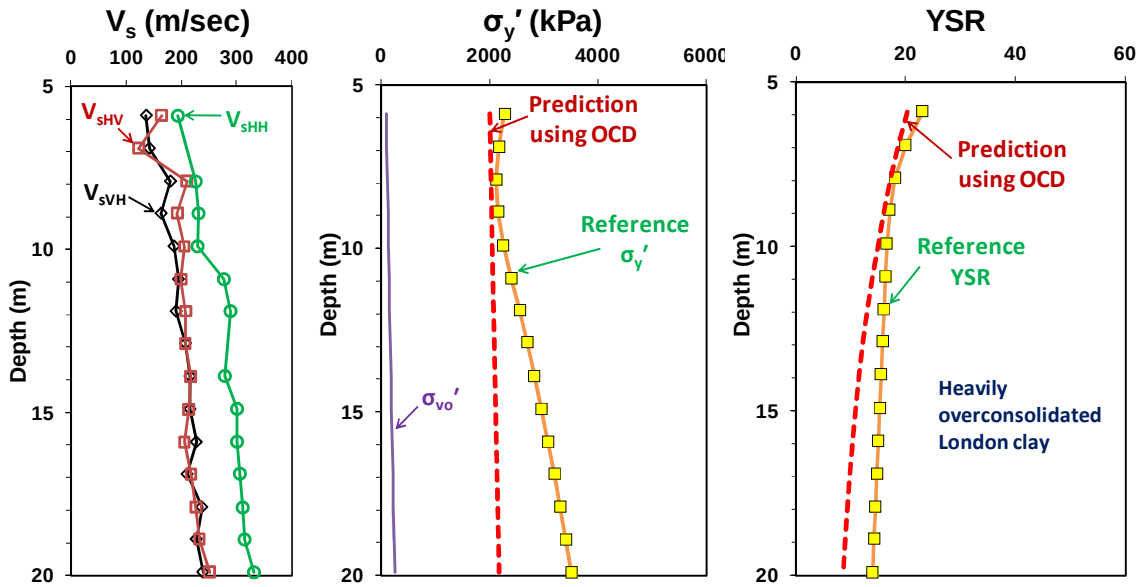

Figure F.3. Paired sets of V_s modes and stress history evaluation using OCD- $G_{0,HH}/G_{0,VH}$ relationship at Heathrow, UK (Stress history reference profile: Gasparre 2005).

D) Southern England (Oxford clay)

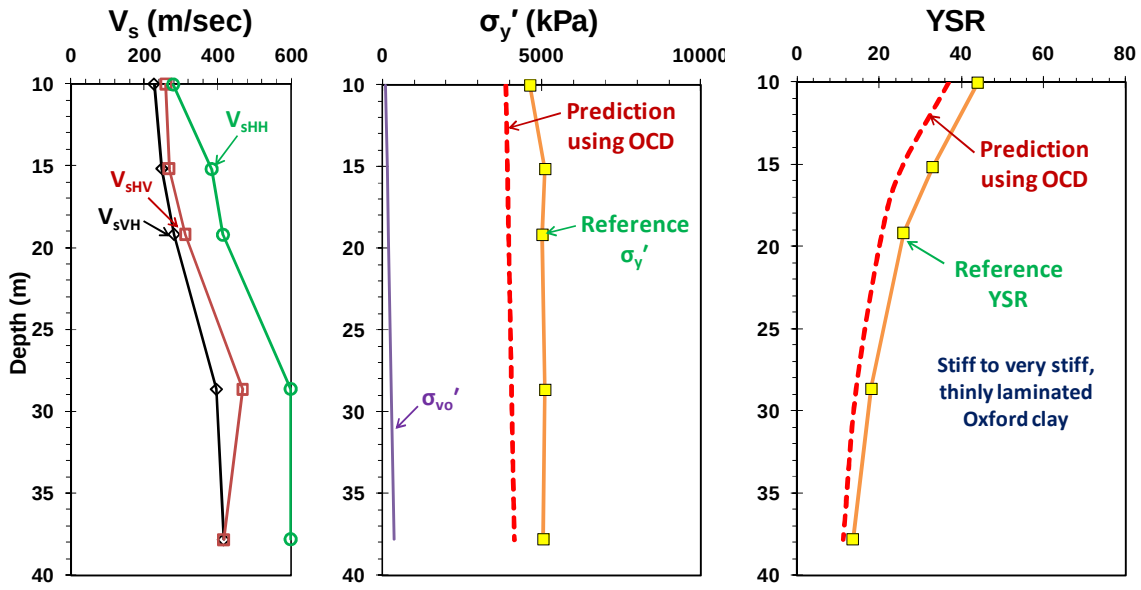

Figure F.4. Paired sets of V_s modes and stress history evaluation using OCD- $G_{0,HH}/G_{0,VH}$ relationship at Southern England (Oxford clay - Stress history reference profile: Hird and Pierpoint 1997).

Note: 10 meter depth shear waves are not included for analysis

E) Cowden

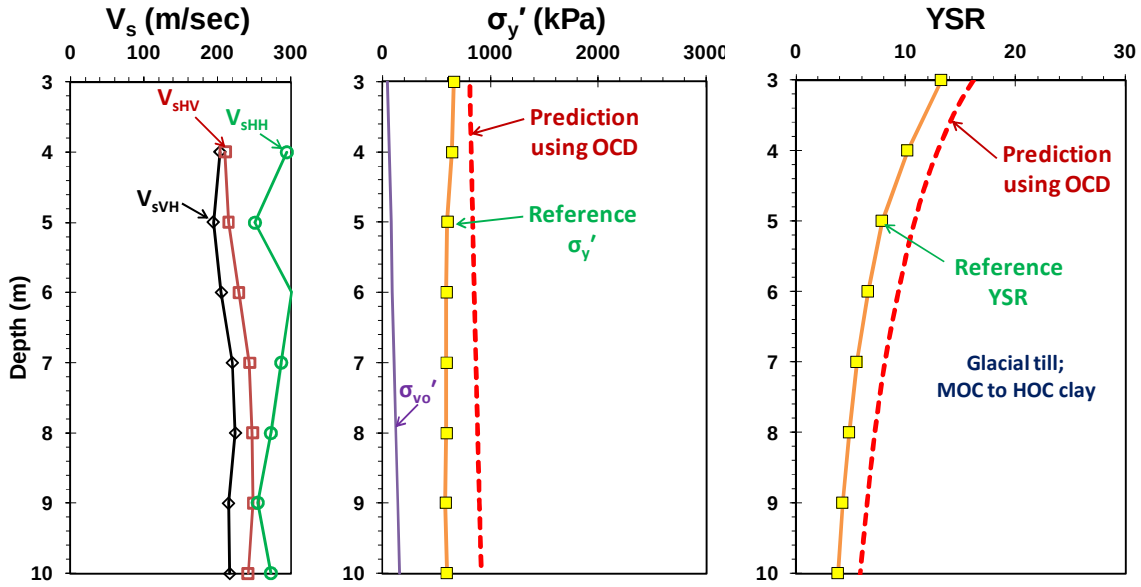

Figure F.5. Paired sets of V_s modes and stress history evaluation using OCD- $G_{0,HH}/G_{0,VH}$ relationship at Cowden, UK (Stress history reference profile: Powell and Butcher 2003).

F) Pisa tower

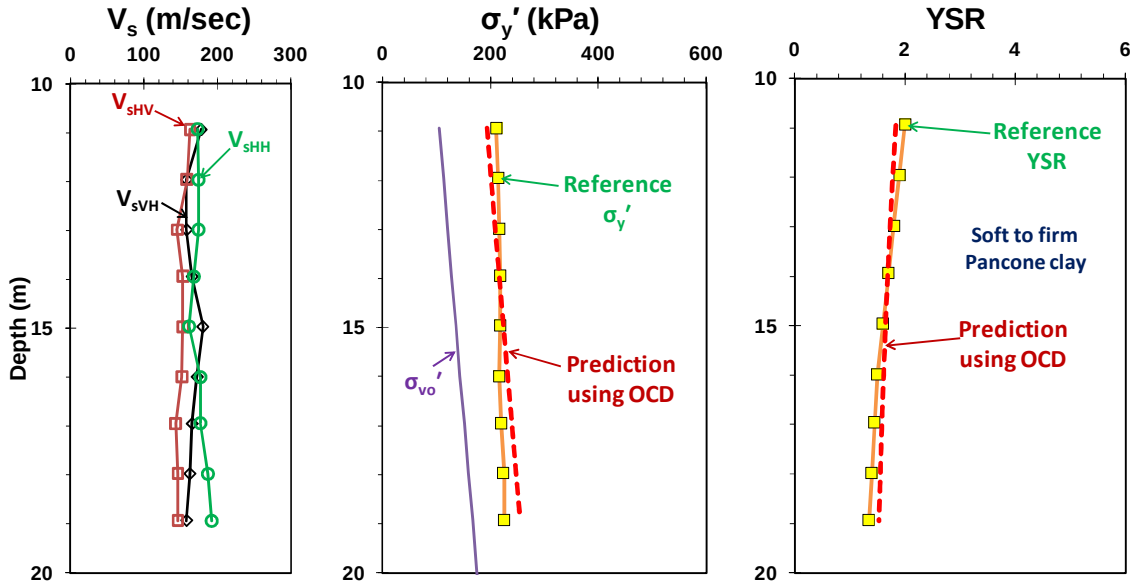

Figure F.6. Paired sets of V_s modes and stress history evaluation using OCD- $G_{0,HH}/G_{0,VH}$ relationship at Pisa tower site, Italy (Stress history reference profile: LoPresti et al. 2003).

G) Amherst

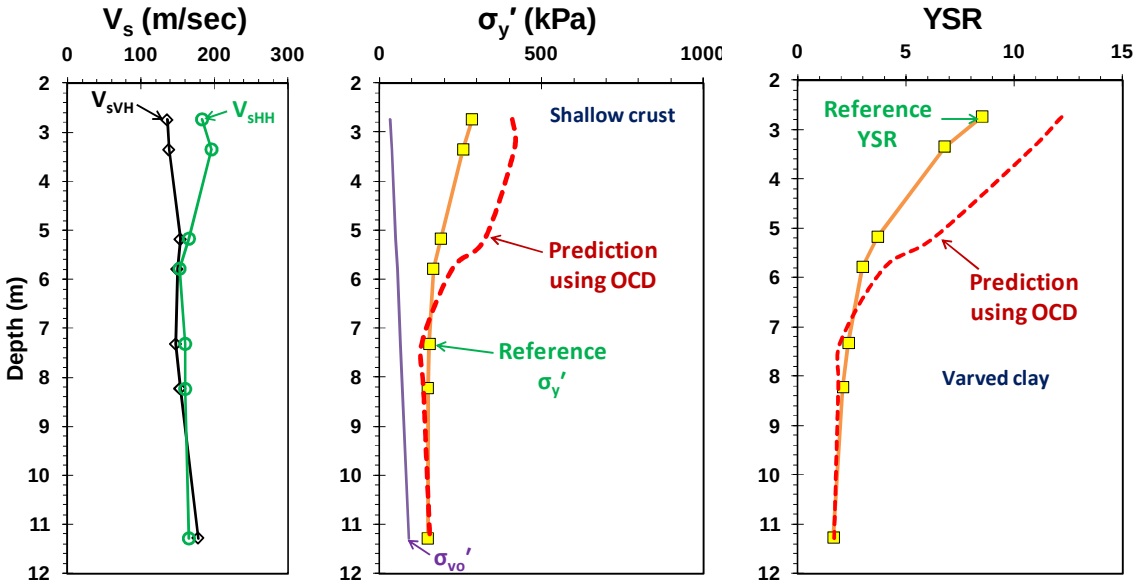

Figure F.7. Paired sets of V_s modes and stress history evaluation using OCD- $G_{0,HH}/G_{0,VH}$ relationship at Amherst (Stress history reference profile: DeGroot and Lutenegger 2003).

Note: upper OC soils and lower NC soils are separately calculated, then middle (transition) area between 5 and 6 meter depths are averaged for stress history evaluation.

H) Higashi-Ohgishima, Japan

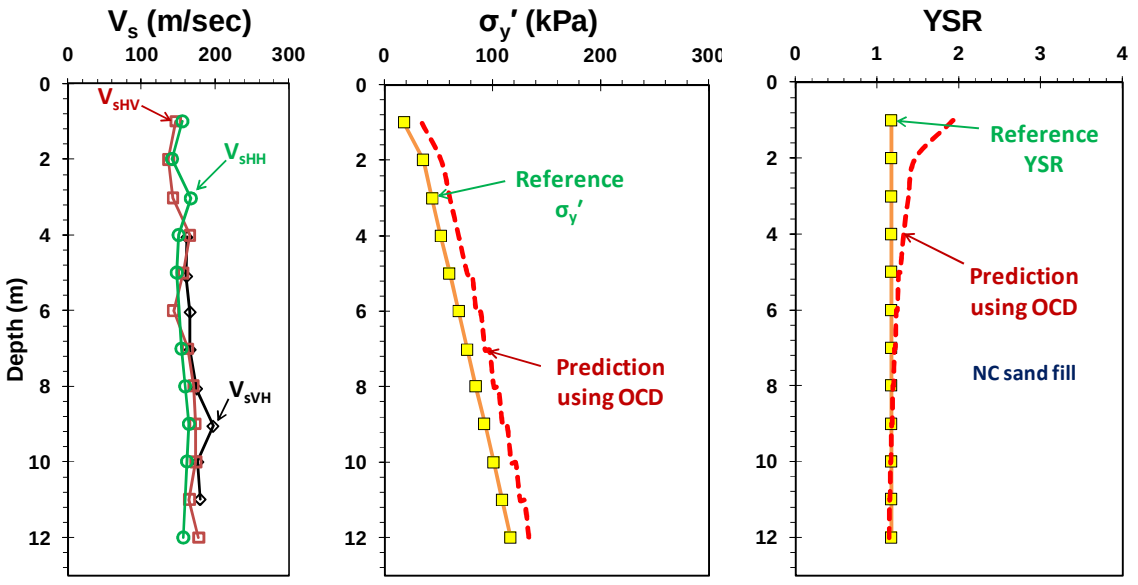

Figure F.8. Paired sets of V_s modes and stress history evaluation using OCD- $G_{0,HH}/G_{0,VH}$ relationship at Higashi-Ohgishima, Japan (Stress history reference profile: assumed NC - Shibuya et al. 1995).

I) Po River, Italy

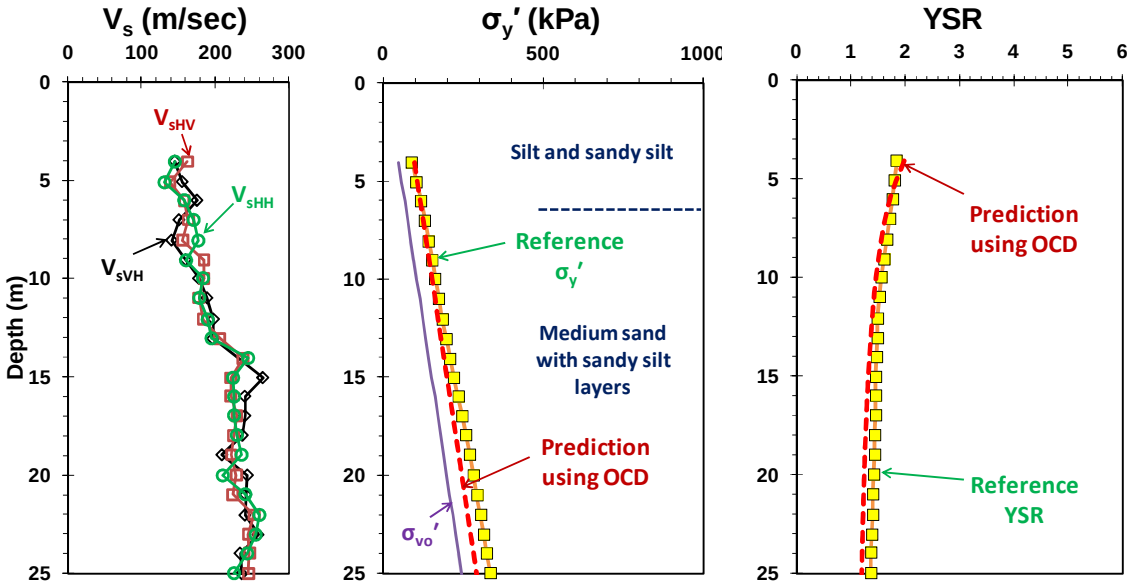

Figure F.9. Paired sets of V_s modes and stress history evaluation using OCD- $G_{0,HH}/G_{0,VH}$ relationship at Po River, Italy (Stress history reference profile: Bruzzi et al. 1985).

J) Opelika, AL

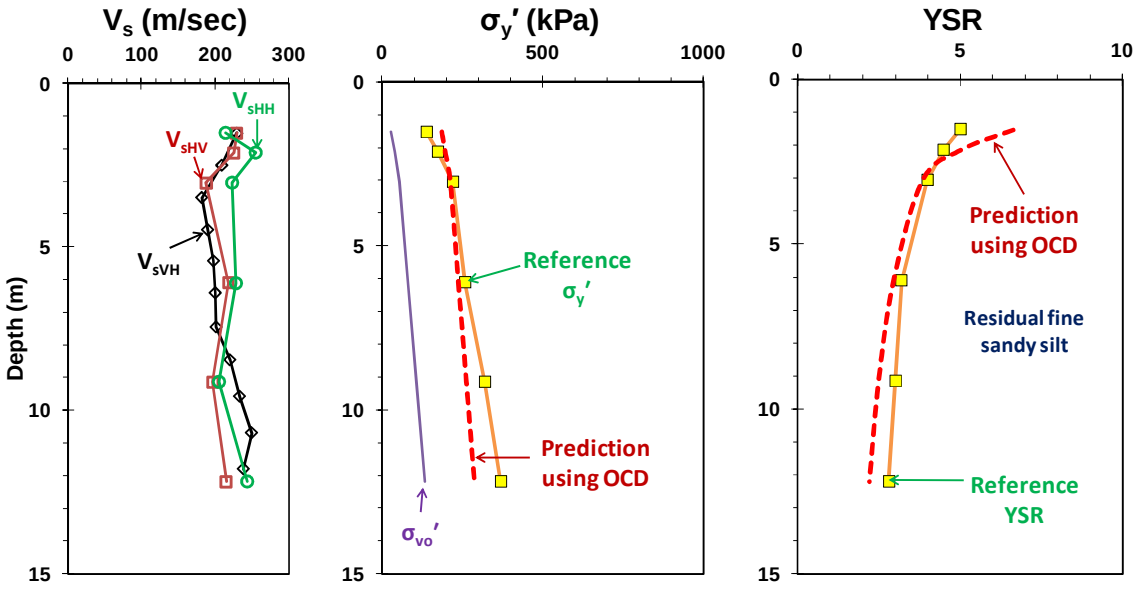

Figure F.10. Paired sets of V_s modes and stress history evaluation using OCD- $G_{0,HH}/G_{0,VH}$ relationship at Opelika, AL (Stress history reference profile: Hoyos and Macari 1999).

K) Treasure Island, CL

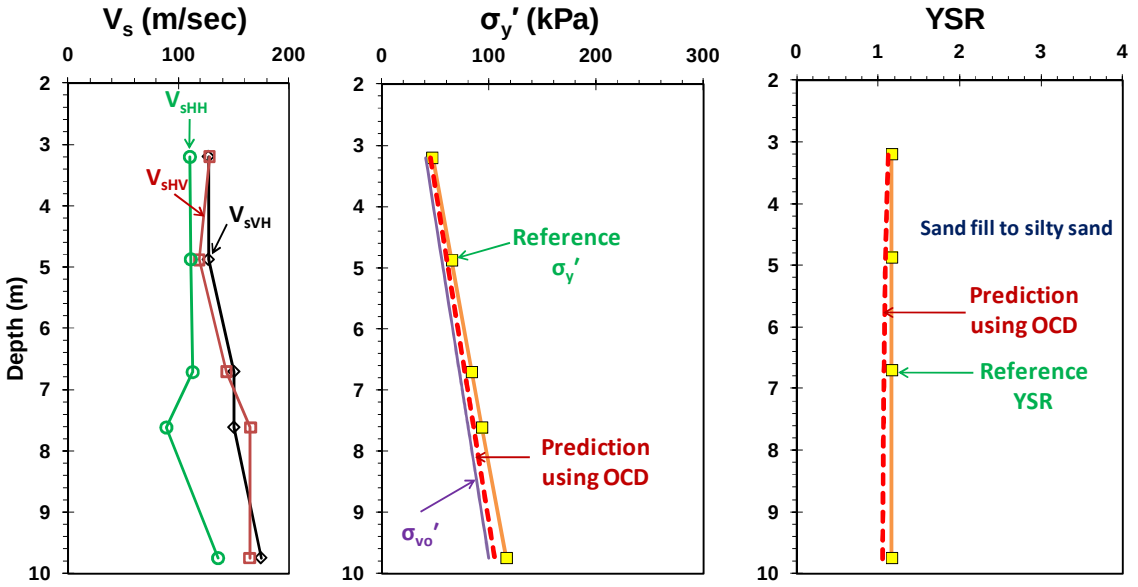

Figure F.11. Paired sets of V_s modes and stress history evaluation using OCD-$G_{0,HH}/G_{0,VH}$ relationship at Treasure Island, CA (Stress history reference profile: assumed NC – Henke and Henke 2002).

L) Bothkennar, UK

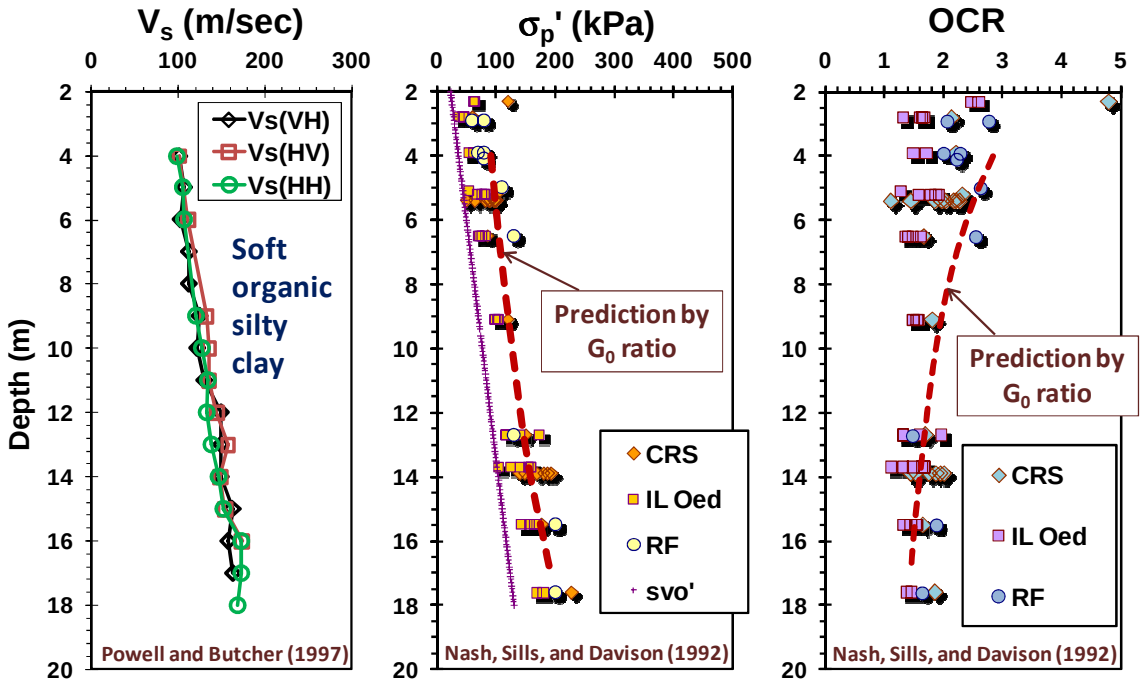

Figure F.12. Profiles at Bothkennar soft clay: (a) directional V_s modes; (b) yield stress profile; and (c) OCR profile from consolidation tests and OCD-G_0 ratio trend (identical to Figure 7.3)

APPENDIX G: CORRELATIONS BETWEEN FIELD TESTS AT SRS

G.1 CPT-SPT Correlations at SRS

Due to the unique geologic conditions at SRS, many existing relationships between in-situ measurements are site-specific. Interrelationships between selected tests were therefore studied by the author to better understand where and perhaps why these trends occurred, as well establish limits of applicability. Some of the derived expressions are detailed in this appendix.

Based on four boreholes advanced at the SRS SWPF site, the SPT N_{60} values were tabulated for study, with corresponding mean grain size (D_{50}) and fines content (FC) data obtained from the laboratory program (Shannon and Wilson, Inc. 2007). For investigation of possible CPT-SPT correlations, nearby piezocone data were also collected for pairings of these two tests (i.e., B33 - CPT82, B34 - CPT50, B35 - CPT53, B36 - CPT55). Figure G.1 shows the trend relationships between the CPT tip resistance (q_t/P_a, P_a = atmospheric pressure = 101.3 kPa) and SPT N_{60} values. In general, the q_t generally increases with N_{60}. Subsequently, the data are sorted by mean grain size (D_{50}, mm) and fines content (FC, %) in Figure G.2 and Figure G.3, respectively. Based on visual examinations, the estimated zones for D_{50} and FC are approximately marked. Whereas the larger D_{50} seems to result in higher q_t at equivalent N_{60} values in Figure G.2, the q_t/N_{60} ratio roughly decreases with high FC in Figure G.3.

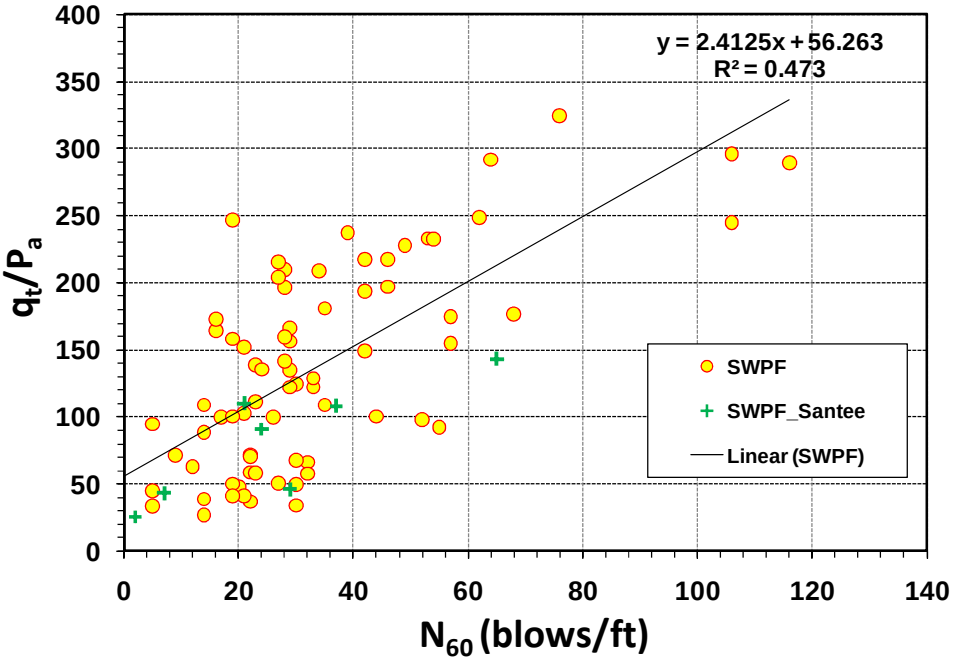

Figure G.1. Linear trend between CPT tip resistance (q_t) and SPT N_{60} at SWPF.

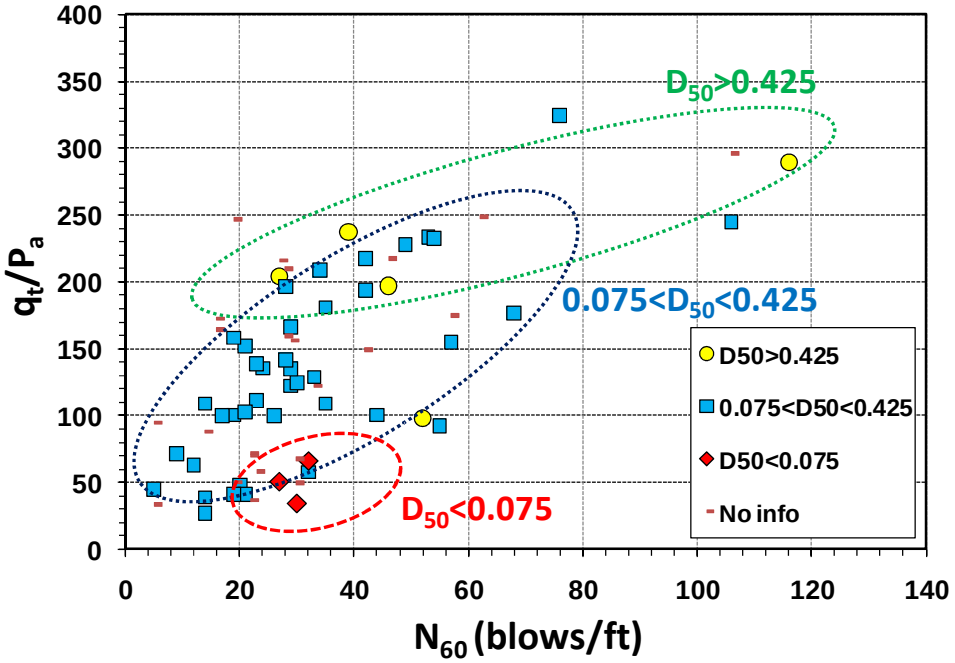

Figure G.2. Grouped trends between CPT tip resistance (q_t) and SPT N_{60} sorted by mean grain size (D_{50}, unit: mm) at SWPF.

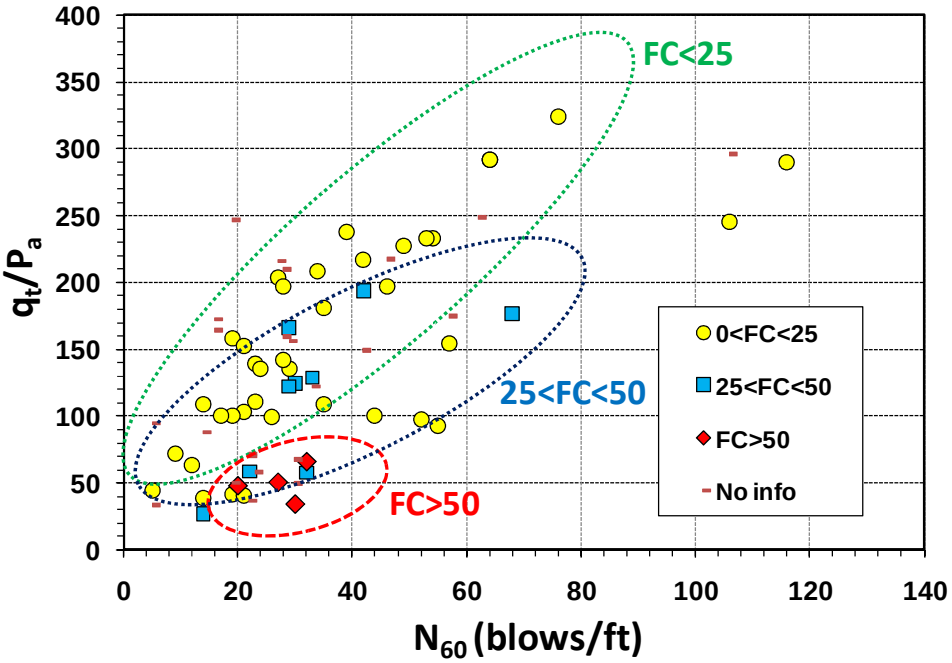

Figure G.3. Grouped trends between CPT tip resistance (q_t) and SPT N_{60} sorted by fines content (FC, unit: %) at SWPF.

In the last several decades, the penetration ratio q_t/N_{60} has been examined in several prior studies. For instance, in Figure G.4, Kulhawy and Mayne (1990) compiled $(q_t/P_a)/N_{60}$ versus D_{50} based on published sources, then eventually suggested a regression line. Similarly, Figure G.5 shows variations of $(q_t/P_a)/N_{60}$ with FC and a recommended line. The data obtained from the SRS are plotted together for comparison, as shown by red and green plus signs. As aforementioned, it is observed that the $(q_t/P_a)/N_{60}$ ratio is proportional to the D_{50} and decreases with FC.

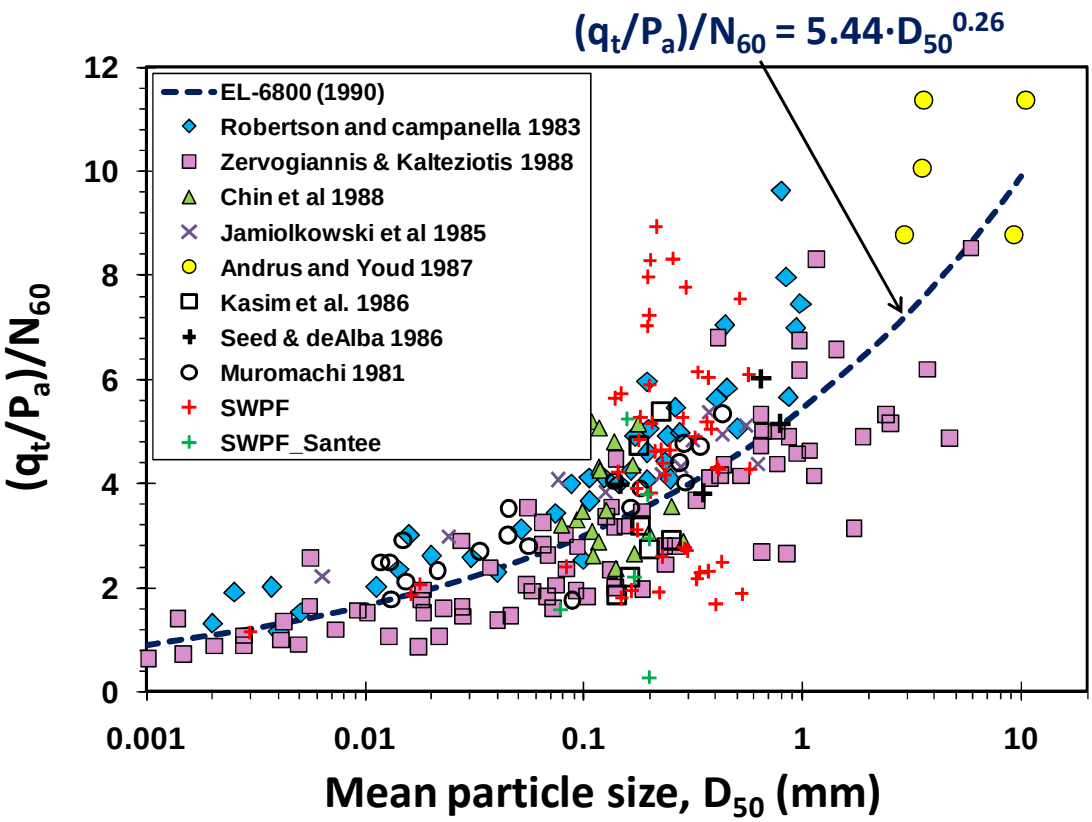

Figure G.4. Observed variation of $(q_t/P_a)/N_{60}$ ratio with D_{50} at SWPF (compiled data source: Kulhawy and Mayne 1990)

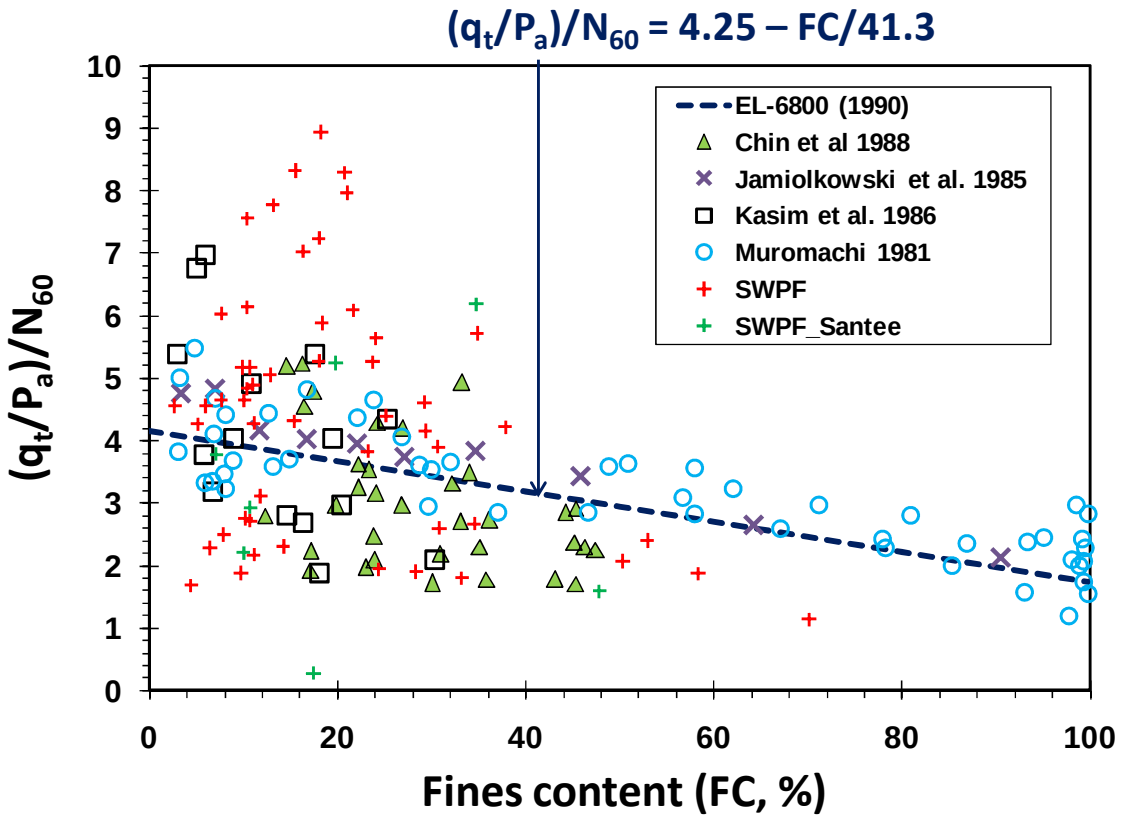

Figure G.5. Observed variation of $(q_t/P_a)/N_{60}$ ratio with FC
(compiled data source: Kulhawy and Mayne 1990)

Interestingly, the $(q_t/P_a)/N_{60}$ ratio seems considerably scattered in vicinity of large D_{50} and/or small FC. These variants might be caused by differences in drainage conditions in the field. In clean sand, whereas the CPT can be assumed as a drained condition during penetration, the SPT maybe result in an undrained testing condition due to cyclic impacts. It is noted that the ratio of drained strength versus undrained strength is inversely proportional to soil density (Tatsuoka et al. 1982; Suzuki et al. 1998). Therefore, the $(q_t/P_a)/N_{60}$ ratio maybe have a scattered range varied counting on the soil density for sands, normally considered "drained". In cohesive soils, both SPT and CPT drainage conditions are assumed undrained. The clayey to silty sands at SRS may have a lower permeability than clean sands because of the unusual plastic fines noted earlier.

Figures G.6 and G.7 show the $(q_t/P_a)/N_{60}$ data vs. mean grain size and percent fines content, respectively, obtained from the SRS site with corresponding regression lines. Although the trend lines observed from the SRS are closely matched with the lines suggested from Kulhawy and Mayne (1990), the data are considerably scattered and produce poor R^2 values. Therefore, site-specific equations are required for improved CPT-SPT correlations at the SRS site. Since, it seems that the $(q_t/P_a)/N_{60}$ ratio does not provide consistent estimations at this site, it may be better to separate the q_t and N_{60} terms. Table G.1 summarizes the site-specific equations and statistic information. It is indicated that the q_t is proportional to approximately $(N_{60})^{0.6}$ from all regressions. Figures G.8 a, b, and c show the plots of measured q_t/P_a and predicted q_t/P_a based on Equations G.1, G.2, and G.3, respectively.

On the other hand, the variation of q_t/N ratio with CPT soil behavior type index (I_c) was investigated without direct consideration of D_{50} and FC (Lunne et al. 1997; Suzuki et al. 1998). Figure G.9 shows the observed variation of the $(q_t/P_a)/N_{60}$ ratio with I_c and the recommended trend line from Lunne et al. 1997. The observed data are significantly scattered, albeit the $(q_t/P_a)/N_{60}$ ratio generally decreases with increasing the I_c. To obtain better correlations, instead of the $(q_t/P_a)/N_{60}$ ratio, the ratio of $(q_t/P_a)/N_{60}{}^{0.5}$ is investigated for practical design purposes. Moreover, it was observed the q_t is approximately proportional to the $(N_{60})^{0.6}$ in multiple regression studies that included D_{50} and/or FC as variables in Table G.1. Eventually, improved correlations were obtained, as shown in Figure G.10. The regression statistics are provided in Table G.2.

Table G.1. Site-specific CPT-SPT correlation in consideration of D_{50} and FC at SRS

Empirical equation	R^2	Number of data	Standard error
Eq.(G.1). $(q_t/P_a) = 22.25 \cdot N_{60}^{0.609} \cdot D_{50}^{0.266}$	0.58	48	47.3
Eq.(G.2). $(q_t/P_a) = 30.27 \cdot N_{60}^{0.617} \cdot FC^{-0.269}$	0.53	51	51.3
Eq.(G.3). $(q_t/P_a) = 18.76 \cdot N_{60}^{0.639} \cdot e^{-0.0168 \cdot FC}$	0.60	51	49.4

Note: All variables are significantly correlated on the basis of t-statistic values.

Table G.2. Site-specific CPT-SPT correlation with I_c at SRS

Empirical equation	R^2	Number of data	Standard error
Eq.(G.4). $(q_t/P_a)/N_{60}^{0.5} = 70.52 \cdot (1-I_c/3.34)$	0.58	74	6.9
Eq.(G.5). $(q_t/P_a)/N_{60}^{0.5} = 133.1 \cdot I_c^{-2.35}$	0.63	74	7.4

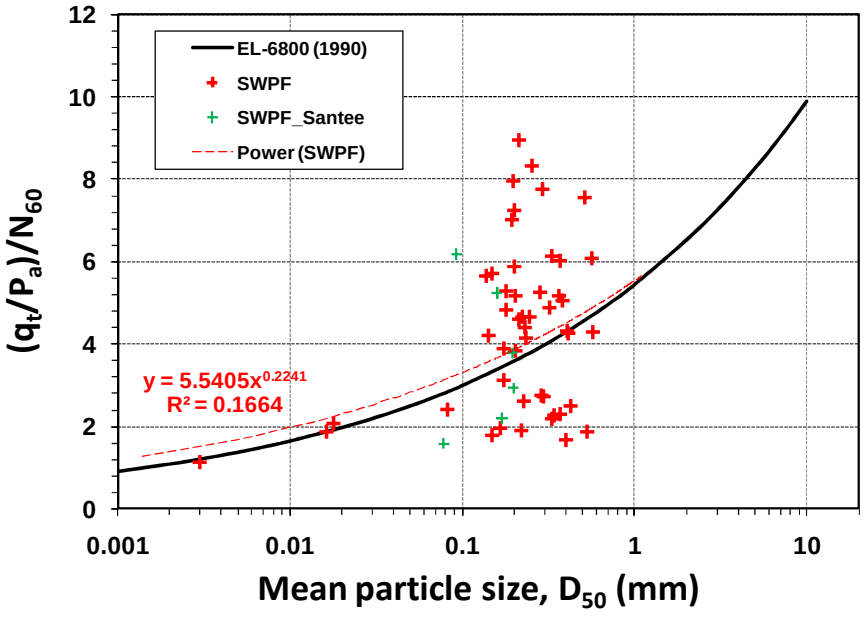

Figure G.6. Observed variation of $(q_t/P_a)/N_{60}$ with D_{50} at SRS.

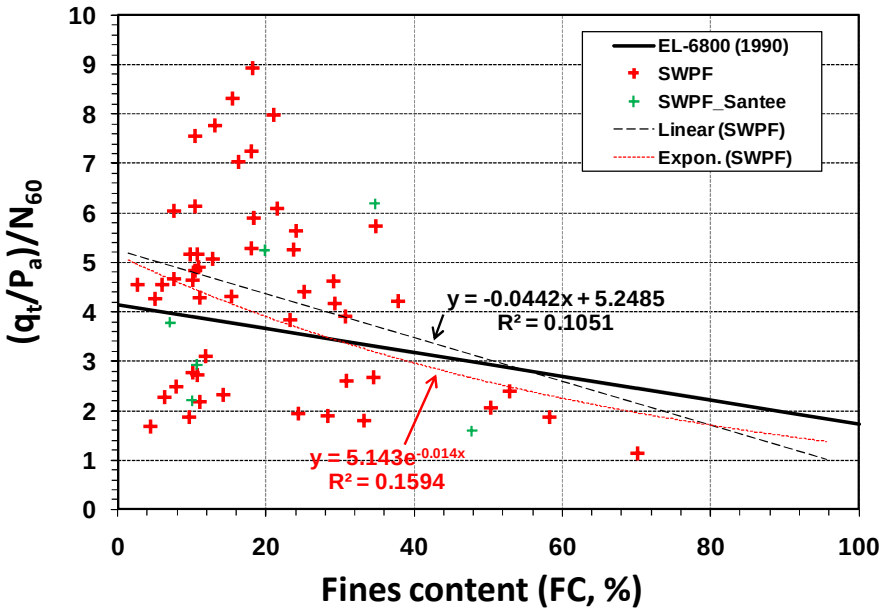

Figure G.7. Observed variation of $(q_t/P_a)/N_{60}$ with FC at SRS.

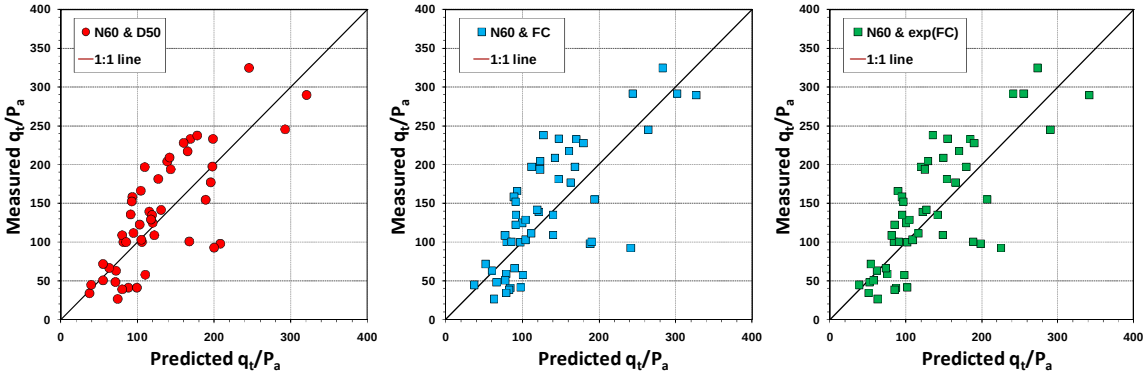

Figure G.8. Comparison of measured q_t/P_a and predicted q_t/P_a as a function of; (a) N_{60} and D_{50} per Eq.G.1, (b) N_{60} and FC per Eq.G.2, (c) N_{60} and e^{FC} per Eq.G.3.

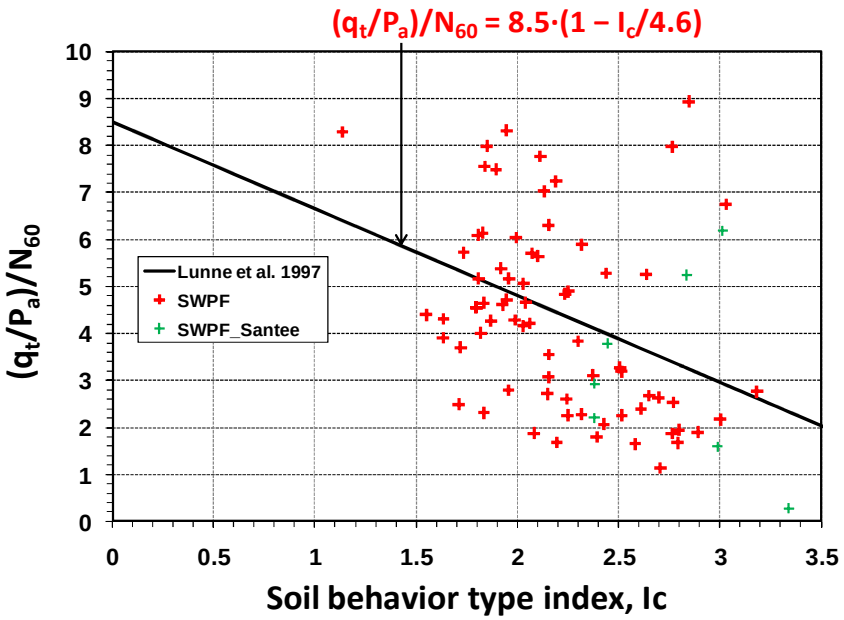

Figure G.9. Observed variation of $(q_t/P_a)/N_{60}$ with I_c at SWPF site.

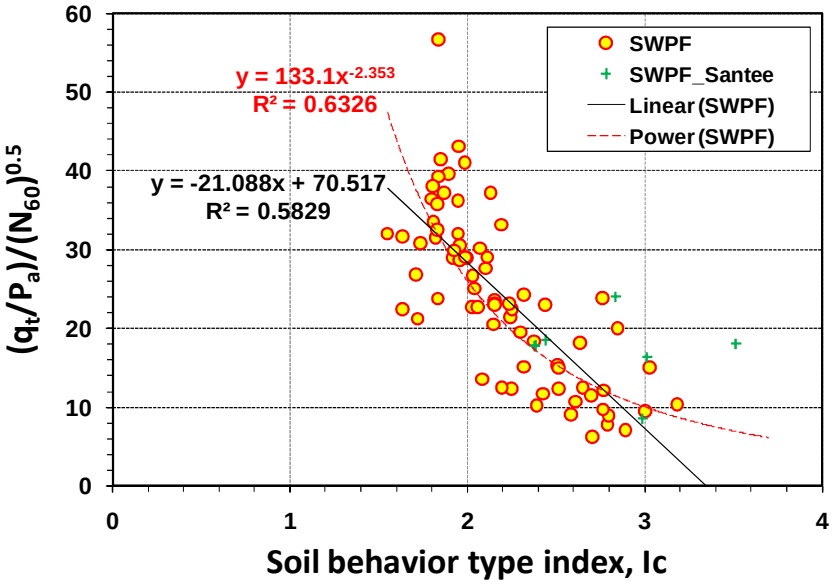

Figure G.10. Observed variation of $(q_t/P_a)/N_{60}^{0.5}$ with I_c at SWPF site.

Based on the suggested empirical relationships (i.e., Eq. G.1 through Eq. G.5), q_t/P_a and/or $(q_t/P_a)/N_{60}^{0.5}$ are estimated from four boreholes at the SRS (i.e., B33 –Figure G.11, B34 – Figure G.12, B35 –Figure G.13, B36 – Figure G.14). Reasonable site-specific CPT-SPT trends were therefore developed for the SRS.

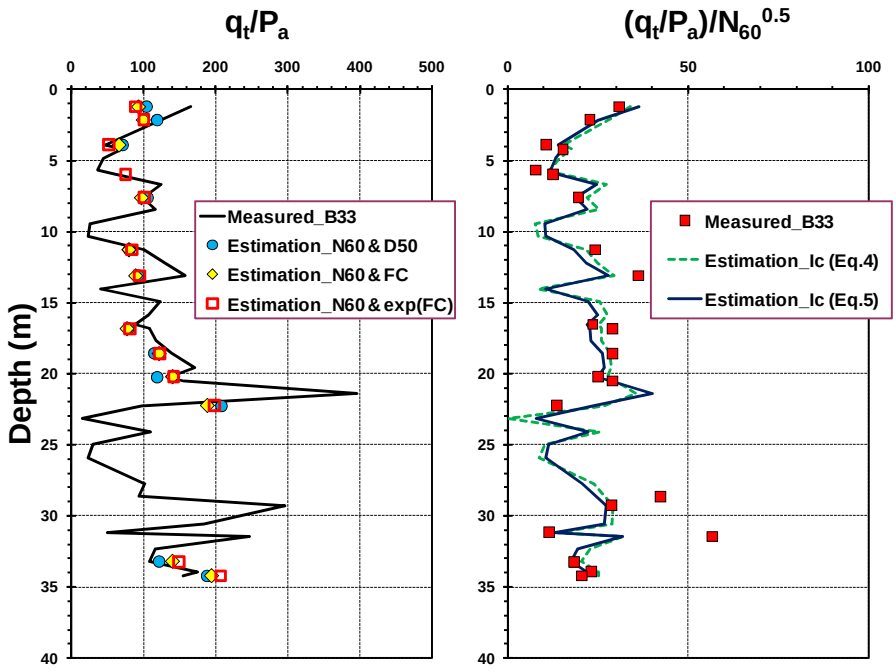

Figure G.11. (a) Measured q_t/P_a versus estimated q_t/P_a using Eq.G.1 fctn (N_{60}, D_{50}), Eq.G.2 fctn (N_{60}, FC), and Eq.G.3 fctn (N_{60}, e^{FC}),(b) Measured $(q_t/P_a)/N_{60}^{0.5}$ versus estimated $(q_t/P_a)/N_{60}^{0.5}$ using Eq. G.4 (linear I_c) and Eq. G.5 (power I_c) at SRS SWPF borehole #33.

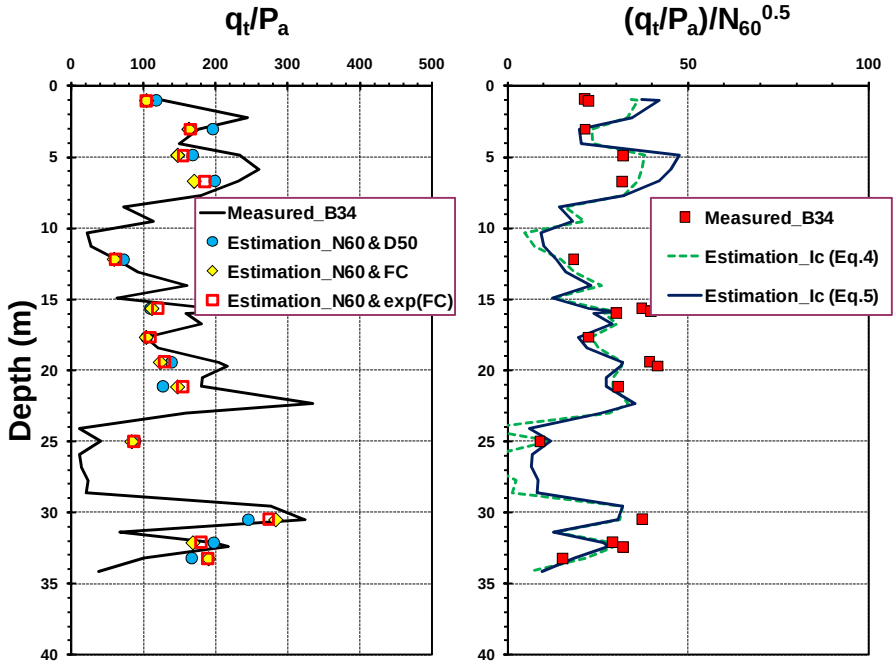

Figure G.12. (a) Measured q_t/P_a versus estimated q_t/P_a using Eq.G.1 fctn (N_{60}, D_{50}), Eq.G.2 fctn (N_{60}, FC), and Eq.G.3 fctn (N_{60}, e^{FC}), (b) Measured $(q_t/P_a)/N_{60}^{0.5}$ versus estimated $(q_t/P_a)/N_{60}^{0.5}$ using Eq.G.4 (linear I_c) and Eq.G.5 (power I_c) at SRS SWPF borehole #34.

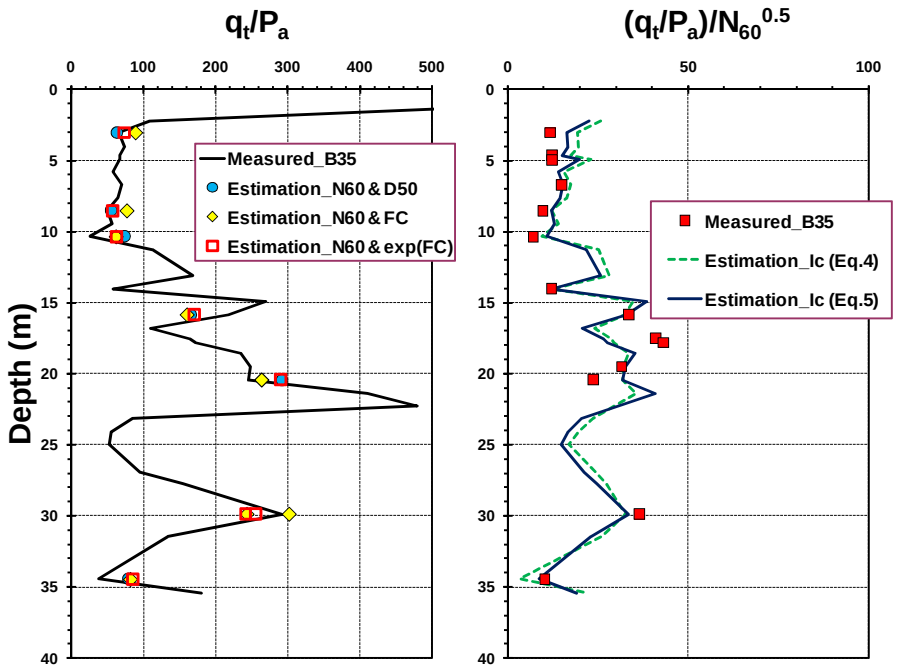

Figure G.13. (a) Measured q_t/P_a versus estimated q_t/P_a using Eq.G.1 fctn (N_{60}, D_{50}), Eq.G.2 fctn (N_{60}, FC), and Eq.G.3 fctn (N_{60}, e^{FC}), (b) Measured $(q_t/P_a)/N_{60}^{0.5}$ versus estimated $(q_t/P_a)/N_{60}^{0.5}$ using Eq. G.4 (linear I_c) and Eq. G.5 (power I_c) at SRS SWPF borehole #35.

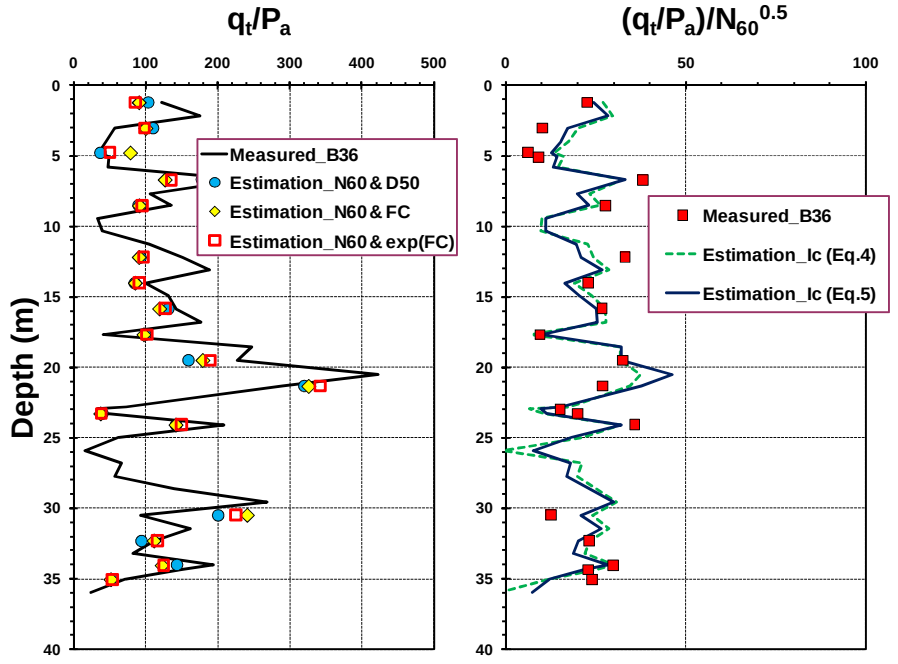

Figure G.14. (a) Measured q_t/P_a versus estimated q_t/P_a using Eq.G.1 fctn (N_{60}, D_{50}), Eq.G.2 fctn (N_{60}, FC), and Eq.G.3 fctn (N_{60}, e^{FC}), (b) Measured $(q_t/P_a)/N_{60}^{0.5}$ versus estimated $(q_t/P_a)/N_{60}^{0.5}$ using Eq.G.4 (linear I_c) and Eq.G.5 (power I_c) at SRS SWPF borehole #36.

G.2 CPT-DMT Correlations at SRS

Robertson (2009) reviewed prior studies concerning CPT-DMT correlations and developed some new trends based on published sources obtained from 19 different sites. Herein, the relationships between CPT and DMT are investigated at SRS. To examine the CPT-DMT trends at SRS, four paired sets of CPTu soundings and DMT soundings were collected from the SRS SWPF site (data from Shannon and Wilson, Inc. Report 2007: CPT#84-DMT#17, CPT#85-DMT#20, CPT#86-DMT#21, CPT#87-DMT#22). Based on these paired data, relationships between CPT and DMT parameters were examined. Figure G.15 shows a general relationship between I_c and I_D from various sites. Similar to Robertson's (2009) findings, the SRS data also have an inversely proportional trend, however the data are more scattered. A more reliable correlation is observed from the plot of E_D/σ_{vo}' (DMT) versus Q_{t1} (CPT) in Figure G.16. The observed site-specific correlation at SRS has a slightly smaller slope, compared to the suggested equation by Mayne and Liao (2004) and Robertson (2009):

- General trend line from various sites: $E_D/\sigma_{vo}' = 5 \cdot Q_{t1}$
- Site-specific correlation at SRS: $E_D/\sigma_{vo}' = 4 \cdot Q_{t1}$

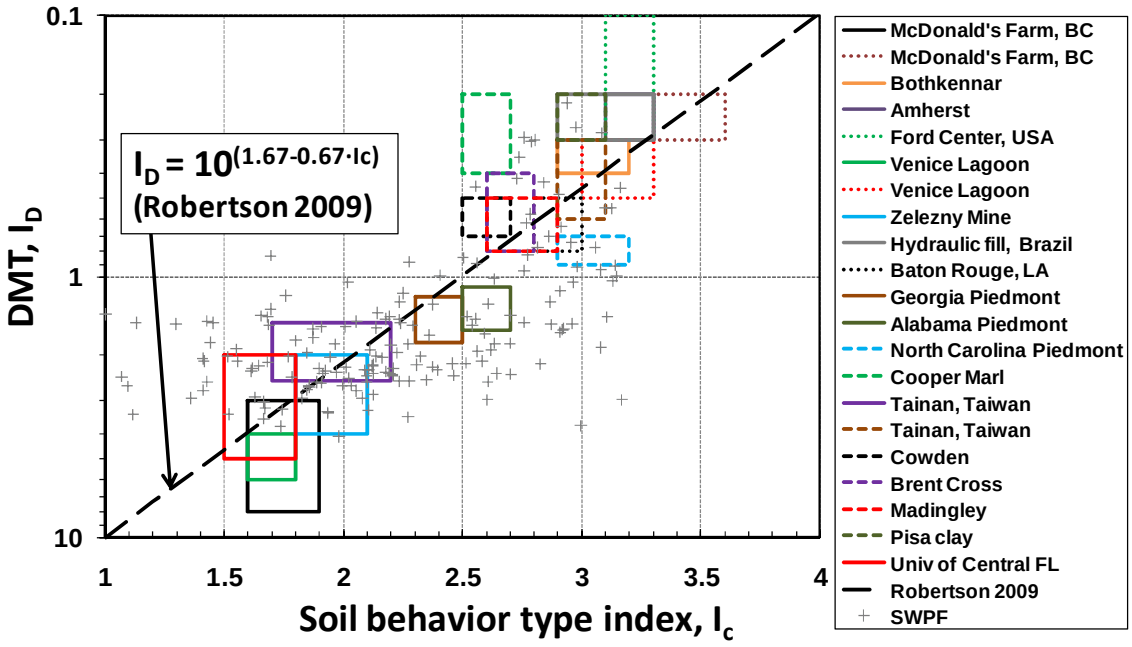

Figure G.15. Relationship between I_D and I_c at various sites and superimposed SRS data.

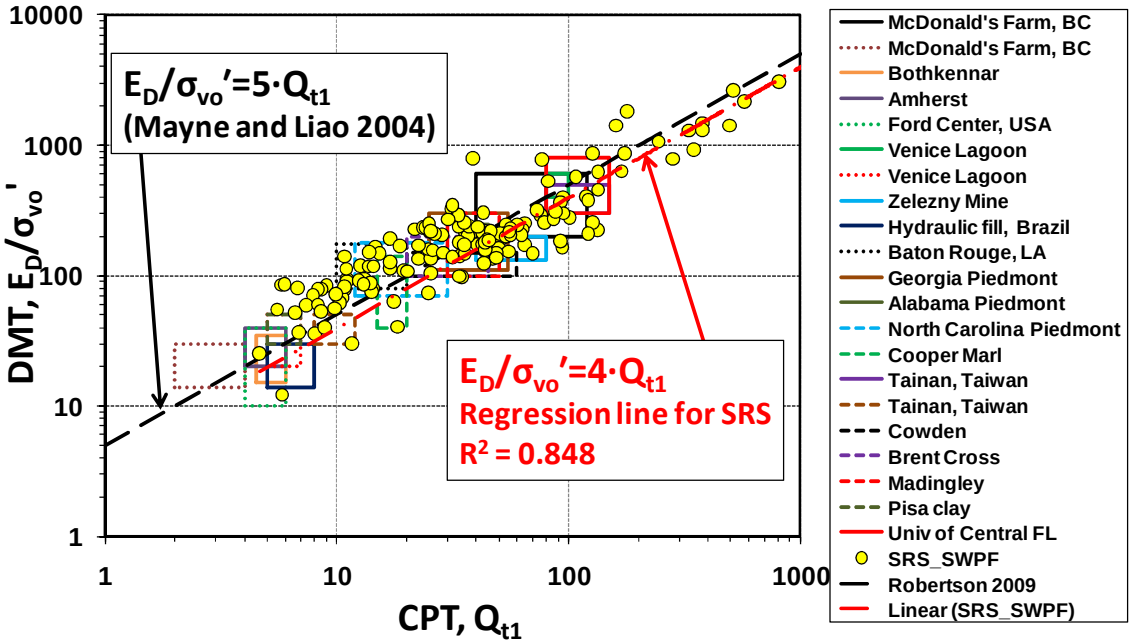

Figure G.16. Relationship between E_D/σ_{vo}' (DMT) and Q_{t1} (CPT) at various sites and observed site-specific correlation at SRS.

REFERENCES

Anderson, D.G. and Stokoe, K.H. (1978). "Shear modulus: a time dependent soil property," Dynamic Geotechnical Testing, ASTM STP 654, American Society for Testing & Materials, West Conshohocken, PA, 66-90.

Andrus, R.D., Mohanan, N.P., Piratheepan, P., Ellis, B.S. and Holzer, T.L. (2007). "Predicting shear wave velocity from cone penetration resistance," Proc. 4th International Conferences on Earthquake Geotechnical Engineering, Thessaloniki, Greece: Paper No. 1454.

Arnal, P.S. (2009). Review and analysis of preconsolidation stress determination methods for laboratory consolidation tests, Thesis, Univ. Valencia/ Georgia Institute of Technology, School of Civil & Environmental Engineering.

Atkinson, J.H. and Sallfors, G. (1991). :Experimental determination of stress-strain-time characteristics in laboratory and in situ tests," Deformation of Soils and Displacements of Structures: Proc. 10th ECSMGE, Vol. 3, Firenze: 915-956.

Bagwell, L. (2008). Geophysical Data, SRNL, DOE-SRS-Georgia Tech Soft Zone Review.

Baldi, G., Bellotti, R., Ghionna, V., Jamiolkowski, M., and Lo Presti, D.C.F. (1989). "Modulus of sands from CPTs and DMTs," Proceedings, XII ICSMFE, Rio de Janeiro, Vol. 1, 165-170.

Baldi, G., Bruzzi, D., Superbo, S., Battaglio, M. and Jamiolkowski, M. (1988). "Seismic cone in Po River sand," Penetration Testing 1988, (Proc. ISOPT-1, Orlando), Vol. 2, Balkema, Rotterdam: 643-650.

Bates, C.R. and Phillips, D.R. (2000). "Multi-component seismic surveying for near surface investigations: examples from central Wyoming and southern England," Journal of Applied Geophysics, 44: 257-273.

Becker, D.B., Crooks, J.H.A., Been, K., and Jefferies, M.G. (1987). "Work as a criterion for determining in situ and yield stresses in clays," Canadian Geotechnical Journal, 24(4): 549–564.

Bellotti, R., Jamiolkowski, M., Lo Presti, D.C.F. and O'Neill, D.A. (1996). "Anisotropy of small strain stiffness in Ticino sand," Geotechnique, 46(1): 115-131.

Benoit, J. and Lutenegger, A.J. (1992). "Determining lateral stress in soft clays," Predictive Soil Mechanics *(*Proc. Wroth Memorial Symp., Oxford), Thomas Telford, London: 135-155.

Benz, T. (2007). "Small-strain stiffness of soils and its numerical consequences," Ph.D Dissertation, Institut fur Geotechnik der Universitat Stuttgart, 193p.

Bjerrum, L. (1972). "Embankments on soft ground, Performance of Earth and Earth-Supported Structures," Vol. 2 (Conf. Proc. Purdue Univ.), ASCE, Reston, VA, 1-54.

Bjerrum, L. and Andersen, K.H. (1972). "In-situ measurement of lateral pressures in clay," Proceedings of 5th ECSMFE (1), Madrid, 11-20.

Bloomfield, P. (2000). Fourier analysis of time series: an introduction, second edition, New York, John Wiley & Sons, Inc., 261 p.

Boone, S.J. (2010). "A critical reappraisal of preconsolidation pressure interpretations using the oedometer test," Canadian Geotechnical Journal, 47(3): 281-296.

Brooker, E.W. and Ireland, H.O. (1965). "Earth pressures at-rest related to stress history," Canadian Geotechnical Journal, 2(1): 1-15.

Brown, L.T., Boore, D.M., and Stokoe II K.H. (2002). "Comparison of shear wave slowness profiles at 10 strong-motion sites from noninvasive SASW measurements and measurements made in boreholes," Bulletin of the Seismological Society of America, 92(8): 3116-3133.

Bruzzi, D., Ghionna, V., Jamiolkowski, M., Lancellotta, R., and Manfredini, G. (1985). "Self boring pressuremeter in Po River sand," The Pressuremeter and Its Marine Applications, (Proc. 2nd ISP, Texas A&M), ASTM STP 950: 57-74.

Burghignoli, A., Cavalera, L., Chieppa, V. and Jamiolkowski, M. (1991). "Geotechnical characterization of Fucino clay," Proc. 10th European Conf. Soil Mechanics & Foundation Engineering, Vol. 1 (Florence), Balkema, Rotterdam, 27-40.

Burland, J.B. (1989). "The 9th Bjerrum Memorial Lecture: Small Is beautiful - the stiffness of soils at small strains," Canadian Geotechnical Journal, 26(4): 499-516.

Burland, J.B. (1990). "On the compressibility and shear strength of natural clays," Geotechnique, 40, 329-378.

Burns and Roe Enterprises Inc. (2001). "Final geotechnical investigation report - Volume I." U.S. Department of Energy, 333p.

Butcher, A.P. and Powell, J.J.M. (1995). "The effect of geological history on the dynamic measurement of the stiffness of the ground," Proc. 11th European Conf. Soil Mechanics and Foundation Engineering, Vol. 1 (Copenhagen), Danish Geotechnical Society: 27-36.

Butcher, A.P. and Powell, J.J.M. (1996). “Practical considerations for field geophysical techniques used to assess ground stiffness,” Proc. Intl. Conf. on Advances in Site Investigation Practice, ICE, Thomas Telford, London: 701-714.

Butcher, A.P. and Powell, J.J.M. (1997). “Determining the modulus of the ground from in situ geophysical testing,” Proc. 14th Intl. Conf. Soil Mechanics and Foundation Engineering, Hamburg, Vol. 1, 449-452.

Butcher, A.P., Campanella, R.G., Kaynia, A.M., and Massarsch, K.R. (2005). “Seismic cone downhole pressure to measure shear wave velocity – a guideline,” TC10 ISSMGE, Proceedings of the International Symposium on Geophysical Testing in Geotechnical Engineering, May, 2006, Osaka, Japan

Cai, G., Liu, S., Puppala, A.J., and Tong, L. (2011). “Assessment of the coefficient of lateral earth pressure at rest (K_0) from in situ seismic tests,” ASTM, Geotechnical Testing Journal, 34 (4): 1-11.

Cameron, A.E., Knapp, C.C., Waddell, M.G., Addison, A.D. and Shafer, J.M. (2010). “Structural and stratigraphic control on the migration of a contaminant plume at the P Reactor area, Savannah River site, South Carolina,” Environmental Geosciences, 17(2): 77-98.

Camp, W.M., (2004). “Site characterization and subsurface conditions for the Cooper River Bridge,” Geo-Trans Conference, Geo-Institute of ASCE, Los Angeles Vol. 1, 347-360.

Campanella, R.G. (1994). “Field methods for dynamic geotechnical testing,” Dynamic Geotechnical Testing II (STP 1213), ASTM, West Conshohocken, PA: 3-23.

Campanella, R.G., Robertson, P.K. and Gillespie, D. (1986). “Seismic cone penetration test,” Proceeding of In-Situ’86, GSP 6, ASCE, Reston, VA, 116-130.

Campanella, R.G. and Stewart, W.P. (1992). “Seismic cone analysis using digital signal processing for dynamic site characterization,” Canadian Geotechnical Journal, 29(3): 477-486.

Casagrande, A. (1936). “The determination of the preconsolidation load and its practical significance,” In Proceedings of the First International Conference on Soil Mechanics and Foundation Engineering, Cambridge, Mass., 22–26 June 1936. Harvard Printing Office, Cambridge, Mass. Vol. 3, 60–64.

Casey, T. J. (2000). Shear wave data collection in Mid America using an automated surface source during seismic cone testing, MS Thesis, School of Civil and Environmental Engineering, Georgia Institute of Technology, Atlanta, 212 p.

Cha, M.-S. and Santamarina, J.C. (2012). Savannah River Site (SRS) Project − Comprehensive GeoCharacterization of Santee Formation and Its Implications for Engineering Behavior at SRS, Bimontly Report, In preparation for paper submission

Chang, C.S., Misra, A. and Sundaram, S. (1991). "Properties of granular packings under low amplitude cyclic loading," Soil Dynamics and Earthquake Engineering 10(4): 201-211.

Chang, I. and Cho, G.C. (2010). "A new Alternative for estimation of geotechnical engineering parameters in reclaimed clays by using shear wave velocity," Geotechnical Testing Journal, ASTM, 33(3): 1-12.

Chen, B.S-Y. and Mayne, P.W. (1994). Profiling the overconsolidation ratio of clays by piezocone tests. Report GIT-CEEGEO-94-1 to National Science Foundation, Civil Engineering, Georgia Tech, Atlanta, GA : 280 p.

Cho, G.C., and Santamarina, J.C. (2001). "Unsaturated particulate materials – particle level studies," Journal of Geotechnical Engineering, ASCE, 127(1): 84-96.

Choo, J., Jung, Y.H. and Chung, C.K. (2011). "Effect of directional stress history on anisotropy of initial stiffness of cohesive soils measured by bender element tests," Soils and Foundations 51(4): 737-747.

Clayton, C.R.I. (2011). "Rankine Lecture: Stiffness at small strain: research and practice," Geotechnique, 61(1): 5-37.

Clementino, R.V. (2005). "An oedometer test study on the preconsolidation stress of glaciomarine clays," Discussion, Canadian Geotechnical Journal, 42(3): 972-974.

Coop, M.R. and Wroth, C.P. (1989). "Field studies of an instrumented model pile in clay," Geotechnique, 39(4): 679-696.

Crilly, M.S., Driscoll, R.M.C. and Chandler, R.J. (1992). "Seasonal ground and water movement observations from an expansive clay site in the UK," Proceedings of 7th International Coference on Expansive Soils, Dallas, Vol. 1, 313-318.

Cruz, I.R. (2009). "An evaluation of seismic flat dilatometer and lateral stress seismic piezocone," MS Thesis, Civil Engineering, University of British Columbia, Vancouver: 180 p.

Cumbest, R.J., Parra, J.O., Zook, B.J., Addington, C., and Price, V. (1996). "Reverse VSP and crosswell seismic imaging at the Savannah River Site: United States," Society of Society of Exploration Geophysicists, 34 p

DeGroot, D.J., Knudsen, S., Lunne, T. (1999). "Correlations among p_c', s_u and the index properties for offshore clays," International Conference on Offshore and Nearshore Geotechnical Engineering, December 2-3, 1999, 173-178.

DeGroot D.J., Lunne T. and Tjelta T.J. (2011). "Recommended best practice for geotechnical site characterisation of cohesive offshore sediments," Frontiers in offshore Geotechnics II, Perth Western Australia Gourvenec & White, eds., Taylor and Francis Group, London, 33-57

DeGroot, D.J. and Lutenegger, A.J. (2003). "Geology and engineering properties of Connecticut Valley Varved Clay," Characterization and Engineering Proprieties of Natural Soils, Vol. 1, Balkema, Rotterdam: 695-724.

Diaz-Rodriguez, J.A., Leroueil, S. and Aleman, J. (1992). "Yielding of Mexico City clay and other natural clays," Journal of Geotechnical Engineering, ASCE, 118(7): 981-995.

Darendeli, M.B. (1991). Development of a new family of normalized modulus reduction and material damping curves, Ph.D. Dissertation, University of Texas at Austin. Texas, USA.

Martin, R.E. and Drahos, E. (1986). "Pressuremeter correlations for preconsolidated clay, Use of In-Situ Tests in Geot. Engrg. (GSP6), ASCE, New York, 206-220.

Ebelhar, R.J., Young, A.G. and Stieben, G.P. (1988). "Cone penetrometer and conductor pullout tests in carbonate soils offshore Africa," Proceedings of the International Conference on Calcareous Sediments, Perth, 1, 155-163.

Elsworth, D. (1993). "Analysis of piezocone dissipation data using dislocation methods," Journal of Geotechnical Engineering, ASCE, 119(10): 1601–1623.

Eslaamizaad, S. and Robertson, P.K. (1996). "Seismic cone penetration test to identify cemented sands," Proc. 49th Canadian Geotech. Conf., St John's Newfoundland, 849-858.

Fahey, M. (1998). "Deformation and in situ stress measurement," Geotechnical Site Characterization, Vol. 1 (Proc. ISC-4, Atlanta), Balkema, Rotterdam: 49-68.

Fernandez, A. and Santamarina, J.C. (2001). "Effect of cementation on the small strain parameters of sands," Canadian Geotechnical Journal, 38(1): 191-199.

Fioravante, V., Jamiolkowski, M. and LoPresti, D.C.F. (1998). "Assessment of the coefficient of earth pressure at rest from shear wave velocity," Geotechnique, 48 (5): 657-666.

Foti, S. (2012). "Combined use of geophysical methods in site characterization," Geotechnical and Geophysical Site Characterization (ISC-4, Brazil), 43-61.

Foti, S., Lancellotta, R., Marchetti, D., Monaco, P. and Totani, G. (2006). "Interpretation of SDMT tests in a transversely isotropic medium," Proceedings, Second Intl. Conf. on the Flat Dilatometer, Washington, D.C., 275-280.

Gasparre, A. (2005). Advanced laboratory characterization of London clay, Ph.D. Thesis, Civil and Environmental Engineering Dept., Imperial College London, 598 p.

Ghionna, V. and Jamiolkowski, M. (1991). "A critical appraisal of calibration chamber testing of sands," Calibration Chamber Testing, Elsevier, Potsdam, N.Y., 13-39.

Gibbens, R.M. and Briaud, J.-L. (1994). "Data and prediction request for a spread footing prediction event," Predicted and Measured Behavior of Five Spread Footings on Sand, GSP 41, ASCE. Reston, VA, 11-85.

Gillespie, D.G. (1990). "Evaluating shear wave velocity and pore pressure data from the seismic cone penetration test," Ph.D. Thesis, Civil Engineering Department, University of British Columbia, Vancouver, B.C.

Graham, J., Pinkney, R.B., Lew, K.V., Trainor, P.G.S. (1981). "Curve-fitting and laboratory data," Canadian Geotechnical Journal, 19(1): 201-205.

Griffin, L.M. and Hiltunen, D.R. (2001). "Field determination of anisotropy and the coefficient of lateral earth pressure," International Center for Aggregates Research 9th Annual Symposium: Aggregates - Concrete, Bases and Fines, 19p.

Hamouche, K.K., Leroueil, S., Roy, M. and Lutenegger, A.J. (1995). "In situ evaluation of K_0 in eastern Canada clays," Canadian Geotechnical Journal, 32(4): 677-688.

Hatanaka, M, Uchida, A., and Taya, Y. (1999). "K_0-value of in situ gravelly soils," Proc. 11th Asian Regional Conference on Soil Mechanics and Geotechnical Engineering, Balkema, Rotterdam: 77-80.

Hardin, B.O. (1978). "The nature of stress-strain behavior for soils," Earthquake Engineering and Soil Dynamics, Vol. 1 (Pasadena), ASCE, Reston, Virginia: 3-90.

Hardin, B. O. and Black, W. L. (1968). "Vibration modulus of normally consolidated clay," Journal of the Soil Mechanics and Foundations Division, ASCE, Vol. 94 (SM2), 353-369

Hardin, B.O. and Blandford, G.E. (1989). "Elasticity of particulate materials," Journal of Geotechnical Engineering ASCE 115(6): 788-805.

Hardin, B.O. and Drnevich, V.P. (1972). "Shear modulus and damping in soils: Design

equations and curves," Proc. ASCE, Journal of the Soil Mechanics and Foundations Division, 98(SM7): 667-692.

Hardin, B.O. and Richart, F.E., Jr. (1963). "Elastic wave velocities in granular soils," Journal of the Soil Mechanics and Foundations Division, ASCE, 89(1): 33-65.

Hegazy, Y.A. and Mayne, P.W. (1995). "Statistical correlations between V_s and CPT data for different soil types," Proc. Cone Penetration Testing (CPT'95), Vol. 2, Linköping, Swedish Geotechnical Society, 173-178.

Henke, R. and Henke, W. (2002). "In situ nonlinear inelastic shearing deformation characteristics of soil deposits inferred using the torsional cylindrical impulse shear test," Bulletin of the Seismological Society of America, 92(5): 1970-1983.

Hight, D.W., Bond, A.J., and Legge, J.D. (1992). "Characterization of the Bothkennar clay: an overview," Geotechnique, 42(2): 303-347.

Hight, D.W., McMillan, F., Powell, J.J.M., Jardine, R.J. and Allenou, C.P. (2003). "Some characteristics of London Clay," Characterization and Engineering Proprieties of Natural Soils, Vol. 2, Balkema, Rotterdam: 851-907

Hiltunen, D.R., Griffin, L.M., and Woods, R.D. (2003). "Liquefaction evaluation of Vincent Thomas Bridge sites via crosshole seismic shear wave measurements," Soil and Rock America 2003 (Proceedings, 12th Pan American Conference on Soil Mechanics & Geotechnical Engineering), Vol. 1, Cambridge, MA: 253-260.

Hird, C.C. and Pierpoint, N.D. (1997). "Stiffness determination and deformation analysis for a trial excavation in Oxford Clay," Geotechnique, 47(3): 665-691.

Hoar, R. J. and Stokoe, K. H. (1978). "Generation and measurement of shear waves in situ," Dynamic Geotechnical Testing, Denver, CO, ASTM Special Technical Publication 654, ASTM, Philadelphia, PA, 3-29.

Howie, J.A., Shozen, T., and Vaid, Y.P. (2002). " Effect of ageing on stiffness of very loose sand," Canadian Geotechnical Journal, 39(1): 149-157.

Hoyos, L.R., Macari, E.J. (1999). "Influence of in situ factors on dynamic response of Piedmont residual soils," Journal of Geotechnical and Geoenvironmental Engineering, ASCE, 125(4): 271-279.

Huntsman , S.R. (1985). "Determination of in-situ lateral pressure of cohesionless soils by static cone penetrometer," Ph.D. Thesis, Dept. of Civil Engineering, University of California at Berkeley.

Hryciw, R.D. and Thomann, T.G. (1993). "Stress-history-based model for G_{max} of cohesionless soils," Journal of Geotechnical Engineering, ASCE, 119(7): 1073-1093.

Hryciw, R.D. and Woods, R.D., (1988). "DMT-Cross Hole Shear Correlations," Penetration Testing 1988, (Proc., ISOPT-1, Orlando), Vol. 1, Balkema, Rotterdam, 527-532.

Iwasaki, T., Tatsuoka, F. and Takagi, Y. (1978). "Shear moduli of sands under cyclic torsional shear loading," Soils and Foundations, 18(1): 39-56.

Jaky, J. (1944). "The coefficient of earth pressure at rest," Journal for Society of Hungarian Architects and Engineers, Budapest, Hungary, pp. 355-358.

Jamiolkowski, M. (2012). "Role of geophysical testing in geotechnical site characterization," 3rd de Mello Lecture – Libson, Portuguese-Brazilian Geotechnical Congress.

Jamiolkowski, M., Ladd, C.C., Germain, J., Lancellotta, R. (1985). "New developments in field and lab testing of soils," Proceedings, 11th International Conference on Soil Mechanics and Foundation Engineering, Vol. 1, San Francisco, 57-154.

Jamiolkowski, M., Lancellotta, R. and Lo Presti, D.C.F. (1995). "Remarks on the stiffness at small strains of six Italian clays," Pre-Failure Deformation Characteristics of Geomaterials, Vol. 2 (IS-Hokkaido, Sapporo). Balkema, Rotterdam, 817-836.

Jamiolkowski, M., LoPresti, D.C.F. and Manassero, M. (2001). "Evaluation of relative density and shear strength of sands from cone penetration test and flat dilatometer test," Soil Behavior and Soft Ground Construction (GSP 119), ASCE, Reston/VA: 201-238.

Jardine, R.J., Davies, M.C.R., Hight, D.W., Smith, A. and Stallebrass, S.E. (1998), editors. Pre-Failure Deformation Behavior of Geomaterials. Thomas Telford/ICE, London: 417.

Jardine, R.J., Gens, A., Hight, D.W., Coop, M.R. (2004). "Developments in understanding soil behavior," Advances in Geotechnical Engineering, Vol. 1 (Proc. Skempton Conference), Institution of Civil Engineers, London, 103-240.

Jefferies, M. and Been, K. (2006). Soil liquefaction – A critical state approach. Taylor and Francis, New York, NY, pp. 580.

Jovicic, V. and Coop, M. (1998). "The measurement of stiffness anisotropy in clays with bender element tests in triaxial apparatus," ASTM, Geotechnical Testing Journal, 21(1): 3-10.

Keaveny, J.M. and Mitchell, J.K. (1986). "Strength of fine-grained soils using PCPT," Use of In-Situ Tests in Geotechnical Engrg. (GSP 6), ASCE, New York, pp. 668-685.

Kim, T.C. and Novak, M. (1981). "Dynamic properties of some cohesive soils of Ontario," Canadian Geotechnical Journal, 18: 371-389.

Kim, Y-S., Shibuya, S., Ochi, K., Shi, D.-M., and Tatsuoka, F. (1991). "Deformation modulus and strength of artificial and natural soft rocks at low strain levels," Proceedings of Symposium on Triaxial Testing Methods, JSSMFE, Tokyo, 265-272.

Kokusho, T. (1980). "Cyclic triaxial test of dynamic soil properties for wide strain range," Soils and Foundations, 20(2): 45-60.

Kokusho, T., Yoshida, Y., and Esashi, Y. (1982). "Dynamic properties of soft clay for wide strain range," Soils and Foundations, 22(4): 1-18.

Konrad, J-M. and Law, K.T. (1987). "Undrained shear strength from piezocone tests," Canadian Geotechnical Journal, 24(3): 392-405.

Ku, T., and Mayne, P.W. (2012a). "Feasibility and sensitivity analysis of at-rest lateral stress coefficient (K_0) prediction using different types of shear wave velocities," Proc. GeoCongress 2012, GSP 225, ASCE, Reston, VA: 2639-2648

Ku, T., and Mayne, P.W. (2012b), "Evaluating the in-situ lateral stress coefficient (K_0) of soils via paired shear wave velocity modes." Journal of Geotechnical and Geoenvironmental Engineering, ASCE, In press (published online in June 2012).

Ku, T., and Mayne, P.W. (2012c) "Frequent-interval SDMT and continuous SCPTu for detailed shear wave velocity profiling in soils." Geotechnical Engineering Journal of the SEAGS & AGSSEA, Vol. 43, No.4, (December 2012) In Press.

Ku, T., Mayne, P.W. and Gutierrez, B.J. (2011). "Hierarchy of V_s modes and stress-dependency in geomaterials," Proc. 5th International Symposium on Deformation Characteristics of Geomaterials (Seoul), Vol. 1, Taylor & Francis Group, London, 533-540.

Ku, T., Mayne, P.W., and Gutierrez, B.J. (2012). "Shear wave profiles in Tertiary marine sediments in west central South Carolina." 4th International Conference on Geotechnical and Geophysical Site Characterization (ISC'4), Brazil, 1259-1265.

Kulhawy, F.H. and Mayne, P.W. (1990). Manual on estimating soil properties for foundation design. Report EPRI EL-6800, Electric Power Research Institute, Palo Alto, 306 pp.

Ladd, C.C. (1991). "Stability evaluation during staged construction," The 22nd Terzaghi Lecture, Journal of Geotechnical Engineering Division, ASCE, 117(4): 540-615.

Ladd, C. C. and DeGroot, D. J. (2003). "Recommended practice for soft ground site characterization: Arthur Casagrande Lecture," 12th Panamerican Conference on Soil Mechanics and Geotechnical Engineering, Soil and Rock America 2003, Boston, MA, VGE, Essen, Germany, 1, 3-57.

Larrahondo-Cruz J.M. (2011). Carbonate diagenesis and chemical weathering in the southeastern United States: some implications on geotechnical behavior, Ph.D. Dissertation, School of Civil and Environmental Engineering, Georgia Institute of Technology, 320 pp.

Lee, C., Lee, J-S., Yoon, H-K., Truong, H.Q., and Cho, T-H. (2006). "Characteristics of Shear Wave Velocity as Stress-induced and Inherent Anisotropies," Journal of Korean Geotechnical Society, 22(11):47-54.

Lee, J.S. and Santamarina, J.C. (2005). "Bender elements: performance and signal interpretation," J. Geotechnical and Geoenvironmental Engineering, 131(9): 1063-1070.

Leroueil, S. & Hight, D.W. (2003). "Behaviour and properties of natural soils and soft rocks," Characterisation & Engineering Properties of Natural Soils, Vol. 1 (Proc. Singapore Workshop), Swets & Zeitlinger, Lisse: 29-254.

Leroueil, S. and Jamiolkowski, M. (1991). "Exploration of soft soil and determination of design parameters," Proceedings, GeoCoast'91,Yokohama, Vol. 2, Port & Harbour Research Institute, 969–998.

Levesque, C.L., Locat, J. and Leroueil, S. (2007). "Characterization of postglacial sediments of the Saguenay Fjord, Quebec," Characterization and Engineering Properties of Natural Soils, Vol. 4 (IS-Singapore), Taylor & Francis Group, London, 2645-2677.

Lew, M. and Campbell, K.W. (1985). "Relationships between shear wave velocity and depth of overburden," Measurement and Use of Shear Wave Velocity for Evaluating Dynamic Soil Properties, ASCE, Reston, Virginia: 63-76.

Li, W.T. (2008). "Prediction of surface settlement due to the displacement of soft zones," Proceedings of Deformational Characteristics of Geomaterials, Vol. 1, IOS Press, Amsterdam: 413-419

Li, Mason, and Williams (2010). Probabilistic seismic hazard assessment available data and current analyses. Internal Report, DOE Savannah River Site, Aiken, SC.

Liao, T. and Mayne, P.W. (2006). "Automated post-processing of shear wave signals," Proc. 8th US National Conference on Earthquake Engineering, San Francisco: 460.1-460.10.

Lohani, T.N., Fujiwara, T., Iwasaki, Y., and Shibuya, S. (2008). "Stiffness characteristics of quick clays in Osaka Bay," Proceedings 4th International Symposium on Deformation Characteristics of Geomaterials, Atlanta, Millpress/IOS Press, Amsterdam, Vol. 1, 153-157.

Lohani, T.N., Imai, G., and Shibuya, S. (1999). "Effect of sample disturbance on G_{max} of Holocene clay deposits," Proceedings of 2nd International Symposium on Pre-failure Deformation Characteristics of Geomaterials (IS-Torino 99), Balkema, Rotterdam, 115-122.

Locat, J., Tanaka, H., Tan, T.S., Dasari, G.R. and Lee, H. (2003). "Natural soils: geotechnical behavior and geological knowledge," Characterisation & Engineering Properties of Natural Soils, Vol. 1 (Proc. Singapore Workshop), Swets & Zeitlinger, Lisse: 3-28.

Lomb, N.R. (1976). "Least-squares frequency analysis of unequally spaced data," Astrophysics and Space Science, Vol. 39: 447-462.

Long, M. and Donohue, S. (2007). "In situ shear wave velocity from multichannel analysis of surface waves (MASW) tests at eight Norwegian research sites," Canadian Geotechnical J., 44(5): 533-544.

Lo Presti, D.C.F., Jamiolkowski, M., Pallara, O. and Cavallaro, A. (1996). "Rate and creep effect on the stiffness of soils," Measuring and Modeling Time Dependent Soil Behavior." Geotechnical Special Publication, Vol. 61. ASCE, 166–180

Lo Presti, D.C.F., Jamiolkowski, M. and Pepe, M. (2003). "Geotechnical characterization of the subsoil of Pisa Tower," Characterization and Engineering Proprieties of Natural Soils, Vol. 2 (Singapore), Balkema, Rotterdam: 909-946.

Lo Presti, D.C.F., Pallara, O., Lancellotta, R., Armandi, M. and Maniscalco, R. (1993). "Monotonic and cyclic loading behavior of two sands at small strains," Geotechnical testing Journal, ASTM, 16(4): 409-424.

Lunne, T. and Mayne, P.W. (1998). Offshore in-situ testing to determine horizontal stress. NGI Report 521552-1 submitted to Statoil, Norwegian Geotechnical Institute, Oslo: 101 p.

Lunne, T., Robertson, P.K., and Powell, J.J.M. (1997). Cone Penetration Testing in Geotechnical Practice. Blackie-EF Spon, Rutledge Publishing, London: 318p.

Lyon, D.A. (2010). “The discrete Fourier Transform, part 6: cross-correlation,” Journal of object technology, 9(2): 17-22.

Mair, R. J. (1993). “Developments in geotechnical engineering research: applications to tunnels and deep excavations,” Unwin Memorial Lecture 1992., Proceedings of Institution of Civil Engineers, Civil Engineering, 27–41.

Marchetti, S., (1980). “In-situ tests by flat dilatometer,” Journal of Geotechnical Engineering, ASCE, 107(3): 832-837.

Marchetti, S. (1997). “The flat dilatometer: design applications,” Proceedings, Third Geotechnical Engineering Conference, Cairo University, Egypt, 1-25.

Marcuson, III, W.F. and Wahls, H.E. (1972). “Time effects on dynamic shear modulus of clays,” Journal of the Soil Mechanics and Foundations Division, ASCE, 98(SM12): 1359-1373.

Martin, G.K. and Mayne, P.W. (1998). “Seismic flat dilatometer tests in Piedmont residual soils,” Geotechnical Site Characterization, Vol. 2, Balkema, Rotterdam: 837-843.

Massarsch, R. (1975). “New method for measurement of lateral earth pressure in cohesive soil,” Canadian Geotechnical Journal, 12(1): 142-146.

Mayne, P.W. (1980). “Cam-Clay Predictions of Undrained Strength,” Journal of Geotechnical Engineering, 106 (11): 1219-1242.

Mayne, P.W. (1988). “Determining OCR in Clays from Laboratory Strength,” Journal of Geotechnical Engineering, 114 (1): 76-92.

Mayne, P.W. (1989). “Site characterization of Yorktown formation for new accelerator,” Foundation Engineering: Current Principles and Practices (GSP No. 22), Vol. 1, ASCE, Reston, Virginia: 1-15.

Mayne, P.W. (1991). “Determination of OCR in clays by piezocone tests using cavity expansion and critical state concepts,” Soils and Foundations 31 (1): 65-76.

Mayne, P.W. (1992). “In-situ characterization of Piedmont residuum in eastern US,” Proc. NSF US-Brazil Geo-Workshop: Application of Classical Soil Mechanics to Structured Soils, Belo Horizonte: 89-93.

Mayne, P.W. (2001). “Stress-strain-strength-flow parameters from enhanced in-situ tests,” Proceedings, Intl. Conf. on In-Situ Measurement of Soil Properties & Case Histories, Bali, Indonesia: pp. 27-48.

Mayne, P.W. (2003). "Class A footing response prediction from seismic cone tests," Deformation Characteristics of Geomaterials, Vol. 1 (Lyon), Swets & Zeitlinger, Lisse, 883-888.

Mayne, P.W. (2005). "Integrated ground behavior: In-situ and lab tests," Deformation characteristics of geomaterials, Vol. 2 (Proc. Lyon, France), Taylor & Francis, London, United Kingdom, pp. 155-177.

Mayne, P.W. (2006). The 2006 James K. Mitchell lecture: "Undisturbed sand strength from seismic cone tests," Geomechanics and Geoengineering, Vol. 1 (4), Taylor and Francis, London: pp. 239-247.

Mayne, P.W. (2007). "In-situ test calibrations for evaluating soil parameters," Characterization and Engineering Properties of Natural Soils, Vol. 3, Taylor & Francis: 1601-1652.

Mayne, P.W. (2012). "Geotechnical Site Exploration in the Year 2012 and Beyond," 16th Nordic Geotechnical Meeting, Copenhagen, Denmark.

Mayne, P.W. and Bachus, R.C. (1989). "Penetration pore pressure in clay by CPTu, DMT, and SBP," Proceedings, 12th ICSMFE, Vol. 1, Rio de Janeiro, 291-294.

Mayne, P.W. and Brown, D.A. (2003). "Site characterization of Piedmont residuum of North America," Characterization and Engineering Properties of Natural Soils. Vol. 2, Swets & Zeitlinger, Lisse, 1323-1339.

Mayne, P.W., Coop, M.R., Springman, S., Huang, A-B., and Zonberg, J. (2009). State-of-the-Art Paper (SOA-1): "Geomaterial behavior and testing," Proc. 17th Intl. Conf. Soil Mechanics & Geotechnical Engineering, Alexandria, Egypt, Millpress/IOS Press Rotterdam, in press.

Mayne, P.W. and Kulhawy, F.H. (1982). "Ko-OCR relationships in soil," Journal of the Geotechnical Engineering Division, ASCE, Vol. 108, GT6, pp. 851-872.

Mayne, P.W. and Kulhawy, F.H. (1982). "Direct and Indirect Measurements of In-Situ K_0 in Clays," Transportation Research Record 1278, Washington, DC: 141-149.

Mayne, P.W. and Liao, T. (2004). "CPT-DMT interrelationships in Piedmont residuum," Geotechnical & Geophysical Site Characterization, Vol. 1, (Proc. ISC-2, Porto), Millpress, Rotterdam, 345-350.

Mayne, P.W. and Pearce, R.A. (2005). "Site characterization of Bootlegger Cove Formation clay for Port of Anchorage,"Frontiers in Offshore Geotechnics (Proc. ISFOG, Perth), Taylor & Francis Group, London: 951-955.

Mayne, P.W, Peuchen, J., and Bouwmeester, D. (2010). "Soil unit weight estimated from CPTu in offshore soils," Frontiers in Offshore Geotechnics II (Proc. ISFOG 2010, Perth), Taylor & Francis Group, London: 371-376.

Mayne, P.W. and Rix, G.J. (1995). "Correlations between shear wave velocity and cone tip resistance in clays," Soils and Foundations, 35(2), 107-110.

Mayne, P.W and Stewart, H.E. (1988). "Pore pressure behavior of K_o-consolidated clays," Journal of Geotechnical Engineering, ASCE, 114(11): 1340-1346.

McGillivray, A.V. (2007). Enhanced integration of shear wave velocity profiling in direct-push site characterization systems, Ph.D Dissertation, School of Civil and Environmental Engineering, Georgia Institute of Technology, 361 pp.

McGillivray, A.V. and Mayne, P.W. (2008). "An automated seismic source for continuous-push shear wave velocity profiling with SCPT and frequent-interval SDMT," Geotechnical & Geophysical Site Characterization, Vol. 2, (Proc. ISC-3, Taipei), Taylor & Francis Group, London, 1347-1352.

Meng, J. (2003). The influence of loading frequency on dynamic soil properties, Ph.D. Dissertation, School of Civil and Environmental Engineering, Georgia Institute of Technology, 176 pp.

Menq, F.Y. (2003). Dynamic properties of sandy and gravelly soils. Ph.D. Dissertation, The University of Texas at Austin. Texas USA,

Mesri, G. and Abdel-Ghaffar, M.E.M. (1993). "Cohesion intercept in effective stess-stability analysis," Journal of Geotechnical Engineering, ASCE, 119(8): 1229-1249.

Mesri, G. and Choi, Y.K. (1979). "Strain rate behavior of Saint-Jean-Vianney clay," Discussion, Canadian Geotechnical Journal, 16(4): 831-834.

Mesri, G. and Choi, Y.K. (1983). "Discussion—dynamic properties of soft clays for wide strain range," Soils and Foundations, 23(1): 125–127.

Mesri, G., Feng, T.W. and Benak, J.M. (1990). "Postdensification penetration resistance of clean sands," Journal of Geotechnical and Geoenvironmental Engineering, ASCE, 116(7): 1095-1115.

Mitachi, T. and Kitago, S. (1976). "Change in undrained shear strength characteristics of saturated remolded clay due to swelling," Soils and Foundations, 16(1): 45-58.

Mitchell, J.K. and Soga, K. (2005). Fundamentals of Soil Behavior, Second Edition, John Wiley & Sons, New York: 577 pp.

Murdoch, L.C., Richardson, J.R., Tan, Q., Malin, S.C., and Fairbanks, C. (2006). "Forms and sand transport in shallow hydraulic fractures in residual soil," Canadian Geotechnical Journal, 43(10): 1061-1073.

Nash, D.F.T., Powell, J.J.M., Lloyd, I.M. (1992). "Initial investigations of the soft clay test site at Bothkennar," Geotechnique, 42(2): 163-181.

Nash, D.F.T., Sills, G.C., and Davison, L.R. (1992). "One-dimensional consolidation testing of soft clay from Bothkennar," Geotechnique, 42(2): 241-256.

Nazarian, S. and Stokoe, K. H. (1984). "In situ shear wave velocities from spectral analysis of surface waves," 8th World Conference on Earthquake Engineering, San Francisco, CA, 3, 31-38.

Ng, C.W.W., Leung, E.H.Y., and Lau, C.K. (2004). "Inherent anisotropic stiffness of weathered geomaterial and its influence on ground deformations around deep excavations," Canadian Geotechnical Journal, 41(1): 12-24.

Ni, S.-H. (1987). "Dynamic properties of sand under true triaxial stress states from resonant column/torsion shear tests," PhD Dissertation, Dept. of Civil Engineering, University of Texas at Austin.

Oda, M. (1977). "Coordination number and its relation to shear strength of granular material," Soils and Foundations, 17(2): 29-42.

O'Neill, M.W. (2000). "The national geotechnical experimentation site: University of Houston, National Geotechnical Experimentation Sites," GSP 93, ASCE. Reston, Virginia, 72-101.

Oppenheim, A.V., and Schafer, R.W. (1989). Discrete-Time Signal Processing. Englewood Cliffs, NJ: Prentice Hall, pp. 284-285.

Park, C. B., Miller, R. D. and Xia, J. (1999). "Multichannel analysis of surface waves," Geophysics, 64(3), 800-808.

Parry, R.H.G. (1970). "Overconsolidation in soft clay deposits," Geotechnique, 20(4): 442-446.

Patel, A. Bartake, P. P., and Singh, D. N. (2009). "An empirical relationship for determining shear wave velocity in granular materials accounting for grain morphology," ASTM, Geotechnical Testing Journal, 32(1): 1-10.

Pennington, D.S., Nash, D.F.T., and Lings, M.L. (1997). "Anisotropy of Go shear stiffness in Gault clay," Geotechnique, 47(3): 391-398.

Piriyakul, K. (2006). “Anisotropic stress-strain behavior of Belgian Boom clay in the small strain region,” Ph.D. thesis, Ghent University, Belgium.

Powell, J.J.M. (1990). “A comparison of four different pressuremeters and their methods of interpretation in a stiff heavily overconsolidated clay,” Pressuremeters (Proc. ISP 3, Oxford), Thomas Telford, London: 287-298.

Powell, J.J.M. and Butcher, A.P. (2003). “Characterisation of a glacial clay till at Cowden, Humberside,” Characterisation and Engineering Properties of Natural Soils, Vol. 2, Balkema, Rotterdam: 983 – 1020.

Press, W.H. Teukolsky, S.A., Vetterling, W.T., and Flannery, B.P. (1992). Numerical Recipes in C: the Art of Scientific Computing, Cambridge Univ. Press, 575-584

Pruska, L. (1973). “Effect of initial stress on the stress–strain relation,” Proc. 8th International Conference on Soil Mechanics and Foundation Engineering, Moscow, Vol. 4: 26–28.

Rankka, K. (1990). “Measuring and predicting lateral earth pressures in slopes, Trasportation Research Record 1278, Washington D.C., 172-182.

Rampello, S., Viggiani, G.M.B. and Amorosi, A. (1997). “Small-strain stiffness of reconstituted clay compressed along constant triaxial effective stress ratio paths,” Geotechnique 47(3): 475-489.

Randolph, M.F. (2004). “Characterization of soft sediments for offshore applications,” Geotechnical & Geophysical Site Characterization, Vol. 1 (Proc. ISC-2, Porto), Millpress, Rotterdam: 209-232.

Reyna, F. and Chameau, J.L. (1991). “Dilatometer based liquefaction potential of sites in the Imperial Valley,” Proceedings, Second Intl. Conference on Recent Advances in Geotechnical Earthquake Engineering and Soil Dynamics, St. Louis, Vol. 1, 385-392.

Ridley, A.M. and Burland, J.B. (1993). “A new instrument for the measurement of soil moisture suction,” Geotechnique, 43(2): 321-324.

Rix, G.J. and Stokoe, K.H. (1991). “Correlation of initial tangent modulus and cone resistance,” Proceedings of International Symposium on Calibration Chamber Testing, Elsevier, New York, 351-362.

Robertson, P.K. (1986). “In-situ testing and its application to foundation engineering,” Canadian Geot. J., 23 (4): 573-594.

Robertson, P.K. (2009). “CPT-DMT correlations,” Journal of Geotechnical and Environmental Engineering, ASCE, 135(11): 1762-1771

Robertson, P.K., Campanella, R.G., Gillespie, D. and Rice, A. (1986). "Seismic CPT to measure in situ shear wave velocity," Journal of Geotechnical Engineering, 112(8): 791-804.

Robertson, P.K. (1990). "Soil classification using the cone penetration test," Canadian Geotechnical Journal, 27 (1): 151-158.

Robertson, P.K. (2009). "Interpretation of cone penetration tests: a unified approach," Canadian Geotechnical Journal, 46(11): 1337-1355.

Robertson, P.K. and Wride, C.E. (1998). "Evaluating cyclic liquefaction potential using the cone penetration test," Canadian Geotechnical Journal, 35(3): 442-459.

Roesler, S. (1979). "Anisotropic shear modulus due to stress anisotropy," Journal of Geotechnical Engineering Division, Vol. 105 (GT7): 871-880

Rollins, K.M., Mchood, M.D., Hryciw, R.D., Homolka, M., and Shewbridge, S.E. (1994). "Ground response on Treasure Island," The Lorna Prieta, California, Earthquake of October 17, 1989-Strong Ground Motion, USGS Professional Paper, A109-A121.

Sandven, R. (1990). Strength and deformation properties of fine grained soils obtained from piezocone tests, Ph.D. Thesis, Norwegian Institute of Technology, Trondheim, Department of Civil Engineering, Trondheim, Norway.

Santagata, M. (2008). "Effects of stress history on the stiffness of a soft clay," Deformation Characteristics of Geomaterials, Vol. 1 (Atlanta), IOS Press, Amsterdam: 95-123.

Santagata, M., Germaine, J.T. and Ladd, C.C. (2005). "Factors affecting the initial stiffness of cohesive soils," Journal of Geotechnical and Geoenvironmental Engineering, 131(4): 430-441

Santagata, M and Kang, Y.I. (2007). "Effects of geologic time on the initial stiffness clays," Engineering Geology, Vol. 89, 98-111

Santamarina, J.C. and Cascante, G. (1996). "Stress anisotropy and wave propagation: A micromechanical view," Canadian Geotechnical Journal 33(5): 770-782.

Santamarina, J.C. and Fratta, D. (1998). Introduction to Discrete Signals and Inverse Problems in Civil Engineering, ASCE Press, Reston, VA: 327 p.

Santamarina, J.C., Klein,K.A. and Fam, M.A. (2001). Soils and Waves – particular materials behavior, characterization and process monitoring, Wiley, New York: 488 p.

Saxena, S.k., Avramidis, A.S., and Reddy, K.R. (1988). "Dynamic moduli and dampingratios for cemented sands at low strains," Canadian Geotechnical Journal, 25(2): 353-368.

Schmertmann, J. H. (1978). "Effect of shear stress on the dynamic bulk modulus of sand," Technical Report S-78-16, Waterways Experiment Station, Vicksburg Miss.

Schmertmann, J.H., (1986). "Suggested method for performing the flat dilatometer test," Geotechnical Testing Journal, 9(2): 93-101.

Schmertmann, J.H. (1991). "The mechanical aging of soils—25th Karl Terzaghi Lecture," Journal of Geotechnical Engineering, ASCE, 117(9): 1288–1330.

Schnaid, F. (2005). "Geo-characterisation and properties of natural soils by in situ tests," Proceedings of 16th International Conference on Soil Mechanics and Geotechnical Engineering (ICSMGE), Osaka, 1: 3-46.

Schnaid, F. (2009). In-situ testing in geomechanics, Taylor & Francis, 329p.

Schnaid, F., Lehane, B.M. and Fahey, M. (2004). "In-situ test characterization of unusual geomaterials," Geotechnical and Geophysical Site Characterization, Vol. 1 (Proc. ISC-2, Porto), Millpress, Rotterdam, 49-74.

Schneider, J.A., Mayne, P.W., and Rix, G.J. (2001). "Geotechnical Site Characterization in the Greater Memphis Area Using Cone Penetration Tests," Engineering Geology, Vol. 62 (Nos. 1-3): 169-184.

Seed, H.B. and Idriss, I.M. (1970). Soil moduli and damping factors for dynamic response analysis, Report 70-10, EERC, Berkeley, CA.

Semple, R. (1988). "State of the art report on engineering properties of carbonate soils," Proceedings of the International Conference on Calcareous Sediments, Perth, 2, 807-836

Senneset, K., Sandven, R. and Janbu, N. (1989). "Evaluation of soil parameters from piezocone tests," Transportation Research Record 1235, National Research Council, Washington, DC: pp. 24-37.

Shannon & Wilson, Inc. (2007). "Geotechnical Engineering Report - Geotechnical Investigation Phase II: Salt Waste Processing Facility," U.S. Department of Energy, 1945p.

Shibuya, S., Hwang, S.C. and Mitachi, T. (1997). "Elastic shear modulus of soft clays from shear wave velocity measurement," Geotechnique 47(3): 593-601.

Shibuya, S., Mitachi, T., Yamashita, S. and Tanaka, H. (1995). "Effects of sample disturbance on G_{max} of soils – A case study," Earthquake Geotechnical Engineering, Balkema, Rotterdam: 77-82.

Shibuya, S., Park, C.-S., Tatsuoka, F., Abe, F., Teachavorasinskun, S., Kohatam, Y. and Sato, T. (1992). "The significance of local lateral strain measurement of soil specimen for a wide range of strain," Soils and Foundations 34(2): 95-105.

Shibuya, S. and Tanaka, H. (1996). " Estimate of elastic shear modulus of Holocene soil deposits," Soils and Foundations, 36(4): 45-55.

Simonini, P. (2004). "Characterization of the Venice lagoon silts from in-situ tests and the performance of a test embankment," Geotechnical and Geophysical Site Characterization Vol. 1 (ISC-2, Porto), Millpress, Rotterdam: 187-207.

Simonini, P., Ricceri, G., and cola, S. (2007). "Geotechnical characterization and properties of Venice lagoon heterogeneous silts," Characterization and Engineering Properties of Natural Soils, Vol. 4, Taylor and Francis, London, 2289-2327.

Skempton, A.W. (1961). "Horizontal stresses in an overconsolidated Eocene clay," Proceedings, 5th International Conference on Soil Mechanics and Foundation Engineering, Vol. 1, Paris, 351-357.

SRS Report (2005). Compilation of SRS soil shear wave velocity data for soil parameterization model, 97p.

Stewart, W.P. (1992). "In-situ measurement of dynamic soil properties with emphasis on damping," Ph.D. Thesis, Civil Engineering Dept., University of British Columbia, Vancouver, B.C.

Stokoe, K.H., Hwang, S.K., Darendeli, M. and Lee, N.J. (1995). Correlation study of nonlinear dynamic soil properties, University of Texas at Austin Final Report for Westinghouse-Savannah River Site.

Stokoe, K.H., Lee, S.H.H., and Knox, D.P. (1985). "Shear moduli under true triaxial stresses," Advances in the Art of Testing Soil Under Cyclic Conditions, ASCE, New York: 166-185.

Stokoe, K.H.II. Lee, J.N.K. and Lee, S.H.H. (1991). "Characterization of Soil in Calibration Chambers with Seismic Waves," Calibration Chamber Testing (Proc. ISOCCT1, Clarkson University), Elsevier Publishing, NY, pp. 363-376.

Stokoe, K.H. and Santamarina, J.C. (2000). "Keynote: Seismic wave-based testing in geotechnical engineering," Proc. GeoEng 2000, Melbourne, Australia: 1490-1536.

Stokoe, K.H. and Woods, R.D. (1972). "In-situ shear wave velocity by cross-hole method," Journal of Soil Mechanics and Foundation Engineering Div., ASCE , 98(5): 443-460.

Sully, J.P. and Campanella, R.G. (1990). "Measurement of lateral stress in cohesive soils by full-displacement in-situ test methods," Transportation Research Record 1278, National Research Council, Washington, DC: 164-171.

Sully, J.P. (1991). "Measurement of in-situ lateral stress during full-displacement penetration tests," Ph.D. Thesis, Civil Engineering, University of British Columbia, Vancouver: 485 p.

Sully, J.P. and Campanella, R.G. (1995). "Evaluation of in-situ anisotropy from crosshole and downhole shear wave velocity measurements," Geotechnique, 45(2): 267-282.

Suzuki, Y., Sanematsu, T. and Tokimatsu, K. (1998). "Correlation between SPT and seismic CPT," Geotechnical Site Characterization, Vol. 2 (Proc. ISC-1, Atlanta), Balkema, Rotterdam, 1375-1380

Svensson, M. and Möller, B. (2001). "Geophysics in soil mechanics – in-situ shear moduli determined by SASW technique and more traditional geotechnical methods," Report 508, Swedish Geotechnical Institute, Linköping: 41 p.

Tatsuoka, F., Iwasaki, T., Fukushima, S., and Sudo, H. (1979). "Stress conditions and stress histories affecting shear modulus and damping of sand under cyclic loading," Soil and Foundations, Japanese Society of Soil Mechanics and Foundation Engineering, 19(2): 29-43.

Tatsuoka, F., Muramatsu, M. and Sasaki, T. (1982). "Cyclic undrained stress-strain behavior of dense sands by torsional simple shear test," Soils and Foundations, 22(2): 55-70

Tatsuoka, F. and Shibuya, S. (1992). "Deformation characteristics of soils and rocks from field and laboratory tests," Proc. 9th Asian Regional Conference on SMFE, Bangkok, pp. 101-190.

Tavenas, F.A., Blanchette, G., Leroueil, S., Roy, M., and LaRochelle, P. (1975). "Difficulties in the in-situ determination of K_0 in soft sensitive clays," Proceedings of In-Situ Measurement of Soil Properties, Vol. 1, Raleigh, ASCE, New York, 450-476.

Terzaghi, K., Peck, R.B. and Mesri, G. (1996). Soil Mechanics in Engineering Practice, 3rd edition, John Wiley & Sons, Inc., New York, 549p.

Toki, S., Shibuya, S., and Yamashita, S. (1995). "Standardization of laboratory test methods to determine the cyclic deformation properties of geomaterials in Japan," Pre-failure Deformations of Geomaterials, Balkema, Rotterdam, Vol 2, 741-784.

Tokimatsu, K., Tamura, S. and Kojima, H. (1992). "Effects of multiple modes on Rayleigh wave dispersion," Journal of Geotechnical Engineering, 118(10): 1529-1543.

Trauth, M.H. (2010). MATLAB Recipes for Earth Sciences, 3rd Edition. Springer**,** 336 p

Tumay, M.T. (1997). In-situ testing at the national geotechnical experimentation sites, Louisiana Transportation Research Center, Baton Rouge.

UniStar Nuclear Services, LLC (UNS) Report. (2010). Calvert Cliffs Nuclear Power Plant Unit 3, Part 2: Final Safety Analysis Report.

Van Zelst, T.W. (1948). "An investigation of factors affecting laboratory consolidation of clay," Proceeding, 2nd International Conf. Soil Mech. Foundation Engrg., Rotterdam, Vol.7, 52-61.

Vesic, A.S. (1977). Design of pile foundations. Synthesis of Highway Practice 42. Transportation Research Board, National Research Council, Washington, D.C., 68 p.Yan, L and Byrne, P.M. (1990). Simulation of Downhole and Crosshole Seismic Tests on Sand Using the Hydraulic Gradient Similitude Method. *Canadian Geotechnical Journal*, Vol. 27, No. 4, pp. 441-460.

Viana da Fonseca, A., Ferreira, C. and Carvalho, J.M. (2005). "The use of shear wave velocities determined in down-hole (V_{sVH}) and cross-hole (V_{sHV}) tests for the evaluation of K_0 in soils," Revista Latino-Americana de Geotecnia 28(3): 271-281.

Viana da Fonseca, A., Silva, S. R. and Cruz, N. (2010). "Geotechnical characterization by in situ and lab tests to the back-analysis of a supported excavation in Metro do Porto," Geotech. Geol. Engrg., 28: 251-264.

Viggiani, G. and Atkinson, J.H. (1995). "Stiffness of fine-grained soil at very small strains," Geotechnique 45(2): 249-265.

Vucetic, M. and Dobry, R. (1991). "Effect of soil plasticity on cyclic response. Journal of Geotechnical Engineering," ASCE, 117(1): 89-107.

Wahls, H.E. (1962). "Analysis of Primary and Secondary consolidation," ASCE Journal of the Soil Mechanics and Foundations Division, 88(SM6): 207-231.

Washington Savannah River Company (WSRC). (2007). “Salt waste processing facility (SWPF) dynamic settlement evaluation (U),” United States Department of Energy, Savannah River Site, Aiken, South Carolina.

Weiler, W.A.J. (1988). “Small-strain shear modulus of clay,” Earthquake Engineering and Soil Dynamics II – Recent Advances in Ground-Motion Evaluation, ASCE, Reston, Virginia: 331-345.

Welch, P. D. (1967). “The use of Fast Fourier Transform for the estimation of power spectra: a method based on time averaging over short, modified periodograms,” IEEE Transactions on Audio and Electroacoustics, AU-15: 70-73.

Whittle, A.J. and Aubeny, C.P. (1993). “The effects of installation disturbance on interpretation of in-situ tests in clay,” Predictive Soil Mechanics, Thomas Telford, UK, 742-767.

Wightman, W.E., Jalinoos, F., Sirles, P., and Hanna, K. (2003). Application of geophysical methods to highway related problems, Federal Highway Administration Manual, 716p.

Woods, R.D. (1978). “Measurement of dynamic soil properties,” Earthquake Engineering and Soil Dynamics, Vol. 1 (Pasadena), ASCE, Reston, VA: 91-178.

Yamashita, S., Hori, T., and Suzuki, T. (2003). “Effects of fabric anisotropy and stress condition on small-strain stiffness of sands,” Deformation Characteristics of Geomaterials, Vol. 1 (Proc. Lyon), Swets & Zeitlinger, Lisse: 187-194.

Yan, L and Byrne, P.M. (1990). “Simulation of downhole and crosshole seismic tests on sand using the hydraulic gradient similitude method,” Canadian Geotechnical Journal, 27(4): 441-460.

Youd, T.L., et al. (2001). “Liquefaction resistance of soils: Summary report from the 1996 NCEER and 1998 NSF Workshops on liquefaction,” Journal of Geotechnical & Geoenvironmental Engineering 127(4): 297-313.

Yu, P. and Richart, F. E., Jr. (1984). “Stress ratio effects on shear modulus of dry sands,” Journal of Geotechnical Engineering, ASCE, 110(3): 331-345.

Zapata-Medina, D.G. (2012). Evaluation of dynamic soil parameter change due to construction-induced stresses, Ph.D. dissertation, Northwestern University, Civil Enginering, 260p.

Zeng, X. and Ni, B. (1999). “Stress-induced anisotropic Gmax of sands and its measurement,” Journal of Geotechnical and Geoenvironmental Engineering, ASCE, 125(9): 741-749.